THE UNIVERSITY *of* EDINBURGH

This thesis has been submitted in fulfilment of the requirements for a postgraduate degree (e. g. PhD, MPhil, DClinPsychol) at the University of Edinburgh. Please note the following terms and conditions of use:

- This work is protected by copyright and other intellectual property rights, which are retained by the thesis author, unless otherwise stated.
- A copy can be downloaded for personal non-commercial research or study, without prior permission or charge.
- This thesis cannot be reproduced or quoted extensively from without first obtaining permission in writing from the author.
- The content must not be changed in any way or sold commercially in any format or medium without the formal permission of the author.
- When referring to this work, full bibliographic details including the author, title, awarding institution and date of the thesis must be given.

Studying Crystallinity Gradients in High Performance Thermoplastic Composites Manufactured by Automated Tape Placement

Helena Pérez Martín

Doctor of Philosophy Thesis

2023

THE UNIVERSITY *of* EDINBURGH

Declaration

I declare that this thesis was composed by myself and that the work contained herein is my own, except where explicitly stated otherwise in the text. This work has not been submitted for any other degree or professional qualification except as specified. Any publications are my own work, except where indicated throughout the thesis. Due references have been provided on all supporting literatures and resources.

Helena Pérez Martín

December 2023

Abstract

Poly(aryletherketone)s (PAEKs) are a family of thermoplastics, used as a matrix in carbon fibre (CF) reinforced composites. These high-performance composites are widely implemented as structural materials in aeronautics, in parts like wing flaps, access panels and floor panels, amongst others. Poly(etherketoneketone) (PEKK), a member of the PAEK family, has aroused interest in recent years due to its excellent properties, as well as the range of available grades of PEKK with different applications. In order for a successful implementation of the material, however, a thorough understanding of the polymer's crystallisation kinetics and morphology is required. Crystallinity refers to the degree of molecular order in the polymer, which plays a crucial part in mechanical, thermal and chemical properties. While some literature exists covering crystallisation morphology of some grades of unreinforced PEKK, such studies on CF/PEKK composites and their mechanical performance are minimal.

Developing such an understanding is of interest within the context of manufacturing, particularly in fast-paced processes such as automated tape placement (ATP). This is a manufacturing process regularly used in the aerospace industry, designed for fast production, automation and repeatability of part manufacturing. However, such fast-manufacturing techniques limit the time the processed material undergoes high temperatures and loads, not only affecting crystallinity development but also part consolidation. This ultimately can have a negative impact on part quality and performance. ATP processing conditions add a further layer of complexity in the case of semicrystalline thermoplastics such as PEKK, as the generation of uniform crystallinity throughout the bulk of a manufactured part is a key requirement for reliable performance during the service life. It is therefore essential to understand how processing conditions affect the crystallinity development across the final part's thickness, which can provide insight into the effectiveness of the manufacturing method and potential areas of improvement during the manufacturing process.

This PhD project aims to explore the variation of crystallinity across the thickness of CF/PEKK laminates manufactured via ATP. In order to achieve this, three main objectives were established, which are addressed throughout this body of work. These, along with the work performed and the results, are summarised below.

Firstly, it was necessary to establish an understanding of the crystallisation nature of PEKK. In order to achieve this, an exhaustive study on crystallisation morphology, behaviour and kinetics of unreinforced PEKK and CF/PEKK composites was performed. Different isothermal holding temperatures were tested, ranging from 220-300°C. These affected the crystallisation morphology, with spherulites increasing in size as the isothermal temperature was increased (from ~2 μm at 220°C to ~5 μm at 300°C). All samples were observed to crystallise fully (~25%). The fastest crystallisation kinetics were achieved at 240-260°C, reaching peak crystallisation kinetics after 0.8 minutes. Non-isothermal cooling cycles were proven to influence the extent of crystallisation, with samples crystallising fully (26%) after cooling from the melt at 5°C/min, while remaining amorphous (<2% crystallinity) when cooled at 150°C/min. Modelling of the crystallisation kinetics was also performed, where time-temperature-transformation contour plots were generated for both the isothermal and non-isothermal cooling conditions.

Once an understanding of the crystallisation nature was established, it was of interest to evaluate the impact of different ATP parameters on the matrix-dominated mechanical properties of CF/PEKK laminates. To do this, CF/PEKK composites were manufactured via compression moulding and ATP, where 5 different compression moulding cycles were chosen based on the studied thermal cycles, and fully crystallised laminates were obtained. The effect of different spherulite sizes in the compression-moulded laminates (as observed in the crystallinity studies) was not evident on the properties investigated, as all compression-moulded laminates (crystallised to the highest extent) performed similarly. A series of ATP laminates were manufactured where the effect of different parameters was tested: tool material (ceramic and mild steel), nip temperature (360, 370, 380 and 390°C), lay-down speed (2 and 4 m/min) and roller pressure (2 and 4 bar). All ATP laminates displayed a significantly lower performance across the investigated mechanical properties when compared to the compression-moulded laminates (ranging from 24 to 73% lower performance across different matrix-dominated properties). When evaluating the impact of individual ATP parameters however, tool material and nip temperatures had the most significant impact on properties, with the ceramic tool and the higher temperatures improving performance.

While the macromechanical testing described above provides an indication of the overall quality of the laminate, this does not solely reflect the crystallinity extent, as mechanical performance can also be influenced by other factors such as void content. Furthermore, this testing does not provide an indication of any variation in crystallinity across the thickness of laminates. Therefore, the final consideration to this work was to study variation in micromechanical properties across different CF/PEKK laminates and their thickness to indirectly evaluate crystallinity content variations throughout a sample's cross-section. Nanoindentation was selected to do this as it allows to test regions small enough to provide different values for fibre, matrix bulk and fibre/matrix properties. The matrix bulk of compression-moulded laminates, which were found to be fully crystallised, performed significantly better than the ATP laminates (22-53% higher), in line with macromechanical testing results. The central region of the ATP laminates performed better than regions close to the top and bottom surfaces (up to 14%), likely due to a higher crystallinity development in the central area. Additionally, a transition region at the fibre/matrix region was observed in all samples.

The present work provides a diligent study on the crystallisation kinetics and morphology of CF/PEKK composites. This offers a solid understanding of crystalline structure development that can be of great value for optimising manufacturing parameters for semicrystalline thermoplastic composites. It also provides significant experimental evidence on crystalline structure development of CF/PEKK composites under compression moulding and ATP, and their impacts on macro and micromechanical performance. The crystallinity gradients developed across the thickness of the CF/PEKK laminates as an effect of ATP processing are studied via nanoindentation. Such scientific understanding can play a big role in optimising ATP manufacturing parameters and increasing the reliability of CF/PEKK products in high-performance applications.

Lay summary

The forecasted increase in demand in the aerospace industry has prompted a need to address its environmental impact. One approach to this involves using lighter materials to manufacture structural components. This can be achieved by replacing heavy, metallic parts with composite materials, consisting of a reinforcement (generally a fibre) and a matrix or binder (typically a polymer). Using such materials does not only result in lighter structures, but also leads to reduced fuel consumption and lower overall aviation emissions. The use of high-performance thermoplastic polymers specifically as a matrix in composites is particularly appealing. These materials offer advantages such as faster manufacturing, single-step processing, reparability and recyclability when compared to the more conventional thermoset polymers, such as epoxy resins.

The introduction of such materials has introduced new manufacturing challenges, leading to an increase in popularity of fast-paced, in-situ manufacturing methods. An example of such a manufacturing technique is automated tape placement (ATP), which uses computer-guided robotics to lay down carbon fibre/thermoplastic composite material in layers. The material is heated and consolidated as it is being laid to form structural components. However, due to the significant impact that the processing conditions have on the properties of thermoplastics, fast-paced manufacturing processes need to be tailored to suit the material's requirements.

The material of interest in this thesis is carbon fibre/poly(etherketoneketone) (CF/PEKK) composites, a high-performance thermoplastic composite of interest in the aerospace industry due to its excellent mechanical, thermal, and chemical properties. However, the existing understanding and research of PEKK regarding its microstructure and response to different processing conditions is limited. This is particularly the case with PEKK in composite form, and its implementation in ATP manufacturing, where parameter optimisation is vital to ultimately deliver high-quality parts and a competitive cost.

The work performed in this thesis strives to develop an understanding of the required processing conditions to achieve the composite's optimum performance. This understanding is achieved by evaluating the effect that different processes have on its morphology at the micron scale, as well as its mechanical performance. An understanding of the effect of different thermal histories was established, which was then used to manufacture a series of laminates via compression moulding (a well-established, slower-paced method of manufacturing high-quality laminates) and test a variety of matrix-dominated properties in the macro and micron scale, showing the strength of the PEKK component within the composite.

The findings indicate that the compression-moulded laminates outperformed the ATP laminates, despite some improvement in ATP performance when varying some manufacturing parameters. When assessing the ATP laminates at the micron scale, differences in properties were observed across the thickness of the laminates, likely a consequence of the differing levels of heat exposure of distinct laminate layers during the manufacturing process.

Overall, the research presented in this thesis develops a scientific understanding of the processing requirements of PEKK and their effect on its performance as part of a composite structure. This knowledge can contribute towards the optimisation of the ATP process and the successful application of CF/PEKK in high-performance scenarios within the aerospace industry.

Acknowledgements

I owe my most heartfelt gratitude to my main supervisor, Dr. Dipa Roy, whose guidance, expertise, and unwavering support have been instrumental over the past 4 years. Your insightful feedback and mentorship have been invaluable in sustaining my motivation and active engagement throughout these years. I am equally indebted to my secondary supervisor, Prof. Conchúr Ó Brádaigh, for your continuous encouragement and scholarly insights that have enriched my work.

I am deeply appreciative of the contributions of my industrial supervisors, Dr. Paul Mackenzie and Dr. Alex Baidak. Your practical insights and real-world perspective have greatly complemented my academic endeavours. The collaboration between academia and industry that you facilitated has been an invaluable asset to my research.

With thanks, I acknowledge financial support National Manufacturing Institute of Scotland (grant reference NMIS-IDP/009) and Hexcel Composites Ltd. for their financial support, as well as all the material provision enabled by Hexcel. I also wish to acknowledge the support of the Henry Royce Institute through the Royce PhD Equipment Access Scheme, enabling access to nanoindentation facilities at the Materials Research Facility (UK Atomic Energy Authority).

I would like to also extend my gratitude to the German Academic Exchange Service, which enabled me to perform some of the work in this thesis at the Leibniz Institute for Composite Materials. A special mention for Dr. Barbara Güttler and Mr. Stefan Buchalik-Bopp for all their guidance and support during my stay. I would also like to acknowledge the University of Limerick, and in particular the help of Mr. David Jones, for the manufacturing of all ATP laminates that were used in this work.

Finally, I am greatly thankful to the Composites group, for the discussions and the camaraderie we've shared. A special mention is due for Mr. Eddie Monteith and Mr. John Blackhurst, for their endless patience and help with everything lab-related; and for Mx. Kit O'Rourke and Mr. Machar Devine, my "PhD siblings" - the memories of conference and holiday travels with you both, as well as our lunches, are not only cherished but have also added a dimension of joy to my academic journey.

I would like to dedicate this thesis, firstly to my parents, Javier and Alicia - Papá, mamá, gracias por ser siempre tan generosos y mi mayor apoyo desde que me fui de casa. Siempre habéis estado ahí para las buenas y las malas, pasara lo que pasara. ¡Lo conseguimos!

To my cherished Edinburgh and Madrid inner circle – thank you for celebrating every little win along the way with me, and putting up with my rants over the years. To my partner in crime, Sergio – your unwavering support throughout these last 10 months has been indispensable, and you have been my loudest cheerleader. I am blessed to have all of you on my team.

Finally, in loving memory of my dearest best friend, Yuli, who left us in 2022. Nothing was more effective at making me get my act together like your tough reality checks and your sarcastic sense of humour. Thank you for always believing in me. I dedicate this thesis to you, celebrating not just my success, but the beautiful soul you were and the indelible mark you've left on my journey.

List of publications

The following publications are the result from work conducted in this thesis.

Journal articles

1. Pérez-Martín H, Mackenzie P, Baidak A, Ó Brádaigh CM, Ray D. Crystallinity studies of PEKK and carbon fibre/PEKK composites: A review. Composites Part B: Engineering 2021;223:109127. https://doi.org/10.1016/j.compositesb.2021.109127.
2. Pérez-Martín H, Mackenzie P, Baidak A, Ó Brádaigh CM, Ray D. Crystallisation behaviour and morphological studies of PEKK and carbon fibre/PEKK composites. Composites Part A: Applied Science and Manufacturing 2022;159:106992. https://doi.org/10.1016/j.compositesa.2022.106992.
3. Pérez-Martín H, Buchalik-Bopp S, Guettler BE, Mackenzie P, Baidak A, Ó Brádaigh CM. Effect of crystallinity and morphology on the mechanical properties of CF/PEKK composites manufactured under compression moulding and Automated Tape Placement. Materials Today Communications 2023;36;106442. https://doi.org/10.1016/j.mtcomm.2023.106442.
4. Pérez-Martín H, Mackenzie P, Baidak A, Ó Brádaigh CM, Ray D. Microstructural and micromechanical property characterisation of CF/PEKK composites using nanoindentation. Materials and Design 2023;234;112359. https://doi.org/10.1016/j.matdes.2023.112359.

Book chapters

1. Ray D, Pérez-Martín H. Chapter 3: Resins for structural Composites. Design and Manufacture of Structural Composites. Editor(s): Lee Harper, Mike Clifford. In Woodhead Publishing Series in Composites Science and Engineering. ISBN 9780128191606. https://doi.org/10.1016/B978-0-12-819160-6.00001-9.

Conference presentations

1. Pérez-Martín H, Mackenzie P, Baidak A, Ó Brádaigh CM, Ray D. Processing and characterisation of carbon fibre/PEKK composites. International Conference on Manufacturing of Advanced Composites, 2021.
2. Pérez-Martín H, Mackenzie P, Baidak A, Ó Brádaigh CM, Ray D. Influence of processing parameters on matrix-dominated properties of carbon fibre/poly(ether-ketone-ketone) composites. SAMPE Europe Conference. Hamburg 2022.
3. Pérez-Martín H, Mackenzie P, Baidak A, Ó Brádaigh CM, Ray D. Crystallisation studies on neat PEKK and carbon fibre/PEKK composites. 23rd International Conference on Composite Materials. Belfast, 2023.

- Scottish Research Partnership in Engineering annual conferences – poster presentations updating on project progress done as part of the National Manufacturing Institute of Scotland industry doctorate programme in 2019, 2021 and 2022.

Contents

Declaration ii
Abstract iii
Lay summary v
Acknowledgements vi
List of publications viii
Journal articles viii
Book chapters viii
Conference presentations viii
List of figures xiii
List of tables xx
Chapter 1. Introduction 1
Chapter references 3
Chapter 2. Literature review 5
2.1. Crystallisation morphology and structure 5
2.1.1. Chain morphology 5
2.1.2. Unit cell structure 9
2.1.3. Spherulitic growth and lamellar structure 11
2.1.4. Carbon fibre/PEKK and transcrystallinity 14
2.2. Crystallisation kinetics 16
2.2.1. Isothermal crystallisation 16
2.2.2. Non-isothermal crystallisation 20
2.2.3. Crystallisation kinetics in composites and effect on mechanical properties 22
2.2.4. Matrix-dominated mechanical properties 25
2.3. Modelling of crystallisation kinetics 31
2.3.1. Isothermal crystallisation kinetics 31
2.3.2. Non-isothermal crystallisation kinetics 38
2.3.3. Modelling of transcrystallinity 43
2.4. Automated tape placement 45
2.5. Chapter summary 50
Chapter references 52
Chapter 3. Research motivation 58

3.1. Gaps in existing knowledge 58
3.2. Research opportunities, thesis aims and objectives 60
Chapter references 61
Chapter 4. Crystallisation studies of PEKK powder and CF/PEKK prepreg tape 63
4.1. Materials and methods for crystallisation studies 63
4.1.1. Materials 63
4.1.2. Acid digestion 64
4.1.3. Thermogravimetric analysis 64
4.1.4. Differential scanning calorimetry (DSC) 64
4.1.5. Scanning electron microscopy (SEM) 65
4.2. Results and discussion 66
4.2.1. Fibre and matrix content 66
4.2.2. Thermal degradation of CF/PEKK in air and nitrogen environments 66
4.2.3. Isothermal crystallisation 67
4.2.4. Non-isothermal crystallisation 77
4.2.5. Manufacturing and end-use applicability 84
4.3. Chapter conclusions 86
Chapter references 86
Chapter 5. Materials and manufacturing: CF/PEKK laminate fabrication via compression-moulding and automated tape placement (ATP) 88
5.1. CF/PEKK prepreg tape 88
5.2. Compression-moulded laminates 90
5.3. Automated Tape Placement 93
5.3.1. First manufacturing campaign 95
5.3.2. Second manufacturing campaign 96
5.3.3. Summary of manufactured ATP laminates and codes 97
5.4. Chapter conclusions 98
Chapter 6. Mechanical testing of CF/PEKK laminates 99
6.1. Materials and methods 99
6.1.1. Materials and manufacturing 99
6.1.2. Ultrasonic non-destructive testing (UT) 100
6.1.3. Microscopy 100
6.1.4. Differential scanning calorimetry (DSC) 100

6.1.5. Chemical etching 101
6.1.6. Mechanical testing 101
6.1.7. Scanning electron microscopy (SEM) 102
6.2. Results and discussion 102
6.2.1. Laminate consolidation 102
6.2.2. Crystallinity and spherulitic morphology 106
6.2.3. Mechanical performance of unidirectional laminates 110
6.2.4. Mechanical performance of cross-ply laminates (in-plane shear testing) 120
6.2.5. ATP manufacturing insights 121
6.3. Chapter conclusions 122
Chapter references 123
Chapter 7. Microstructural and micromechanical property characterisation of CF/PEKK laminates using nanoindentation 125
7.1. Materials and methods 127
7.1.1. Materials and manufacturing 127
7.1.2. Nanoindentation 127
7.1.3. Nanoindentation 132
7.2. Chapter conclusions 143
Chapter references 144
Chapter 8. Thesis contributions and future work 147
8.1. Crystallinity studies 147
8.2. Prepreg quality 147
8.3. Manufacturing and mechanical testing of CF/PEKK laminates 148
8.4. Nanoindentation work 149
Chapter references 150
Chapter 9. Thesis conclusions 152
Appendix A. Calculating fibre volume fraction 156
A.1. Derivation 156
A.2. Calculations 157
Appendix B. Calculating LTE:HTE ratio for overlapping endotherms 158
Appendix C. Manufacturing trials and challenges 161
C.1. Initial ATP manufacturing trials 161
C.2. Issues with ATP manufacturing with a heated tool 161

Appendix D. Process data sheets 163
Appendix E. Ultrasound scan 187
Appendix F. Mechanical testing error analysis 188
Appendix G. ANOVA analysis of nanoindentation matrix bulk properties 189
G.1 Comparison across compression-moulded data 190
Hardness 190
Elastic modulus 190
G.2 Comparison across ATP-380 data 191
Hardness 191
Elastic modulus 191
G.3 Comparison across ATP-360 data 194
Hardness 194
Elastic modulus 194
G.4 Comparison across MID locations (compression-moulded vs. ATP-380) 195
Hardness 195
Elastic modulus 196
G.5 Comparison across MID locations (compression-moulded vs. ATP-360) 197
Hardness 197
Elastic modulus 197
Appendix H. Fibre/matrix interphase of ATP laminates 198
Appendix I. Peer-reviewed publications 201

List of figures

Figure 2.1: Chemical reaction for production of 1,4- (top) and 1,3- (bottom) substituted PEKK, by combining diphenyl ether (DPE) with terephthalic acid (T) or isophthalic acid (I). 6
Figure 2.2: Chemical reaction for prodution of PEEK by combining 4, 4' difluorobenzophenone, hydroquinone and potassium carbonate. Drawn after [17]. 7
Figure 2.3: Chemical structures and chain packing of (a) PEEK and PEKK with various T/I ratios: (b) 100/0, (c) 50/50, (d) 0/100. 8
Figure 2.4: Crystal packing models of PEKK of form 1 (two-chain orthorhombic); form 2 (i) (one-chain orthorhombic as per Gardner et al. [12]); and form 2 (ii) (two-chain orthorhombic as per Blundell and Newton [20]) and unit cell dimensions. 9
Figure 2.5: 3D schematic of crystal packing models of PEKK, based on Figure 2.4. 10
Figure 2.6: "Phase diagram" showing the occurrence of the two crystalline polymorphisms in PEKK as a function of the T/I ratio and the crystallisation conditions. Adapted from [3]. 11
Figure 2.7: A schematic showing homogeneous nucleation, where a polymer chain commences nucleation without the presence of a foreign phase or particle. 11
Figure 2.8: A schematic showing heterogeneous nucleation, where a polymer chain commences nucleation on the surface of a foreign particle. 12
Figure 2.9: Crystalline morphology schematic, showing lamellae (crystal) and amorphous regions of a spherulite. Magnitude increases from left to right. Drawn after [4,23]. 12
Figure 2.10: Spherulite formation schematic. Drawn after [23]. 12
Figure 2.11: Micrographs of PEKK 60/40 crystallised from the melt at 270°C during (a) 20 min, (b) 30 min and (c) 40 min [9]. 12
Figure 2.12: Optical micrographs of PEEK with carbon fibres: samples held at 390°C for (1) 0.5h; (2) 2h; (3) 3h; (4) 4h and cooled (0.5°C/min) to 270°C, followed by quenching to room temperature [24]. 13
Figure 2.13: Diagram of transcrystalline interface growth on the fibre surface. Not to scale. Drawn after [25]. 14
Figure 2.14: Left: spherulite nucleation in PEEK in contact with an unsized AS4 fibre. Right: transcrystallinity in PEEK in contact with unsized HMS fibre [32]. 15
Figure 2.15: DSC thermograms of isothermally crystallised PEKK 60/40 at different temperatures (as indicated) for 60 min [15]. 17
Figure 2.16: DSC thermograms of isothermally crystallised PEKK 60/40 at 245°C for different time periods [15]. 17
Figure 2.17: DSC scans of PEKK specimens annealed at different temperatures: (a) PEKK 90/10, (b) PEKK 80/20, (c) PEKK 70/30 (d) PEKK 60/40, (e) PEKK (50/50) [12]. 19
Figure 2.18: DSC thermograms of PEKK at 10°C/min after different cooling rates. Plot **a**, PEKK 60/40: (a) 2°C/min, (b) 5/C min, (c) 10°C/min, (d) 20°C/min, (e) 40°C/min, and (f) quenched. Plot **b**, PEKK 70/30: (a)10°C/min, (b) 20°C/min, (c) 40°C/min, (d) 60°C/min, and (e) quenched. Plot **c**, PEKK 80/20: (a) 5°C/min, (b) 10°C/min, (c) 20°C/min, (d) 40°C/min, (e) 60°C/min, and (f) quenched [15]. 20

Figure 2.19: Crystallisation peak time vs. temperature for PEKK resin ◊ and its AS4/PEKK carbon fibre-reinforcement composite +. The dotted curve represents the fit from a second-order polynomial equation [14]. 23
Figure 2.20: Comparison of half-time values for unreinforced PEEK (450PF in red) and CF/PEEK (450CA30 in black). Adapted from [54] 23
Figure 2.21: Scanning electron micrographs of fracture surfaces of CF/PEEK cooled at (a) 1°C/min and (b) 1800°C/min [29]. 24
Figure 2.22: Young's modulus and stress at yield vs. crystallinity at room temperature of neat PEKK crystallised at 230°C from the glassy state. Adapted from [65]. 26
Figure 2.23: Tensile strength, Young's modulus and crystallinity of neat PEEK as a function of cooling rate. Adapted from [29]. 26
Figure 2.24: Comparison of IFSS, ILSS and degree of crystallinity as a function of cooling rate [29] ... 30
Figure 2.25: Avrami crystallisation plots for the isothermal crystallisation of neat PEEK at 307°C, 310°C, 312°C, 315°C, showing the existence of two competing crystallisation processes [30] 33
Figure 2.26: Double logarithm vs. ln(time) (from left to right: 230°C, 220°C, 210°C, 200°C), Avrami model (dashed curves) and Hillier model (solid curves, discussed below) for PEKK 60/40 isothermal crystallisation from the melt [9]. 33
Figure 2.27: PEKK 60/40 DSC thermograms during isothermal crystallisation from the melt at 230°C (solid line) and 210°C (dashed line) [9] 35
Figure 2.28: Isotherm of total volume crystallinity of PEKK (A) separated into a primary volume crystallinity (B) and a secondary volume crystallinity (C). The data were obtained from an isotherm at 298°C [14] 35
Figure 2.29: Time-temperature-transformation diagram of the relative crystallinity of PEKK (a) 6002 and (b) 7002 crystallised from the melt [35]. 36
Figure 2.30: Ozawa plot of $log\ [-ln1-\alpha T]$ versus $log\varphi$ at the indicated temperatures. Lines as guides to the eye [39]. 39
Figure 2.31: Avrami crystallisation plot of $log\ [-ln1-a]$ vs. $logt$, for non-isothermal crystallisation at -1°C/min, -5°C/min, -10°C/min and -20°C/min, where a is relative crystallinity. The lines are guides to the eye [26]. 39
Figure 2.32: Volume fraction crystallinity versus time for the non-isothermal crystallisation of (a) neat PEEK resin and (b) PEEK resin in APC2 at various cooling rates. Lines represent predictions obtained by fitting the data to the parallel model, with best fit dynamic parameters [30] 40
Figure 2.33: Comparison of the experimental data (points) with the calculated values (lines) from using only the heterogeneous term $kNtn$ in Eqn. (2.21) at the cooling rates (●) 5°C/min, (■) 3°C/min, and (▲) 2°C/min [91]. 42
Figure 2.34: Comparison of the experimental data (points) with the calculated values (lines) from using only the heterogeneous term $kNtn$ in Eqn. (2.21) at the cooling rates (○) 50°C/min, (□) 20°C/min, and (Δ) 10°C/min [91] 42
Figure 2.35: Optical micrograph observation of the transcrystalline phase of CF/PEKK at 320°C isotherm [92] 43
Figure 2.36: Pixel colouring simulation of a polymeric film in the presence of two carbon fibres after locating nucleation sites as per the identified zones in optical micrographs [92] 44

Figure 2.37: Illustration of a location substrate where the microstructural modelling is considered [96]. 44
Figure 2.38: Comparison of spherulitic microstructure observations obtained from simulation between two extreme processing conditions at different relative crystallinities “c”. For both cases, incidence angle is 60°, torch exit diameter is 8mm, and torch distance to target is 32mm [96]. 45
Figure 2.39: Diagram of ATP manufacturing process. 46
Figure 2.40: 3D X-ray tomography of prepreg material, showing (i) carbon fibre (yellow and voids) blue, and (ii) the elongated nature of voids oriented in the fibre direction [71]. 47
Figure 2.41: Microstructure and void content of (a), (c) laser ATP and (b), (d) autoclave specimens for (a), (b) ILSS testing and (c), (d) open-hole compression testing [71]. 47
Figure 2.42: CF/PEEK prepreg tape (APC2-AS4) showing excessive surface roughness and void content [103]..... 48
Figure 3.1: Schematic of a laminate consolidated by Automated Tape Placement (left) and autoclave (right). Different shades of blue show crystallinity variation within the matrix. ATP schematic drawn after [3]. 59
Figure 4.1: (a) PEKK powder and (b) CF/PEKK prepreg tape images. 63
Figure 4.2: DSC heat cycle of all samples undergoing (a) isothermal crystallisation analysis and (b) non-isothermal or dynamic crystallisation analysis. The dotted sections of the plot indicate (a) the isothermal hold of the cycle, which can be at 220, 240, 260, 280 or 300°C; and (b) the cooling section of the cycle, which can be 5, 10, 20, 40, 60 100 or 150°C/min cooling rate. 65
Figure 4.3: TGA analysis of CF/PEKK samples under nitrogen (blue and grey curves) and air (yellow curve) environments. Note that the blue and grey curves overlap. 66
Figure 4.4: DSC thermograms (second heating cycles in Figure 4.2(a) of (a) unreinforced PEKK powder and (b) CF/PEKK prepreg tape after undergoing isothermal crystallisation at different temperatures with a hold time of 60 minutes. Dotted lines in the 300°C curve in (a) demonstrate how the area corresponding to each endotherm (LTE and HTE) was calculated in instances where the two peaks overlap. 67
Figure 4.5: Variation of LTE and HTE with isothermal temperature for unreinforced PEKK powder and CF/PEKK prepreg tape. Solid and dotted lines are exponential lines of best fit. 69
Figure 4.6: Schematic showing spherulite size at low and high temperature isotherms, and the consequent interlamellar spacing in which secondary crystallisation takes place. 69
Figure 4.7: Schematic representation of spherulitic development in unreinforced PEKK and CF/PEKK, depicting the difference in growth kinetics at different times as a consequence of CFs inhibiting spherulitic growth. Schematics of CF/PEKK are based on an SEM micrograph of the cross-section of a CF/PEKK prepreg sample. The regions marked with an X indicate areas in the two different samples that crystallised at the same time t. 70
Figure 4.8: SEM of cryofractured CF/PEKK samples after undergoing an isothermal hold of (a) 220°C, (b) 260°C and (c) 300°C from the melt. Red annotations highlight spherulitic structures, with a red dot providing an example of a nucleus location. 71
Figure 4.9: DSC thermograms of (a) unreinforced PEKK powder and (b) CF/PEKK prepreg tape while undergoing isothermal holds at different temperatures showing peak crystallisation kinetics times in minutes. In (a), samples undergoing 220 and 240°C isotherms crystallise before

reaching the isothermal temperatures, and therefore do not show crystallisation peaks during the isothermal hold. In (b), the fastest crystallisation kinetics can be observed between 240 and 260°C. 72
Figure 4.10: Relative crystallinity against time of unreinforced PEKK (dotted lines) and CF/PEKK (solid lines) at different isothermal holds. 73
Figure 4.11: Avrami plots of the relative crystallinity of unreinforced PEKK and CF/PEKK. 74
Figure 4.12: Relative crystallinity against time of (a) unreinforced PEKK and (b) CF/PEKK at different isothermal holds, showing a comparison of the Velisaris-Seferis model with the experimental data, as well as the contribution of primary and secondary crystallisation mechanisms to the model. 75
Figure 4.13: Logarithmic plot of (a) k_1 and (b) k_2 against isothermal temperature for unreinforced PEKK and CF/PEKK. Dotted lines show the Hoffmann-Lauritzen models fitted to the experimental data..... 76
Figure 4.14: DSC thermograms of (a) unreinforced PEKK and (b) CF/PEKK prepreg at 20°C/min heat ramp after different cooling rates..... 77
Figure 4.15: SEM of cryofractured CF/PEKK sample after undergoing a cooling rate of (a) 5°C/min from the melt to room temperature (25.6% crystallintiy) and (b) 100°C/min from the melt to room temperature (6.9% crystallinity). 79
Figure 4.16: DSC thermograms of (a) Unreinforced PEKK powder and (b) CF/PEKK prepreg tape while undergoing different cooling rates. 79
Figure 4.17: Relative crystallinity against time of unreinforced PEKK (dotted lines) and CF/PEKK (solid lines) at different cooling rates. 80
Figure 4.18: Dual Nakamura model fits to non-isothermal crystallisation experimental data of unreinforced PEKK powder undergoing a range of cooling rates. 81
Figure 4.19: Variation of crystallisation relative content (w_1 and w_2) with cooling rate for crystallisation kinetics modelling of unreinforced PEKK powder. 82
Figure 4.20: Single Nakamura model fits to non-isothermal crystallisation experimental data of CF/PEKK composite undergoing a range of cooling rates. 83
Figure 4.21: Single Nakamura with correction coefficient fits to non-isothermal crystallisation experimental data of CF/PEKK composite undergoing a range of cooling rates. 83
Figure 4.22: Time-temperature-transformation diagrams of relative crystallinity development for (a) unreinforced PEKK and (b) CF/PEKK at different isothermal holds. A relative crystallinity of 1 means the material has achieved its full crystallisation potential, based on the crystallinity values shown in Table 4.2. 84
Figure 4.23: Time-temperature-transformation diagrams of relative crystallinity development for (a) unreinforced PEKK and (b) CF/PEKK when undergoing different cooling rates. The coloured straight lines denote the performed cooling rates in this study. A relative crystallinity of 1 refers to the total crystallinity achieved after cooling at 5°C/min. 85
Figure 5.1: CF/PEKK prepreg tape as received from Hexcel Composites Ltd. for (a) compression-moulding (150 mm wide)and (b) ATP manufacturing (6.5 mm wide). 88
Figure 5.2: Prepreg tape imaging of lighter and darker regions. 89
Figure 5.3: Schematic of frame and plates used for compression-moulding manufacturing..... 91
Figure 5.4: Prepreg tape preparation for laminate manufacturing via compression-moulding. 91

Figure 5.5: Summary of processing parameters for the compression-moulded laminates. 92
Figure 5.6: I-220-370 laminate after manufacturing..... 92
Figure 5.7: Schematic of ATP lay-up process and processing parameters. ATP schematic drawn after [5]..... 93
Figure 5.8: Images of (a) ATP equipment and (b) (c) ATP head close-ups. 93
Figure 5.9: Schematic of ATP laying programme. 94
Figure 5.10: Image of ATP manufacturing process, showing the first layer of a laminate being laid down on a mild steel tool. Double-sided tape is highlighted, showing how the first layer of tape is held in place. 94
Figure 5.11: Images of ATP-manufactured (a) unidirectional laminates for 0° flexural, 90° flexural and ILSS testing, and (b) cross-ply laminates for in-plane shear testing.. 95
Figure 5.12: (a) Schematic of original concept for multi-thickness laminate and (b) image of final manufactured multi-thickness laminate. 96
Figure 6.1: UD compression-moulded laminates c-scans from ultrasonic testing and image of example laminate (I-220-370) highlighting high- and low-ultrasound penetration regions..... 103
Figure 6.2: UD ATP laminates c-scans from ultrasonic testing (a) as received (16dB), and (b) after the gain was increased by 16.6 dB..... 104
Figure 6.3: Microscopy images of the cross sections of (a) compression-moulded laminates and (b) ATP-manufactured laminates with annotations highlighting examples of interply voids (blue squares) and intraply voids (red arrows)..... 105
Figure 6.4: Sample DSC heat scans of CF/PEKK laminates manufactured under different processing conditions..... 107
Figure 6.5: SEM micrographs of etched CF/PEKK samples from different compression-moulded laminates: (a) Laminate I-220-270 (b) Laminate I-260-370 and (c) Laminate I-300-370 (d) example of partially etched sample showing remaining fibrillar networks in the matrix as a consequence of partial etching..... 109
Figure 6.6: Mechanical testing results of compression-moulded and ATP CF/PEKK laminates. Error bars show the data range. 111
Figure 6.7: Representative stress strain curves for flexural 0° coupons of compression-moulded and ATP laminates. 112
Figure 6.8: SEM images of 0° flexural fracture surfaces of specimens extracted from (a) I-220-370 (compression moulded) and (b) 390-4-2 (ATP-manufactured) laminates at ×40 magnification, with labelled tension and compression failure regions. 113
Figure 6.9: SEM images of 0° flexural fracture surfaces of specimens extracted from (a) I-300-370 (compression moulded) and (b) 390-4-2 (ATP). 114
Figure 6.10: Representative stress-strain curves for flexural 90° coupons of compression-moulded and ATP laminates. 115
Figure 6.11: SEM images of 90° flexural fracture surfaces of specimens extracted from (a) I-300-370 (compression-moulded) and (b) 390-4-2 (ATP). 116
Figure 6.12: Representative ILSS stress-extension curves of compression-moulded and ATP laminates. 117

Figure 6.13: Schematics and SEM images of cast ILSS specimens extracted from (a) I-300-370 (compression moulded) and (b) ATP-380-2-2 with sketches highlighting failure modes. Images are of the side of the specimens.....118
Figure 6.14: SEM image of an untested ATP laminate sample showing intraply voids. 118
Figure 6.15: Representative stress-strain curves for in-plane shear coupons of ATP laminates after undergoing different post-processing conditions.....120
Figure 6.16: SEM images of failure regions of in-plane shear tested coupons extracted from (a) ATP-360-4-2, (b) ATP-360-4-2-P220 and (c) ATP-360-4-2-P300.....121
Figure 7.1: (a) Nanoindentation loading and unloading schematic; and (b) sample load-displacement curve generated from a nanoindentation test 128
Figure 7.2: (a) Micrograph of 2 μm depth indentation at a matrix pocket; and (b) elastic modulus-displacement plot of said indentation. 129
Figure 7.3: Schematics of laminate cross-sections, showing the location of performed indentations with a square □.....130
Figure 7.4: Schematic example of an indentation array and fibre and matrix indents on an ATP sample. In this case, 19 indentations were performed per location marked with a square □, with each of them giving hardness and elastic modulus data.....130
Figure 7.5: A micrograph showing array and a matrix indent. A close-up of two indentations shows nanoindentation distances to the closest fibre surface marked with red arrows, measured using ImageJ. 131
Figure 7.6: Load-displacement results of nanoindentation experiments on (a) CM-220 and (b) the top location of ATP-380-4-2.....132
Figure 7.7: (a) Hardness and (b) elastic modulus results against indentation distance from fibre surface for CM-260. The experimental data includes the nanoindentation array and individual indents performed on matrix pockets and fibres. The curves are fitted to the experimental data, and correspond to Eq. (6.8) and (6.9) for (a) and (b) respectively. 134
Figure 7.8: (a) Matrix bulk hardness and (b) matrix bulk elastic modulus of all compression-moulded laminates and ATP laminates manufactured at T_{nip} = 380°C. Top-right schematic shows the locations where the indentations were performed, measured from the bottom of the laminate (taken from Figure 7.3).....136
Figure 7.9: Schematic of contribution to crystallinity development of the ATP unheated tool acting as a heat sink and the heat repasses seen by a layer of material as more layers are placed on top. 138
Figure 7.10: (a) Matrix bulk hardness and (b) matrix bulk elastic modulus of all compression-moulded laminates and ATP laminates manufactured at T_{nip} = 360°C. Schematics in (c) show the locations where the indentations were performed, measured from the bottom of the laminate (taken from Figure 7.3).....139
Figure 7.11: (a) Hardness and (b) elastic modulus exponential decay curve fittings to nanoindentation test results of compression-moulded samples, with 95% confidence intervals shown by the shaded regions. Note that the curves for I-220-370 and I-300-370 overlap in both plots. ...140
Figure 7.12: Schematic demonstrating the effect of temperature on crystal growth in CF/PEKK, based on general polymeric nucleation theory, where $T_1 < T_2 < T_3$. Red markings indicate crystals growing from the fibre surface. 141

Figure 7.13: (a) Hardness and (b) elastic modulus exponential decay curve fittings to nanoindentation test results of I-260-370, ATP-380-4-2 and ATP-360-4-2-2mm, with confidence intervals shown by the shaded regions. 142
Figure 9.1: Summary of the key findings in Chapter 4. Plots show primary to secondary crystallisation proportions present in unreinforced PEKK and CF/PEKK samples when undergoing (a) different isothermal holds and (b) different cooling rates. Additionally, (a) shows time for peak crystallisation kinetics at each isothermal hold (where all samples fully crystallised), and (b) shows total crystallinity development. 153
Figure 9.2: Radar chart summarising the key findings of Chapter 6. Axis minimum and maximum values are provided in square brackets for scaling purposes. * The IPS values marked with an **X** are for graphing purposes only (these laminates did not undergo IPS testing).. IPS results for I-220-270 and I-300-370 are ATP laminates post-processed via compression moulding (please refer to Chapter 5 for further details on manufacturing of laminates ATP-360-4-2-P220 and ATP-360-4-2-P300). 154
Figure 9.3: Summary of the key findings in Chapter 7. Plots show CF/PEKK matrix bulk properties tested via nanoindentation. The results are across different laminates (as shown in the figure legend) and at different points across the laminate thicknesses (indicated in the x axis). 155
Figure B.1: Example of overlapping double endotherm, with LTE and HTE areas coloured in orange and green respectively. 158
Figure B.2: Double endotherm diagram showing the breakdown of different regions within the double endotherm. 158
Figure B.3: Double endotherm diagram showing imaginary lines to aid in the calculation of lengths AB, AC and BC. 159
Figure B.4: Double endotherm diagram showing the triangle regions that correspond to the LTE (orange) and HTE (green). 160
Figure B.5: Example of overlapping double endotherm, with LTE and HTE areas coloured in orange and green respectively. 160
Figure C.1: Cuboid tool for laminate manufacturing, including (a) tool, (b) part obtained with said tool via ATP manufacturing, and (c) resulting laminates obtained after trimming rounded edges. 161
Figure C.2: Image of 3rd layer being laid during ATP laminate manufacturing with T_{nip} = 380°C and tool temperature of 260°C. Lifting of tapes in layers 2 and 3 is highlighted wit harrows. ... 162
Figure E.1: Ultrasound c-scan of autoclaved CF/PEKK laminate with a 5 mm Perspex reference to the right. 187
Figure H.1: (a, b, c) Hardness and (d, e, f) elastic modulus exponential decay curve fittings of ATP CF/PEKK T_{nip} = 380°C nanoindentation testing results. Each plot has the curve fittings of all locations of a single sample. 198
Figure H.2: (a, b) Hardness and (c. d) elastic modulus exponential decay curve fittings of ATP CF/PEKK T_{nip} = 360°C nanoindentation testing results. Each plot has the curve fittings of all locations of a single sample. 199

List of tables

Table 1.1: Thesis chapter to publication mapping. 3
Table 2.1: Polymer repeat units for PEEK, poly(etherketone) (PEK), poly(etherketoneetherketoneketone) (PEKEKK) and PEKK. Drawn after [3]. 6
Table 2.2: KEPSTAN(R) PEKK commercial range grades, based on T/I ratio and viscosity (adapted from webinar presentation) [19]. 9
Table 2.3: Dimensions for the different unit cell forms of PEKK. 10
Table 2.4: Transition temperatures and crystallinity of PEKK 60/40 after annealing. Table excerpt from [15] 18
Table 2.5: Crystallinity percentage for PEKK samples subjected to cooling at various cooling rates. Table excerpt from [15]. 20
Table 2.6: Crystallinity, shear modulus (GPa) and Young's modulus (GPa) of ±45° of PEKK composites manufactured under different conditions, tested at room temperature and 180°C. Adapted from [28]. 27
Table 2.7: Crystallinity, shear modulus (GPa) and Young's modulus (GPa) of ±45° of PEKK composites held at different isothermal conditions, tested at room temperature and 180°C. Adapted from [28] 27
Table 2.8: Void content, crystallinity and ILSS (MPa) of CF/PEKK composites after undergoing different processing and post-processing conditions. Adapted from [66] 28
Table 2.9: Compilation of matrix-dominated properties of CF/PEEK offered by various authors. 29
Table 2.10: Relation between the Avrami exponent and the morphological unit. Adapted from [9,76]. . 32
Table 2.11: Relation between crystallisation rate constant k and the morphological unit. Adapted from [9,35]. 32
Table 2.12: Micrographs of CF/PEKK for different processing conditions and post-processing methods. Adapted from [66]. 48
Table 4.1: CF/PEKK prepreg tape sample weights before and after acid digestion. 66
Table 4.2: Average values for transition temperatures, melting enthalpies and total crystallinity of unreinforced PEKK powder and CF/PEKK prepreg tape after undergoing different isothermal holds. 68
Table 4.3: Summary of Velisaris-Seferis model parameters for the isothermal crystallisation modelling of unreinforced PEKK and CF/PEKK. w_1 and w_2 are extracted from the LTE:HTE ratios in Table 4.2. 75
Table 4.4: Parameters used for Hoffmann-Lauritzen modelling. 77
Table 4.5: Average values for transition temperatures, enthalpies and total crystallinity of PEKK powder and CF/PEKK prepreg tape after undergoing different cooling rates. 78
Table 5.1: CF/PEKK prepreg tape sample weights before and after acid digestion. 95
Table 5.2: CF/PEKK prepreg tape sample weights before and after acid digestion. 96
Table 5.3: Summary of processing parameters for unidirectional ATP-manufactured laminates. 97
Table 5.4: Summary of reprocessing parameters for cross-ply ATP-manufactured laminates. 97
Table 5.5: Summary of processing parameters for multi-thickness laminate. 97
Table 6.1: Summary of processing parameters for the compression-moulded and ATP-manufactured laminates. 99

Table 6.2: Laminate thickness and void content of compression-moulded and ATP laminates, taken from microscopy images in Figure 6.3. 104
Table 6.3: Average values for glass transition temperatures, enthalpies and total crystallinity of CF/PEKK laminates manufactured under different processing conditions. 107
Table 6.4: Mechanical testing results of compression-moulded and ATP CF/PEKK laminates. 110
Table 6.5: Flexural 0° strength results in this work and in literature. 114
Table 6.6: ILSS results in this work and in literature. 119
Table 6.7: In-plane shear testing of results of ATP CF/PEKK laminates after undergoing different post-processing conditions. 120
Table 7.1: Summary of processing parameters for the compression-moulded and ATP-manufactured laminates. 127
Table 7.2: Summary of B_H and B_M values and 95% confidence intervals for the exponential decay modelling of compression-moulded CF/PEKK samples. 140
Table 7.3: Summary of B_H and B_M values and 95% confidence intervals (CI) for the exponential decay modelling of I-260-370, ATP-380-4-2 and ATP-360-4-2-2mm. 142
Table F.1: Property and error calculation equations for mechanical testing performed in this work. 188
Table F.2: Reading error in the equipment used. 188
Table H.1: Summary of and B_H and B_M values for the exponential decay modelling of ATP CF/PEKK samples manufactured at T_{nip} = 380°C (on a metal tool). Values are given for each tested location on each sample. The cells shaded the darkest grey in the tables are a guide to the eye of the highest B values for each laminate (the steepest slope and the shortest fibre-matrix transition). The lower the B value, the lighter the cell shading is, with white cells indicating the lowest B value of each laminate (the softest gradient, and the longest fibre-matrix transition). 198
Table H.2: Summary of and B_H and B_M values for the exponential decay modelling of ATP CF/PEKK samples manufactured at T_{nip} = 360°C (on a ceramic tool). Values are given for each tested location on each sample. The cells shaded the darkest grey in the tables are a guide to the eye of the highest B values for each laminate (the steepest slope and the shortest fibre-matrix transition). The lower the B value, the lighter the cell shading is, with white cells indicating the lowest B value of each laminate (the softest gradient, and the longest fibre-matrix transition). 199

Chapter 1. Introduction

High-performance thermoplastics are increasingly being studied and used as a matrix in carbon fibre composites destined for aerospace industry applications. Introducing such materials offers several advantages over the more traditional thermosetting matrices, namely recyclability, impact resistance, reparability, extended shelf life, and reduced energy consumption. The absence of a curing reaction also leads to potentially shorter processing times or single-step processing, enabling the combination and tailoring of different features and materials to suit the requirements of any particular application [1]. An example of such polymers are poly(aryletherketone)s (PAEKs), a family of semicrystalline thermoplastics used due to their excellent properties, including good impact, chemical and oxidation resistance, high-temperature performance and low density. These are commonly used in parts like wing structures such as flaps, access panels and floor panels, amongst others [1–8].

Poly(etheretherketone) (PEEK) is the most widely studied polymer of the PAEK family, and has been one of the main candidates as a thermoplastic matrix for high-performance composite applications [9–14]. Poly(etherketoneketone) (PEKK), the main focus of this thesis, has been less studied to date, but is becoming an increasingly attractive option for advanced applications [1,3,6,13,15–19]. An advantage that PEKK possesses over PEEK is the range of grades obtainable during its synthesis. This results in the capability of fine-tuning some of PEKK's properties, such as crystallisation extent. Crystallisation refers to the arrangements of polymeric chains into a regular pattern, and is an aspect of PEKK that is thoroughly assessed in this body of work. The extent to which crystallisation can take place in a polymer is generally dictated by molecular structure, and the presence of crystallinity significantly impacts properties such as strength, stiffness, chemical resistance and melting temperature. In some commercial grades of PEKK, melting temperature can range between 305-358°C [20]; whereas PEEK's melting temperature is limited to 343°C [20]. This can be used to a manufacturer's advantage, enabling processing of some grades of PEKK at lower temperatures than with PEEK. This, along with PEKK's excellent mechanical properties (comparable to that of PEEK) make it an interesting candidate for high-performance applications as well.

Despite these advantages, there are challenges associated with introducing thermoplastics into aerospace applications, including material cost and the need to develop specialized manufacturing processes. With such high-performance polymers in particular, difficulties arise with regards to fibre impregnation due to higher viscosity, leading to a poor fibre-matrix interface, porosity and partial impregnation during production. This becomes particularly exacerbated during fast-paced, in-situ manufacturing processes, where achieving the desired mechanical properties in a manufactured part undergoing short processing windows can be highly challenging [9,21–24]. In addition, achieving the desired level of crystallinity in semicrystalline thermoplastics is critical in high-performance applications, requiring optimum thermal cycles.

An example of such an in-situ manufacturing process is automated tape placement (ATP), an advanced manufacturing technique using computer-guided robotics to deposit layers of preimpregnated carbon fibre tape (prepreg) on a mould or tool in order to manufacture a composite part. It offers advantages such as the ability to create complex geometries, consistent quality, reduced material waste, and increased production efficiency [25–27]. However, the fast nature of the manufacturing process can result in steep

temperature gradients and short exposure to consolidation pressures [15,21]. When using this processing technique to manufacture semicrystalline thermoplastic composite parts, it is essential to use optimal processing parameters in order to achieve the required properties for the intended application.

This thesis follows a structure based on peer-reviewed publications. These collectively offer a comprehensive insight into the crystallisation kinetics and morphology of unreinforced PEKK and CF/PEKK composite, exploring how these factors influence mechanical properties, as well as the effects of various manufacturing processes. An outline of the chapters is provided below:

- Chapter 2 provides background to the body of work, offering a literature of PEKK's crystallisation morphology, kinetics and any existing modelling. Comparisons to PEEK are regularly drawn throughout, due to this being a better established polymer and therefore more literature being available on PEEK. Some context on existing research performed on Automated Tape Placement manufacturing of CF/PEEK and CF/PEKK composites is also included.
- Chapter 3 describes the research motivation and outlines the thesis aims and objectives, based on the gaps found in the literature review.
- Chapter 4 presents work performed on the crystallisation studies of unreinforced PEKK and CF/PEKK composite, evaluating crystal morphology, kinetics when undergoing different thermal cycles, and modelling of the crystallisation process.
- Chapter 5 describes the manufacturing processes that a variety of CF/PEKK laminates underwent, later used in Chapter 6 and Chapter 7.
- Chapter 6 presents characterisation of CF/PEKK laminates described in Chapter 5, covering a variety of microscopic techniques and mechanical testing.
- Chapter 7 delves into micromechanical property characterisation of CF/PEKK laminates via nanoindentation testing, comparing matrix bulk properties of laminates manufactured via different processing conditions. Variation in matrix bulk properties across the thickness of laminates is also evaluated, along with any presence of a fibre-matrix interphase.
- Chapter 8 summarises the main thesis contributions to the scientific knowledge, and highlights recommendations for future work.
- Chapter 9 provides a summary of the thesis' main findings.

The chapter to publication mapping is shown in Table 1.1. Further information on these articles can be found in the List of publications in page viii. With the exception of the literature review paper, which is not open access, the publications can be found in Appendix I.

Table 1.1: Thesis chapter to publication mapping.

Chapter	Publication Title	Journal [Impact factor]	Status
Chapter 2. Literature review	Crystallinity studies of PEKK and carbon fibre/PEKK composites: A review.	Composites Part B: Engineering [13.1]	Published (2021)
Chapter 4. Crystallisation studies of PEKK and CF/PEKK prepreg tape	Crystallisation behaviour and morphological studies of PEKK and carbon fibre/PEKK composites.	Composites Part A: Applied Science and Manufacturing [8.7]	Published (2022)
Chapter 6. Mechanical testing of CF/PEKK laminates	Effect of crystallinity and morphology on the mechanical properties of CF/PEKK composites manufactured under compression moulding and Automated Tape Placement.	Materials Today Communications [3.8]	Published (2023)
Chapter 7. Microstructural and micromechanical property characterisation of CF/PEKK laminates	Microstructural and micromechanical property characterisation of CF/PEKK composites using nanoindentation.	Materials and Design [8.4]	Published (2023)

Chapter references

[1] Donadei V, Lionetto F, Wielandt M, Offringa A, Maffezzoli A. Effects of blank quality on press-formed PEKK/Carbon composite parts. Materials 2018;11. https://doi.org/10.3390/ma11071063.

[2] Blundell DJ, Crick RA, Fife B, Peacock J, Keller A, Waddon A. Spherulitic morphology of the matrix of thermoplastic PEEK/carbon fibre aromatic polymer composites. J Mater Sci 1989;24:2057–64. https://doi.org/10.1007/BF02385421.

[3] Choupin T, Fayolle B, Régnier G, Paris C, Cinquin J, Brulé B. Isothermal crystallization kinetic modeling of poly(etherketoneketone) (PEKK) copolymer. Polymer 2017;111:73–82. https://doi.org/10.1016/j.polymer.2017.01.033.

[4] Mazur RL, Oliveira PC, Rezende MC, Botelho EC. Environmental effects on viscoelastic behavior of carbon fiber/PEKK thermoplastic composites. J Reinf Plast Compos 2014;33:749–57. https://doi.org/10.1177/0731684413515955.

[5] Hassan EAM, Ge D, Yang L, Zhou J, Liu M, Yu M, et al. Highly boosting the interlaminar shear strength of CF/PEEK composites via introduction of PEKK onto activated CF. Compos Part Appl Sci Manuf 2018;112:155–60. https://doi.org/10.1016/j.compositesa.2018.05.029.

[6] Quiroga Cortés L, Caussé N, Dantras E, Lonjon A, Lacabanne C. Morphology and dynamical mechanical properties of poly ether ketone ketone (PEKK) with meta phenyl links. J Appl Polym Sci 2016;133:1–10. https://doi.org/10.1002/app.43396.

[7] Reitman M, Jaekel D, Siskey R, Kurtz SM. Morphology and Crystalline Architecture of Polyaryletherketones. 2nd ed. Elsevier Inc.; 2012. https://doi.org/10.1016/B978-1-4377-4463-7.10004-1.

[8] Cheng SZD, Ho RM, Hsiao BS, Gardner KH. Polymorphism and crystal structure identification in poly(aryl ether ketone ketone)s. Macromolecules 1996;197:185–213. https://doi.org/10.1002/macp.1996.021970115.

[9] Comer AJ, Ray D, Obande WO, Jones D, Lyons J, Rosca I, et al. Mechanical characterisation of carbon fibre–PEEK manufactured by laser-assisted automated-tape-placement and autoclave. Compos Part Appl Sci Manuf 2015;69:10–20. https://doi.org/10.1016/j.compositesa.2014.10.003.

[10] Flanagan M, Goggins J, Doyle A, Weafer B, Ward M, Bizeul M, et al. Out-of-autoclave manufacturing of a stiffened thermoplastic carbon fibre PEEK panel. AIP Conf Proc 2017;1896. https://doi.org/10.1063/1.5008001.

[11] Deignan A, Stanley WF, McCarthy M. Insights into wide variations in carbon fibre/polyetheretherketone rheology data under automated tape placement processing conditions. J Compos Mater 2018;52:2213–28. https://doi.org/10.1177/0021998317740733.

[12] Lee Y, Porter RS. Crystallization of poly(etheretherketone) (PEEK) in carbon fiber composites. Polym Eng Sci 1986;26:633–9. https://doi.org/10.1002/pen.760260909.

[13] Gardner KH, Hsiao BS, Faron KL. Polymorphism in poly (aryl ether ketone). Polymer 1994;35:2290–5.

[14] Tencé-Girault S, Quibel J, Cherri A, Roland S, Fayolle B, Bizet S, et al. Quantitative Structural Study of Cold-Crystallized PEKK. ACS Appl Polym Mater 2021;3:1795–808. https://doi.org/10.1021/acsapm.0c01380.
[15] Esguerra-Arce I, Martín MI, Pérez-Pastor A, García-Martínez V. Evolution of crystallinity with multiple lamination steps in high performance thermoplastic composites by in-situ consolidation process. Twenty-Second Int Conf Compos Mater 2019.
[16] Gardner KCH, Hsiao BS, Matheson RR, Wood BA. Structure, crystallization and morphology of poly (aryl ether ketone ketone). Polymer 1992;33:2483–95. https://doi.org/10.1016/0032-3861(92)91128-O.
[17] Ho RM, Cheng SZD, Hsiao BS, Gardner KH. Crystal morphology and phase identifications in poly(aryl ether ketone)s and their copolymers. 3. Polymorphism in a polymer containing alternated terephthalic acid and isophthalic acid isomers. Macromolecules 1995;28:1938–45. https://doi.org/10.1021/ma00110a030.
[18] Hsiao BS, Chang IY, Sauer BB. Isothermal crystallization kinetics of poly(ether ketone ketone) and its carbon-fibre-reinforced composites. Polymer 1991;32:2799–805. https://doi.org/10.1016/0032-3861(91)90111-U.
[19] Choupin T, Debertrand L, Fayolle B, Régnier G, Paris C, Cinquin J, et al. Influence of thermal history on the mechanical properties of poly(ether ketone ketone) copolymers. Polym Cryst 2019;2:e10086. https://doi.org/10.1002/pcr2.10086.
[20] Arkema. Introduction to ultra high-performance Kepstan® PEKK 2020.
[21] Stokes-Griffin CM, Compston P. The effect of processing temperature and placement rate on the short beam strength of carbon fibre-PEEK manufactured using a laser tape placement process. Compos Part Appl Sci Manuf 2015;78:274–83. https://doi.org/10.1016/j.compositesa.2015.08.008.
[22] Lamontia M, Gruber M. Remaining developments required for commercializing in situ thermoplastic ATP. SAMPE Eur Conf 2007:1–15.
[23] Qureshi Z, Swait T, Scaife R, El-Dessouky HM. In situ consolidation of thermoplastic prepreg tape using automated tape placement technology: potential and possibilities. Compos Part B Eng 2014;66:255–67. https://doi.org/10.1016/j.compositesb.2014.05.025.
[24] Shadmehri F, Hoa SV, Fortin-Simpson J, Ghayoor H. Effect of in situ treatment on the quality of flat thermoplastic composite plates made by automated fiber placement (AFP). Adv Manuf Polym Compos Sci 2018;4:41–7. https://doi.org/10.1080/20550340.2018.1444535.
[25] August Z, Ostrander G, Michasiow, John, Hauber D. Recent developments in automated fiber placement of thermoplastic composites. SAMPE J 2014;50:30–7.
[26] Lukaszewicz DHJA, Ward C, Potter KD. The engineering aspects of automated prepreg layup: history, present and future. Compos Part B Eng 2012;43:997–1009. https://doi.org/10.1016/j.compositesb.2011.12.003.
[27] Oromiehie E, Prusty BG, Compston P, Rajan G. Automated fibre placement based composite structures: Review on the defects, impacts and inspections techniques. Compos Struct 2019;224:110987. https://doi.org/10.1016/j.compstruct.2019.110987.

Chapter 2. Literature review

As described in Chapter 1, the superior properties of the PAEK family of polymers make them great candidates as composite matrices in high-performance applications. PEEK, in particular, has been widely studied over the last 30 years, with the focus on the processing of PEEK-based composites increasing in the past decade [1–8]. Poly(etherketoneketone) (PEKK), on the other hand, has been investigated much less extensively. The tuneability PEKK offers, discussed in the following sections, along with its excellent mechanical properties and lower processing temperatures than PEEK, has aroused interest as a matrix for composite structural parts only in the recent years [3,9–15].

This chapter provides an analysis of PEKK crystallisation morphology and kinetics, factors affecting this, and how the inclusion of carbon fibres impacts these behaviours. This is followed by an overview of the most relevant models used for the crystallisation kinetics of neat and composite PEKK, as well as an overview of some relevant transcrystallinity simulations. It is important to develop an understanding of unreinforced PEKK before considering its behaviour as part of a composite material, and therefore this chapter offers a review of unreinforced PEKK wherever possible prior to any discussion of CF/PEKK composites. Due to the limited literature on PEKK, a comparison is drawn from the more extensive literature available for PEEK and CF/PEEK whenever it is relevant.

In addition, a brief review of the ATP manufacturing process is provided, briefly discussing the nature of the process, advantages, limitations, and some published work on ATP-manufactured CF/PEEK and CF/PEKK laminates.

2.1. Crystallisation morphology and structure

The properties of PEKK, as well as that of any other PAEK, are a direct result of the molecular weight, polymer backbone, molecular organisation upon solidification, and any morphological changes that occur during subsequent thermal exposure [16]. The mode in which the polymers are crystallised also impacts the morphology, affecting the thermal stability of the resultant semicrystalline structure. This section will cover the differences in the structure of PAEKs and the various grades of PEKK, the morphology of crystallised PEKK at molecular and micron level, and will discuss how crystal nucleation and growth is impacted by the inclusions of carbon fibres, potentially resulting in a transcrystalline phase at the fibre-matrix interface.

2.1.1. Chain morphology

The backbone of all PAEK polymers consists of aromatic rings connected by ether or ketone linkages, the order of which gives the name to the specific polymer as shown in Table 2.1. The stiffness that aromatic rings bring to the backbone chain, combined with a high chain linearity and little to no branching (a continuous arrangement of monomer units) [3,16] results in thermoplastics suitable for high-performance composite applications. Ketone linkages are also stiffer than ether linkages, which gives rise to PEKK being the stiffest of the four polymers shown in Table 2.1.

Table 2.1: Polymer repeat units for PEEK, poly(etherketone) (PEK), poly(etherketoneetherketoneketone) (PEKEKK) and PEKK. Drawn after [3].

Functional groups in PAEKs	Structure	Name	Ketone (%)
Ether 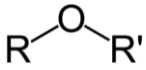	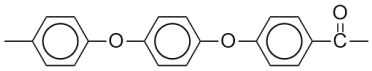	PEEK	33
	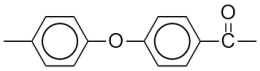	PEK	50
Ketone 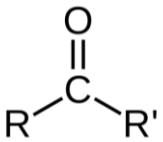	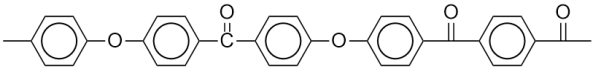	PEKEKK	60
	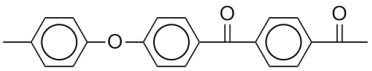	PEKK	67

In some thermoplastics from the PAEK family, material properties can be further modified by controlling the inclusion of different isomers during synthesis. In the case of PEKK, this is created by combining diphenyl ether (DPE) with terephthalic acid (T) or isophthalic acid (I). These result in the creation of para- and meta- isomers respectively as per Figure 2.1. Different contents of these linkages result in different grades of PEKK, and these are often classified with a T/I ratio (terephthalic/isophthalic content). A low T/I ratio entails a higher content of meta- linkages, resulting in more flexible chains and a decreased melting temperature [3,15]. This facilitates composite manufacturing, but at the cost of achieved crystallinity as a consequence of the angle between ketone groups by the meta- linkage (visible when comparing terephthalic and isophthalic acids in Figure 2.1), which causes disruption of the crystal packing [12].

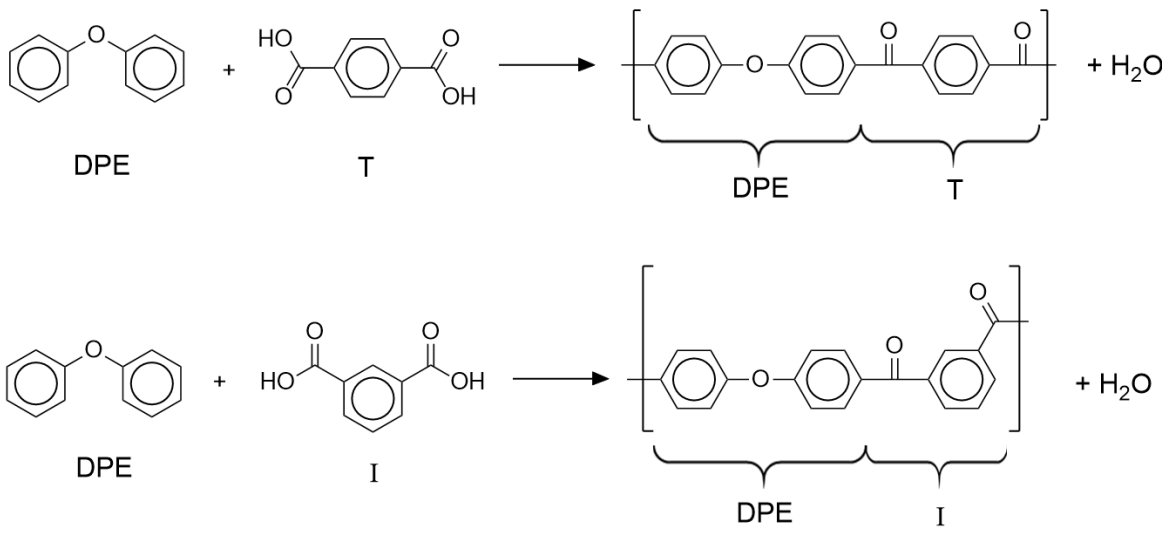

Figure 2.1: Chemical reaction for production of 1,4- (top) and 1,3- (bottom) substituted PEKK, by combining diphenyl ether (DPE) with terephthalic acid (T) or isophthalic acid (I).

In the case of PEEK, there is no way of achieving these differences in grades by varying para/meta linkages. The polymer is often produced by reacting 4, 4' difluorobenzophenone, hydroquinone and potassium carbonate, as per Figure 2.2 [17]. A lower ketone content makes PAEK polymers more malleable, allowing PEEK to crystallise more readily than PEKK.

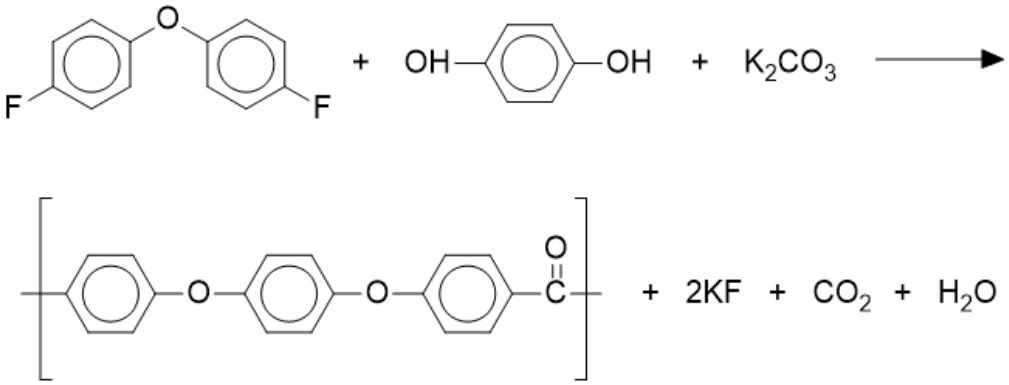

Figure 2.2: Chemical reaction for prodution of PEEK by combining 4, 4' difluorobenzophenone, hydroquinone and potassium carbonate. Drawn after [17].

Overall, the PAEK family of polymers crystallises easily due to the ether and ketone linkages they contain [17]: while the aromatic rings present in the backbone chain bring rigidity to the material, the flexible ether linkages provide some flexibility and allow for processability. The ketone linkages, despite being stiffer than ether linkages, have very similar bond angles (approximately 110° and 120° for ether and ketone respectively), allowing for neighbouring molecules to pack together without necessarily having identical sequencing. This is key in the potential for crystallisation. In the case of PEEK, as this is a highly even polymer with no meta- phenyl links, chain packing is more readily achievable. The higher ketone content in PEKK results in a heavier, stiffer chain structure and generally a more viscous polymer with slower crystallisation kinetics. As mentioned in page 6, crystallisation is also dependent on the T/I ratio, thereby making PEKK a more tuneable but challenging material to optimise [12,15,18]. This is conveyed in Figure 2.3, which shows a comparison of the chain packing of PEEK and of different T/I ratios of PEKK when sequencing is not identical.

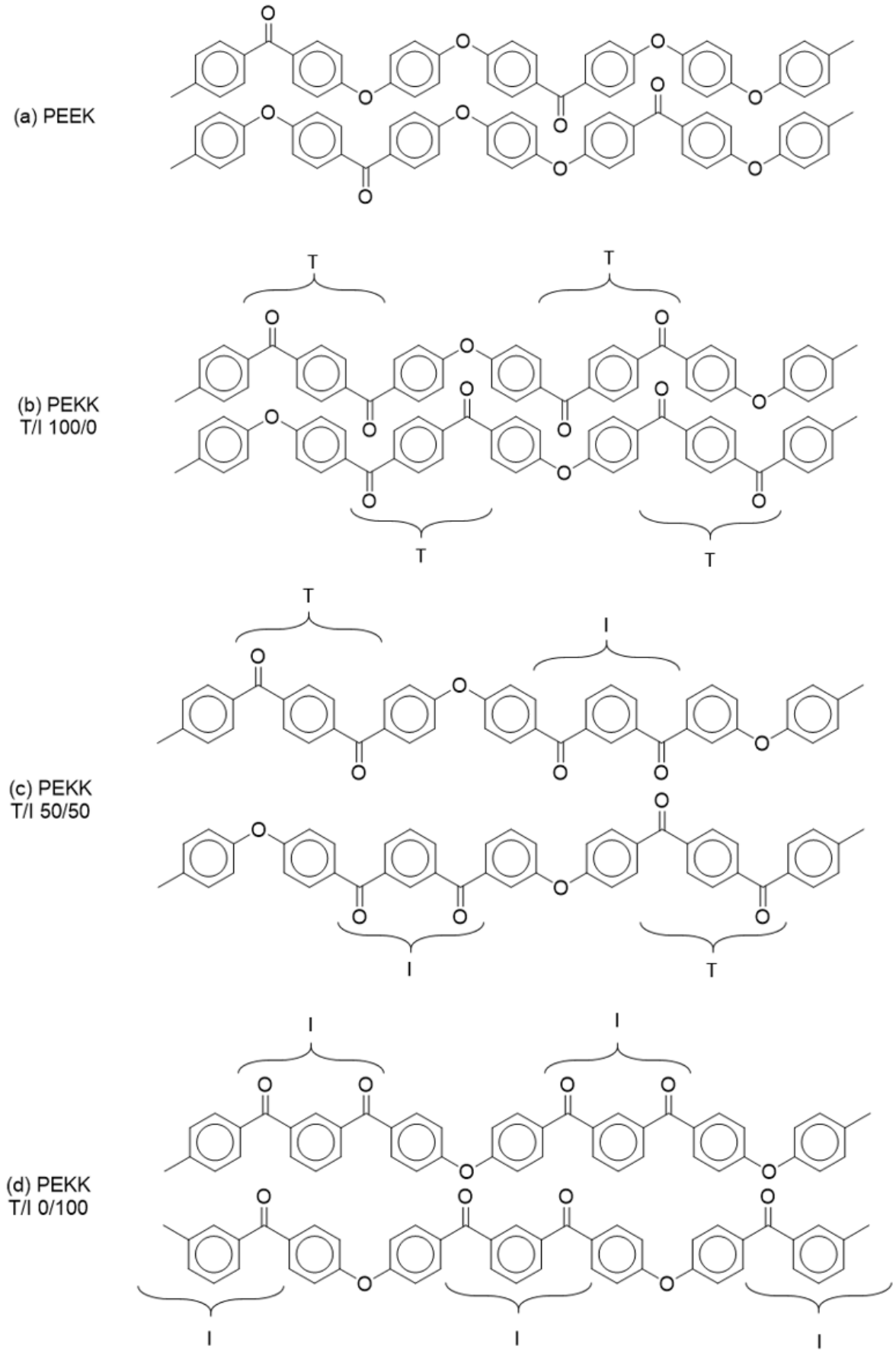

Figure 2.3: Chemical structures and chain packing of (a) PEEK and PEKK with various T/I ratios: (b) 100/0, (c) 50/50, (d) 0/100.

Table 2.2 shows different grades of KEPSTAN® PEKK offered by Arkema, where both the T/I ratio and the viscosity are varied [19]. An increase in the melt volume index within a specific T/I ratio as denoted in the second row suggests a lower viscosity.

Table 2.2: KEPSTAN(R) PEKK commercial range grades, based on T/I ratio and viscosity (adapted from webinar presentation) [19].

Viscosity level	**1**	**2**	**3**	**4**
Melt Volume Index*	11-24**	4-8	8-16	16-25
6000 series (T/I 60/40)	6001	6002	6003	6004
7000 series (T/I 70/30)	7001	7002	7003	7004
8000 series (T/I 80/20)	8001	8002	8003	8004

* MVI in cc per 10', at 380°c and under 1kg
** MVI measured under 5 kg for level 1 viscosity

2.1.2. Unit cell structure

All polymers contain an amorphous fraction of material due to polydispersity, material "defects" such as chain ends, and the entangled nature of polymer chains, preventing full crystallisation [16]. As described previously, the higher ketone content in PEKK results in higher chain stiffness, adding to the crystallisation difficulty. Nonetheless, PEKK can be crystallised during the manufacturing process or with subsequent annealing. Depending on the crystallisation conditions (from the melt, cold or solvent), not only one but two unit cell forms of crystallised PEKK may be present [3,4,13]. Unit cells are the simplest repeating unit within a crystal form, and are the building blocks of the spherulitic structures that form in PEKK. Spherulite formation is discussed further in Section 2.1.3.

These two different unit cell forms have been identified by Gardner et al. [12] as follows, and can be observed in Figure 2.4 and Figure 2.5 (form 1 and form 2 (i)). Both have been observed to be orthorhombic, with Form 1 accommodating two polymer chains, located at the centre and corner of the cell, with edge-to-face phenyl interactions. Form 2, on the other hand, was identified to accommodate a single chain, with face-to-face phenyl interactions. An alternative form 2 unit cell was identified by Blundell and Newton [20], with a 2-chain orthorhombic structure and face-to-face phenyl interactions, shown in Figure 2.4 (form 2 (ii)) [13,20–22]. There is no dual unit cell form in the case of PEEK due to its higher ether content, and so it only crystallises as form 1 [20].

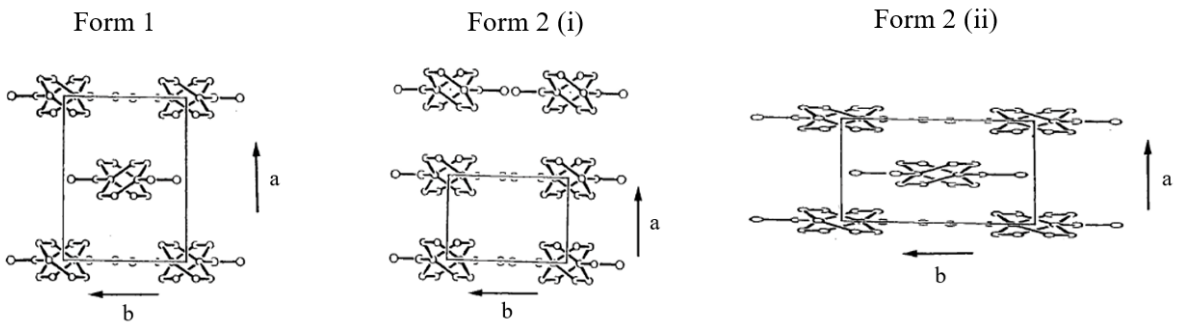

Figure 2.4: Crystal packing models of PEKK of form 1 (two-chain orthorhombic); form 2 (i) (one-chain orthorhombic as per Gardner et al. [12]); and form 2 (ii) (two-chain orthorhombic as per Blundell and Newton [20]) and unit cell dimensions.

Based on Figure 2.4, a three-dimensional schematic of each unit cell is included in Figure 2.5. The dimensions of each unit cell are available in Table 2.3.

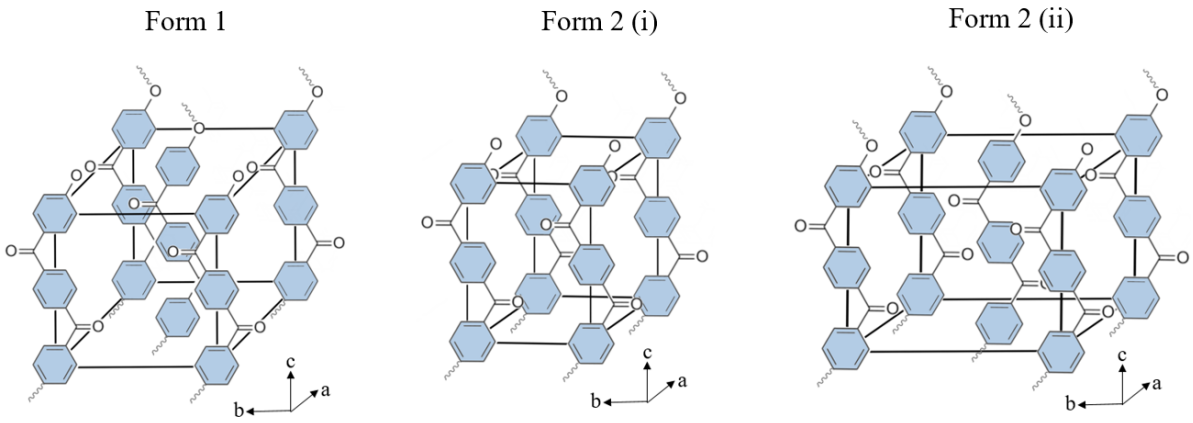

Figure 2.5: 3D schematic of crystal packing models of PEKK, based on Figure 2.4.

Table 2.3: Dimensions for the different unit cell forms of PEKK.

Unit cell	Dimensions (nm)			Reference
	a	b	c	
Form 1	0.769	0.606	1.016	[12]
	0.767	0.606	1.008	[22]
Form 2 (i)	0.393	0.575	1.016	[12]
Form 2 (ii)	0.417	1.134	1.008	[20,22]

This polymorphism has also been reported in other PAEKs. The presence of forms 1 and 2 has been found to depend on two factors:

a) Crystallisation mode, with melt crystallisation favouring form 1; and cold or solvent crystallisation favouring form 2 [3,13,21,22].
b) Chain stiffness, which increases in PAEKs with higher ketone content and with a higher T/I ratio, and favours form 2 [3,20,21].

In the case of PEKK, Gardner et al. [3] summarised the impact of T/I ratio and crystallisation method in the "phase diagram" shown in Figure 2.6. Further details on the impact of these variables can be found in their work, as well as in [12,13,20–22].

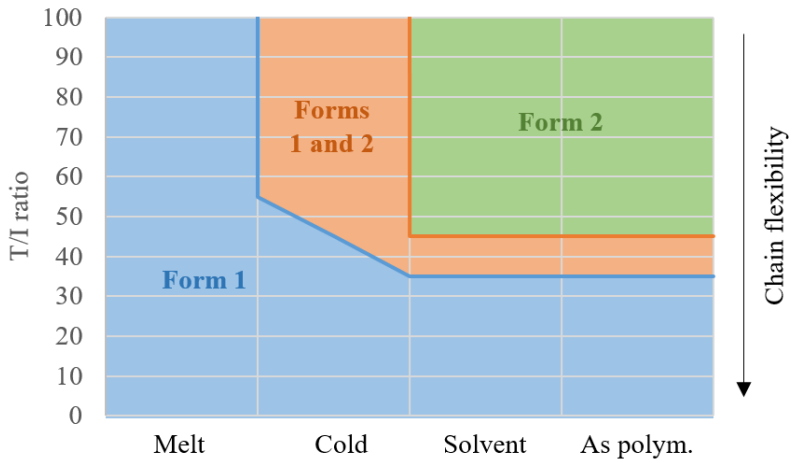

Figure 2.6: "Phase diagram" showing the occurrence of the two crystalline polymorphisms in PEKK as a function of the T/I ratio and the crystallisation conditions. Adapted from [3].

2.1.3. Spherulitic growth and lamellar structure

Regardless of the unit cell form that PEKK chains organise into when crystallising, these unit cells begin to form upon nucleation as shown in Figure 2.7 and Figure 2.8. Nucleation occurs during the cooling or solidification of a polymer melt, where polymer chains arrange themselves into ordered structures. This transition faces a thermodynamic barrier, where an initial nucleus has to be formed. It can be initiated by various factors, such as a temperature reduction changing the kinetics energy of the polymer chains; or the presence of sites that allow for nucleation to take place. Examples of these could be nucleating agents, or pre-existing polymer particles or sites that have not fully melted. Once a nucleation site has developed, this allows PEKK chains to further arrange themselves to form individual lamellae, as per Figure 2.9. These are separated by an amorphous zone consisting of chain ends and entangled segments. Lamellae then develop into sheaf-like structures which grow further in and out of plane to form spherulites, as shown in Figure 2.10 [1,4,17,23]. Choupin et al. [9] observed the spherulitic growth of PEKK 60/40 with hot stage microscopy, shown in Figure 2.11. The crystalline entities can be observed to grow independently with the same size until impingement, typical of instantaneous nucleation.

Figure 2.7: A schematic showing homogeneous nucleation, where a polymer chain commences nucleation without the presence of a foreign phase or particle.

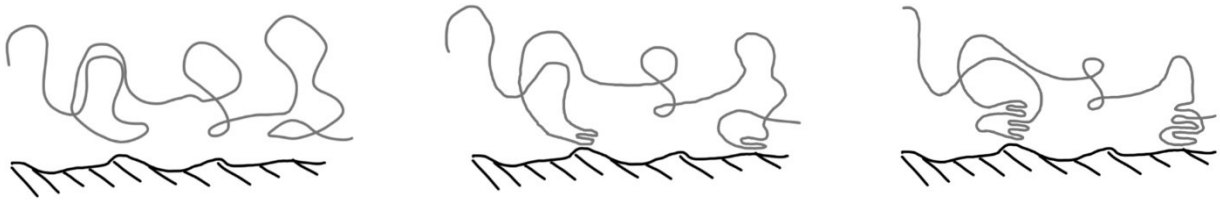

Figure 2.8: A schematic showing heterogeneous nucleation, where a polymer chain commences nucleation on the surface of a foreign particle.

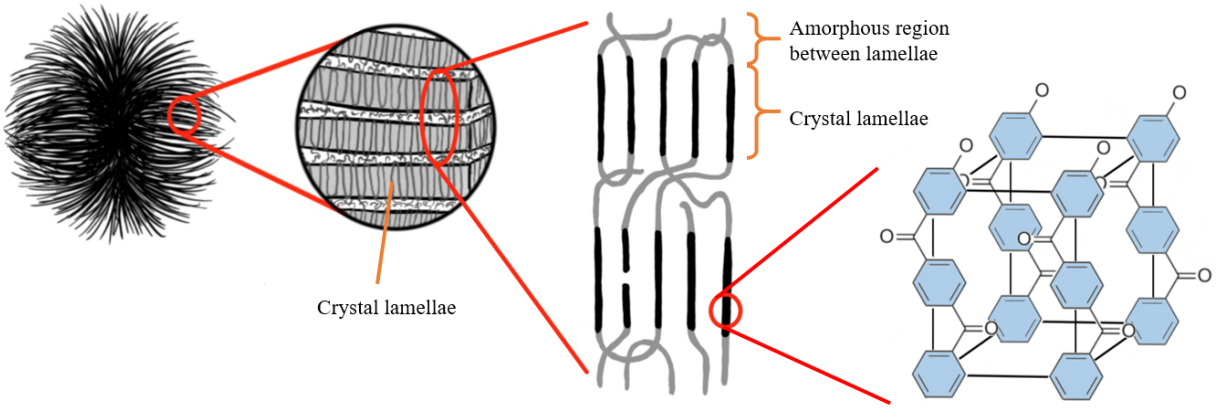

Figure 2.9: Crystalline morphology schematic, showing lamellae (crystal) and amorphous regions of a spherulite. Magnitude increases from left to right. Drawn after [4,23].

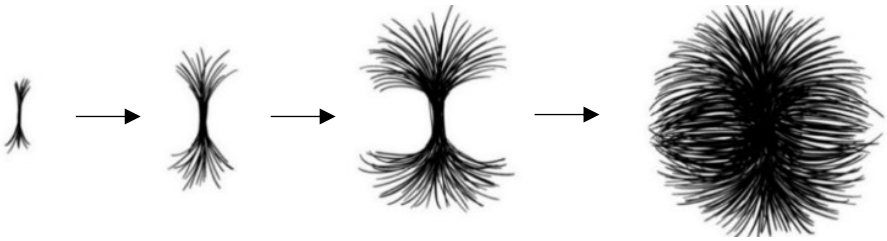

Figure 2.10: Spherulite formation schematic. Drawn after [23].

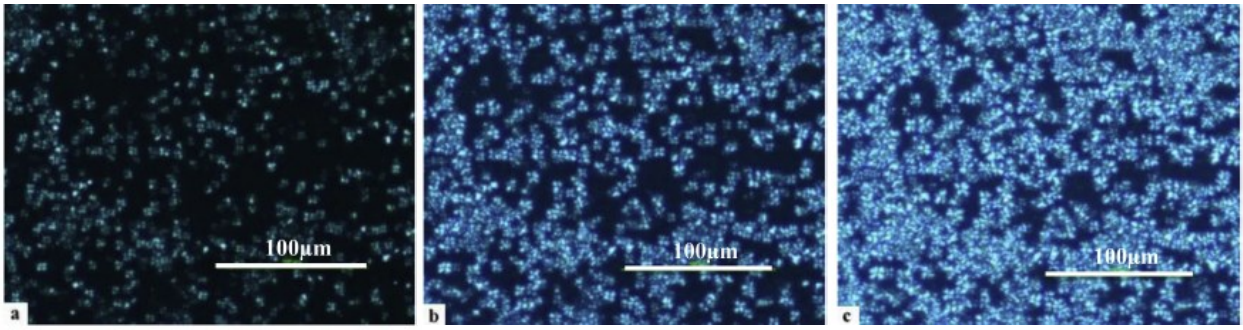

Figure 2.11: Micrographs of PEKK 60/40 crystallised from the melt at 270°C during (a) 20 min, (b) 30 min and (c) 40 min [9].

Spherulitic nucleation and growth are dependent on several factors. A low nucleation density and therefore large spherulites can be obtained if the polymer is held in the melt during extended periods of time, enough to destroy any pre-existing nucleation sites. The temperature can then be dropped to crystallise the material, in which spherulites will grow for as long as the material is held at crystallisation temperature, or until two spherulitic fronts meet and impinge on each other. Alternatively, higher nucleation densities can be obtained if the polymer is not held in the melt long enough, or if annealed, which may be common in fast-paced manufacturing techniques. Lee and Porter [24] observed this phenomenon, where they held PEEK samples with carbon fibres at 390°C (in the melt) for different lengths of time, and cooled to 270°C at 0.5°C/min, followed by quenching to room temperature. The results can be observed in Figure 2.12 below.

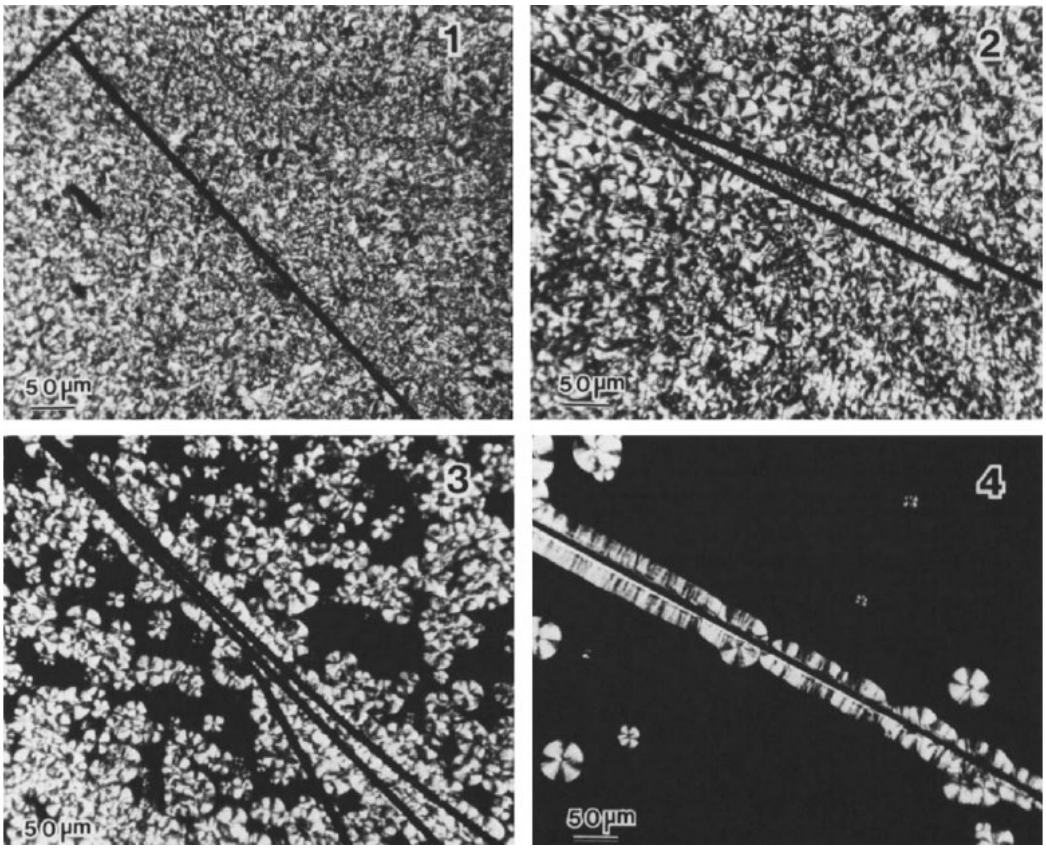

Figure 2.12: Optical micrographs of PEEK with carbon fibres: samples held at 390°C for (1) 0.5h; (2) 2h; (3) 3h; (4) 4h and cooled (0.5°C/min) to 270°C, followed by quenching to room temperature [24].

The matrix bulk in sample 4 (held for the longest time) can be observed to have fewer but larger spherulites of approximately 50 µm, whereas the opposite happens with the shorter times, resulting in the impingement of small spherulites in sample 1, with dimensions ranging between approximately 5-20 µm. Nucleation on fibre surfaces as observed in Lee and Porter's findings [24] will be discussed in the following section.

Blundell et al. [1] also observed such high nucleation densities in the bulk of CF/PEEK samples when the material was melted at a temperature not high enough to melt the last traces of crystallinity. They melted a sample at 355°C for 10 minutes (15°C above the peak melting point in a DSC scan), followed by cooling at 10°C/min. This resulted in self-seeding of the crystallisation process, resulting in a very high nucleation density and the prevention of spherulitic growth by mutual impingement, and therefore sheaf-like

structures were formed instead. This is in contrast to samples held in the melt at 400°C for 10 minutes and then cooled at 10°/min, where nucleation density was much lower and spherulite structures were clearly formed. SEM images of this can be found in their work [1].

2.1.4. Carbon fibre/PEKK and transcrystallinity

The use of fibres with high-performance thermoplastics has become increasingly popular in the aerospace and automotive industries, and is almost a necessity, due to their high strength and stiffness per unit weight. This makes composites an attractive replacement for previously used heavier materials for the same applications, such as steels, titanium and aluminium. The fibre/matrix interface plays an essential role in their performance, due to it being responsible for the transmission of stress from the matrix to the fibres. A transcrystalline interface has been observed in thermoplastic composites, the presence and size of which is dependent on the nucleating activity of the fibre surface as well as the crystallisation kinetics of the matrix [25].

In the case of carbon fibres, transcrystalline growth has often been related to the presence of small, graphitic crystals on the fibre surface, as well as the higher thermal conductivity promoting a conductivity mismatch between fibre and matrix [1,25]. In the case of CF/PEEK and CF/PEKK in particular, Hsiao et al. [14] concluded that, on top of these two factors, a similarity in unit cells is also a potential source of nucleation. The high nucleation density on the fibre surface causes neighbouring nuclei to impinge, resulting in a compact, unidirectional growth of crystals normal to the fibre surface, often referred to as "epitaxial" growth. This is in contrast to the spherulitic nature of crystallisation in the matrix bulk [24–31]. A schematic applicable to the crystallisation of PEEK and PEKK is shown in Figure 2.13.

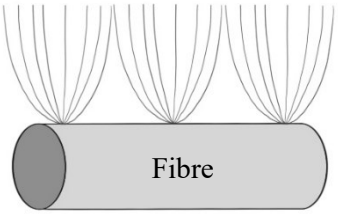

Figure 2.13: Diagram of transcrystalline interface growth on the fibre surface. Not to scale. Drawn after [25].

The presence of transcrystallinity on CF/PEEK and CF/PEKK composites is still a topic under investigation, as different observations have been reported by authors. Blundell et al. [1] observed no evidence of transcrystalline growth in etched CF/PEEK samples, but instead observed spherulitic growths on the fibre surface as per in the matrix bulk. On the other hand, Lustiger [32] observed differences in the transcrystallinity of CF/PEEK depending on the type of fibre used, something also noted by Chen and Hsiao [25] in CF/PEKK. The following paragraphs will investigate the source of these discrepancies.

In Lustiger's study [32], clear differences in the transcrystalline region were observed between low-modulus (AS4) and high-modulus (HMS) carbon fibres, where the surface energy played a critical role in the form of the transcrystalline region. The unsized fibres were placed in molten PEEK and held long enough in the melt to minimise any potential nucleation sites in the bulk, and to allow for large spherulitic growth. Flat-on lamellae were observed to grow on the AS4 fibres, whereas a high nucleation density was

observed on the HMS fibres, resulting in impingement before spherulites can fully form and therefore causing transcrystallinity. This has been attributed to differences in the fibres' surface energy: AS4 fibres have higher surface energy, inviting the amorphous interlamellar regions to interact with them, resulting in lamellae lying flat-on; whereas HMS fibres are relatively inert resulting in little attraction between the fibre surface and the amorphous polymer, and therefore lamellae can form perpendicular to the fibre surface. SEM micrographs displaying this behaviour are shown in Figure 2.14. These observations have been made in other literature [24,29,31–33] where it was concluded that the graphitic nature of HMS fibres results in a higher nucleation tendency, consistently generating transcrystallinity in PEEK and other semi-crystalline polymers. This is in line with the observations by Blundell et al. [1] mentioned earlier, as the carbon fibres used were AS4 (higher surface energy and therefore no transcrystallinity).

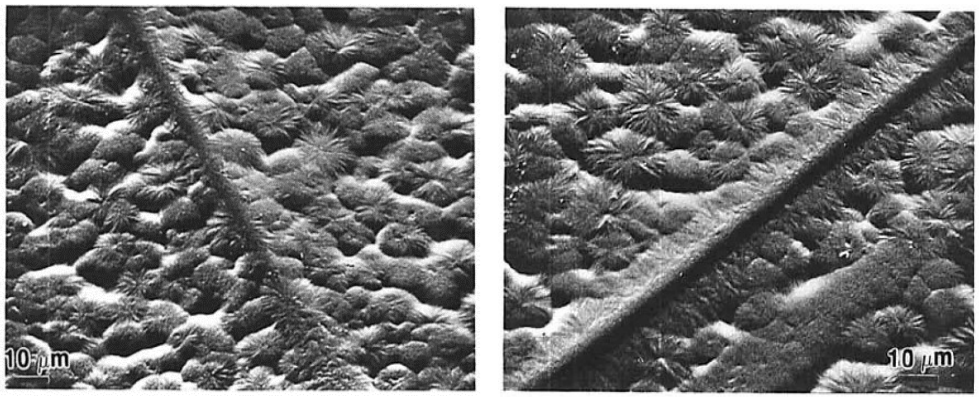

Figure 2.14: Left: spherulite nucleation in PEEK in contact with an unsized AS4 fibre. Right: transcrystallinity in PEEK in contact with unsized HMS fibre [32].

Chen and Hsiao [25], who studied the transcrystallinity of PEEK and PEKK on different fibres, observed a transcrystalline interface on pitch-based carbon fibres, taking the characteristic epitaxial form; while this was not the case on PAN-based AU4 carbon fibres. Pitch-based carbon fibre has interactive edge planes which result in a topographical match with the matrix crystal structure, whereas PAN-based carbon fibre is mostly defect-free, hindering nucleation on the fibre surface.

Lee and Porter [24] studied the nucleation ability of PEEK on Thornel 300 carbon fibres (PAN-based) supplied by Union Carbide, which clearly developed a transcrystalline region, particularly when CF/PEEK samples were held in the melt for long times and few spherulites are seen in the bulk, as shown in Figure 2.12. It is unclear, however, where Thornel 300 fibres fall in comparison with the previously mentioned fibres with regards to their strength and modulus. In fact, a connection between pitch vs. PAN-based fibres, as well as high-strength vs. high-modulus, and their connection and influence on transcrystallinity, is not clearly outlined in literature, and would be interesting to investigate further.

Overall, it can be concluded that PEEK and PEKK have the capability to form transcrystalline interfaces in the presence of carbon fibres, as long as said fibre has the correct surface characteristics to do so. There is some uncertainty, however, regarding the presence of transcrystallinity and its influence on mechanical properties, as literature has reported contradictory conclusions. The fibre volume fraction (FVF) of CF/PEKK and CF/PEEK composites has been observed to have an effect on this interface phenomenon. A higher fibre content results in a lower matrix spacing between fibres, limiting crystallisation growth both in the bulk and on the fibres [25,28,29]. While Chen and Hsiao [25] observed a 48% increase in force

during microdebonding tests of a single AU-4 filament/PEKK composite with a transcrystalline region (compared to its transcrystallinity-free counterpart), an increase in FVF decreased this difference, reducing to 0% difference at a FVF of 60%. Waddon et al. [31] observed preferential fracture along the line where two transcrystalline growth fronts met in a CF/poly(etherketone) sample, due to a structural discontinuity which is more susceptible to fracture. The presence of two neighbouring transcrystalline regions is most likely to occur in samples with high fibre content. This may be a reason for the reduced impact of transcrystallinity in higher FVF composites.

The development of a transcrystalline interface is also heavily reliant on the composite's processing: melting and crystallisation temperatures, holding times and cooling rates. This, as well as its effects on mechanical properties, is elaborated on in Section 2.2.3, after presenting the crystallisation kinetics of unreinforced PEKK.

2.2. Crystallisation kinetics

As discussed above, the properties of PEKK and any semi-crystalline thermoplastic polymer depend on the degree of crystallinity and their morphology. The understanding of crystallisation mechanisms is of fundamental importance in the case of high-performing thermoplastic materials, and plays a fundamental role in composites processing. This section will therefore provide a review of both isothermal and non-isothermal crystallisation kinetics of unreinforced PEKK. Isothermal crystallisation refers to holding the material at a constant temperature between glass transition temperature and melting temperature, allowing for the material to crystallise during this hold. Non-isothermal crystallisation refers to cooling the material from the melt at a constant cooling rate, throughout which the material will crystallise to a major or minor extent depending on the crystallisation kinetics the material possesses. The effect that carbon fibre reinforcement might have on these kinetics is also discussed in this section. A selection of graphs and data from various articles is included, showing the variation of matrix-dominated mechanical properties with respect to the manufacturing cycle the material undergoes. Studies covering the impact of thermal cycles on specifically crystallinity and mechanical behaviour are sparse, particularly on CF/PEKK. Thus, some data covering unreinforced PEKK, PEEK and CF/PEEK composites is included.

2.2.1. Isothermal crystallisation

Quiroga Cortés et al. [15] assessed the effect of both holding temperature and holding time on the crystallisation of unreinforced PEKK 60/40 (PEKK KEPSTAN 6003, supplied by Arkema). The results of this are shown in Figure 2.15 and Figure 2.16. Two endotherms can be observed: the standard melting peak, referred to as the high temperature endotherm (HTE) at around 300°C, and a smaller peak, called the lower temperature endotherm (LTE) at approximately 10°C above the holding temperature.

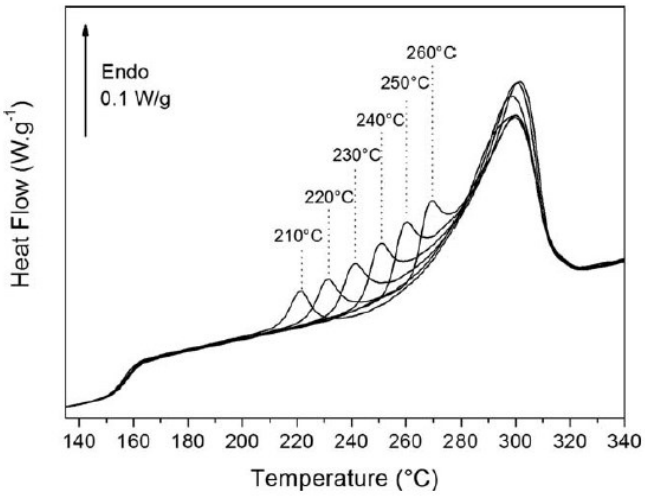

Figure 2.15: DSC thermograms of isothermally crystallised PEKK 60/40 at different temperatures (as indicated) for 60 min [15].

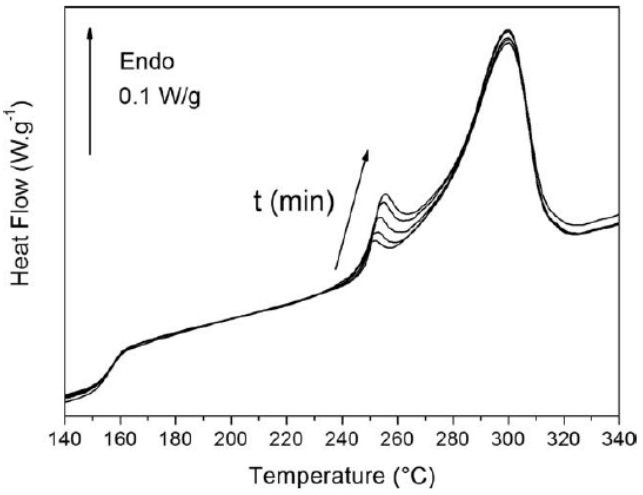

Figure 2.16: DSC thermograms of isothermally crystallised PEKK 60/40 at 245°C for different time periods [15].

Double melting behaviour has been observed by several authors in PEKK isothermal crystallisation [9,12,13,15,18,34,35], as well as in PEEK [4,36–49] during DSC. This additional low temperature endotherm (LTE) is reported to appear 10-20°C above the isothermal crystallisation temperature to which the polymer is subjected to, in PEEK and different grades of PEKK. This is shown in Figure 2.15, where each endothermic peak is labelled with the isotherm that the material has undergone. For example, the first peak labelled as 210°C occurs at approximately 220°C. The size of the endothermic peak is affected by the time the polymer is held at the isotherm for, increasing in size and slightly increasing in peak temperature with time as per Figure 2.16 [15]. The temperature at which the higher temperature endotherm (HTE) takes place, related to classic melting, is not affected by the annealing temperature or time.

The LTE in PEEK has been associated with different hypotheses: crystal reorganisation during heating, and the melting of less thermally stable crystallites [15,36,40,42,45]. Spherulites are formed of branching individual lamellae during primary crystallisation, with additional subsequent infilling between the lamellae. In PEKK, this has been attributed to the melting of this secondary structure within the spherulites [9,12,15,35,50]. It can therefore be established that PEKK crystallises with two different crystallisation processes: a primary crystallisation of amorphous material which takes place at the early stages of crystallisation, during which spherulitic entities are formed (as described in Section 2.1.3); and a secondary stage, during which interlamellar crystalline structures grow. These two processes are not independent: a structure developed by primary crystallisation must be established before secondary crystallisation can take place.

Quiroga Cortés et al. [15] also assess the crystallinity evolution of PEKK. A summary of this is presented in Table 2.4. As expected, crystallinity increases as the material is held for longer at the isotherm. With regards to the annealing temperature, results show that PEKK 60/40 reaches its highest crystallisation at around 250°C (even though further tests at 240°C would perhaps provide more clarity to this value). The total crystallinity achieved within the specified timeframe used in these experiments is heavily linked to the crystallisation kinetics of the material at different isothermal temperatures.

Table 2.4: Transition temperatures and crystallinity of PEKK 60/40 after annealing. Table excerpt from [15].

Holding temp.	Holding time	Low temp. endotherm	High temp. endotherm	Total crystallinity
210°C	60 min	221.0°C	300.0°C	22.2%
220°C		231.5°C	300.0°C	24.3%
230°C		241.5°C	299.5°C	26.2%
250°C		260.0°C	300.5°C	27.3%
260°C		270.0°C	301.5°C	26.5%
245°C	5 min	251.5°C	300.0°C	22.5%
	10 min	252.5°C	300.0°C	23.4%
	20 min	253.5°C	300.0°C	24.5%
	40 min	255.0°C	300.0°C	25.6%
	60 min	255.5°C	300.5°C	26.4%

Holding isotherms at different temperatures was further explored by Gardner et al. [12] with different grades of PEKK. The results of this can be observed in Figure 2.17. PEKK 90/10, 80/20 and 70/30 show a clear double-melting behaviour. However, PEKK 60/40 and 50/50 show a more complicated melting. This is likely due to the increase in meta- linkages, which, as discussed previously, increases chain flexibility. There are two relative rotations of phenyl rings across a meta- linkage, which may result in different, more complex packing interactions in PEKK grades with higher meta- linkage content [12]. On top of this, PEKK 50/50 is also a homopolymer, while the rest of the grades are random copolymers. This not only makes PEKK 50/50 the specimen with the highest flexibility, but also with the highest chain regularity, potentially complicating the crystallisation and melting behaviour of the material [12].

It is worth noting that the slightly more complicated melting behaviour observed in Gardner et al.'s results for PEKK 60/40 [12] is not visible in Quiroga Cortés et al.'s work [15]. This may be due to other differences in the polymers, such as polymer synthesis process, average molecular weight and molecular weight distribution, since the material suppliers are different for each article.

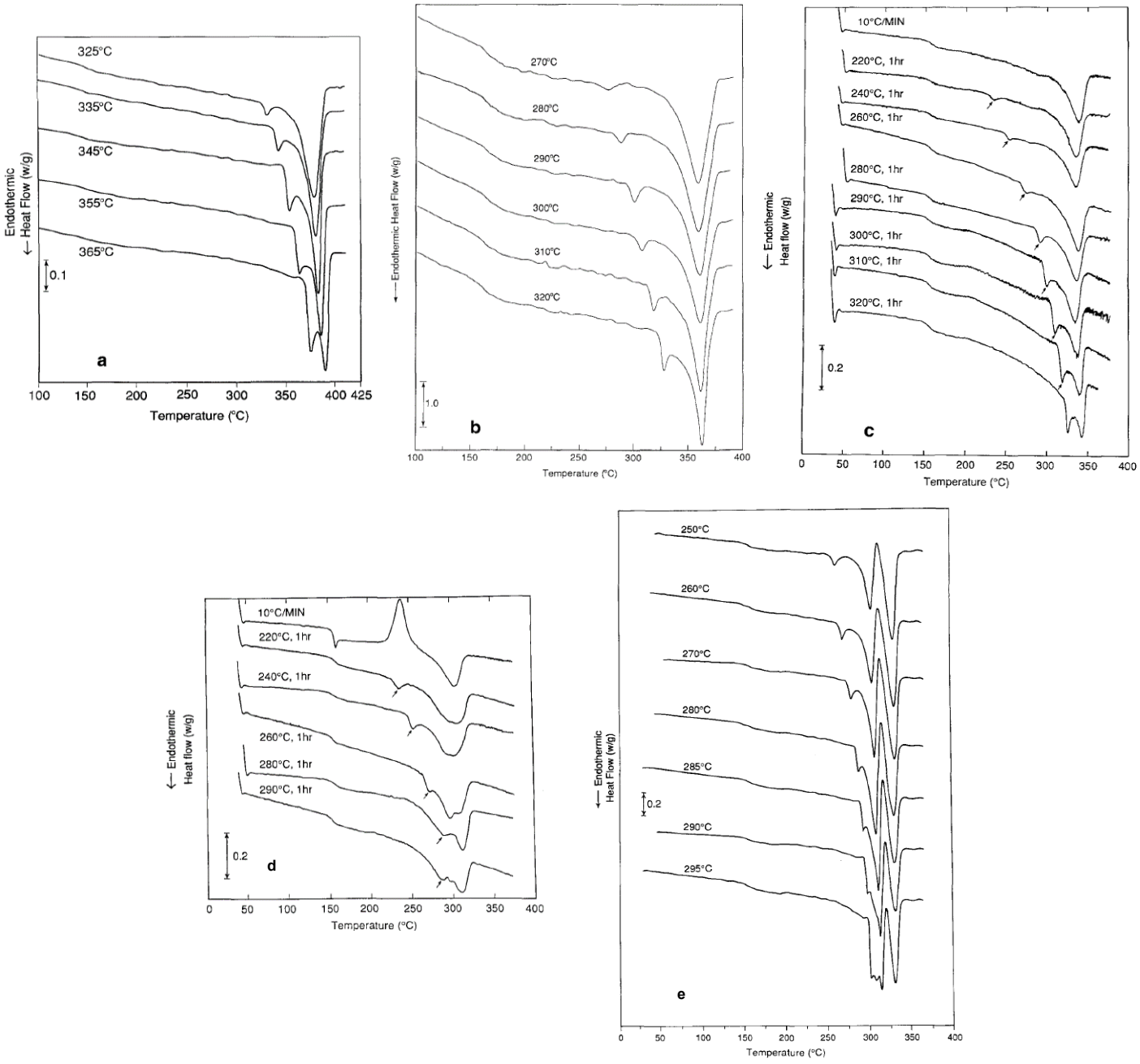

Figure 2.17: DSC scans of PEKK specimens annealed at different temperatures: (a) PEKK 90/10, (b) PEKK 80/20, (c) PEKK 70/30 (d) PEKK 60/40, (e) PEKK (50/50) [12].

In comparison to PEEK, overall crystallinity is lower in PEKK, which is to be expected due to PEEK's higher content of the more flexible and less bulky ether linkages, which facilitate faster crystallisation; as well as the exclusive para- linkages that PEEK has, enabling the polymer chain to be locally straight. In PEKK, particularly with lower T/I ratios, meta- linkages do not allow for this, hindering chain packing, as shown in Figure 2.3 [3,13,15,17,22].

2.2.2. Non-isothermal crystallisation

Crystallisation in any thermoplastic polymer is affected by the cooling rate that it undergoes. Assessing crystallisation under non-isothermal conditions is perhaps a more realistic way of understanding the crystallisation process in fast-paced manufacturing environments. Quiroga Cortés et al. [15] performed a thorough study on several grades of KEPSTAN PEKK supplied by Arkema, subjecting the materials to a variety of cooling rates after erasing any thermal history. The resultant DSC heating scans with different cooling rates are shown in Figure 2.18, and crystallinities from each cooling rate are summarised in Table 2.5 below.

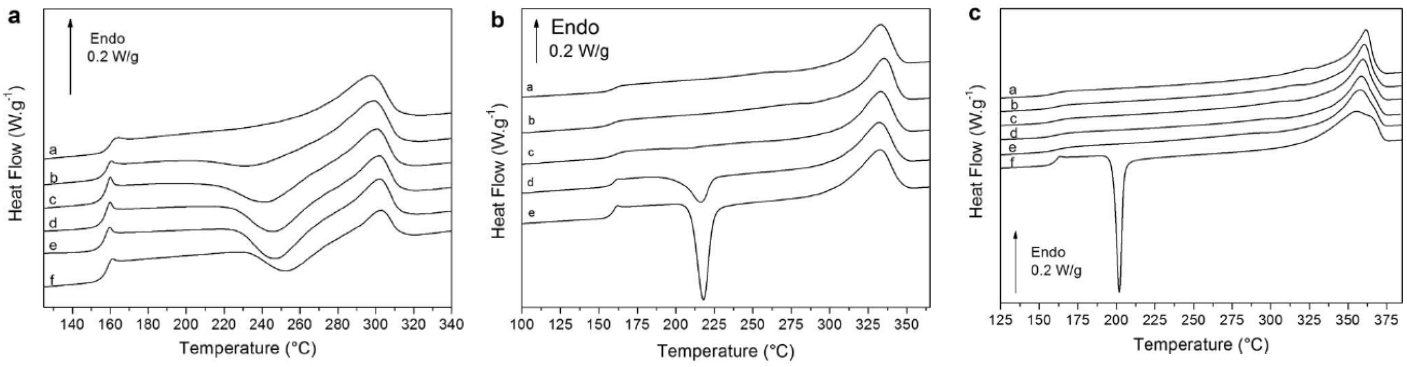

Figure 2.18: DSC thermograms of PEKK at 10°C/min after different cooling rates.
*Plot **a**, PEKK 60/40: (a) 2°C/min, (b) 5/C min, (c) 10°C/min, (d) 20°C/min, (e) 40°C/min, and (f) quenched.*
*Plot **b**, PEKK 70/30: (a)10°C/min, (b) 20°C/min, (c) 40°C/min, (d) 60°C/min, and (e) quenched.*
*Plot **c**, PEKK 80/20: (a) 5°C/min, (b) 10°C/min, (c) 20°C/min, (d) 40°C/min, (e) 60°C/min, and (f) quenched [15].*

Table 2.5: Crystallinity percentage for PEKK samples subjected to cooling at various cooling rates. Table excerpt from [15].

PEKK grade T/I ratio	Cooling rate	Crystallinity
KEPSTAN 6003 60/40	0.5°C/min	28.4%
	1°C/min	27.0%
	2°C/min	21.6%
	5°C/min	14.1%
	10°C/min	2.5%
	20°C/min	2.7%
	40°C/min	2.5%
	60°C/min	2.5%
	Quenched	0.5%
KEPSTAN 7003 70/30	10°C/min	27.7%
	20°C/min	28.1%
	40°C/min	25.2%
	60°C/min	15.8%
	Quenched	3.2%
KEPSTAN 8002 80/20	5°C/min	34.0%
	10°C/min	33.8%
	20°C/min	33.2%
	40°C/min	32.9%
	60°C/min	31.5%
	Quenched	7.1%

These results show, as expected, that a higher cooling rate results in a lower crystallinity percentage. A higher cooling rate inhibits any chain reorganisation that takes place when cooling from the melt, hindering crystal structure formation. This increases the amount of amorphous phase present, which undergoes cold crystallisation during subsequent heating. The cold crystallisation peak is therefore larger with a higher cooling rate [15]. PEKK with lower T/I ratios becomes progressively more susceptible to the cooling rate, and has a lower crystallisation, further reinforcing the discussion in Section 2.1.1.

Chang and Hsiao [34] briefly cover the effect of cooling rates on PEKK as well. The grade of the polymer is unknown, however, the melting temperature obtained (338°C) suggests that the T/I ratio may be approximately 70/30. Despite not reporting any quantitative values of crystallinity developed, their cooling DSC thermograms show a melt crystallisation exotherm occurring at progressively lower temperatures with higher cooling rates. This suggests that melt crystallisation requires a larger gap between melting and crystallisation temperatures (a larger supercooling) as the cooling rate increases [34]. The crystallisation start, peak and end temperatures are therefore strongly dependent on the cooling conditions, also observed in PEEK [37,51].

Similar to PEKK, the crystallisation percentage of PEEK decreases with an increase in cooling rate. However, the decrease is substantially smaller, particularly when compared to PEKKs with lower T/I ratios. As per the isothermal crystallisation analysis, PEEK also seems to obtain a higher crystallinity than PEKK when cooled at the same rate. This is due to the higher ether content and purely para- linkages that PEEK possesses, as discussed previously, resulting in faster crystallisation kinetics. Gao and Kim [29] in fact observe a small cold crystallisation exotherm for PEEK at 600°C/min cooling rate while achieving a crystallinity of 26%, and go up to 1500°C/min where a crystallinity of 17% was observed.

Unlike during isotheral crystallisation, associating the primary and secondary crystalline phases to the presence of two distinct endothermic peaks poses a limitation in the case of non-isothermal crystallisation studies. The DSC melting curves in Figure 2.18 showed a single melting endotherm, corresponding to conventional melting (the HTE), as well as a cold crystallisation exotherm in some curves, indicating the presence of amorphous material in the samples as a consequence of the faster cooling rates. The absence of an LTE is not addressed in this case. Bessard et al. [37] performed a similar study on PEEK, where they observed a shoulder at the beginning of the single melting endotherm for the slower cooling rates, indicating some contribution from the secondary crystallisation. Similar observations were made by Regis et al. [52] and by Lustiger et al. [53] in their work on PEEK and carbon fibre (CF)/PEEK. The presence of secondary crystallisation in slow-cooled PEEK can be explained by the faster kinetics that PEEK possesses compared to PEKK, due to PEEK's higher chain linearity and lower ketone content. Since the development of secondary crystallisation is determined by time, it is therefore logical that there will be a lower contribution of secondary crystallisation (if at all) at faster cooling rates. The absence on an LTE in non-isothermal PEKK studies may suggest that there is no secondary crystallisation phase present in PEKK after undergoing dynamic cooling from the melt, however this has not been explored or discussed in depth to date.

2.2.3. Crystallisation kinetics in composites and effect on mechanical properties

The introduction of carbon fibres into PAEKs has been observed to have an effect on its crystallisation kinetics and transcrystalline interface. Literature covering the effect of this in PEKK, however, is minimal. This section will therefore include some reporting of PEKK in theses, but will mainly focus on published literature covering the effect of these inclusions in PEEK, particularly when discussing transcrystallinity.

Gao and Kim [29] obtained 1-5% lower overall crystallinities in CF/PEEK than in its neat counterpart when undergoing different cooling rates. They suggested this may be due to the presence of densely packed fibres suppressing spherulitic growth, as discussed previously. Velisaris and Seferis [30] explained this as being due to the presence of carbon fibres decreasing the extent to which the primary crystallisation process takes place, causing a drop in the final degree of crystallinity. They used different grades of PEEK in their work however (450P powder for neat PEEK, and APC2 tape for the composite, which is similar to 150P PEEK grade [14]), so a direct comparison may not be applicable. In the case of PEKK, Hsiao et al. [14] reported that the presence of fibres had little effect on the relative volume fraction crystallinity under isothermal conditions, possibly due to its rapid nucleation ability.

The impact of fibres on kinetics has been investigated to some extent. Hsiao et al. [14] reported once again that the inclusion of fibres had minimal impact on the crystallisation rate of PEKK under isothermal conditions, as shown by the very similar crystallisation peak times reported in Figure 2.19. On the other hand, higher fibre contents in Lee and Porter's work [24] with CF/PEEK showed faster kinetics than unreinforced PEEK under dynamic conditions, where the peak crystallisation temperature shifted from 283°C at 0% carbon fibre volume content to 286°C at 18.5% carbon fibre volume content while cooling at 20°C/min. A potential reason for this is discussed later in this section and in Section 2.3.3, where fibre surface energy may be inducing transcrystalline growth and increasing nucleation and crystallisation rate. However, as will be discussed, the reasons behind this are not elaborated on in literature.

A larger temperature range study is offered by Harris in their thesis [54], where they compared crystallisation kinetics of PEEK and CF/PEEK between 310°C and 318°C. They found that kinetics are similar at low isothermal temperatures, whereas PEEK composites crystallise faster at higher temperature isotherms. Harris attributed this behaviour to the fact that at higher temperatures, nucleation kinetics in the bulk will be low and the carbon fibres act as stress initiators for nucleation; whereas at lower temperatures, nucleation kinetics in the bulk are incentivised, and fibres hinder the matrix macromolecular chain mobility. This behaviour can be observed in Figure 2.20, where the half-times for the composite can be seen to be considerably lower at high temperatures, and closer to unreinforced PEEK at lower temperatures.

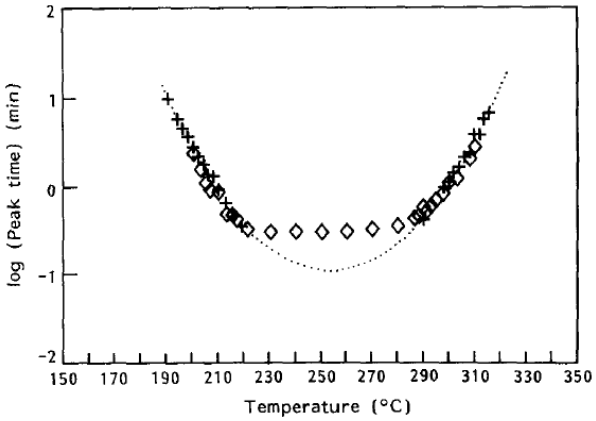

Figure 2.19: Crystallisation peak time vs. temperature for PEKK resin ◊ and its AS4/PEKK carbon fibre-reinforcement composite +. The dotted curve represents the fit from a second-order polynomial equation [14].

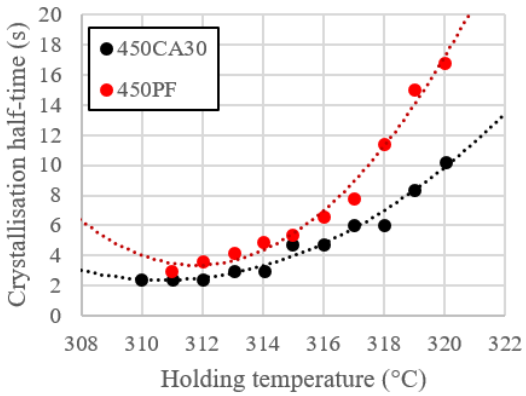

Figure 2.20: Comparison of half-time values for unreinforced PEEK (450PF in red) and CF/PEEK (450CA30 in black). Adapted from [54].

A similar conclusion was reached by Choupin in their thesis work [28], where they observed kinetics of PEKK and CF/PEKK (grade 60/40) at a variety of isotherms, ranging from 200°C to 275°C. At temperatures above 265°C, crystallisation kinetics in the bulk are slower and thus the main crystallisation mechanism takes place on the carbon fibre surfaces, resulting in a faster crystallisation in the composite material; whereas at temperatures below 265°C, nucleation kinetics in the bulk dominate and the fibres play a lesser role, and therefore the difference in kinetics is smaller.

Primary crystallisation has overall been observed to be hindered by the fibre, resulting in less perfect crystalline entities and an increased secondary crystallisation.

The phenomenon of transcrystallinity, in particular, is also directly impacted by holding temperature and cooling rate. This is linked to the above discussion of Choupin's work [28], where high isothermal crystallisation temperatures coming from the melt favour the occurrence of transcrystallinity in PEKK, due to the carbon fibres acting as nucleation agents, whereas the opposite happens at low crystallisation temperatures. Similarly, slower cooling rates from the melt will allow for larger crystallisation growth from the fibre surface, and less nucleation from the bulk. Gao and Kim [29] observed a large amount of fibre nucleated spherulites in slow-cooled (1°C/min) AS4 CF/PEEK composites, where the developed crystallisation is well defined and larger in size, whereas fast-cooled (1000°C/min) specimens displayed a mixture of smaller, isolated and fibre-nucleated spherulites. Tung and Dynes [55] also observed a noticeably developed transcrystalline region in slow-cooled samples (1.5°C/min), while that was not very apparent in fast-cooled samples (70°C/min, 2500°C/min) of CF/PEEK.

The presence of transcrystallinity is also dependent on the holding time of the material in the melt, now that this will determine the extent to which traces of previous spherulites or "defects" in the matrix are still present as nucleation sites. A longer holding time will increase the homogeneity in the bulk, leaving fewer nucleation sites available in the matrix and therefore allowing for a more developed transcrystalline region [24,56]. On the other hand, simply annealing a sample will create a high nucleation density and will not allow for any further development of transcrystallinity. This can be observed in Lee and Porter's work [24] shown in Figure 2.12 in Section 2.1.3, where the CF/PEEK sample held the longest in the melt (4 hours) developed a clear transcrystalline region, whereas the sample held for the shortest time (0.5 hours) developed a very high nucleation density in the matrix and no visible transcrystallinity.

The morphological impact that different processing conditions have on CF/PAEK composites also play a crucial role in the performance and failure mechanisms of the materials and their fibre-matrix interface. Gao and Kim [29] collected data on interfacial shear strength (IFSS) of identical AS4 CF/PEEK systems [57–60], which were found to vary widely (40-110 MPa) partly as a consequence of the different processing and testing conditions used. Overall, Gao and Kim [29] observed a much better fibre-matrix adhesion at slow cooling rates with fibre pull-out tests, these being characterised by brittle fracture with little matrix deformation along the fibre. This was likely due to a crystal structure developing at the interface, resulting in a better fibre-matrix load transmission during mechanical testing. Fast cooled specimens, on the other hand, displayed extensive plastic yielding, a common behaviour typical of amorphous phases. This is observable in their SEM images in Figure 2.21, where ordered structures are visible on the fibre surface of the slow-cooled sample at 1°C/min (with a crystallinity of 33%), and a smooth surface in the fast cooled counterpart at 1800°C/min (with a crystallinity of 12%) [29,56]. This is due to the time that the polymer is exposed to higher temperatures. PEEK molecules tend to uncoil further when undergoing slow cooling rates or higher temperature isotherms, and therefore get adsorbed more onto the fibre surfaces.

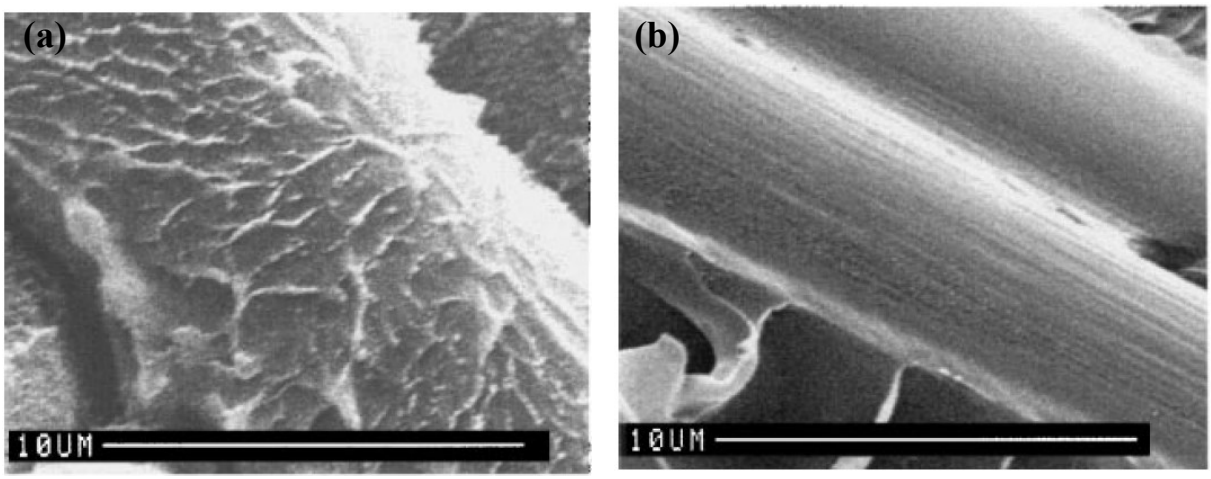

Figure 2.21: Scanning electron micrographs of fracture surfaces of CF/PEEK cooled at (a) 1°C/min and (b) 1800°C/min [29].

Gao and Kim's studies [29] compliment Saiello et al.'s findings [61] on how different isotherms affect fibre/matrix adhesion. They observed differences on the surfaces of cryo-fractured CF/PEEK samples that had undergone cold crystallisation at 180°C, or had been held in the melt and then crystallised at 320°C for 60 minutes each. SEM results showed some ordered structures in the matrix of the annealed sample, as expected from holding in an isotherm, however the fibre surfaces were clean, indicating little fibre-matrix interaction (adhesive failure). On the other hand, the fibres of the specimen crystallised from the melt were still covered by the matrix after fracture, which could be observed to have some form of order (cohesive failure). These observations were in line with further SEM observations that they made with as-received amorphous (<5%) and crystalline (30%) CF/PEEK samples in the same work. Figures showing these results are available in their work [61].

The above discussion tackles the effect of fibre-matrix adhesion in general, but does not provide a focus on transcrystallinity in particular. In fact, despite the above findings, the effect of transcrystallinity on mechanical properties and interfacial strength is a topic of controversy. There is a consensus on its properties being different to that of the matrix bulk [25,29,62–64], however the results reported in

literature are somewhat conflicting across different matrix materials. Chen and Hsiao [25] carried out micro-debonding tests on carbon fibres embedded in a PEKK matrix, prepared by heating a sandwich of matrix film and fibres. The test was performed by applying a stepwise compression loading on a single fibre until debonding takes place, identified by a microscope. They concluded that the presence of a transcrystalline region increases the strength of CF/PEKK by 40% when compared to its amorphous counterpart. Saiello et al. [61] agreed on the fact that having some form of crystalline fibre-matrix adhesion has a positive effect on the interface properties in comparison to having a fully amorphous interface.

When compared to bulk crystallinity, however, there is uncertainty regarding whether a transcrystalline region is beneficial for the composite's strength or not. Gao and Kim [29] proposed that the build-up of thermal stresses during the transcrystallisation process can reduce interfacial shear strength, whereas the presence of a transcrystalline region decreases the mismatch of moduli between fibre and matrix, improving the stress transfer across the interface and hence the composite's mechanical properties. This hypothesis is not supported uniformly across the available literature: Lustiger [32] compared the low and high modulus fibres discussed previously, showing that CF/PEEK systems with a transcrystalline region have a lower ILSS and transverse flexural strength, dropping by almost 25% and 50% respectively. This was further reinforced by visual inspection, where AS4 fibres (with no developed transcrystallinity) were well coated with the matrix material, while HMS fibres (which showed a transcrystalline region) appeared clean. On the other hand, Lee and Porter [24] concluded that a transcrystalline region in CF/PEEK systems results in twice the strength in transverse tensile tests when compared to other samples with no interface but of similar crystallinity.

Overall, the crystallisation kinetics of CF/PAEK systems and the effects of transcrystallinity need further research. While some literature is available reporting differences in crystallisation kinetics between the two, this is either not peer-reviewed (such as the theses by Choupin and Harris) or is not in-depth. Further to this, literature focusing on PEKK in particular is minimal. Even though PEEK and PEKK behave comparably, further research is needed in CF/PEKK systems in order to further quantify and understand this material's behaviour.

2.2.4. Matrix-dominated mechanical properties

This section offers a brief review of the mechanical properties of unreinforced PEKK, PEEK and matrix-dominated properties of CF/PEKK and CF/PEEK when undergoing a range of different manufacturing cycles observed by several authors. As the impact of crystallinity on the composite's performance has already been discussed in Section 2.2.3, this section will focus on providing a collection of data available in literature, and discussion is kept to a minimum.

While there is limited data available on the impact of crystallinity on the performance of CF/PEEK or CF/PEKK, some literature does cover this in the case of unreinforced PEKK and PEEK. This is the case of Figure 2.22 and Figure 2.23, adapted from Choupin et al. [65] and Gao and Kim [29] respectively, which show tensile properties of PEKK and PEEK. While the samples in each figure have been prepared differently (the PEKK samples underwent different isothermal holds, whereas the PEEK samples underwent various cooling rates), the plots still allow for a comparison between mechanical performance

and crystallinity. A higher crystallinity induces a higher strength and stiffness in both materials, due to the presence of ordered molecular chains. This results in tighter molecular and crystal packing, which leads to increased resistance to deformation and hinders any slipping of material in the crystal structures. [29]. A lower crystallinity therefore results in a more ductile material, with lower strength and stiffness.

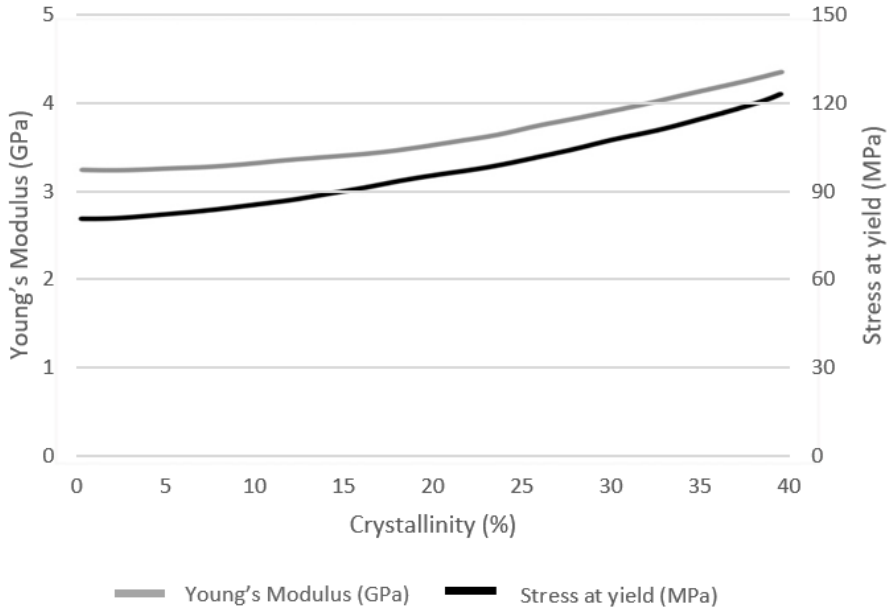

Figure 2.22: Young's modulus and stress at yield vs. crystallinity at room temperature of neat PEKK crystallised at 230°C from the glassy state. Adapted from [65].

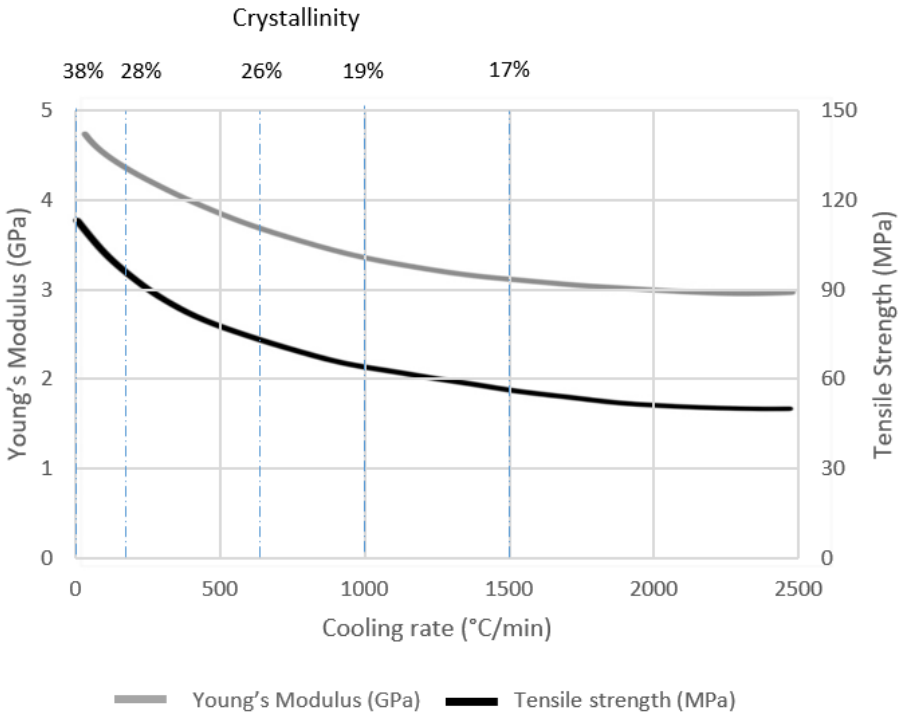

Figure 2.23: Tensile strength, Young's modulus and crystallinity of neat PEEK as a function of cooling rate. Adapted from [29].

A study covering matrix-dominated properties of CF/PEKK composites was performed by Choupin in their thesis work [28], the results of which are shown in Table 2.6. While these do not show a spectrum of crystallinities and the impact of this on matrix behaviour, they show the difference between fully crystallised and amorphous matrix composites where possible. In PEKK 6002 (T/I ratio 60/40), a clear decrease in the properties can be observed for the amorphous samples, which becomes much more distinct when tested at 180°C. More information on this can be found in their work [28].

Table 2.6: Crystallinity, shear modulus (GPa) and Young's modulus (GPa) of ±45° of PEKK composites manufactured under different conditions, tested at room temperature and 180°C. Adapted from [28].

Material	**Processing conditions**	**Crystallinity**	**Shear modulus (±45° tensile test)**		**Young's Modulus (±45° tensile test)**	
			Test temperature		Test temperatures	
			T_{room}	**180°C**	**T_{room}**	**180°C**
CF/PEKK 6002	Autoclave (10 min at 360°C, followed by 2h at 230°C)	30%, fully crystallised	5.6	0.53	16.5	1.9
	Press (10 min at 360°C, followed by 2h at 230°C)	30%, fully crystallised	5.1	0.49	17.3	1.7
	Press (10 min at 360°C, followed by 20°C/min cooling rate)	5%, amorphous	3.7	0.046	15.4	0.33
CF/PEKK 7002	Autoclave (10 min at 380°C, followed by 20°C/min cooling rate)	33%, fully crystallised	4.4	0.39	17.9	1.6
	Press (10 min at 380°C, followed by 20°C/min cooling rate)	28%, fully crystallised	4.6	0.33	17.8	1.2

Choupin [28] also performed high (from the melt) and low (from the glassy state) isothermal holds to observe potentially high and low amounts of transcrystalline phases respectively. Due to low residual nuclei, the isothermal hold from the melt would allow for a transcrystalline region to form, whereas when crystallising from the glassy state, this is unlikely to be the case. The results of ±45° tensile tests are available in Table 2.7. The shear modulus and Young's modulus can be observed to be 22% and 2% higher at room temperature, and 12% and 38% higher at 180°C respectively for CF/PEKK composites crystallised at a higher temperature. This behaviour could be attributed to a higher amount of transcrystalline region present in the sample crystallised at a higher temperature, resulting in a better load transfer between fibre and matrix, as per the discussion in Section 2.2.3.

Table 2.7: Crystallinity, shear modulus (GPa) and Young's modulus (GPa) of ±45° of PEKK composites held at different isothermal conditions, tested at room temperature and 180°C. Adapted from [28].

Material	**Processing conditions**	**Crystallinity**	**Shear modulus (±45° tensile test)**		**Young's Modulus (±45° tensile test)**	
			Test temperature		**Test temperature**	
			T_{room}	**180°C**	**T_{room}**	**180°C**
CF/PEKK 6002	Autoclave (10 min at 360°C, followed by 4h at 260°C)	28%, fully crystallised	4.7	0.51	17.76	2.4
	Press (10 min at 360°C, followed by 20°C/min to room temperature, then 4h at 200°C)[66]	30%, fully crystallised	3.68	0.45	17.44	1.5

In a recent study, Hoang et al. [66] manufactured a series of CF/PEKK laminates via automated tape placement, which they then post-processed under different conditions and performed interlaminar shear strength testing. A summary of the results is shown in Table 2.8. While the study reports crystallinity values obtained, the presence of voids dominated the mechanical response of the laminates, and so the effect of crystallinity could not be observed effectively.

Table 2.8: Void content, crystallinity and ILSS (MPa) of CF/PEKK composites after undergoing different processing and post-processing conditions. Adapted from [66]

Material	Processing conditions	Post-processing conditions	Void content	Crystallinity	ILSS (MPa)
AS4D CF/PEKK	ATP manufacturing. • Laser power: 3349 W • Nip temp.: 417°C • Lay-down speed: 2.4 m/min	None	6.1%	3%	20
		Annealing 120 min at 270°C, cooled at 40°C/min	6.3%	17%	21
		Vacuum bag at 1 bar for 30 min at 380°C, cooled at 3°C/min	0.9%	22%	71
		Compression moulding for 10 min at 380°C, cooled at 16°C/min (pressure higher than VB)	0.4%	20%	90
	ATP manufacturing. • Laser power: 3460 W • Nip temp.: 430°C • Lay-down speed: 2.4 m/min	None	5.8%	4%	20
		Annealing 120 min at 270°C, cooled at 40°C/min	2.8%	20%	22
		Vacuum bag at 1 bar for 30 min at 380°C, cooled at 3°C/min	1.1%	18%	56
		Compression moulding for 10 min at 380°C, cooled at 16°C/min (pressure higher than VB)	0.4%	19%	89
	ATP manufacturing. • Laser power: 3460 W • Nip temp.: 430°C • Lay-down speed: 6 m/min	None	6.8%	3%	20
		Annealing 120 min at 270°C, cooled at 40°C/min	6.7%	21%	22
		Vacuum bag at 1 bar for 30 min at 380°C, cooled at 3°C/min	3.0%	20%	48
		Compression moulding for 10 min at 380°C, cooled at 16°C/min (pressure higher than VB)	0.3%	21%	92

Outside of the above, no studies covering matrix-dominated properties of CF/PEKK composites were found, and so a compilation of various articles on CF/PEEK is presented in Table 2.9 instead.

Table 2.9: Compilation of matrix-dominated properties of CF/PEEK offered by various authors.

Material	Crystallinity/processing conditions		Crystallinity	Transverse tensile strength (MPa)	Transverse flexural strength (MPa)	Interlaminar shear strength (MPa)	Interfacial shear bond strength (MPa)	Ref.
AS4/PEEK	Hot pressed in a vacuum furnace at 450°C at 2MPa, for 10-40min (see to the right). Followed by 400°C/min cooling.	10 min					49.9	[29, 58]
		20 min					55.4	
		30 min					73.2	
		40 min					96.7	
AS4/PEEK	Molten at 390. Followed by:	Quenched in iced water					74	[29, 67]
		Slowly cooled in air					97	
		Annealed at 320°C for 60 min, then quenched in iced water					112	
AS4/PEEK	Unknown				152	38.9		[32]
HMS/PEEK	Unknown				76.4	29.7		
T300 CF/PEEK	30 min preheating at ambient pressure 390°C, followed by compression moulding at 390°C at 2 MPa for 30 min, and cooled at different rates:	0.6°C/min	45%	60				[24]
		7°C/min	42%	63				
	100 min preheating at ambient pressure 390°C, followed by compression moulding at 390°C at 2 MPa for 30 min, and cooled at different rates:	0.6°C/min	36%	106				
		7°C/min	43%	111				
AS4/PEEK	Hot pressed at 400°C at 1MPa for 60 min, followed by cooling at different rates (pressure removed for cooling):	3°C/min (9% void content)			60*			[68]
		10°C/min (6% void content)			90*			
		175°C/min (4% void content)			110*			
AS4/PEEK	Hot pressed at 400°C for 60 min at 1MPa, followed by 3°C/min cooling rate at different pressures:	Ambient pressure		55				[69]
		0.2MPa		125				
		0.4MPa		130				
		1MPa		120				
APC2 (CF/PEEK tape)	Held at 400°C for 15 min, then cooled at different rates:	0.33°C/min	31%		172	117		[70]
		22-23°C/min	26%		154	108		
AS4/PEEK	Held 420°C for 15 min, then cooled at different rates:	0.33°C/min	36%		114	103		
		22-23°C/min	26%		146	101		

IM7/PEEK	Autoclave – held at 375°C for 20 min at 7 bar, then cooled at 3°C/min	40%	112		[71]
	Automated tape placement – lay down speed 8m/min, roller pressure 1.2 bar. (High heating and cooling rates)	18%	78		
AS4/PEEK	Held at 400°C for 10 min in an oven, then cooled between 1-1500°C/min.	14-38% (see Figure 2.24)	50-80 (see Figure 2.24)	75-115 (see Figure 2.24)	[29]
*** = while these results may seem that a slower cooling rates results in a lower performance, this is actually a consequence of the void content of the different laminates, which is highest at the 3°C/min (12%) sample and lowest at the 170°C/min (4%).**					

As seen in Table 2.9, a thorough evaluation of matrix mechanical properties as a function of crystallinity under different processing conditions is scarce. Some papers do mention a correlation between superior mechanical properties with a higher crystallinity content [58,70], but only a few of them cited in Table 2.9 offer crystallinity values for the different processing cycles that their samples underwent. None of these studies offer a diligent review of the impact of thermal cycles (varying holding times, varying cooling rates) on composite crystallinity and their consequent effect on the matrix performance. An exception to this is Gao and Kim's paper [29] mentioned in the previous paragraph and in the last row of Table 2.9, which does offer information on the variation of ILSS, IFSS and crystallinity with respect to cooling rate, shown in Figure 2.24.

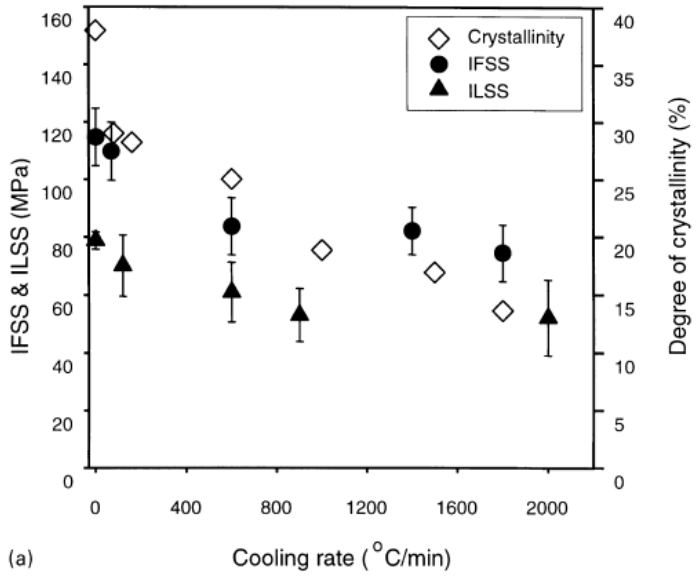

Figure 2.24: Comparison of IFSS, ILSS and degree of crystallinity as a function of cooling rate [29].

Thorough studies on the impact of thermal cycles on the crystallinity and performance of composite matrices are essential for a better understanding of how thermoplastic composite materials can be reliably used in industry. This is perhaps less significant with PEEK as it is a fast-crystallising material, but with PEKK, particularly grades with lower T/I ratios (and therefore slower crystallisation kinetics), the thermal cycle that the material undergoes is paramount to its crystallinity and mechanical behaviour.

2.3. Modelling of crystallisation kinetics

As discussed in Section 2.2, the dual crystallisation mechanism that takes place in PEKK is paramount in the understanding of its crystallisation kinetics. When plotted against time, the evolution of crystallinity has a sigmoidal shaped curve. In the initial stages of crystallisation, spherulites start to nucleate and grow, followed by a faster spherulitic growth period, namely primary crystallisation. Once spherulites begin to impinge on each other, crystallisation slows down, but even after maximum volume of crystallisation has been achieved, crystallisation continues in the form of interlamellar crystalline structures. This is known as secondary crystallisation, corresponding to the upper tail of the curve.

Modelling this double crystallisation behaviour in PEKK (and other PAEKs) has been the object of several studies, and an overview of several models is presented in this section. The main background theory of polymer crystallisation kinetics is outlined first, followed by an explanation of the most relevant models and a discussion of any similarities and discrepancies found in literature, as well as any extra commentary on reinforcement with carbon fibres where literature is available. Isothermal crystallisation kinetics is discussed first, followed by non-isothermal crystallisation kinetics. Notation is consistent throughout the entirety of Section 2.3, and so may not be the same as that used in the discussed papers. Finally, a brief overview of two transcrystallisation simulations is given.

2.3.1. Isothermal crystallisation kinetics

The initial stages of crystallisation, where crystals grow independently, has often been modelled in terms of the Avrami equation [72]:

$$\alpha(t) = 1 - \exp(-kt^n) \tag{2.1}$$

where the quantity $\alpha(t)$ is a measure of the relative volume fraction of crystallinity at time t, k is the crystallisation rate constant, and the Avrami exponent n is related to the nature of crystal growth for the first mechanism. The equation is a simple sigmoidal function that has been extensively used to model the progress of phase transformations in materials systems [73]. Assessment of whether the Avrami equation correctly models the crystallisation process can be done by plotting $\log[-ln(1-\alpha)]$ against $\log t$. If successful, the plot would result in a straight line of gradient n and intercept $\log k$.

The Avrami exponent n is understood to be equal to the number of directions that crystal growth takes place with instantaneous nucleation, leading to rods, discs or spheres for n = 1, 2 or 3 respectively. However, a value of 2 for the Avrami exponent could also be associated with a one-dimensional growth with sporadic nucleation; which is how an exponent of up to 4 can be achieved with 3-dimensional growth and sporadic nucleation. The relation between the exponent, geometry and nucleation type is shown in Table 2.10. However, it is worth noting that the Avrami equation should be used with caution, as non-integer values for n_I are often found to fit experimental data, and the shape of the morphological unit predicted is not always correct [9,23]. This will be observed in the results obtained for PEEK and PEKK by several authors in this section. Potential reasons for this can be that nucleation occurs as a combination of the instantaneous and sporadic mechanisms, as well as crystallisation growth not being exclusively spherulitic for instance, but rather being a mix of structures of different dimensions [30,74,75]. The latter

may be particularly relevant in the case of composites where a one-dimensional growth may occur at the fibre-matrix interface, as described in Section 2.1.4.

Table 2.10: Relation between the Avrami exponent and the morphological unit. Adapted from [9,76].

Growth unit	Geometry	n_1 with instantaneous nucleation	n_1 with sporadic nucleation
Spherulites	3D	3	4
Discs	2D	2	3
Rods	1D	1	2

The crystallisation rate constant k varies with the growth unit and nucleation type, and can be expressed as a function of the initial number of potential nuclei N and the crystal growth rate G. Table 2.11 below provides a summary of these.

Table 2.11: Relation between crystallisation rate constant k and the morphological unit. Adapted from [9,35].

Growth unit	k with instantaneous nucleation	k with sporadic nucleation
Spherulites	$\frac{4\pi NG^3}{3}$	$\frac{\pi NG^3}{3}$
Discs	πNG^2	$\frac{4\pi NG^2}{3}$
Rods	NG	$\frac{1}{2}NG$

In the case of PEKK, as mentioned in Section 2.1.3, nucleation is instantaneous.

According to Hoffman and Lauritzen theory [77], the crystal growth rate in polymers can be expressed as follows:

$$G_i(T) = G_{0i}\exp\left(-\frac{U^*}{R(T-T_\infty)}\right)\exp\left(-\frac{K_{gi}}{T\times\Delta T\times f}\right) \quad (2.2)$$

G_{0i} is a pre-exponential factor independent of temperature. The first exponential term corresponds to the contribution of macromolecular chain diffusion in the melt, where U^* is the activation energy of the molecular transfer from the melt to the crystal interface, T_∞ is the temperature below which diffusion stops ($T_\infty = T_g$ - 30 K), and R is the gas constant. The second exponential term contains the contribution of the nucleation process, where K_{gi} is the activation energy of nucleation for a crystal with a critical size, ΔT is the degree of supercooling ($\Delta T=T_m^0-T$) with T_m^0 as the equilibrium melting temperature, and f is a correction coefficient accounting for the temperature dependence of the melting enthalpy ($f=2T/(T_m^0+T)$). The index i for G_i, G_{0i}, and K_{gi} is equal to 1 for primary crystallisation and 2 for secondary crystallisation. Further details of the Hoffman Lauritzen theory can be found in their work [77], and specifically applied to PEKK in [9,35,74].

It is also worth noting that the use of the Avrami equation alone completely ignores the existence of a secondary growth stage, which has been repeatedly observed in PEKK and PEEK. This is observable in Velisaris and Seferis' work on PEEK [30], where the Avrami plot shown in Figure 2.25 displays two competing crystallisation mechanisms, and therefore two distinct gradients corresponding to different Avrami exponents. Choupin et al. [9] show similar behaviour for PEKK, as per Figure 2.26.

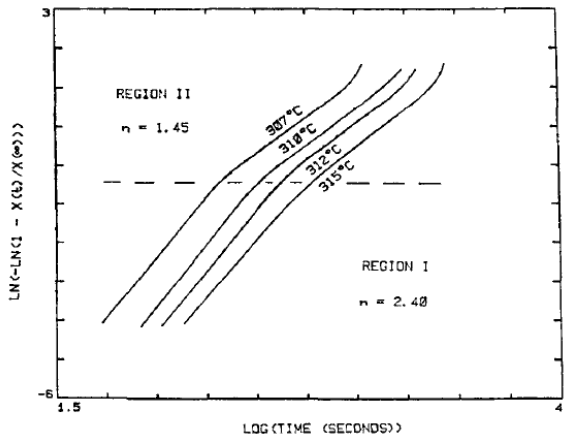

Figure 2.25: Avrami crystallisation plots for the isothermal crystallisation of neat PEEK at 307°C, 310°C, 312°C, 315°C, showing the existence of two competing crystallisation processes [30].

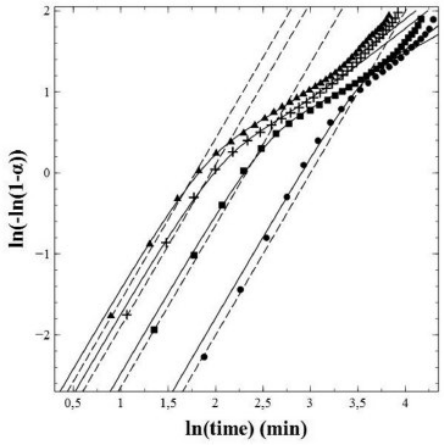

Figure 2.26: Double logarithm vs. ln(time) (from left to right: 230°C, 220°C, 210°C, 200°C), Avrami model (dashed curves) and Hillier model (solid curves, discussed below) for PEKK 60/40 isothermal crystallisation from the melt [9].

Velisaris and Seferis [30] tackled this by proposing two separate Avrami crystallisation processes taking place in parallel, as per Equation (2.3), which they tested on both unreinforced and CF/PEEK.

$$\alpha(t) = w_1\alpha_1(t) + w_2\alpha_2(t) \tag{2.3}$$

which, substituting for α_1 and α_2:

$$\alpha(t) = w_1[1 - \exp(-k_1 t^{n_1})] + w_2[1 - \exp(-k_2 t^{n_2})] \tag{2.4}$$

In the above equations, w_1 and w_2 are the weight factors corresponding to primary and secondary crystallisation respectively, providing the relative importance of each crystallisation mode ($w_1 + w_2 = 1$). All quantities with subscripts 1 and 2 refer to primary and secondary crystallisations respectively. Using 2.5 and 1.5 for n_1 and n_2 respectively (which provided the best fit to their data), they concluded that the model provided a good description of the crystallisation process for both neat and fibre-reinforced PEEK, achieving an average deviation from experimental data of 4%. It was observed that both rate constants for CF/PEEK were higher than those for its neat counterpart. As previously mentioned in Section 2.2.3, however, the PEEK grades used by Velisaris and Seferis in the neat and composite PEEK systems were different [14]. Crystallisation kinetics are therefore not comparable between the two.

Prior to this, Hillier [50] postulated a different model, where a primary Avrami type crystallisation took place followed by a first-order crystallisation process ($n_2 = 1$) growing from the primary crystallisation. Equation (2.5) shows the proposed expression for secondary crystallisation, and Equation (2.6) provides the overall crystallisation.

$$\alpha_2(t) = \int_0^t \alpha_1(\tau) \times \frac{\mathrm{d}}{\mathrm{dt}}[1 - \exp(-k_2(t-\tau)^{n_2})]d\tau \tag{2.5}$$

$$\alpha(t) = w_1[1 - \exp(-k_1 t^{n_1})] + w_2 k_2 \int_0^t [1 - \exp(-k_1 \tau^{n_1})] \times \exp[-k_2(t-\tau)]\, d\tau \tag{2.6}$$

Here, τ is the time at which a volume element has been included in the lamellae and secondary crystallisation begins. This model differs from the one Velisaris and Seferis [30] proposed, since the Hillier model assumes that this secondary crystallisation occurs after time τ, as opposed to both growths taking place independently and simultaneously from $t = 0$.

These two models were tested on PEKK and CF/PEKK by Hsiao et al. [14], who concluded that, after a modification of the exponent of the secondary crystallisation, the Hillier model provided a better fit than the Velisaris Seferis model. This was because the Hillier model has a better physical reasoning to describe the secondary crystallisation taking place within lamellae, as some primary crystallisation must exist before the secondary step begins. In this modified Hillier model, the secondary crystallisation is not assumed to be of the first order, and therefore the total crystallinity is:

$$\begin{aligned} \alpha(t) &= w_1[1 - \exp(-k_1 t^{n_1})] \\ &+ w_2 k_2 n_2 \int_0^t [1 - \exp(-k_1 \tau^{n_1})] \times (t-\tau)^{n_2 - 1} \exp[-k_2(t-\tau)]\, d\tau \end{aligned} \tag{2.7}$$

In order to identify the relative crystallinity and crystallisation kinetics parameters, the model must be fitted to the relative crystallinity, which can be calculated via the integration of heat flows measured using DSC:

$$\alpha(t) = \frac{\int_0^t Q(t)\, dt}{\int_0^{t\infty} Q(t)\, dt} \tag{2.8}$$

where *Q(t)* is the heat flow measured at time *t*, and t_∞ is the time when the polymer is fully crystallised. This integration becomes a challenge to perform due to unstable heat flow signals resulting from the DSC switching from heating/cooling to isothermal. This is reflected as a shortening of the beginning of the crystallisation peak. This truncation becomes more prominent with lower temperature isotherms from the melt, and at temperatures at which faster crystallisation kinetics are favoured. An example of this is shown in Figure 2.27, where kinetics are faster at 230°C, resulting in a shorter peak as indicated by the arrows. This was commented on in Hsiao et al.'s work [14], and was later identified by Choupin et al. [9].

To tackle this, Hsiao et al. [14] simply used the results where the instrumental fluctuations did not interfere with the crystallisation signal. They found the Avrami exponents to be 4 and 2 respectively, representing a nucleation growth that is assumed to be three-dimensional and sporadic (time-dependent) during primary crystallisation, and two-dimensional or diffusion-controlled in the secondary stage. This is in disagreement with what Hillier previously assumed, where secondary crystallisation obeys a first-order law ($n_2 = 1$). Hsiao et al. argued that this assumption may oversimplify the secondary stage. Figure 2.28 demonstrates when primary and secondary crystallisation develop as per this modified Hillier model. In

this study, the inclusion of carbon fibres in PEKK was not found to have an effect on the crystallisation rate constant or the relative volume fraction crystallinity for each crystallisation stage.

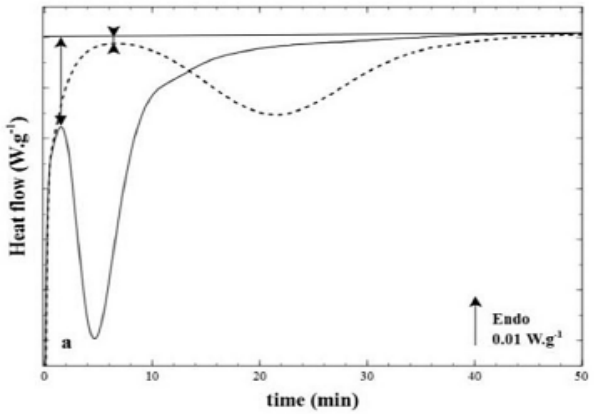

Figure 2.27: PEKK 60/40 DSC thermograms during isothermal crystallisation from the melt at 230°C (solid line) and 210°C (dashed line) [9].

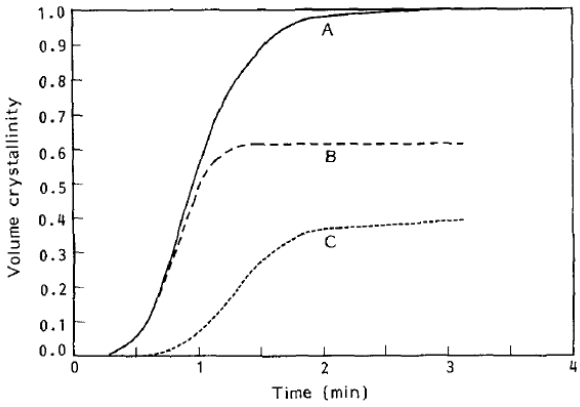

Figure 2.28: Isotherm of total volume crystallinity of PEKK (A) separated into a primary volume crystallinity (B) and a secondary volume crystallinity (C). The data were obtained from an isotherm at 298°C [14].

This initial truncation of the crystallisation signal proved to be a larger problem in Choupin's work on neat PEKK as shown in Figure 2.27, which was initially tackled by the introduction of an induction time [9]. This was defined by the intersection of the baseline and the extrapolation line of the crystallisation peak beginning, without which the model coefficients were not able to provide a good fit of the experimental data. This method produced an Avrami exponent of approximately $n_1=2$, however, which contradicted their microscopic observations of spherulitic entities as this exponent suggests lower dimensional growths (instantaneous nucleation with disc-like growths or sporadic nucleation with rod-like structures).

Furthermore, Choupin et al. suggested in later work [35] that the introduction of a crystallisation induction time is inconsistent with overall crystallisation kinetics theories, and proposed a further modification to the Hillier model. This new method considers only reliable DSC measurements and does not need extrapolation, called the derivative Hillier method. A more thorough explanation of the following derivation is available in their paper [35].

Equation (2.8) can be differentiated to obtain

$$\frac{d\alpha(t)}{dt} = \frac{Q(t)}{\int_0^{t\infty} Q(t)dt} = \frac{Q(t)}{\Delta H_m} \tag{2.9}$$

where ΔH_m is the total melting enthalpy.

The derivatives of the primary crystallisation and secondary crystallisation rate equations (Equation (2.1) and (2.5)) are as follows:

$$\frac{d\alpha_1(t)}{dt} = k_1 n_1 t^{n_1-1} \exp(-k_1 t^{n_1}) \tag{2.10}$$

$$\frac{d\alpha_2(t)}{dt} = k_2 n_2[1 - \exp(-k_1 t^{n_1})] + k_2 n_2 \int_0^t [1 - \exp(-k_1 \tau^{n_1})] \times \exp[-k_2 (t-\tau)^{n_2}] \times [(n_2 - 1)(t-\tau)^{n_2 - 2} - k_2 n_2 (t-\tau)^{n_2 - 2} d\tau \quad (2.11)$$

The derivative of the total crystallinity is therefore

$$\frac{d\alpha(t)}{dt} = w_1 \frac{d\alpha_1(t)}{dt} + w_2 \frac{d\alpha_2(t)}{dt} \quad (2.12)$$

with w_1 and w_2 corresponding to the weight factors for the primary and secondary crystallisation respectively. Choupin et al. [35] found the best fits to take place when n_2 =1, simplifying Equations (2.10) - (2.12) to:

$$\frac{d\alpha(t)}{dt} = w_1 k_1 n_1 t^{n_1 - 1}(1 - \alpha_1(t)) + w_2 k_2 (\alpha_1(t) - \alpha_2(t)) \quad (2.13)$$

Choupin et al. [35] tested this model on neat PEKK 60/40 and 70/30 (KEPSTAN 6002 and 7002 respectively, by Arkema), in order to validate it under different crystallisation rates. The same Avrami exponents for primary crystallisation were chosen for both samples, n_1 = 3 and n_2 = 1, which is in line with the instantaneous nucleation growth of spherulitic nature observed in PEKK. They also performed parameter modelling according to Hoffmann and Lauritzen theory as discussed previously, and appropriate crystallisation rate constants k_1 and k_2 were selected as per Table 2.11. Further details of this can be found in Choupin et al.'s work [35]. Their findings can be summarised in the time-temperature-transformation diagrams for PEKK shown below.

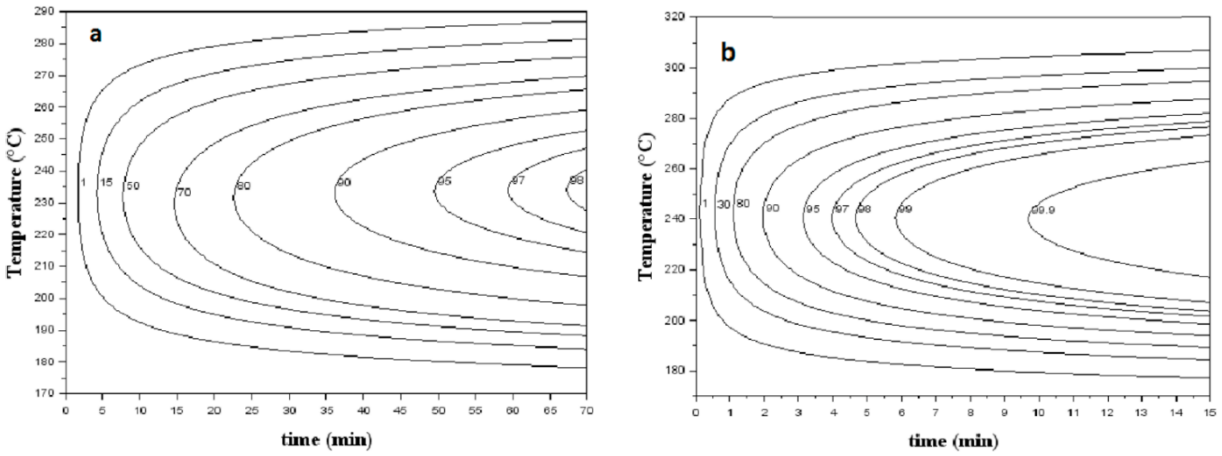

Figure 2.29: Time-temperature-transformation diagram of the relative crystallinity of PEKK (a) 6002 and (b) 7002 crystallised from the melt [35].

The same model (derivative Hillier) was later implemented by Chelaghma et al. [74] on neat PEKK 70/30 (KEPSTAN 7003 by Arkema), where n_1 was also found to be 3, but a different secondary exponent was obtained, n_2 = 2.7. Neither Choupin et al. nor Chelaghma et al. modelled kinetics of CF/PEKK composites.

The discrepancy on n_1 between Hsiao et al. [14], Choupin et al. [35] and Chelaghma et al. [74] lies in the nature of the nucleation of PEKK: Hsiao et al. [14] defend that the nucleating density is clearly a function of time as observed in thermal optical analysis (hence sporadic), and therefore as per Table 2.10, should follow that $n_1 = 4$. On the other hand, Choupin et al.'s optical microscopy results in Figure 2.11 [9] depict crystalline entities of the same size, and therefore instantaneous nucleation can be assumed, which is, for spherulitic growth, $n_1 = 3$ [35]. Chelaghma et al.'s hot stage microscopy studies [74] also demonstrate instantaneous nucleation. The difference between the models used by Hsiao et al. [14] (Modified Hillier model) and Choupin et al. [35] and Chelaghma et al. [74] (derivative Hillier model) may be the reason as to why one constant fits better, and therefore has been selected over the other.

The discrepancies regarding n_2 are perhaps less conclusive. Hsiao et al.'s selection for $n_2 = 2$ [14] is somewhat arbitrary, but suggest that Hillier's initial choice of $n_2 = 1$ [50], indicating that secondary crystallisation within the spherulite follows first-order growth, may be an oversimplification. The value $n_2 = 1$ was used by Choupin et al. as well [35], who simply selected the exponent which showed the best fit with the derivative Hillier model, and therefore represents 1-dimensional growth. Chelaghma et al. [74] however identified n_2 as 2.7, and suggest that the secondary crystallisation mechanism is not necessarily related to a unique process, but the formation of structures of different dimensions.

With regards to the proportion in which each of these crystallisation stages is observed in PEKK, the literature discussed above agrees on the secondary crystallisation becoming more prominent with higher isothermal crystallisation temperatures. The w_1/w_2 ratio varies with PEKK's T/I ratio and molecular weight. Choupin et al. [35] found a consistent decrease in primary crystallisation of PEKK 60/40 with an increase in temperature, whereas with PEKK 70/30 its value seemed considerably more constant. This could be attributed to a more organised chain packing as a consequence of the higher para- linkage presence, as discussed in Section 2.1.1. When using PEKK 70/30 of a lower molecular weight, Chelaghma et al. [74] found w_1 to decrease more significantly. Hsiao et al. [14] also observed a consistent decrease of w_1 with temperature in their PEKK samples (believed to be 70/30, by DuPont). There are discrepancies in the range of these values, likely due to slight differences in the chosen models and parameters as discussed above, as well as in the grade of PEKK. But overall, w_1 has been observed to vary between 0.9 and 0.55 for PEKK 70/30 in an isothermal temperature range of 270-310°C; and between 0.7 and 0.4 in an isothermal temperature range of 200-275°C for PEKK 60/40.

With the help of the models, Choupin et al. [35] plotted the variation of k_1 and k_2 for both PEKK 60/40 and PEKK 70/30 (Arkema), finding the fastest kinetics to take place at 235°C and 245°C respectively. Both crystallisation stages achieved this peak at the same temperatures for each grade. Hsiao et al. [14] found this temperature to be 255°C for PEKK 70/30 (DuPont), again, likely due to variation in molecular weight.

Implementation of isothermal crystallisation kinetics models on CF/PEEK and CF/PEKK composites is sparse – from the above literature, Velisaris and Seferis [30], as well as Hsiao et al., [14] obtained successful fits on composite systems with the models they previously implemented on unreinforced PEEK and PEKK. Choupin also did this in their thesis work [28], and found that using the same primary Avrami exponent as he used for unreinforced PEKK ($n_1 = 3$) provided a good fit for low isothermal temperatures, whereas for higher temperatures, using $n_1 = 2$ created a more successful fit. The reason for this has been

discussed in detail in Section 2.2.3, but at higher temperatures, crystallisation kinetics in the bulk are considerably slower. This results in the main crystallisation mechanism occurring on the carbon fibre surfaces, where the high nucleation density can cause impingement and therefore an epitaxial growth rather than spherulitic, reducing the value of the Avrami exponent.

Regardless, further investigation is necessary to verify the suitability of the discussed models, particularly the ones developed in the more recent years, since there is little literature covering the implementation of these in unreinforced PEKK, and virtually none on CF/PEKK.

Overall, the understanding of the primary crystallisation of PEKK seems to be better established, and a consensus on spherulitic growth has been reached. Some discrepancies exist in the literature on whether the nucleation process is instantaneous or sporadic, but recent literature leans in favour of the former. Understanding of the secondary crystallisation mechanism is less clear however, due to it not being readily observable by microscopy methods. The model adaptations to accommodate for this are somewhat novel, particularly the derivative Hillier model. Investigation of the crystallisation kinetics of CF/PEKK is sparse for older models (Velisaris-Seferis, modified Hillier), and non-existent for the newer models (derivative Hillier). Further work needs to be carried out in this ambit in order to better understand the secondary crystallisation kinetics of PEKK, and the overall crystallisation kinetics process for CF/PEKK.

2.3.2. Non-isothermal crystallisation kinetics

Available literature of models for non-isothermal crystallisation kinetics is considerably sparser than the isothermal counterpart. Several models have been developed based on the Avrami equation, such as the Nakamura [78] and Ziabicki [79] models, where non-isothermal crystallisation is predicted using isothermal crystallisation data; a differential Nakamura model, proposed by Patel and Spruiell [80]; or the Ozawa model, where an infinite number of isothermal steps are assumed to form the non-isothermal process [81]. The Ozawa model is perhaps the most attempted one on non-isothermal crystallisation kinetics model on our materials of interest (as explained below), and takes the following form:

$$\alpha(T) = 1 - \exp\left(-\frac{K^*(T)}{\varphi^m}\right) \tag{2.14}$$

where $K^*(T)$ is a heating/cooling function dependent on temperature, φ is the cooling rate the sample undergoes (a constant), and m is assumed to be constant and independent of temperature. The crystallisation in this model is dependent on temperature, and therefore relies on crystallinity sampling at different temperatures during crystallisation at different cooling rates. If a crystallisation process is correctly modelled by Ozawa analysis, a plot of $\log[-\ln(1-\alpha(T))]$ against $\log\varphi$ would result in a series of parallel lines with slope m and intercept K^* [39,81,82].

The aforementioned models have the same limitation as the Avrami model as they cannot model dual crystallisation behaviour, and are therefore not ideal for modelling PEKK or other PAEKs, where secondary crystallisation is significant [26,37,39,81,83,84]. This is obvious in Cebe and Hong's [39] attempt to use the Ozawa and Avrami equations to model non-isothermal crystallisation of unreinforced PEEK with cooling rates between 2 and 20°/min, shown in Figure 2.30. With the Ozawa model, they

obtained a distinct curvature in their results, likely due to the inaccurate assumption in the model that the constants are independent of temperature. With Avrami fitting, they found that for low degrees of conversion up to 0.20, the model was linear for the entire range of cooling rates applied. This therefore implies that it is after this relative crystallinity is obtained that secondary crystallisation starts taking place – Cebe and Hong stated this happens within the range of 0.24-0.35 at the faster rates used in their study. It is worth noting that the meaning that the Avrami exponent *n* holds during isothermal crystallisation is lost in this case and is not representative of crystallisation morphology.

In a later study, Cebe [26] implemented the same Avrami equation on CF/PEEK when undergoing various cooling rates, and found the data to be linear over a very wide range of degrees of conversion. While it is likely that there are molecular weight differences between Cebe's [26] and Cebe and Hong's [39] studies, linear ranges can be observed in the range of 0.1-0.8 in cooling rates between 1 and 20°C/min in Figure 2.31. Departures from linearity at the beginning and end of the crystallisation process are explained as an exaggeration of small errors in the assignment of the crystallisation starting time, and as a switch between primary and secondary crystallisation respectively. It is observed that in comparison to neat PEEK crystallisation, crystallisation initiates and peaks at higher temperatures (implying faster kinetics) in the composite. While this may be due to molecular weight differences, it is also possible that the carbon fibres act as sites for nucleation and transcrystalline growth, as discussed in previous sections.

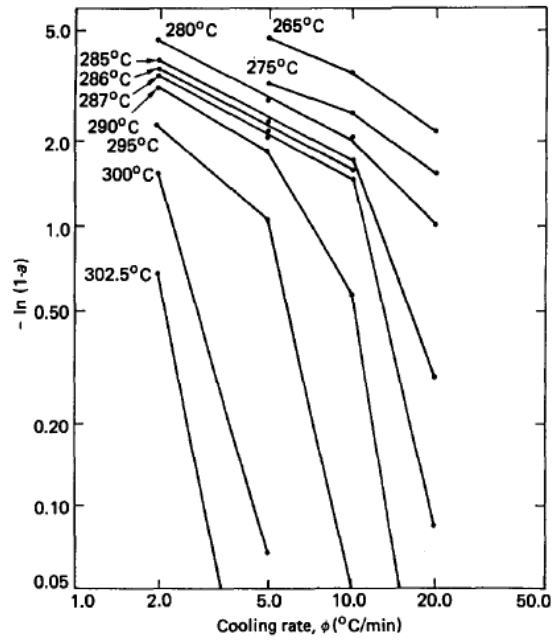

Figure 2.30: Ozawa plot of $log\ [-ln(1-\alpha(T))]$ *versus* $log\ \varphi$ *at the indicated temperatures. Lines as guides to the eye [39].*

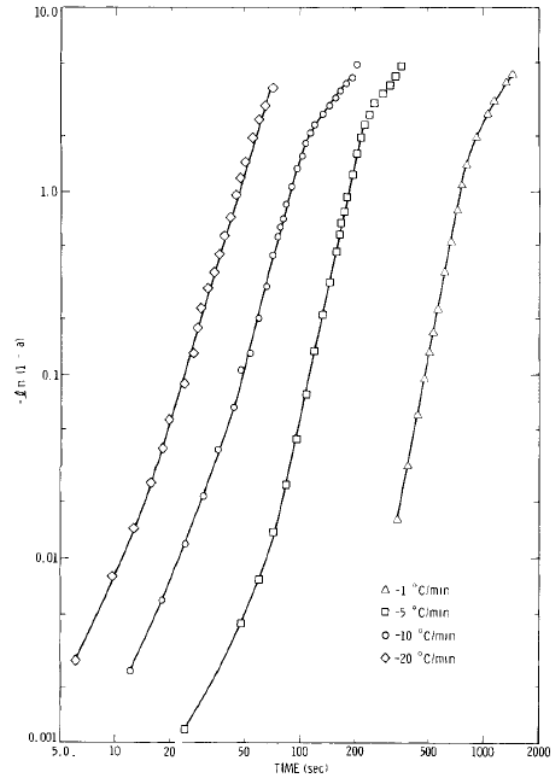

Figure 2.31: Avrami crystallisation plot of $log\ [-ln(1-a)]$ *vs.* $log\ t$*, for non-isothermal crystallisation at -1°C/min, -5°C/min, -10°C/min and -20°C/min, where a is relative crystallinity. The lines are guides to the eye [26].*

Velisaris and Seferis [30] extended their model (discussed in Section 2.3.1) to the non-isothermal case on PEEK by utilising an integral Avrami expression. Each crystallisation rate process *i* is modelled as follows:

$$\alpha_i(t) = 1 - \exp\left[-\int_0^t k(T)_i n_i t^{n_i - 1}\, dt\right] \tag{2.15}$$

where the crystallisation rate $k(T)_i$ is now temperature-dependent. Extended for a dual crystallisation mechanism (i = 1, 2), this becomes:

$$\alpha(t) = w_1\left[1 - \exp\left[-\int_0^t k(T)_1 n_1 t^{n_1 - 1}\, dt\right]\right] + w_2\left[1 - \exp\left[-\int_0^t k(T)_2 n_2 t^{n_2 - 1}\, dt\right]\right] \tag{2.16}$$

It is worth noting that in these authors' work [30], $\alpha(t)$ is printed as $X_{vc}X_{vc\infty}$, where X_{vc} is the volume fraction crystallinity and $X_{vc\infty}$ is the equilibrium volume fraction crystallinity. Other authors that use this model [27,85] define $\alpha(t)$ as $X_{vc}/X_{vc\infty}$, following the commonly used definition of relative volume fraction crystallinity. Further explanation of this model can be found in the Velisaris and Seferis' paper [30].

Applying this model to neat PEEK, they obtained the best model with n_1 = 2.5 and n_2 = 1.5, as per their isothermal modelling. The results show a good correspondence with experimental values, with perhaps a slight deviation from experimental results towards the end of the crystallisation process, as shown in Figure 2.32 below; however, as discussed previously, the neat and composite samples contain different grades of PEEK, and therefore the achieved volume fraction crystallinities and kinetics are not comparable.

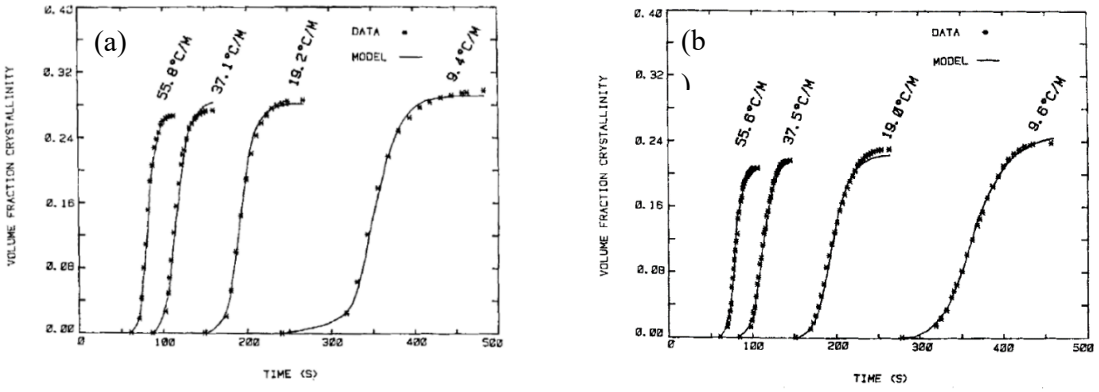

Figure 2.32: Volume fraction crystallinity versus time for the non-isothermal crystallisation of (a) neat PEEK resin and (b) PEEK resin in APC2 at various cooling rates. Lines represent predictions obtained by fitting the data to the parallel model, with best fit dynamic parameters [30].

Choupin [28] developed a non-isothermal model in their thesis work which takes into account this dual crystallisation and is applicable for any thermoplastic. The model is not reliant on material-specific parameters, and was applied to neat PEKK 60/40 and 70/30. The work is based on the models proposed by Hillier [50] and Patel and Spruiell [80], and considers non-isothermal crystallisation cycles as a succession of brief isotherms. This allows for the addition of the relative crystallinity formed during each small isotherm, in order to determine the crystallinity obtained for the entire non-isothermal crystallisation. The derivation of the model can be found in Choupin's work [28], where its final form is as follows:

$$\frac{d\alpha(t)}{dt} = w_1 n_1 k_1^{\frac{1}{n_1}}\left[-\ln\left(1-a_1(t)\right)\right]^{\frac{n_1-1}{n_1}}[1-\alpha_1(t)] + w_2 k_2[\alpha_1(t)-\alpha_2(t)] \quad (2.17)$$

This model tends to over-predict crystallisation kinetics, due to not accounting for an induction time for nucleation. Choupin argued that this phenomenon is due to the assumption that nucleation and growth kinetics are proportional, which may not be true for non-isothermal crystallisation.

Seo et al. [86] took a similar path to Velisaris and Seferis, extending the Nakamura model into a dual form to model the crystallisation kinetics of PEEK. Nakamura [78] adapted the Avrami equation as follows:

$$\alpha(t) = 1 - exp\left[-\left(\int_0^t K\,dt\right)^n\right] \quad (2.18)$$

where K is temperature dependent and connected with the isothermal crystallisation rate constant k through the relation:

$$K = k^{1/n} \quad (2.19)$$

where k can be expressed as a function of the initial number of potential nuclei and the crystallisation growth rate, as defined in 2.3.1. Seo et al. [86] proposed a parallel dual Nakamura model as:

$$\alpha(t) = w_1\left(1 - exp\left[-\left(\int_0^t K_1\,dt\right)^{n_1}\right]\right) + w_2\left(1 - exp\left[-\left(\int_0^t K_2\,dt\right)^{n_2}\right]\right) \quad (2.20)$$

and then equated $w_1 = 1-\alpha(t)$ and $w_2 = \alpha(t)$, associating w_1 and w_2 with varying weight fractions of amorphous phase and crystalline phase. Further details of their work can be found in [86,87].

Another model worth mentioning which takes a different approach to dual crystallisation modelling is the following one developed by Tobin [88–90]. Tobin argued that the Avrami equation is not suitable for crystallisation modelling of any polymer, as it assumes the system to be completely melted with no residual nuclei, only obtaining adequate fits below 10-30% conversion. They proposed models for heterogeneous and homogeneous nucleation, as well as a mixed-mode model which simply consists of a linear combination of the first two expressions:

$$\frac{\alpha(t)}{1-\alpha(t)} = kNt^n + KI^*\int_0^\tau (t-\tau)^n[1-\alpha(\tau)]d\tau \quad (2.21)$$

where $\alpha(t)$ is the relative crystallinity at time t, k is a constant containing nucleation and growth parameters, n is an integer similar to the Avrami exponent, the value of which depends on the nucleation mechanism and the crystal growth form; N is the initial number of heterogeneous nuclei and I^* is the rate of homogeneous nucleation. The first term, kNt^n, represents heterogeneous nucleation and growth, and the integral term corresponds to homogeneous nucleation and growth.

Choe and Lee [91] applied this model to unreinforced PEEK in later work, therefore taking a different approach to other authors studying this polymer: instead of considering a primary and secondary crystallisation mode, nucleation type (heterogeneous or homogeneous) is considered. They adapted the

Tobin equation to non-isothermal modelling by transforming it to differential form and verified the model again with a range of cooling rates 2-50°C/min. Details of this can be found in their work.

It was found that at slow cooling rates, where the material is exposed to the higher temperatures for longer, heterogeneous growth dominates, and using only the first term of the equation kNt^n was suitable, obtaining very high correlations as shown in Figure 2.33. Homogeneous nucleation does not occur in this case because the free energy of nuclei formation is very high, and instead growth processes dominate crystallisation. At higher cooling rates, on the other hand, using only the heterogeneous term kNt^n resulted in a poor fit, as per Figure 2.34. This is because the two processes are present, and when using a contribution of both heterogeneous and homogeneous nucleation processes in the model, a good correlation was obtained.

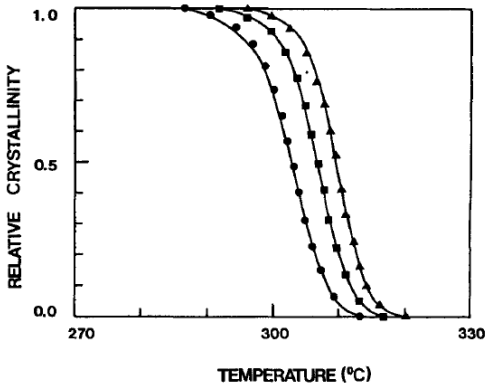

Figure 2.33: Comparison of the experimental data (points) with the calculated values (lines) from using only the heterogeneous term kNt^n in Eqn. (2.21) at the cooling rates (●) 5°C/min, (■) 3°C/min, and (▲) 2°C/min [91].

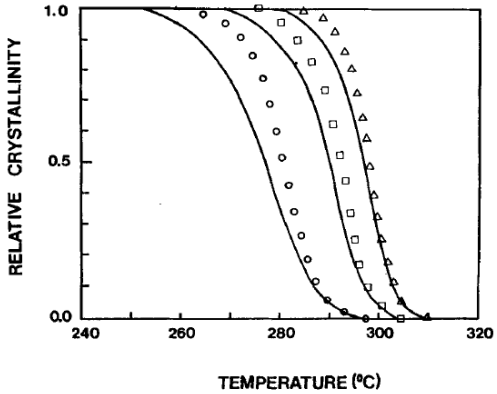

Figure 2.34: Comparison of the experimental data (points) with the calculated values (lines) from using only the heterogeneous term kNt^n in Eqn. (2.21) at the cooling rates (○) 50°C/min, (□) 20°C/min, and (Δ) 10°C/min [91].

To the knowledge of the author, this model has not been used as extensively as the Avrami model and subsequent models based on it. A reason for this may be that, while the presence of heterogeneity and homogeneity is a valid argument, primary and secondary crystallisation have been proven to be the key processes taking place in PEEK and PEKK, and cannot be disregarded. As the majority, if not all, of these models have been implemented on experimental data obtained via DSC, where a small amount of material is held in the melt and therefore it is likely that there are no residual nuclei, this may contribute to the fact that the Avrami-based models effectively fit results. Implementing Tobin's model on composite systems may result in different approaches, as carbon fibres have been shown to act as nucleation sites at times; or possibly obtaining experimental results from samples with a variety of residual nuclei would result in different outcomes for all of the above models.

Overall, the investigation into the crystallisation kinetics of unreinforced PEEK and PEKK under non-isothermal conditions is not notably conclusive, and no particular model has been widely used in literature. This is likely due to a lack of understanding around kinetics under isothermal conditions to begin with, until perhaps more recently. Evaluation of non-isothermal crystallisation kinetics of composite systems is even sparser, potentially due to the same reasons. A better understanding of isothermal conditions is necessary prior to developing accurate models under non-isothermal conditions.

2.3.3. Modelling of transcrystallinity

Existing modelling of transcrystallinity is seen to take a different approach to the rest of this section, as it does not only depend on thermal conditions, but also on the fibre in question, as previously discussed. The effect of the fibre type on crystallisation kinetics can be one of three: speed up, slow down, or none. Some authors maintain that the presence of a transcrystalline region lowers the Avrami exponent, due to the one-dimensional growth occurring at the fibre surface instead of three-dimensional spherulitic growth, as discussed in Section 2.3.1.

Apart from this, there is no further mention of any potential impact that the presence of a transcrystalline phase may have on the aforementioned crystallisation kinetics models. There is little literature focusing on the kinetics of transcrystalline growth and its modelling on PEKK or PEEK, one of these being Chelaghma et al. [92] with a pixel colouring technique, a method previously studied and implemented by Ruan et al. [93–95] in a neat matrix system and with short carbon fibre inclusions. Here, crystalline nuclei are randomly dispersed and identified by a colour, which grow in a spherulitic manner at a constant radial speed until different spherulites come into contact, causing impingement and therefore stopping further growth. Nucleation and growth rates were determined by previous microscopic analysis. Three different models were created, making the following assumptions:

- Model 1: Fibres with entire surfaces acting as nucleation sites.
- Model 2: Fibres with nucleation sites on surfaces matching microscopy results (only parts of the fibre acted as nucleation sites – shown in Figure 2.35 and Figure 2.36).
- Model 3: Fibre surfaces that had no effect on the matrix's nucleation.

These proved to be a good method to model primary crystallisation of PEKK, confirming that fibres whose surfaces act as nucleation sites accelerate the overall crystallisation process, causing the formation of a transcrystalline zone. A kinetics comparison between these and the empirical results was performed, showing that model 2 had the best fit, which only develops transcrystallinity on zones observed to do so. While the authors do not discuss the reasons why some locations on the fibre do not act as nucleation sites, this may a consequence of differences in the fibre surface energy locally. This could be due to local crystal disparities or uneven fibre sizing along the length of the fibres, for instance, resulting in these differences in the transcrystalline presence as discussed in Section 2.1.4.

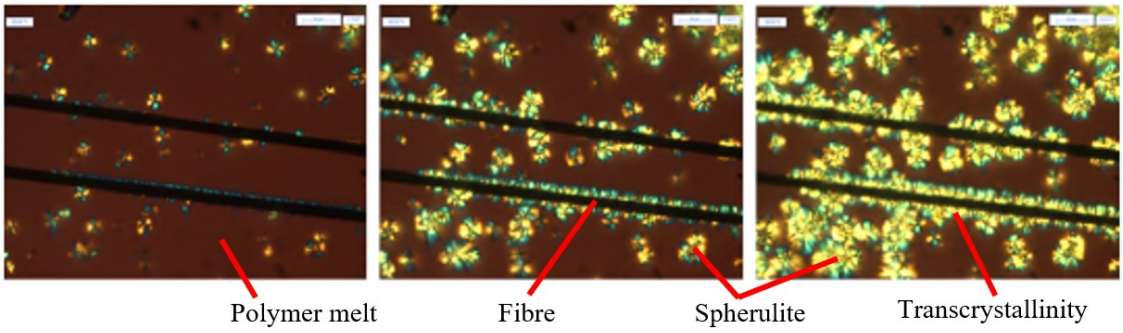

Figure 2.35: Optical micrograph observation of the transcrystalline phase of CF/PEKK at 320°C isotherm [92].

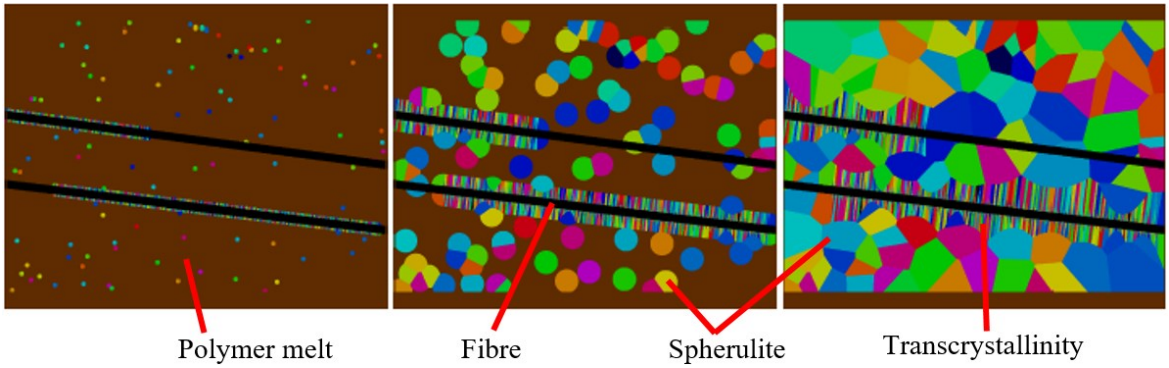

Figure 2.36: Pixel colouring simulation of a polymeric film in the presence of two carbon fibres after locating nucleation sites as per the identified zones in optical micrographs [92].

There are still some elements that remain to be integrated into the above model, in order for this to be realistic. Secondary crystallisation is not included in this model, likely due to the difficulty in observing this phenomenon taking place the same way that spherulitic growth does. The author also points out the assumption of temperature homogeneity across the sample, which may have not been the case; as well as the thermal contribution linked to crystallisation being ignored [92].

Another composite modelling approach worth mentioning is that presented by Guan and Pitchumani [96], which focused on the tow-placement process of CF/PEEK. This model does take into account spatial temperature variation and thermal history (as a consequence of the manufacturing process' heat source). The model domain focuses on a small area located at one of the interfaces between substrate prepreg layers, bound at the top and bottom by neighbouring fibres, as shown in Figure 2.37. Further details of the model, as well as the heat transfer boundary conditions and further mathematical details of the analysis, can be found in [96,97].

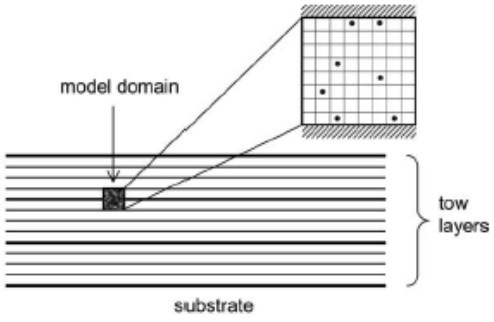

Figure 2.37: Illustration of a location substrate where the microstructural modelling is considered [96].

Studied parameters were based on using a hot gas torch as a heating source: incidence angle, torch exit diameter, torch distance to the target, hot gas temperature, gas velocity, line speed, and number of layers in the tow substrate. The discussion of the results is lengthy and focuses on optimising the manufacturing process, which lies outside of the scope of this literature review. The model, however, effectively shows the dependence of transcrystallinity on the different processing parameters, and demonstrates a larger development of this phase with longer exposure times. The model follows the impact that nucleation density in the bulk has: with a lower nucleation density, the transcrystalline region can grow for longer periods before coming into contact with any spherulites growing in the matrix bulk. This correlates with larger spherulite sizes in the bulk, since there are fewer nucleation sites and therefore spherulites grow for

longer before they reach impingement. A figure comparing two simulations with extreme processing conditions, showing the largest and smallest spherulites and transcrystallinity development in CF/PEEK can be seen in Figure 2.38, including snapshots at different relative crystallinities.

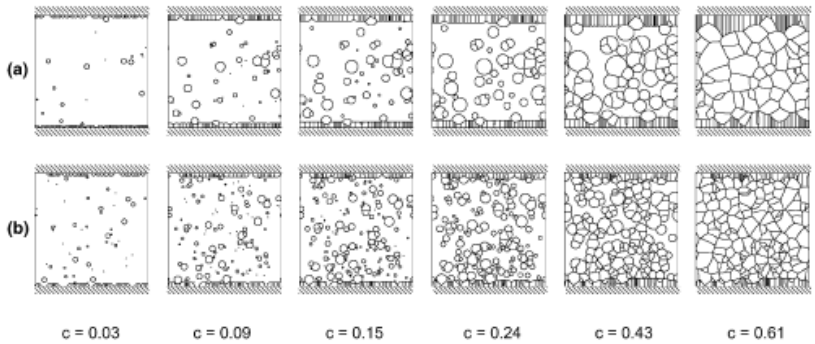

Case	(a)	(b)
Hot gas temperature (°C)	900	700
Gas velocity (m/s)	650	590
Line speed (mm/s)	10	20

Figure 2.38: Comparison of spherulitic microstructure observations obtained from simulation between two extreme processing conditions at different relative crystallinities "c". For both cases, incidence angle is 60°, torch exit diameter is 8mm, and torch distance to target is 32mm [96].

Results show that various spherulitic morphologies can be achieved with different processing conditions that will produce the same overall degree of crystallinity, and therefore processing parameters can be optimised in order to achieve the desired mechanical properties. The model focuses, however, on a small segment of the composite during the manufacturing process, not considering other factors such as degradation, interlaminar surface contact or bonding. Experimental verification of the authors' findings would provide further grounds for the success of this model.

2.4. Automated tape placement

The use of high-performance thermoplastic matrices such as PEKK is of high interest in the aerospace industry. This is not only due to having a better starting point to mechanically recycle the components at their end of life, but also driven by the need to eliminate the high capital cost and the bottlenecks caused by autoclave manufacturing, as well as any post-processing techniques that increase the cost of manufacturing of these parts. An example of such a single-step, in-situ manufacturing process is automated tape placement (ATP), the manufacturing technique that is central to this thesis. This consists of a computer-guided robotic arm with a tape-laying head attached to it, which lays prepreg tape over a tool surface. A schematic of this can be seen in Figure 2.39. Such processes are designed for fast production, cost reduction, automation, manufacturing repeatability and the capability to produce complex geometries [98,99]. This poses an advantage over better-established processing techniques such as autoclaving, in which part size is limited by the equipment size, requires a high capital cost, long cycle times, and manufacturing complex geometries with internal cavities requires complex tooling and/or bagging [99].

However, the fast manufacturing nature of ATP (consolidation times of seconds or a fraction of a second [6]) can result in lower quality and performance of products when compared to slower processing techniques like autoclaving (compression moulding and autoclaving often provide consolidation times of 20-60+ minutes [8,69,71]). The temperature, pressure and environmental control that autoclave manufacturing provides is often considered the gold standard in composite manufacturing. When compared to this, the fast-paced nature of the ATP manufacturing process results in very short exposure

times to high temperatures and pressures. This limits the time window for resin flow, adhesion between the laid plies and void reduction, which are factors that play key roles in consolidation quality, part integrity and properties [6,71,100–102].

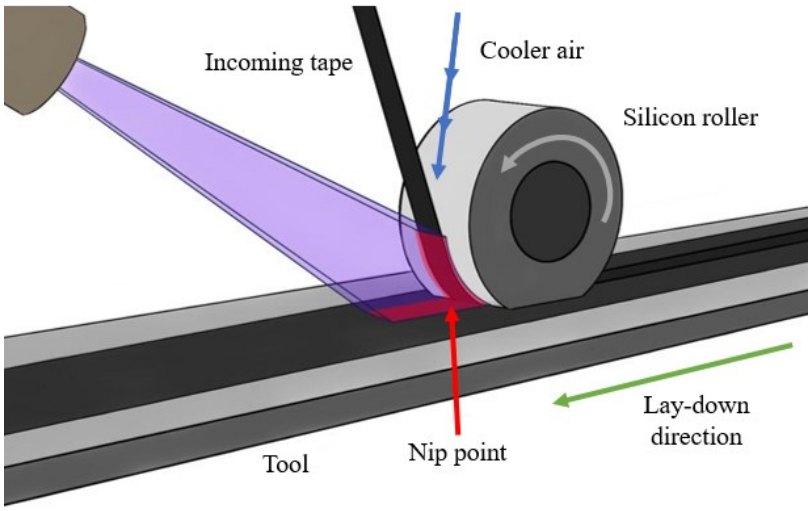

Figure 2.39: Diagram of ATP manufacturing process.

The use of thermoplastics for in-situ manufacturing comes with further challenges regarding their processing. Thermoplastics possess high viscosities in molten conditions when compared to thermosetting resins, hindering fibre impregnation, interply contact and polymer chain reptation. These difficulties are highlighted in literature, where microscopy of manufactured laminates via different routes shows drastic differences in the consolidation quality. Figure 2.40 by Comer et al. [71] shows voids observed via x-ray tomography present in CF/PEEK prepreg material, which are shown in Figure 2.41a and c to remain after ATP manufacturing as intra-ply voids. Inter-ply voids, observable between prepreg layers in Figure 2.41a and c, are generally governed by the prepreg's surface roughness and processing parameters, where resin-rich surfaces and adequate nip temperatures contribute towards achieving a good intimate interlayer contact [71,103]. Both types of voids initiate fibre/matrix debonding and negatively impact mechanical performance. In the autoclaved samples shown in Figure 2.41b and d, on the other hand, these voids are not present, due to the longer holding times under high temperatures and pressures resulting in a homogenisation of the fibre/matrix distribution and a better interply adhesion. Gruber et al [103] observed similar findings for CF/PEEK, highlighting the necessity for better quality prepregs in order to achieve better mechanical performance in in-situ manufacturing. In their work, the prepreg tapes shown in Figure 2.42 display excessive tape roughness and void content, and that is reflected in the ATP laminates they manufactured. This was observed in the case of CF/PEKK in Hoang et al.'s recently published work [66], where ATP manufacturing vs. ATP followed by hydraulic press post-processing achieved very different consolidations (~6% vs. ~0.5% void content respectively), as observed in Table 2.12. Void content measurement, as well as crystallinity and ILSS performance of these laminates are given in Table 2.8 in Section 2.2.4.

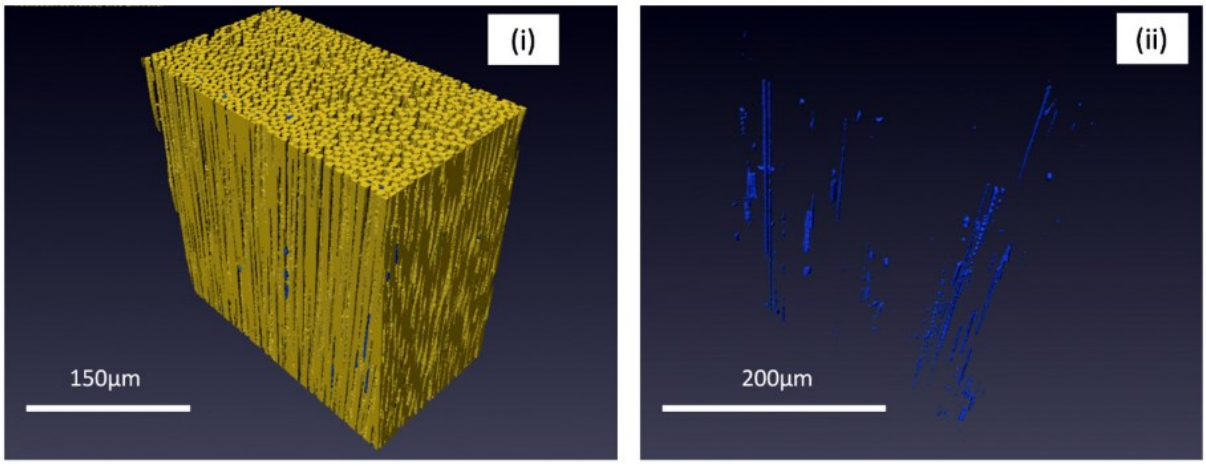

Figure 2.40: 3D X-ray tomography of prepreg material, showing (i) carbon fibre (yellow and voids) blue, and (ii) the elongated nature of voids oriented in the fibre direction [71].

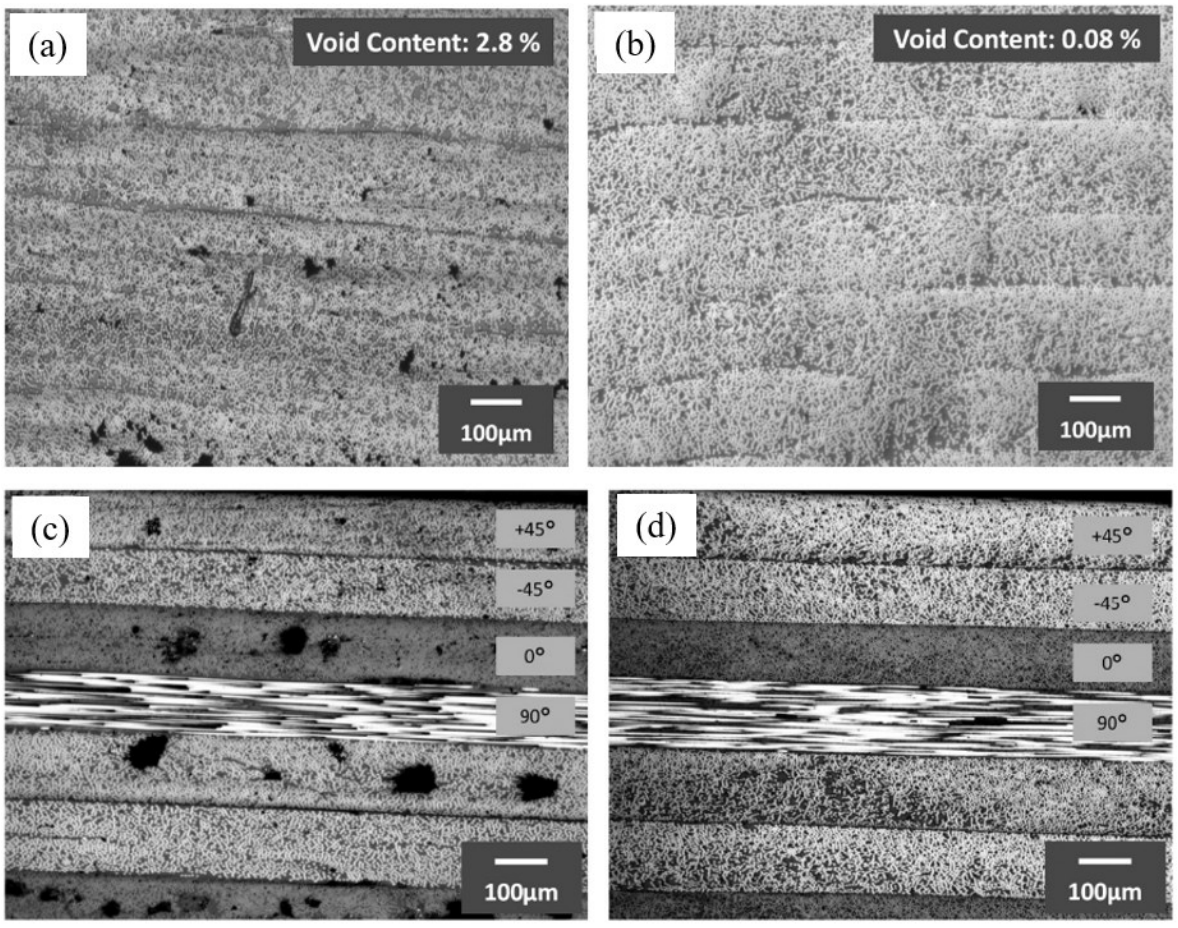

Figure 2.41: Microstructure and void content of (a), (c) laser ATP and (b), (d) autoclave specimens for (a), (b) ILSS testing and (c), (d) open-hole compression testing [71].

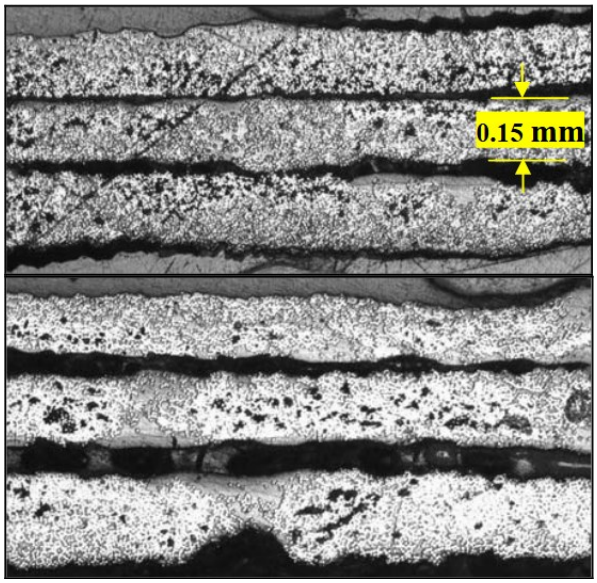

Figure 2.42: CF/PEEK prepreg tape (APC2-AS4) showing excessive surface roughness and void content [103].

Table 2.12: Micrographs of CF/PEKK for different processing conditions and post-processing methods. Adapted from [66].

ATP parameters used	ATP only	ATP and hydraulic press post-processing
Laser power: 3349 W Nip temp: 417°C Lay-down speed: 2.4 m/min	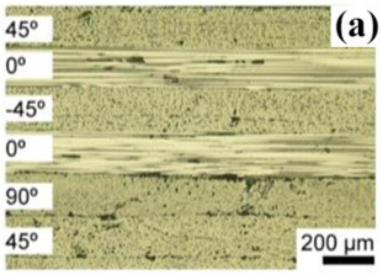	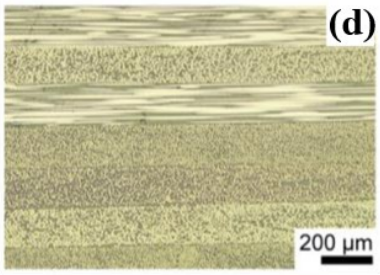
Laser power: 3460 W Nip temp: 430°C Lay-down speed: 2.4 m/min	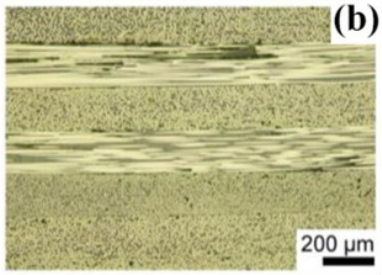	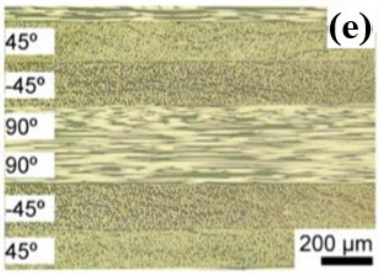
Laser power: 3460 W Nip temp: 430°C Lay-down speed: 6 m/min	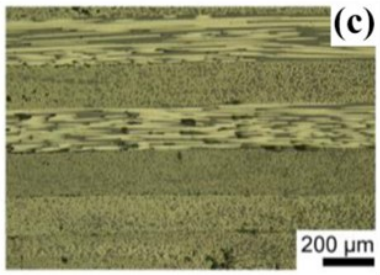	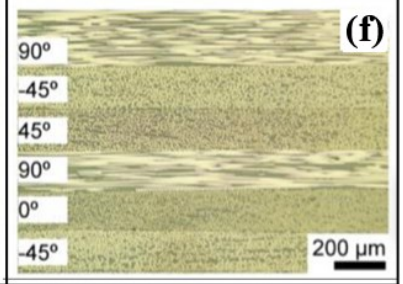

Apart from prepreg tape quality, optimised use of parameters during ATP manufacturing is also essential to ensure good laminate performance. This can affect not only void content and interply adhesion, but also crystallinity in the case of thermoplastics such as CF/PEEK and CF/PEKK. Literature has highlighted melting temperature, lay-down speed and consolidation pressure as the three most significant factors contributing towards robust manufacturing of ATP laminates. While the following paragraphs provide a brief overview of the impact of these ATP parameters on CF/PEEK (and CF/PEKK where available), review articles by Oromiehie et al. [104] and Martin et al. [105] provide further insight into defects and inspection techniques [104], as well as thermal modelling, adhesion, crystallinity development and thermal degradation [105].

One of the main parameters affecting material properties of composites during ATP manufacturing is temperature, namely nip temperature and the use of a heated tool. In the case of semicrystalline thermoplastics specifically, allowing for crystallinity to develop is paramount due to the strong impact it has on mechanical and chemical performance [6,106,107], and the thermal history that the material experiences is essential for this. Esguerra-Arce et al. [11] observed significantly higher crystallinities in CF/PEKK laminates manufactured with a heated tool at 200°C compared to an unheated tool at 20°C. In the case of the unheated tool, a crystallinity gradient was observed ranging from 15-35%, where the layers closer to the tooling achieved a lower crystallisation. This is due to the material experiencing abrupt cooling profiles at the layers closer to the tooling, and as more tapes are laid, the material in place retains heat better. This not only allows for annealing, but also allows the newly laid tape to remain at higher temperatures for longer, resulting in slower cooling rates which may aid with further crystallisation. This is further confirmed by Sonmez and Hahn's modelling of crystallinity development during ATP manufacturing [108]. Lamontia and Gruber [100], who performed a study manufacturing CF/PEKK laminates on a heated aluminium tool at 175°C and on an unheated insulated tool, also observed significant crystallinity variation across the thickness of the two laminates. However, neither work achieved the maximum crystallinity of the PEKK polymer, in this case 26-29%. In the case of the heated tool, the first laid ply reached 23% crystallinity due to the annealing it underwent by being in contact with the heated tooling, however all remaining layers achieved crystallinities below 14%, many of these below 4%. Achieved crystallinities were even lower in the case of the unheated tool. Disparities between the work of Esguerra-Arce et al. [11] and Lamontia and Gruber [100] regarding the success of the work and the crystallisation ability of PEKK are likely due to the use of different grades of PEKK, which are not disclosed in either work.

Literature reports lay-down speed to have a lesser effect on the aforementioned properties. Slower lay-down speeds impact the time that a portion of the material is exposed to nip temperature for, and therefore is more of an indirect effect of temperature exposure. Stokes-Griffin and Compston [6] investigated different lay-down rates in their work on CF/PEEK and found that slower lay-down speeds contribute towards a longer time under heat exposure and therefore benefit the laminate performance. Similar results were observed in Qureshi et al.'s work [101]. However, this may result in excessive exposure to high temperatures, resulting in polymer degradation, adversely impacting properties, also observed in Pitchumani et al.'s work [109]. In Hoang et al.'s work on CF/PEKK [66], variations in both lay-down speed and nip temperature had minimal effect on the performance of the resulting laminates, these being considerably lower than what is achieved via conventional methods. The reason for this disparity could be due to CF/PEKK possessing lower crystallisation temperatures, as well as the limited temperature range

that was assessed in Hoang et al.'s work compared to work on CF/PEEK. It is important to note however, that slower lay-down speeds which may contribute to better properties may not lead to optimum fabrication times.

Consolidation pressure during ATP manufacturing is likely to have a lesser effect on the crystallinity development, but more on the interply adhesion and void content. Combined with heat, it may positively contribute to molecular diffusion across plies when in contact with one another, as well as facilitating resin flow into the intraply voids. However, some studies point out that this is the factor that affects the quality of ATP manufactured laminates the least, and in some cases has minimal effect on properties [101,103]. Roller pressure on plies works for very short periods during lay-down, resulting in a very limited window for resin flow, as well as pressure releases while the material is often still above glass transition temperature. This may result in void rebound, where voids that had initially been compressed during the roller pass re-emerge [109]. Gruber et al. [103] also found layer permeability to be an issue, where fibre-rich regions close-pack and lock up existing voids, not allowing resin flow.

The effect of the aforementioned parameters on laminate consolidation and crystallinity development inevitably impacts the mechanical performance of the polymer composites. For instance, Stokes-Griffin and Compston's work [6] on the effect of a wide range of nip temperatures and lay-down speeds on CF/PEEK highlighted this, achieving short-beam shear strengths comparable to conventionally prepared laminates. On the other hand, Hoang et al.'s work [66] on CF/PEKK ATP laminates varying nip temperature and lay-down speed did not show significant improvements, and ATP performance was significantly lower than that of compression-moulded specimens. Further literature discussion on the impact of ATP parameters on mechanical performance can be found in Chapter 6, where results reported in literature are compared with the findings of this body of work.

Apart from these parameters, accurate placement of plies during lay-down is also essential to achieve the desired part performance. Placement and steering-induced defects are out of the scope of this thesis, but worth highlighting briefly, as lay-down can become challenging with increasingly complex part geometries. Formation of gaps and overlaps, tow drop coverage, wrinkling or bridging defects due to tension are some examples of defect sources. An in-depth review of such placement and steering-induced defects can be found in Oromiehie et al.'s work [104].

Overall, optimising the processing parameters of ATP is of paramount importance for thermoplastics, particularly offering temperature and pressure control and exposure times catered to the material being used. In order to fully optimise the processing of such materials, however, it is important to establish an understanding of the effect of thermal history on the morphology and properties of the composite matrix.

2.5. Chapter summary

An understanding of the crystallinity development in CF/PEKK composites is important to establish the reliability of such products in high-performance applications such as the aerospace or the oil and gas sectors. There are studies on the crystalline morphology of PEKK, its terephthalic/isophthalic content ratios and its influence on crystallisation. The external factors that affect crystallisation are also clearly

identified, such as crystallisation mode and thermal history, and their effects on the unit cell and spherulite morphology.

The effect of carbon fibre reinforcement on the crystallisation morphology of PEKK at the fibre-matrix interface is not as obvious as crystallisation in the bulk. Literature covering this is sparse, so a comparison with PEEK has been drawn whenever relevant. Overall, the presence of transcrystallinity is still a topic under investigation and different observations have been reported. There is a likely dependence on the fibre surface energy, where a low surface energy results in little attraction between the fibre and matrix and therefore lamellae form perpendicular to the surface, creating a transcrystalline phase of epitaxial form; whereas high-energy surfaces invite lamellae to grow flat-on, and therefore growths take on a more spherulitic shape and no transcrystallinity is formed. Transcrystalline growth is also observed to be incentivised by high isothermal temperatures and slow cooling rates, which allows for larger crystallisation growth from the fibre surface and less nucleation in the bulk. Simulations have been developed that successfully demonstrate the development of this phase. Literature reports different findings, however, when assessing whether the presence of transcrystallinity benefits or hinders composite mechanical properties. Further investigations on different carbon fibre types and their interactions with PEKK polymers are needed in order to reach a consensus on this topic.

A dual crystallisation mode is reported for PEKK in both unreinforced and carbon fibre reinforced composite form, consisting of a primary, spherulitic growth followed by a secondary stage, where interlamellar crystalline structures grow. Quantifying the primary and secondary crystalline phases present has been the object of study particularly when modelling crystallisation kinetics, mainly in the case of unreinforced PEKK. The impact of thermal processing cycles on this is clearly reported, where holding temperature and time are observed to influence the extent and nature of crystallinity developed in the material. Robust models have been developed for the isothermal crystallisation cases of PEKK, but further refinement is needed in the case of non-isothermal crystallisation kinetics.

In the case of CF/PEKK composites, crystallisation kinetics studies are minimal. The available literature reports higher isothermal temperatures resulting in faster kinetics for the composites, potentially due to fibres acting as nucleation sites and kinetics in the bulk being low; whereas at lower isothermal temperatures the difference is not notable, since nucleation in the bulk is faster and fibres hinder macromolecular chain mobility. A few of the aforementioned crystallisation kinetics models applied to unreinforced PEEK and PEKK have also been implemented to their composite counterparts with some success, however, once again this is less diligent than for neat PEEK and PEKK, and existing models may need some adaptation to account for the inclusion of carbon fibres.

Within fast-paced manufacturing contexts such as ATP, high-performance thermoplastics of the likes of PEKK not only pose challenges due to the limited understanding of the polymer's crystallisation capabilities, but also due to high viscosity in molten states, affecting fibre impregnation, interply contact, and polymer chain movement. These issues lead to variable consolidation quality in manufactured laminates, which in turn affect mechanical performance. To optimize thermoplastic processing within such manufacturing techniques, understanding the influence of thermal history on matrix morphology and properties is essential.

Chapter references

[1] Blundell DJ, Crick RA, Fife B, Peacock J, Keller A, Waddon A. Spherulitic morphology of the matrix of thermoplastic PEEK/carbon fibre aromatic polymer composites. J Mater Sci 1989;24:2057–64. https://doi.org/10.1007/BF02385421.

[2] Deignan A, Stanley WF, McCarthy M. Insights into wide variations in carbon fibre/polyetheretherketone rheology data under automated tape placement processing conditions. J Compos Mater 2018;52:2213–28. https://doi.org/10.1177/0021998317740733.

[3] Gardner KH, Hsiao BS, Faron KL. Polymorphism in poly (aryl ether ketone). Polymer 1994;35:2290–5.

[4] Jin L, Ball J, Bremner T, Sue HJ. Crystallization behavior and morphological characterization of poly(ether ether ketone). Polymer 2014;55:5255–65. https://doi.org/10.1016/j.polymer.2014.08.045.

[5] Rodríguez-Lence F, Zuazo M, Calvo S, Lorenzo E. Activities on in-situ consolidation by automated placement technologies. 16th Eur Conf Compos Mater 2014:22–6.

[6] Stokes-Griffin CM, Compston P. The effect of processing temperature and placement rate on the short beam strength of carbon fibre-PEEK manufactured using a laser tape placement process. Compos Part Appl Sci Manuf 2015;78:274–83. https://doi.org/10.1016/j.compositesa.2015.08.008.

[7] Zhu K, Tan H, Wang Y, Liu C, Ma X, Wang J, et al. Crystallization and mechanical properties of continuous carbon fiber reinforced polyether-ether-ketone composites. Fibers Polym 2019;20:839–46. https://doi.org/10.1007/s12221-019-8791-5.

[8] Kilroy JP, Ó Brádaigh CM, Semprimoschnig COA. Mechanical and physical evaluation of a new carbon fibre/PEEK composite system for space applications. SAMPE J 2008:1–12.

[9] Choupin T, Fayolle B, Régnier G, Paris C, Cinquin J, Brulé B. Isothermal crystallization kinetic modeling of poly(etherketoneketone) (PEKK) copolymer. Polymer 2017;111:73–82. https://doi.org/10.1016/j.polymer.2017.01.033.

[10] Donadei V, Lionetto F, Wielandt M, Offringa A, Maffezzoli A. Effects of blank quality on press-formed PEKK/Carbon composite parts. Materials 2018;11. https://doi.org/10.3390/ma11071063.

[11] Esguerra-Arce I, Martín MI, Pérez-Pastor A, García-Martínez V. Evolution of crystallinity with multiple lamination steps in high performance thermoplastic composites by in-situ consolidation process. Twenty-Second Int Conf Compos Mater 2019.

[12] Gardner KCH, Hsiao BS, Matheson RR, Wood BA. Structure, crystallization and morphology of poly (aryl ether ketone ketone). Polymer 1992;33:2483–95. https://doi.org/10.1016/0032-3861(92)91128-O.

[13] Ho RM, Cheng SZD, Hsiao BS, Gardner KH. Crystal morphology and phase identifications in poly(aryl ether ketone)s and their copolymers. 3. Polymorphism in a polymer containing alternated terephthalic acid and isophthalic acid isomers. Macromolecules 1995;28:1938–45. https://doi.org/10.1021/ma00110a030.

[14] Hsiao BS, Chang IY, Sauer BB. Isothermal crystallization kinetics of poly(ether ketone ketone) and its carbon-fibre-reinforced composites. Polymer 1991;32:2799–805. https://doi.org/10.1016/0032-3861(91)90111-U.

[15] Quiroga Cortés L, Caussé N, Dantras E, Lonjon A, Lacabanne C. Morphology and dynamical mechanical properties of poly ether ketone ketone (PEKK) with meta phenyl links. J Appl Polym Sci 2016;133:1–10. https://doi.org/10.1002/app.43396.

[16] Reitman M, Jaekel D, Siskey R, Kurtz SM. Morphology and Crystalline Architecture of Polyaryletherketones. 2nd ed. Elsevier Inc.; 2012. https://doi.org/10.1016/B978-1-4377-4463-7.10004-1.

[17] Cogswell FN. Thermoplastic matrix resins: Polyetheretherketone. Thermoplast. Aromat. Polym. Compos. Study Struct. Process. Prop. Carbon Fibre Reinf. Polyetheretherketone Relat. Mater., Butterworth-Heinemann Ltd; 1992, p. 21–30.

[18] Hsiao BS, Gardner KH, Cheng SZD. Crystallization of poly(aryl ether ketone ketone) copolymers containing terephthalate/isophthalate moieties. J Polym Sci Part B Polym Phys 1994;32:2585–94. https://doi.org/10.1002/polb.1994.090321604.

[19] Arkema. Introduction to ultra high-performance Kepstan® PEKK 2020.

[20] Blundell DJ, Newton AB. Variations in the crystal lattice of PEEK and related para-substituted aromatic polymers: 2. Effect of sequence and proportion of ether and ketone links. Polymer 1991;32:308–13. https://doi.org/10.1016/0032-3861(91)90019-F.
[21] Cheng SZD, Ho RM, Hsiao BS, Gardner KH. Polymorphism and crystal structure identification in poly(aryl ether ketone ketone)s. Macromolecules 1996;197:185–213.
[22] Ho RM, Cheng SZD, Hsiao BS, Gardner KH. Crystal Morphology and Phase Identifications in Poly(aryl ether ketone)s and Their Copolymers. 1. Polymorphism in PEKK. Macromolecules 1994;27:2136–40. https://doi.org/10.1021/ma00086a023.
[23] Painter PC, Coleman MM. Polymer Morphology. Fundam. Polym. Sci. Introd. Text. 2nd edition, Routledge; 1997, p. 250–3.
[24] Lee Y, Porter RS. Crystallization of poly(etheretherketone) (PEEK) in carbon fiber composites. Polym Eng Sci 1986;26:633–9. https://doi.org/10.1002/pen.760260909.
[25] Chen EJH, Hsiao BS. The effects of transcrystalline interphase in advanced polymer composites. Polym Eng Sci 1992;32:280–6. https://doi.org/10.1002/pen.760320408.
[26] Cebe P. Non-isothermal crystallization of poly(etheretherketone) aromatic polymer composite. Polym Compos 1988;9:271–9. https://doi.org/10.1002/pc.750090405.
[27] Cebe P. Application of the parallel Avrami model to crystallization of poly(etheretherketone). Polym Eng Sci 1988;28:1192–7. https://doi.org/10.1002/pen.760281809.
[28] Choupin T. Mechanical performances of PEKK thermoplastic composites linked to their processing parameters. École nationale supérieure d'arts et métiers, 2017.
[29] Gao S-L, Kim J-K. Cooling rate influences in carbon fibre/PEEK composites. Part I. Crystallinity and interface adhesion. Compos Part Appl Sci Manuf 2000;31:517–30. https://doi.org/10.1016/S1359-835X(00)00009-9.
[30] Velisaris CN, Seferis JC. Crystallization kinetics of polyetheretherketone (peek) matrices. Polym Eng Sci 1986;26:1574–81. https://doi.org/10.1002/pen.760262208.
[31] Waddon AJ, Hill MJ, Keller A, Blundell DJ. On the crystal texture of linear polyaryls (PEEK, PEK and PPS). J Mater Sci 1987;22:1773–84. https://doi.org/10.1007/BF01132406.
[32] Lustiger A. Morphological aspects of the interface in the PEEK-carbon fiber system. Polym Compos 1992;13:408–12. https://doi.org/10.1002/pc.750130511.
[33] Hobbs SY. Row nucleation of isotactic polypropylene on graphite fibres. Nat Phys Sci 1971;234. https://doi.org/10.1038/physci234012a0.
[34] Chang IY, Hsiao BS. Thermal properties of high performance thermoplastic composites based on poly(ether ketone ketone) (PEKK). 36th Int SAMPE Symp 1991:1587–601.
[35] Choupin T, Fayolle B, Régnier G, Paris C, Cinquin J, Brulé B. A more reliable DSC-based methodology to study crystallization kinetics: Application to poly(ether ketone ketone) (PEKK) copolymers. Polymer 2018;155:109–15. https://doi.org/10.1016/j.polymer.2018.08.060.
[36] Bassett DC, Olley RH, Al Raheil IAM. On crystallization phenomena in PEEK. Polymer 1988;29:1745–54. https://doi.org/10.1016/0032-3861(88)90386-2.
[37] Bessard E, De Almeida O, Bernhart G. Unified isothermal and non-isothermal modelling of neat PEEK crystallization. J Therm Anal Calorim 2014;115:1669–78. https://doi.org/10.1007/s10973-013-3308-8.
[38] Blundell DJ, Osborn BN. The morphology of poly(aryl-ether-ether-ketone). Polymer 1983;24:953–8. https://doi.org/10.1016/0032-3861(83)90144-1.
[39] Cebe P, Hong S-D. Crystallization behaviour of poly(ether-ether-ketone). Polymer 1986;27:1183–92. https://doi.org/10.1016/0032-3861(86)90006-6.
[40] Cheng SZD, Cao MY, Wunderlich B. Glass transition and melting behavior of poly(oxy-1,4-phenyleneoxy-1,4-phenylenecarbonyl-1,4-phenylene) (PEEK). Macromolecules 1986;19:1868–76. https://doi.org/10.1021/ma00161a015.
[41] Ko TY, Woo EM. Changes and distribution of lamellae in the spherulites of poly(ether ether ketone) upon stepwise crystallization. Polymer 1996;37:1167–75. https://doi.org/10.1016/0032-3861(96)80843-3.
[42] Lattimer MP, Hobbs JK, Hill MJ, Barham PJ. On the origin of the multiple endotherms in PEEK. Polymer 1992;33:3971–3. https://doi.org/10.1016/0032-3861(92)90391-9.
[43] Lee Y, Porter RS, Lin JS. On the double-melting behavior of poly(ether ether ketone). Macromolecules 1989;22:1756–60. https://doi.org/10.1021/ma00194a043.

[44] Medellín-Rodríguez FJ, Phillips PJ. Bulk crystallization of poly(aryl ether ether ketone) (PEEK). Polym Eng Sci 1996;36:703–12. https://doi.org/10.1002/pen.10457.
[45] Tan S, Su A, Luo J, Zhou E. Crystallization kinetics of poly(ether ether ketone) (PEEK) from its metastable melt. Polymer 1999;40:1223–31. https://doi.org/10.1016/S0032-3861(98)00275-4.
[46] Tardif X, Pignon B, Boyard N, Schmelzer JWP, Sobotka V, Delaunay D, et al. Experimental study of crystallization of PolyEtherEtherKetone (PEEK) over a large temperature range using a nano-calorimeter. Polym Test 2014;36:10–9. https://doi.org/10.1016/j.polymertesting.2014.03.013.
[47] Verma RK, Hsiao BS. Some new insights into the crystallization and melting mechanism in semicrystalline semistiff polymers. Trends Polym Sci 1996;9:312–9.
[48] Wei C-L, Chen M, Yu F-E. Temperature modulated DSC and DSC studies on the origin of double melting peaks in poly(ether ether ketone). Polymer 2003;44:8185–93. https://doi.org/10.1016/j.polymer.2003.10.009.
[49] Zhang Z, Zeng H. Effects of thermal treatment on poly(ether ether ketone). Polymer 1993;34:3648–52. https://doi.org/10.1016/0032-3861(93)90049-G.
[50] Hillier IH. Modified avrami equation for the bulk crystallization kinetics of spherulitic polymers. J Polym Sci A 1965;3:3067–78. https://doi.org/10.1002/pol.1965.100030902.
[51] Yuan M, Galloway JA, Hoffman RJ, Bhatt S. Influence of molecular weight on rheological, thermal, and mechanical properties of PEEK. Polym Eng Sci 2011;51:94–102. https://doi.org/10.1002/pen.21785.
[52] Regis M, Zanetti M, Pressacco M, Bracco P. Opposite role of different carbon fiber reinforcements on the non-isothermal crystallization behavior of poly(etheretherketone). Mater Chem Phys 2016;179:223–31. https://doi.org/10.1016/j.matchemphys.2016.05.034.
[53] Lustiger A, Uralil FS, Newaz GM. Processing and structural optimization of PEEK composites. Polym Compos 1990;11:65–75. https://doi.org/10.1002/pc.750110109.
[54] Harris L. A study of the crystallisation kinetics on PEEK and PEEK composites. University of Birmingham, 2011.
[55] Tung CM, Dynes PJ. Morphological characterization of polyetheretherketone–carbon fiber composites. J Appl Polym Sci 1987;33:505–20. https://doi.org/10.1002/app.1987.070330218.
[56] Gao S-L, Kim J-K. Crystallinity and interphase properties of carbon fibre/PEEK matrix composites. ICCM12 Conf Paris Fr 1999.
[57] Ye L, Scheuring T, Friedrich K. Matrix morphology and fibre pull-out strength of T700/PPS and T700/PET thermoplastic composites. J Mater Sci 1995;30:4761–9. https://doi.org/10.1007/BF01154482.
[58] Zou YL, Netravali AN. Ethylene/ammonia plasma polymer deposition for controlled adhesion of graphite fibers to PEEK. J Adhes Sci Technol 1995;9:1505–20. https://doi.org/10.1163/156856195X00158.
[59] Beehag A, Ye L. Fibre/Matrix adhesion in thermoplastic composites : is transcrystallinity a key? Proc ICCM-11 1997.
[60] Folkes MJ, Kalay G, Ankara A. The effect of heat treatment on the properties of PEEK and APC2. Compos Sci Technol 1993;46:77–83. https://doi.org/10.1016/0266-3538(93)90083-S.
[61] Saiello S, Kenny J, Nicolais L. Interface morphology of carbon fibre/PEEK composites. J Mater Sci 1990;25:3493–6. https://doi.org/10.1007/BF00575375.
[62] Kwei TK, Schonhorn H, Frisch HL. Dynamic mechanical properties of the transcrystalline regions in two polyolefins. J Appl Phys 1967;38:2512–6. https://doi.org/10.1063/1.1709938.
[63] Matsuoka S, Daane JH, Bair HE, Kwei TK. A further study of the properties of transcrystalline regions in polyethylene. J Polym Sci [B] 1968;6:87–91. https://doi.org/10.1002/pol.1968.110060117.
[64] Zhang M, Xu J, Zhang Z, Zeng H, Xiong X. Effect of transcrystallinity on tensile behaviour of discontinuous carbon fibre reinforced semicrystalline thermoplastic composites. Polymer 1996;37:5151–8. https://doi.org/10.1016/0032-3861(96)00341-2.
[65] Choupin T, Debertrand L, Fayolle B, Régnier G, Paris C, Cinquin J, et al. Influence of thermal history on the mechanical properties of poly(ether ketone ketone) copolymers. Polym Cryst 2019;2:e10086. https://doi.org/10.1002/pcr2.10086.
[66] Hoang V-T, Kwon B-S, Sung J-W, Choe H-S, Oh S-W, Lee S-M, et al. Postprocessing method-induced mechanical properties of carbon fiber-reinforced thermoplastic composites. J Thermoplast Compos Mater 2023;36:432–47. https://doi.org/10.1177/0892705720945376.

[67] Kobayashi H, Hayakawa E, Kikutani T, Takaku A. Effect of quenching and annealing on fiber pull-out from crystalline polymer matrices. Adv Compos Mater 1991;1:155–68. https://doi.org/10.1163/156855191X00252.
[68] Beehag A, Ye L. Influence of cooling rate on interlaminar fracture properties of unidirectional commingled CF/PEEK composites. Appl Compos Mater 1995;2:135–51. https://doi.org/10.1007/BF00567748.
[69] Beehag A, Ye L. Role of cooling pressure on interlaminar fracture properties of commingled CF/PEEK composites. Compos Part Appl Sci Manuf 1996;27:175–82. https://doi.org/10.1016/1359-835X(95)00027-Y.
[70] Weiss R. Influence of production parameters on the mechanical behaviour of CF/PEEK. Dev. Sci. Technol. Compos. Mater., Stuttgart: 1990, p. 1007–12.
[71] Comer AJ, Ray D, Obande WO, Jones D, Lyons J, Rosca I, et al. Mechanical characterisation of carbon fibre–PEEK manufactured by laser-assisted automated-tape-placement and autoclave. Compos Part Appl Sci Manuf 2015;69:10–20. https://doi.org/10.1016/j.compositesa.2014.10.003.
[72] Avrami M. Kinetics of phase change. I: General theory. J Chem Phys 1939;7:1103–12. https://doi.org/10.1063/1.1750380.
[73] Shirzad K, Viney C. A critical review on applications of the Avrami equation beyond materials science. J R Soc Interface 2023;20:20230242. https://doi.org/10.1098/rsif.2023.0242.
[74] Chelaghma SA, De Almeida O, Margueres P, Passieux J, Perie J, Vinet A, et al. Identification of isothermal crystallization kinetics of poly(ether-ketone-ketone) based on spherulite growth measurements and enthalpic data. Polym Cryst 2020;3. https://doi.org/10.1002/pcr2.10141.
[75] Banks W, Sharples A, Hay JN. The effect of simultaneously occurring processes on the course of polymer crystallization. J Polym Sci A 1964;2:4059–67. https://doi.org/10.1002/pol.1964.100020923.
[76] Cowie JMG. The crystalline state: Kinetics of crystallization. Polym. Chem. Phys. Mod. Mater. 2nd edition, Blackie Academic & Professional; 1998.
[77] Hoffman JD, Lauritzen JI. Crystallization of bulk polymers with chain folding: theory of growth of lamellar spherulites. J Res Natl Bur Stand Sect Phys Chem 1961;65A:297–336. https://doi.org/10.6028/jres.065a.035.
[78] Nakamura K, Katayama K, Amano T. Some aspects of nonisothermal crystallization of polymers. II. Consideration of the isokinetic condition. J Appl Polym Sci 1973;17:1031–41. https://doi.org/10.1002/app.1973.070170404.
[79] Ziabicki A. Theoretical analysis of oriented and non isothermal crystallization. Colloid Polym Sci 1974;252:207–21.
[80] Patel RM, Spruiell JE. Crystallization kinetics during polymer processing—Analysis of available approaches for process modeling. Polym Eng Sci 1991;31:730–8. https://doi.org/10.1002/pen.760311008.
[81] Ozawa T. Kinetics of non-isothermal crystallization. Polymer 1971;12:150–8. https://doi.org/10.1016/0032-3861(71)90041-3.
[82] Bianchi O, Oliveira RVB, Fiorio R, Martins JDN, Zattera AJ, Canto LB. Assessment of Avrami, Ozawa and Avrami–Ozawa equations for determination of EVA crosslinking kinetics from DSC measurements. Polym Test 2008;27:722–9. https://doi.org/10.1016/j.polymertesting.2008.05.003.
[83] Di Lorenzo ML, Silvestre C. Non-isothermal crystallization of polymers. Prog Polym Sci 1999;24:917–50. https://doi.org/10.1016/S0079-6700(99)00019-2.
[84] Long Y, Shanks RA, Stachurski ZH. Kinetics of polymer crystallisation. Prog Polym Sci 1995;20:651–701. https://doi.org/10.1016/0079-6700(95)00002-W.
[85] Tierney JJ, Gillespie JW. Crystallization kinetics behavior of PEEK based composites exposed to high heating and cooling rates. Compos Part Appl Sci Manuf 2004;35:547–58. https://doi.org/10.1016/j.compositesa.2003.12.004.
[86] Seo J, Zhang X, Schaake RP, Rhoades AM, Colby RH. Dual Nakamura model for primary and secondary crystallization applied to nonisothermal crystallization of poly(ether ether ketone). Polym Eng Sci 2021;61:2416–26. https://doi.org/10.1002/pen.25767.
[87] Seo J, Gohn AM, Dubin O, Takahashi H, Hasegawa H, Sato R, et al. Isothermal crystallization of poly(ether ether ketone) with different molecular weights over a wide temperature range. Polym Cryst 2019;2:e10055. https://doi.org/10.1002/pcr2.10055.

[88] Tobin MC. Theory of phase transition kinetics with growth site impingement. I. Homogeneous nucleation. J Polym Sci Polym Phys Ed 1974;12:399–406. https://doi.org/10.1002/pol.1974.180120212.
[89] Tobin MC. The theory of phase transition kinetics with growth site impingement. II. Heterogeneous nucleation. J Polym Sci Polym Phys Ed 1976;14:2253–7. https://doi.org/10.1002/pol.1976.180141210.
[90] Tobin MC. Theory of phase transition kinetics with growth site impingement. III. Mixed heterogeneous–homogeneous nucleation and nonintegral exponents of the time. J Polym Sci Polym Phys Ed 1977;15:2269–70. https://doi.org/10.1002/pol.1977.180151217.
[91] Choe CR, Lee KH. Nonisothermal crystallization kinetics of poly(etheretherketone) (PEEK). Polym Eng Sci 1989;29:801–5. https://doi.org/10.1002/pen.760291208.
[92] Chelaghma S, Passieux J-C, Almeida OD, Périé J-N, Marguères P, Vinet A. Modélisation Pixel Coloring de la cristallisation du PEKK. Comptes Rendus JNC 21 - Bordx INP 2019:9.
[93] Ruan C, Ouyang J, Liu S, Zhang L. Computer modeling of isothermal crystallization in short fiber reinforced composites. Comput Chem Eng 2011;35:2306–17. https://doi.org/10.1016/j.compchemeng.2010.11.011.
[94] Ruan C, Guo L, Liang K, Li W. Computer modeling and simulation for 3D crystallization of polymers. II. Non-isothermal case. Polym-Plast Technol Eng 2012;51:816–22. https://doi.org/10.1080/03602559.2012.671413.
[95] Ruan C, Liang K, Guo L, Li W. Computer modeling and simulation for 3D crystallization of polymers. I. Isothermal case. Polym-Plast Technol Eng 2012;51:810–5. https://doi.org/10.1080/03602559.2012.671412.
[96] Guan X, Pitchumani R. Modeling of spherulitic crystallization in thermoplastic tow-placement process: Spherulitic microstructure evolution. Compos Sci Technol 2004;64:1363–74. https://doi.org/10.1016/j.compscitech.2003.10.023.
[97] Guan X, Pitchumani R. Modeling of spherulitic crystallization in thermoplastic tow-placement process: heat transfer analysis. Compos Sci Technol 2004;64:1123–34. https://doi.org/10.1016/j.compscitech.2003.08.011.
[98] August Z, Ostrander G, Michasiow, John, Hauber D. Recent developments in automated fiber placement of thermoplastic composites. SAMPE J 2014;50:30–7.
[99] Flanagan M, Goggins J, Doyle A, Weafer B, Ward M, Bizeul M, et al. Out-of-autoclave manufacturing of a stiffened thermoplastic carbon fibre PEEK panel. AIP Conf Proc 2017;1896. https://doi.org/10.1063/1.5008001.
[100] Lamontia M, Gruber M. Remaining developments required for commercializing in situ thermoplastic ATP. SAMPE Eur Conf 2007:1–15.
[101] Qureshi Z, Swait T, Scaife R, El-Dessouky HM. In situ consolidation of thermoplastic prepreg tape using automated tape placement technology: potential and possibilities. Compos Part B Eng 2014;66:255–67. https://doi.org/10.1016/j.compositesb.2014.05.025.
[102] Shadmehri F, Hoa SV, Fortin-Simpson J, Ghayoor H. Effect of in situ treatment on the quality of flat thermoplastic composite plates made by automated fiber placement (AFP). Adv Manuf Polym Compos Sci 2018;4:41–7. https://doi.org/10.1080/20550340.2018.1444535.
[103] Gruber MB, Lockwood IZ, Dolan TL, Funck SB, Tierney JJ, Simacek P, et al. Thermoplastic in situ placement requires better impregnated tapes and tows. Int SAMPE Tech Conf 2012.
[104] Oromiehie E, Prusty BG, Compston P, Rajan G. Automated fibre placement based composite structures: Review on the defects, impacts and inspections techniques. Compos Struct 2019;224:110987. https://doi.org/10.1016/j.compstruct.2019.110987.
[105] Martin I, Saenz del Castillo D, Fernandez A, Güemes A. Advanced Thermoplastic Composite Manufacturing by In-Situ Consolidation: A Review. J Compos Sci 2020;4:149. https://doi.org/10.3390/jcs4040149.
[106] Chanteli A, Bandaru AK, Peeters D, O'Higgins RM, Weaver PM. Influence of repass treatment on carbon fibre-reinforced PEEK composites manufactured using laser-assisted automatic tape placement. Compos Struct 2020;248:112539. https://doi.org/10.1016/j.compstruct.2020.112539.
[107] Denault J, Dumouchel M. Consolidation Process of PEEK/Carbon Composite for Aerospace Applications. Adv Perform Mater 1998;5:83–96. https://doi.org/10.1023/A:1008638105370.

[108] Sonmez FO, Hahn HT. Modeling of Heat Transfer and Crystallization in Thermoplastic Composite Tape Placement Process. J Thermoplast Compos Mater 1997;10:198–240. https://doi.org/10.1177/089270579701000301.
[109] Pitchumani R, Gillespie JW, Lamontia MA. Design and Optimization of a Thermoplastic Tow-Placement Process with In-Situ Consolidation. J Compos Mater 1997;31:212–314. https://doi.org/10.1177/002199839703100302.

Chapter 3. Research motivation

Based on the literature review presented in Chapter 2, certain gaps in current knowledge deserve immediate attention. From a subset of these gaps, the aims and objectives of this body of work have been formulated.

3.1. Gaps in existing knowledge

The existing literature shows some limited understanding of PEKK's crystallisation behaviour, morphology and structure, but research on the impact of carbon fibre reinforcement in PEKK is much less conclusive. As has been reported in Chapter 2, it is clear that the nature of the fibre surface can have an effect on the matrix crystallisation and the transcrystalline phase at the fibre/matrix interface. It is difficult, however, to understand transcrystallinity and to correlate its presence (or lack thereof) across different fibres without an understanding of the similarities and differences between said fibres and their surfaces. This is something that is not thoroughly reported in the literature assessing the effect of transcrystallinity in CF/PEEK and CF/PEKK, and leads to confusion. The fibre type, modulus and surface finish can all play a role in the surface energy and therefore influence the presence of transcrystallinity.

Furthermore, reporting on the mechanical behaviour of the transcrystalline phase is also inconclusive. Some literature shows that the presence of a transcrystalline phase results in better mechanical performance, improved fibre-matrix adhesion and higher load transfer, while other authors describe the opposite. Further investigations to clarify this is important, particularly with PEKK, where these studies are sparse.

Once the understanding of transcrystallinity in unreinforced PEEK and PEKK is better developed, then kinetics modelling may develop further into their fibre-reinforced composites. Current models used for unreinforced PEKK need to be further verified and then adapted to the composite counterparts. Transcrystallinity simulations, even though sparse, have proved to be successful [1,2]. It will be interesting to see further implementation of this modelling, or new models that can lead to new findings and investigations on the kinetics of neat and composite PEKK.

Finally, and perhaps the largest challenge to overcome, is the meaning and applicability of this research to industry. The majority of CF/PEKK studies covered in this chapter focus on small scale morphology and properties, developed and evaluated under highly controlled conditions. An example of this is DSC, where samples weighing between 5-20mg undergo a controlled thermal cycle in an inert environment.

While it is paramount to develop an understanding of the material behaviour performing in small scale lab tests, these are far from emulating the conditions of real-life manufacturing, where thick composite sections and a variety of manufacturing techniques may cause thermal gradients, exposure to high heating and cooling rates, and even thermal degradation due to exposure to more reactive environments. It is therefore key to correlate lab-scale studies to industrial manufacturing scenarios and performance. An in-depth understanding of the relationship between manufacturing, crystallinity development and the final mechanical properties will help to improve the reliability and paths to certification of thermoplastic

composite structures in high-performing industrial applications which are currently dominated by epoxy composites. Press and autoclave manufacturing, for example, offer controlled cooling conditions even at a large industrial scale (less controlled than the DSC - due to the size of the equipment, metal moulds and the varied thickness of the manufactured parts). As previously described, automated higher-speed, out-of-autoclave manufacturing techniques such as ATP are of increasing interest, however the limitations outlined in Section 2.4 can result in crystallinity variations across the laminate thickness, a schematic of which is shown in Figure 3.1. The figure outlines the crystallinity distribution uncertainty in the resulting laminate from ATP, and the current need of post-processing in order to obtain a uniform and controlled crystallinity.

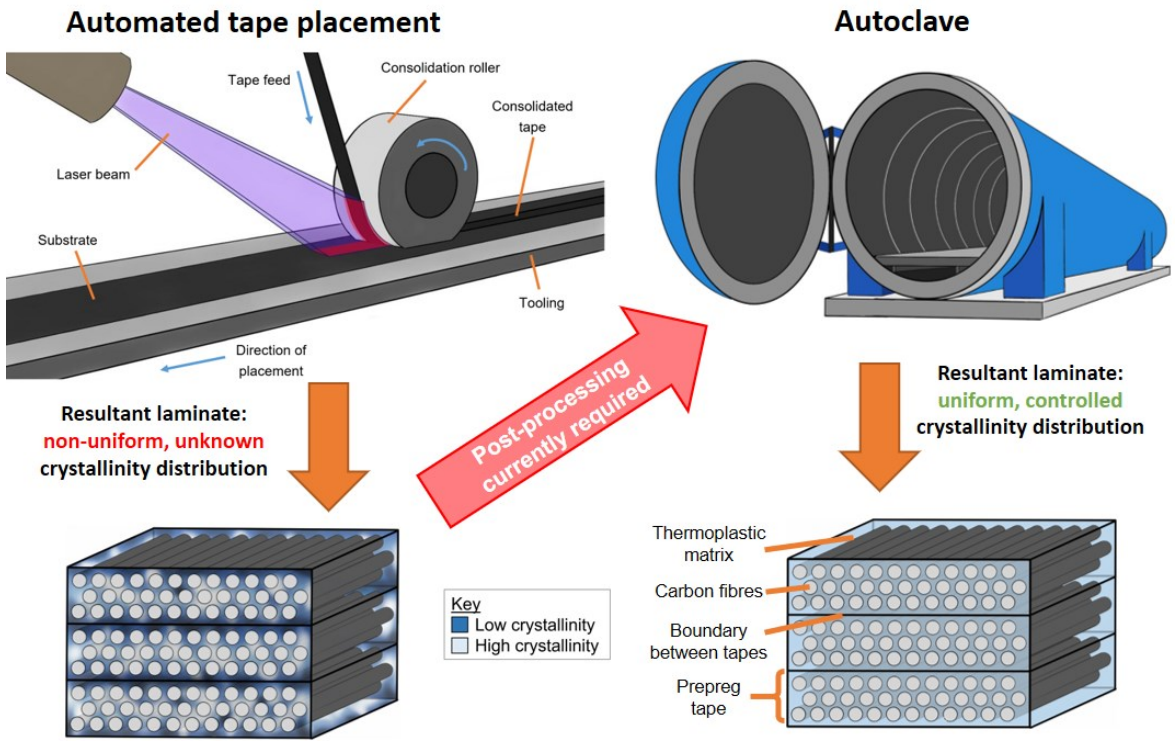

Figure 3.1: Schematic of a laminate consolidated by Automated Tape Placement (left) and autoclave (right). Different shades of blue show crystallinity variation within the matrix. ATP schematic drawn after [3].

This is not a challenge only applicable to PEKK, but to any semicrystalline thermoplastic matrix composite consolidated by ATP [4]. There are several studies available on ATP-manufactured CF/PEEK laminates focusing on mechanical characterisation and consolidation quality [3,5–11], and fewer in the case of CF/PEKK [9], however literature covering variation in crystallinity specifically is sparse [12,13]. Therefore, studies on samples extracted from processes like ATP would be key in understanding how CF/PEKK composites behave, and their applicability in high-performance applications.

Another manufacturing challenge is the introduction of PEKK and short CF/PEKK composites to 3D printing. This is an additive manufacturing technique which deposits molten polymer to create a three-dimensional object. This exposes the material to uncontrolled cooling rates without any consolidation pressure, which may result in uneven interlayer bonding, crystallinity gradients and anisotropic mechanical properties if the processing conditions and their impact on the printing material are not well understood. 3D-printed composite forms of PEKK and other PAEKs are also attractive in similar high-performance applications as ATP, such as aerospace, automotive or off-shore oil and gas exploration [14],

but unreinforced PAEKs are particularly interesting in medical applications, due to their biocompatibility, chemical resistance and antibacterial properties, as well as possessing similar mechanical properties to human bones [15–17].

While some studies on crystallinity are available for PEEK and other PAEKs [18,19], research on PEKK and CF/PEKK 3D printing covers the impact of infill density, topology and T/I ratio on mechanical performance [14,15,20], with no mention of the effect of the printing process on crystallinity. Namely, an understanding of the impact of nozzle temperature on the polymer melting, crystallisation and interface between printing layers is necessary, as well as the influence of nozzle size and deposition speeds on cooling rates, and any potential need and effect of post-processing, in order to establish a good understanding of PEKK's behaviour in 3D printing.

3.2. Research opportunities, thesis aims and objectives

Motivated by the interest from industry in combining the use of high-performance thermoplastics with high-speed manufacturing processes, the aim of this body of work is to evaluate any variation in crystallinity across the thickness of CF/PEKK laminates manufactured by ATP. This evaluation seeks to assess the viability of combining both material and manufacturing process.

Based on the gaps observed in the existing literature in Chapter 2 and those highlighted in Section 3.1, there are several research opportunities that arise in order to ultimately achieve this aim. While not all of the identified gaps in Section 3.1 could be investigated throughout the course of this project, the following objectives have been studied and presented in this thesis:

1. Establish an understanding of the crystallisation kinetics and morphology of PEKK. In order to successfully manufacture composite components in accordance with industry specifications, it is essential to develop the knowledge of how to achieve optimum crystallinity levels aligned with the required performance. This part of the study, presented in Chapter 4, explores how the crystallinity evolution of PEKK is impacted by a variety of isothermal and non-isothermal thermal histories, in both unreinforced and composite form.
2. Evaluate the impact of different ATP parameters on the mechanical performance of CF/PEKK laminates. Based on existing literature, a series of ATP laminates were manufactured, varying nip point temperature, lay-down speed and roller pressure. In order to have benchmark values of conventionally-manufactured laminates, a series of compression-moulded laminates were also manufactured, with heating programs based on the developed knowledge during the crystallinity studies. These then underwent a variety of matrix-dominated mechanical testing, evaluating the effect of different crystalline morphologies and crystallinity levels on performance. Details of the manufacturing procedures are given in Chapter 5, with mechanical testing results presented in Chapter 6.
3. Study any variation in micromechanical properties in different CF/PEKK laminates, as well as across their thickness, to indirectly evaluate the crystallinity content of the sample. As discussed in Section 2.4, the fast-paced nature of ATP manufacturing may lead to uneven cooling rates across a laminate's thickness as it is being manufactured, which may result in a crystallinity gradient across the laminate thickness. This part of the study therefore indirectly evaluates differences in

crystallinity across the thickness of ATP laminates via nanoindentation. Nanoindentation provides micromechanical properties which indirectly reflect crystallinity content. Compression-moulded laminates are once again used as benchmarks for conventionally-manufactured laminates with highest levels of crystallinity. The results of this work are given in Chapter 7.

Finally, insights achieved from the performed work, as well as future research that can be performed based on that presented in this thesis is discussed in detail.

Chapter references

[1] Chelaghma S, Passieux J-C, Almeida OD, Périé J-N, Marguères P, Vinet A. Modélisation Pixel Coloring de la cristallisation du PEKK. Comptes Rendus des JNC 21 - Bordeaux INP 2019:9.

[2] Guan X, Pitchumani R. Modeling of spherulitic crystallization in thermoplastic tow-placement process: Spherulitic microstructure evolution. Composites Science and Technology 2004;64:1363–74. https://doi.org/10.1016/j.compscitech.2003.10.023.

[3] Stokes-Griffin CM, Compston P. The effect of processing temperature and placement rate on the short beam strength of carbon fibre-PEEK manufactured using a laser tape placement process. Composites Part A: Applied Science and Manufacturing 2015;78:274–83. https://doi.org/10.1016/j.compositesa.2015.08.008.

[4] Hosseini SMA, Schäkel M, Baran I, Janssen H, van Drongelen M, Akkerman R. Non-uniform crystallinity and temperature distribution during adjacent laser-assisted tape winding process of carbon/PA12 pipes. Int J Adv Manuf Technol 2020;111:3063–82. https://doi.org/10.1007/s00170-020-06215-8.

[5] Kilroy JP, Ó Brádaigh CM, Semprimoschnig COA. Mechanical and physical evaluation of a new carbon fibre/PEEK composite system for space applications. SAMPE Journal 2008:1–12.

[6] Comer AJ, Ray D, Obande WO, Jones D, Lyons J, Rosca I, et al. Mechanical characterisation of carbon fibre–PEEK manufactured by laser-assisted automated-tape-placement and autoclave. Composites Part A: Applied Science and Manufacturing 2015;69:10–20. https://doi.org/10.1016/j.compositesa.2014.10.003.

[7] Flanagan M, Goggins J, Doyle A, Weafer B, Ward M, Bizeul M, et al. Out-of-autoclave manufacturing of a stiffened thermoplastic carbon fibre PEEK panel. AIP Conference Proceedings 2017;1896. https://doi.org/10.1063/1.5008001.

[8] Gruber MB, Lockwood IZ, Dolan TL, Funck SB, Tierney JJ, Simacek P, et al. Thermoplastic in situ placement requires better impregnated tapes and tows. International SAMPE Technical Conference 2012.

[9] Lamontia M, Gruber M. Remaining developments required for commercializing in situ thermoplastic ATP. SAMPE Europe Conference 2007:1–15.

[10] Qureshi Z, Swait T, Scaife R, El-Dessouky HM. In situ consolidation of thermoplastic prepreg tape using automated tape placement technology: potential and possibilities. Composites Part B: Engineering 2014;66:255–67. https://doi.org/10.1016/j.compositesb.2014.05.025.

[11] Shadmehri F, Hoa SV, Fortin-Simpson J, Ghayoor H. Effect of in situ treatment on the quality of flat thermoplastic composite plates made by automated fiber placement (AFP). Advanced Manufacturing: Polymer and Composites Science 2018;4:41–7. https://doi.org/10.1080/20550340.2018.1444535.

[12] Esguerra-Arce I, Martín MI, Pérez-Pastor A, García-Martínez V. Evolution of crystallinity with multiple lamination steps in high performance thermoplastic composites by in-situ consolidation process. Twenty-Second International Conference on Composite Materials 2019.

[13] Lamontia MA, Gruber MB. Limitations on mechanical properties in thermoplastic laminates fabricated by two processes: automated thermoplastic tape placement and filament winding. SAMPE Europe Conference and Exhibition 2005.

[14] Kishore V, Ajinjeru C, Duty C. Rheological characteristics of fiber reinforced poly(ether ketone ketone) (PEKK) for melt extrusion additive manufacturing, 2017, p. 9.

[15] Cheng K, Liu Y, Wang R, Zhang J, Jiang X, Dong X, et al. Topological optimization of 3D printed bone analog with PEKK for surgical mandibular reconstruction. Journal of the Mechanical Behavior of Biomedical Materials 2020;107:103758. https://doi.org/10.1016/j.jmbbm.2020.103758.
[16] Wang M, Bhardwaj G, Webster T. Antibacterial properties of PEKK for orthopedic applications. IJN 2017;Volume 12:6471–6. https://doi.org/10.2147/IJN.S134983.
[17] Panayotov IV, Orti V, Cuisinier F, Yachouh J. Polyetheretherketone (PEEK) for medical applications. J Mater Sci: Mater Med 2016;27:118. https://doi.org/10.1007/s10856-016-5731-4.
[18] Yang C, Tian X, Li D, Cao Y, Zhao F, Shi C. Influence of thermal processing conditions in 3D printing on the crystallinity and mechanical properties of PEEK material. Journal of Materials Processing Technology 2017;248:1–7. https://doi.org/10.1016/j.jmatprotec.2017.04.027.
[19] Yi N, Davies R, Chaplin A, McCutchion P, Ghita O. Slow and fast crystallising poly aryl ether ketones (PAEKs) in 3D printing: Crystallisation kinetics, morphology, and mechanical properties. Additive Manufacturing 2021;39:101843. https://doi.org/10.1016/j.addma.2021.101843.
[20] Nachtane M, Tarfaoui M, Ledoux Y, Khammassi S, Leneveu E, Pelleter J. Experimental investigation on the dynamic behavior of 3D printed CF-PEKK composite under cyclic uniaxial compression. Composite Structures 2020;247:112474. https://doi.org/10.1016/j.compstruct.2020.112474.

Chapter 4. Crystallisation studies of PEKK powder and CF/PEKK prepreg tape

Based on the review of existing literature presented in Chapter 2, it is clear that a better understanding of the crystallisation development and kinetics of CF/PEKK is necessary prior to any manufacturing. Developing such an understanding will contribute towards selecting appropriate processing parameters. Therefore, an in-depth study of the crystallisation behaviour, morphology and kinetics of unreinforced PEKK and CF/PEKK composite tape was completed along with crystallisation kinetics modelling, and is presented in this chapter.

4.1. Materials and methods for crystallisation studies

4.1.1. Materials

In this study, KEPSTAN PEKK 7002PT by Arkema is used in powder form, provided by Hexcel Composites Ltd. This grade of PEKK has a T/I ratio of 70/30, with glass transition temperature and melting temperature measured at 161°C and 338°C respectively. This grade in particular is intended for the manufacturing of unidirectional prepreg tape with carbon fibres [1], and was studied in this work due to Hexcel's interest in this material. Images of the powder are shown in Figure 4.1a.

The composite material used is unsized AS7 CF/PEKK unidirectional prepreg tape, 150 mm wide and 0.2 mm thick, provided by Hexcel Composites Ltd. Images of the tape are shown in Figure 4.1b. The PEKK matrix in the tape is the same grade as the powder. An exhaustive description and evaluation of the prepreg tape is given in Section 5.1.

(a) PEKK powder

(b) CF/PEKK prepreg tape

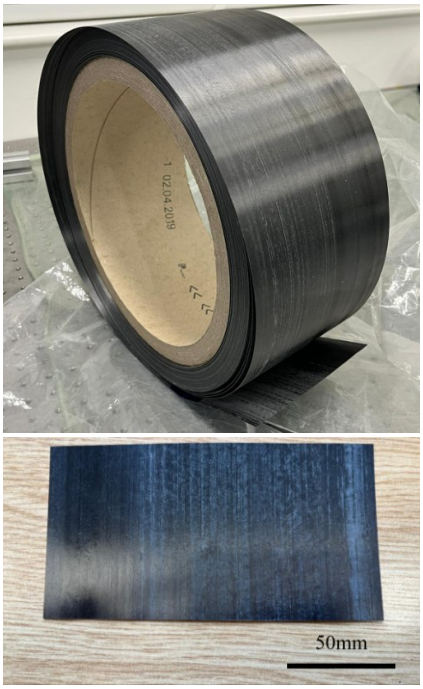

Figure 4.1: (a) PEKK powder and (b) CF/PEKK prepreg tape images.

4.1.2. Acid digestion

Acid digestion was performed as per BS ISO 14127 Procedure A3: Digestion in a sulphuric acid/hydrogen peroxide mixture. This was done to determine the fibre content of the prepreg tape. Two samples of weights 200-500 mg were taken from prepreg tape provided by Hexcel Composites Ltd. This tape was later used for compression-moulding manufacturing (see Chapter 5). The followed procedure is given below:

1. 30 mL concentrated sulphuric acid was heated with the sample until it begins to fume (180°C ± 10°C).
2. When solution became dark in colour with no noticeable change for 5 minutes, 20 mL hydrogen peroxide were slowly added. Once the solution became clear, an extra 2 mL were added. The solution was then heated for a further 10 minutes.
3. The contents of the beaker were filtered through a glass fibre filter.
4. The fibres were washed in the filter with ~500 mL distilled water, followed by acetone.
5. The fibres were then dried in an air-circulation oven at 105°C ± 5°C for 90 minutes.
6. Fibres were weighed to the nearest 0.1 mg.

4.1.3. Thermogravimetric analysis

Thermogravimetric analysis was performed by Ruston Services Ltd. with a PerkinElmer Pyris 1 TGA analyser, using platinum sample pans. CF/PEKK samples of approximately 7-8 mg underwent thermogravimetric analysis under a nitrogen environment, where samples were heated at 10°C/min up to 600°C, and then held at 600°C for 45 minutes. Two samples were run under a nitrogen environment, and an additional run under air to observe the material's exposure limitations under more common industrial-level manufacturing conditions.

4.1.4. Differential scanning calorimetry (DSC)

Isothermal and non-isothermal crystallisation analyses were carried out using a PerkinElmer DSC 8000, with aluminium pans non-hermetically sealed with aluminium lids. Indium was used to calibrate the temperature and heat of fusion prior to any experiments. Sample weights of 5-7 mg of neat PEKK powder were used, whereas sample weights of 10-12 mg of CF/PEKK prepreg tape were used. All experiments were run twice in order to ensure repeatability under a nitrogen environment.

In order to erase any thermal history, samples were initially heated to 370°C, and held in the melt for 5 minutes. For isothermal analysis, samples were cooled at a rate of 150°C/min down to the temperature of interest (220, 240, 260, 280, or 300°C), held for 60 minutes, and then further cooled at a rate of 150°C/min to room temperature. These temperatures were selected based on previous work that had been done on PEKK in literature [2,3]. For non-isothermal crystallisation analysis, samples were cooled at the rate of interest (5, 10, 20, 40, 60, 100 or 150°C/min) from the melt to room temperature. The cooling rates were based on previous studies available in literature [4] and the DSC's cooling capability (maximum cooling rate of 150°C/min). All samples then underwent a second heat ramp at 20°C/min to measure the effect of the crystallisation cycle on the glass transition, melting temperature and crystallinity. The temperature-time plots of these thermal cycles are shown in Figure 4.2.

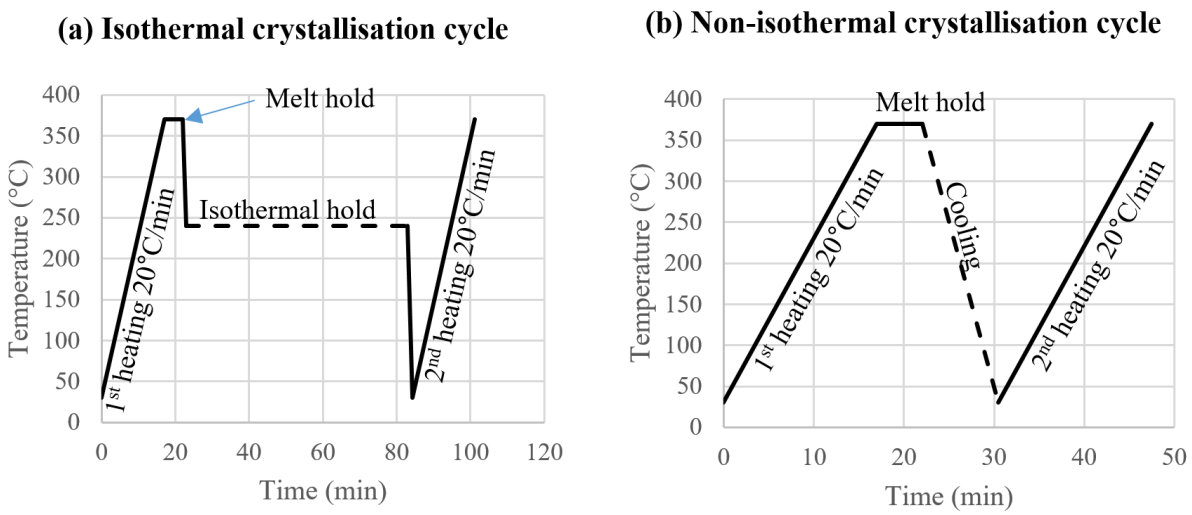

Figure 4.2: DSC heat cycle of all samples undergoing (a) isothermal crystallisation analysis and (b) non-isothermal or dynamic crystallisation analysis. The dotted sections of the plot indicate (a) the isothermal hold of the cycle, which can be at 220, 240, 260, 280 or 300°C; and (b) the cooling section of the cycle, which can be 5, 10, 20, 40, 60 100 or 150°C/min cooling rate.

Performing the second heat ramp at the end of the cycle removes all thermal history. In order to later observe the impact of the thermal history at microscopic scale under scanning electron microscopy (SEM), CF/PEKK samples underwent the same cycle once again with the exception of the final heating ramp.

The crystallinity of a sample can be estimated with:

$$\chi = \frac{\Delta H_m - \Delta H_{cc}}{\alpha \times \Delta H_{100\%}} \tag{4.1}$$

Where ΔH_m is the melting enthalpy, ΔH_{cc} is the cold crystallisation enthalpy, α is the weight fraction of matrix content (100% in the case of the unreinforced PEKK powder, 31.7% in the case of CF/PEKK prepreg tape) and $\Delta H_{100\%}$ is the theoretical melting enthalpy of 100% crystalline PEKK. This has been calculated to be 130J/g by Chang and Hsiao [2]. Enthalpies were calculated using Pyris Manager Software, provided by PerkinElmer.

4.1.5. Scanning electron microscopy (SEM)

SEM was performed on cryofractured CF/PEKK prepreg tape samples after undergoing the DSC cycles described above, in order to qualitatively examine the effect that crystallinity had on fibre-matrix interfacial adhesion and matrix morphology. Cryofracture involved submerging the samples in liquid nitrogen, followed by fracturing to expose their cross-sections. Samples were prepared with a 15nm sputter coating of gold to enhance surface conductivity, and then imaged with a JEOL JSM-IT100 instrument at 20 kV.

4.2. Results and discussion

4.2.1. Fibre and matrix content

Acid digestion results are shown in Table 4.1. The average fibre (and resin) content by weight was 68% (and 32%), which translated to a fibre volume fraction of 61% (the calculations for which can be found in Appendix A).

Table 4.1: CF/PEKK prepreg tape sample weights before and after acid digestion.

	Weight before test (mg)	Weight after test (mg)	Fibre content by weight (%)	Resin content by weight (%)
Sample 1	399.9	273.9	68.5	31.5
Sample 2	412.7	281.3	68.2	31.8

4.2.2. Thermal degradation of CF/PEKK in air and nitrogen environments

Thermogravimetric analysis results are shown in Figure 4.3. These showed that, in both air and nitrogen environments, any form of thermal degradation is minimal up to approximately 500°C. The initial decomposition observed up until approximately 50 minutes into the cycle (~500°C) was the same across all curves. After this, approximately 11% of the weight of the samples held under a nitrogen environment was lost, plateauing during the 600°C hold. This demonstrated that the sample is unlikely to degrade any further in a nitrogen environment at such temperatures. Under an air environment, with the presence of oxygen, the polymer degraded much further, along with extensive carbon fibre oxidation, resulting in almost 100% sample weight reduction by the end of the thermal cycle.

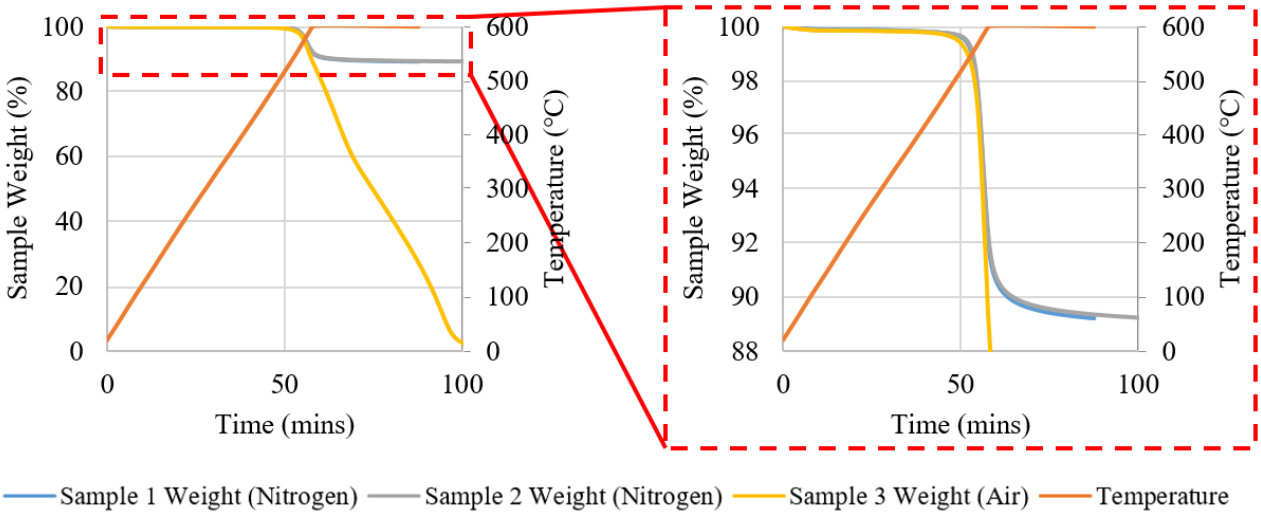

Figure 4.3: TGA analysis of CF/PEKK samples under nitrogen (blue and grey curves) and air (yellow curve) environments. Note that the blue and grey curves overlap.

As PEKK's melting temperature is approximately 337°C, this allows for all crystallisation studies and manufacturing to be performed comfortably bringing the material up to 360-390°C without any risk of oxidation or thermal degradation in neither nitrogen or air environments.

4.2.3. Isothermal crystallisation

4.2.3.1. Crystallisation at different isothermal temperatures

Figure 4.4 shows the heat flow variation of one set of runs of unreinforced PEKK powder and CF/PEKK prepreg tape, during a heat ramp of 20°C/min from room temperature to 370°C, after undergoing different isothermal temperatures from the melt held for 60 minutes. Table 4.2 shows average data from this portion of the cycle for both performed runs.

Two melting endotherms are observed in the heat scans in Figure 4.4, corresponding to the LTE and HTE as discussed in Section 2.2.1. The LTE is approximately 15°C above the isothermal temperature throughout for both unreinforced and composite PEKK. In the case of the 280°C and 300°C isothermal holds where the two endotherms overlap, the area corresponding to each endotherm was calculated by drawing a line perpendicular to the baseline, crossing the curve at its inflection point between the two peaks. This is illustrated on the 300°C isothermal curve in Figure 4.4a. The software used to calculate enthalpies is unable to perform this operation, and so this problem was solved trigonometrically. Its derivation is given in Appendix B.

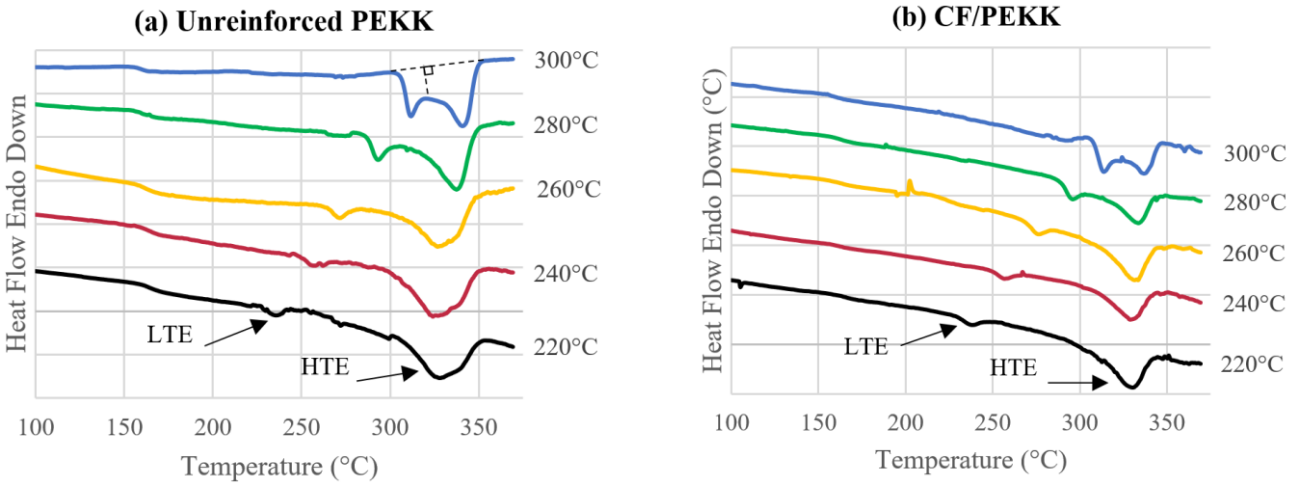

Figure 4.4: DSC thermograms (second heating cycles in Figure 4.2(a) of (a) unreinforced PEKK powder and (b) CF/PEKK prepreg tape after undergoing isothermal crystallisation at different temperatures with a hold time of 60 minutes. Dotted lines in the 300°C curve in (a) demonstrate how the area corresponding to each endotherm (LTE and HTE) was calculated in instances where the two peaks overlap.

Table 4.2: Average values for transition temperatures, melting enthalpies and total crystallinity of unreinforced PEKK powder and CF/PEKK prepreg tape after undergoing different isothermal holds.

Isothermal temp. (°C)	Unreinforced PEKK						
	T_g (°C)	T_{LTE} (°C)	ΔH_{LTE} (J/g)	T_{HTE} (°C)	ΔH_{HTE} (J/g)	LTE:HTE	χ (%)
220	165.5 ± 1.1	239.6 ± 4.4	1.8 ± 0.2	328.6 ± 0.5	29.7 ± 0.1	5:95 ± 1	24.2 ± 0.2
240	163.5 ± 0.3	258.4 ± 2.0	2.3 ± 0.3	324.0 ± 0.2	29.1 ± 0.4	7:93 ± 1	24.1 ± 0.2
260	162.0 ± 0.8	274.9 ± 3.3	2.5 ± 0.2	331.9 ± 5.0	26.9 ± 0.2	8:92 ± 1	22.6 ± 0.1
280	159.7 ± 0.8	298.1 ± 4.9	7.3 ± 0.3	337.5 ± 0.1	28.4 ± 0.4	20:80 ± 1	27.5 ± 0.5
300	158.5 ± 0.1	315.5 ± 3.8	10.4 ± 0.5	341.7 ± 0.5	20.4 ± 1.8	34:66 ± 3	23.7 ± 1.1
	CF/PEKK						
220	164.3 ± 0.9	239.8 ± 2.1	1.0 ± 0.1	329.4 ± 0.3	9.1 ± 0.1	10:90 ± 0	24.3 ± 0.6
240	158.5 ± 1.8	258.9 ± 2.5	1.1 ± 0.2	329.2 ± 0.3	8.5 ± 0.1	10:90 ± 1	23.0 ± 0.5
260	160.4 ± 1.4	277.0 ± 1.2	1.1 ± 0.2	334.1 ± 2.7	8.2 ± 0.5	12:88 ± 1	22.5 ± 1.5
280	159.6 ± 2.8	300.4 ± 5.0	3.1 ± 0.4	335.5 ± 2.2	7.9 ± 0.1	28:72 ± 2	26.6 ± 1.2
300	161.4 ± 2.0	316.3 ± 2.8	4.7 ± 0.5	338.8 ± 2.1	5.2 ± 0.1	47:53 ± 3	23.7 ± 1.0

T_g: Glass transition temperature
T_{LTE}: Low temperature endotherm
ΔH_{LTE}: Low temperature endotherm enthalpy
T_{HTE}: High temperature endotherm
ΔH_{HTE}: High temperature endotherm enthalpy
LTE:HTE: Low temperature endotherm to high temperature endotherm ratio
χ: Total crystallinity

As the isothermal hold temperature increases, the LTE:HTE ratio can be seen to increase, the variation of which can be observed in Table 4.2 and Figure 4.5. The reasoning for this may be as follows. In order for secondary crystallisation to take place, primary crystallisation (formation of spherulites) must be established first. As primary crystallisation takes place and spherulites develop, the spherulites' lamellae expand and branch out, becoming larger and therefore creating more interlamellar space for secondary crystallisation to happen. The extent to which spherulites grow is determined by general polymeric nucleation theory, where at lower temperatures the formation of new spherulite nuclei takes precedence over spherulitic growth. This results in a high number of small spherulites. On the other hand, at higher temperatures, spherulitic growth predominates over the formation of new nuclei, resulting in a smaller number of spherulites but larger in size. It is therefore possible that, at higher isothermal temperatures, there is more interlamellar space created by the larger spherulites, allowing for a larger volume of interlamellar growth (secondary crystallisation) to take place than at low isothermal temperatures. This therefore results in a larger presence of secondary crystallites, and a larger LTE:HTE endotherm ratio. A schematic portraying this is shown in Figure 4.6.

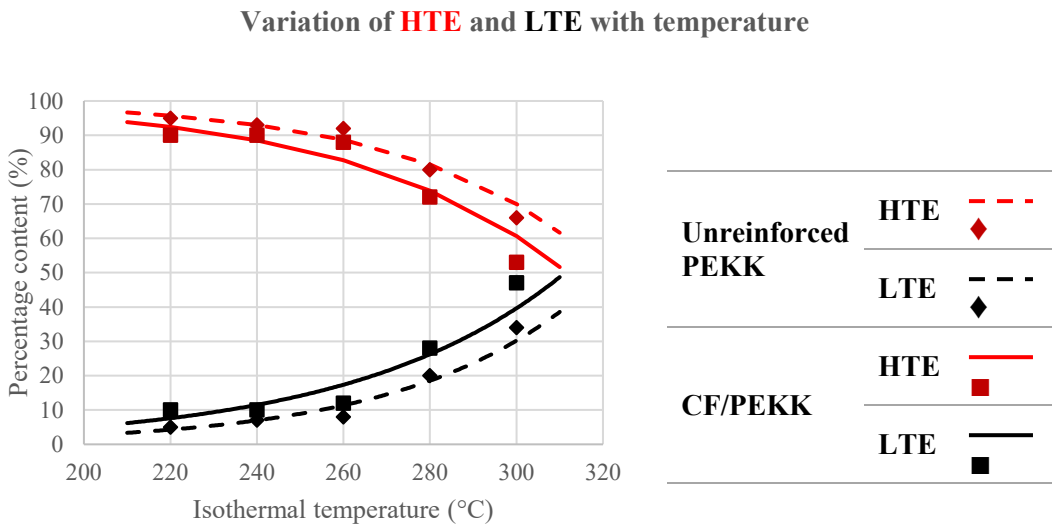

Figure 4.5: Variation of LTE and HTE with isothermal temperature for unreinforced PEKK powder and CF/PEKK prepreg tape. Solid and dotted lines are exponential lines of best fit.

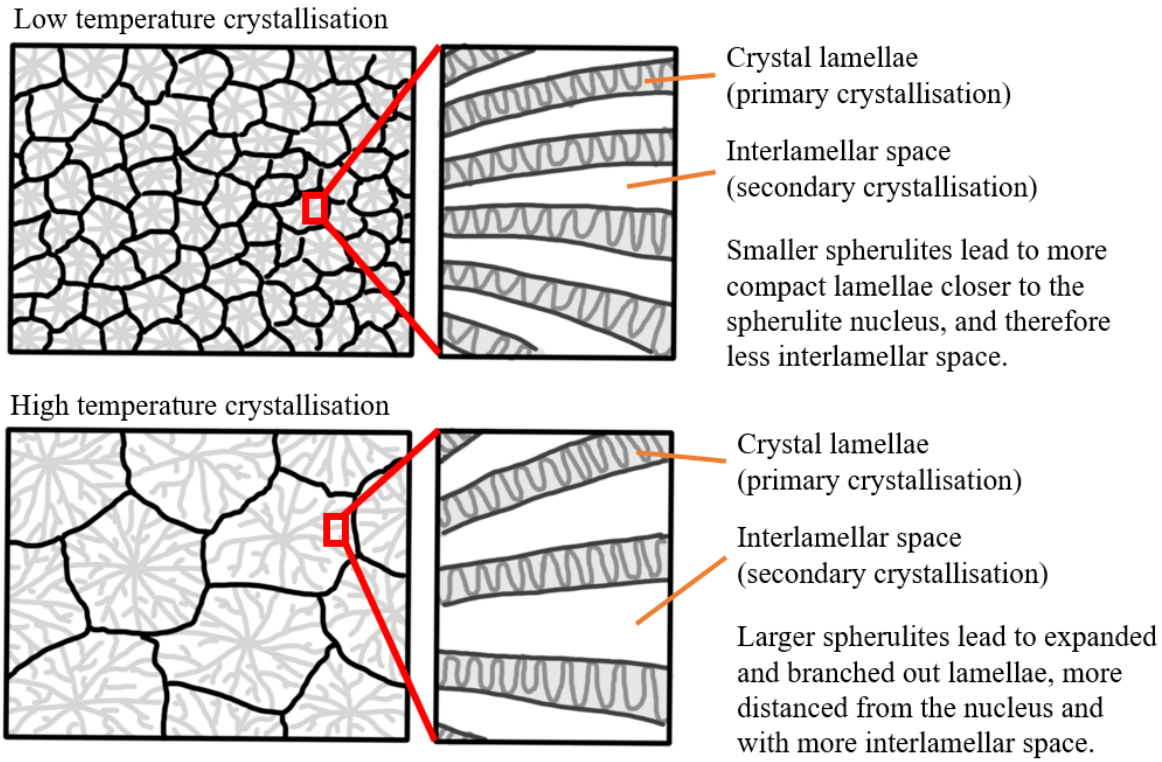

Figure 4.6: Schematic showing spherulite size at low and high temperature isotherms, and the consequent interlamellar spacing in which secondary crystallisation takes place.

From the above results in Table 4.2 and Figure 4.5, it can also be observed that CF/PEKK has a slightly larger LTE:HTE ratio (a higher presence of secondary crystallisation) than the unreinforced PEKK throughout all isothermal hold temperatures. A possible reason for this could be the presence of densely-packed fibres supressing spherulitic development, causing a slower growth of the primary crystallisation phase in CF/PEKK compared to the neat samples at a given time *t*, as shown in Figure 4.7.

Spherulitic growth is governed by primary crystallisation, which in turn affects the extent to which secondary crystallisation can take place. However, secondary crystallisation takes place at a smaller scale and does not require major molecular rearrangement in the manner that primary crystallisation does (since it occurs in already established interlamellar regions), and it is therefore possible that it *locally* progresses at the same speed as in the unreinforced case. This would result in a larger percentage of the crystallinity contribution in CF/PEKK being from the secondary phase, resulting in a larger LTE:HTE ratio as seen in Figure 4.5.

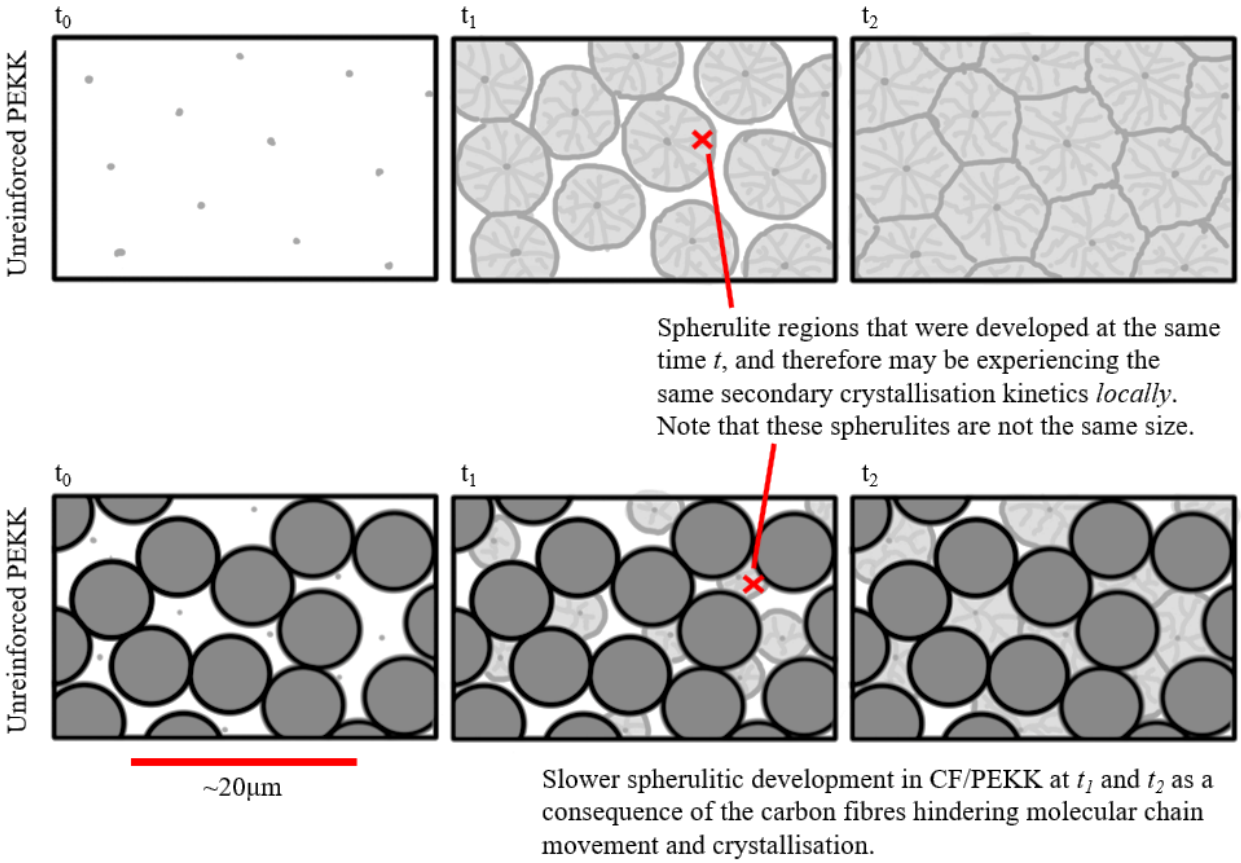

Figure 4.7: Schematic representation of spherulitic development in unreinforced PEKK and CF/PEKK, depicting the difference in growth kinetics at different times as a consequence of CFs inhibiting spherulitic growth. Schematics of CF/PEKK are based on an SEM micrograph of the cross-section of a CF/PEKK prepreg sample. The regions marked with an X indicate areas in the two different samples that crystallised at the same time t.

Another potential explanation for the larger proportion of the LTE could be a different nucleation density and crystal growth at the fibre surface. Fibres may be a source of heterogeneous nucleation and transcrystallinity, which may possess a higher fraction of secondary crystallisation than spherulites developed in the bulk of the matrix via homogeneous nucleation.

Figure 4.8a, b and c show SEM images of cryofractured CF/PEKK samples after undergoing the previously described DSC isothermal cycles at 220, 260 and 300°C respectively. Spherulite structures can be observed in Figure 4.8c (~5 µm in diameter), these becoming smaller and slightly less defined in Figure 4.8b and even less so in Figure 4.8a (~2 µm). As described previously, higher isothermal hold temperatures induce a lower nucleation density and larger spherulitic growth, which is the case in the 300°C isotherm. Consequently, the largest and most defined spherulites can be observed in Figure 4.8c. On the other hand, at lower isothermal temperatures, nucleation density is higher and therefore smaller spherulites are formed due to an early impingement between growth fronts. This may be the reason why

spherulitic structures in Figure 4.8a are the least defined. However, this could also be due to the proximity of the fibres limiting the crystallisation growth to purely perpendicular to the fibre surface.

Another potential explanation for the matrix morphology seen in these figures is the presence of transcrystallinity. It is possible that with lower isothermal hold temperatures, the growth of a transcrystalline interface is incentivised as a consequence of primary nucleation dominating at lower temperatures and the fibre surfaces inducing such nucleation. In Figure 4.8b (260°C isotherm), some epitaxial growth can be observed perpendicular to the fibre surfaces, which then seem to change orientation and form more spherulite-like structures in the bulk. In Figure 4.8a, this perpendicular growth seems to be the most obvious.

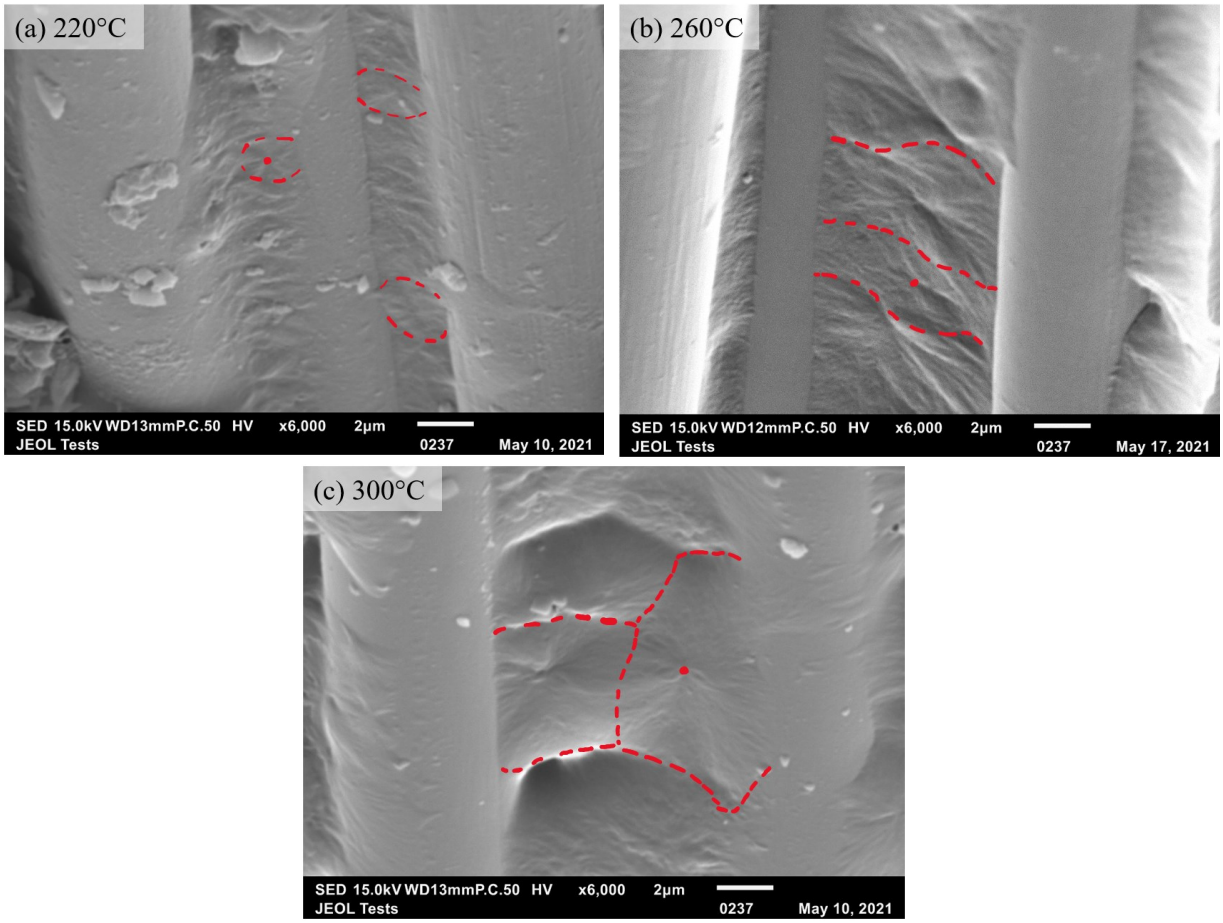

Figure 4.8: SEM of cryofractured CF/PEKK samples after undergoing an isothermal hold of (a) 220°C, (b) 260°C and (c) 300°C from the melt. Red annotations highlight spherulitic structures, with a red dot providing an example of a nucleus location.

4.2.3.2. Crystallisation kinetics at different isothermal holds

Figure 4.9 shows heat flow – time thermograms of unreinforced PEKK and CF/PEKK samples during the DSC isothermal holds. Crystallisation occurs in the first minutes of the isothermal hold, and therefore only the first 20 minutes of the 60-minute hold are shown (minutes 20-60 do not show any variation in heat flow).

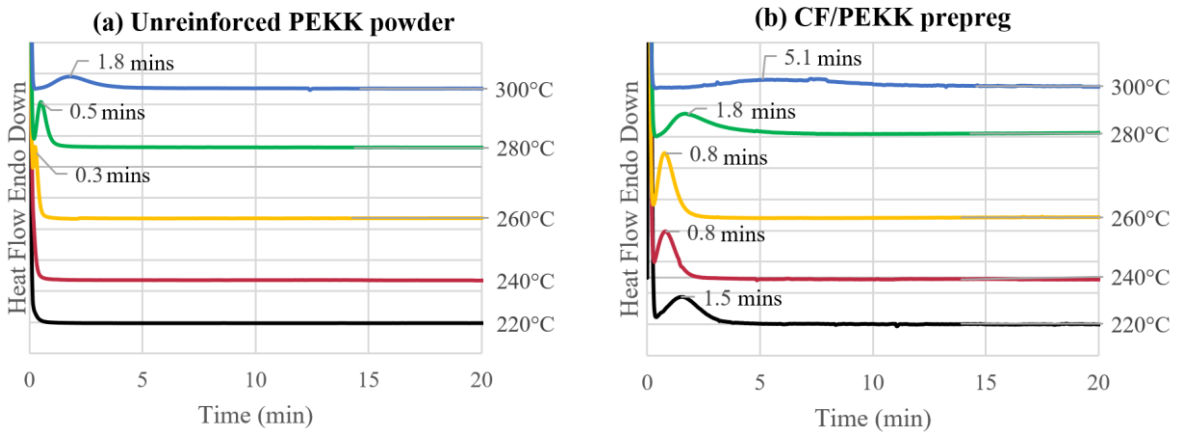

Figure 4.9: DSC thermograms of (a) unreinforced PEKK powder and (b) CF/PEKK prepreg tape while undergoing isothermal holds at different temperatures showing peak crystallisation kinetics times in minutes. In (a), samples undergoing 220 and 240°C isotherms crystallise before reaching the isothermal temperatures, and therefore do not show crystallisation peaks during the isothermal hold. In (b), the fastest crystallisation kinetics can be observed between 240 and 260°C.

In the case of unreinforced PEKK, crystallisation kinetics curves for 220°C and 240°C are not present and the peak for 260°C is only partially present. This is because unreinforced PEKK is already partially crystallised when reaching these isothermal temperatures. When cooling from the melt at 150°C/min, crystallisation takes place in the temperature range 260-210°C (shown later in Figure 4.16a in Section 4.2.4, where crystallisation kinetics under non-isothermal conditions is discussed). By the time that the isothermal temperature (240 or 220°C) is reached when cooling from the melt, crystallisation has already occurred. Therefore, by the time the isothermal hold is recorded to begin, there is no crystallisation taking place. In order to assess the crystallisation kinetics at the lower isotherms, a faster cooling rate would have to be applied. Kinetics and modelling of unreinforced PEKK will therefore only be discussed for the isothermal holds at 260, 280 and 300°C henceforth.

Other authors have assessed the crystallisation kinetics of unreinforced PEKK in literature. Choupin et al. [5] used unreinforced KEPSTAN PEKK 7002 in their studies, a similar grade of PEKK with the same T/I ratio as the one used in this article (KEPSTAN PEKK 7002PT). While they found peak kinetics to take place at approximately 245°C (which would be in line with this article's results), kinetics were considerably slower. They observed a clear crystallisation peak at ~0.8 min during an isothermal hold of 250°C after cooling at 40°C/min, a cooling rate which they determined was fast enough to not result in any crystallisation before reaching the isothermal temperature. This is not the case in this study, where both unreinforced and composite PEKK do crystallise at rates above 40°C/min, as will be shown in Section 4.2.4. This is due to the grade of PEKK possessing faster crystallisation kinetics than in Choupin et al.'s work, which may be because of a different molecular chain length or an additive in the polymer. This is information that Hexcel did not disclose when providing the material for this work.

In a different article, Chelaghma et al. [6] used unreinforced KEPSTAN PEKK 7003, which also possesses a T/I ratio of 70/30 but has a lower viscosity than the KEPSTAN PEKK 7002 series [7]. This material still displayed slower crystallisation kinetics (~1.8 min peak time at 270°C) than the grade being studied in this article (~0.5 min peak time at 280°C). This may be a consequence of different syntheses or modifications of the different grades, as they are intended for different applications [1].

A comparison of the rest of the unreinforced PEKK isothermal holds with their composite counterparts clearly revealed that CF/PEKK has slower crystallisation kinetics, peaking between 240-260°C. This is likely due to the high carbon fibre content hindering the growth and development of spherulites as previously discussed, resulting in slower kinetics. Hsiao et al. [8] found peak kinetics to take place at

255°C and reported minimal impact of fibres on the crystallisation rate of PEKK under isothermal conditions, however there could be differences in the matrix composition, which in Hsiao et al.'s case was provided by DuPont. It is also possible that the different carbon fibres used (AS4 carbon fibres in the case of Hsiao et al.'s work) cause the difference in results.

4.2.3.3. Modelling of isothermal crystallisation kinetics

In order to perform crystallisation kinetics modelling, a plot of the relative crystallinity of each sample against time is needed. This can be obtained by dividing the area under the curves in Figure 4.9 at time t by the area under the entire curve. This is defined by Equation (4.2):

$$\alpha(t) = \frac{\int_0^t Q(t)\,dt}{\int_0^{t\infty} Q(t)\,dt} \tag{4.2}$$

where $Q(t)$ is the heat flow measured at time t, and t_∞ is the time when the polymer is fully crystallised. The resulting relative crystallinity-time curves are shown in Figure 4.10. In the cases where some data points at the beginning of the isothermal crystallisation exotherm are missing in Figure 4.9 as a consequence of partial crystallisation during the cooling step, the curves shown in Figure 4.10 do not start at a relative volume crystallinity of 0.

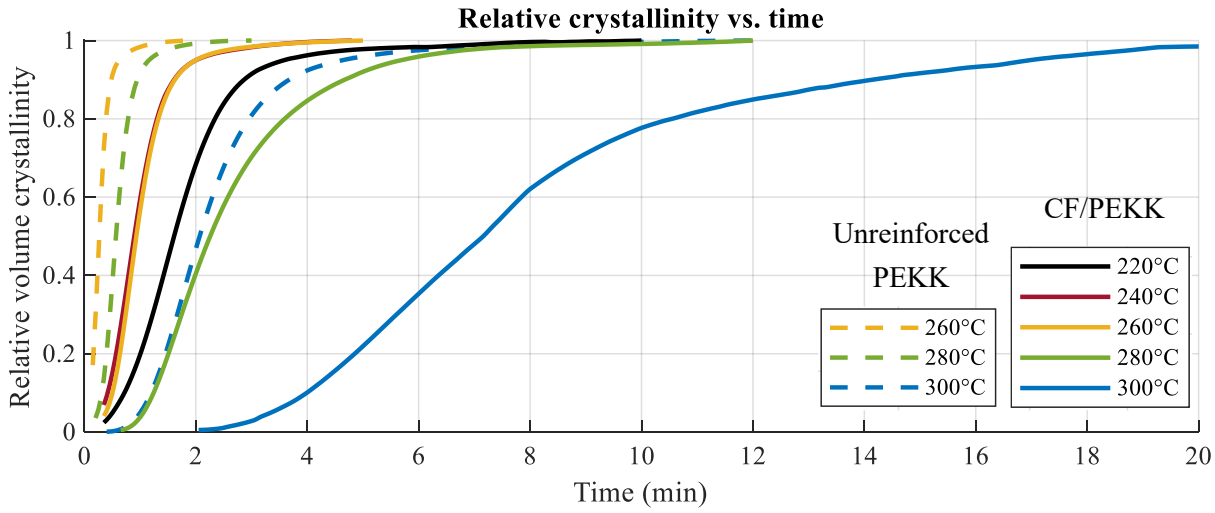

Figure 4.10: Relative crystallinity against time of unreinforced PEKK (dotted lines) and CF/PEKK (solid lines) at different isothermal holds.

Avrami plots can be obtained by plotting $\ln[-\ln(1-\alpha)]$ against $\ln(t)$, shown in Figure 4.11. As discussed in Section 2.3.1, these do not provide a straight line of best fit, implying that there is more than a single crystallisation mechanism taking place. An estimated Avrami exponent for the primary crystallisation stage can be obtained by calculating the slope of the first part of the curves [3,8,9]. Therefore, for the remaining of this modelling section, the Velisaris-Seferis model introduced in Section 2.3.1 was implemented, repeated below in Equation (4.3):

$$\alpha(t) = w_1[1-\exp(-k_1 t^{n_1})] + w_2[1-\exp(-k_2 t^{n_2})] \tag{4.3}$$

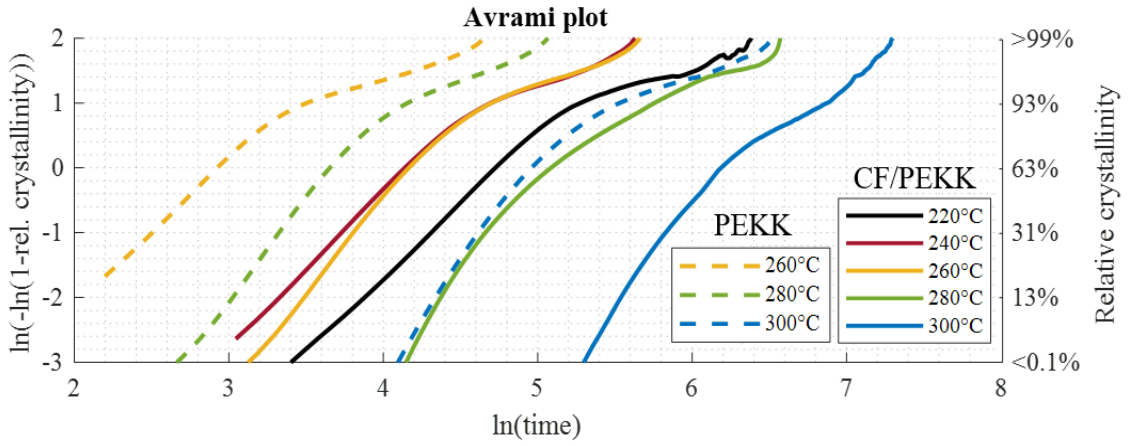

Figure 4.11: Avrami plots of the relative crystallinity of unreinforced PEKK and CF/PEKK.

In the case of unreinforced PEKK, the linear sections of the plots (corresponding to n_1) average to 2.9, making 3 the closest integer. This is in line with the instantaneous nature of crystallisation, as observed by other authors in hot stage microscopy [3,6], as well as its three-dimensional, spherulitic form. For CF/PEKK however, these slopes average to 2.5. A potential cause for this could be restricted growth as a consequence of fibre proximity, which may limit the three-dimensional spherulitic growth in the matrix bulk, inducing early impingement and reducing the value of n_1. High nucleation density on the fibre surface may be another reason for the lower n_1 value: this may cause a transcrystalline region, which resembles a unidirectional growth from the nucleation site as opposed to the three-dimensional growth of spherulites in the bulk.

Values for n_2 were not determined from the Avrami plots in Figure 4.11, now that the gradients obtained at the upper tail of the curves varied between 0.6-0.8, and these proved to provide very poor fits. Further to this, other authors have used both integer and non-integer values ranging between 1-3 to model secondary crystallisation kinetics of PEEK and PEKK with Avrami-based models [5,6,9,10]. This value would be picked based on which one provided the best fit with the experimental data, and some authors allowed the value for n_2 to vary with the isothermal hold temperature [11]. This further highlights the more complicated nature of secondary crystallisation, which suggests that the growth of secondary crystallisation structures may consist of different dimensions, the proportions of which may vary with isothermal holding temperature.

For modelling purposes, the Avrami exponents (n_1 and n_2) were kept constant across different temperatures in this work. The Velisaris-Seferis model was scripted in MATLAB, setting n_1 to 3 and 2.5 for unreinforced PEKK and CF/PEKK respectively. A value for n_2 was determined by the script that provided the best fit for all curves, which for both unreinforced and composite PEKK was $n_2 = 2$. w_1 and w_2 were set according to the LTE:HTE ratios calculated in Table 4.2 for each individual isotherm, with w_1 representing primary crystallisation (HTE) and w_2 representing secondary crystallisation (LTE). k_1 and k_2 were optimised by the script using a non-linear least squares method, these corresponding to the individual rates of primary and secondary crystallisation respectively. All parameters are summarised in Table 4.3. As expected from the results, the highest values for the rate constants can be found at the isothermal temperatures that resulted in the fastest kinetics. Values for k_1 are higher than for k_2 due to primary crystallisation being a faster process than secondary crystallisation.

Table 4.3: Summary of Velisaris-Seferis model parameters for the isothermal crystallisation modelling of unreinforced PEKK and CF/PEKK. w_1 and w_2 are extracted from the LTE:HTE ratios in Table 4.2.

Isothermal temperature (°C)	**Unreinforced PEKK (n_1 = 3, n_2 = 2)**				**CF/PEKK (n_1 = 2.5, n_2 = 2)**			
	w_1	w_2	k_1	k_2	w_1	w_2	k_1	k_2
220	-	-	-	-	0.90	0.10	0.236	0.056
240	-	-	-	-	0.90	0.10	1.011	0.191
260	0.92	0.08	38.86	1.306	0.88	0.12	0.912	0.254
280	0.80	0.20	4.368	1.017	0.74	0.26	0.111	0.047
300	0.69	0.31	0.096	0.084	0.55	0.45	0.007	0.008

w_1: primary crystallisation weight factor
w_2: secondary crystallisation weight factor
k_1: primary crystallisation rate constant
k_2: secondary crystallisation rate constant

The obtained models are shown in Figure 4.12. The Velisaris Seferis model (solid lines) achieves a good fit with the provided Avrami exponents (n_1 and n_2) and weight factors (w_1 and w_2), and with the optimised crystallisation rate constants (k_1 and k_2). The contributions of the primary and secondary crystallisations to the overall model are depicted by the different dotted lines in the plots.

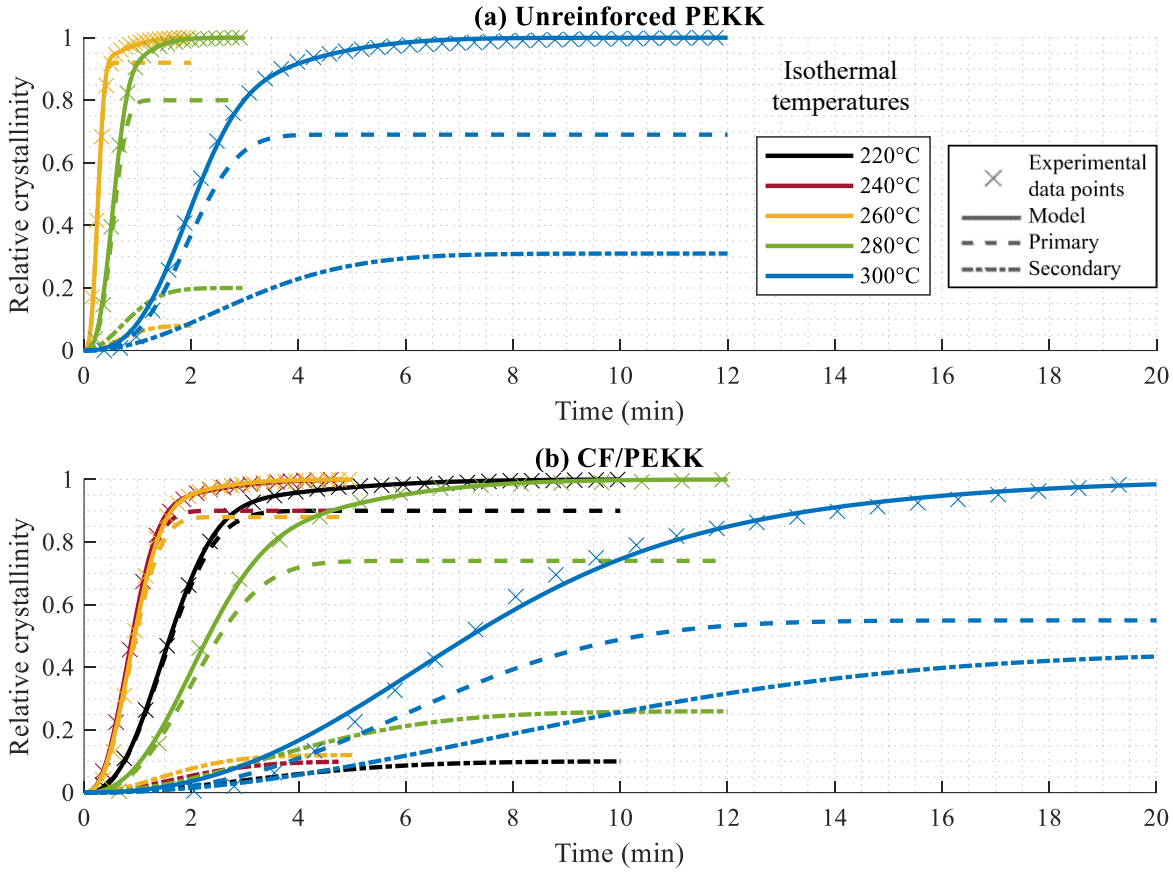

Figure 4.12: Relative crystallinity against time of (a) unreinforced PEKK and (b) CF/PEKK at different isothermal holds, showing a comparison of the Velisaris-Seferis model with the experimental data, as well as the contribution of primary and secondary crystallisation mechanisms to the model.

Plots showing the variation of ln (k_1) and ln (k_2) against the isothermal temperatures are shown in Figure 4.13. Hoffmann-Lauritzen models (introduced in Section 2.3.1) were fitted to these values, which will be used when modelling crystallisation kinetics at different cooling rates in Section 4.2.4.3. The equations for these curves are summarised below.

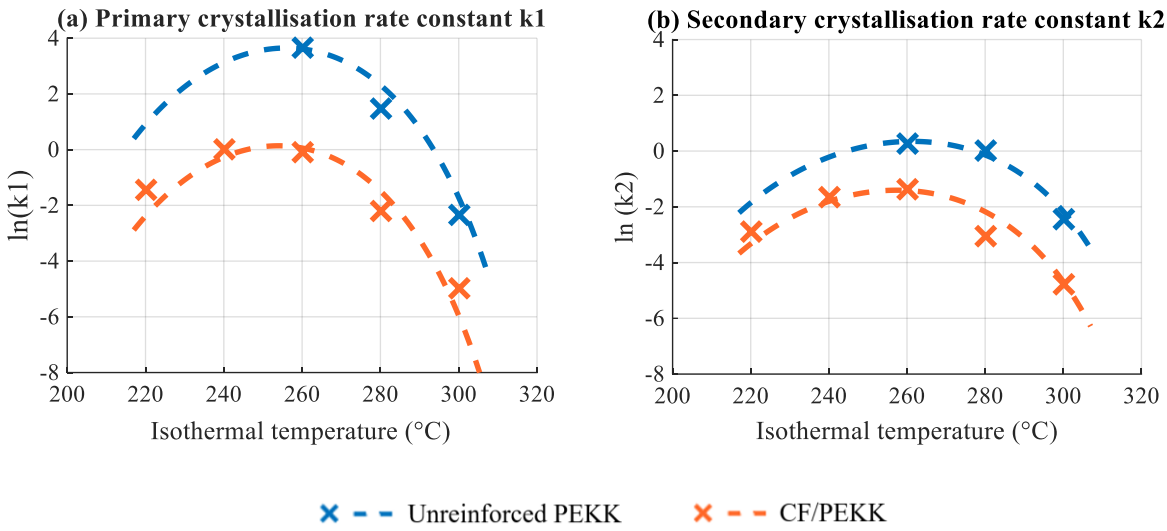

Figure 4.13: Logarithmic plot of (a) k_1 and (b) k_2 against isothermal temperature for unreinforced PEKK and CF/PEKK. Dotted lines show the Hoffmann-Lauritzen models fitted to the experimental data.

For spherulitic growth during primary crystallisation, k_1 is expressed as per Equation (4.4) (see Table 2.11), which results in the Hoffmann-Lauritzen model in Equation (4.5) used in Figure 4.13a.

$$k_1 = \frac{4}{3}\pi N_{01} G_1^3 \tag{4.4}$$

$$k_1 = k_{01}\left[\exp\left(-\frac{3U^*}{R(T-T_\infty)}\right) \times \exp\left(-\frac{3K_{g1}}{T\Delta Tf}\right)\right] \tag{4.5}$$

where $k_{01} = \frac{4}{3}\pi N_{01} G_{01}^3$. G_1 is the crystal growth rate described in Section 2.3.1 (Equation (2.2)). N_{01} is the initial number of potential nuclei and G_{01} is a pre-exponential factor independent of temperature.

For crystal growth during secondary crystallisation, k_2 is expressed as per Equation (4.6) (see Table 2.11) and Equation (4.7), used in Figure 4.13b.

$$k_2 = \pi N_{02} G_2^2 \tag{4.6}$$

$$k_2 = k_{02}\left[\exp\left(-\frac{2U^*}{R(T-T_\infty)}\right) \times \exp\left(-\frac{2K_{g2}}{T\Delta Tf}\right)\right] \tag{4.7}$$

where $k_{02} = \pi N_{02} G_{02}^2$. Parameter definitions are as per Equations (4.4) and (4.5). Table 4.4 provides the parameters used for the models, as well as results for k_{01}, k_{02}, K_{g1} and K_{g2}. Note that, while all temperature values are given in °C, modelling was performed with temperature in units of Kelvin.

Table 4.4: Parameters used for Hoffmann-Lauritzen modelling.

Parameters	Unreinforced PEKK	CF/PEKK
U^* (J mol^{-1})	4700 (Ref [5])	4700 (Ref [5])
R (m^3 Pa K^{-1} mol^{-1})	8.314	8.314
T_m^0 (used for T_∞, ΔT and f) (°C)	356 (Ref [2])	356 (Ref [2])
T_∞ (°C)	131	131
k_{01} (min^{-3})	1.500×10^{14}	1.5460×10^{13}
k_{02} (min^{-2})	5.041×10^{7}	3.593×10^{7}
K_{g1} (K^2)	2.486×10^{5}	2.687×10^{5}
K_{g2} (K^2)	2.025×10^{5}	2.359×10^{5}

Figure 4.13a and Figure 4.13b show slower crystallisation kinetics for the secondary crystallisation mechanism k_2, due to this step requiring an established primary crystallisation and a longer time to develop. This is in line with what was previously discussed in Section 2.2.1.

Hoffmann-Lauritzen model fitting show that the fastest crystallisation kinetics for both unreinforced PEKK and PEKK composites occur at circa 255°C and 260°C for k_1 and k_2 respectively. This is in line with what has been reported in literature to date, where the fastest kinetics were identified to take place at approximately 255°C [8].

4.2.4. Non-isothermal crystallisation

4.2.4.1. Crystallisation at different cooling rates

Figure 4.14 shows the heat flow variation of one set of runs of PEKK powder and CF/PEKK respectively, when heated from room temperature to 370°C at a rate of 20°C/min, after undergoing different cooling rates. Table 4.5 shows average data from this portion of the cycle for both performed runs.

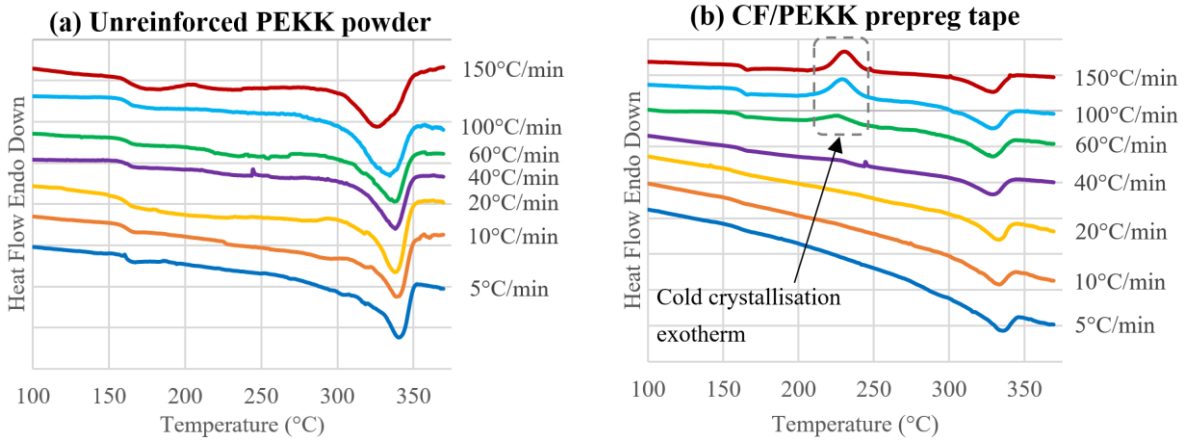

Figure 4.14: DSC thermograms of (a) unreinforced PEKK and (b) CF/PEKK prepreg at 20°C/min heat ramp after different cooling rates.

Table 4.5: Average values for transition temperatures, enthalpies and total crystallinity of PEKK powder and CF/PEKK prepreg tape after undergoing different cooling rates.

Cooling rate (°C/min)	Unreinforced PEKK					
	T_g (°C)	T_{cc} (°C)	ΔH_{cc} (J/g)	T_m (°C)	ΔH_m (J/g)	χ (%)
5	160.9 ± 0.8	-	-	341.5 ± 1.5	33.1 ± 0.3	25.5 ± 0.2
10	161.1 ± 0.7	-	-	340.0 ± 1.2	29.2 ± 3.1	22.5 ± 2.5
20	162.8 ± 1.8	-	-	338.0 ± 0.3	27.2 ± 0.1	20.9 ± 0.1
40	164.0 ± 1.9	-	-	337.4 ± 0.4	28.3 ± 1.0	21.8 ± 0.8
60	161.4 ± 0.1	-	-	337.0 ± 0.4	27.4 ± 1.2	21.1 ± 0.9
100	161.9 ± 0.7	212.3 ± 4.7	0.6 ± 0.2	331.9 ± 2.4	26.2 ± 0.6	19.7 ± 0.3
150	159.5 ± 3.9	210.9 ± 8.7	1.9 ± 0.1	326.0 ± 0.8	26.7 ± 0.4	19.0 ± 0.2
				CF/PEKK		
5	159.2 ± 1.8	-	-	334.4 ± 0.7	10.6 ± 0.0	25.7 ± 0.0
10	160.6 ± 3.6	-	-	335.0 ± 2.2	7.8 ± 0.7	18.9 ± 1.6
20	158.8 ± 3.0	-	-	334.9 ± 2.5	7.0 ± 0.0	16.9 ± 0.2
40	161.9 ± 1.5	-	-	333.1 ± 4.6	6.6 ± 0.7	16.1 ± 0.6
60	161.2 ± 0.1	222.0 ± 4.2	2.1 ± 1.6	333.2 ± 3.3	7.8 ± 1.6	14.0 ± 0.1
100	162.8 ± 0.8	226.8 ± 2.2	5.8 ± 1.3	331.9 ± 3.5	8.7 ± 1.4	6.8 ± 0.1
150	162.0 ± 1.4	226.1 ± 4.7	7.7 ± 0.4	330.9 ± 1.8	8.3 ± 0.7	1.5 ± 0.8

T_g: Glass transition temperature
T_{cc}: Cold crystallisation temperature
ΔH_{cc}: Cold crystallisation enthalpy
Tm: High temperature endotherm enthalpy
ΔH_m: Melting enthalpy
χ: Total crystallinity

The crystallinity of unreinforced PEKK powder decreases with an increase in cooling rate, due to faster temperature drops inhibiting chain movement and therefore limiting diffusion onto the growing crystal front [12]. There is therefore a small cold crystallisation peak developed at the faster cooling rates (100°C/min, 150°C/min). This agrees with results from Quiroga Cortés et al. [4], where this peak takes place at the fastest cooling rates across different PEKK grades. However, as observed in the isothermal studies in this work, the crystallisation kinetics of the grade of PEKK in unreinforced form are faster than those observed in literature.

The crystallinity of CF/PEKK, on the other hand, is affected more significantly by the cooling rate, as is observable from Table 4.5. An increasingly larger cold crystallisation peak develops with higher cooling rates in Figure 4.14b, and therefore a drop in crystallinity from 25.7% at 5°C/min to 1.5% at 150°C/min takes place. This drastic difference is likely due to carbon fibres hindering the macromolecular chain mobility of PEKK, and therefore, at higher cooling rates, the polymer chains do not have time to rearrange and crystallise. It is possible that, while carbon fibre surfaces can act as nucleation sites, densely packed fibres are likely to suppress chain mobility and spherulitic growth, and will have a larger impact in the overall crystallisation. Similar observations were made by Gao and Kim [12] when evaluating the impact of CF inclusions on the crystallisation capability of PEEK. They observed lower crystallinities in CF/PEEK with a fibre volume fraction of 61% in comparison to PEEK powder when undergoing different cooling rates.

As discussed in Section 2.2.2, the characteristic double melting endotherm observed in Figure 4.4 is not present during non-isothermal crystallisation. This absence could be a consequence of secondary crystallisation being a slower mechanism that requires an established primary crystallisation and time to develop, both of which are reduced with increasingly faster cooling rates.

Figure 4.15 shows SEM images of cryofractured CF/PEKK samples after undergoing 5°C/min and 100°C/min cooling rates respectively, with high and low crystallinities. Figure 4.15a shows highly coated fibres, whereas clean, exposed fibres are observed in the lower crystallinity case in Figure 4.15b. Similar behaviour has been observed in CF/PEEK, as shown in Figure 2.21 in Chapter 2 [12,13]. This suggests that higher crystallinity in the matrix will improve fibre-matrix adhesion when compared to a more amorphous matrix.

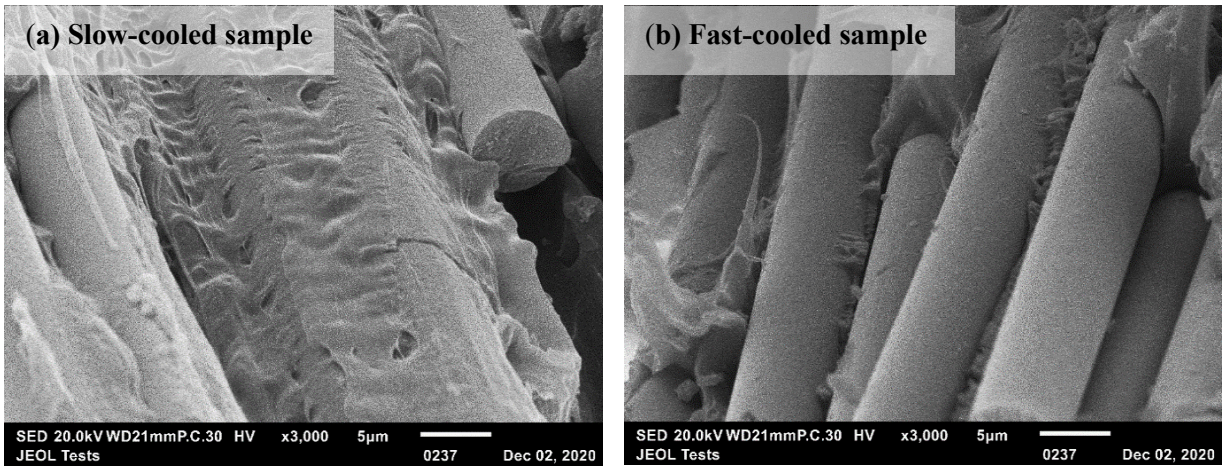

Figure 4.15: SEM of cryofractured CF/PEKK sample after undergoing a cooling rate of (a) 5°C/min from the melt to room temperature (25.6% crystallintiy) and (b) 100°C/min from the melt to room temperature (6.9% crystallinity).

4.2.4.2. Crystallisation kinetics at different cooling rates

Figure 4.16 shows heat flow – temperature thermograms of PEKK and CF/PEKK samples while undergoing different cooling rates, showing melt crystallisation exotherms as the material cools and solidifies.

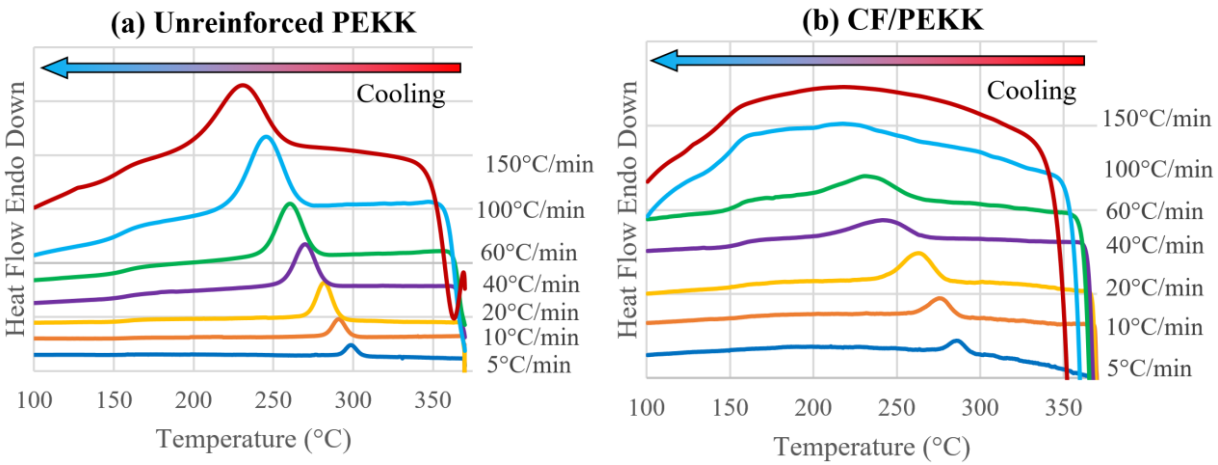

Figure 4.16: DSC thermograms of (a) Unreinforced PEKK powder and (b) CF/PEKK prepreg tape while undergoing different cooling rates.

In both unreinforced PEKK and CF/PEKK composite, crystallisation takes place at progressively lower temperatures with faster cooling rates. At slower rates, chains have more time to move, and therefore begin to crystallise at higher temperatures. As the cooling rate is progressively increased, the polymer commences diffusion at lower temperatures.

Comparing PEKK and CF/PEKK, the composite samples in Figure 4.16b consistently begin crystallisation at lower temperatures than their neat counterparts in Figure 4.16a. The introduction of carbon fibres clearly obstructs the crystallisation mechanism of the matrix, resulting in a delayed crystallisation compared to unreinforced PEKK. This progressively lowers the total crystallinity developed with faster cooling rates, as discussed in the previous section. The crystallisation peak completely disappears at the fastest cooling rates for CF/PEKK in Figure 4.16b, whereas unreinforced PEKK in Figure 4.16a still shows a crystallisation peak at 150°C/min cooling rate.

4.2.4.3. Modelling of non-isothermal crystallisation kinetics

Similar to isothermal crystallisation kinetics, relative crystallinity plots of each sample are required to implement any model. Using Equation (4.2), such a plot is obtained, shown in Figure 4.17. The kinetics for CF/PEKK at 150°C/min are not evaluated, as the achieved crystallinity was very low (0.7%). Note that, while all samples reach a relative volume crystallinity of 1 in Figure 4.17, this does not mean that all samples achieved the same level of absolute crystallinity (listed in Table 4.5). As observed in Figure 4.16, unreinforced PEKK undergoes a faster crystallisation than its composite counterpart for each given cooling rate.

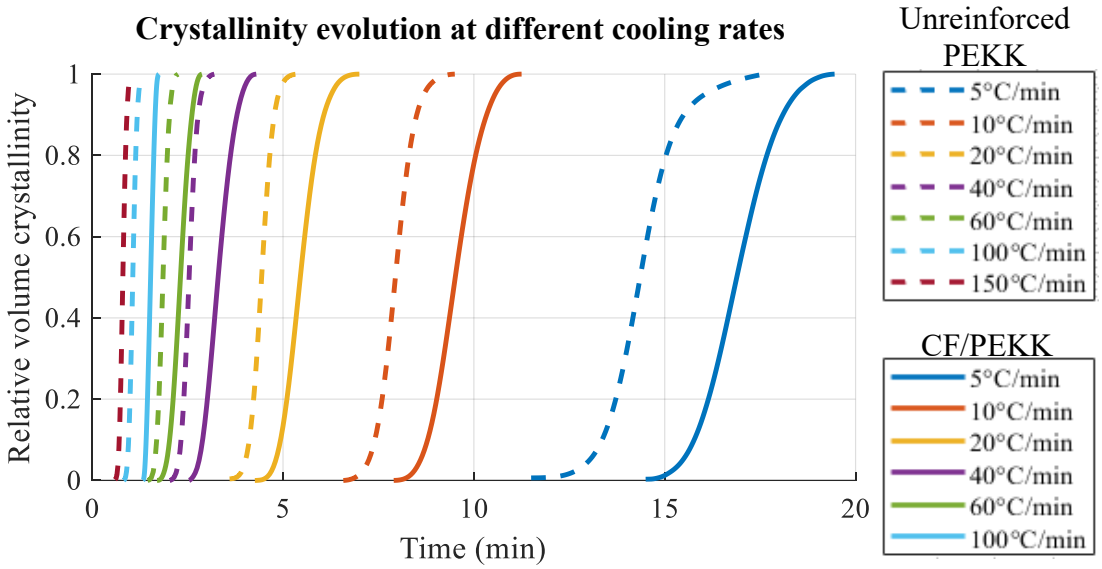

Figure 4.17: Relative crystallinity against time of unreinforced PEKK (dotted lines) and CF/PEKK (solid lines) at different cooling rates.

As discussed in Section 2.3.1, Avrami-based modelling includes the temperature-dependent crystallisation rate constant k. Therefore, creating an Avrami plot as shown in Figure 4.11 (by plotting $\ln[-\ln(1-\alpha)]$ against $\ln(t)$) in order to find information on the possible primary crystallisation mechanism (a value for n_1) is not suitable in this instance, now that k varies with temperature under non-isothermal conditions.

Further to this, changing the thermal cycle that the sample undergoes is not likely to change the spherulitic (or otherwise) nature of crystallisation, but rather the extent to which it occurs (the total crystallinity achieved). Therefore, n_1 and n_2 have been kept the same as in Section 4.2.3: $n_1 = 3$ and $n_2 = 2$ for unreinforced PEKK; and $n_1 = 2.5$ and $n_2 = 2$ for CF/PEKK composite.

In order to model dynamic behaviour and account for a dual crystallisation mechanism, the Nakamura model discussed in Section 2.3.2 was extended into a dual Nakamura model, where, in a similar manner

to the Velisaris-Seferis model, the secondary mechanism can be accounted for by having two separate Nakamura models acting in parallel, representing primary and secondary crystallisation respectively:

$$\alpha(t) = w_1\left(1 - exp\left[-\left(\int_0^t k_1^{1/n_1}\,dt\right)^{n_1}\right]\right) + w_2\left(1 - exp\left[-\left(\int_0^t k_2^{1/n_2}\,dt\right)^{n_2}\right]\right) \tag{4.8}$$

where $K_1 = k_1^{1/n_1}$ and $K_2 = k_2^{1/n_2}$ as described in Section 2.3.2. The integral terms in this case represent how the rates for primary and secondary crystallisation vary over time as the temperature changes. Substituting k_1 and k_2 with Hoffmann-Lauritzen model Equations (4.5) and (4.7) yields the following model:

$$\begin{aligned}\alpha(t) = w_1\left(1 - exp\left[-\left(\int_0^t \left(k_{01}\left[\exp\left(-\frac{3U^*}{R(T-T_\infty)}\right)\times \exp\left(-\frac{3K_{g1}}{T\Delta Tf}\right)\right]\right)^{1/n_1} dt\right)^{n_1}\right]\right) + \\ w_2\left(1 - exp\left[-\left(\int_0^t \left(k_{02}\left[\exp\left(-\frac{2U^*}{R(T-T_\infty)}\right)\times \exp\left(-\frac{2K_{g2}}{T\Delta Tf}\right)\right]\right)^{1/n_2} dt\right)^{n_2}\right]\right)\end{aligned} \tag{4.9}$$

T is the temperature at time t, dependent on the cooling rate r:

$$T = T_m - rt \tag{4.10}$$

where T_m is the melt temperature from which the cooling begins (in this case, 370°C). This model was scripted and implemented on MATLAB using the non-isothermal data of PEKK and CF/PEKK, using the identified parameters in Table 4.4.

Unreinforced PEKK

The heat scan curves of unreinforced PEKK in Figure 4.14 show a single melting endotherm, and therefore values for w_1 and w_2 cannot be set according to LTE:HTE ratios as in the isothermal modelling. Therefore, the ratio of w_1 and w_2 was optimised by the script. The resulting fits are shown in Figure 4.18. These show a decreasing contribution of secondary crystallisation as the cooling rate increases, in line with the observations by Bessard et al. [14] and Regis et al. [15] on the presence of secondary crystallisation under non-isothermal crystallisation. The resulting variation of w_1 and w_2 with cooling rate is shown in Figure 4.19.

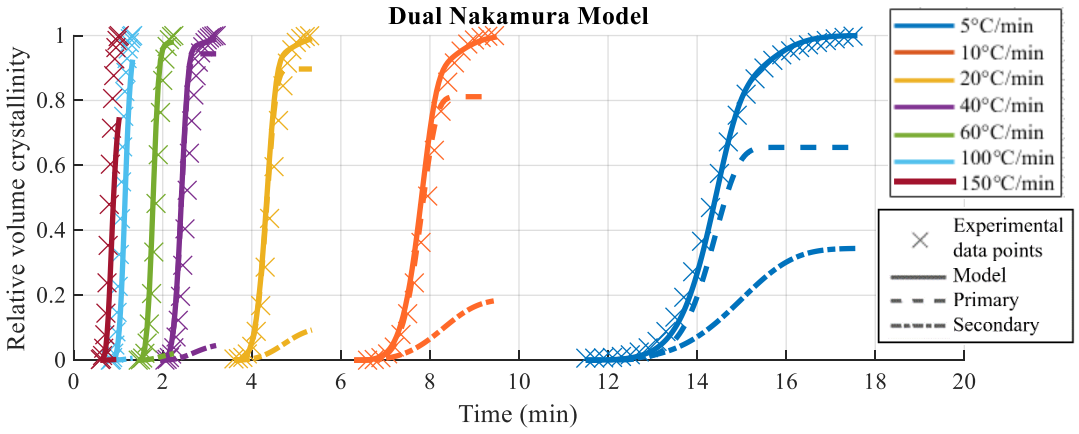

Figure 4.18: Dual Nakamura model fits to non-isothermal crystallisation experimental data of unreinforced PEKK powder undergoing a range of cooling rates.

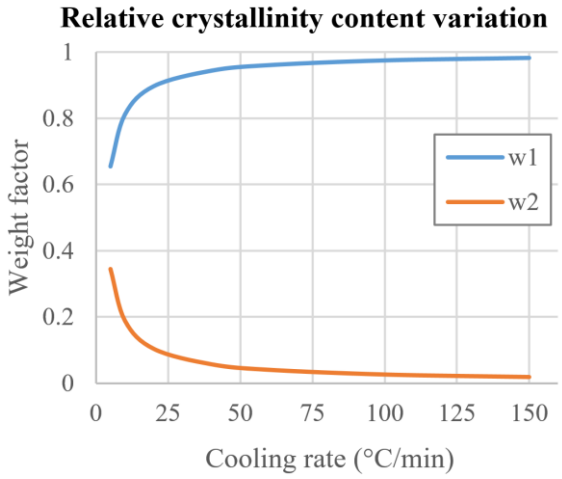

Figure 4.19: Variation of crystallisation relative content (w_1 and w_2) with cooling rate for crystallisation kinetics modelling of unreinforced PEKK powder.

The model can be adapted to account for this variation in w_1 by introducing Equation (4.11) (obtained from the fit in Figure 4.19) in Equation (4.9) and remembering that $w_1 + w_2 = 1$.

$$w_1 = -1.399r^{-0.8707} + 1 \tag{4.11}$$

where r is the applied cooling rate.

The contribution of w_2 necessary to achieve a better fit in the models above suggests that there may be some secondary crystallisation taking place in the material, despite no presence of an LTE endotherm in Figure 4.14a. While the LTE:HTE ratio may be a good estimate of primary and secondary crystallisation content in the case of isothermal studies, this is not the case in non-isothermal studies. Therefore, a LTE may not be the sole indicator of presence of secondary crystallisation in PEKK.

CF/PEKK composite

In the case of CF/PEKK composite, performing the fitting while allowing the script to optimise the values of w_1 and w_2 resulted in $w_1 = 1$ for all curves. It is likely that only primary crystallisation occurs in the case of CF/PEKK, now that kinetics are slower than in unreinforced PEKK and there may not be enough time for the slower secondary crystallisation mechanism to take place.

Even when only accounting for primary crystallisation, however, the model underpredicts the kinetics of the composite, and at increasingly faster rates the crystallinity achieved in the experiments is not reached by the model. This is shown in Figure 4.20. This may be due to the crystallisation rate equation for k_1 (Equation (4.6)) underestimating the crystallisation capability of the polymer under non-isothermal conditions, particularly at higher cooling rates. Including a secondary crystallisation step would only delay kinetics further, as this is a slower mechanism than primary crystallisation.

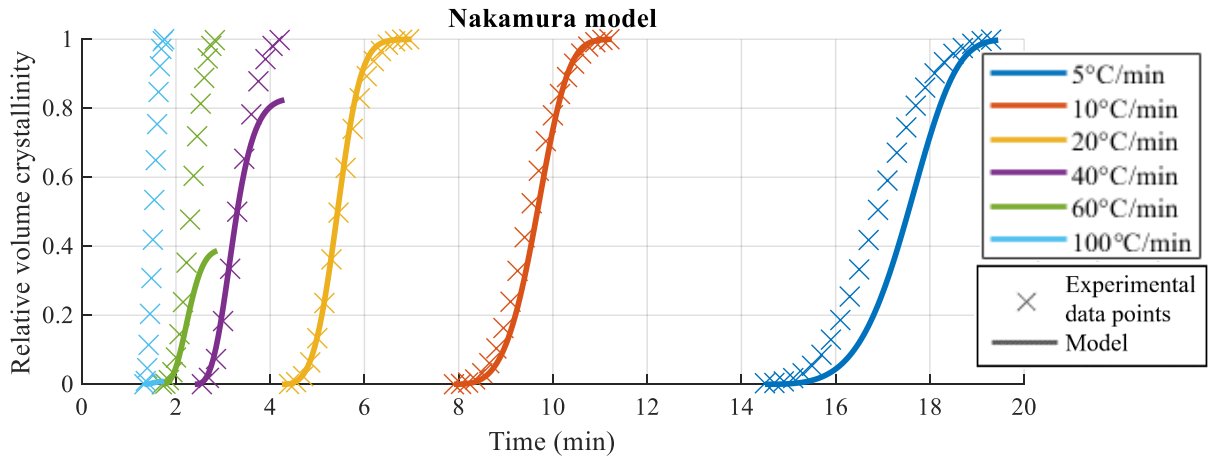

Figure 4.20: Single Nakamura model fits to non-isothermal crystallisation experimental data of CF/PEKK composite undergoing a range of cooling rates.

In order to successfully model dynamic crystallisation of composite PEKK, a z coefficient was introduced to Equation (4.9), which was optimised by the MATLAB script. This coefficient is bespoke for the specific grade of composite PEKK, as it would be beneficial to use for instance in the modelling of crystallinity development across a laminate experiencing different temperature gradients and distributions.

Since, as discussed above, $w_1 = 1$ and $w_2 = 0$, the second half of Equation (4.9) can be ignored, and becomes:

$$\alpha(t) = z\left(1 - \exp\left[-\left(\int_0^t \left(k_{01}\left[\exp\left(-\frac{3U^*}{R(T-T_\infty)}\right) \times \exp\left(-\frac{3K_{g1}}{T\Delta Tf}\right)\right]\right)^{1/n_1} dt\right)^{n_1}\right]\right) \tag{4.12}$$

The expression obtained for z is shown in Equation (4.13), where r is the cooling rate, and the resulting fittings are shown in Figure 4.21.

$$z = 0.00229\exp(0.109r) + 1 \tag{4.13}$$

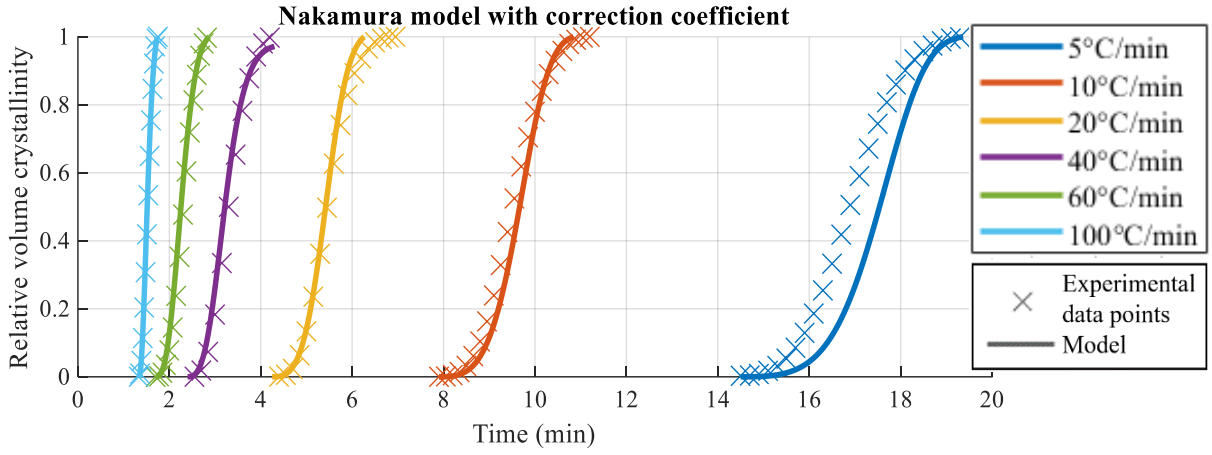

Figure 4.21: Single Nakamura with correction coefficient fits to non-isothermal crystallisation experimental data of CF/PEKK composite undergoing a range of cooling rates.

4.2.5. Manufacturing and end-use applicability

It is of interest to reflect on which of the studied processing conditions would result in the best performance of CF/PEKK composites within the context of manufacturing and high-performance applications. A high crystallinity content may be desirable [16,17] in order to achieve specific performance requirements, such as high strength, stiffness, or chemical resistance, which usually entails using slow cooling rates or isothermal holds. Deciding what isothermal temperature hold or cooling rate will result in a better response is therefore worth investigating and discussing. In this work, different applied thermal cycles have been observed to influence the formation of crystals. Some literature has reported that larger spherulite sizes reduce the mechanical performance of PEEK [18,19] and other polymers [20,21]. Larger crystal sizes in PEKK and CF/PEKK are shown here to develop at high isothermal hold temperatures, and are also likely developed at slow cooling rates (crystallisation takes place at higher temperatures with slower rates, as seen in Figure 4.16). This suggests lower isothermal holds, in the range of 220-260°C, may result in improved mechanical properties, and may therefore be more attractive to designers and manufacturers. The higher end of this range (240-260°C), while resulting in slightly larger spherulites, will undergo faster crystallisation kinetics, which may lead to shorter processing times. The mechanical performance of CF/PEKK laminates manufactured under different conditions based on the crystallisation studies of this chapter is investigated in Chapter 6.

Time-temperature-transformation diagrams based on the isothermal crystallisation studies and the Velisaris-Seferis modelling have been included in Figure 4.22, which allow for the relative crystallinity of the material to be determined at any holding temperature and time. A relative crystallinity of 1 means the material has reached its full crystallisation potential, absolute percentage values of which are presented in Table 4.2.

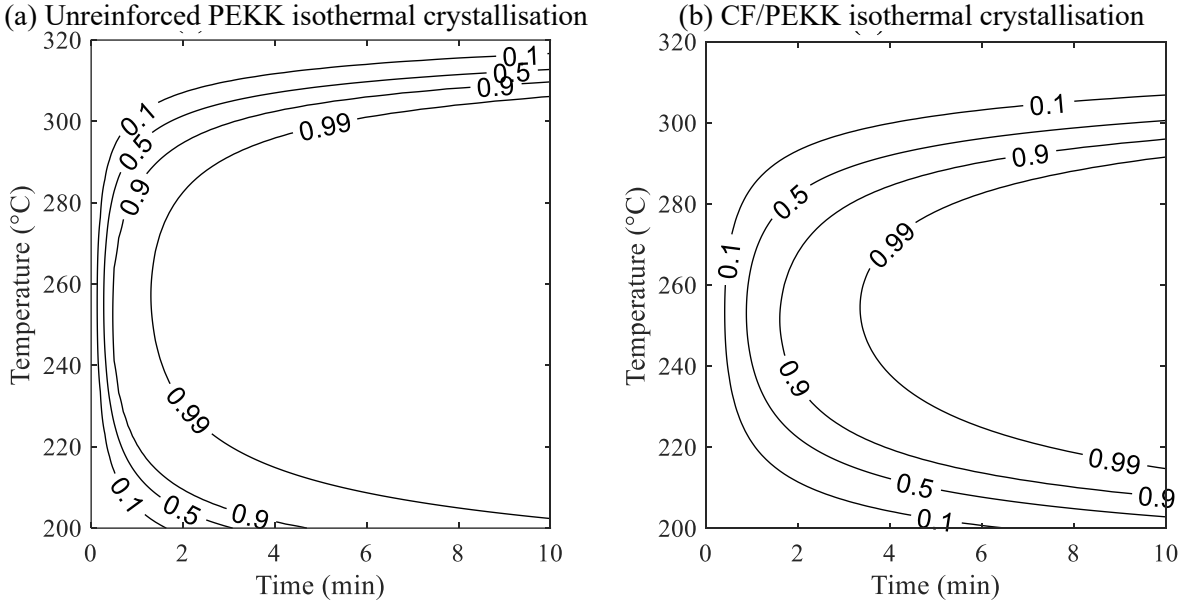

Figure 4.22: Time-temperature-transformation diagrams of relative crystallinity development for (a) unreinforced PEKK and (b) CF/PEKK at different isothermal holds. A relative crystallinity of 1 means the material has achieved its full crystallisation potential, based on the crystallinity values shown in Table 4.2.

Time-temperature transformation diagrams have also been included for non-isothermal instances in Figure 4.23, based on the performed Nakamura modelling. In this instance, a relative crystallinity of 1 refers to the crystallinity achieved by cooling at 5°C/min (absolute crystallinity of 25.5% and 25.7% for unreinforced PEKK and CF/PEKK respectively). As faster cooling rates are performed (indicated by the labelled slopes), lower crystallinities are achieved, as outlined in Table 4.5.

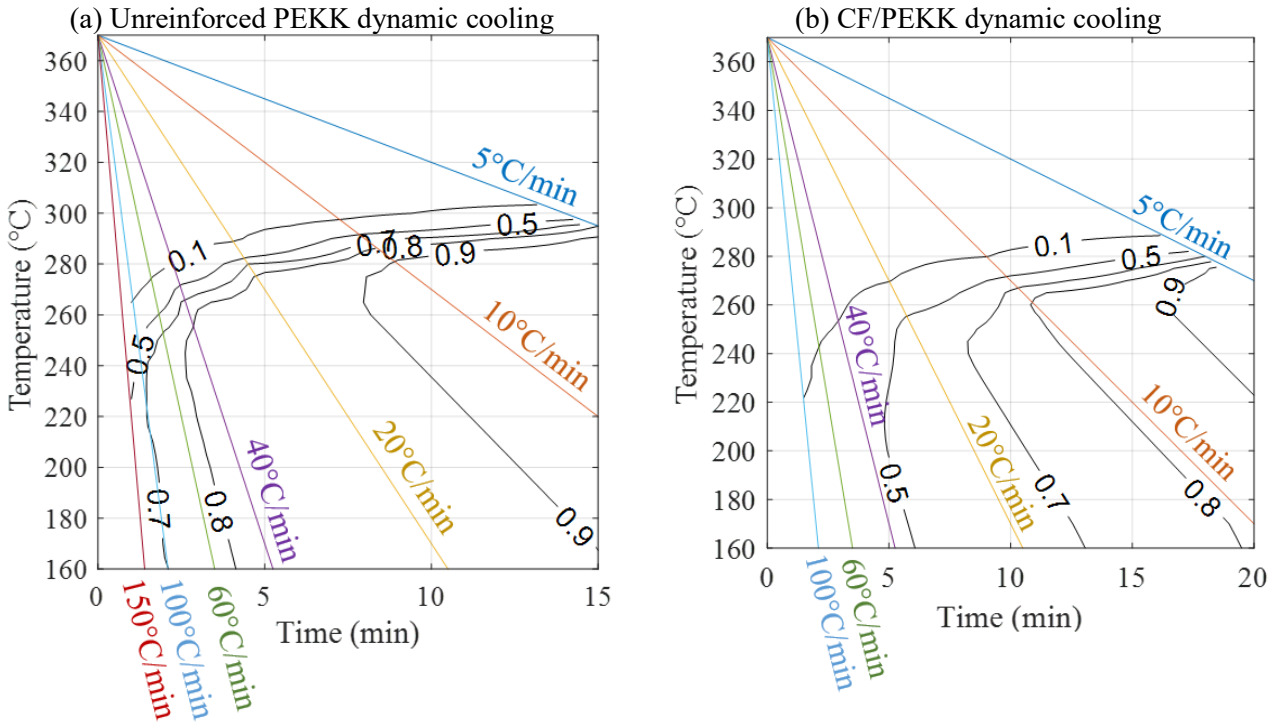

Figure 4.23: Time-temperature-transformation diagrams of relative crystallinity development for (a) unreinforced PEKK and (b) CF/PEKK when undergoing different cooling rates. The coloured straight lines denote the performed cooling rates in this study. A relative crystallinity of 1 refers to the total crystallinity achieved after cooling at 5°C/min.

It is worth considering, however, that holding temperature or cooling rate are not the only factors influencing physical and mechanical properties. The melt temperature will have a large effect on resin flow and part consolidation, as will the application of sufficient processing pressure, without which defects like voids or non-homogeneous consolidation may arise, possibly impacting mechanical performance. Further to this, the experiments performed in this work have all focussed on small amounts of material under the highly controlled, inert environment that DSC provides. This may not be directly applicable to an industrial manufacturing setting, where larger parts are unlikely to undergo highly controlled cooling and may experience a temperature gradient across their thickness. Due to this, manufacturing and mechanical testing of laminates is performed and discussed in the following chapters. The results in this chapter, however, form a solid guideline for industrial-scale processing of CF/PEKK composite parts.

4.3. Chapter conclusions

When undergoing non-isothermal crystallisation, PEKK in unreinforced form crystallises even at the fastest cooling rate tested in this study (150°C/min, achieving partial crystallisation), whereas CF/PEKK, possessing slower crystallisation kinetics, remains amorphous at the fastest cooling rate. Fibre-matrix adhesion is enhanced in more crystalline samples than in amorphous ones, as observed in cryofractured CF/PEKK samples. During dynamic crystallisation, the secondary crystallisation behaviour is not obvious, due to the slower nature of this mechanism. Slow-cooled CF/PEKK samples with higher levels of crystallinity were observed to have a stronger fibre-matrix interphase than amorphous (fast-cooled) samples, as examined by SEM.

Crystallisation kinetics for both isothermal and non-isothermal conditions have been studied using Avrami-based models, where two parallel Avrami-based expressions are used to account for primary and secondary crystallisation respectively. For the isothermal instances, the Velisaris-Seferis model was implemented, and a correlation between the isothermal holding temperature and the crystallisation rate constants was established. This was then used in the non-isothermal crystallisation cases in the implementation of adapted versions of the Nakamura model: a dual Nakamura model with a decreasing contribution of secondary crystallisation with faster cooling rates for unreinforced PEKK, and a single Nakamura model with a material-specific correction factor for CF/PEKK. Successful fits were achieved in all instances, which allows for the prediction of crystallisation evolution at other different rates and isothermal holds.

Overall, the findings of this work lead to a better understanding of the effect that different processing cycles might have on crystal structure development in CF/PEKK composite parts. Given the results in this chapter, a preliminary isothermal holding temperature range that provides optimum spherulitic development for its intended application in high-performance environments is found at 220-260°C. The limitations of this work within the context of industrial applications must, however, be taken into account, namely the differences in scale, processing parameters and environment control when comparing small scale DSC studies and industrial-scale manufacturing. Consequently, the following chapters will cover the manufacturing and testing of CF/PEKK laminates, with cycles based on the knowledge developed as a consequence of the crystallisation studies performed in this chapter.

Chapter references

[1] Arkema. Kepstan® PEKK Brochure 2018.

[2] Chang IY, Hsiao BS. Thermal properties of high performance thermoplastic composites based on poly(ether ketone ketone) (PEKK). 36th Int SAMPE Symp 1991:1587–601.

[3] Choupin T, Fayolle B, Régnier G, Paris C, Cinquin J, Brulé B. Isothermal crystallization kinetic modeling of poly(etherketoneketone) (PEKK) copolymer. Polymer 2017;111:73–82. https://doi.org/10.1016/j.polymer.2017.01.033.

[4] Quiroga Cortés L, Caussé N, Dantras E, Lonjon A, Lacabanne C. Morphology and dynamical mechanical properties of poly ether ketone ketone (PEKK) with meta phenyl links. J Appl Polym Sci 2016;133:1–10. https://doi.org/10.1002/app.43396.

[5] Choupin T, Fayolle B, Régnier G, Paris C, Cinquin J, Brulé B. A more reliable DSC-based methodology to study crystallization kinetics: Application to poly(ether ketone ketone) (PEKK) copolymers. Polymer 2018;155:109–15. https://doi.org/10.1016/j.polymer.2018.08.060.

[6] Chelaghma SA, De Almeida O, Margueres P, Passieux J, Perie J, Vinet A, et al. Identification of isothermal crystallization kinetics of poly(ether-ketone-ketone) based on spherulite growth measurements and enthalpic data. Polym Cryst 2020;3. https://doi.org/10.1002/pcr2.10141.
[7] Arkema. Introduction to ultra high-performance Kepstan® PEKK 2020.
[8] Hsiao BS, Chang IY, Sauer BB. Isothermal crystallization kinetics of poly(ether ketone ketone) and its carbon-fibre-reinforced composites. Polymer 1991;32:2799–805. https://doi.org/10.1016/0032-3861(91)90111-U.
[9] Velisaris CN, Seferis JC. Crystallization kinetics of polyetheretherketone (peek) matrices. Polym Eng Sci 1986;26:1574–81. https://doi.org/10.1002/pen.760262208.
[10] Hsiao BS, Gardner KH, Cheng SZD. Crystallization of poly(aryl ether ketone ketone) copolymers containing terephthalate/isophthalate moieties. J Polym Sci Part B Polym Phys 1994;32:2585–94. https://doi.org/10.1002/polb.1994.090321604.
[11] Tardif X, Pignon B, Boyard N, Schmelzer JWP, Sobotka V, Delaunay D, et al. Experimental study of crystallization of PolyEtherEtherKetone (PEEK) over a large temperature range using a nano-calorimeter. Polym Test 2014;36:10–9. https://doi.org/10.1016/j.polymertesting.2014.03.013.
[12] Gao S-L, Kim J-K. Cooling rate influences in carbon fibre/PEEK composites. Part I. Crystallinity and interface adhesion. Compos Part Appl Sci Manuf 2000;31:517–30. https://doi.org/10.1016/S1359-835X(00)00009-9.
[13] Saiello S, Kenny J, Nicolais L. Interface morphology of carbon fibre/PEEK composites. J Mater Sci 1990;25:3493–6. https://doi.org/10.1007/BF00575375.
[14] Bessard E, De Almeida O, Bernhart G. Unified isothermal and non-isothermal modelling of neat PEEK crystallization. J Therm Anal Calorim 2014;115:1669–78. https://doi.org/10.1007/s10973-013-3308-8.
[15] Regis M, Zanetti M, Pressacco M, Bracco P. Opposite role of different carbon fiber reinforcements on the non-isothermal crystallization behavior of poly(etheretherketone). Mater Chem Phys 2016;179:223–31. https://doi.org/10.1016/j.matchemphys.2016.05.034.
[16] Choupin T, Debertrand L, Fayolle B, Régnier G, Paris C, Cinquin J, et al. Influence of thermal history on the mechanical properties of poly(ether ketone ketone) copolymers. Polym Cryst 2019;2:e10086. https://doi.org/10.1002/pcr2.10086.
[17] Comer AJ, Ray D, Obande WO, Jones D, Lyons J, Rosca I, et al. Mechanical characterisation of carbon fibre–PEEK manufactured by laser-assisted automated-tape-placement and autoclave. Compos Part Appl Sci Manuf 2015;69:10–20. https://doi.org/10.1016/j.compositesa.2014.10.003.
[18] Schultz JM, Chu JN. The influence of microstructure on the failure behaviour of PEEK. J Mater Sci 1990;25:3746–52. https://doi.org/10.1007/BF00575414.
[19] Lustiger A, Uralil FS, Newaz GM. Processing and structural optimization of PEEK composites. Polym Compos 1990;11:65–75. https://doi.org/10.1002/pc.750110109.
[20] Ehrenstein GW, Theriault RP. Polymeric Materials: Structure, Properties, Applications. Hanser Publishers; 2001.
[21] Starkweather Jr. HW, Brooks RE. Effect of spherulites on the mechanical properties of nylon 66. J Appl Polym Sci 1959;1:236–9. https://doi.org/10.1002/app.1959.070010214.

Chapter 5. Materials and manufacturing: CF/PEKK laminate fabrication via compression-moulding and automated tape placement (ATP)

As discovered in Chapter 4, it is beneficial to apply the acquired knowledge during the crystallisation studies within the context of larger-scale manufacturing. This is not only to assess the mechanical performance of the developed crystallinities, but also how well small-scale studies translate to more industrial settings. Compression-moulding was chosen to manufacture laminates with high crystallinity contents due to the ability to hold and control processing temperature and pressure. This manufacturing process was also chosen to act as benchmark values for what is expected of a well-consolidated, crystalline laminate when assessing the behaviour of ATP-manufactured laminates, in which differences in consolidation and crystallinity development were expected when compared to compression moulding (due to the fast nature of the process). This chapter describes in detail the materials and processing conditions that were used during compression-moulding and ATP manufacturing of the laminates that undergo testing in Chapter 6 and Chapter 7.

5.1. CF/PEKK prepreg tape

AS7 CF/PEKK prepreg tape was used for all manufacturing performed in this work. This was provided by Hexcel Composites Ltd, who manufactured this tape via aqueous powder impregnation, with PEKK powder provided by Arkema (KEPSTAN PEKK 7002PT, the same that was used in the crystallisation studies in Chapter 4). The resulting tape had an average thickness of 0.2 mm, and a width of 150 mm. Hexcel also provided 6.5 mm-wide tape for ATP manufacturing, already wound up in spools appropriate for the ATP equipment. The nominal resin weight as stated by the manufacturers was 34%, which was further verified for each batch used in each manufacturing process. The measured weights are discussed in the following sections. Images of the two tape presentations are shown in Figure 5.1.

(a) Prepreg tape roll for compression-moulding (b) Prepreg tape in spool for ATP manufacturing

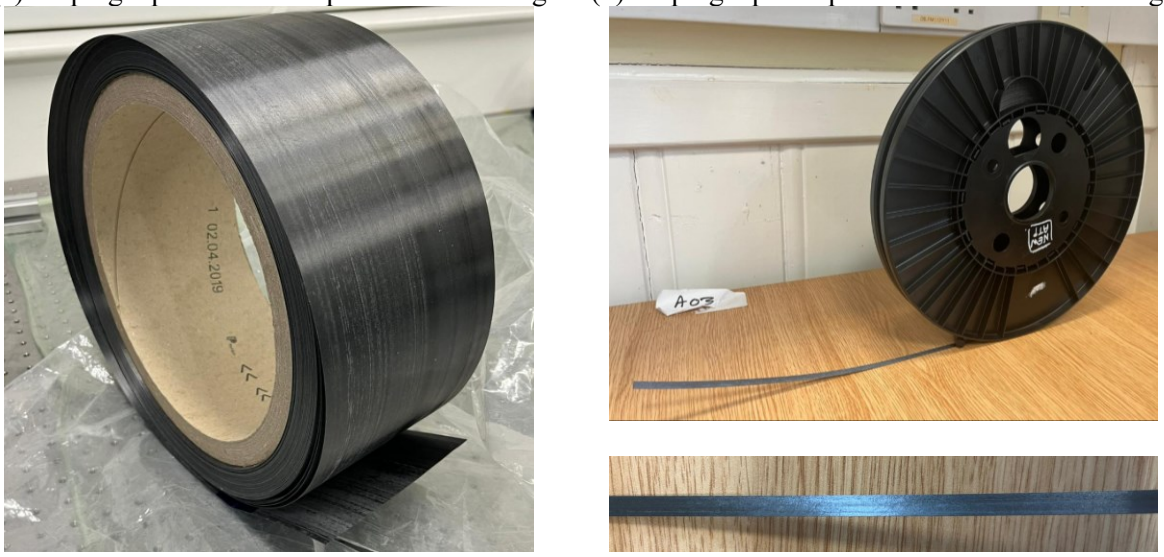

Figure 5.1: CF/PEKK prepreg tape as received from Hexcel Composites Ltd. for (a) compression-moulding (150 mm wide)and (b) ATP manufacturing (6.5 mm wide).

A sample of the resulting prepreg, along with SEM images at different magnifications, can be observed in Figure 5.2. The specifications of the SEM set-up are shown in Section 4.1.5. Visual inspection of the prepreg tape (Figure 5.2a) showed lighter and darker regions. These areas were thoroughly examined to understand whether this may have any impact on laminate quality. Looking at the prepreg tape surface under SEM showed pooling of resin on the tape surface in the lighter regions and more exposed fibres on the darker regions (Figure 5.2b). This is also clear in the cross-section imaging (Figure 5.2c and Figure 5.2d), where the surfaces of the dark region mainly show bare fibres, whereas in the light regions, more matrix can be observed on the surface. This potentially highlights uneven spreading of the powder during prepreg manufacture in some areas. Figure 5.2c and Figure 5.2d also show an uneven spread of fibre and matrix across the thickness of the prepreg, which in some cases may result in the presence of voids in fibre-rich regions as highlighted in Figure 5.2d and Figure 5.2e. The effect of this is likely to be minimal during compression-moulding, where the long holding times under high temperatures and pressures allow for thorough resin flow and fibre impregnation. However, this may pose challenges during fast in-situ manufacturing, where these conditions do not take place over extended periods.

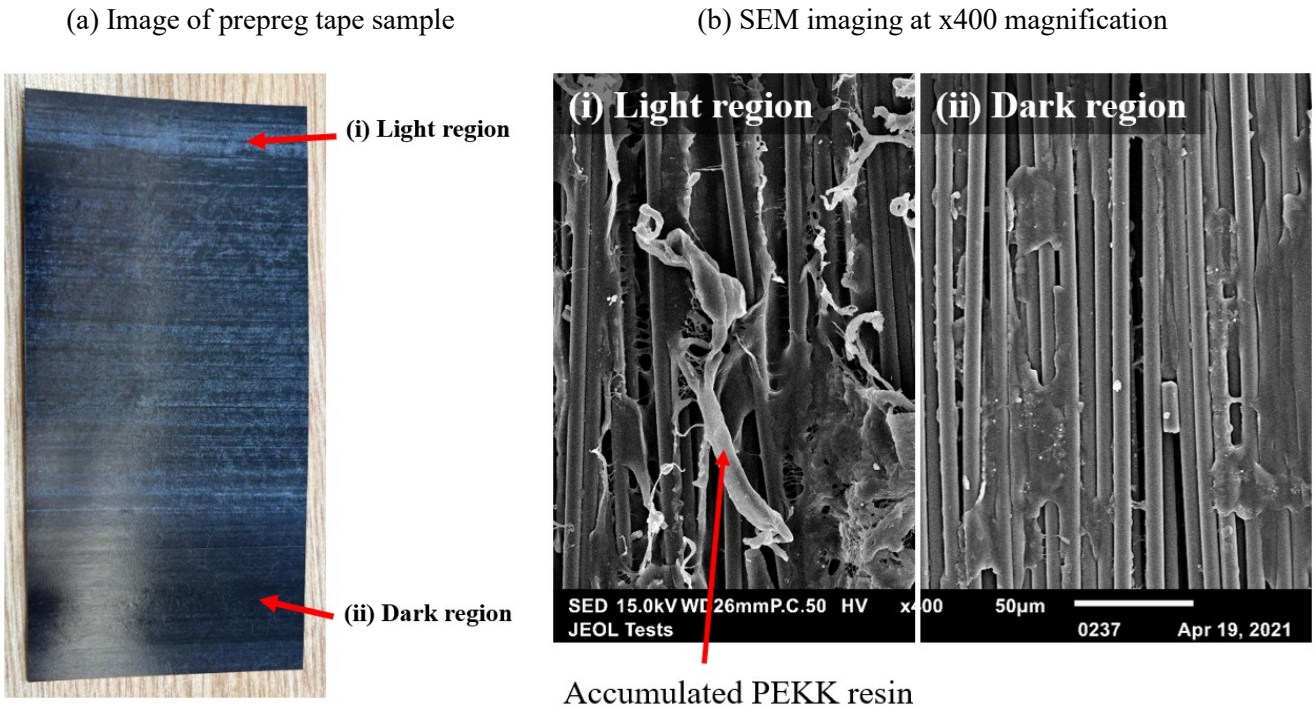

Figure 5.2: Prepreg tape imaging of lighter and darker regions.

(c) Light region cross-section SEM at x400 magnification

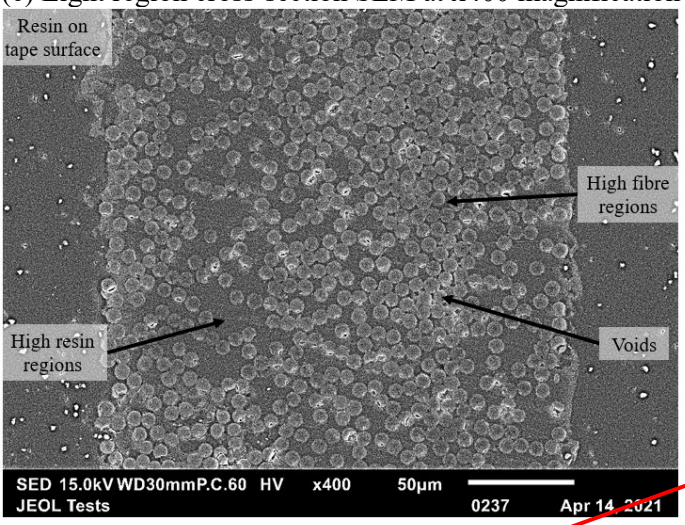

(d) Dark region cross-section SEM at x400 magnification

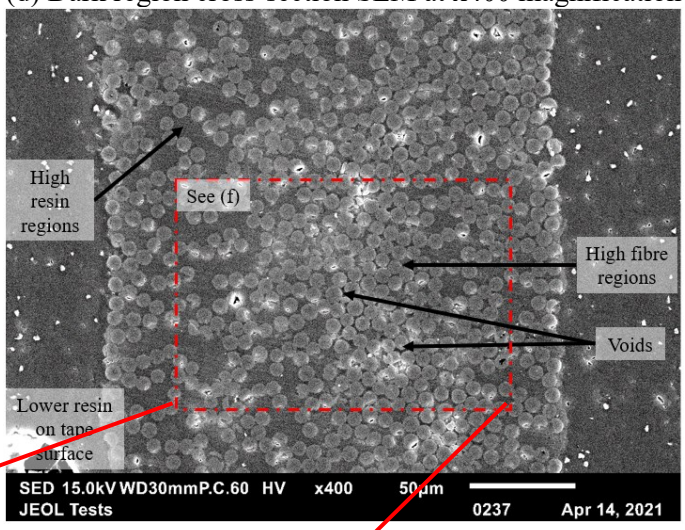

(e) Dark region cross-section SEM at x800 magnification highlighting voids

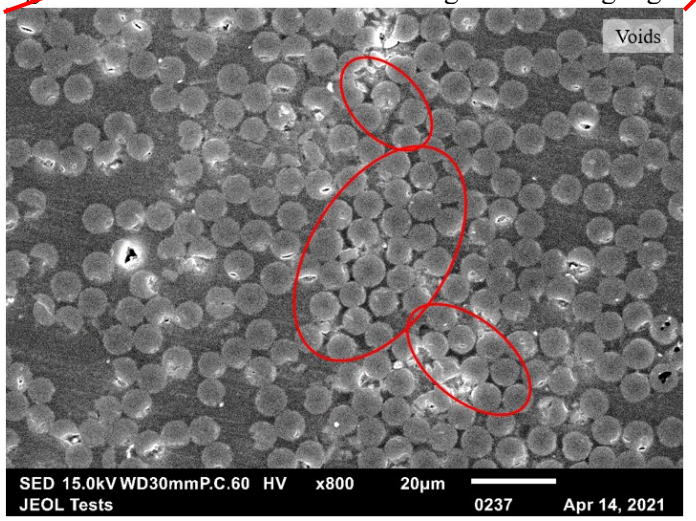

Figure 5.2: (cont): Prepreg tape imaging of lighter and darker regions.

5.2. Compression-moulded laminates

For the compression-moulded laminates, prepreg tape was used from the same roll that was used for the crystallisation studies in Chapter 4 (see Section 4.1.1). This tape came in a 150 m long roll and was 150 mm wide and approximately 0.2 mm thick. As discussed in Section 4.2.1, fibre content by weight was found to be 68% via acid digestion (resin content of approximately 32%). This translated to a fibre volume fraction of 61%. The calculations for this can be found in Appendix A.

Unidirectional laminates were manufactured in a Pinette Emidecau Industries (PEI) LAB 450 P hydraulic press. Cooling of the press is provided by an integrated Frigosystem chiller. All laminates were made by stacking 10 plies of prepreg sheets with a layup $[0°]_{10}$ to achieve a thickness of 2 mm. A 3-part mould was used, consisting of a 2mm-thick frame and a top and bottom plate, as shown in Figure 5.3.

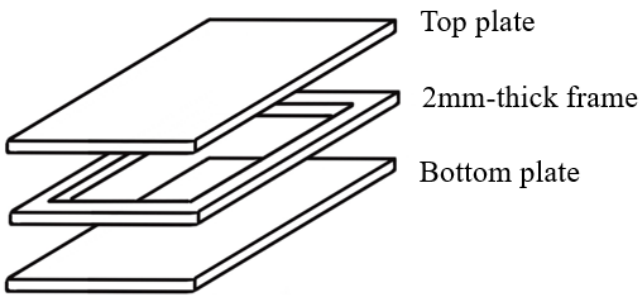

Figure 5.3: Schematic of frame and plates used for compression-moulding manufacturing.

This resulted in laminates with dimensions 300 mm x 150 mm x 2 mm. Prepreg plies were cut down to this length with a guillotine. As the prepreg plies were not sticky, maintaining 0° alignment while setting up for compression moulding proved to be challenging. A soldering iron kit was used to melt the corners of the plies together while stacking them, to circumvent this issue, as shown in Figure 5.4. The laminate frame was used to keep the plies in place during melting, minimising ply misalignment. Samples for mechanical testing were later extracted at least 10 mm away from the edges of the laminate, so testing was unaffected by this preparation step.

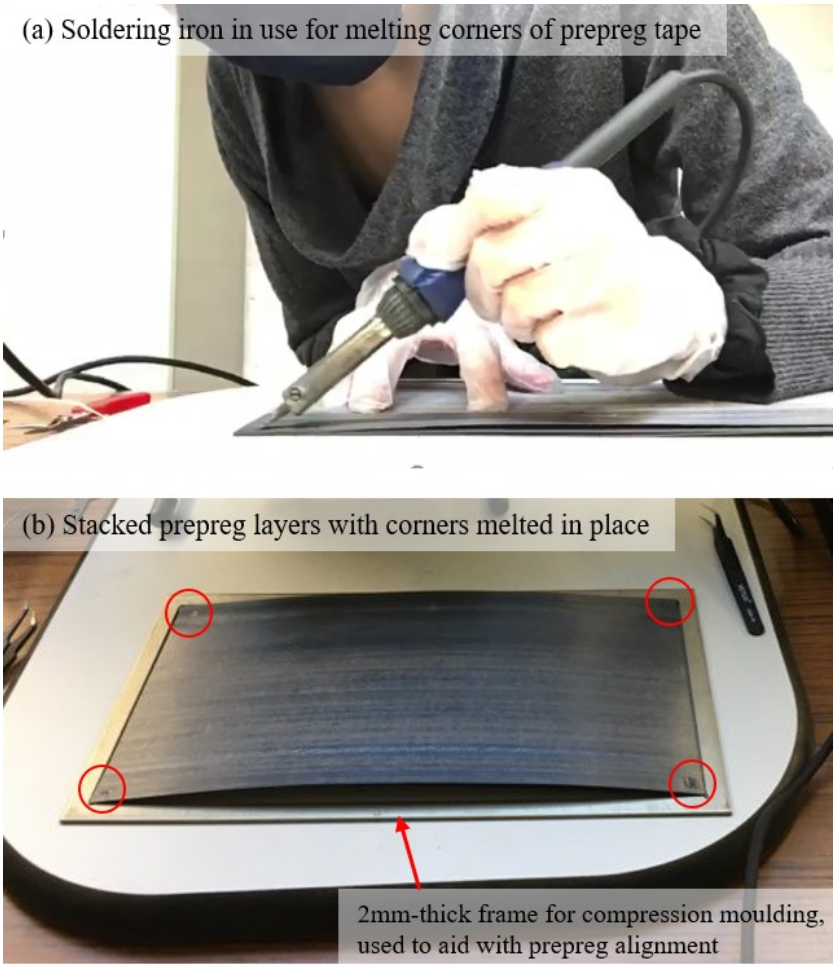

Figure 5.4: Prepreg tape preparation for laminate manufacturing via compression-moulding.

Four laminates were manufactured undergoing the following processing cycles. The selected isothermal and holding temperatures in the melt were chosen based on the study presented in Chapter 4 on the crystallisation behaviour and morphology of PEKK and CF/PEKK composites.

1. Heat from room temperature to holding temperature in the melt (370°C or 380°C) at 10°C/min.
2. Hold in the melt for 25 min.
3. Cool down to isothermal temperature (220°C, 260°C or 300°C) at 10°C/min.
4. Hold at the isothermal temperature for 60 min.
5. Cool from the isothermal temperature to room temperature at 10°C/min.

An additional laminate was manufactured undergoing a different processing cycle with dynamic cooling having no isothermal hold:

1. Heat from room temperature to holding temperature in the melt (370°C) at 10°C/min.
2. Hold in the melt for 25 min.
3. Cool from the melt temperature to room temperature at 5°C/min.

A temperature-time plot of the programmed cycles is shown in Figure 5.5. All laminates underwent a pressure of 1 bar during the heating step, and 28 bar for the remainder of the processing cycle. The laminates were named as shown in Figure 5.5. The laminate code consists of three parts, denoting the nature of cooling ("I" for isothermal or "C" for dynamic cooling) followed by isothermal hold temperature (220°C, 260°C or 300°C) or a cooling rate (5°C/min), and finally the holding temperature in the melt (370°C or 380°C). An example of what the laminates looked like is shown in Figure 5.6.

Compression-moulded laminates

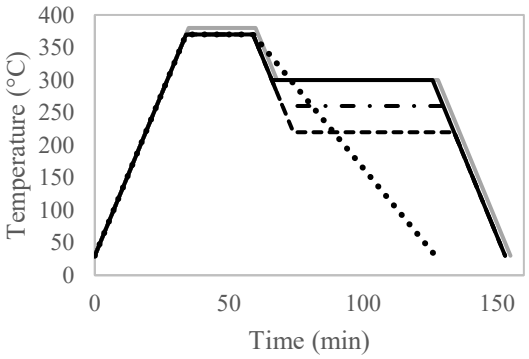

Legend	Laminate code	Hold melt temp. (°C)	Isothermal hold temp. (°C)
- - -	I-220-370	370	220
— · ·	I-260-370	370	260
——	I-300-370	370	300
——	I-300-380	380	300

Legend	Laminate number	Hold melt temp. (°C)	Cooling rate (°C/min)
▪▪▪▪	C-5-370	370	5

Figure 5.5: Summary of processing parameters for the compression-moulded laminates.

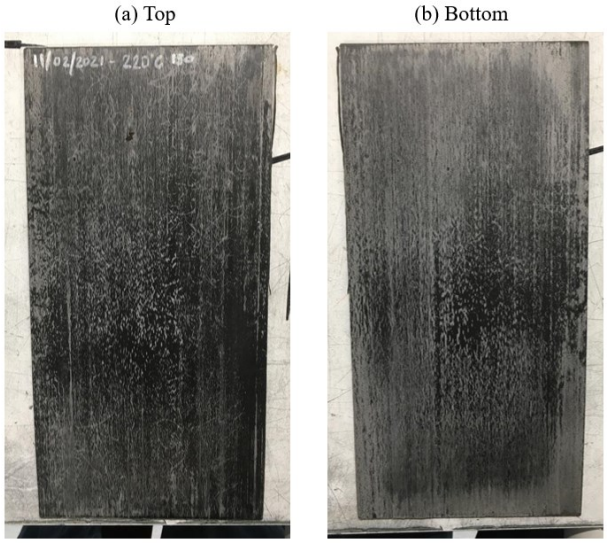

Figure 5.6: I-220-370 laminate after manufacturing.

5.3. Automated Tape Placement

Unidirectional ATP laminates were manufactured at the University of Limerick, Ireland, using a laser-assisted tape placement head (AFPT, GmbH) attached to a robot arm (Kuka, KR240 L210-2). A total of 10 layers of prepreg tape were placed per laminate, as per the compression-moulded laminates, resulting in 2 mm-thick laminates. A diagram of the process highlighting the ATP settings is shown in Figure 5.7, and labelled images of the equipment are available in Figure 5.8. The parameters that were studied in this work were nip temperature, lay-down speed and roller pressure.

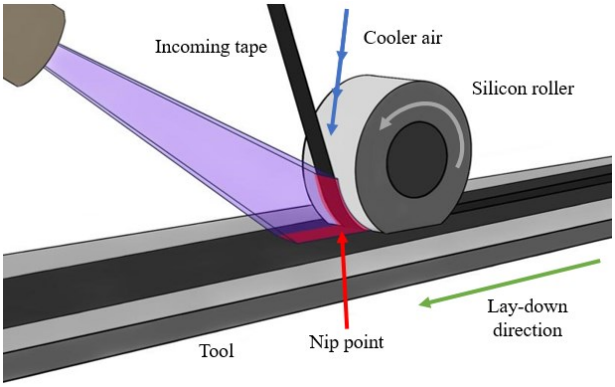

Cooler air pressure	1 bar
Incoming tape dimensions	6.4 mm wide x 0.2 mm thick
Laser-nip point optical distance	170 mm
Laser power limit	1000 W
Tape/laminate laser split	Approx. 50/50
Tool temperature	Unheated

Figure 5.7: Schematic of ATP lay-up process and processing parameters. ATP schematic drawn after [5].

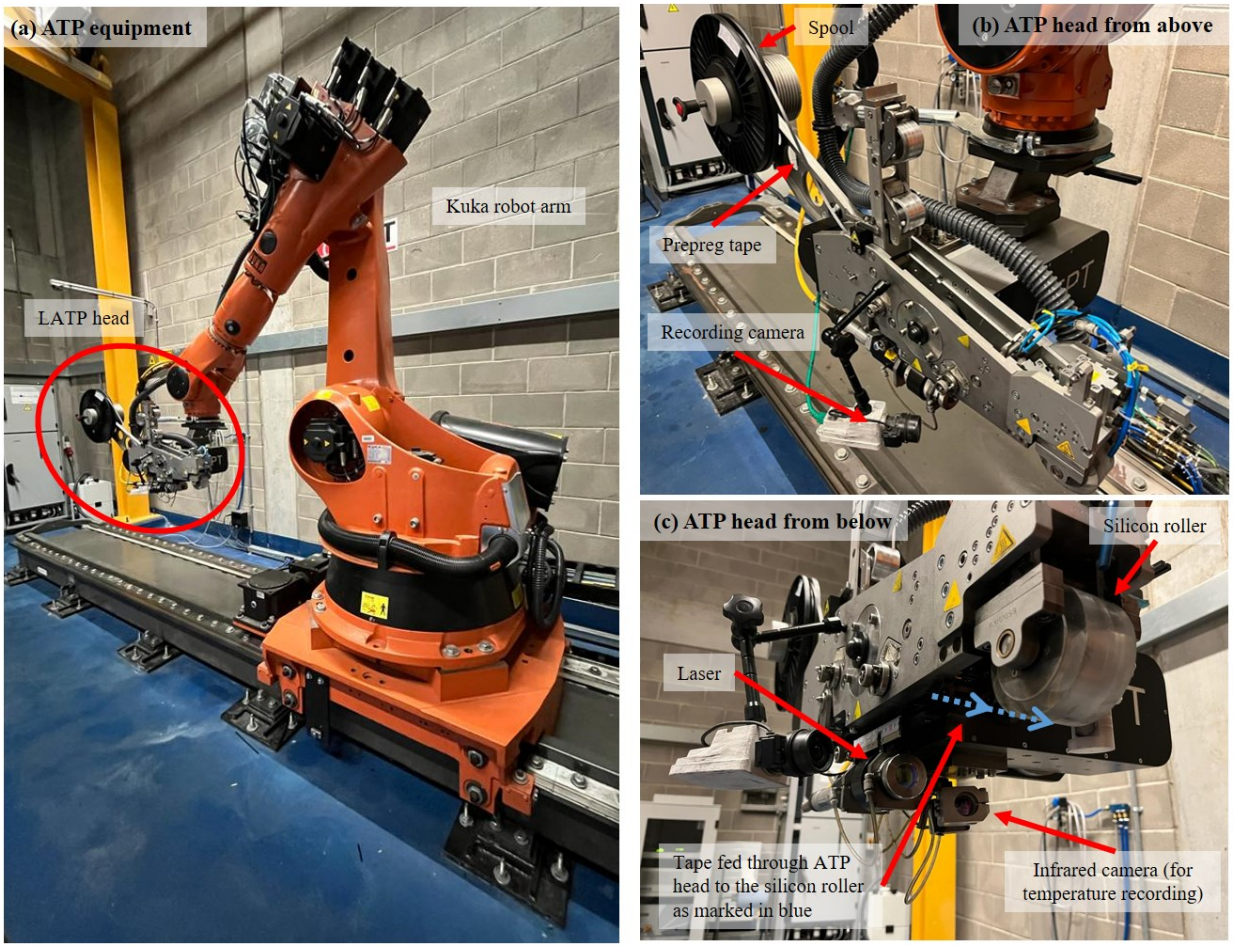

Figure 5.8: Images of (a) ATP equipment and (b) (c) ATP head close-ups.

Figure 5.9 shows a schematic of the laying station programme provided by the ATP operator. The desired programme parameters are only achieved along the panel length portion of the lay-down process. As the prepreg tape is not tacky, double-sided tape was placed on the tool surface for the first layer of prepreg tape to remain in place, at the beginning and end of the panel length. This is shown in Figure 5.10. The remaining laminate layers adhered to the previous layer during lay-down. Any exceptions to this are discussed in the following sections.

Laminates were manufactured in two separate batches, which will be discussed in the following sections.

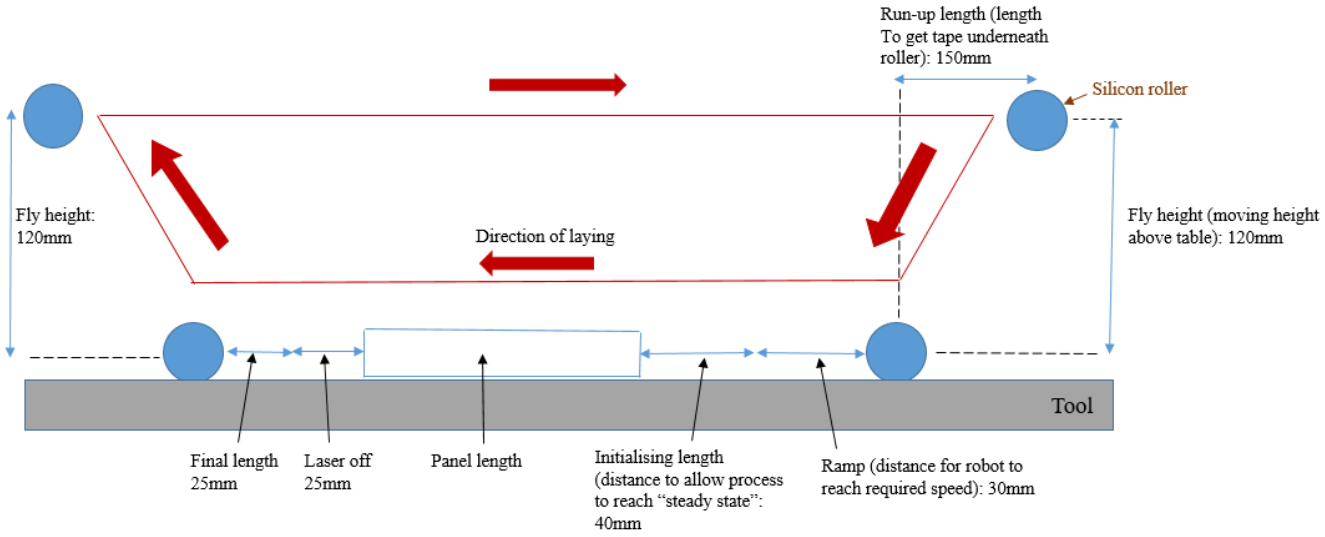

Figure 5.9: Schematic of ATP laying programme.

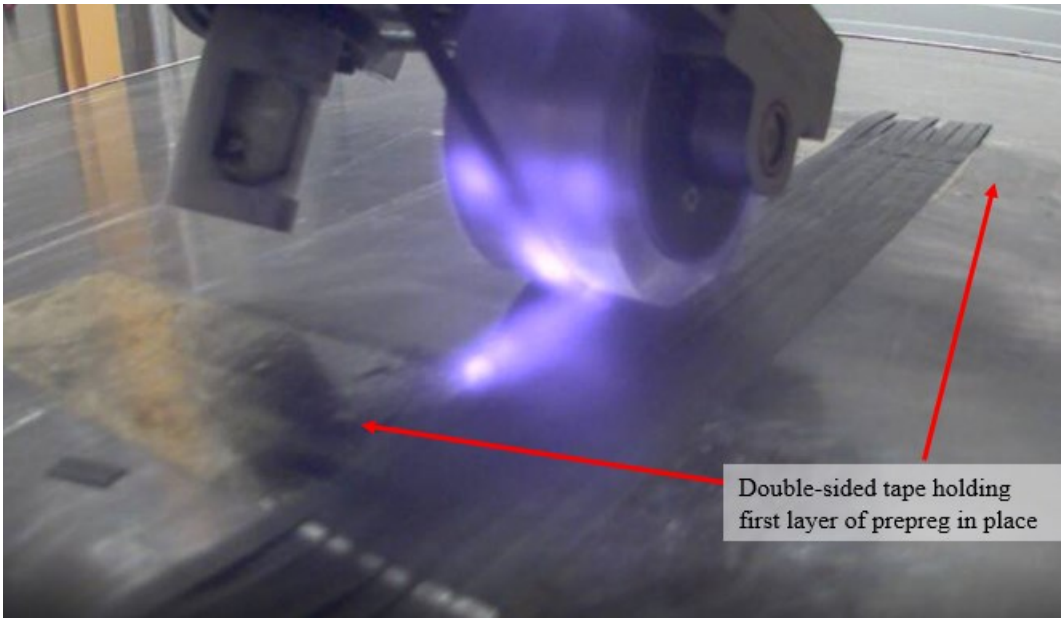

Figure 5.10: Image of ATP manufacturing process, showing the first layer of a laminate being laid down on a mild steel tool. Double-sided tape is highlighted, showing how the first layer of tape is held in place.

5.3.1. First manufacturing campaign

In the first manufacturing campaign, the prepreg tape used was from the same batch (manufactured at the same time) as the tape used in the crystallinity studies in Chapter 4 and for the compression-moulded laminates. However, this tape was slit into 6.35mm-wide tapes, in order to be compatible with the ATP head, and wound up on compatible spools by the manufacturer. Another acid digestion test campaign was performed on samples from this to ensure the adequate fibre (or resin) content was recorded. The results are shown in Table 4.1, providing a fibre (or resin) weight average of 67% (or 33%). This translated to a fibre volume fraction of 59% (see Appendix A).

Table 5.1: CF/PEKK prepreg tape sample weights before and after acid digestion.

	Weight before test (mg)	Weight after test (mg)	Fibre content by weight (%)	Resin content by weight (%)
Sample 1	507.4	342.8	67.6	32.4
Sample 2	493.2	327.0	66.3	33.7

Initial manufacturing trials were attempted on a square tool, details of which can be found in Appendix C.1. Finally, a flat, unheated ceramic tool was used with a nip temperature T_{nip} = 360°C. This temperature was later deemed to be slightly low, which led to the second batch of laminate manufacturing discussed in the next section.

Unidirectional laminates ($[0]_{10}$) were manufactured to perform mechanical testing of flexural 0°, flexural 90° and interlaminar shear stress testing. Additionally, cross-ply laminates were manufactured ($[0/90]_{3s}$), to perform ±45 tensile testing. Examples of these are shown in Figure 5.11. Two of the cross-ply laminates were reprocessed via compression moulding, following the same cycles as I-220-370 and I-300-370 (see Figure 5.5).

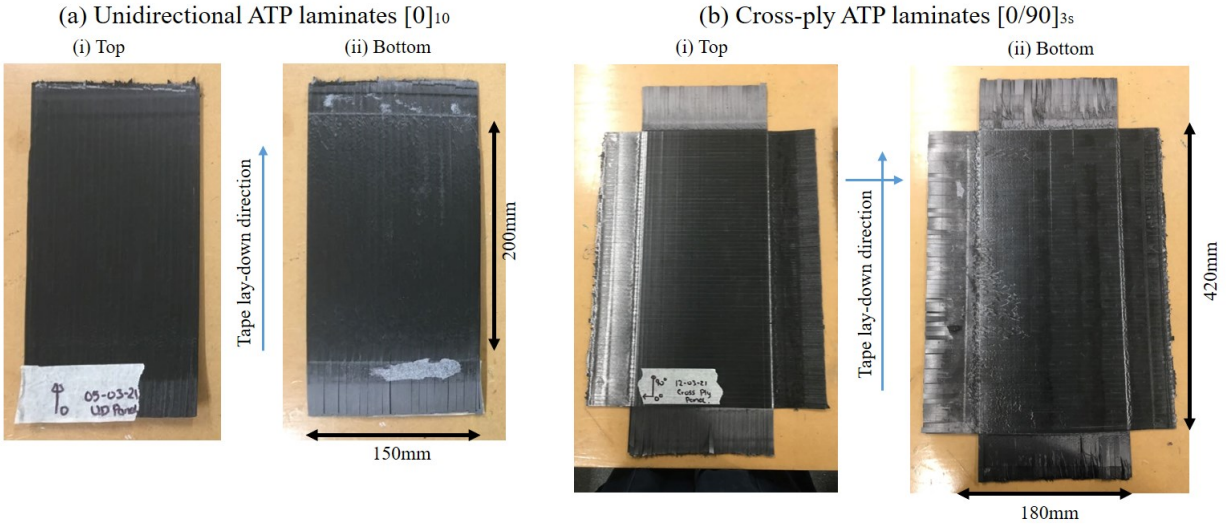

Figure 5.11: Images of ATP-manufactured (a) unidirectional laminates for 0° flexural, 90° flexural and ILSS testing, and (b) cross-ply laminates for in-plane shear testing..

Additionally, a multi-thickness laminate was manufactured to perform crystallinity gradient studies. Initially, thicknesses from 2 to 10 mm in 2 mm steps were intended as per Figure 5.12a. However, due to warping of the laminate as more layers of prepreg tape were laid, tape laying was stopped after completing the 6 mm layer. The resulting laminate is shown in Figure 5.12b.

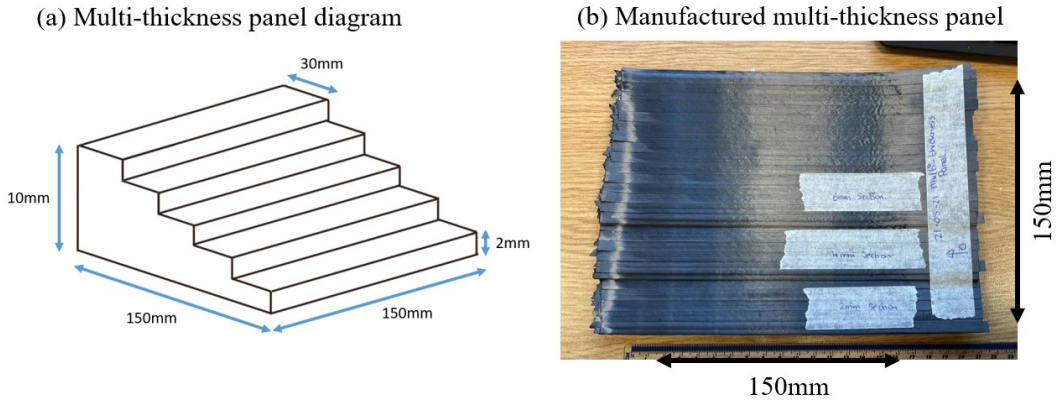

Figure 5.12: (a) Schematic of original concept for multi-thickness laminate and (b) image of final manufactured multi-thickness laminate.

A summary of these manufactured laminates is given in Section 5.3.3.

5.3.2. Second manufacturing campaign

For the second manufacturing campaign, new prepreg rolls were supplied by Hexcel with the same carbon fibre and PEKK powder as the prepreg batches used for compression moulding and previous ATP manufacturing. Another acid digestion test was performed to verify fibre (or resin) content, the results of which are shown in Table 5.2. Fibre (or resin) content were found to be 65% (or 35%) on average, which translated to a fibre volume fraction of 58% (see Appendix A). Both this tape batch and the batch from the first campaign were used for the manufacturing of these laminates. Section 5.3.3 provides further details of what tape was used for each laminate.

Table 5.2: CF/PEKK prepreg tape sample weights before and after acid digestion.

	Weight before test (mg)	**Weight after test (mg)**	**Fibre content by weight (%)**	**Resin content by weight (%)**
Sample 1	479.2	310.3	64.8	35.2
Sample 2	480.6	318.1	66.2	33.8

In this case, it was decided that the effect of different nip temperatures would be tested, along with different lay-down speeds and roller pressure. Initially, using a heated tool was to be trialled as well, however due to adhesion problems between layers this could not be done. To avoid any delay, manufacturing was carried out with a cold metal tool. The details of heated tool trials and problems faced are given in Appendix C.2.

A total of 5 laminates were manufactured, where T_{nip} of 370, 380 and 390°C, lay-down speeds of 2 and 4 m/min, and roller pressures of 2 and 4 bar were used. These were then used to perform flexural 0°, flexural 90° and ILSS mechanical testing.

5.3.3. Summary of manufactured ATP laminates and codes

Table 5.3, Table 5.4 and Table 5.5 show laminate codes and all parameters for the manufactured unidirectional ATP laminates, including the manufacturing campaign and the tape that was used for each of them. The tape batch that was used for all the manufacturing of the first campaign is referred to as "1st tape", and the new tape batch that was introduced during the second manufacturing campaign is named "2nd tape".

The codes of the laminates consist of the manufacturing process (ATP), nip temperature (360, 370, 380 or 390°C), lay-down speed (2 or 4 m/min) and roller pressure (2 or 4 bar). The cross-ply laminates that have been reprocessed have an extra code term indicating they have then been compression-moulded at 220 or 300°C (P220 or P300), see Table 5.4. The different sections from the multi-thickness panel also include the respective thickness of each section in the laminate code (2, 4 or 6 mm), see Table 5.5. Process data sheets for each panel are available in Appendix D.

Table 5.3: Summary of processing parameters for unidirectional ATP-manufactured laminates.

Laminate code	Manuf. campaign	Tape used	Nip temp. (°C)	Lay-down speed (m/min)	Roller pressure (bar)	Tool material
ATP-360-4-2	1	1st tape	360	4	2	Ceramic
ATP-370-4-2	2	Layers 1-4: 1st tape Layers 5-10: 2nd tape	370	4	2	Mild steel
ATP-380-4-2	2	1st tape	380	4	2	Mild steel
ATP-390-4-2	2	1st tape	390	4	2	Mild steel
ATP-380-2-2	2	2nd tape	380	2	2	Mild steel
ATP-380-4-4	2	2nd tape	380	4	4	Mild steel

Table 5.4: Summary of reprocessing parameters for cross-ply ATP-manufactured laminates.

Laminate code	Manuf. campaign; tape used	ATP parameters				Post Processing	
		Nip temp. (°C)	Lay-down speed (m/min)	Roller pressure (bar)	Tool material	Hold melt temp. (°C)	Isothermal hold temp. (°C)
ATP-360-4-2	1; 1st tape	360	4	2	Ceramic	-	-
ATP-360-4-2-P220	1; 1st tape	360	4	2	Ceramic	370	220
ATP-360-4-2-P300	1; 1st tape	360	4	2	Ceramic	370	300

Table 5.5: Summary of processing parameters for multi-thickness laminate.

Laminate code	Manuf. campaign; tape used	Nip temperature (°C)	Lay-down speed (m/min)	Roller pressure (bar)	Tool material	Laminate thickness (mm)
ATP-360-4-2-2mm	1; 1st tape	360	4	2	Ceramic	2
ATP-360-4-2-4mm	1; 1st tape	360	4	2	Ceramic	4
ATP-360-4-2-6mm	1; 1st tape	360	4	2	Ceramic	6

5.4. Chapter conclusions

The knowledge gained on PEKK's crystallinity development has been applied towards laminate manufacturing, in an attempt to observe the effect of crystallinity on the mechanical performance of CF/PEKK composites. A variety of laminates have been manufactured via compression-moulding and ATP to obtain different crystallinity extents and morphologies. In the following chapters, these laminates are tested for their flexural and ILSS properties and/or the microstructural properties are assessed, and links to the crystallinity development observed in Chapter 3 are made. The provided codes in Table 5.3, Table 5.4 and Table 5.5 will be used to refer to each laminate for clarity purposes.

Chapter 6. Mechanical testing of CF/PEKK laminates

Previous chapters have established an understanding of the crystallisation nature, morphology and kinetics of CF/PEKK composites. The results obtained were used to manufacture a series of CF/PEKK laminates via compression-moulding, in an effort to observe whether different crystallisation morphologies develop in a similar way in larger-scale settings; as well as whether the mechanical performance differs in any way. Further to this, a series of laminates were manufactured via the faster ATP process, to evaluate its effectiveness in producing laminates with a comparable performance to the compression-moulded laminates.

While the main focus of this thesis is the crystallisation nature of the polymer, it would be misleading to discuss the macromechanical performance of these laminates with regards to solely crystallinity. Therefore, the current chapter evaluates the effect of the different processing conditions on the crystallinity development, as well as the consolidation quality of the laminates and their mechanical performance.

6.1. Materials and methods

6.1.1. Materials and manufacturing

CF/PEKK prepreg tape, provided by Hexcel Composites Ltd., was used to manufacture UD and cross-ply compression-moulded and ATP laminates. The details of the laminates tested in this chapter are given in Table 6.1, with further manufacturing details provided in Chapter 5.

Table 6.1: Summary of processing parameters for the compression-moulded and ATP-manufactured laminates.

Laminate code (Compression-moulded laminates)	Hold melt temperature (°C)	Isothermal hold temperature (°C)
I-220-370	370	220
I-260-370	370	260
I-300-370	370	300
I-300-380	380	300
C-5-370	370	5°C/min (cooling rate)

Laminate code (ATP laminates)	Tool material	Nip temp (°C)	Lay-down speed (m/min)	Roller pressure (bar)
ATP-360-4-2	Ceramic (unheated)	360	4	2
ATP-370-4-2	Mild steel (unheated)	370	4	2
ATP-380-4-2	Mild steel (unheated)	380	4	2
ATP-390-4-2	Mild steel (unheated)	390	4	2
ATP-380-2-2	Mild steel (unheated)	380	2	2
ATP-380-4-4	Mild steel (unheated)	380	4	4

6.1.2. Ultrasonic non-destructive testing (UT)

Ultrasonic testing was performed by Hexcel Composites Ltd. on the manufactured UD laminates to assess the consolidation quality of these. The testing was conducted using a Tomoscan Focus LT by Olympus Scientific (now called Evident). The ultrasound transducer used was an Olympus 5MHz 128 element phased-array immersion probe. The inspection and analysis software used was Olympus Tomoview. Testing was performed with the laminates mounted and immersed in water using 5MHz ultrasound and a 0.6 mm pitch. 5 mm-thick Perspex block was used for reference across all testing, with an initial gain set at 16 dB across all laminates in order to make them comparable. In some instances, which will be described in Section 6.2.1, the gain was increased when required.

6.1.3. Microscopy

Void content was calculated using optical microscopy images taken with a Leica DM6000 M microscope after casting, grinding and polishing the UD laminate samples. These images were then analysed with ImageJ software. Void content was taken from images that encompassed the entire thickness of a laminate cross-section ignoring defects close to the laminate surfaces (6 images per laminate). The total evaluated area per laminate was approximately 1250 µm x 1400 µm.

Microscopy of cross-ply laminates was not performed as they follow the same processing parameters as reported for UD laminates ATP-360-4-2 and compression-moulded laminates I-220-370 and I-300-370.

6.1.4. Differential scanning calorimetry (DSC)

Crystallinity measurements were obtained by cutting three samples from randomly selected locations of each UD laminate. Scans at dynamic heating rates of 20°C/min from room temperature to 370°C were carried out using a Mettler Toledo DSC 3+, with aluminium pans non-hermetically sealed with aluminium lids. Sample masses of 10-20mg were used. All experiments were performed under a nitrogen environment to avoid any sample degradation. Indium was used to calibrate the temperature and heat of fusion prior to any experiments.

As per Equation 4.1 in Chapter 4, the crystallinity of a sample was estimated with:

$$\chi = \frac{\Delta H_m - \Delta H_{cc}}{\alpha \times \Delta H_{100\%}} \tag{2.1}$$

where ΔH_m is the melting enthalpy, ΔH_{cc} is the cold crystallisation enthalpy, α is the weight fraction of matrix content (31.7% for the compression moulding tape and 34.5% for the ATP tape) and $\Delta H_{100\%}$ is the theoretical melting enthalpy of 100% crystalline PEKK. This has been calculated to be 130J/g by Chang and Hsiao [15]. Enthalpies were calculated using StarE Evaluation Software, compatible with the exported files from the DSC software.

DSC of cross-ply laminates was not performed as they follow the same processing parameters as reported for UD laminates ATP-360-4-2 and compression-moulded laminates I-220-370 and I-300-370.

6.1.5. Chemical etching

Chemical etching was performed on laminates I-220-370, I-260-370 and I-300-370 to observe the impact of isothermal temperature on the matrix morphology. Cross-section samples of the laminates were cast and polished. These were then etched following the steps below, based on the etching methods reported in literature for CF/PEEK [1,2]:

1. Immerse in a stirred solution of 1% potassium permanganate in a 5:2:2 solution of sulphuric acid, orthophosphoric acid and distilled water.
2. Carefully wash in a 7:2 solution of sulphuric acid and distilled water.
3. Wash in 30% hydrogen peroxide solution.
4. Wash in distilled water.

This procedure was performed twice on the same samples. The first time, steps 1 and 2 were carried out for 7 and 3 minutes respectively; the second time they were carried out for 10 and 5 minutes respectively.

6.1.6. Mechanical testing

6.1.6.1. Flexural testing

0° and 90° flexural testing were performed on the UD laminates in accordance with ASTM D7264, using a span-to-thickness ratio of 32:1 and a specimen length about 20% longer than the support span. This resulted in coupon dimensions of 80 mm x 13 mm, and a span of 64 mm. Eight coupons were tested per laminate in each orientation. A crosshead speed of 3 mm/min was used until failure on an Instron 3369 testing system with a 10 kN load cell.

6.1.6.2. Interlaminar shear strength (ILSS)

Interlaminar shear performance was assessed on the UD laminates in accordance with ASTM D2344, using a span-to-thickness ratio of 4:1, a length-to-thickness ratio of 6:1 and a width to thickness ratio of 2:1. Eight coupons were tested per laminate. Coupon dimensions were therefore 12 mm x 4 mm, with a span of 8 mm. Testing was performed at 1 mm/min on an Instron 3369 testing system with a 10 kN load cell.

6.1.6.3. In-plane shear (±45° tensile testing)

In-plane shear response was evaluated by tensile testing of the cross-ply laminates, in accordance with ASTM D3518. Coupon dimensions were 200 mm x 25 mm, and testing was performed at 2 mm/min on an Instron 3369 testing system with a 50 kN load cell. Digital image correlation was used to measure longitudinal and transverse strain using a video gauge extensometer to track speckles drawn on the coupon surfaces.

6.1.6.4. Error analysis

Error analysis, estimating the potential scatter range in mechanical properties as a consequence of measurement uncertainty, was performed for all mechanical testing. Sources of error included measurements of load, displacement and coupon dimensions. Details on the calculation of these can be found in Appendix F.

6.1.7. Scanning electron microscopy (SEM)

SEM was performed on post-mortem flexural, ILSS and IPS coupons in order to qualitatively assess failure behaviour. Flexural and IPS coupons were cut down to a size that allowed for SEM observation of the fracture area, taking care to not affect the region of interest. ILSS coupons were cast exposing the edges of the samples and polished. SEM was also performed on the aforementioned etched samples, in order to observe differences in the crystalline structures. Samples were prepared with a 15nm sputter coating of gold to enhance surface conductivity and imaged with a JEOL JSM-IT100 instrument at 15kV.

6.2. Results and discussion

The manufactured laminates were examined for their consolidation quality and crystalline morphology, and were tested for flexural (longitudinal and transverse), interlaminar shear strength and in-plane shear properties. The following sections discuss the results of these tests.

6.2.1. Laminate consolidation

Figure 6.1 shows c-scans obtained from ultrasonic testing on compression-moulded and ATP UD laminates as obtained from the scans. As shown in the colour guide in the figure, red/orange/yellow colours indicate a better ultrasound penetration through the laminate, with green/blue/white showing a worse penetration. A better ultrasound penetration generally indicates a higher consolidation quality. An example of a high-penetration ultrasound scan obtained with a CF/PEKK autoclaved laminate manufactured by Hexcel is given in Appendix E.

All compression-moulded laminates show a similar colour range, with I-300-370 and C-5-370 seemingly displaying a better sound penetration. Upon visual inspection of the laminates, it was observed that some of the regions with poorer results were in fact a consequence of surface defects, likely generated during manufacturing; whereas the regions which achieved the highest sound penetration displayed a darker finish post-manufacturing. Examples of these are highlighted in Figure 6.1.

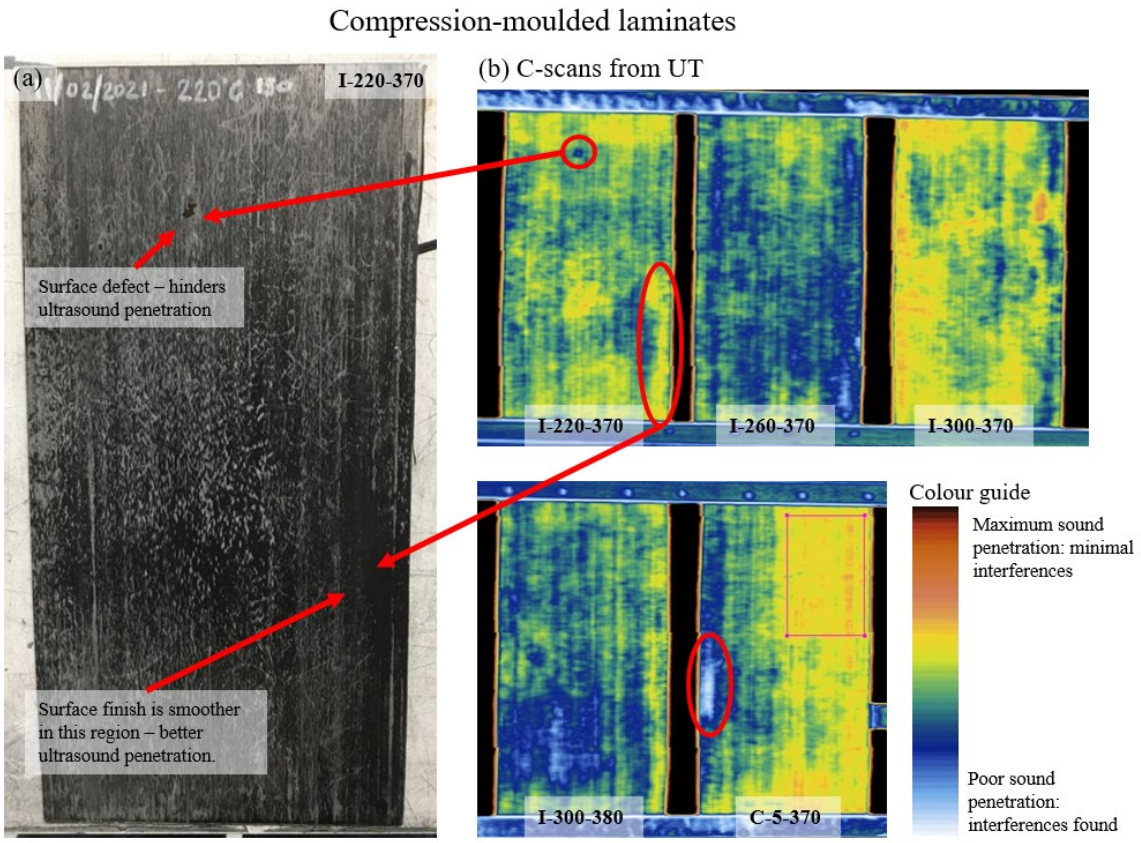

Figure 6.1: UD compression-moulded laminates c-scans from ultrasonic testing and image of example laminate (I-220-370) highlighting high- and low-ultrasound penetration regions.

Figure 6.2a shows c-scans from ultrasonic testing of the ATP laminates, performed at the same settings as the compression-moulded laminates. There is a considerable difference in colour between the two sets, indicating that there is comparatively poor ultrasound penetration in the ATP laminates. This may be due to poorer consolidation as a consequence of the manufacturing process, which is explored further in this section. In order to better compare sound penetration ability across the ATP laminates, the gain of the acquired signal was increased by 16.6 dB. The resulting c-scans are shown in Figure 6.2b. This showed the highest sound penetration in ATP-380-4-4, which could be expected to be the laminate that achieved the best consolidation out of all the ATP laminates, due to it being processed at the highest pressure. ATP-380-2-2 also demonstrated some better sound penetration regions than the remaining laminates, potentially due to the slower lay-down speed achieving a better consolidation than faster lay-downs. ATP-370-4-2 showed the poorest sound penetration, with ATP-360-4-2 doing better despite the lower nip temperature. This may be due to the tool material of ATP-360-4-2 being ceramic, retaining heat better than the mild steel tool used for the rest of the laminates, and potentially causing a better consolidation than ATP-370-4-2.

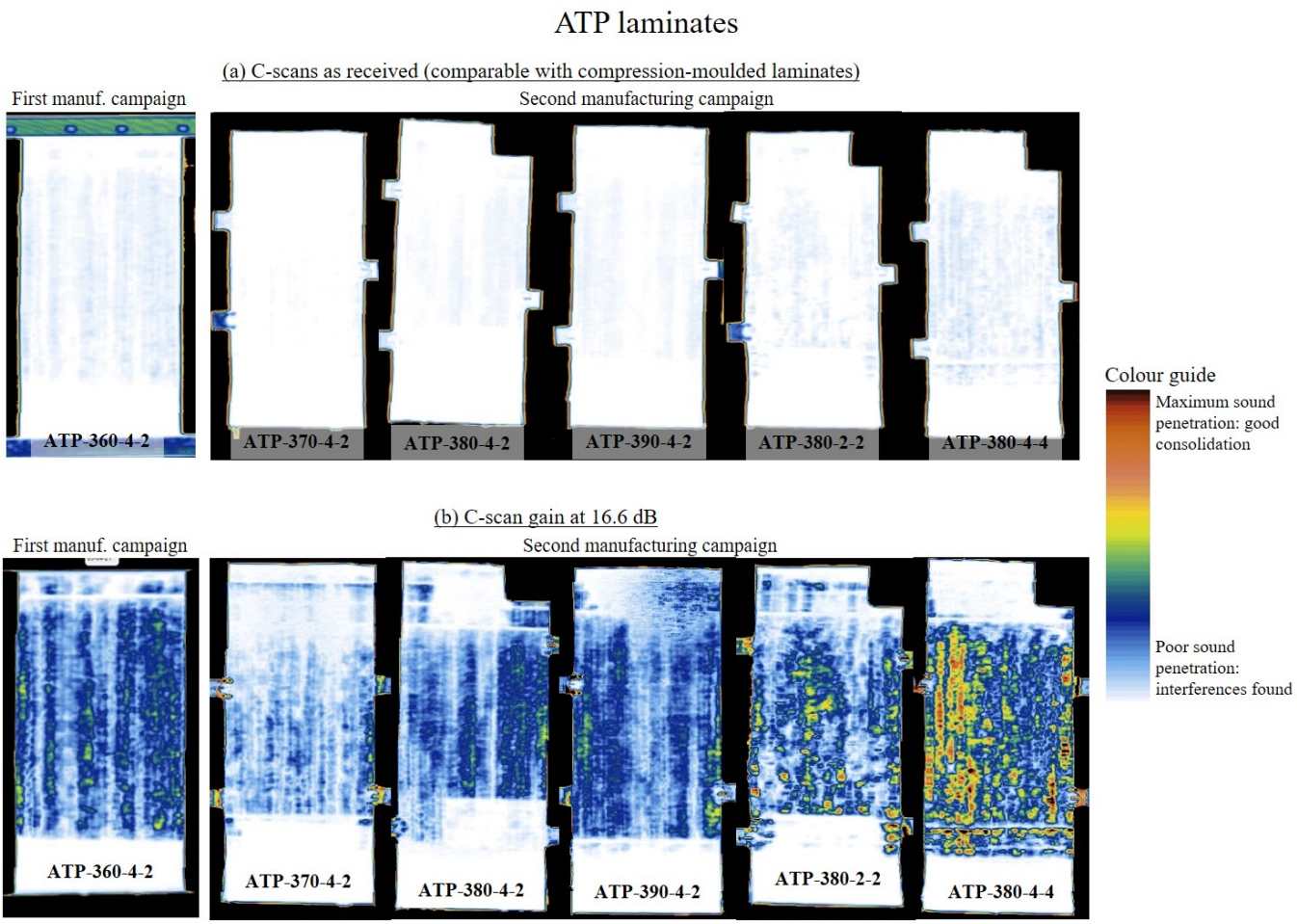

Figure 6.2: UD ATP laminates c-scans from ultrasonic testing (a) as received (16dB), and (b) after the gain was increased by 16.6 dB.

Figure 6.3 shows sample microscopy images of mounted and polished compression-moulded and ATP samples, where fibre, matrix and any voids present can be observed. Table 6.2 shows the average thickness and % void content for each laminate taken from Figure 6.3.

Table 6.2: Laminate thickness and void content of compression-moulded and ATP laminates, taken from microscopy images in Figure 6.3.

	Laminate	Laminate thickness (mm)	Void content (%)
Compression-moulded	I-220-370	1.92 ± 0.00	0.4 ± 0.2
	I-260-370	1.89 ± 0.01	0.1 ± 0.1
	I-300-370	1.93 ± 0.00	0.1 ± 0.1
	I-300-380	1.92 ± 0.01	0.2 ± 0.0
	C-5-370	1.91 ± 0.01	0.4 ± 0.1
ATP	ATP-360-4-2	2.11 ± 0.02	3.9 ± 2.2
	ATP-370-4-2	2.20 ± 0.03	7.9 ± 2.7
	ATP-380-4-2	2.13 ± 0.01	8.0 ± 1.1
	ATP-390-4-2	2.11 ± 0.03	3.7 ± 0.5
	ATP-380-2-2	1.95 ± 0.02	6.0 ± 0.5
	ATP-380-4-4	2.24 ± 0.02	5.7 ± 1.8

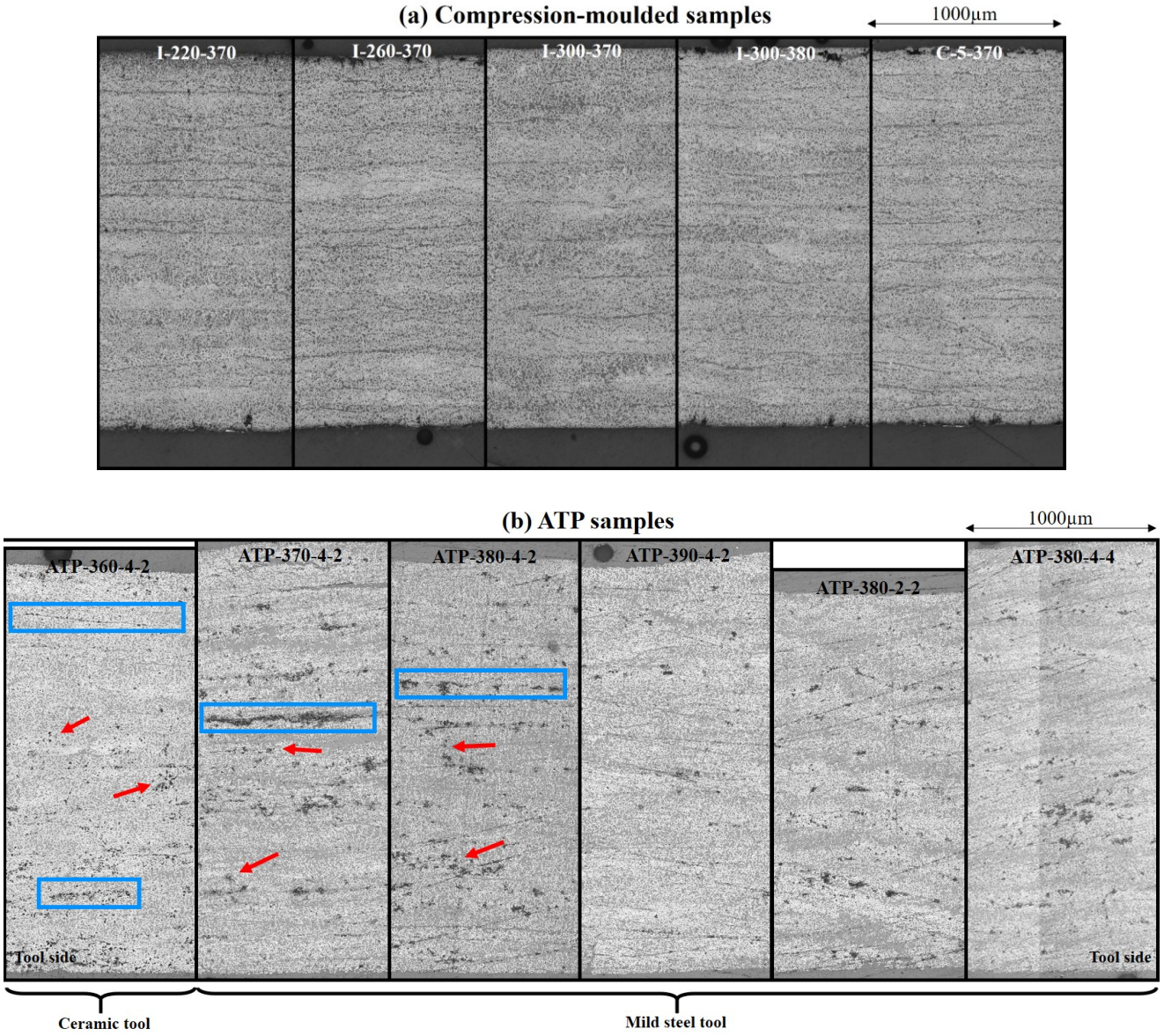

Figure 6.3: Microscopy images of the cross sections of (a) compression-moulded laminates and (b) ATP-manufactured laminates with annotations highlighting examples of interply voids (blue squares) and intraply voids (red arrows).

Overall, no significant variability was observed in the thickness or void content across the compression-moulded laminates. Although the thermal history of each laminate is different, these were held in the melt and at the isothermal temperatures for long times (60 minutes) under high pressure (28 bar), and therefore a low void content was expected. This processing, along with the frame used, limited the laminate thickness of the compression-moulded laminates to the thickness of the frame, explaining the low variability in thickness across the different laminates. The different prepreg layers are still distinguishable in the micrographs of all the laminates (Figure 6.3a).

On the other hand, the ATP laminates showed a significantly higher void content. This is a consequence of the much shorter exposure time to high temperatures and pressures which limit flow of the matrix into voids and the extent of interply contact, evident in the interply voids highlighted with blue squares in Figure 6.3b. Intraply voids (highlighted with red arrows) are also present, which could be attributed to the inadequate penetration of the matrix into the fibres in the prepreg tape. The pressure during compression

moulding is high enough to minimise these, but not during the ATP lay-down process. Other authors have made similar observations when comparing CF/PEEK ATP-manufactured laminates with autoclaved laminates. For example, in Comer et al.'s work [3], void content was measured at 2.83% and 0.08% in ATP and autoclaved laminates respectively. They also cited other works on ATP-manufactured CF/PEEK laminates [4–6] where void content varied from 1.65-7%, in line with the observations in this study. Qureshi et al. [7] also drew qualitative comparisons between microscopy images of autoclaved and ATP CF/PEEK laminates where the higher void content in the ATP-manufactured laminates was evident.

The effect of the lower pressure applied for shorter times also became obvious when comparing the ATP laminate thicknesses with that of the compression moulded laminates: with the same number of plies, thicknesses were 1.89-1.93 mm for the compression-moulded laminates and 1.95-2.24 mm for the ATP laminates.

Some differences, albeit less significant, can also be observed across the different ATP laminates manufactured on a mild steel tool. A slower lay-down speed resulted in a thinner laminate, less defined interply boundaries and a lower void content, visible when comparing laminates ATP-380-4-2 and ATP-380-2-2. Roller pressure may have also impacted the presence of voids: interply voids appear more localised in ATP-380-4-4, whereas in ATP-380-4-2 they seem more elongated and distributed along interply boundaries.

Higher nip temperatures clearly caused a decrease in void content, particularly noticeable in Figure 6.3b when comparing ATP-370-4-2 and ATP-390-4-2. A higher temperature likely resulted in the polymer being held at a lower viscous state for longer, resulting in better interply adhesion. Consequently, the thickness also decreased with a higher nip temperature, but this is less significant.

Comparing the ceramic tool laminate ATP-360-4-2 against the mild steel laminate ATP-370-4-2, it is clear that even processing with a lower nip temperature, a lower laminate thickness and void content are obtained. The cross-section images for these laminates in Figure 6.3 display a better consolidation for the ceramic tool laminate, the overall quality of which seems comparable to ATP-390-4-2 on a steel tool based on the above evaluations. A metallic tool will have a higher thermal conductivity than ceramic, drawing heat away from the laminate faster and requiring higher processing temperatures to obtain a similar consolidation quality to that obtained with a ceramic tool at lower nip temperatures.

6.2.2. Crystallinity and spherulitic morphology

Table 6.3 shows the average glass transition temperatures, enthalpies and total crystallinities achieved in the manufactured UD laminates, with Figure 6.4 showing heat flow variation against temperature in DSC for one sample of each laminate. All the compression-moulded laminates crystallised to the maximum extent (~29%), whereas the ATP-manufactured laminates only achieved 6-9.9% crystallinity and contained a significant amorphous fraction. This amorphous content is denoted by the cold crystallisation peak and the much more prominent glass transition in the ATP sample curves in Figure 6.4.

Table 6.3: Average values for glass transition temperatures, enthalpies and total crystallinity of CF/PEKK laminates manufactured under different processing conditions.

	Laminate	T_g (°C)	T_{LTE} (°C)	ΔH_{LTE} (J/g)	T_{HTE} (°C)	ΔH_{HTE} (J/g)	LTE:HTE	X (%)
Compression-moulded	I-220-370	155.5 ± 1.4	231.6 ± 0.5	0.27 ± 0.01	341.3 ± 0.6	11.8 ± 0.6	2:98 ± 0	29.3 ± 1.4
	I-260-370	157.0 ± 3.2	271.0 ± 0.7	0.38 ± 0.03	340.8 ± 0.6	10.7 ± 0.4	3:97 ± 0	27.0 ± 1.0
	I-300-370	156.6 ± 205	309.9 ± 0.2	2.9 ± 0.2	341.4 ± 0.8	9.1 ± 0.5	24:76 ± 1	29.1 ± 1.3
	I-300-380	160.2 ± 0.4	306.6 ± 0.1	2.9 ± 0.2	340.9 ± 0.7	10.0 ± 0.4	22:78 ± 1	31.2 ± 0.4
	C-5-370	151.9 ± 0.8	-	-	341.7 ± 1.1	11.7 ± 0.2	-	28.5 ± 0.4

		T_g (°C)	T_{cc} (°C)	ΔH_{cc} (J/g)	T_m (°C)	ΔH_m (J/g)	-	X (%)
ATP	ATP-360-4-2*	160.8 ± 0.7	212.5 ± 0.3	9.1 ± 0.1	337.2 ± 1.1	13.2 ± 0.3	-	9.9 ± 0.3
	ATP-370-4-2	162.6 ± 1.0	220.5 ± 0.3	9.0 ± 0.5	337.8 ± 1.3	11.7 ± 0.7	-	6.0 ± 0.5
	ATP-380-4-2	165.3 ± 4.1	220.2 ± 3.8	9.1 ± 0.3	339.2 ± 2.7	12.5 ± 0.5	-	6.8 ± 1.3
	ATP-390-4-2	164.7 ± 0.4	223.5 ± 2.6	9.0 ± 1.0	339.2 ± 0.4	11.8 ± 1.0	-	6.1 ± 0.5
	ATP-380-2-2	162.6 ± 0.3	217.8 ± 0.4	8.6 ± 0.2	338.2 ± 0.6	12.5 ± 0.9	-	8.3 ± 1.0
	ATP-380-4-4	163.8 ± 2.1	220.5 ± 1.3	9.0 ± 0.1	338.4 ± 1.7	11.7 ± 0.7	-	6.0 ± 1.6

T_g = glass transition temperature
T_{LTE} = low endotherm temperature
ΔH_{LTE} = low endotherm enthalpy
T_{HTE} = high endotherm temperature
ΔH_{HTE} = high endotherm enthalpy
LTE:HTE = low endotherm to high endotherm ratio
X = total crystallinity
T_{cc} = cold crystallisation temperature
ΔH_{cc} = cold crystallisation enthalpy
T_m = melting temperature
ΔH_m = melting enthalpy
* = Ceramic tool used. The rest of ATP laminates used a mild steel tool.

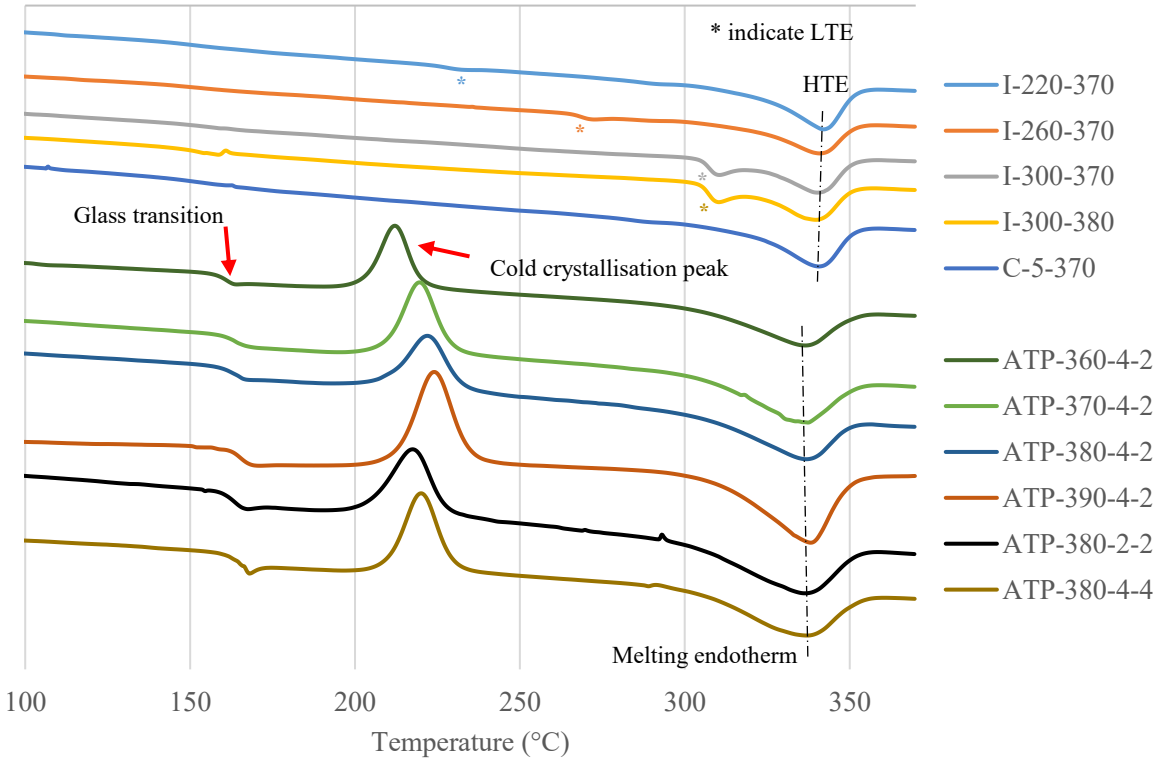

Figure 6.4: Sample DSC heat scans of CF/PEKK laminates manufactured under different processing conditions.

The melting behaviour of the isothermally compression-moulded laminates in DSC denote a dual crystallisation mechanism previously observed for both PEEK and PEKK systems [2,8–14]. The LTEs (marked * in Figure 6.4) are observed to shift, depending on the isothermal temperature (T_{iso}) the material underwent, always remaining approximately 10°C above T_{iso}. The proportion of LTE:HTE also increased

with T_{iso}, as observed in Chapter 4. The proportion of HTE is higher in the current study, which may be a consequence of the slower cooling rate the material undergoes to reach T_{iso} (10°C/min instead of 150°C/min used in DSC), as well as the sample size: the laminates consist of 10 layers of prepreg tape across which heat flow may be slower than the small prepreg sample used in the previous DSC studies. During non-isothermal processing (as per laminate C-5-370), PEKK does not display this dual melting behaviour, but rather a single melting peak (corresponding to the HTE in the isothermal laminates).

In the case of laminates I-300-370 and I-300-380, where the holding temperatures in the melt were 370°C and 380°C respectively and isothermal hold temperature was 300°C, both endotherms in Figure 6.4 (LTE and HTE) began to overlap, as observed in previous studies [8,11]. In this case, the area corresponding to each endotherm was calculated as done in Section 4.2.3.1. There is no significant difference observed as a consequence of the different holding temperatures in the melt.

The ATP-manufactured laminates, on the other hand, achieved a lower crystallinity than what the prepreg tape originally contained, and did not show any form of dual melting behaviour in the DSC heat scan. This may be attributed to the slower crystallisation kinetics of PEKK compared to PEEK and the short time that the matrix is exposed to temperatures at which it can undergo crystallisation. The polymer may therefore develop a limited amount of primary crystallisation and no secondary crystallisation phase due to its slower forming nature. This is further evidenced by the cold crystallisation peak that takes place during heating (Figure 6.4), showing that the matrix did not fully crystallise during processing. Laminate ATP-380-2-2, with a slower lay-down speed of 2 m/min, achieved a slightly higher crystallisation than the remaining ATP laminates manufactured on a mild steel tool, likely due to this lower speed resulting in longer exposure times of the material to temperatures within crystallisation range (between glass transition temperature and melting temperature). Nip temperature and roller pressure did not seem to have an effect on the crystallinity extent. Using a ceramic tool, however, did result in the highest developed crystallinity despite using the lowest nip temperature when compared to the mild steel tool ATP laminates. The better heat retention of the ceramic likely allowed PEKK to sit within crystallisation-range temperatures, resulting in a more developed crystalline structure, albeit lower than that achieved by the compression-moulded laminates.

Figure 6.5a, b and c show etched samples from laminates I-220-370, I-260-370 and I-300-370 respectively. These samples were selected to observe the effect of different isothermal holding temperatures on the developed matrix morphology. Figure 6.5d shows a partially etched sample, where the top layer of the matrix has not been fully etched. Here the fibrillar networks in the matrix can be observed to be the last to remain from the top matrix layer as the etchant exposes the lower layer of the matrix. These networks are likely to be remnants of the primary crystal structure of the matrix, with amorphous material being etched first, followed by secondary crystals, and finally the primary crystalline structures.

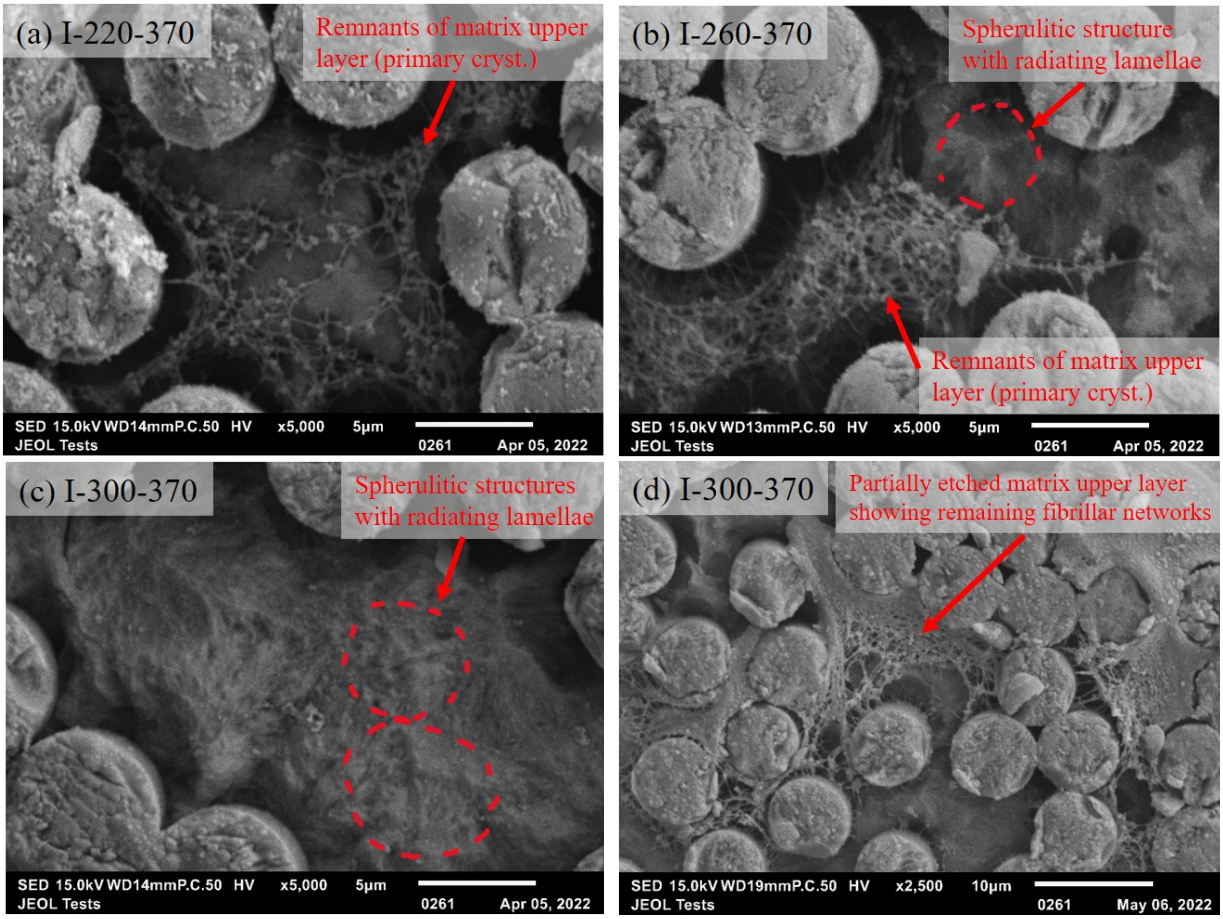

Figure 6.5: SEM micrographs of etched CF/PEKK samples from different compression-moulded laminates: (a) Laminate I-220-270 (b) Laminate I-260-370 and (c) Laminate I-300-370 (d) example of partially etched sample showing remaining fibrillar networks in the matrix as a consequence of partial etching.

Across all images in Figure 6.5 it is obvious that the fibre-matrix interface region was more severely impacted by the etching than the bulk matrix. This suggests a fibre-matrix interface with a lower chemical resistance than the matrix bulk. This could be due to the presence of a transcrystalline region with lower chemical resistance.

In the bulk matrix of the samples in Figure 6.5b and Figure 6.5c, the preferential etching of the amorphous regions revealed radiating patterns typical of spherulitic crystallisation. The spherulite size is larger in Figure 6.5c where the sample was held at the higher isotherm (300°C), a consequence of the lower nucleation density at higher isothermal temperatures. The spherulite sizes are therefore expected to be the smallest in Figure 6.5a with the highest nucleation density out of the three samples. These are not particularly obvious potentially due to spherulites being very small, as well as the network-like structure present over the etched surface in Figure 6.5a. While these network structures were present in all samples, these were observed the most in the etched sample of laminate I-220-370 and I-260-370, and the least in the laminate I-300-370. From the DSC results shown in Figure 6.4 and Table 6.3, there is a larger proportion of material that melts under the HTE in samples undergoing lower T_{iso}, and therefore a larger proportion of the more stable primary crystalline structure. It is therefore logical that there is more of this residual primary structure present in Figure 6.5a, and the least in Figure 6.5c.

6.2.3. Mechanical performance of unidirectional laminates

The results of the mechanical testing of the manufactured unidirectional laminates are discussed in this section. Overall, there was no significant difference in the performance of the different compression-moulded laminates, except for a marginally improved performance of laminate I-300-380 in flexural 90° testing. On the other hand, lower properties were observed in the ATP-manufactured laminates across all tests, with the laminate manufactured on the ceramic tool performing the best despite having the lowest nip temperature. A summary of all mechanical testing results is presented in Table 6.4 and **Error! Reference source not found.**, and will be discussed in detail in the following sub-sections. Mechanical testing data reported in literature for ATP-manufactured CF/PEKK (AS7 fibres as used in this study) laminates is scarce, and therefore available results on CF/PEEK with different fibre types (AS4, IM7) are also included for comparative purposes.

Table 6.4: Mechanical testing results of compression-moulded and ATP CF/PEKK laminates.

	Laminate	**Flexural 0°**		**Flexural 90°**		**ILSS**
		Strength (MPa)	Modulus (GPa)	Strength (MPa)	Modulus (GPa)	SBS Strength (MPa)
Compression -moulded	I-220-370	1824 ± 119	120.1 ± 1.7	75.5 ± 2.0	8.6 ± 0.2	97.9 ± 0.5
	I-260-370	1825 ± 135	120.6 ± 2.6	75.8 ± 3.0	8.6 ± 0.2	97.9 ± 1.8
	I-300-370	1770 ± 107	120.1 ± 1.7	77.6 ± 7.3	8.6 ± 0.2	99.4 ± 3.0
	I-300-380	1772 ± 95	119.2 ± 2.5	93.9 ± 7.0	8.6 ± 0.2	100.1 ± 3.1
	C-5-370	1855 ± 64	121.2 ± 2.0	81.0 ± 3.5	8.7 ± 0.1	93.0 ± 4.6
ATP	ATP-360-4-2	795.0 ± 123.8	100.8 ± 3.1	34.5 ± 2.3	4.5 ± 0.2	29.5 ± 1.7
	ATP-370-4-2	457.8 ± 35.8	88.8 ± 7.4	20.8 ± 4.9	2.2 ± 0.6	22.0 ± 1.6
	ATP-380-4-2	718.8 ± 73.1	95.8 ± 2.8	31.3 ± 2.3	3.4 ± 0.3	24.4 ± 2.0
	ATP-390-4-2	755.7 ± 58.9	91.9 ± 6.1	27.1 ± 4.4	2.6 ± 0.5	29.3 ± 1.7
	ATP-380-2-2	761.0 ± 50.1	87.1 ± 4.8	24.1 ± 2.1	2.9 ± 0.6	27.0 ± 2.4
	ATP-380-4-4	741.7 ± 98.9	86.9 ± 8.7	24.1 ± 1.6	3.1 ± 0.2	26.6 ± 2.0

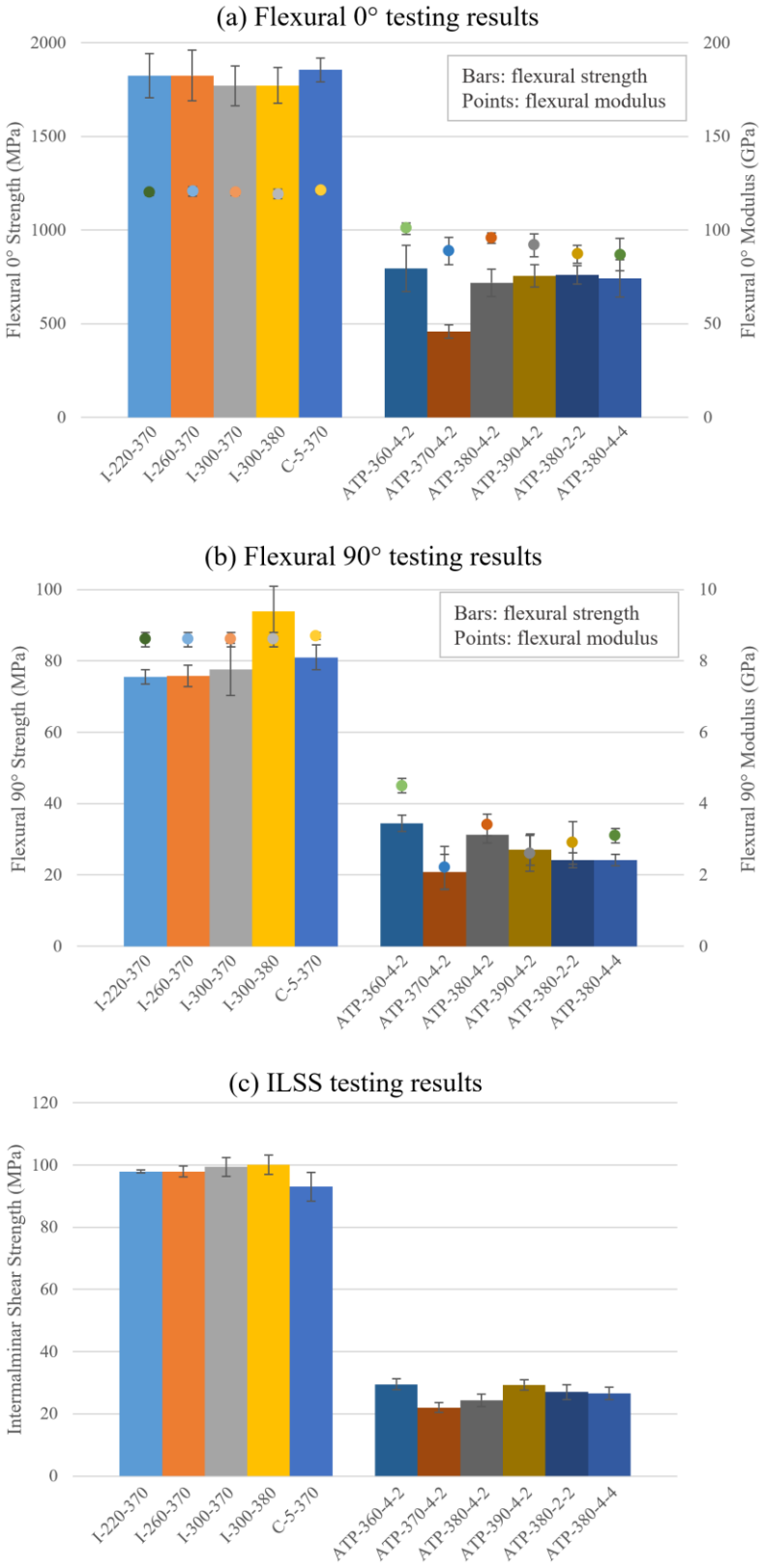

Figure 6.6: Mechanical testing results of compression-moulded and ATP CF/PEKK laminates. Error bars show the data range.

6.2.3.1. *Flexural 0° (longitudinal) testing*

Representative flexural 0° stress-strain curves for each laminate are shown in Figure 6.7. Coupon failure in this testing mode commenced by compression on the top surface of the specimens (where the load was being applied), followed by tension failure on the bottom surface. While flexural 0° testing response is dominated by the fibres, the matrix also plays a role in providing compression strength in particular, and therefore may influence flexural properties to some extent.

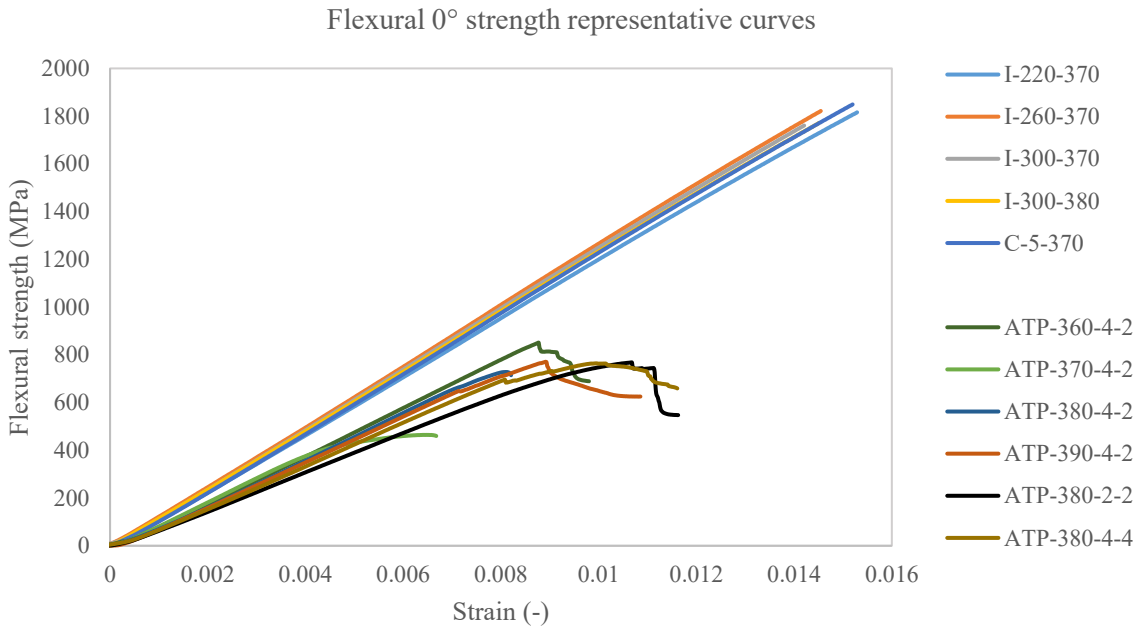

Figure 6.7: Representative stress strain curves for flexural 0° coupons of compression-moulded and ATP laminates.

No significant difference in flexural strength or modulus was observed across the different compression-moulded laminates, implying that differences in the crystal morphology, as a consequence of the differing isothermal holds or holding temperatures in the melt, have not resulted in significant differences in the behaviour of the matrix when loaded under 0° flexure. This was expected, as longitudinal flexural testing is dominated by fibre strength rather than the matrix. The failure of the composites was also abrupt and explosive, with the majority of the samples splitting in two when reaching the maximum load. It is obvious, however, that processing conditions did have an effect on flexural 0° performance to a certain extent, as shown by the lower flexural strength and modulus of the ATP specimens by 61% and 24% respectively on average. The higher void content is likely to lead to lower mechanical properties; as well as the amorphous nature of the matrix in the ATP specimens resulting in a more ductile behaviour (due to a lower elastic modulus). This therefore resulted in sample deformation and failure under lower loads (a lower strength) than the compression-moulded specimens. This more plastic behaviour is also reflected in the fact that, unlike the compression-moulded specimens, the ATP flexural specimens did not experience an explosive fracture nor completely split into two. Instead, a jagged fracture curve was observed in Figure 6.7, indicating that the ATP samples failed in various steps. This is due to the poorer consolidation of the laminates observed in Section 6.2.1, which resulted in different groups of plies failing at different stages. This is visible in the SEM images of the fracture surfaces shown in Figure 6.8 – in the

compression-moulded sample, single compression and tension regions are visible, whereas in the ATP sample these can be seen to alternate, indicating several steps to failure.

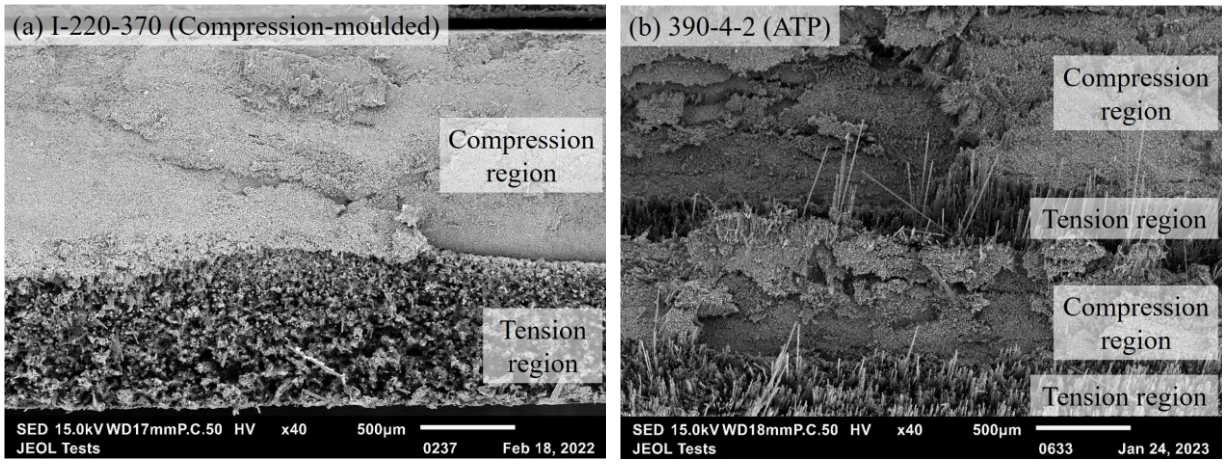

Figure 6.8: SEM images of 0° flexural fracture surfaces of specimens extracted from (a) I-220-370 (compression moulded) and (b) 390-4-2 (ATP-manufactured) laminates at ×40 magnification, with labelled tension and compression failure regions.

Comparing the results in Table 6.4 for the different ATP laminates, it is obvious that higher nip temperatures (380 and 390°C) increase 0° flexural performance, particularly flexural strength, possibly a consequence of achieving a better interlayer adhesion during material lay-down. A slower lay-down speed likely had the same impact, marginally increasing the performance of ATP-380-2-2 compared to ATP-380-4-2. This may have also been influenced by the slightly higher crystallinity content resulting from a slower lay-down speed. ATP-380-4-4, with a higher roller pressure, did not show any significant difference, potentially indicating that at this nip temperature and lay-down speed, increasing roller pressure does not have an impact on laminate consolidation. ATP-360-4-2, manufactured on a ceramic tool, showed the highest performance out of the ATP laminates despite having the lowest nip temperature. This again further reinforces the effect of heat retention by the ceramic material on the consolidation and crystallinity development, resulting in a stronger, stiffer composite. The better performance of the ATP samples with higher nip temperatures and slower lay-down speeds (which exposes the material to higher temperatures for longer times) also highlights the temperature dependence of consolidation and crystallinity. The flexural strength displayed, however, is still significantly lower than that achieved by the compression-moulded laminates.

Higher magnification SEM images of the fracture surfaces of a compression-moulded specimen and an ATP specimen are shown in Figure 6.9. This figure resembles Figure 2.21 in Chapter 2, and Figure 4.15 in Chapter 4, highlighting the effect of processing conditions on the fibre-matrix adhesion. Across all compression-moulded specimens, fibre surfaces were observed to be coated with matrix, with no major differences across the different samples, whereas the ATP specimens showed bare fibres. This suggests that the processing conditions influenced the fibre-matrix interface, with a higher crystallinity resulting in better adhesion of the matrix to the fibre surface.

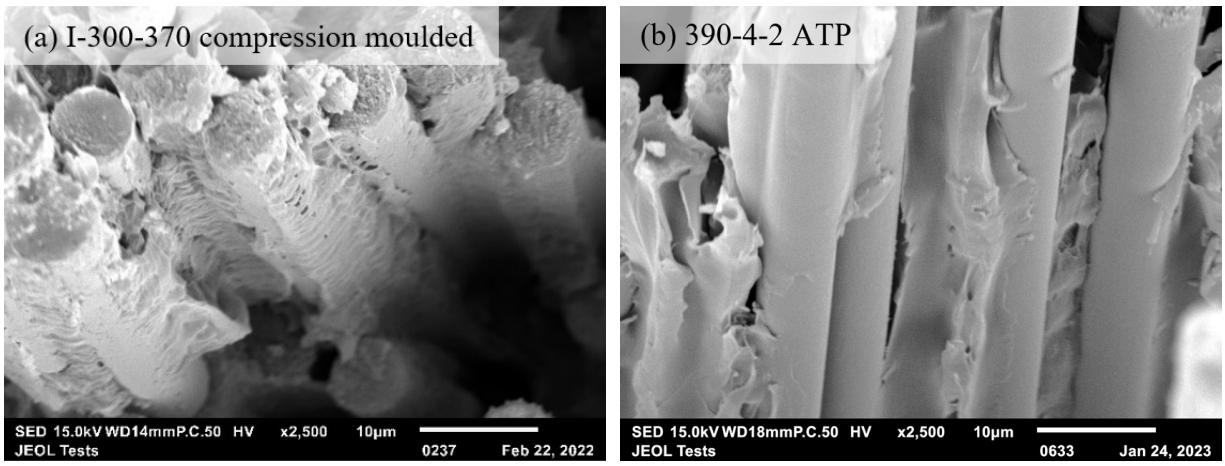

Figure 6.9: SEM images of 0° flexural fracture surfaces of specimens extracted from (a) I-300-370 (compression moulded) and (b) 390-4-2 (ATP).

A comparison of the above results of CF/PEKK with results from the literature on CF/PEEK is given in Table 6.5. The compression-moulded CF/PEKK samples performed comparably to autoclaved CF/PEEK samples, whereas the ATP laminates tested in this work underperformed in comparison to reported ATP CF/PEEK values. This may be a consequence of the ATP process parameters selected in the current study limiting interply consolidation and resulting in a higher void content, as discussed in Section 6.2.1.

Table 6.5: Flexural 0° strength results in this work and in literature.

Material [Ref]	**Autoclave**	**Laser ATP**					
	Flexural 0° Strength (MPa)	Nip temp. (°C)	Tool temp. (°C)	Tool material	Lay-down speed (m/min)	Roller pressure (bar)	Flexural 0° Strength (MPa)
AS4/PEEK [15]	1650	420	Unheated	Stainless steel	9	3.8	1143
AS4/PPS/PEEK [15]	1650	400	Unheated	Stainless steel	9	3.8	1035
This work, AS7/PEKK	1770-1855 (comp. moulding)	360	Unheated	Ceramic	4	2	795.0
		370	Unheated	Mild steel	4	2	457.8
		380	Unheated	Mild steel	4	2	718.8
		390	Unheated	Mild steel	4	2	755.7
		380	Unheated	Mild steel	2	2	761.0
		380	Unheated	Mild steel	4	4	741.7

6.2.3.2. Flexural 90° (transverse) testing

Representative flexural 90° stress-strain curves for each laminate are shown in Figure 6.10. In this testing mode, failure was caused purely by tension, which began on the bottom surface of the samples (side under tension). Fibre contribution to strength and stiffness is minimal in this case, and therefore this test can provide a better indication of any variation in matrix properties as a consequence of processing.

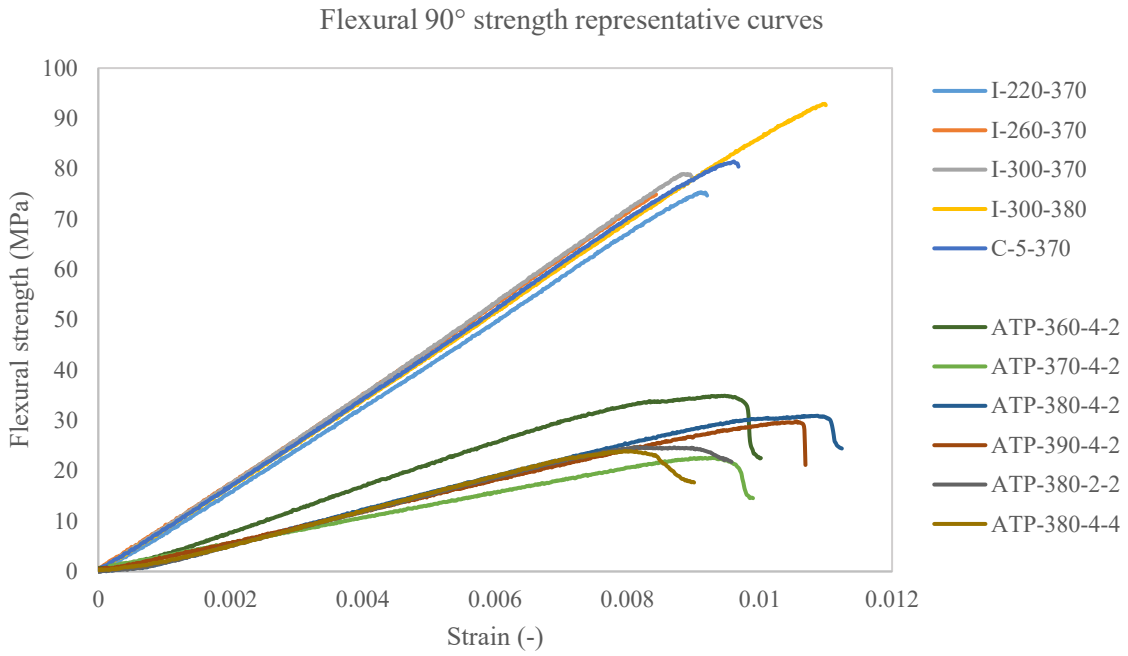

Figure 6.10: Representative stress-strain curves for flexural 90° coupons of compression-moulded and ATP laminates.

There was a significant increase of approximately 23% in the 90° flexural strength of laminate I-300-380 compared to the remaining compression-moulded laminates, which showed no significant difference in performance. This suggests that a different crystalline morphology as a consequence of different isothermal holds (large vs. small spherulites) does not majorly dictate flexural performance when loaded under 90° flexure as long as the material is crystallised to its maximum extent (~29%). The crystallinity of laminate I-300-380 (shown in Table 6.3) was also the highest, which may contribute to the better performance. All compression-moulded samples exhibited an immediate load drop after reaching the peak load.

The ATP specimens showed significantly lower flexural strength and modulus (~67% and 64% lower respectively) compared to the compression-moulded laminates. The more amorphous nature of the matrix resulted in lower material strength and stiffness, as mentioned before. The higher ductility in the material is once again apparent in the representative curves in Figure 6.10, where the load did not immediately drop after failure. ATP-360-4-2, manufactured on the ceramic tool, performed the best out of all ATP laminates, likely due to a better interply consolidation as observed in Section 6.2.1. Out of the ATP laminates manufactured on the mild steel tool, those with higher nip temperatures (380 and 390°C) performed best, indicating that higher processing temperatures contributed towards a better performance. This may be a consequence of the lower void content and an overall better consolidation as observed in the laminate thickness in Section 6.2.1. A slower lay-down speed and a higher roller pressure did not seem to have a significant impact in changing matrix flexural strength in this case.

SEM images of the 90° flexural fracture surfaces of compression-moulded and ATP specimens in Figure 6.11 show coated fibres in the compression-moulded specimen, and clean fibres in the ATP sample. This suggests a weak fibre-matrix interface with an amorphous matrix in the ATP specimen, causing failure at said interface rather than in the matrix bulk.

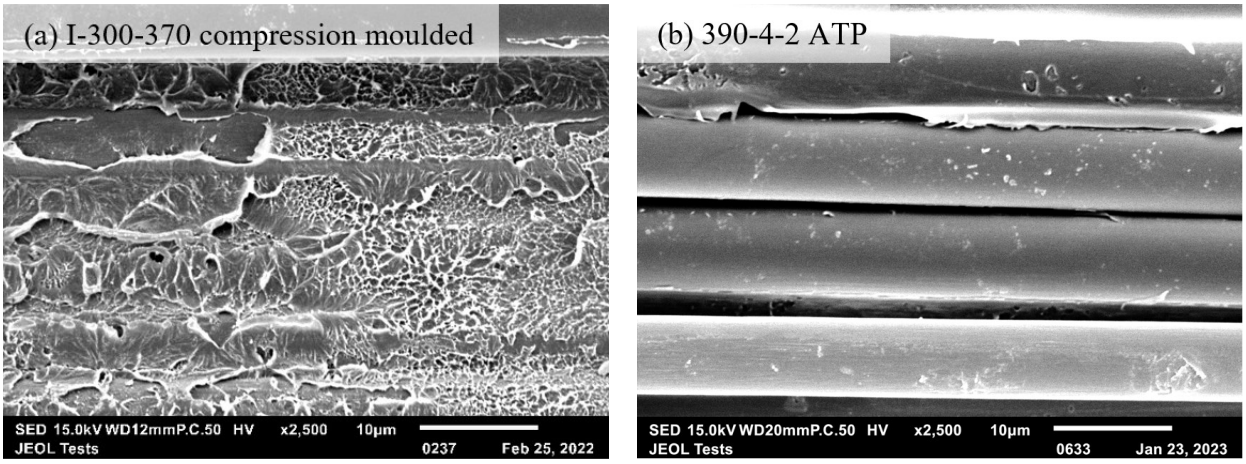

Figure 6.11: SEM images of 90° flexural fracture surfaces of specimens extracted from (a) I-300-370 (compression-moulded) and (b) 390-4-2 (ATP).

Comparing the flexural 90° results to literature, the compression-moulded CF/PEKK laminates in this study (75-94 MPa) performed comparably with CF/PEEK laminates manufactured via autoclave (~90 MPa [16]) and compression moulding (55-130MPa [17,18]). Literature covering flexural 90° testing of ATP-manufactured CF/PEEK or CF/PEKK laminates has not been found.

6.2.3.3. Interlaminar shear strength (ILSS)

Representative stress-displacement curves from the ILSS tests are shown in Figure 6.12. No significant variation in performance was observed across the isothermally compression-moulded laminates, with a marginally lower performance in the ILSS of dynamically cooled laminate C-5-370 (-6%). As this laminate underwent non-isothermal cooling at a rate of 5°C/min, there was a steady decrease in the matrix molecular movement with the drop in temperature as the material cooled down. The laminate was also exposed to temperatures in which interply consolidation could happen above glass transition temperature for a shorter time than the rest of the compression-moulded laminates. This is visible in Figure 5.5, where the temperature in laminate C-5-370 dropped below 160°C (T_g) after 100 minutes, whereas the rest of the compression-moulded laminates dropped below 160°C after approximately 140 minutes. Therefore, it is possible that a slower cooling rate, particularly at the temperature range where a better interply consolidation can be achieved (above T_g), might improve this result. However, if the difference in performance is marginal between laminates undergoing a slower cooling rate or undergoing an isothermal hold at a higher temperature for a definite period of time, then the more energy-efficient cycle should be considered in large-scale manufacturing.

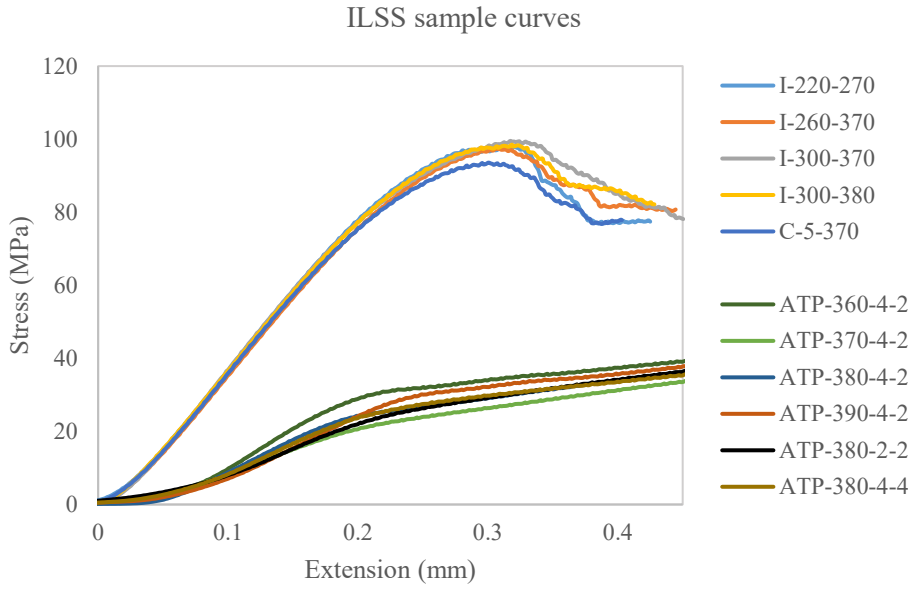

Figure 6.12: Representative ILSS stress-extension curves of compression-moulded and ATP laminates.

The ATP laminate specimens, on the other hand, exhibited 73% lower ILSS compared to the compression-moulded laminates. This is very likely due to the much shorter exposure times to heat and pressure experienced during ATP manufacturing, which resulted in a higher void content and lower interply consolidation than that achieved by compression moulding. It can also be observed in Figure 6.12 that the response of the ATP specimens was unlike the other specimens and not what is commonly seen in an ILSS load-displacement curve (no ILSS peak). Instead, they displayed much more plastic deformation after the initial linear portion of the graph. A similar behaviour was observed in Chanteli et al.'s work [19], where the influence of repass on laser-ATP-manufactured laminates was studied, and no distinct peak was observed in their load-displacement curves. In this case, the authors argued that the non-linear response was a consequence of the viscoelastic behaviour of the matrix. As with the previous testing, the performance of the laminates can be observed to marginally increase with a higher nip temperature, again potentially indicating a better interlayer adhesion; as well as with the use of the ceramic tool even with lower nip temperatures. As per the 0° flexural testing, there was also a marginal increase in ILSS with a slower lay-down speed (ATP-380-2-2) and a higher roller pressure (ATP-380-4-4) when compared to ATP-380-4-2. This is likely due to the better consolidation reflected in the lower void content observed in Section 6.2.1.

The difference in performance between compression-moulded and ATP ILSS coupons becomes obvious in the SEM images shown in Figure 6.13. The compression-moulded laminates showed a kink in the fibres under the location of the loading nose (flexural failure by compression) and/or ply separation (interlaminar shear) (Figure 6.13a). On the other hand, the ATP specimens did not show either of these features, and instead displayed inelastic deformation (Figure 6.13b). The voids visible in Figure 6.13b (iv) have also been observed in untested specimens to a lesser extent (see Figure 6.14). It is possible that the voids already present in the untested samples were exacerbated during ILSS testing, specifically those present between plies (particularly obvious in Figure 6.13b(iv)).

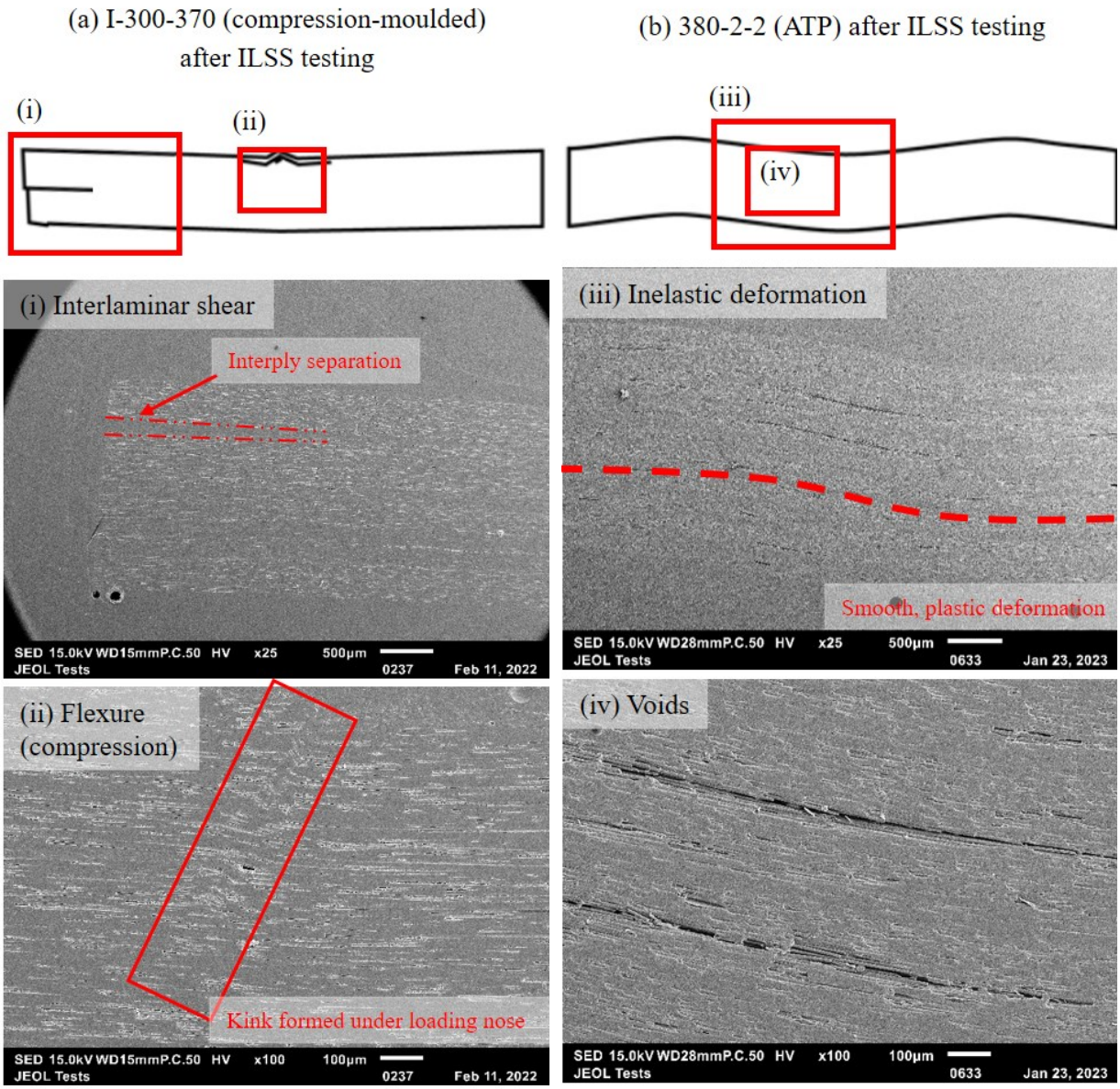

Figure 6.13: Schematics and SEM images of cast ILSS specimens extracted from (a) I-300-370 (compression moulded) and (b) ATP-380-2-2 with sketches highlighting failure modes. Images are of the side of the specimens.

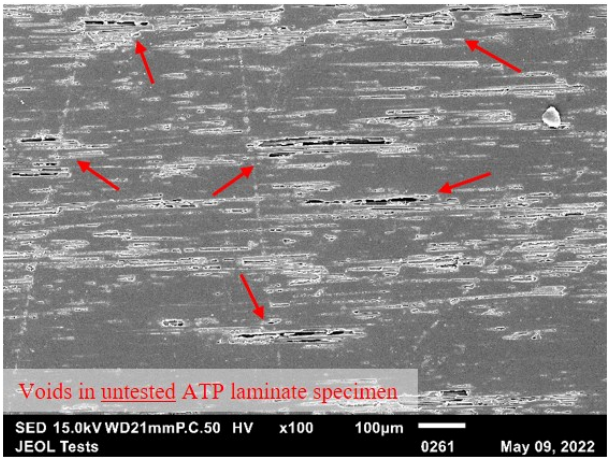

Figure 6.14: SEM image of an untested ATP laminate sample showing intraply voids.

A comparison of ILSS results of CF/PEKK with that of CF/PEEK in literature, as well as a recent study on CF/PEKK, is given in Table 6.6. The compression-moulded laminates in our work performed similarly to the autoclaved CF/PEEK [19,20] and CF/PEKK [21] laminates reported in literature. This was also the case for the ATP laminates when compared to published work with similar nip temperatures and an unheated tool (materials 3 and 4 in Table 6.6), showing a significant drop of 57% for CF/PEEK [19] and 77% for CF/PEKK [21] when compared to their respective autoclaved results.

However, when using nip temperatures significantly above melting temperature on CF/PEEK (material 1 [22] in Table 6.6), ILSS results comparable to autoclave manufacturing or compression moulding were reached (while noting that at high enough temperatures and lower lay-down speeds, polymer degradation may take place). On the other hand, using similar temperatures for CF/PEEK as the ones used in this study, but with the introduction of a heated tool, as per material 2 [20], again achieved ILSS results close to autoclave manufacturing.

Table 6.6: ILSS results in this work and in literature.

Material	**Autoclave**	**Laser ATP**					
	ILSS (MPa)	Nip temp (°C)	Tool temp (°C)	Tool material	Lay-down speed (m/min)	Roller pressure/ load	ILSS (MPa)
1. AS4/PEEK [22]	-	400	Unheated	Aluminium	6	500N	94
		450	Unheated	Aluminium	6	500N	98
		500	Unheated	Aluminium	6	500N	98
		550	Unheated	Aluminium	6	500N	95
		600	Unheated	Aluminium	6	500N	84
		400	Unheated	Aluminium	24	500N	75
		450	Unheated	Aluminium	24	500N	83
		500	Unheated	Aluminium	24	500N	88
		550	Unheated	Aluminium	24	500N	94
		600	Unheated	Aluminium	24	500N	93
2. AS4/PEEK [20]	87	340-370	200	Not specified	1	-	71
		370-400	200	Not specified	1	-	78
		400-430	200	Not specified	1	-	70
3. IMS65/PEEK [19]	105	380	Unheated	Aluminium	3	2.5 bar	42.5
4. AS4D/PEKK [21]	~90	417	Unheated	Not specified	2.4	1000N	~20
		430	Unheated	Not specified	2.4	1000N	~20
		430	Unheated	Not specified	6	1000N	~20
This work, AS7/PEKK	93-101 (compression moulding)	360	Unheated	Ceramic	4	2 bar	29.5
		370	Unheated	Mild steel	4	2 bar	22.0
		380	Unheated	Mild steel	4	2 bar	24.4
		390	Unheated	Mild steel	4	2 bar	29.3
		380	Unheated	Mild steel	2	2 bar	27.0
		380	Unheated	Mild steel	4	4 bar	26.6

6.2.4. Mechanical performance of cross-ply laminates (in-plane shear testing)

The results of the in-plane shear testing of the ATP and post-processed cross-ply laminates are given in Table 6.7, with representative curves shown in Figure 6.15.

Table 6.7: In-plane shear testing of results of ATP CF/PEKK laminates after undergoing different post-processing conditions.

Laminate	Shear stress at 5% shear strain (MPa)
ATP-360-4-2	33.9 ± 0.9
ATP-360-4-2-P220	72.3 ± 3.2
ATP-360-4-2-P300	74.3 ± 4.6

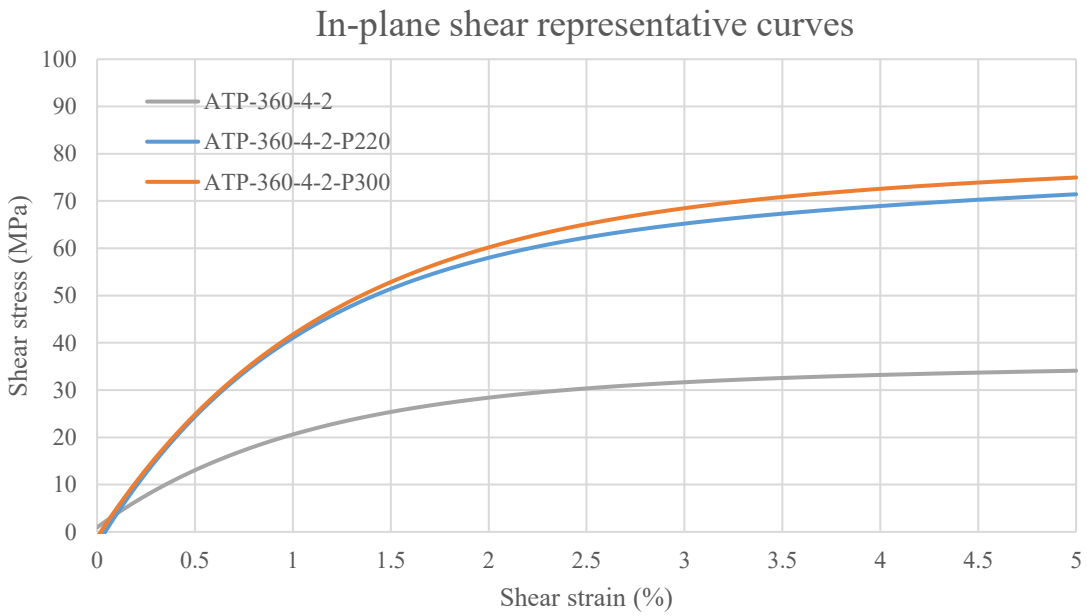

Figure 6.15: Representative stress-strain curves for in-plane shear coupons of ATP laminates after undergoing different post-processing conditions.

The laminates that underwent post-processing via compression moulding displayed similar shear stress behaviour, implying that any differences in the crystal morphology formed due to the different post-processing conditions did not cause a significant difference in shear performance. ATP-360-4-2, however, which did not undergo any post-processing, displayed a shear stress that was 54% lower than that of the post processed laminates at 5% shear strain.

This is likely due to the higher consolidation achieved by the post-processing of ATP-360-4-2-P220 and ATP-360-4-2-P300, achieving a better inter-ply adhesion than the ATP-360-4-2 cross-ply laminate. This is obvious in the post-mortem SEM images in Figure 6.16, where the surface for the unprocessed sample in Figure 6.16b not only shows voids, but resembles the prepreg image shown in Figure 5.2:b(ii). This shows that interply adhesion and matrix flow was poor during ATP manufacturing. On the other hand, matrix remnants from other plies can be observed in Figure 6.16c and Figure 6.16d for the post-processed samples, demonstrating a better interply consolidation.

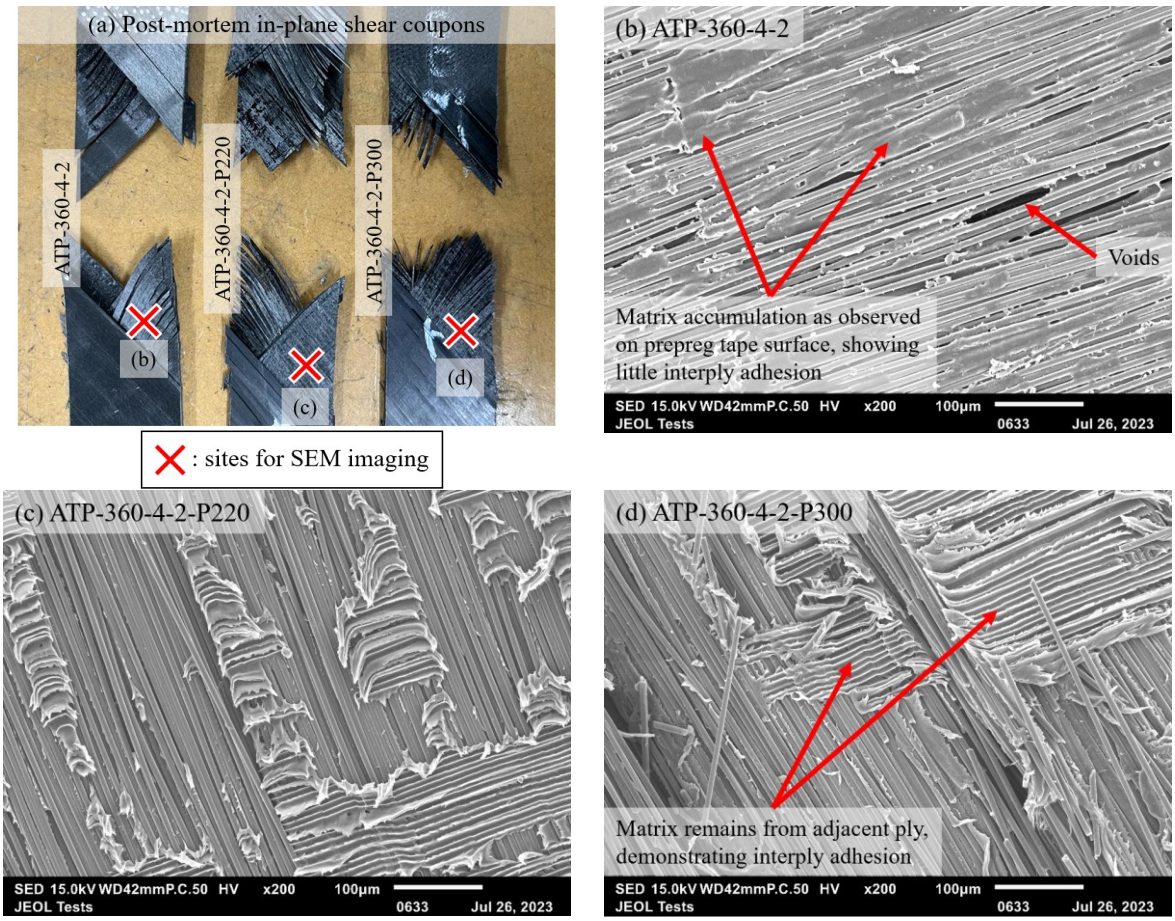

Figure 6.16: SEM images of failure regions of in-plane shear tested coupons extracted from (a) ATP-360-4-2, (b) ATP-360-4-2-P220 and (c) ATP-360-4-2-P300.

Compared to in-plane shear results in literature, the post-processed CF/PEKK laminates in this work (72-74 MPa) performed slightly below autoclaved CF/PEKK (~95 MPa) and CF/PEEK laminates (~78 MPa) [23]. The difference in performance in the case of CF/PEKK could be due to differences in the processing conditions, as well as the use of different fibre (Tenax®-E HTS45 12 K) and matrix (Tenax®-E TPUD PEKK-HTS45) grades to the ones used in this work. Any literature covering in-plane shear testing of ATP-manufactured CF/PEEK of CF/PEKK laminates has not been found.

6.2.5. ATP manufacturing insights

As evidenced in Section 6.2 and previously in Chapter 2, not many reference papers are published on ATP manufacturing and testing of CF/PEKK. The ATP laminates studied in this work displayed inferior performance when compared to the compression-moulded laminates and other ATP-manufactured CF/PEEK laminates reported in literature. PEEK has faster crystallisation kinetics than PEKK [24], which is generally beneficial for achieving higher crystallinities in ATP manufacturing; and PEKK has different grades that may respond differently in fast manufacturing environments such as ATP. This study has developed a basic scientific understanding that can be used in future studies to decide the optimum ATP process parameters for CF/PEKK laminates. Applying optimised process parameters increases the chances of manufacturing high-quality CF/PEKK laminates with ATP. The use of a ceramic tool, which possesses better heat retention, resulted in a slightly better performance despite using the lowest nip temperature. This shows that temperature exposure and heat retention is paramount in order to obtain a better performance from ATP laminates. This was also apparent for CF/PEKK in Hoang et al.'s work [21]

with an unheated tool (of unspecified material), where with slightly higher nip temperatures (417-430°C) than in the current study (370-390°C), ILSS testing resulted in very similar values to the work presented in this article. Exposure to higher temperatures for longer periods will lower polymer viscosity during tape placement, which could result in improved interply bonding and polymer chain reptation [25,26]. This was particularly evident in Stokes-Griffin et al.'s work on CF/PEEK [22] as discussed in Section 6.2.3, where nip temperatures significantly higher than melting temperature (400-600°C, significantly higher than those used in this work) resulted in an ATP laminate ILSS performance comparable to autoclaved counterparts. Introducing a heated tool is likely to help with the material's exposure to higher temperatures, aiding with interply consolidation and crystallisation development while working at lower nip temperatures. This was demonstrated in Esguerra-Arce et al.'s work [24], where using a heated tool at 200°C reduced void content and improved the crystallinity of CF/PEKK. Saenz-Castillo et al.'s work on CF/PEEK [20] also observed similar results, where using similar nip temperatures to this study but with a heated tool at 200°C resulted in an ILSS performance close to autoclaved samples.

However, as discussed in Section 2.4, literature has highlighted the problem of void rebound if the material is held at higher temperatures once roller pressure is removed (the re-emergence of pre-existing voids after these have been compressed during tape lay-down) [3,25,27]. This therefore poses conflicting mechanisms for PEKK, where high temperatures and slow cooling are desirable for adequate crystallinity levels and interply chain reptation, but prolonged exposure to temperatures above T_g with no consolidation pressure may result in void rebound. Further to this, high lay-down speeds have been shown to not offer sufficient compaction time to achieve a good interply bond [27]. This requires an optimisation exercise of material temperature, tool temperature, lay-down speed and roller pressure, to establish optimal parameters regarding exposure to heat and compressive loads, and achieve acceptable levels of crystallinity, interply consolidation and void reduction for the composite material in question. These parameters will be highly dependent on the material type and its inherent crystallisation ability, average molecular weight and molecular weight distribution, and polydispersity index. Lamontia and Gruber [28] suggested a modular lay-down head providing further heating, compaction and cooling steps, however these result in bulkier equipment pieces which may limit the equipment's ability to manufacture geometrically complex shapes, which is an attractive quality of ATP manufacturing.

6.3. Chapter conclusions

In this work, CF/PEKK laminates were processed using different cycles under compression moulding (holding temperatures in the melt of 370 and 380°C, followed by isothermal holds of 220, 260 and 300°C or a cooling rate of 5°C/min) and ATP (metallic and ceramic tools, nip temperatures of 360, 370, 380 and 390°C, lay-down speeds of 2 and 4 m/min, and roller pressures of 2 and 4 bar). Their consolidation quality, crystallinity development in the matrix and flexural and interlaminar performance were evaluated. Overall, it was observed that compression-moulded laminates achieved a very good consolidation and all compression-moulded laminates performed similarly regardless of their processing history, with a marginally higher transverse flexural performance of the laminate manufactured at a higher holding temperature in the melt. The highest extent of crystallinity development was achieved across all the compression-moulded laminates. Differences were observed in their morphology as expected by general polymeric theory, where higher isothermal temperatures result in a lower nucleation density and therefore larger spherulitic entities. Chemical etching to expose these structures also highlighted the potential

presence of a transcrystalline region at the fibre-matrix interface that the chemical etching attacked more aggressively.

Comparing the ATP laminates' performance with the compression-moulded laminates showed overall lower properties and quality. This is expected, due to the differences between the two processing techniques. The more rapid heating and cooling in the ATP manufacturing process resulted in poor consolidation quality, a higher void content, lower crystallinity and a significant reduction in mechanical performance. This is more prominent in slower crystallising PEKK than that in faster crystallising PEEK-based composites. In this study, increasing the exposure to heat of the manufactured laminate via using a tool material with better heat retention or a higher nip temperature had the most noticeable effect on mechanical performance, followed by a slower lay-down speed resulting in a lower void content and marginal increase in both mechanical performance and crystallinity. However, these differences were not significant when compared to the performance of the compression-moulded laminates. Optimising the parameters of ATP manufacturing to better suit the PEKK matrix would likely improve all of the above properties. Specifically, the use of a higher temperature at nip and the use of a heated tool is likely to improve the consolidation quality and crystallinity of ATP laminates; and a higher roller pressure may contribute to void content reduction.

Chapter references

[1] Blundell DJ, Crick RA, Fife B, Peacock J, Keller A, Waddon A. Spherulitic morphology of the matrix of thermoplastic PEEK/carbon fibre aromatic polymer composites. J Mater Sci 1989;24:2057–64. https://doi.org/10.1007/BF02385421.

[2] Bassett DC, Olley RH, Al Raheil IAM. On crystallization phenomena in PEEK. Polymer 1988;29:1745–54. https://doi.org/10.1016/0032-3861(88)90386-2.

[3] Comer AJ, Ray D, Obande WO, Jones D, Lyons J, Rosca I, et al. Mechanical characterisation of carbon fibre–PEEK manufactured by laser-assisted automated-tape-placement and autoclave. Compos Part Appl Sci Manuf 2015;69:10–20. https://doi.org/10.1016/j.compositesa.2014.10.003.

[4] Lamontia MA, Gruber MB, Systems A, Drive S, Tierney J, Gillespie JW. Modeling the Accudyne Thermoplastic In Situ ATP Process. Proc SAMPE Conf 2009:8.

[5] Schledjewski R, Miaris A. Thermoplastic tape placement by means of diode laser heating. vol. 54, 2009.

[6] Chen J, Yousefpour A, Hojjati M, Cai X, Hoa S. Automated fiber placement of thermoplastic composites—lessons learned, 2013.

[7] Qureshi Z, Swait T, Scaife R, El-Dessouky HM. In situ consolidation of thermoplastic prepreg tape using automated tape placement technology: potential and possibilities. Compos Part B Eng 2014;66:255–67. https://doi.org/10.1016/j.compositesb.2014.05.025.

[8] Quiroga Cortés L, Caussé N, Dantras E, Lonjon A, Lacabanne C. Morphology and dynamical mechanical properties of poly ether ketone ketone (PEKK) with meta phenyl links. J Appl Polym Sci 2016;133:1–10. https://doi.org/10.1002/app.43396.

[9] Choupin T, Fayolle B, Régnier G, Paris C, Cinquin J, Brulé B. Isothermal crystallization kinetic modeling of poly(etherketoneketone) (PEKK) copolymer. Polymer 2017;111:73–82. https://doi.org/10.1016/j.polymer.2017.01.033.

[10] Hsiao BS, Chang IY, Sauer BB. Isothermal crystallization kinetics of poly(ether ketone ketone) and its carbon-fibre-reinforced composites. Polymer 1991;32:2799–805. https://doi.org/10.1016/0032-3861(91)90111-U.

[11] Gardner KCH, Hsiao BS, Matheson RR, Wood BA. Structure, crystallization and morphology of poly (aryl ether ketone ketone). Polymer 1992;33:2483–95. https://doi.org/10.1016/0032-3861(92)91128-O.

[12] Ho RM, Cheng SZD, Hsiao BS, Gardner KH. Crystal morphology and phase identifications in poly(aryl ether ketone)s and their copolymers. 3. Polymorphism in a polymer containing alternated terephthalic acid and isophthalic acid isomers. Macromolecules 1995;28:1938–45. https://doi.org/10.1021/ma00110a030.
[13] Blundell DJ, Osborn BN. The morphology of poly(aryl-ether-ether-ketone). Polymer 1983;24:953–8. https://doi.org/10.1016/0032-3861(83)90144-1.
[14] Tardif X, Pignon B, Boyard N, Schmelzer JWP, Sobotka V, Delaunay D, et al. Experimental study of crystallization of PolyEtherEtherKetone (PEEK) over a large temperature range using a nano-calorimeter. Polym Test 2014;36:10–9. https://doi.org/10.1016/j.polymertesting.2014.03.013.
[15] Risteska S, Petkoska AT, Samak S, Drienovsky M. Annealing Effects on the Crystallinity of Carbon Fiber-Reinforced Polyetheretherketone and Polyohenylene Laminate Composites Manufactured by Laser Automatic Tape Placement. Mater Sci 2020;26:308–16. https://doi.org/10.5755/j01.ms.26.3.21489.
[16] Kilroy JP, Ó Brádaigh CM, Semprimoschnig COA. Mechanical and physical evaluation of a new carbon fibre/PEEK composite system for space applications. SAMPE J 2008:1–12.
[17] Beehag A, Ye L. Role of cooling pressure on interlaminar fracture properties of commingled CF/PEEK composites. Compos Part Appl Sci Manuf 1996;27:175–82. https://doi.org/10.1016/1359-835X(95)00027-Y.
[18] Beehag A, Ye L. Influence of cooling rate on interlaminar fracture properties of unidirectional commingled CF/PEEK composites. Appl Compos Mater 1995;2:135–51. https://doi.org/10.1007/BF00567748.
[19] Chanteli A, Bandaru AK, Peeters D, O'Higgins RM, Weaver PM. Influence of repass treatment on carbon fibre-reinforced PEEK composites manufactured using laser-assisted automatic tape placement. Compos Struct 2020;248:112539. https://doi.org/10.1016/j.compstruct.2020.112539.
[20] Saenz-Castillo D, Martín MI, Calvo S, Rodríguez-Lence F, Güemes A. Effect of processing parameters and void content on mechanical properties and NDI of thermoplastic composites. Compos Part Appl Sci Manuf 2019. https://doi.org/10.1016/j.compositesa.2019.03.035.
[21] Hoang V-T, Kwon B-S, Sung J-W, Choe H-S, Oh S-W, Lee S-M, et al. Postprocessing method-induced mechanical properties of carbon fiber-reinforced thermoplastic composites. J Thermoplast Compos Mater 2023;36:432–47. https://doi.org/10.1177/0892705720945376.
[22] Stokes-Griffin CM, Compston P. The effect of processing temperature and placement rate on the short beam strength of carbon fibre-PEEK manufactured using a laser tape placement process. Compos Part Appl Sci Manuf 2015;78:274–83. https://doi.org/10.1016/j.compositesa.2015.08.008.
[23] Ramaswamy K, Modi V, Rao PS, Martin PP, McCarthy CT, O'Higgins RM. An investigation of the influence of matrix properties and fibre–matrix interface behaviour on the mechanical performance of carbon fibre-reinforced PEKK and PEEK composites | Elsevier Enhanced Reader 2023. https://doi.org/10.1016/j.compositesa.2022.107359.
[24] Esguerra-Arce I, Martín MI, Pérez-Pastor A, García-Martínez V. Evolution of crystallinity with multiple lamination steps in high performance thermoplastic composites by in-situ consolidation process. Twenty-Second Int Conf Compos Mater 2019.
[25] Gruber MB, Lockwood IZ, Dolan TL, Funck SB, Tierney JJ, Simacek P, et al. Thermoplastic in situ placement requires better impregnated tapes and tows. Int SAMPE Tech Conf 2012.
[26] Deignan A, Stanley WF, McCarthy M. Insights into wide variations in carbon fibre/polyetheretherketone rheology data under automated tape placement processing conditions. J Compos Mater 2018;52:2213–28. https://doi.org/10.1177/0021998317740733.
[27] Clancy G, Peeters D, Oliveri V, Jones D, O'Higgins RM, Weaver PM. A study of the influence of processing parameters on steering of carbon fibre/PEEK tapes using laser-assisted tape placement. Compos Part B Eng 2019;163:243–51. https://doi.org/10.1016/j.compositesb.2018.11.033.
[28] Lamontia M, Gruber M. Remaining developments required for commercializing in situ thermoplastic ATP. SAMPE Eur Conf 2007:1–15.

Chapter 7. Microstructural and micromechanical property characterisation of CF/PEKK laminates using nanoindentation

In previous chapters, the crystallisation kinetics of PEKK and CF/PEKK composites have been characterised, and the acquired knowledge has been used to manufacture and mechanically test a set of compression-moulded and ATP laminates, in an attempt to observe the effect of crystallinity on mechanical performance. These results overall reflected how compression-moulded laminates outperformed ATP. However, this was likely due to the crystallinity (27-31% for compression-moulded and 6-10% for ATP) and void content (0.1-0.4% for compression-moulded and 3.7-8.0% for ATP) having a joint effect on the laminate performance.

Further to this, any potential variation in crystallinity across the thickness of laminates as a consequence of manufacturing parameter variation cannot be identified via macromechanical testing. The presence of a crystallinity gradient is particularly likely in the case of ATP manufacturing, where the material undergoes fast cooling rates and repeated annealing.

Work has been done on tracking the evolution of heat transfer during ATP manufacturing [1,2] and its modelling [3–6], as well as some investigations on how this impacts crystallinity development [2,6]. The generation of uniform crystallinity throughout the bulk of a manufactured part is a key requirement for reliable performance during the service life. This is quite challenging to achieve when a thermoplastic part is manufactured using ATP. The measurement of crystallinity across the thickness of laminates can provide insight into the effectiveness of the manufacturing method and potential areas of improvement during the manufacturing process. Differential scanning calorimetry (DSC) has been used by many researchers to evaluate crystallinity and morphology of ATP samples [2,7–10], however, DSC provides an average value of the entire sample being assessed. Lamontia and Gruber [11] assessed crystallinity variation of a CF/PEKK ATP laminate by milling different layers of a sample and then performing DSC, however, this is a quite laborious and time-intensive process. A different way of indirectly evaluating through-thickness crystallinity requiring less sample preparation is via micromechanical property characterisation with nanoindentation.

Nanoindentation is a technique that can be used to measure elastic modulus and hardness at micron and nano scales, which can thereby infer crystallinity. A method most commonly used in the field of metals and ceramics, it is increasingly used on a variety of polymers to test local properties [12–15]. Recent studies on unreinforced semicrystalline thermoplastics have shown that nanoindentation can be used to indirectly measure crystallinity of a sample by measuring their micromechanical properties. Christöfl et al. [14] successfully measured the variation in elastic modulus across an injection-moulded polyoxymethylene sample cross-section as a consequence of crystallinity and morphology variation. Indentations close to the sample surface displayed a lower elastic modulus than indentations in the bulk, due to top and bottom surfaces being in contact with injection-moulding tooling and cooling at a faster rate during manufacturing, therefore having a lower crystallinity. These results agreed with polarised light microscopy results performed in the same work, which revealed less crystallinity close to the sample edges. A similar behaviour has been observed in unreinforced PEEK [13,15,16], where a higher crystallinity

resulted in increased hardness and elastic modulus values. A bimodal behaviour in fully crystallised PEEK was reported by Iqbal et al. [13], which was initially associated with the semicrystalline nature of the material. However, the indentation depths (6 μm) and reported spherulitic sizes of PEEK spherulites (10-20 μm) most likely provided the homogenised properties of the polymer rather than the two different phases, due to the resulting indentation being too large (a triangle with sides of about 30 μm [15]) to distinguish between the phases within a spherulitic structure. Voyiadjis et al. [15] suggested that this bimodal behaviour could therefore be due to surface inhomogeneities and studied the importance of surface finish in tough polymers (specifically PEEK) for nanoindentation to obtain consistent results. To the knowledge of the authors, no nanoindentation testing on unreinforced PEKK has been published.

The use of nanoindentation to characterise composite materials has risen since the 2000s, with research characterising the reinforcement and matrix constituents of composites. The performance of the polymer matrix during nanoindentation experiments is influenced by the presence of fibres, particularly at large penetration depths [17], and polymer hardness and elastic modulus values are generally greater as a matrix in a composite than in neat form [18,19]. Nanoindentation has also been used to assess reinforcement-matrix interface and interphase properties. Interface generally refers to interfacial shear strength between fibre and matrix, where nanoindentation is used for fibre push-in testing; whereas interphase refers to a "third" transition phase between the fibre and matrix, tested via grid nanoindentation. Gibson [18] provides a review of work done on interfaces and interphases for a variety of polymer composites.

Nanoindentation research on specifically PEEK and PEKK composites is sparse: Ray et al. [17] performed nanoindentation on CF/PEEK autoclaved and ATP laminates, corroborating previous findings that the presence of crystallinity results in a performance increase. Molazemhosseini et al. [20] studied PEEK-based composites with short CFs and nano-silica, successfully characterising fibre, matrix and interphase performance, as well as demonstrating an improvement in the performance of PEEK composites compared to its unreinforced form. Gain et al. [21] performed a study where the impact of consolidation force and hot gas torch temperature on the matrix and interphase properties were assessed, finding that increasing both parameters resulted in hardness and elastic modulus increases during nanoindentation testing. Additionally, nanoindentation has been used to evaluate the effect of ion irradiation on the micromechanical properties of unreinforced PEKK, [22] as well as its thermal degradation behaviour as a consequence of laser heating [23].

Nano-indentation research on CF/PEKK, on the other hand, is more limited, with no literature available on ATP-manufactured CF/PEKK composites. Gaillard and Amiot [24] performed nanoindentation testing on CF/PEKK in an attempt to observe and model the presence of an interphase with very low maximum loads of 60 μN (and therefore very small indentations), achieving a very high spatial resolution. The matrix regions close to the fibre were found to be affected by the presence of the fibre, presenting a fibre-to-matrix modulus gradient ring around the fibre of approximately 800 nm thickness. It is important to keep in mind, however, that very small indentations (<50 nm depth), and therefore low indenter tip contact areas, may produce unreliable results that are influenced by tip blunting or surface roughness [25]. Ramaswamy et al. [26] employed a nanoindenter to characterise fibre/matrix interfacial shear strength via fibre-pushout tests on autoclave-manufactured CF/PEKK laminates. Any further nanoindentation studies on crystallinity, the effects of varying parameters in a manufacturing process, or interphase characterisation of CF/PEEK or CF/PEKK have not been found by the authors of this work.

The work presented in this chapter evaluates micromechanical properties of CF/PEKK laminates manufactured via compression moulding and ATP using nanoindentation, in order to indirectly measure crystallinity development and variation. DSC is initially used to assess the average crystallinity developed in each laminate as a consequence of the processing conditions. The impact of varying manufacturing parameters on the micromechanical properties is then studied via nanoindentation, as well as any variation in properties across the thickness of the ATP laminates. Additionally, the presence of any fibre/matrix property transition is evaluated.

7.1. Materials and methods

7.1.1. Materials and manufacturing

CF/PEKK prepreg tape, provided by Hexcel Composites Ltd., was used to manufacture UD compression-moulded and ATP laminates. The details of laminates tested in this chapter are given in Table 7.1, with further manufacturing details and laminate codes provided in Figure 5.7, Table 5.3 and Table 5.5 in Chapter 5.

Table 7.1: Summary of processing parameters for the compression-moulded and ATP-manufactured laminates.

Laminate code (Compression-moulded laminates)	**Hold melt temperature (°C)**		**Isothermal hold temperature (°C)**		
I-220-370	370		220		
I-260-370	370		260		
I-300-370	370		300		
Laminate code (ATP laminates)	**Tool material**	**Nip temp (°C)**	**Lay-down speed (m/min)**	**Roller pressure (bar)**	**Laminate thickness (mm)**
ATP-380-4-2	Mild steel (unheated)	380	4	2	2
ATP-380-2-2	Mild steel (unheated)	380	2	2	2
ATP-380-4-4	Mild steel (unheated)	380	4	4	2
ATP-360-4-2-2mm	Ceramic (unheated)	360	4	4	2
ATP-360-4-2-4mm	Ceramic (unheated)	360	4	4	4
ATP-360-4-2-6mm	Ceramic (unheated)	360	4	4	6

7.1.2. Nanoindentation

Samples measuring approximately 1 cm x 1 cm (2 mm thick) were cut out of the laminates with a hand saw and were mounted in epoxy resin, exposing the cross-section of the laminate. These were polished with silicon carbide discs of up to P2500, followed by diamond suspension polishing down to 1 μm particle size.

The nanoindentation tests were performed using a KLA iMicro Nanoindenter, with a diamond Berkovich-type indenter tip (ID: DC2/BERKOVICH/015). An initial calibration was performed with silica and glassy carbon to measure the frame stiffness and the area function of the tip.

Load-unload indentation cycles were performed using continuous stiffness measurement testing, at an indentation strain rate of $0.2s^{-1}$, a frequency of 110Hz and frequency amplitude of 2nm. Elastic modulus

and hardness can be determined from the load-displacement curves obtained during testing, an example of which is shown in Figure 7.1.

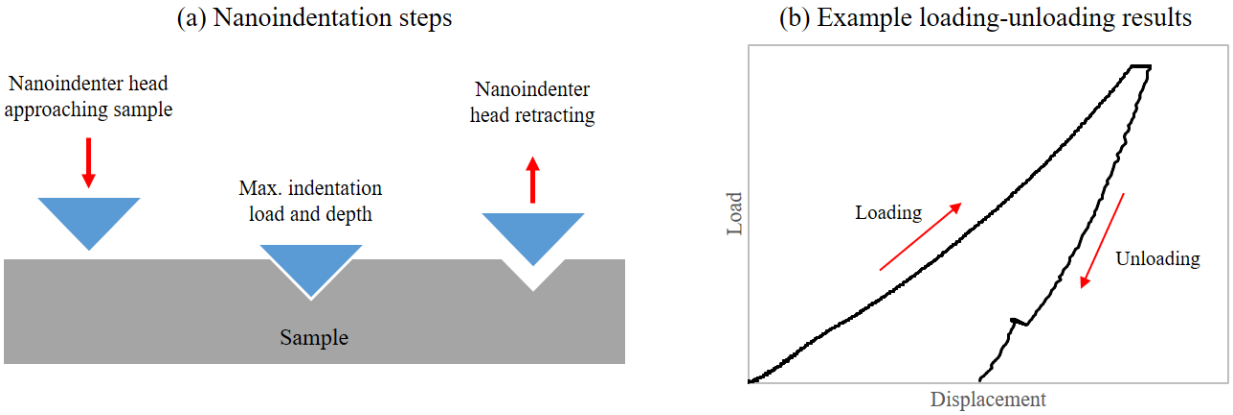

Figure 7.1: (a) Nanoindentation loading and unloading schematic; and (b) sample load-displacement curve generated from a nanoindentation test

Commonly used properties in nanoindentation to evaluate material performance are elastic modulus and hardness. Elastic modulus in particular assumes a linear stress-strain relationship, which, as will be observed, is not the case in this work, particularly with indentation performed in the matrix bulk. However, this is a convenient parameter to use, and has been used in literature on PEEK and CF/PEEK providing curves with similar shapes [20,21,23,27]. For the purposes of comparing the mechanical properties of different locations across a laminate's thickness in order to evaluate variations in crystallinity, the use of elastic modulus has been successfully used previously [14], as discussed in this chapter's introduction.

The contact stiffness S, which is the initial slope at the beginning of the unloading curve, can be expressed as defined by Pharr and Oliver [28]:

$$S = \frac{2\beta}{\sqrt{\pi}} \times E_r \sqrt{A_c} \tag{6.1}$$

where E_r is the reduced elastic modulus and A_c is the indenter contact area (a function of the indenter depth in contact with the sample during testing). β is an indenter geometry constant introduced by Hay et al. [29] to account for different indenter tip geometries. E_r represents the elastic deformation that takes place in both the indenter and the sample, and is given by:

$$E_r = \left(\frac{1 - \nu_i^2}{E_i} + \frac{1 - \nu_s^2}{E_s} \right)^{-1} \tag{6.2}$$

where ν is Poisson's ratio, and the subscripts i and s denote the indenter and sample materials respectively. Assuming that $E_i \gg E_s$, the first term of Eq. (6.2) becomes negligible. Substituting Eq. (6.2) into Eq. (6.1) and rearranging,

$$E_s = (1 - \nu_s^2) \times \frac{\sqrt{\pi}}{2\beta} \times \frac{S}{\sqrt{A_c}} \tag{6.3}$$

If the indenter is considered to be much stiffer than the sample, the sample hardness H can be defined by [30]:

$$H = \frac{P_{max}}{A_c} \tag{6.4}$$

where P_{max} is the maximum loading force achieved.

A 2 μm trial indentation in a matrix pocket, as shown in Figure 7.2a, was performed to determine an adequate indentation depth. Figure 7.2b shows that, above 1100 μm, there is a sharp increase in elastic modulus, indicating that fibres in the vicinity significantly influenced the matrix response at these depths. A lower depth is therefore preferable, in order to successfully evaluate the response of the composite's different constituents [18]. It is worth noting that, at very low displacements, no modulus data was provided by the software. This is likely due to the low contact area at this stage resulting in non-representative modulus values, as discussed in the introduction of this chapter. Such behaviour has been observed in Ray et al.'s work on CF/PEEK [17], where an initial elastic modulus of 18 GPa at approximately 10nm depth dropped to approximately 8 GPa for indentation depths of 50-500nm.

Based on the discussed observations, a target indentation depth of 400 nm was chosen to take all elastic modulus and hardness values. In Figure 7.2a, a 2 μm-deep indentation can be observed to be too large to do this in matrix areas closer to the fibre surface.

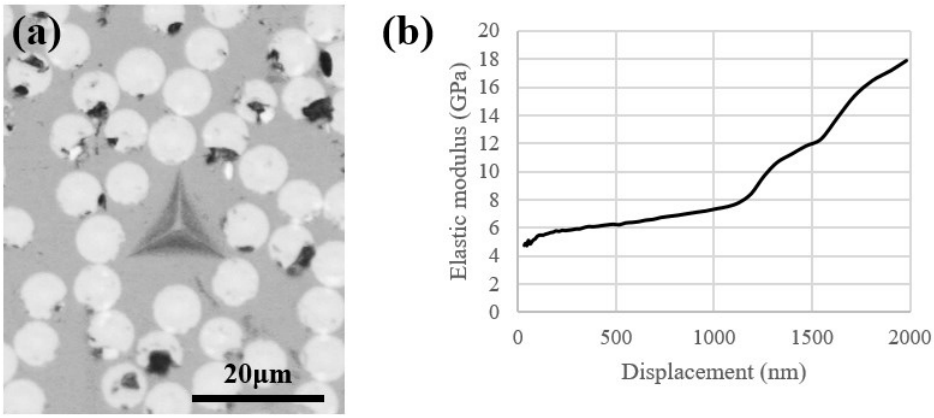

Figure 7.2: (a) Micrograph of 2 μm depth indentation at a matrix pocket; and (b) elastic modulus-displacement plot of said indentation.

All samples were indented at locations marked with a square □ as shown in Figure 7.3. At each location, a series of indentations were performed as given below:

- An array of nanoindentations to obtain hardness and elastic modulus values of the fibres and the matrix at different distances from the fibre surface, as shown with triangles △ in Figure 7.4;
- Two individual indents on matrix pockets to obtain matrix bulk properties, shown with stars ☆ in Figure 7.4 (to ensure matrix bulk properties are characterised);
- Two individual indents on fibres to obtain fibre properties, as shown with crosses ✕ in Figure 7.4 (to ensure fibre properties are characterised).

A micrograph of an array and a matrix indent is shown in Figure 7.5. The distance of the indentations to the closest fibre surface was measured using ImageJ software from the centre of the indentations to the surface of the nearest fibre edge.

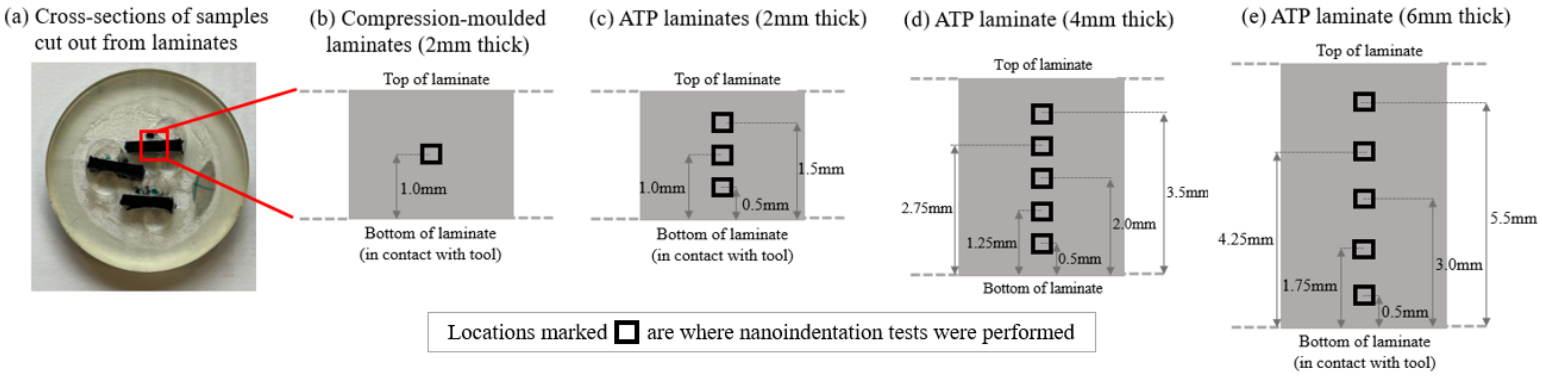

Figure 7.3: Schematics of laminate cross-sections, showing the location of performed indentations with a square □.

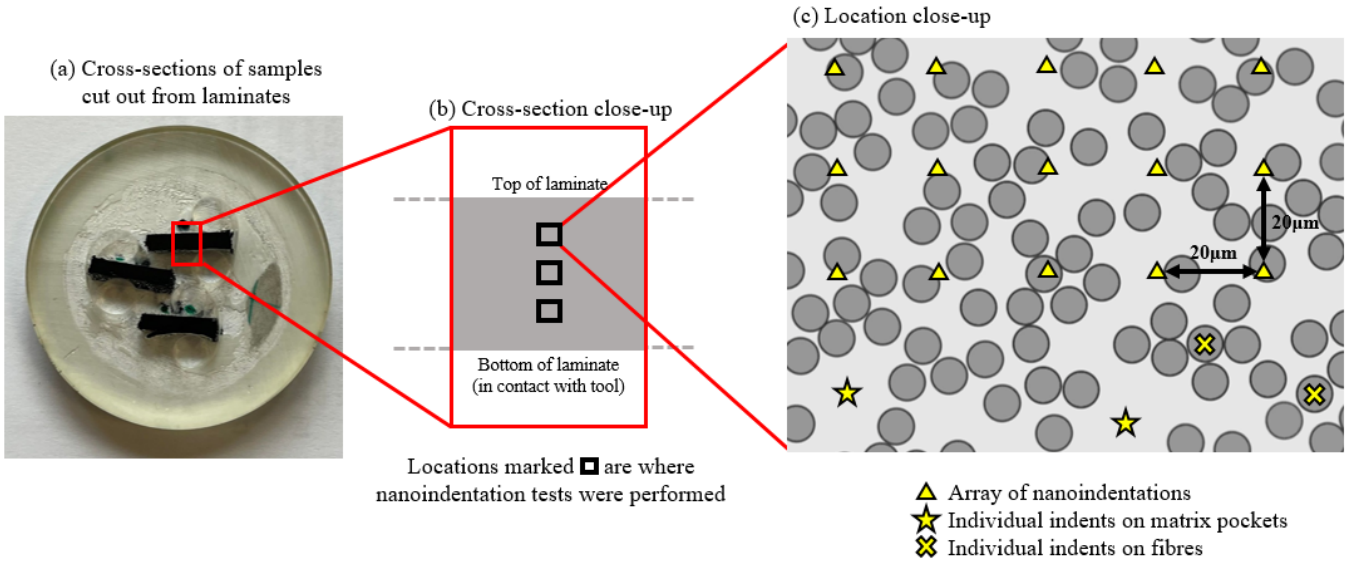

Figure 7.4: Schematic example of an indentation array and fibre and matrix indents on an ATP sample. In this case, 19 indentations were performed per location marked with a square □, with each of them giving hardness and elastic modulus data.

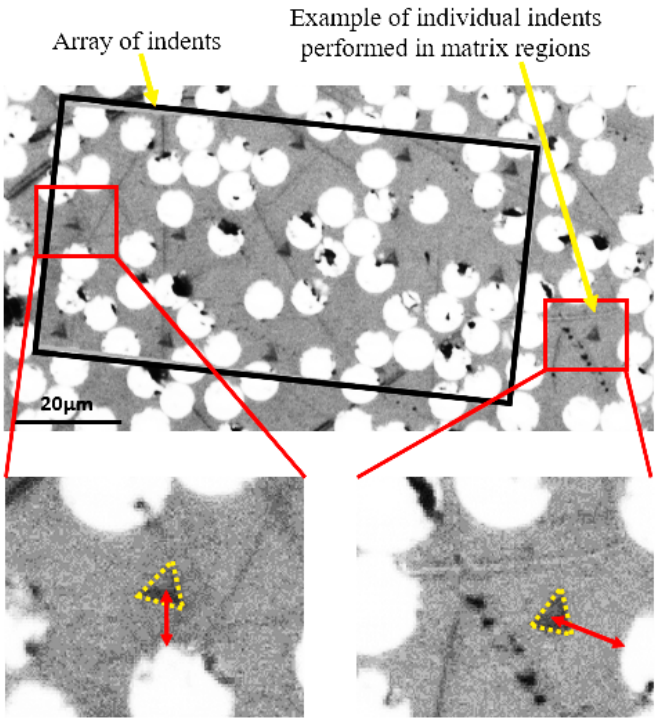

Figure 7.5: A micrograph showing array and a matrix indent. A close-up of two indentations shows nanoindentation distances to the closest fibre surface marked with red arrows, measured using ImageJ.

The location and amount of nanoindentation arrays performed were chosen based on the expected crystallinity distribution across the thickness of the laminates. In the case of the compression-moulded laminates, crystallinity and morphology were assumed to be constant throughout the thickness due to the long holding times at crystallisation temperatures. The work done on these laminates reported in Chapter 6 supports this assumption, showing homogeneous consolidation, high average crystallinity content and good mechanical performance. Therefore, a 5 x 5 array, two matrix indentations and two fibre indentations were performed at a single location (as shown in Figure 7.4b) on compression-moulded samples, totalling 29 indentations per location (shown with the symbol □).

On the other hand, the fast nature of ATP manufacturing is likely to result in a difference in crystallinity and morphology across the laminate thickness. This is supported by observations of poor laminate consolidation and low average crystallinity as shown in Chapter 6, as well as a varying crystallinity content across the thickness of CF/PEEK and CF/PEKK ATP laminates as reported in literature [2,11]. Therefore, 3 x 5 arrays plus two matrix and two fibre indentations (as shown in Figure 7.4c) were performed at several locations across thicknesses of the ATP samples to assess this variation, resulting in 19 indentations on each location □. For 2 mm-thick ATP laminates, 3 locations were tested as shown in Figure 7.3c; for the 4 mm-thick laminate, 5 locations were tested as per Figure 7.3d; and for the 6 mm-thick laminate, 5 locations were tested as shown in Figure 7.3e.

Results and discussion

7.1.3. Nanoindentation

The following sections discuss the differences observed in load-displacement curves for compression-moulded and ATP laminates. This is followed by a brief explanation of the data processing procedure. Then matrix bulk properties are analysed and compared across different laminates and locations, as well as any variation in properties across the fibre/matrix interphase.

7.1.3.1. Load-displacement curves

Figure 7.6a and Figure 7.6b show load-displacement curves for all indentations done on sample I-220-370 and the top location of ATP-380-4-2 respectively. These are provided as representative examples of the response of compression-moulded and ATP laminates, as this section draws a general comparison of the two manufacturing techniques, and not of the individual laminates. In these, as well as the rest of the nanoindentation results, three distinct responses can be observed, denoted as "fibre", "matrix" and "interphase" in Figure 7.6. Note that results obtained by indentations marked with a star ☆ in Figure 7.4 fall in the matrix response, and results obtained by indentations marked with a cross ✕ fall in the fibre response. Indentations marked with a triangle △ may fall within any of these three categories, depending on where the indentation is made (on the fibre, in the matrix bulk, or in the matrix closer to a fibre surface).

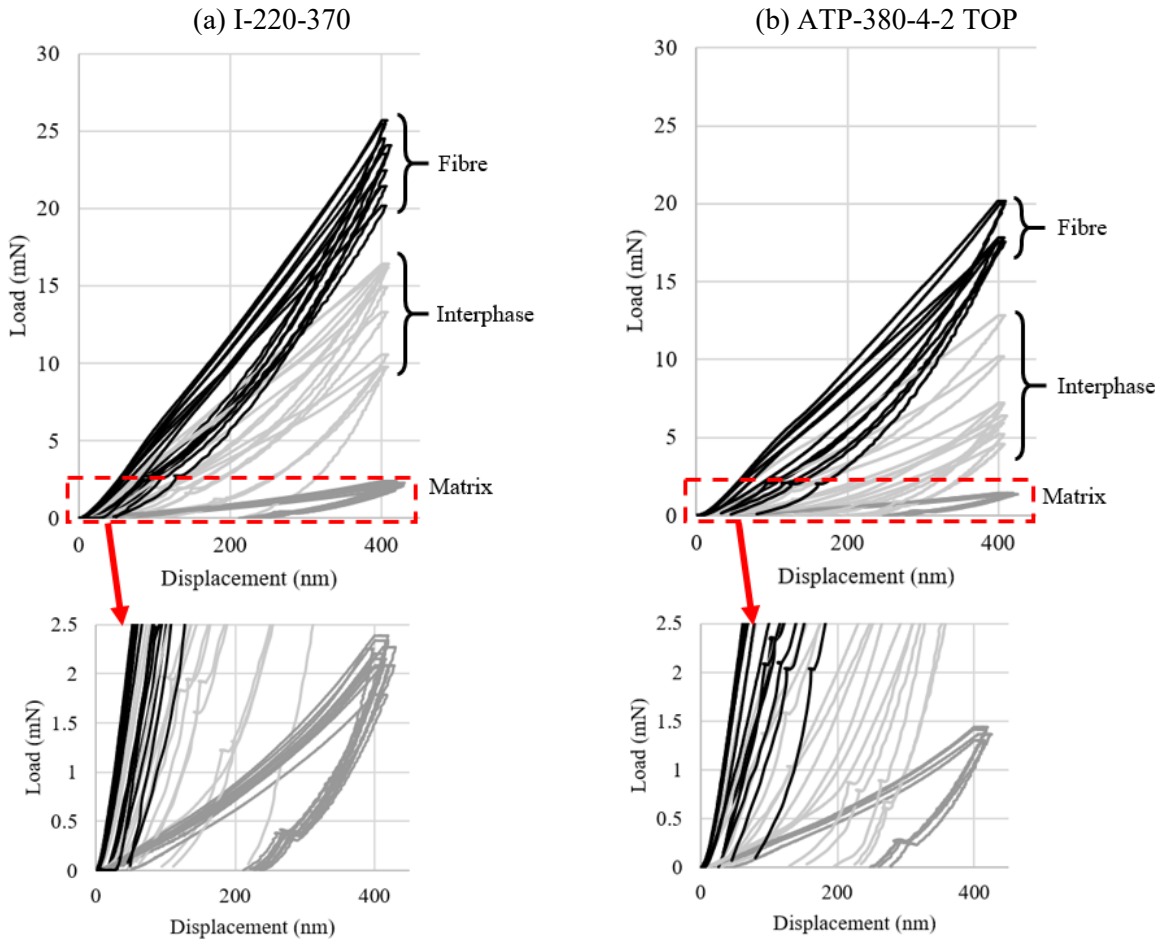

Figure 7.6: Load-displacement results of nanoindentation experiments on (a) CM-220 and (b) the top location of ATP-380-4-2.

The fibre response is the stiffest among all regions, experiencing the largest elastic recovery compared to matrix and interphase responses. This is observed in existing nanoindentation work on CF/PEEK [20]. While the fibres in all samples are identical, a lower peak load response in the ATP sample of 17-20 mN can be observed, against 20-25 mN of the compression-moulded sample. This may be due to the fibre behaving as part of a composite during nanoindentation rather than in isolation. Due to the elastic response of the fibre, no permanent dents were left after nanoindentation testing – this is visible in the nanoindentation array in Figure 7.5, where permanent dents on matrix regions are visible but those that fell on fibres are not. Because of this, the indentation distance from the centre of the fibre could not be measured.

Matrix behaviour refers to the bulk response far away from any fibres, where performance remained similar across all load-displacement curves irrespective of the distance from fibre surfaces. An example location of this can be seen in Figure 7.4 marked with stars ☆. A prominent hysteresis loop can be observed, related to the viscoelastic behaviour of PEKK. This suggests that the polymer's behaviour is impacted by the strain rate it undergoes. Due to this, indentation speed has been kept constant throughout all testing. The compression-moulded sample withstood a higher load and experienced a smaller hysteresis loop. This is visible in the zoomed-in plots in Figure 7.6a and Figure 7.6b, where the indentation depth retained after the nanoindenter head is withdrawn ranges from 210-235 nm for the compression-moulded sample and 245-280 nm for the ATP sample (values read from the x-axes in Figure 7.6). This can be attributed to the high crystallinity content in the compression-moulded samples, where the presence of ordered, spherulitic structures resulted in a stiffer, more elastic response compared to that observed in the amorphous matrix of the ATP sample.

The interphase region refers to the response that does not match the fibre or matrix bulk response, but instead varies with the distance from the fibre surface at which the indentation was made. In the following section, it will be observed that nanoindentation tests closer to the fibre surface resulted in a stiffer response. The stiffer responses shown in Figure 7.6 (higher loads at the same displacement) also possess smaller hysteresis loops, in line with the more elastic response as indentations are performed closer to fibre surfaces.

Similar observations have been made for a variety of polymers and polymer composites in literature. Molazemhosseini et al. [20] performed nanoindentation testing on short CF/PEEK samples (some reinforced with nano silica particles) and reported similar fibre/matrix/interphase responses as observed in this work. In their case, fibres exhibited perfect elastic response, likely due to the lower depth of indentations in all the testing (10-70 nm). Shen et al. [31] observed an increase in indentation resistance with a higher crystallinity content in unreinforced PA6, in a similar way to the stiffer performance of the more crystallised compression-moulded samples in this work. Klapperich et al. [12] tested a range of unreinforced PE grades with different molecular weights, and found those with lower crystallinity to exhibit a more pronounced hysteresis loop, and experience a significantly higher amount of deformation under the same load due to a more compliant response of the amorphous fraction in the sample.

7.1.3.2. Hardness and elastic modulus against indentation distance from fibre surface: curve fitting

The nanoindentation results for each location marked with a square □ in Figure 7.3 provided hardness and elastic modulus data, which were plotted against the distance from the fibre surface at which each data point was taken. An example of this is given in Figure 7.7, where hardness and elastic modulus results for the single location in laminate I-260-370 are plotted. These results show a plateau far away from the fibre surface. For results analysis and comparative purposes, an exponential decay function was fitted to the results of each location. Examples of these are shown with the dotted curves in Figure 7.7.

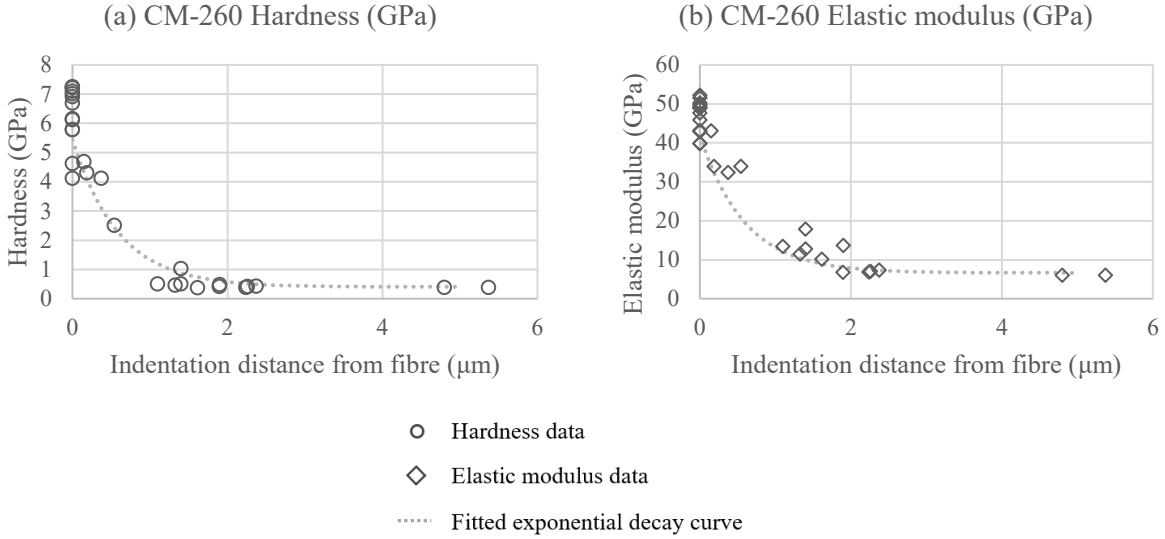

Figure 7.7: (a) Hardness and (b) elastic modulus results against indentation distance from fibre surface for CM-260. The experimental data includes the nanoindentation array and individual indents performed on matrix pockets and fibres. The curves are fitted to the experimental data, and correspond to Eq. (6.8) and (6.9) for (a) and (b) respectively.

The exponential decay equation in question has the following form:

$$y = Aexp(-Bx) + C \tag{6.5}$$

where x is the distance from the fibre surface (μm), y is fibre hardness (or elastic modulus) (GPa), and A, B and C are constants. The number of constants to be found can be reduced by introducing the following boundary conditions:

- When $x = 0$, $y = H_F$ (or M_F), the fibre hardness (or fibre elastic modulus). This value remains the same across all locations, as they all use the same fibre type. Substituting and rearranging:

$$y = Aexp(-Bx) + H_F - A \tag{6.6}$$

$$y = Aexp(-Bx) + M_F - A \tag{6.7}$$

- When $x = \infty$, $y = H_M$ (or M_M), the matrix hardness (or matrix elastic modulus). This value changes with each location, now that the processing conditions will affect the matrix morphology and crystallinity, and therefore its properties. This includes different locations within the same sample, as is the case with ATP samples. Substituting and rearranging:

$$y = (H_F - H_M)\exp(-B_H x) + H_M \tag{6.8}$$

$$y = (M_F - M_M)\exp(-B_M x) + M_M \tag{6.9}$$

Values for H_F and M_F were found by averaging the fibre indentation results across all locations, and were found to be H_F = 5.44 GPa and M_F = 41.9 GPa. Values for H_M and M_M are discussed in Section 7.1.3.3, and were found by averaging the matrix indentation results of each individual location after they stabilised into a plateau. For example, in Figure 7.7a and Figure 7.7b, this would be after $x \approx 1.75$ μm and $x \approx 2$ μm respectively.

A one-way ANOVA test was used to evaluate whether there was a significant difference in H_M and M_M results across the different tested locations (across the thickness of samples and across the same location of different samples), with a probability threshold value $\alpha = 0.05$. Whenever a significant difference is found, a one-way ANOVA test does not highlight which groups differ specifically. Therefore, when this happened, different result sets were tested together, and a T-test was performed whenever necessary to evaluate exactly which groups had a significant difference. This analysis can be found in Appendix X.

Once these values were established, a MATLAB script was used to fit Eq. (6.8) and (6.9) to the raw data and find B_H (for hardness) and B_M (for elastic modulus) at each location □. These constants represent the gradient of the exponential decay function – the larger the value, the faster the transition from fibre to matrix hardness (or elastic modulus).

7.1.3.3. Matrix bulk properties (H_M and M_M)

In this section, a general comparison between compression-moulding and ATP results is drawn, followed by discussions within individual manufacturing processes (compression-moulded, ATP with T_{nip} 380°C and ATP with T_{nip} 360°C) addressed separately.

Note that ATP laminates with different nip temperatures are manufactured on different types of tools (T_{nip} = 360°C on a ceramic tool and T_{nip} = 380°C on a mild steel tool). As concluded in Chapter 6, this likely resulted in different cooling profiles in the laminates due to the different thermal conductivity of the tools. Therefore, results are not directly comparable.

Compression-moulded vs. ATP-380 laminates

The graphs in Figure 7.8a and Figure 7.8b show matrix bulk hardness and elastic modulus results for the compression-moulded laminates (single location tested as shown in Figure 7.3b) and across the thickness of the ATP laminates with T_{nip} = 380°C (3 locations tested as shown in Figure 7.3c). These show that the compression-moulded laminates have significantly higher hardness (34-53%) and elastic modulus (22-48%) values than the ATP laminates (analysis of statistical significance available in Appendix G.4). This is expected due to the extended holding times at crystallisation temperatures during manufacturing resulting in a crystalline matrix, whereas ATP laminates experienced fast-cooling, resulting in a softer, amorphous structure and lower hardness and elastic modulus responses.

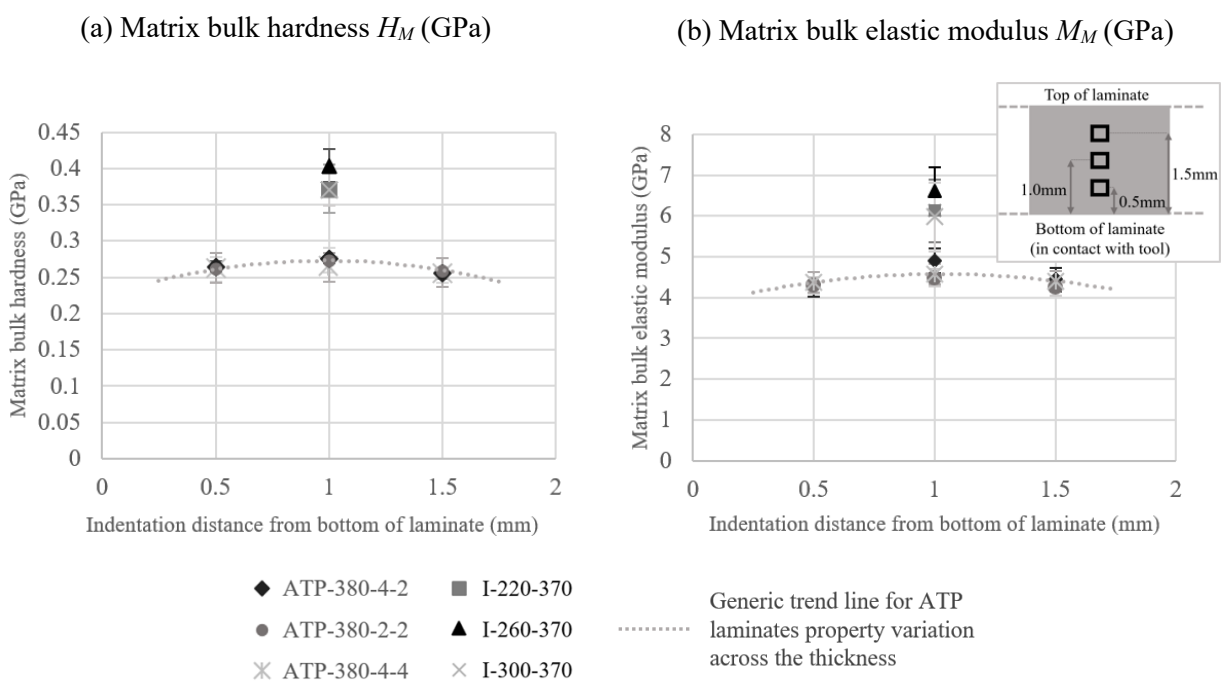

Figure 7.8: (a) Matrix bulk hardness and (b) matrix bulk elastic modulus of all compression-moulded laminates and ATP laminates manufactured at T_{nip} = 380°C. Top-right schematic shows the locations where the indentations were performed, measured from the bottom of the laminate (taken from Figure 7.3).

Differences in compression-moulded laminates

Among the compression-moulded laminates, I-260-370 performed marginally better than I-220-370 and I-300-370 (~9% higher hardness and 8-11% higher elastic modulus), even though this difference was found not statistically significant (see Appendix G.1). I-220-370 and I-300-370 performed similarly, as observed in Figure 7.8. The crystallisation studies in Chapter 4 showed that isotherms held at 260°C (which is the case for laminate I-260-370) exhibited the fastest crystallisation rates. I-220-270 and I-300-370 possessed the smallest (~2 µm diameter) and largest (~6 µm) spherulites respectively, with I-260-370 having intermediate-sized spherulites, ~4 µm. The faster crystallisation rates that I-260-370 experienced might be an indication that these processing conditions are optimal for the polymer's most effective crystallisation, which has been reflected in its performance during nanoindentation testing.

On the other hand, mechanical properties of these samples reported in Chapter 6 (ILSS, 0° and 90° flexural) did not show any significant effect of the spherulitic size. Tensile testing on other polymers with similar spherulite sizes (unreinforced PP-PE, 3-7 µm diameter) [32] reported similar findings. Polymers with larger variations in spherulitic diameter (1-30 µm), however, have shown a variation in mechanical performance (tensile and flexural), with unreinforced PA66 achieving a higher flexural modulus and yield point and a lower ultimate elongation with smaller spherulites [33]. Therefore, it might be possible that small variations in spherulite size may not have a significant impact on all mechanical properties at the macro scale, but their effects are more detectable at micron or nano-scale. The knowledge and understanding of such microstructures can improve the performance and failure at macroscopic level during the service life.

Differences in ATP-380 laminates (metal tool)

The results of all the ATP laminates (2 mm thick) shown in Figure 7.8 follow a similar trend: a peak in properties in the middle of the laminate compared to the tested locations close to the bottom (tool side) and top surfaces. Percentage differences between the performance of the middle location and the top/bottom locations in the ATP laminates are as follows:

- ATP-380-4-2: 5-9% hardness increase, 11-14% elastic modulus increase.
- ATP-380-2-2: ~5% hardness increase, 4-5% elastic modulus increase.
- ATP-380-4-4: 0-3% hardness increase, 4-5% elastic modulus increase.

This is likely due to the presence of two competing mechanisms during ATP manufacturing that influence crystallinity and mechanical properties:

- Proximity to the metal tool: the tool surface acts as a heat sink, contributing towards the fast cooling of the prepreg tape laid on it. As more layers of the laminate are laid, there is more material between the new prepreg layers and the tool. This can result in better heat retention and a reduction in the cooling speed, which contributes to crystallinity development. This has been observed for CF/PEEK [2], where prepreg layer crystallinity was found to be higher the further away the layer was from the bottom of the laminate (which was in contact with the tool surface), eventually plateauing to the maximum achievable crystallinity given the heat retention capability of the material and the ATP parameters. Ref. [2] also showed similar results on CF/PEKK, however, due to slower crystallisation kinetics, maximum achievable crystallinity was reached after a higher number of layers. The contribution of the proximity to the tool to crystallinity development is represented in Figure 7.9 with a grey line, which resembles the results reported in [2] for the crystallinity evolution for every added layer.
- Heat repasses: as the prepreg layers are laid, the incoming heat diffuses into the layers that are already in place. This causes annealing of the polymer, which contributes towards enhanced crystallisation. The lower layers of the laminate undergo more of these repasses than the top layers. The through-thickness temperature profile of ATP-manufactured CF/PEEK laminates has been validated via thermocouples during manufacturing [3,4,34] and modelled [3,5,34] in literature. The published literature shows that already laid material is repeatedly heated as more layers are placed. The contribution of heat repasses to crystallinity development is represented in Figure 7.9 with a black line.

The combination of these two mechanisms will influence the temperatures reached by the material locally, which will affect the amount of annealing that the material undergoes. If melting temperatures are reached, these will affect how much melting the material undergoes and therefore the amount of pre-existing crystallinity and nucleation sites available for further crystallisation. Following this, the cooling rate dictated by these two competing mechanisms will influence to what extent spherulitic growth takes place. Based on the above descriptions and the results from the nanoindentation work performed, the highest crystallinity development may be reached around the middle layers of the laminate. The contribution of each mechanism is likely to change along with manufacturing parameters and the type of tool.

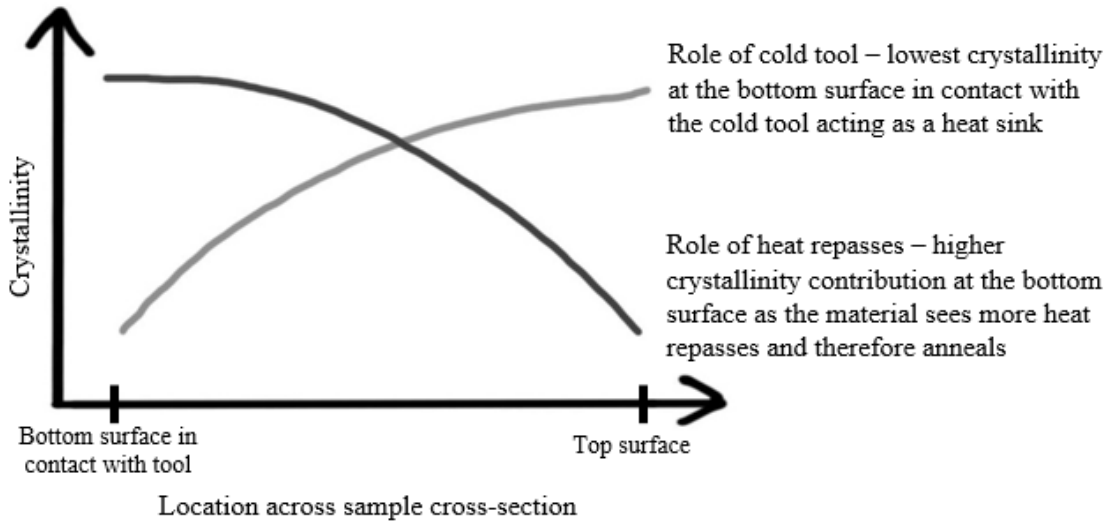

Figure 7.9: Schematic of contribution to crystallinity development of the ATP unheated tool acting as a heat sink and the heat repasses seen by a layer of material as more layers are placed on top.

The difference in hardness and elastic modulus between ATP-380-4-2, ATP-380-2-2 and ATP-380-4-4 at the top and bottom locations is negligible and showed no statistically significant differences (see Appendix G.2). This is likely due to the proximity to the tool on the bottom surface and the low number of (if any) repasses experienced by the top layers, where any variation in manufacturing parameters likely had a negligible effect on performance. It is therefore hypothesised that the fast-cooling and/or minimal annealing resulted in lower crystallinity compared to the middle location.

The middle location of the ATP-380-4-2 sample displayed a slightly higher hardness and elastic modulus than in the other two laminates, (2-5% increase in hardness and 7-10% in elastic modulus). The difference in elastic modulus particularly was statistically significant (see Appendix G.2).

Differences in ATP-360 laminates (ceramic tool)

The plots in Figure 7.10 show matrix hardness and elastic modulus results for the compression-moulded laminates (single location tested as shown in Figure 7.3b) and across the thickness of the 2 mm, 4 mm and 6 mm laminates with T_{nip} = 360°C (3 locations tested as shown in Figure 7.3c). At the top two locations of the 4 mm-thick laminate (at 2.75 mm and 3.5 mm from the bottom surface), the bulk hardness and elastic modulus values can be seen to not follow the trend that the rest of the laminates in this work do, where the middle locations performed better than the top/bottom regions. This is suspected to be due to data points being collected less than 4 μm away from the fibre surface, which may not be far away enough to be truly representative of the matrix bulk properties. Therefore, for the remaining analysis, these two matrix bulk values are not considered, shown in Figure 7.10 by the dotted line.

The difference in performance between the compression-moulded laminates and the ATP-360 laminates (42-56% hardness and 38-49% elastic modulus) is similar to the ATP-380 laminates, for the same reasons as previously discussed, and is also statistically significant (see Appendix G.5). ATP-360 laminates also displayed the same behaviour as the ATP-380 laminates, where the middle location of the laminates performed better than the top/bottom locations, with percentage differences as follows:

- 2 mm-thick laminate: 9-11% hardness increase, 1-3% elastic modulus increase.
- 4 mm-thick laminate: 6% hardness increase, 9% elastic modulus increase (difference between bottom and middle locations only).
- 6 mm-thick laminate: 5-7% hardness increase, 3-12% elastic modulus increase.

This might be due to the central location having a higher crystallinity than the other tested locations, as described for the ATP-380 laminates. These differences were not statistically significant (see Appendix G.3).

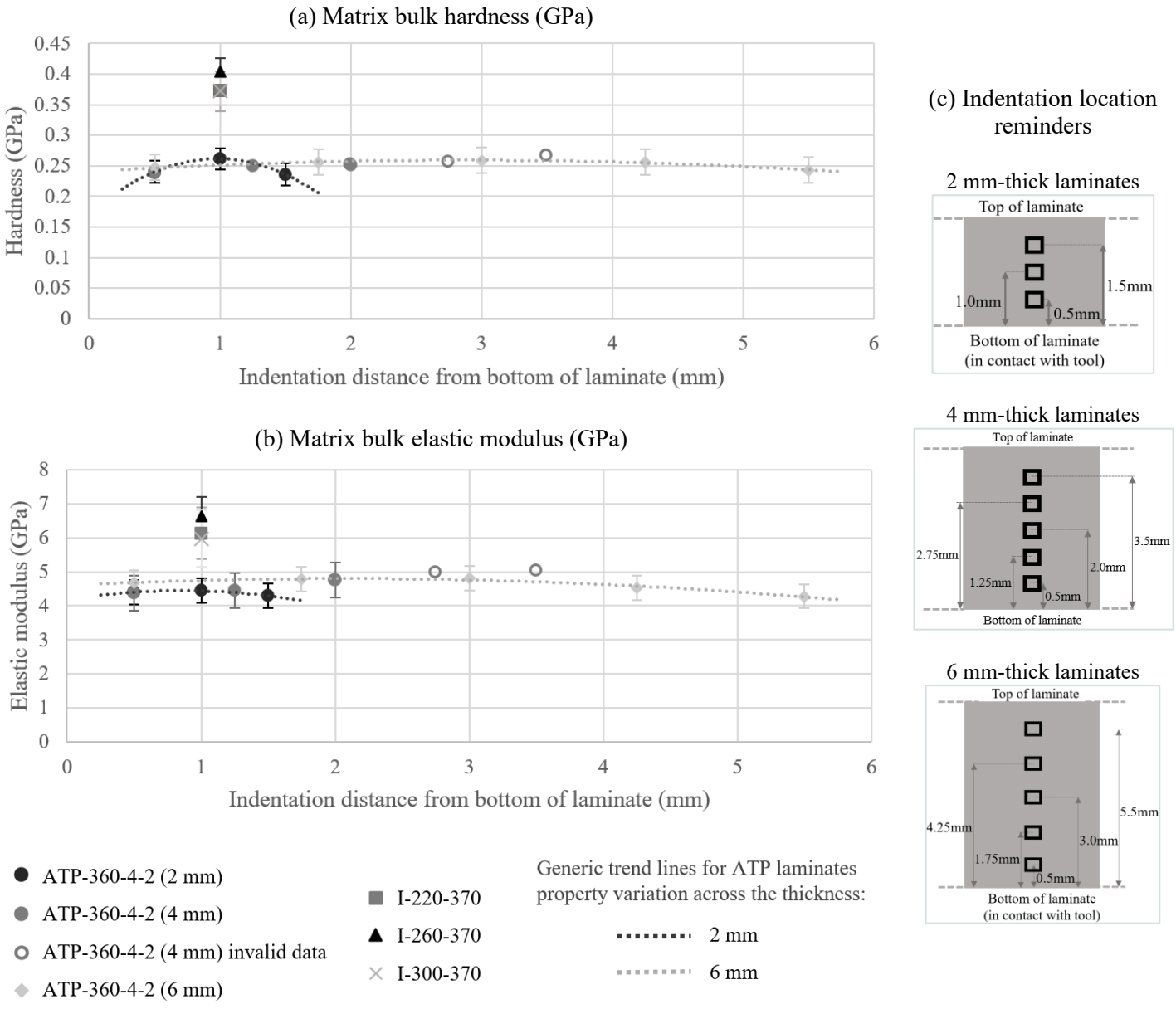

Figure 7.10: (a) Matrix bulk hardness and (b) matrix bulk elastic modulus of all compression-moulded laminates and ATP laminates manufactured at T_{nip} = 360°C. Schematics in (c) show the locations where the indentations were performed, measured from the bottom of the laminate (taken from Figure 7.3).

7.1.3.4. Fibre/matrix interphase

As observed in Section 7.1.3.1, there is a fibre/matrix property transition in samples, whose response varies with the distance from the fibre surface. Section 7.1.3.2 introduced Eq. (6.8) and (6.9) to model this transition where B_H and B_M control the gradient of the fitted curves for hardness and elastic modulus data respectively. This section comments on any observed variations on these gradients across all compression-moulded laminates, as well as the middle locations of ATP-380-4-2 and ATP-360-4-2-2 mm as representative ATP laminates to compare with the compression-moulding results. The curves for the remaining ATP laminates were not very different. This indicates that the changes in the ATP parameters were not significant enough to introduce changes at the fibre/matrix interface of the ATP manufactured laminates. The curves for the remaining ATP laminates and locations can be found in Appendix H.

Compression-moulded laminates

Table 7.2 provides B_H and B_M values and their 95% confidence intervals for the compression-moulded laminates as calculated in MATLAB. Figure 7.11 shows the fitted exponential decay curves with the confidence intervals applied to the curves with shaded regions.

Table 7.2: Summary of B_H and B_M values and 95% confidence intervals for the exponential decay modelling of compression-moulded CF/PEKK samples.

Laminate code	**I-220-370**		**I-260-370**		**I-300-370**	
	Value	**95% confidence interval**	**Value**	**95% confidence interval**	**Value**	**95% confidence interval**
B_H (Hardness)	1.918	± 0.394	1.687	± 0.344	1.924	± 0.723
B_M (Elastic modulus)	1.421	± 0.286	1.200	± 0.197	1.411	± 0.374

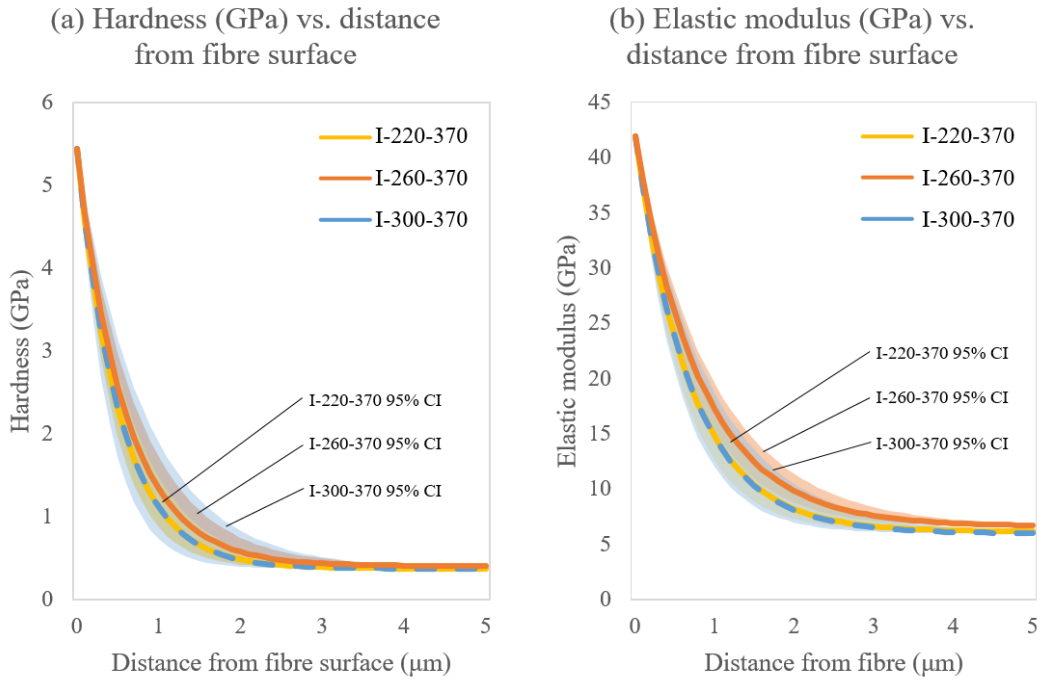

Figure 7.11: (a) Hardness and (b) elastic modulus exponential decay curve fittings to nanoindentation test results of compression-moulded samples, with 95% confidence intervals shown by the shaded regions. Note that the curves for I-220-370 and I-300-370 overlap in both plots.

While gradient differences are subtle and all confidence intervals overlap with the plotted curves, these show that I-260-370 is the laminate with the lowest B_H and B_M (the softest gradients), implying that this sample might have a slightly larger interphase than the other compression-moulded samples. This phenomenon could be explained with general polymeric nucleation theory, along with previous observations made on spherulite sizes of CF/PEKK at the temperatures used for compression moulding in this work. Figure 7.12 has been included to aid with the explanation that follows.

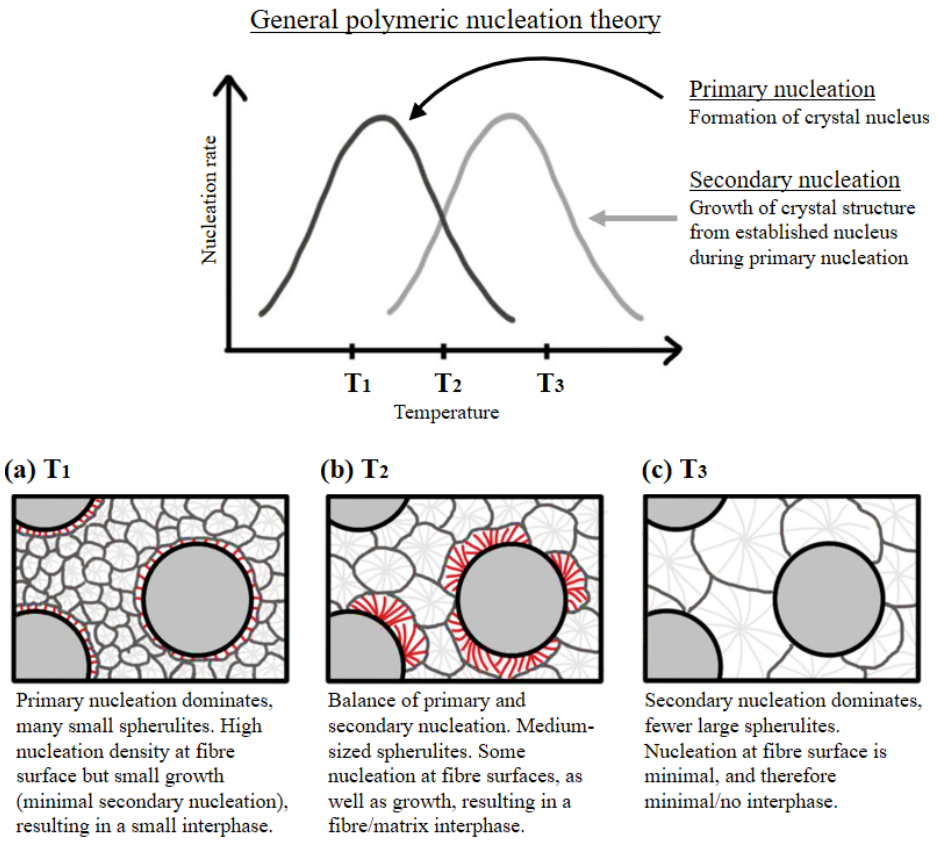

Figure 7.12: Schematic demonstrating the effect of temperature on crystal growth in CF/PEKK, based on general polymeric nucleation theory, where $T_1 < T_2 < T_3$. Red markings indicate crystals growing from the fibre surface.

- At lower crystallisation temperatures (the holding isothermal temperature at which the material is allowed to crystallise), primary nucleation dominates and there is minimal secondary nucleation. This means there will be a higher number of small spherulites, as shown in Figure 7.12a. This is likely to also contribute towards the establishment of crystal nuclei (primary nucleation) on the fibre surface, but crystal growth as a consequence of secondary nucleation will be minimal. This might also result in a transcrystalline region at the fibre/matrix interface where any lamellar growth from the fibre is potentially very short and perpendicular to the fibre surface. This is likely the case for I-220-370, as reported in Chapter 4 where SEM imaging of cryofractured CF/PEKK prepreg samples isothermally crystallised at 220°C showed the formation of small spherulites, with some growth perpendicular to the fibre surface.
- At higher crystallisation temperatures, on the other hand, secondary nucleation dominates, resulting in a lower number of spherulites, but larger in size, as shown in Figure 7.12c. This results in minimal primary nucleation taking place at the fibre surface, and so any crystals growing from the fibre surface will likely resemble spherulites from the bulk. It is therefore unlikely for there to be a significant

interphase present. This is likely to be the case for I-300-370, where large spherulitic structures were observed on CF/PEKK samples isothermally crystallised at 300°C in Chapter 4.

- At the mid-range of crystallisation temperatures, however, there is a balance of both nucleation mechanisms, resulting in medium-sized spherulites. This might also allow for some primary nucleation to take place at the fibre surfaces but also for these nucleation sites to undergo secondary nucleation and develop a crystal structure/transcrystalline interphase between the fibre and the matrix. This is shown in Figure 7.12b, and is likely representative of I-260-370. CF/PEKK prepreg tape isothermally crystallised at 260°C was observed to develop spherulites of intermediate size and perpendicular crystal growth from fibre surfaces, as reported in Chapter 4.

Compression-moulded vs. ATP laminates

Table 7.3 provides B_H and B_M values and their 95% confidence intervals for I-260-370, ATP-380-4-2 and ATP-360-4-2-2mm as example laminates that underwent compression moulding, ATP with T_{nip} = 380°C (with a metallic tool) and T_{nip} = 360°C (with a ceramic tool). Figure 7.13 shows the fitted exponential decay curves for each of these laminates, with their corresponding 95% confidence intervals indicated by the shaded regions. CM-260 properties can be observed to plateau at a slightly higher value than the ATP laminates. This is due to the higher matrix bulk properties that compression-moulded samples possess, as discussed in Section 7.1.3.3.

Table 7.3: Summary of B_H and B_M values and 95% confidence intervals (CI) for the exponential decay modelling of I-260-370, ATP-380-4-2 and ATP-360-4-2-2mm.

Laminate code	I-260-370		ATP-380-4-2 (MID)		ATP-360-4-2-2mm (MID)	
	Value	95% CI	Value	95% CI	Value	95% CI
***B_H* (Hardness)**	1.687	± 0.344	3.816	± 0.592	3.096	± 0.885
***B_M* (Elastic modulus)**	1.200	± 0.197	1.687	± 0.191	0.985	± 0.211

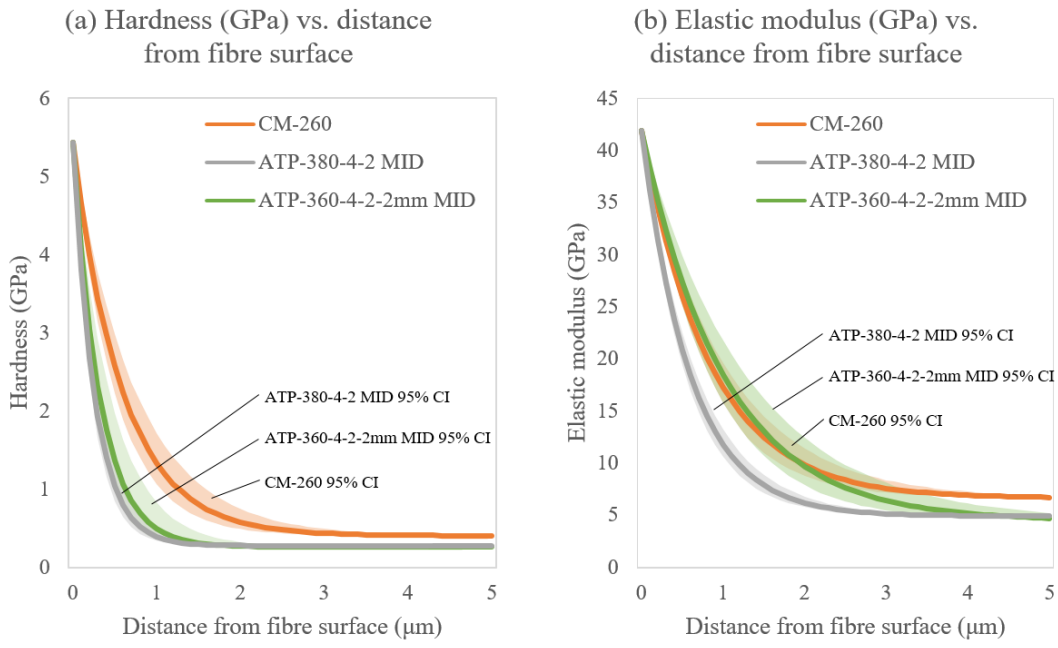

Figure 7.13: (a) Hardness and (b) elastic modulus exponential decay curve fittings to nanoindentation test results of I-260-370, ATP-380-4-2 and ATP-360-4-2-2mm, with confidence intervals shown by the shaded regions.

In the case of the ATP laminates, the fast nature of the manufacturing is not ideal for developing a crystalline structure, as determined by the DSC results in Chapter 6. This is also the case for any fibre-matrix interphase formation. Even in the event of polymer melting during heating, the cooling rates that the material undergoes are too fast for any significant crystallinity to form in this grade of CF/PEKK. Any further crystallinity content developed during heat repasses is likely to take place at a smaller scale in the matrix bulk rather than at the interphase, due to molecular movement being considerably more restricted during annealing than during melt crystallisation. Therefore, any major rearrangement forming an interphase is unlikely.

The effect of overall crystallinity achieved is clearly reflected in the hardness results shown in Figure 7.13a. Hardness is dictated by the load applied as per Eq. (6.4), and is more influenced by surface properties. Both ATP laminates possess a similar hardness response in the fibre/matrix transition region, whereas the compression-moulded laminate (with much higher crystallinity) shows a distinctly longer transition from fibre to matrix properties. This behaviour is not as obvious in Figure 7.13b, where I-260-370and ATP-360-4-2-2mm follow a similar transition path for the first micron from the fibre surface, after which I-260-370 plateaus first to a higher value. The elastic modulus is influenced by the stiffness of the sample, as shown in Eq. (6.3), which is more interlinked with matrix bulk properties rather than surface properties as is the case of hardness. The marginally enhanced fibre-matrix transition behaviour in ATP-360-4-2 might be attributed to the enhanced heat retention with the ceramic tool.

It is worth noting, however, that a more complex evaluation of the modulus may benefit the analysis of interphase regions. As discussed in Section 7.1.2, this property assumes a linear stress-strain relationship. Further investigations on the non-linear relationship between load and displacement (as observed in Figure 7.6) may provide further insight in any differences that the interfaces created by different processing conditions possess.

7.2. Chapter conclusions

In this chapter, nanoindentation experiments were performed that measured the hardness and elastic modulus of samples extracted from compression-moulded and ATP CF/PEKK laminates, reflecting their microstructural differences. A significant difference was observed in the performance of the matrix bulk across the different manufacturing techniques and conditions. A distinct variation in properties of the matrix bulk across the thickness of the ATP laminates was evident, showing the presence of a crystallinity gradient. The presence of a fibre-matrix interphase and its variation under different processing conditions was also observed.

The matrix bulk of the compression-moulded laminates performed better than that of the ATP laminates by 34-53% in hardness and 22-48% in elastic modulus. This is expected, due to the higher crystallinity content of the compression-moulded laminates as a consequence of the longer holding times at crystallisation temperatures. I-260-370, which had been observed to possess the fastest crystallisation rates in Chapter 4, performed the best among all the compression-moulded laminates by 9% in hardness and 8-11% in elastic modulus.

Variation in hardness and elastic modulus across the thickness of the ATP laminates was observed, with these properties being the highest in the middle of the laminate in all instances. This was likely due to the central region of the laminate cross-section achieving higher crystallinity, due to a combined effect of heat repasses from the added layers of material on top, and heat retention of the already laid material, allowing this middle section to hold heat for longer undergoing annealing.

Chapter references

[1] Stokes-Griffin CM, Compston P. The effect of processing temperature and placement rate on the short beam strength of carbon fibre-PEEK manufactured using a laser tape placement process. Compos Part Appl Sci Manuf 2015;78:274–83. https://doi.org/10.1016/j.compositesa.2015.08.008.

[2] Esguerra-Arce I, Martín MI, Pérez-Pastor A, García-Martínez V. Evolution of crystallinity with multiple lamination steps in high performance thermoplastic composites by in-situ consolidation process. Twenty-Second Int Conf Compos Mater 2019.

[3] Kollmannsberger A, Lichtinger R, Hohenester F, Ebel C, Drechsler K. Numerical analysis of the temperature profile during the laser-assisted automated fiber placement of CFRP tapes with thermoplastic matrix. J Thermoplast Compos Mater 2018;31:1563–86. https://doi.org/10.1177/0892705717738304.

[4] Lamontia MA, Gruber MB, Systems A, Drive S, Tierney J, Gillespie JW. Modeling the Accudyne Thermoplastic In Situ ATP Process. Proc SAMPE Conf 2009:8.

[5] Tierney J, Gillespie JW. Modeling of heat transfer and void dynamics for the thermoplastic composite tow-placement process. J Compos Mater 2003;37:1745–68. https://doi.org/10.1177/002199803035188.

[6] Tierney JJ, Gillespie JW. Crystallization kinetics behavior of PEEK based composites exposed to high heating and cooling rates. Compos Part Appl Sci Manuf 2004;35:547–58. https://doi.org/10.1016/j.compositesa.2003.12.004.

[7] Risteska S, Petkoska AT, Samak S, Drienovsky M. Annealing Effects on the Crystallinity of Carbon Fiber-Reinforced Polyetheretherketone and Polyohenylene Laminate Composites Manufactured by Laser Automatic Tape Placement. Mater Sci 2020;26:308–16. https://doi.org/10.5755/j01.ms.26.3.21489.

[8] Saenz-Castillo D, Martín MI, Calvo S, Rodríguez-Lence F, Güemes A. Effect of processing parameters and void content on mechanical properties and NDI of thermoplastic composites. Compos Part Appl Sci Manuf 2019. https://doi.org/10.1016/j.compositesa.2019.03.035.

[9] Chanteli A, Bandaru AK, Peeters D, O'Higgins RM, Weaver PM. Influence of repass treatment on carbon fibre-reinforced PEEK composites manufactured using laser-assisted automatic tape placement. Compos Struct 2020;248:112539. https://doi.org/10.1016/j.compstruct.2020.112539.

[10] Comer AJ, Ray D, Obande WO, Jones D, Lyons J, Rosca I, et al. Mechanical characterisation of carbon fibre–PEEK manufactured by laser-assisted automated-tape-placement and autoclave. Compos Part Appl Sci Manuf 2015;69:10–20. https://doi.org/10.1016/j.compositesa.2014.10.003.

[11] Lamontia MA, Gruber MB. Limitations on mechanical properties in thermoplastic laminates fabricated by two processes: automated thermoplastic tape placement and filament winding. SAMPE Eur Conf Exhib 2005.

[12] Klapperich C, Komvopoulos K, Pruitt L. Nanomechanical Properties of Polymers Determined From Nanoindentation Experiments. J Tribol 2000;123:624–31. https://doi.org/10.1115/1.1330736.

[13] Iqbal T, Briscoe BJ, Yasin S, Luckham PF. Nanoindentation response of poly(ether ether ketone) surfaces-A semicrystalline bimodal behavior. J Appl Polym Sci 2013:n/a-n/a. https://doi.org/10.1002/app.39723.

[14] Christöfl P, Czibula C, Seidlhofer T, Berer M, Macher A, Helfer E, et al. Morphological characterization of semi-crystalline POM using nanoindentation. Int J Polym Anal Charact 2021;26:692–706. https://doi.org/10.1080/1023666X.2021.1968122.

[15] Voyiadjis GZ, Samadi-Dooki A, Malekmotiei L. Nanoindentation of high performance semicrystalline polymers: A case study on PEEK. Polym Test 2017;61:57–64. https://doi.org/10.1016/j.polymertesting.2017.05.005.
[16] Murray BR, Doyle A, Feerick PJ, Semprimoschnig COA, Leen SB, Ó Brádaigh CM. Rotational moulding of PEEK polymer liners with carbon fibre/PEEK over tape-placement for space cryogenic fuel tanks. Mater Des 2017;132:567–81. https://doi.org/10.1016/j.matdes.2017.07.026.
[17] Ray D, Comer AJ, Lyons J, Obande W, Jones D, Higgins RMO, et al. Fracture toughness of carbon fiber/polyether ether ketone composites manufactured by autoclave and laser-assisted automated tape placement. J Appl Polym Sci 2015;132. https://doi.org/10.1002/app.41643.
[18] Gibson RF. A review of recent research on nanoindentation of polymer composites and their constituents. Compos Sci Technol 2014;105:51–65. https://doi.org/10.1016/j.compscitech.2014.09.016.
[19] Gregory JR, Spearing SM. Nanoindentation of neat and in situ polymers in polymer–matrix composites. Compos Sci Technol 2005;65:595–607. https://doi.org/10.1016/j.compscitech.2004.09.001.
[20] Molazemhosseini A, Tourani H, Naimi-Jamal MR, Khavandi A. Nanoindentation and nanoscratching responses of PEEK based hybrid composites reinforced with short carbon fibers and nano-silica. Polym Test 2013;32:525–34. https://doi.org/10.1016/j.polymertesting.2013.02.001.
[21] Gain AK, Oromiehie E, Prusty BG. Nanomechanical characterisation of CF-PEEK composites manufactured using automated fibre placement (AFP). Compos Commun 2022;31:101109. https://doi.org/10.1016/j.coco.2022.101109.
[22] Oromiehie E, Nair V, Short K, Wei T, Bhattacharyya D, Gangadhara Prusty B. Effect of He 2+ Ion Irradiation on the Mechanical Properties of Automated Fibre Placement (Afp) Cf-peek Thermoplastics Composites 2023. https://doi.org/10.21203/rs.3.rs-3027646/v1.
[23] Gaitanelis D, Chanteli A, Worrall C, Weaver PM, Kazilas M. A multi-technique and multi-scale analysis of the thermal degradation of PEEK in laser heating. Polym Degrad Stab 2023;211:110282. https://doi.org/10.1016/j.polymdegradstab.2023.110282.
[24] Gaillard Y, Amiot F. Grid nano-indentation as full-field measurements. Compos Part Appl Sci Manuf 2020;132:105807. https://doi.org/10.1016/j.compositesa.2020.105807.
[25] Hardiman M, Vaughan TJ, McCarthy CT. A review of key developments and pertinent issues in nanoindentation testing of fibre reinforced plastic microstructures. Compos Struct 2017;180:782–98. https://doi.org/10.1016/j.compstruct.2017.08.004.
[26] Ramaswamy K, Modi V, Rao PS, Martin PP, McCarthy CT, O'Higgins RM. An investigation of the influence of matrix properties and fibre–matrix interface behaviour on the mechanical performance of carbon fibre-reinforced PEKK and PEEK composites | Elsevier Enhanced Reader 2023. https://doi.org/10.1016/j.compositesa.2022.107359.
[27] Bedi HS, Tiwari M, Agnihotri PK. Quantitative determination of size and properties of interphases in carbon nanotube-based multiscale composites. Carbon 2018;132:181–90. https://doi.org/10.1016/j.carbon.2018.02.059.
[28] Pharr GM, Oliver WC, Brotzen FR. On the generality of the relationship among contact stiffness, contact area, and elastic modulus during indentation. J Mater Res 1992;7:613–7. https://doi.org/10.1557/JMR.1992.0613.
[29] Hay JC, Bolshakov A, Pharr GM. A critical examination of the fundamental relations used in the analysis of nanoindentation data. J Mater Res 1999;14:2296–305. https://doi.org/10.1557/JMR.1999.0306.
[30] Oliver WC, Pharr GM. An improved technique for determining hardness and elastic modulus using load and displacement sensing indentation experiments. J Mater Res 1992;7:1564–83. https://doi.org/10.1557/JMR.1992.1564.
[31] Shen L, Phang IY, Liu T. Nanoindentation studies on polymorphism of nylon 6. Polym Test 2006;25:249–53. https://doi.org/10.1016/j.polymertesting.2005.09.019.
[32] Viana JC, Cunha AM, Billon N. The effect of the skin thickness and spherulite size on the mechanical properties of injection mouldings. J Mater Sci 2001;36:4411–8.
[33] Starkweather HW, Brooks RE. Effect of spherulites on the mechanical properties of nylon 66. J Appl Polym Sci 1959;1:236–9. https://doi.org/10.1002/app.1959.070010214.

[34] Gruber MB, Lockwood IZ, Dolan TL, Funck SB, Tierney JJ, Simacek P, et al. Thermoplastic in situ placement requires better impregnated tapes and tows. Int SAMPE Tech Conf 2012.

Chapter 8. Thesis contributions and future work

The aim of this body of work was to evaluate any variation in crystallinity across the thickness of CF/PEKK laminates manufactured by ATP. To do this, a series of objectives were identified, outlined in Section 3.2 and addressed throughout this thesis. The work performed has provided new scientific insights into the crystalline nature of PEKK and its performance as a matrix on carbon fibre composites. The following sections will discuss the contributions to the current state of knowledge that this body of work has provided, with Sections 8.1, 8.3 and 8.4 corresponding to objectives 1, 2 and 3 respectively as identified in Section 3.2. Further to this, each section offers recommendations for future work.

8.1. Crystallinity studies

The crystallisation morphology and nature of the studied grade of PEKK and CF/PEKK was successfully characterised in this work. A thorough understanding of kinetics was established through DSC studies encompassing a range of isothermal holds and cooling conditions. Additionally, the application of kinetics modelling allowed for crystallinity development extrapolation across various isothermal temperatures and cooling rates. While this approach had been performed on different grades of unreinforced PEKK [1–3], this had not been explored within the context of CF/PEKK composites. These models hold practical value in industrial manufacturing applications, and can also be integrated in simulation software, where thermal history can be linked to crystallinity development.

Future work to further understand the crystallinity evolution could be done in relation to the fibre content and fibre type of composite samples. As observed in Chapter 4, the composite sample had slower crystallisation kinetics than neat PEKK. Investigating how different fibre volume fractions impact the crystallinity kinetics of PEKK could be beneficial for fast-manufacturing contexts. In addition to that, studying the impact of fibre surface chemistry on the development of transcrystalline phase could add valuable scientific information in this area of research.

Further exploration on the morphology created as a consequence of different isothermal holds could also be beneficial. Observations in this work included cryofracture (Chapter 4) and chemical etching (Chapter 6). Chemical etching procedures are delicate, and may require entire experimental campaigns to optimise etching conditions like solvent concentrations and holding times. The procedures used in this work were based on chemical etching performed on PEEK [4,5]; this same procedure could be further investigated with PEKK to observe different spherulitic sizes, as well as the presence of transcrystallinity.

8.2. Prepreg quality

Admittedly, prepreg quality was a factor that was not explored in depth in this body of work. Due to the primary emphasis on crystallisation studies, laminate manufacturing and testing, coupled with time limitations, this aspect was not given precedence. Nonetheless, prepreg quality plays a significant role in achieving high-quality laminates in fast manufacturing environments concerning void content, interply adhesion and fibre/matrix homogeneity [6,7]. In light of the prepreg observations in Chapter 5, further

research on prepreg surface roughness and matrix distribution (both on the tape surface and within its structure) would contribute towards an improved manufacturing process.

8.3. Manufacturing and mechanical testing of CF/PEKK laminates

In this work, a variety of laminates were successfully manufactured via compression-moulding and ATP for property evaluation. Different parameters were varied to assess the influence of these on crystallinity extent and morphology. Prior research has performed comparable studies concerning CF/PEEK, primarily focused on laminate consolidation, mechanical performance and void content [6,8–11]. While some work has been recently published on CF/PEKK [8,12], it remains sparse and scarcely focuses on the effect of crystallinity.

The novelty of the work presented in this thesis concerning the compression-moulded cycles lies in the utilisation of different thermal cycles and facilitating the development of different crystal morphologies. This is then followed by matrix-dominated property testing, in an effort to observe the impact of different crystallinity contents and morphologies on performance. Literature has not investigated the impact of different crystal morphologies on the mechanical performance of CF/PEKK.

The variation of different ATP parameters also introduced a novel aspect to the work performed on CF/PEKK, particularly considering the limited existing literature on this material. The study presented in this thesis established a scientific foundation for future investigation. There is scope for further experimentation by further varying the parameters, particularly the nip and tool temperatures, to delve deeper into potential benefits, not only for crystallinity development, but also consolidation quality.

Expanding on this, further investigation into the use of a heated tool for manufacturing ATP laminates would be beneficial. As described in Chapter 5 and Appendix C, the challenges faced during manufacturing trials led to manufacturing exclusively on a cold tool. However, drawing from insights in literature, there is a strong indication that that integrating a heated tool into the fabrication of CF/PEKK laminates would benefit the crystallinity development of the laminates and their mechanical performance. This aspect is a strong recommendation for future work.

The performed mechanical testing primarily focused on matrix-dominated properties, namely 0° flexural, 90° flexural, ILSS and IPS testing. While these tests did not produce significant differences in performance across the different compression-moulded cycles or across the ATP laminates, they did highlight substantial differences between the two manufacturing techniques. In order to evaluate any potential differences within each distinct manufacturing technique, further testing is encouraged. This could encompass compression testing, drop-weight impact testing and compression after impact testing; as well as further investigation into IPS testing, including fibre rotation measurements during testing. Such mechanical testing may highlight further differences regarding the performance of different crystal morphologies across the different compression-moulded laminates, as well as ATP laminates once a further range of parameters are tested. Further evaluation of voids (namely their shape and size) as a consequence of the different processing conditions may also provide valuable insight into the mechanical performance of the laminates.

Further to this, water absorption and chemical resistance experiments may also shed light on differences in performance arising from different morphologies and crystallinity levels. Such analyses could be performed using chemicals commonly used in aerospace applications such as aviation fuels, hydraulic fluids or de-icing agents.

In order to better understand the reasons behind the crystal structures developed and the mechanical testing results, tracking of temperature variation within the material during manufacturing would be beneficial. Implementing thermal imaging equipment online during ATP manufacturing in particular may help towards this understanding, as well as thermal modelling of the heat retention and dissipation of the material during part manufacturing. This would also contribute towards a better understanding of the different crystallinities developed across laminates' thickness.

Another aspect of PEKK that could be further investigated to better understand its behaviour is the impact of strain rate in its mechanical response. The viscoelastic nature of PEKK has been briefly mentioned throughout this work, becoming increasingly obvious in the more amorphous samples (for example during ILSS testing of ATP-manufactured laminates). Performing testing of similarly manufactured laminates at different strain rates may provide further insight into CF/PEKK viscoelastic response as a consequence of different crystallinity levels.

8.4. Nanoindentation work

Nanoindentation was conducted on different CF/PEKK samples to evaluate the micromechanical properties of these specimens. This successfully provided a method to indirectly measure crystallinity extent in samples, as was observed by the difference in performance between compression-moulded and ATP samples. These results aligned well with previous crystallinity measurements. Moreover, a subtle variation in properties across the thickness of the ATP laminates was observed, potentially showing a crystallinity gradient. This phenomenon could be attributed to differences in thermal history throughout the thickness as a consequence of the nature of ATP manufacturing, resulting in differences in the local crystallinity. Some nanoindentation work has been performed on various polymers reflecting the effect of crystallinity on micromechanical property performance (including PEKK) [13–17], as well as grid-nanoindentation work on CF/PEKK as an exercise to measure heterogeneous properties in materials [18]. To the author's knowledge, however, no nanoindentation work has been performed on CF/PEKK composites to date aimed at specifically characterising discrepancies in crystallinity development across different laminates, or crystallinity gradients across the laminate thickness.

Nanoindentation was also used to understand the fibre/matrix interface by identifying the property transitions from the fibre to the matrix bulk. This evaluation encompassed all samples and locations as per the matrix bulk properties described in Chapter 7. However, due to time constraints during the experimental phase, a portion of the results did not provide conclusive evidence. As discussed in Appendix H, where these results are presented, this may be due to the limited magnitude of parameter variation in ATP manufacturing, insufficient to generate discernible differences at the interface. This could potentially change with a wider range in ATP parameters.

Another aspect which may positively impact fibre/matrix interface testing involves modifying experimental parameters. Reducing the nanoindentation depth would minimise any overlap of the indenter tip with the fibre, particularly when testing matrix regions close to the fibre surface. This may result in more obvious differences in transition regions attributable to parameter differences within the context of ATP manufacturing. Additionally, using nanoindentation equipment that would allow for exact indentation placement could result in a better data distribution of the interface region, reducing the inherent randomness of indent locations obtained from array testing performed in this work.

As mentioned towards the end of the discussion at the end of Section 7.2.1.4, investigating the non-linear relationship between load and displacement, due to PEKK's viscoelastic behaviour, may provide further insight regarding the differences in interphases across different samples and locations. It may also be of interest to perform testing at different strain rates in nanoindentation testing, to assess the impact of this on different crystal morphologies and phases of the composite.

Further to the above, alternative experimental approaches could be explored as a means to indirectly measure crystallinity. Confocal Raman spectroscopy could be used to evaluate the crystallinity extent across different samples and sample locations, similar to previous work conducted on PEEK [19,20]. Additionally, atomic force microscopy (AFM) could be employed to evaluate distinct local moduli, potentially imaging spherulitic entities as well.

Chapter references

[1] Quiroga Cortés L, Caussé N, Dantras E, Lonjon A, Lacabanne C. Morphology and dynamical mechanical properties of poly ether ketone ketone (PEKK) with meta phenyl links. J Appl Polym Sci 2016;133:1–10. https://doi.org/10.1002/app.43396.

[2] Choupin T, Fayolle B, Régnier G, Paris C, Cinquin J, Brulé B. Isothermal crystallization kinetic modeling of poly(etherketoneketone) (PEKK) copolymer. Polymer 2017;111:73–82. https://doi.org/10.1016/j.polymer.2017.01.033.

[3] Choupin T, Fayolle B, Régnier G, Paris C, Cinquin J, Brulé B. A more reliable DSC-based methodology to study crystallization kinetics: Application to poly(ether ketone ketone) (PEKK) copolymers. Polymer 2018;155:109–15. https://doi.org/10.1016/j.polymer.2018.08.060.

[4] Blundell DJ, Crick RA, Fife B, Peacock J, Keller A, Waddon A. Spherulitic morphology of the matrix of thermoplastic PEEK/carbon fibre aromatic polymer composites. J Mater Sci 1989;24:2057–64. https://doi.org/10.1007/BF02385421.

[5] Bassett DC, Olley RH, Al Raheil IAM. On crystallization phenomena in PEEK. Polymer 1988;29:1745–54. https://doi.org/10.1016/0032-3861(88)90386-2.

[6] Comer AJ, Ray D, Obande WO, Jones D, Lyons J, Rosca I, et al. Mechanical characterisation of carbon fibre–PEEK manufactured by laser-assisted automated-tape-placement and autoclave. Compos Part Appl Sci Manuf 2015;69:10–20. https://doi.org/10.1016/j.compositesa.2014.10.003.

[7] Gruber MB, Lockwood IZ, Dolan TL, Funck SB, Tierney JJ, Simacek P, et al. Thermoplastic in situ placement requires better impregnated tapes and tows. Int SAMPE Tech Conf 2012.

[8] Esguerra-Arce I, Martín MI, Pérez-Pastor A, García-Martínez V. Evolution of crystallinity with multiple lamination steps in high performance thermoplastic composites by in-situ consolidation process. Twenty-Second Int Conf Compos Mater 2019.

[9] Stokes-Griffin CM, Compston P. The effect of processing temperature and placement rate on the short beam strength of carbon fibre-PEEK manufactured using a laser tape placement process. Compos Part Appl Sci Manuf 2015;78:274–83. https://doi.org/10.1016/j.compositesa.2015.08.008.

[10] Chanteli A, Bandaru AK, Peeters D, O'Higgins RM, Weaver PM. Influence of repass treatment on carbon fibre-reinforced PEEK composites manufactured using laser-assisted automatic tape placement. Compos Struct 2020;248:112539. https://doi.org/10.1016/j.compstruct.2020.112539.

[11] Denault J, Dumouchel M. Consolidation Process of PEEK/Carbon Composite for Aerospace Applications. Adv Perform Mater 1998;5:83–96. https://doi.org/10.1023/A:1008638105370.
[12] Hoang V-T, Kwon B-S, Sung J-W, Choe H-S, Oh S-W, Lee S-M, et al. Postprocessing method-induced mechanical properties of carbon fiber-reinforced thermoplastic composites. J Thermoplast Compos Mater 2023;36:432–47. https://doi.org/10.1177/0892705720945376.
[13] Iqbal T, Briscoe BJ, Yasin S, Luckham PF. Nanoindentation response of poly(ether ether ketone) surfaces-A semicrystalline bimodal behavior. J Appl Polym Sci 2013:n/a-n/a. https://doi.org/10.1002/app.39723.
[14] Christöfl P, Czibula C, Seidlhofer T, Berer M, Macher A, Helfer E, et al. Morphological characterization of semi-crystalline POM using nanoindentation. Int J Polym Anal Charact 2021;26:692–706. https://doi.org/10.1080/1023666X.2021.1968122.
[15] Voyiadjis GZ, Samadi-Dooki A, Malekmotiei L. Nanoindentation of high performance semicrystalline polymers: A case study on PEEK. Polym Test 2017;61:57–64. https://doi.org/10.1016/j.polymertesting.2017.05.005.
[16] Murray BR, Doyle A, Feerick PJ, Semprimoschnig COA, Leen SB, Ó Brádaigh CM. Rotational moulding of PEEK polymer liners with carbon fibre/PEEK over tape-placement for space cryogenic fuel tanks. Mater Des 2017;132:567–81. https://doi.org/10.1016/j.matdes.2017.07.026.
[17] Ray D, Comer AJ, Lyons J, Obande W, Jones D, Higgins RMO, et al. Fracture toughness of carbon fiber/polyether ether ketone composites manufactured by autoclave and laser-assisted automated tape placement. J Appl Polym Sci 2015;132. https://doi.org/10.1002/app.41643.
[18] Gaillard Y, Amiot F. Grid nano-indentation as full-field measurements. Compos Part Appl Sci Manuf 2020;132:105807. https://doi.org/10.1016/j.compositesa.2020.105807.
[19] Stuart BH. Polymer crystallinity studied using Raman spectroscopy. Vib Spectrosc 1996;10:79–87. https://doi.org/10.1016/0924-2031(95)00042-9.
[20] Ellis G, Naffakh M, Marco C, Hendra PJ. Fourier transform Raman spectroscopy in the study of technological polymers Part 1: poly(aryl ether ketones), their composites and blends. Spectrochim Acta A Mol Biomol Spectrosc 1997;53:2279–94. https://doi.org/10.1016/s1386-1425(97)00168-6.

Chapter 9. Thesis conclusions

This thesis has explored the use of PEKK as a matrix in carbon-fibre composites destined for high-performance applications, with the aim of evaluating any variation in crystallinity across the thickness of CF/PEKK laminates manufactured via ATP. A literature review was initially performed to assess the state of the art, highlighting the limited research available for PEKK, and particularly CF/PEKK composites. Based on this review, a series of objectives were identified in order to achieve the aim of this work:

1. Establish an understanding of the crystallisation kinetics and morphology of PEKK;
2. Evaluate the impact of different ATP parameters on the mechanical performance of CF/PEKK laminates; and
3. Study any variation in micromechanical properties in different CF/PEKK laminates, as well as across their thickness, to indirectly evaluate the crystallinity content of the sample.

These have been addressed in the main body of this work, the main conclusions of which are summarised below.

Crystallisation studies were performed on unreinforced PEKK and CF/PEKK samples, in order to understand the effect of thermal history on the crystallisation kinetics and morphology of the material. It was found that isothermal holding temperatures between 240-260°C resulted in the fastest crystallisation kinetics, with spherulitic size varying according to general polymeric nucleation theory (a higher number of smaller spherulites at lower temperatures, and a lower number of larger spherulites at higher temperatures). The presence of carbon fibres slowed down crystallisation kinetics and changed the proportion at which the primary and secondary crystallisation phases were developed. The presence of crystallinity enhanced the fibre/matrix interfacial adhesion, as shown by cryofractured samples. Crystallisation kinetics were successfully modelled with Avrami-based equations reflecting the dual crystallisation nature of PEKK, allowing for the prediction of crystallisation evolution at other isothermal holds and cooling rates. A summary of the results can be seen in Figure 9.1. Additionally, time-temperature-transformation diagrams, showing crystallinity development with respect to thermal history and time, can be found in Section 4.2.5 for both isothermal and dynamic conditions (Figure 4.22 and Figure 4.23).

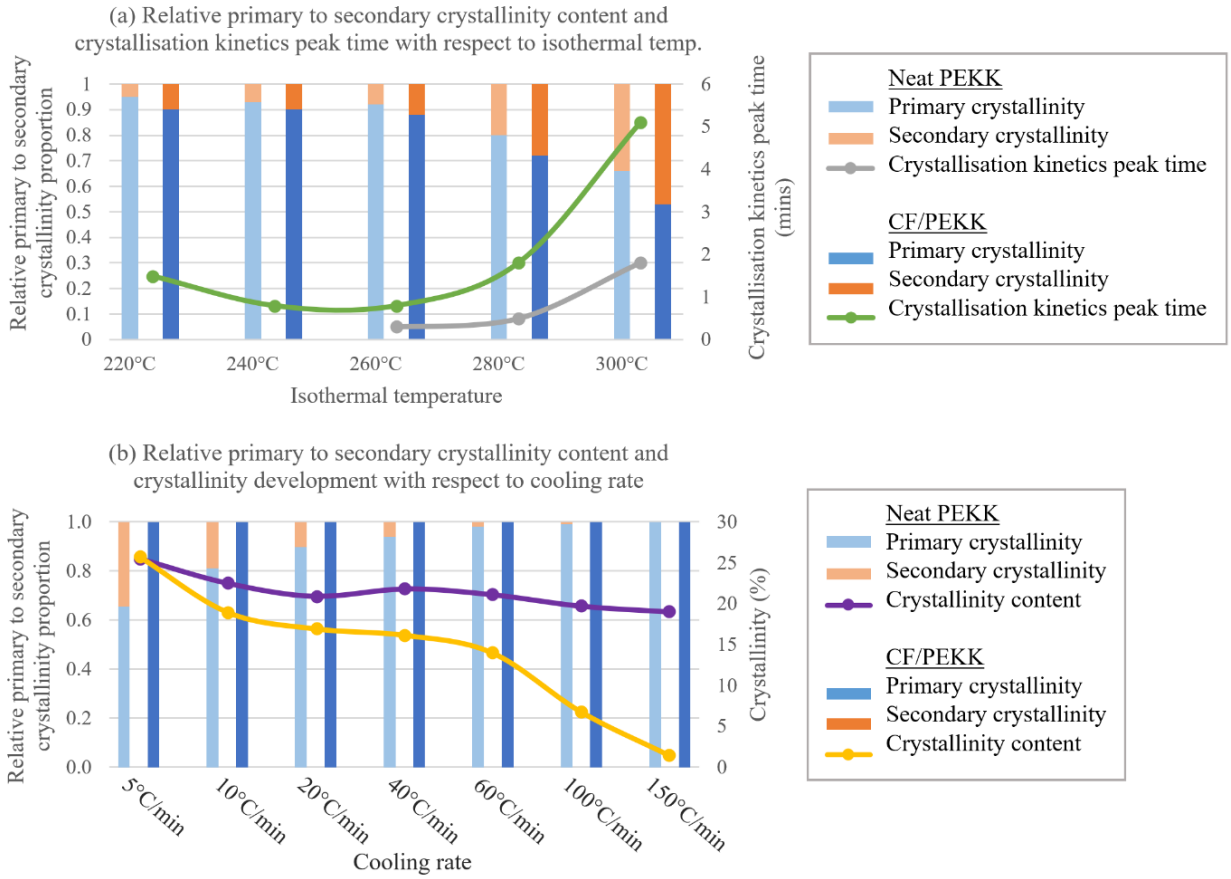

Figure 9.1: Summary of the key findings in Chapter 4. Plots show primary to secondary crystallisation proportions present in unreinforced PEKK and CF/PEKK samples when undergoing (a) different isothermal holds and (b) different cooling rates. Additionally, (a) shows time for peak crystallisation kinetics at each isothermal hold (where all samples fully crystallised), and (b) shows total crystallinity development.

A series of compression-moulded laminates were manufactured based on the aforementioned crystallisation studies performed, along with ATP laminates in which nip temperature, lay-down speed and roller pressure were varied. Compression-moulded laminates were found to have low void contents and were crystallised to the highest extent, which was not the case for the ATP laminates. These laminates then underwent mechanical testing, where the ATP laminates demonstrated an overall lower performance compared to the compression-moulded laminates. Morphological variations across the different compression-moulded laminates did not reflect in the studied mechanical properties. In the case of ATP laminates, using a ceramic tool with a better heat retention than a metal tool, and higher nip temperatures had the most noticeable effect on the properties. A summary of these results can be seen in Figure 9.2.

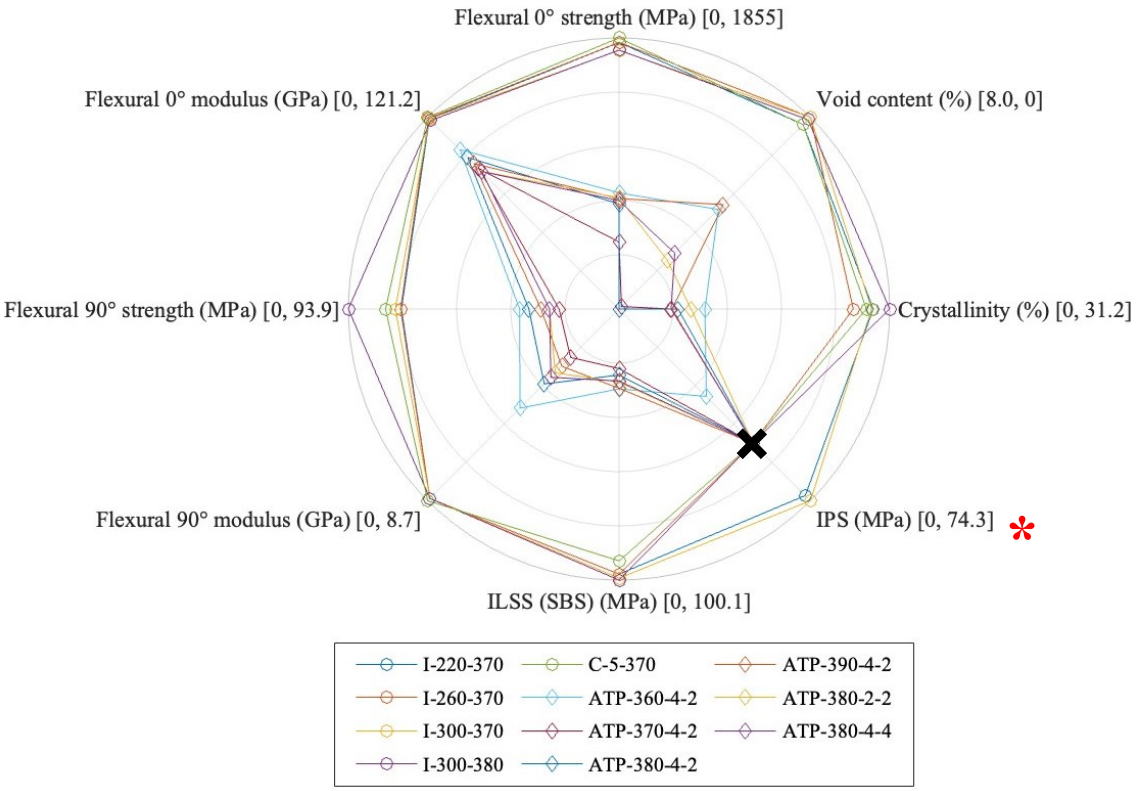

Figure 9.2: Radar chart summarising the key findings of Chapter 6. Axis minimum and maximum values are provided in square brackets for scaling purposes.

* *The IPS values marked with an **X** are for graphing purposes only (these laminates did not undergo IPS testing).. IPS results for I-220-270 and I-300-370 are ATP laminates post-processed via compression moulding (please refer to Chapter 5 for further details on manufacturing of laminates ATP-360-4-2-P220 and ATP-360-4-2-P300).*

While mechanical testing can provide an indication of crystallinity, other factors such as laminate consolidation can also have an impact on mechanical performance. Macromechanical testing also cannot provide insight into variation in crystallinity across a laminate's thickness. This is particularly likely to be the case in ATP-manufactured laminates, where the material undergoes fast cooling and repeated annealing, resulting in differences in the thermal history throughout the laminate's thickness. Nanoindentation experiments were therefore performed to indirectly evaluate local crystallinity via micromechanical property measurement across different laminates, namely hardness and elastic modulus. Property variations across the thickness of ATP laminates were also studied, as well as the presence of a fibre/matrix transition region. As with the mechanical testing, a significant difference was observed between the performance of the compression-moulded and ATP manufactured laminates, due to the higher crystallinity of the compression-moulded laminates. The variation in properties across the thickness of the ATP laminates was observed, with the middle of the laminates exhibiting the highest properties. This is likely due to this region developing the highest crystallinity as a consequence of the combined effect of heat retention of the already laid material and the heat repasses from the added layer of material. A summary of these can be found in Figure 9.3. A transition in response from the fibre to the matrix bulk was observed across all samples via nanoindentation testing.

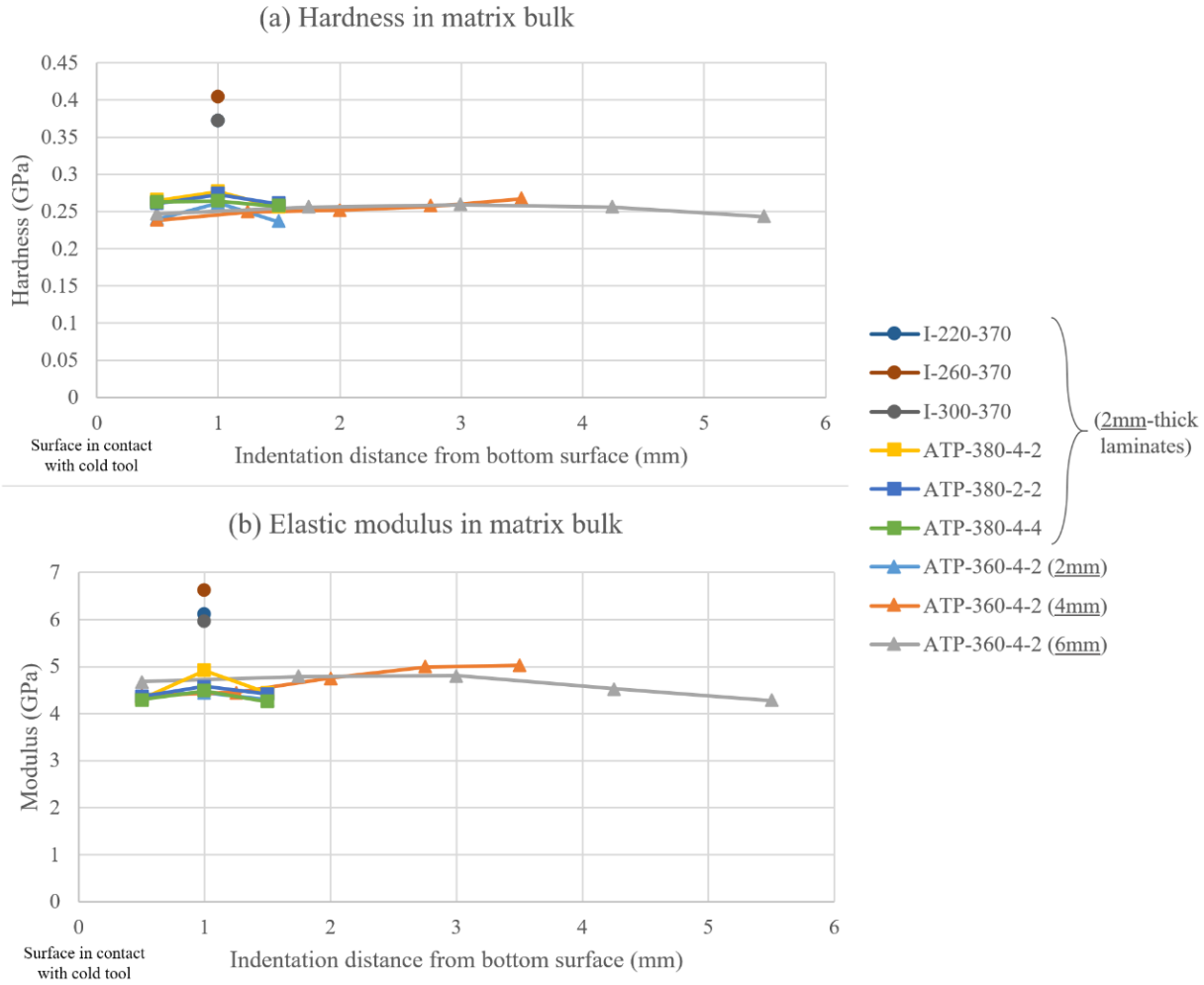

Figure 9.3: Summary of the key findings in Chapter 7. Plots show CF/PEKK matrix bulk properties tested via nanoindentation. The results are across different laminates (as shown in the figure legend) and at different points across the laminate thicknesses (indicated in the x axis).

Overall, the work presented in this thesis establishes a scientific basis for the production of CF/PEKK laminates intended for high-performance applications. The research develops a thorough understanding of the crystallisation nature of the polymer and the influence of different processing conditions (and therefore the thermal history the composite undergoes) on its mechanical performance. Furthermore, micromechanical property characterisation via nanoindentation was used to indirectly measure and compare crystallinity differences across laminates manufactured via different techniques; as well as offering a method to indirectly observe crystallinity variation across the thickness of laminates.

The findings of this study will contribute towards further investigating the effects of varying ATP parameters and improving the manufacturing process, resulting in laminates of superior quality. Furthermore, the research has potential to offer novel processes to control patterns serving micromechanical properties.

Appendix A. Calculating fibre volume fraction

A.1. Derivation

Step 1: Finding fibre volume fraction in terms of density and rearranging for ρ_T.

$$m_C = m_F + m_M$$

$$\rho_C V_C = \rho_F V_F + \rho_M V_M$$

$$\rho_C V_C = \rho_F V_C \varphi_F + \rho_M V_C (1 - \varphi_F)$$

$$\rho_C = \rho_F \varphi_F + \rho_M (1 - \varphi_F)$$

Step 2: Finding fibre mass fraction in terms of density and rearranging for ρ_C.

$$V_C = V_F + V_M$$

$$\frac{m_C}{\rho_C} = \frac{m_F}{\rho_F} + \frac{m_M}{M}$$

$$\frac{m_C}{\rho_C} = \frac{m_C \psi_F}{\rho_F} + \frac{m_C (1 - \psi_F)}{\rho_M}$$

$$\frac{1}{\rho_C} = \frac{\psi_F}{\rho_F} + \frac{(1 - \psi_F)}{\rho_M}$$

$$\frac{1}{\rho_C} = \frac{\psi_F \rho_M + (1 - \psi_F)\rho_F}{\rho_F \rho_M}$$

$$\rho_C = \frac{\rho_F \rho_M}{\psi_F \rho_M + (1 - \psi_F)\rho_F}$$

Step 3: Equating ρ_C and rearranging for φ_F:

$$\rho_F \varphi_F + \rho_M (1 - \varphi_F) = \frac{\rho_F \rho_M}{\psi_F \rho_M + (1 - \psi_F)\rho_F}$$

$$\rho_F \varphi_F + \rho_M - \rho_M \varphi_F = \frac{\rho_F \rho_M}{\psi_F \rho_M + (1 - \psi_F)\rho_F}$$

$$\varphi_F (\rho_F - \rho_M) = \frac{\rho_F \rho_M}{\psi_F \rho_M + (1 - \psi_F)\rho_F} - \rho_M$$

$$\varphi_F = \left[\frac{\rho_F \rho_M}{\psi_F \rho_M + (1 - \psi_F)\rho_F} - \rho_M\right] \times \frac{1}{(\rho_F - \rho_M)}$$

A.2. Calculations

- Known values: fibre mass fraction ψ_F, fibre density ρ_F = 1.79g/cc, polymer density ρ_M = 1.28g/cc.
- Value to find: fibre volume fraction φ_F.
- V = volume; m = mass; ρ = density.
- Subscripts C, F and M stand for "composite", "fibre" and "matrix" respectively.

Tape used for compression-moulding, ψ_F = 68.4%:

$$\varphi_F = \left[\frac{1.79 \times 1.28}{1.28 \times 0.684 + 1.79(1 - 0.684)} - 1.28\right] \times \frac{1}{(1.79 - 1.28)} = 0.608 = \mathbf{60.8}\%$$

1st tape used for ATP manufacturing, ψ_F = 67.0%:

$$\varphi_F = \left[\frac{1.79 \times 1.28}{1.28 \times 0.670 + 1.79(1 - 0.670)} - 1.28\right] \times \frac{1}{(1.79 - 1.28)} = 0.592 = \mathbf{59.2}\%$$

2nd tape used for ATP manufacturing, ψ_F = 65.5%:

$$\varphi_F = \left[\frac{1.79 \times 1.28}{1.28 \times 0.655 + 1.79(1 - 0.655)} - 1.28\right] \times \frac{1}{(1.79 - 1.28)} = 0.575 = \mathbf{57.5}\%$$

Appendix B. Calculating LTE:HTE ratio for overlapping endotherms

In the case of two endotherms overlapping, as shown in Figure B.1, the area corresponding to each endotherm was calculated by drawing a line perpendicular to the baseline (CD), crossing the curve at its inflection point between the two peaks.

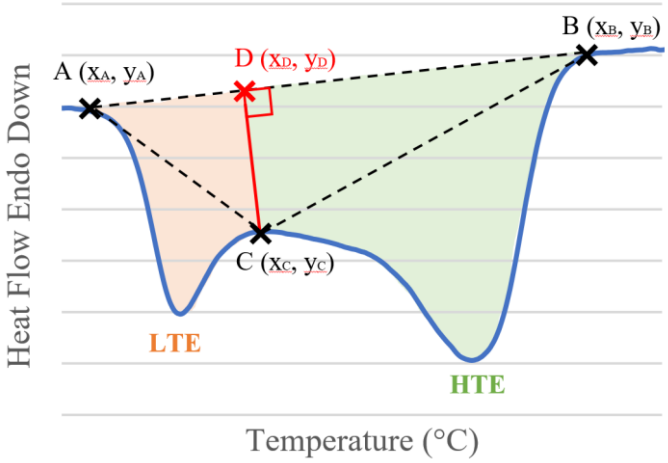

Figure B.1: Example of overlapping double endotherm, with LTE and HTE areas coloured in orange and green respectively.

The x and y coordinates of points A, B and C can be found using the Pyris software used to analyse all DSC curves in Chapter 4. With these, the area under lines AC and BC are also known (white regions in Figure B.2), as well as the area under line AB (entire area of the double endotherms). Subtracting the enthalpies corresponding to AC and BC from AB gives us the enthalpy value corresponding to triangle ABC, shown in yellow in Figure B.2.

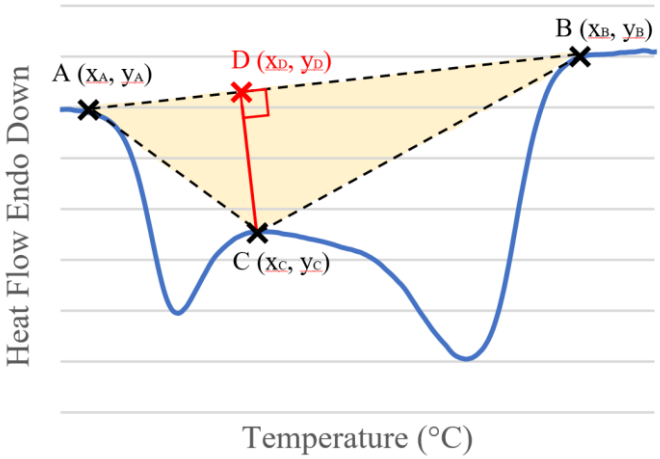

Figure B.2: Double endotherm diagram showing the breakdown of different regions within the double endotherm.

Calculating the areas of triangles ACD and BCD using the known x and y coordinates will provide the area fractions of the triangle ABC that correspond to the LTE and HTE. These can then be used to calculate the enthalpies that correspond to areas ACD and BCD. D is unknown at this point, but lengths AD, BD and CD can be found following these steps:

- In order to calculate the area, lengths AC, BC and AB have to be found first using the known coordinates to draw imaginary right-angled triangles (shown with green, orange and grey dotted lines in X), making the lengths of interest the hypotenuse of the triangle. The Pythagoras theorem, $x^2 = y^2 + z^2$, can then be used to find these lengths.

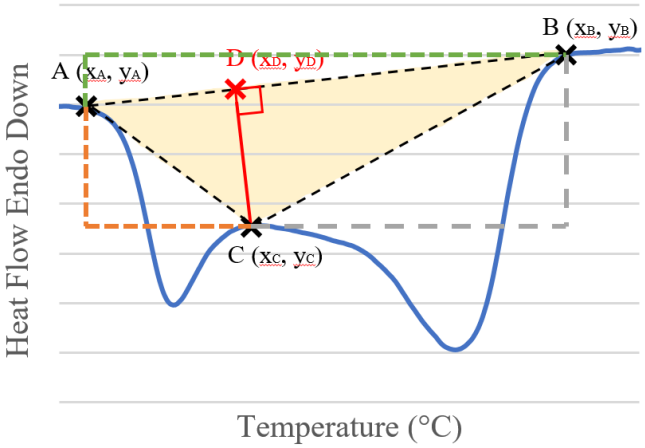

Figure B.3: Double endotherm diagram showing imaginary lines to aid in the calculation of lengths AB, AC and BC.

- Then, angle A can be found using the cosine rule: $BC = \sqrt{AB^2 + AC^2 - 2(AB)(AC)cos\alpha}$.
- Lengths CD, AD and BD can then be found using the relationships between the angles and sides of a right triangle (see below), using line CD to form right-angled triangles with lines AD, AC, BD and BC:

$$\sin(\theta) = \frac{opposite}{hypotenuse}; \cos(\theta) = \frac{adjacent}{hypotenuse}; \text{ and } \tan(\theta) = \frac{opposite}{adjacent}$$

The area of triangles ACD and BCD can then be found using 0.5 x base x perpendicular height, with the bases being AD and BD, and the perpendicular height being CD. These areas are shown in orange and green respectively in Figure B.4.

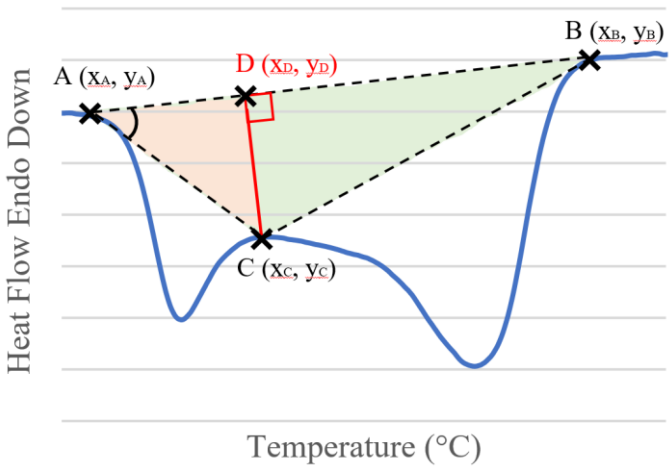

Figure B.4: Double endotherm diagram showing the triangle regions that correspond to the LTE (orange) and HTE (green).

In order to find the enthalpy that corresponds to ACD and BCD, the **area fraction** is needed. This can be easily found by dividing ACD (or BCD) by the total area of the triangle ABC (given by 0.5 x length AB x length CD).

We can then multiply these area fractions by the enthalpy value corresponding to triangle ABC to calculate the enthalpy values of ACD and BCD.

- Adding enthalpy values of ACD and enthalpy below line AC provides the enthalpy value of LTE.
- Adding enthalpy values of BCD and enthalpy below line BC provides the enthalpy value of HTE.

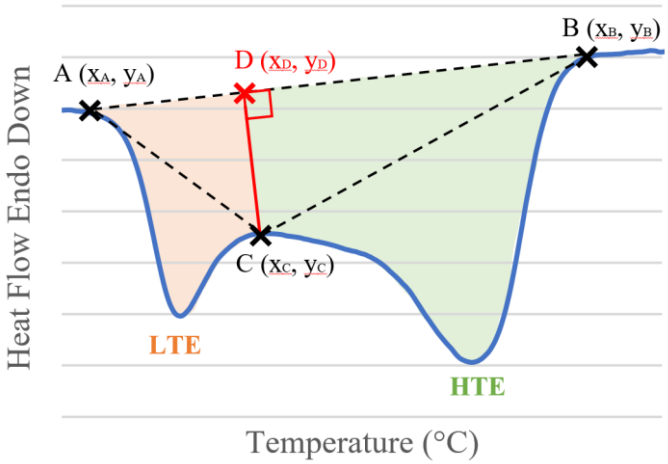

Figure B.5: Example of overlapping double endotherm, with LTE and HTE areas coloured in orange and green respectively.

Appendix C. Manufacturing trials and challenges

C.1. Initial ATP manufacturing trials

During the first manufacturing campaign, initial trials with nip temperature (T_{nip}), lay-down speed and roller pressure were based on previous ATP manufacturing performed at the University of Limerick with CF/PEEK (380°C, 4m/min and 2 bar). Initially, a cuboid tool was to be used as per Figure C.1a, where the cuboid would rotate and the prepreg tape would be wrapped around it. Laminates would then be extracted by trimming the edges of the manufactured CF/PEKK cuboids, along the dotted red lines shown in Figure C.1b. An example of this with previously manufactured CF/PEEK laminates is shown in Figure C.1c.

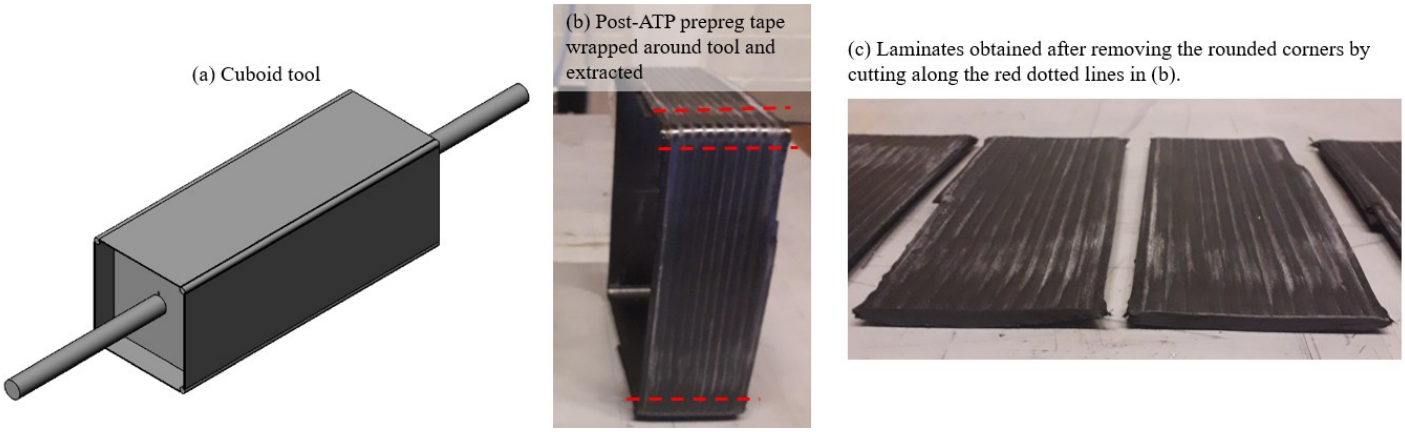

Figure C.1: Cuboid tool for laminate manufacturing, including (a) tool, (b) part obtained with said tool via ATP manufacturing, and (c) resulting laminates obtained after trimming rounded edges.

Initial trials of this showed very large spikes in laser power and therefore very high T_{nip} values close to the rounded edges, and so the initially proposed T_{nip} value of 380°C was deemed too high. Further trialling at T_{nip} = 360°C provided better temperature control close to the cuboid edges. However, after some lay-up trials, a flat tool was suggested for the manufacture of laminates. Therefore, a flat, unheated ceramic tool was used, and the T_{nip} = 360°C was kept for this first batch of manufacturing.

C.2. Issues with ATP manufacturing with a heated tool

During the second manufacturing campaign, it was initially decided that the effect of using a heated tool on the performance of ATP laminates was to be trialled along with the rest of the parameters discussed in Section 5.3.2. However, these trials resulted in significant issues with the adhesion of layers. Based on the crystallisation studies from Chapter 4, it was decided that a tool temperature of 260°C may result in the fastest crystallisation. At this temperature, it was not possible to use the double-sided tape used with the unheated tool, and therefore PEI film was used to hold the first layer in place during lay-up. The first layer was successfully placed. When laying the second layer however, the first tape was placed successfully, but once the roller came down to place the second tape, the weight of the consolidation roller forced the first tape to move and lift. This was the case for the remaining tapes in

layer 2. The ATP operator attempted different tool temperatures as well as different nip temperatures without any success.

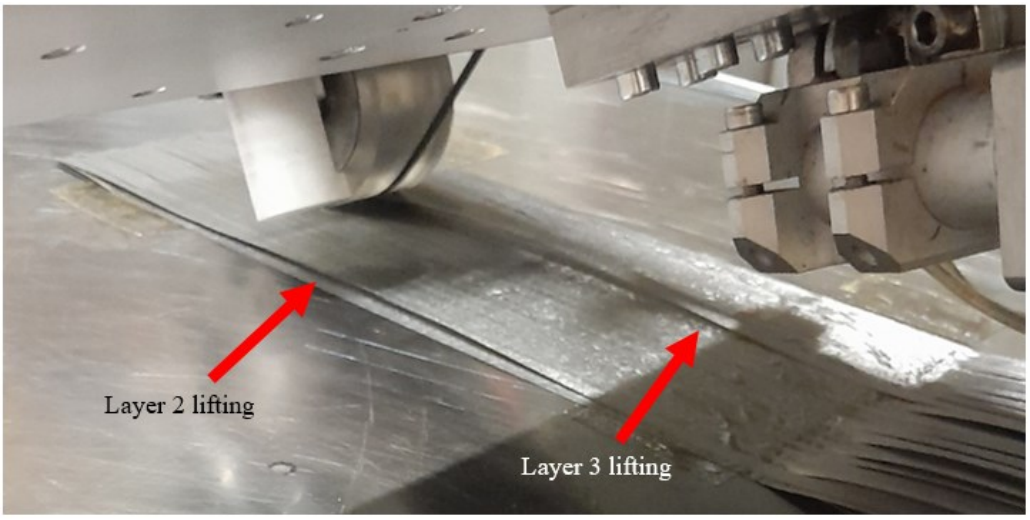

Figure C.2: Image of 3rd layer being laid during ATP laminate manufacturing with T_{nip} = 380°C and tool temperature of 260°C. Lifting of tapes in layers 2 and 3 is highlighted wit harrows.

These trials, along with other ongoing work at the University of Limerick, caused significant delays to this batch of manufacturing, so it was finally decided to manufacture all laminates keeping the tool unheated. When doing this however, the laminates were manufactured on a mild steel tool instead of the ceramic tool that was used in the first manufacturing campaign. This was not intentional, now that the thermal properties of these two materials are different, and this causes the laminates from the two different campaigns to not be comparable.

Appendix D. Process data sheets

UD ATP-360-4-2

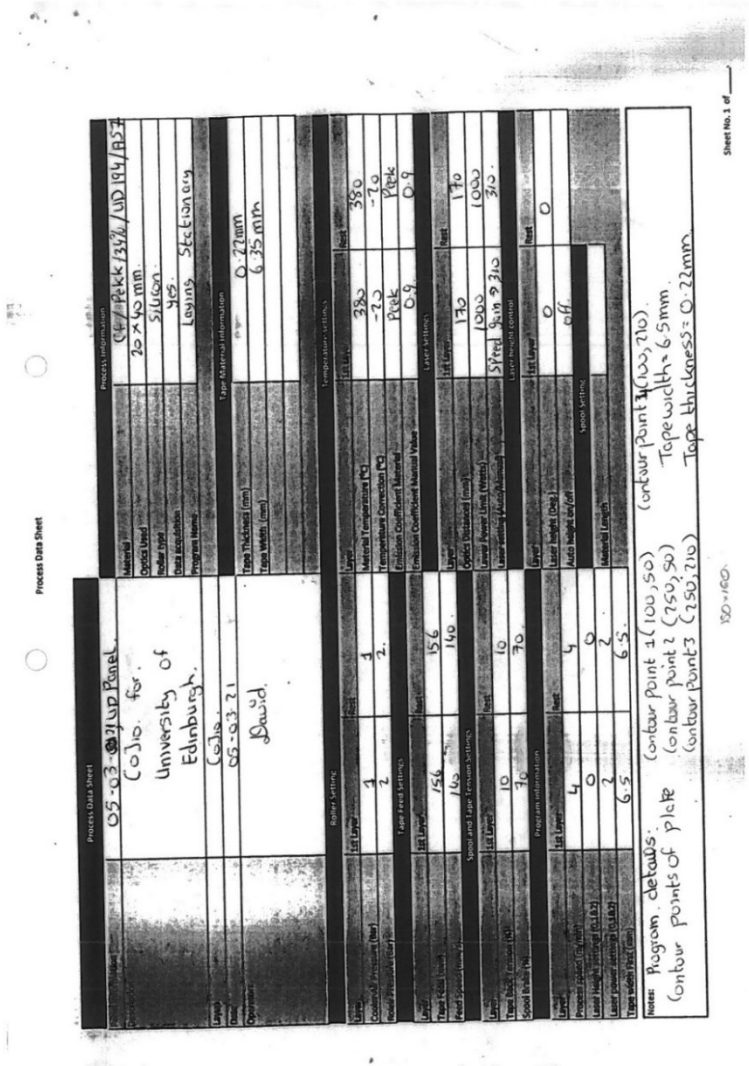

Process Data Sheet

05-03-21 UD Panel

Colin. for. University of Edinburgh.

Colin.

05-03-21

David.

Process information: CF/PEKK/37%/UD 194/AS7; 250 x 400 mm; Silicon; Yes; Layup Section 0.9

Tape Material Information: Tape Thickness (mm) 0.22mm; Tape Width (mm) 6.35 mm

Roller Setting: 1st Layer 1; 2.

Temperature Settings: 1st Layer; Material Temperature (°C) 380; Temperature Correction (°C) -7.0; Emissivity Coefficient Used Peek; Emissivity Coefficient Material Value 0.9

Layer Feed Settings: 1st Layer 156; 140

Layer Settings: 1st Layer 170; Optics Distance (mm) 1000; Laser Power Unit (Watts) Steel 340 & 340

Spool and Tape Tension Settings: 1st Layer 10; 30

Layer Height Control: 1st Layer 0

Program Information: 1st Layer; Process protect (y/n/aut) 4; Laser Height Control (y/n) 0; Laser power control (y/n/aut) 2; Tape Width Trim (mm) 6.5

Laser On/Off: 1st Layer 0; Auto Mode at layer eff

Spool Setting: Material Length

Notes: Program details: Contour Point 1 (100,50) Contour Point 2 (750,50) Contour Point 3 (750,210) Contour Point 4 (100,210). Tape width = 6.5mm. Tape thickness = 0.22mm.

Contour points of plate

Sheet No. 1 of ____

150 x 160

Layup of panel

Ply	Orientation	Offset	Comments
1	0	0	
2	0	50%	
3	0	0	
4	0	50%	
5	0	0	
6	0	50%	
7	0	0	
8	0	50%	
9	0	0	
10	0	50%	

Notes: Panel 05-03-21, UD Panel.

Program data:

flyheight = 120 mm.

Runup length = 150mm

ramp = 30mm

Initialising length = 40mm.

Layinglength min = 80mm.

finalising length = 50mm.

laseroff = 25mm.

Tapespeed = 4 m/mPn.

Process Data Sheet

Process Information			
Date	05-03-21	Operators	David
Layup	Coj10		
Material	CF/Pekk.		
Program	laying Stationary		

Panel Information: 05-03-21, UD Panel

Date	Time	Layer No.	Orientation	Comments
05/03/21		1	0	RP= 2.00
				CP= 1.00
				TCP x value= 12.5.
				Material used= 11.0m
		2	0.	RP= 2.00
				CP= 1.00
				TCP x value= 12.5
				Material used= 21.6 m
		3	0	RP= 2.00
				CP= 1.00
				TCP x value= 12.5
				Material used= 31.9m.
		4	0	RP= 2.00
				CP = 1.00
				TCP x value = 12.5
				Material used = 44.0m.
		5	0	RP= 2.00
				CP= 1.00
				TCP x value= 12.5
				Material used= 54.2m.
		6	0	RP= 2.00
				CP= 1.00
				TCP x value= 12.5
				Material used= 64.3m.

Sheet No. ___ of ___

Process Data Sheet

Process Information			
Date	05-03-21	Operators	David.
Layup	Coj10		
Material	CF/Pekk.		
Program	laying Stationary.		

Panel Information: 05-03-21, UD Panel

Date	Time	Layer No.	Orientation	Comments
		7	0	RP= 2.00
				CP= 1.00
				TCP x value= 12.5
				Material used= 74.4m
		8	0	RP= 2.00
				CP= 1.00
				TCP x value= 12.5
				Material used= 84.5m
		9	0	RP= 2.00
				CP= 1.00
				TCP x value= 12.5
				Material used= 94.6m
		10	0	RP= 2.00
				CP= 1.00
				TCP x value= 12.5.
				Material used = 104.7m
		10a.		Re laser repass on layer 10.
				laser set @ 600 watts.
05/03/21	16.55.			Panel completed.

Sheet No. ___ of ___

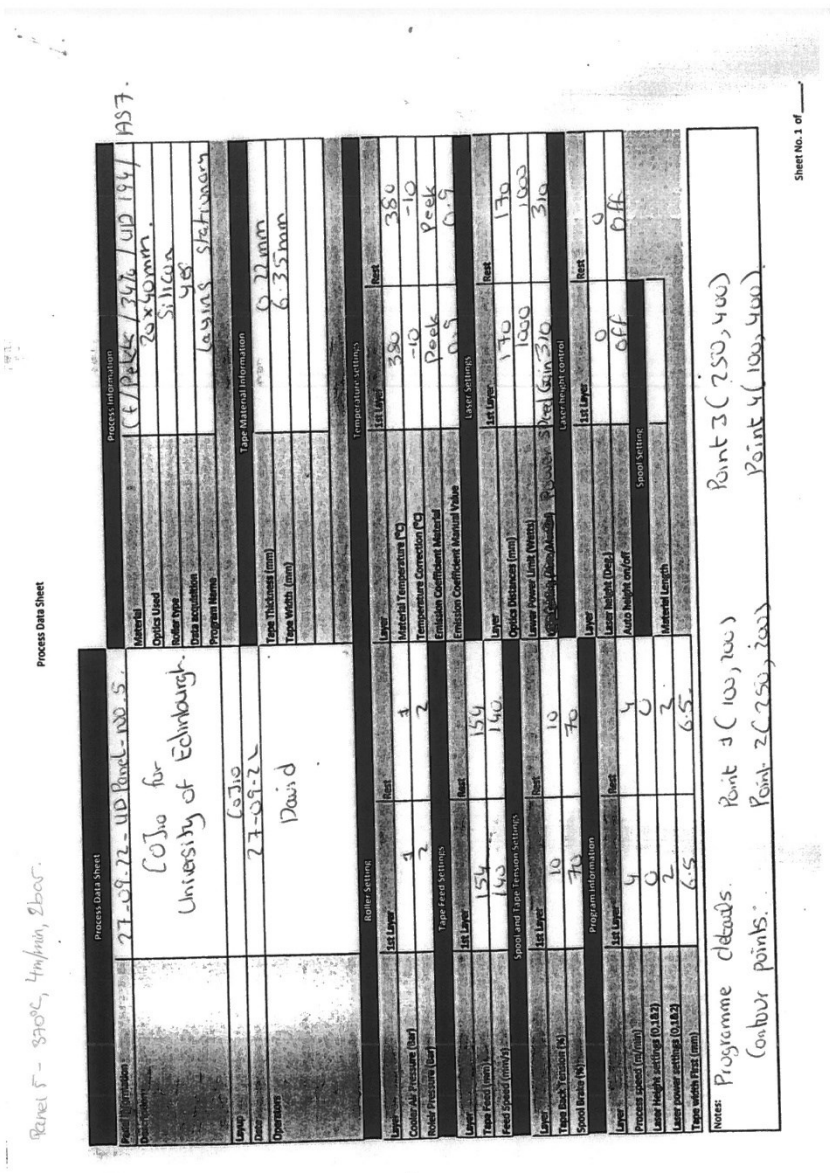

Panel F - 330°C, 4m/min, 2bar.

Process Data Sheet

Process Information	
Panel Identification	27-09-22 - UD Panel - NO.5.
Description	COJO for University of Edinburgh.
Layup	CoJo
Date	27-09-22
Operators	David

Process Information	
Material	CF/PEEK/APC/UD 194/ 197.
Optics Used	20×40mm.
Roller type	Silicon
Data acquisition	Yes
Program Name	Layup Stationary

Roller Setting	1st Layer	Rest
Cooler Air Pressure (bar)	1	1
Roller Pressure (bar)	2	2

Tape Material Information	
Tape Thickness (mm)	0.22mm
Tape Width (mm)	6.35mm

Tape Feed Settings	1st Layer	Rest
Tape Feed (mm)	154	154
Feed Speed (mm/s)	140	140

Temperature Settings	1st Layer	Rest
Material Temperature (°C)	390	350
Temperature Correction (°C)	-10	-10
Emission Coefficient Material	Peek	Peek
Emission Coefficient Manual Value	0.9	0.9

Spool and Tape Tension Settings	1st Layer	Rest
Tape Back Tension (%)	10	10
Spool Brake (%)	70	70

Laser Settings	1st Layer	Rest
Optics Distances (mm)	170	170
Laser Power Limit (Watts)	1000	1000
Laser Power Material	Peek Steel Gen 310	310

Program Information	1st Layer	Rest
Process speed (m/min)	4	4
Laser Height settings (0,1,2)	0	0
Laser power settings (0,1,2)	2	2
Tape width First (mm)	6.5	6.5

Laser Height Control	1st Layer	Rest
Laser height (Dist.)	0	0
Auto height on/off	Off	Off

Spool Setting	
Material Length	

Notes: Programme cleards. Point 1 (100, 200) Point 3 (250, 400)
Contour points. Point 2 (250, 200) Point 4 (100, 400).

Sheet No. 1 of ___

Layup of panel

Ply	Orientation	Offset	Comments
1	0	50%	
2	0	50%	
3	0	50%	
4	0	50%	
5	0	50%	
6	0	50%	
7	0	50%	
8	0	50%	
9	0	50%	
10	0	50%	

Notes: 27-09-22 - UD Panel - NO.5.

Programme data:

flyheight = 120mm.
Runup height = 150mm.
ramp = 30mm.

initialising length = 40mm.
laying length = 80mm
finalising length = 50mm
laseroff = 25mm.
Tapespeed = 4m/min

Process Data Sheet

Process Information			
Date	27-09-22.	Operators	David.
Layup	Cojo.		
Material	CF/PEKK.		
Program	Laying Stationary.		

Panel Information:
27-09-22-UD Panel-NO 5.

Date	Time	Layer No.	Orientation	Comments
				Material from 2021 batch.
		1	0	RP = 2.00 CP: 0.92
				TCP X value = +8.5
				Material used: 11.9m.
		2	0	RP: 2.00 CP: 0.97.
				TCP X value = +8.5.
				Material used = 22.7m.
				Spool changed @ end of layer 2
		3	0	RP=2.00 CP = 0.97
				TCP x value = +8.5.
				Material used = 33.6m.
		4	0	RP = 2.00 CP = 0.99
				TCP x value = +8.5.
				Material used = 45.1m
			⇒	new spool fitted @ end of layer.
				Material from 2022 batch.
		5	0	
				RP = 2.00 CP = 0.98
				TCP x value = +8.5.
				Material used = 56.1m
		6	0	RP = 2.00 CP = 0.98
				TCP x value = +8.5.
				Material used = 67.0m.
		7	0	RP = 2.00 CP = 0.98
				TCP x value = +8.5.
				Material used = 78.0m

Sheet No. ___ of ___

Process Data Sheet

Process Information			
Date	27-09-22	Operators	David.
Layup	Cojo.		
Material	CF/PEKK.		
Program	Laying Stationary.		

Panel Information:
27-09-22-UD Panel-NO.5.

Date	Time	Layer No.	Orientation	Comments
		8	0	RP = 2.00 CP = 0.97.
				TCP x value = +8.5.
				Material used = 89.0m
		9	0	RP = 2.00 CP = 0.97.
				TCP x value = +8.5.
				Material used = 100.0m.
		10	0	RP = 2.00 CP = 0.97
				TCP x value = +8.5.
				Material used = 110.6m
		10a	0	Repass @ 600watts on layer 10
				Panel completed.

Sheet No. ___ of ___

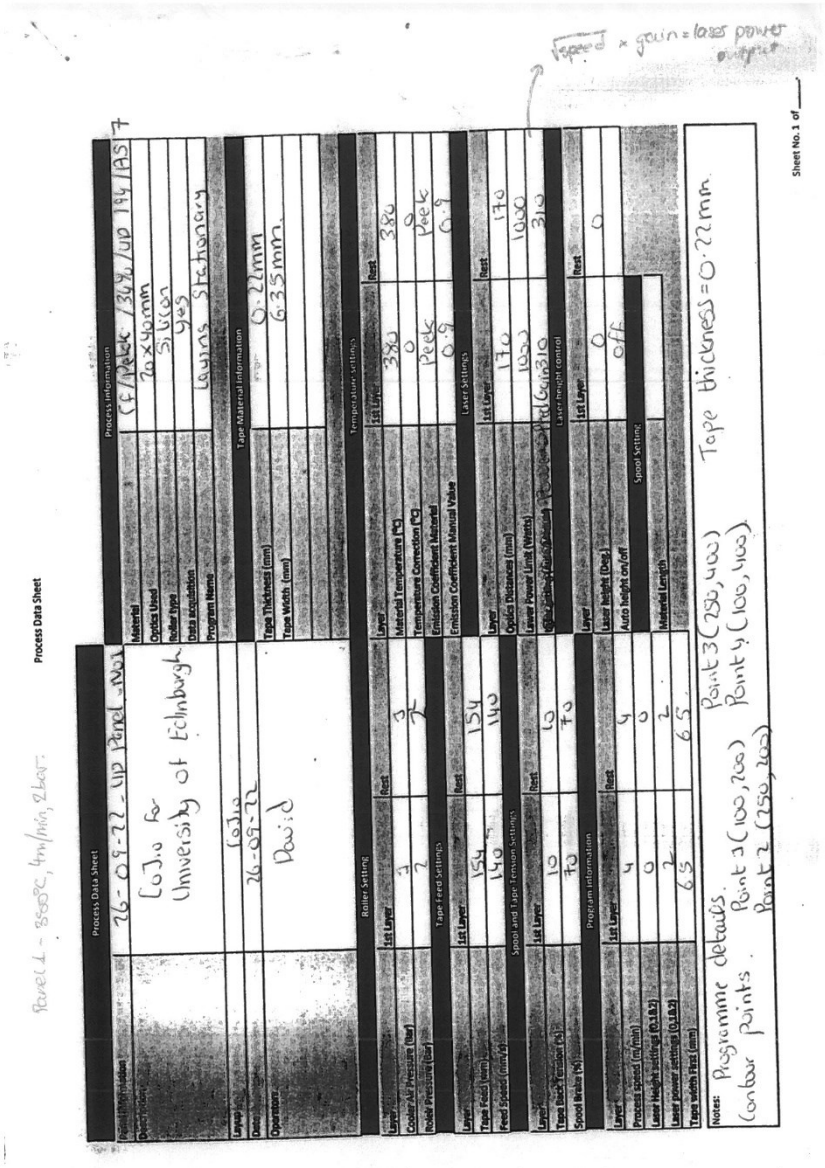

Process Data Sheet

Process Information

Material	CF/PEEK /34% /UD 194 /AS7
Optics Used	20x30mm
Roller type	Silicon
Data acquisition	yes
Program Name	Lauras Stationary

Tape Material Information

Tape Thickness (mm)	0.22mm
Tape Width (mm)	635mm.

Roller Setting

Layer	1st Layer	Rest
Cooler Air Pressure (bar)	1	3
Roller Pressure (bar)	2	7

Temperature Settings

Layer	1st Layer	Rest
Material Temperature (°C)	380	380
Temperature Correction (°C)	0	0
Emission Coefficient Material	Peek	Peek
Emission Coefficient Manual Value	0.9	0.9

Tape Feed Settings

Layer	1st Layer	Rest
Tape Feed (mm)	154	154
Feed Speed (mm/s)	140	140

Laser Settings

Layer	1st Layer	Rest
Optics Distances (mm)	170	170
Laser Power Limit (Watts)	1020	1020
Offset Points of Perforation (Watts)		
Laser Power Control	310	310

Spool and Tape Tension Settings

Layer	1st Layer	Rest
Tape Back Tension (%)	10	10
Spool Brake (%)	70	70

Laser Height Control

Layer	1st Layer	Rest
Laser Height (Dist.)	0	0
Auto height on/off	off	

Program Information

Layer	1st Layer	Rest
Process speed (m/min)	4	4
Laser Height settings (0,1,2)	0	0
Laser power settings (0,1,2)	2	2
Tape Width Tess (mm)	65	65

Spool Setting

Material Length	

Notes: Programme details.
Contour Points. Point 1 (100, 200) Point 3 (250, 400) Tape thickness = 0.22mm
Point 2 (250, 200) Point 4 (100, 400).

Sheet No. 1 of ___

Tapespeed × gain = laser power output

Panel 1 - 350°C, 4m/min, 2bar.

Layup of panel

Ply	Orientation	Offset	Comments
1	0	0%	
2	0	50%	
3	0	0%	
4	0	50%	
5	0	0%	
6	0	50%	
7	0	0%	
8	0	50%	
9	0	0%	
10	0	50%	

Notes: [redacted] 26-09-22-UD Panel-NO1.

Programme data:
Flyheight = 120mm.
Runupheight = 150mm.
ramp = 30mm

Initialising length = 40mm.
laying length = 80mm.
finalising length = 50mm.
Laseroff = 25mm
Tapespeed = 4m/min

Process Data Sheet

Process Information

Date	26-09-2022	Operators	David.
Layup	Co Jio.		
Material	Cf/Pekk.		
Program	laying Stationary.		

Panel Information:

26-09-22 - UD Panel - NO 1.

Date	Time	Layer No.	Orientation	Comments
		1	0	
				Material used from 2021
				RP = 2.00 CP = 1.00
				TCP x value = 8.5.
				Material used = 11.1
		2	0	RP = 2.00 CP = 1.0
				TCP x value = 8.5.
				Material used = 77.4m
		3	0	RP = 2.00 CP = 1.0.
				TCP x value = 8.5.
				Material used = 33.6m
		4	0	RP = 2.00 CP = 1.0.
				TCP x value = 8.5.
				Material used = 44.6m
		5	0.	RP = 2.00 CP = 1.00
				TCP x value = 8.5.
				Material used = 55.6m
		6	0	RP = 2.00 CP = 1.00
				TCP x value = 8.5
				Material used = 66.6m
		7	0	RP = 2.00 CP = 1.00.
				TCP x value = 8.5.
				Material used = 77.6m

Sheet No. ___ of ___

Process Data Sheet

Process Information

Date	26-09-22	Operators	David.
Layup	Co Jio.		
Material	Cf/Pekk.		
Program	laying Stationary.		

Panel Information:

26-09-22 - UD Panel - NO 1.

Date	Time	Layer No.	Orientation	Comments
		8	0	RP = 2.00 CP = 1.0.
				TCP x value = 8.5.
				Material used = 88.8m.
		9	0	RP = 2.00 CP = 1.0
				TCP x value = 8.5.
				Material used = 99.8m.
		10	0	RP = 2.00 CP = 1.00
				TCP x value = 8.5.
				Material used = 110.8m
				Panel Completed

Sheet No. ___ of ___

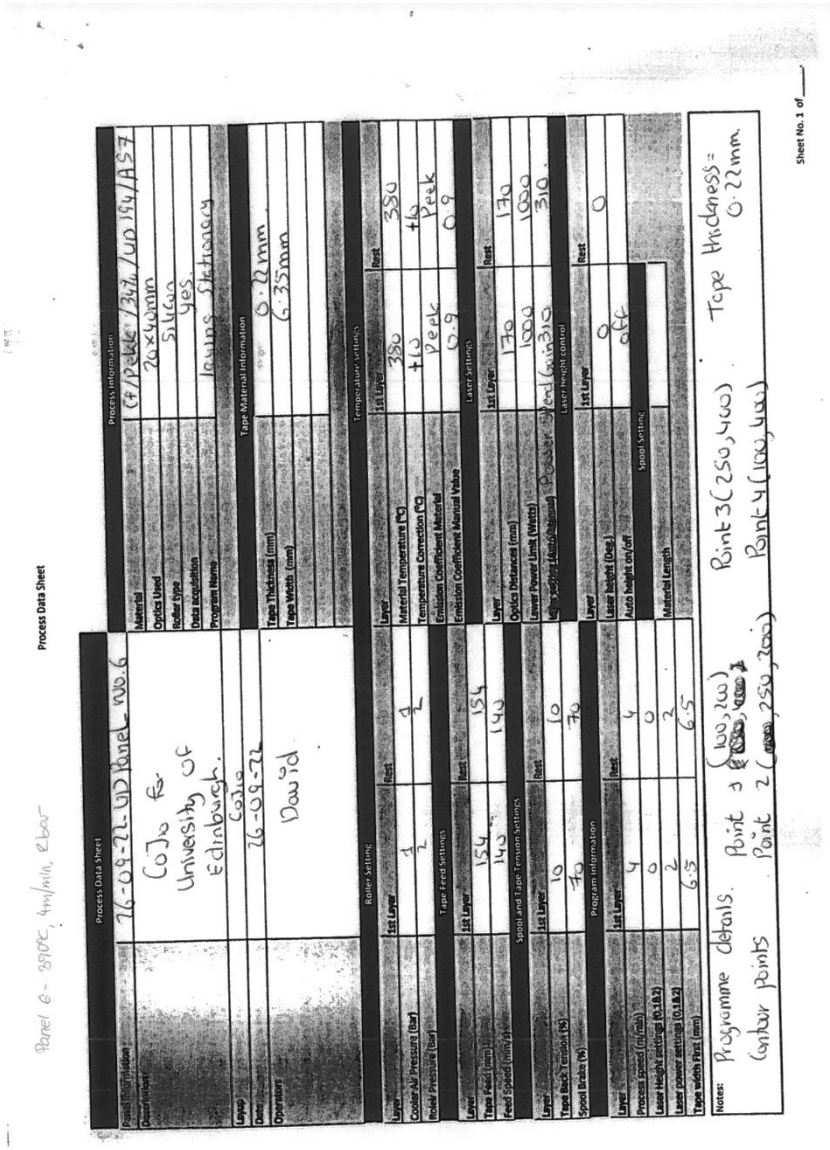

Panel 6 - 390C, 4m/min, Clear

Process Data Sheet

Process Data Sheet		Process Information	
Panel Description	26-09-22-UD Panel_no.6	Material	C/Peek/34%/UD194/AS7
Customer	CoJo for University of Edinburgh.	Optics Used	24×40mm
		Roller type	Silicon
		Duty acquisition	Yes
Layup	Cobe	Program Name	Joints Stationary
Date	26-09-22	Tape Material Information	
Operators	David	Tape Thickness (mm)	0.22mm
		Tape Width (mm)	6.35mm

Roller Setting			Temperature Settings		
Layer	1st Layer	Rest	Layer	1st Layer	Rest
Cooler Air Pressure (Bar)	1	1	Material Temperature (°C)	390	350
Roller Pressure (Bar)	2	2	Temperature Correction (°C)	+10	+10
Tape Feed Settings			Emission Coefficient Material	Peek	Peek
Layer	1st Layer	Rest	Emission Coefficient Material Value	0.9	0.9
Tape Feed (mm/min)	154	154	Laser Settings		
Feed Speed (mm/min)	140	140	Layer	1st Layer	Rest
Spool and Tape Tension Settings			Optics Distances (mm)	130	130
Layer	1st Layer	Rest	Laser Power Link (Watts)	1000	1000
Tape Back Tension (%)	10	10	Laser Power Material	Poker Steel Gain 310	310
Spool Brake (%)	70	70	Laser Height control		
Program Information			Layer	1st Layer	Rest
Layer	1st Layer	Rest	Laser Height (Deg.)	0	0
Process speed (m/min)	4	4	Auto height on/off	off	
Laser Height setting (0.1 to 2)	0	0	Spool Setting		
Laser power setting (0.1 to 2)	2	2	Material Length		
Tape width First (mm)	6.5	6.5			

Notes: Programme details. Point 1 (100,200) Point 3 (250,400) Tape thickness = 0.22mm.
Contour points Point 2 (250,200) Point 4 (100,400)

Sheet No. 1 of ____

Layup of panel

Ply	Orientation	Offset	Comments
1	0	0%	
2	0	50%	
3	0	0%	
4	0	50%	
5	0	0%	
6	0	50%	
7	0	0%	
8	0	50%	
9	0	0%	
10	0	50%	

Notes: 26-09-22-UD Panel_no.6.

Programme data:

Flyheight = 120mm
Runup height = 150mm
ramp = 30mm

initialising length = 40mm
Laying length = 80mm
finalising length = 50mm

laseroff = 75mm
Tapespeed = 4m/min

Process Data Sheet

Process Information

Date	26-09-22	Operators	David.
Layup	CoJo.		
Material	CF/Pekk.		
Program	laying Stationary.		

Panel Information: 26-09-22-UD Panel No 6

Date	Time	Layer No.	Orientation	Comments
				Material from 2021
		1	0	RP= 2.00 CP= 1.00
				Tcp x value = +8.5
				Material used = 10.3m
		2	0	RP = 2.00 CP = 1.00
				Tcp x value = +8.5
				Material used = 21.2m
		3	0	RP = 2.00 CP = 1.00
				Tcp x value = +8.5
				Material used = 32.2m
		4	0	RP = 2.00 CP = 0.98
				Tcp x value = +8.5
				Material used = 43.2m
		5	0	RP = 2.00 CP = 0.97
				Tcp x value = +8.5
				Material used = 54.3m
		6	0	RP = 2.00 CP = 0.95
				Tcp x value = +8.5
				Material used = 65.3m
		7	0	RP = 2.00 CP = 0.97
				Tcp x value = +8.5
				Material used =

Sheet No. ___ of ___

Process Data Sheet

Process Information

Date	26-09-22	Operators	David
Layup	CoJo		
Material	CF/Pekk		
Program	laying Stationary		

Panel Information: 26-09-22-UD Panel - No. 6

Date	Time	Layer No.	Orientation	Comments
		8	0	RP = 2.00 CP = 0.97.
				Tcp x value = +8.5
				Material used = 87.2m
		9	0	RP = 2.00 CP = 0.97.
				Tcp x value = +8.5.
				Material used = 98.2m.
		10	0	RP = 2.00 CP = 0.97.
				Tcp x value = +8.5.
				Material used = 109.1m
		10a	0	Repass @ 600 watts on layer 10.
				Panel Completed.

Sheet No. ___ of ___

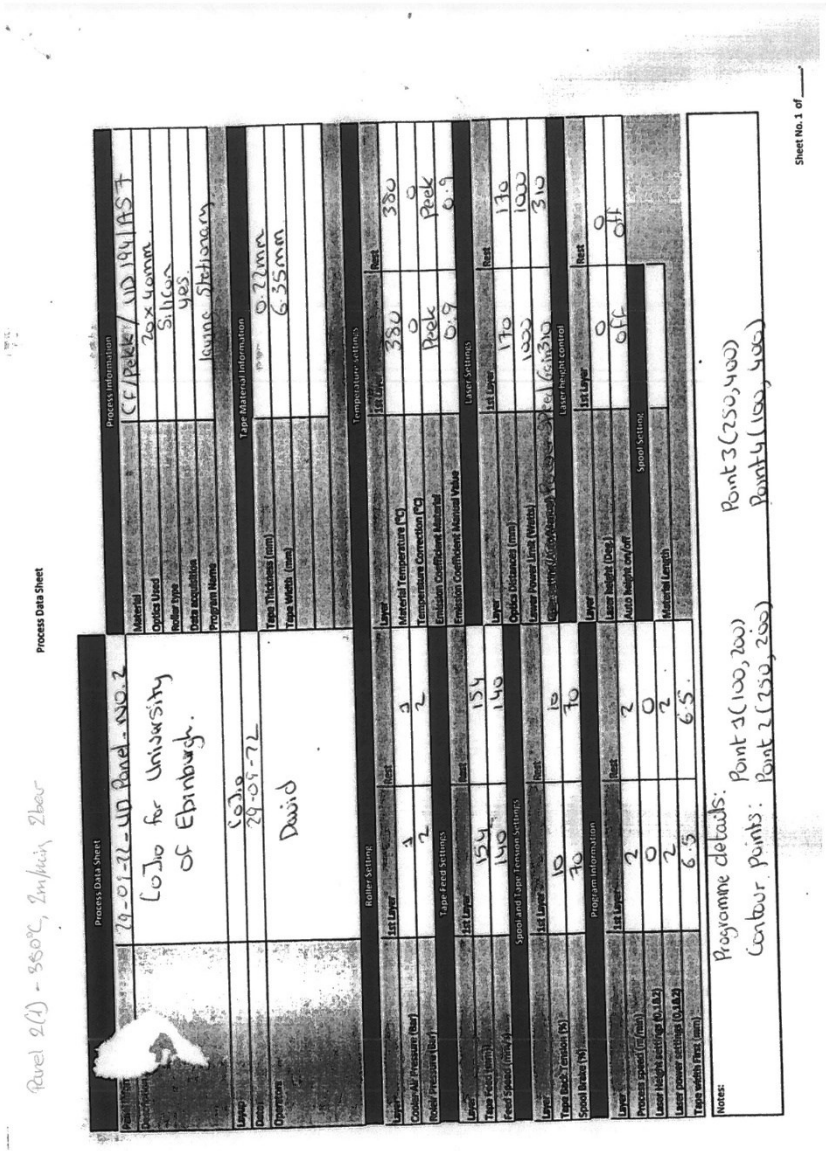

Process Data Sheet

Panel Name: 29-01-22-UD Panel-NO.2
Description: Lojo for University of Edinburgh.
Layup: Lojo
Date: 29-01-22
Operators: David

Process Information
Material: CF/PEEK/UD 194/AST
Optics Used: 2 x 4mm
Roller type: Silicon
Data acquisition: Yes
Program Name: Jenne Stefanacy

Tape Material Information
Tape Thickness (mm): 0.22mm
Tape Width. (mm): 6.35mm

Roller Setting

Layer	1st Layer	Rest
Cooler Air Pressure (Bar)	1	1
Radial Pressure (Bar)	2	2

Temperature Settings

Layer	1st Layer	Rest
Material Temperature (°C)	380	380
Temperature Correction (°C)	0	0
Emission Coefficient Material	Peek	Peek
Emission Coefficient Manual Value	0.9	0.9

Tape Feed Settings

Layer	1st Layer	Rest
Tape Feed (mm/s)	154	154
Feed Speed (mm/s)	140	140

Laser Settings

Layer	1st Layer	Rest
Optics Distance (mm)	170	170
Laser Power Limit (Watts)	1333	1333
Laser power (Watts)	310	310

Spool and Tape Tension Settings

Layer	1st Layer	Rest
Tape Back Tension (N)	10	10
Spool Brake (N)	70	70

Laser Height Control

Layer	1st Layer	Rest
Laser Inlets (Deg)	0	0
Auto Height On/Off	Off	Off

Program Information

Layer	1st Layer	Rest
Process speed (m/min)	2	2
Laser Height setting (0.1-2)	0	0
Laser power settings (0.1-2)	2	2
Tape width Pass (mm)	6.5	6.5

Spool Setting

Material Length		

Notes:
Programme details:
Contour Points: Point 1 (100, 200) Point 2 (250, 250) Point 3 (250, 400) Point 4 (100, 400)

Sheet No. 1 of ____

Panel 2(1) - 350°C, 2m/min, 2bar

Layup of panel

Ply	Orientation	Offset	Comments
1	0	0%	
2	0	50%	
3	0	0%	
4	0	50%	
5	0	0%	
6	0	50%	
7	0	0%	
8	0	50%	
9	0	0%	
10	0	50%	

Notes: 29-09-22_UD Panel_NO.2

Programme data.

flyheight = 120mm
Runup length = 150mm
ramp = 30mm

initialising length = 40mm
laying length = 80mm
finalising length = 50mm

Laser off = 25mm
Top speed = 2M/MIN

Process Data Sheet

Process Information			
Date	29-09-22	Operators	David
Layup	Cojo		
Material	CF/PEEK		
Program	laying Stationary		

Panel Information:
29-09-29 - UD Panel - NO 2

Date	Time	Layer No.	Orientation	Comments
				Material from 2022 batch
				Batch number = 600m00792708
				Spool No = 60m00792700042
		1	0	RP = 2.00 CP = 1.00
				Tcp x value = +8.5.
				Material used = 11.3m.
				Speed = 2 m/min.
		2	0	RP = 2.00 CP = 1.00
				Tcp x value = +8.5
				Material used = 23.0m
		3	0	RP = 7.00 CP = 1.00
				Tcp x value = +8.5
				Material used = 34.1m
		4	0	RP = 7.00 CP = 1.00
				Tcp x value = +8.5.
				Material used = 45.0.
				Power Speed Gain Changed to 335
		5	0.	RP = 7.00 CP = 1.00.
				Tcp x value = +8.5.
				Material used = 56.2m
		6	0	RP = 2.00 CP = 1.00
				Tcp x value = +8.5.
				Material used = 67.2m

Sheet No. ___ of ___

Process Data Sheet

Process Information			
Date	29-09-22	Operators	David
Layup	Cojo		
Material	CF/PEEK		
Program	laying Stationary		

Panel Information:
29-09-29 - UD Panel - NO 2.

Date	Time	Layer No.	Orientation	Comments
		7	0	RP = 2.00 CP = 1.00
				Tcp x value = +8.5
				Material used = 78.3m
		8	0	RP = 2.00 CP = 1.00
				Tcp x value = +8.5.
				Material used = 89.1m.
		9	0	RP = 7.00 CP = 1.00
				Tcp x value = +8.5
				Material used = 100.0m
		10	0	RP = 2.00 CP = 1.00
				Tcp x value = +8.5.
				Material used = 111.1m
		10A	0.	repass on layer 10 @ 450 watts
				Panel completed.

Sheet No. ___ of ___

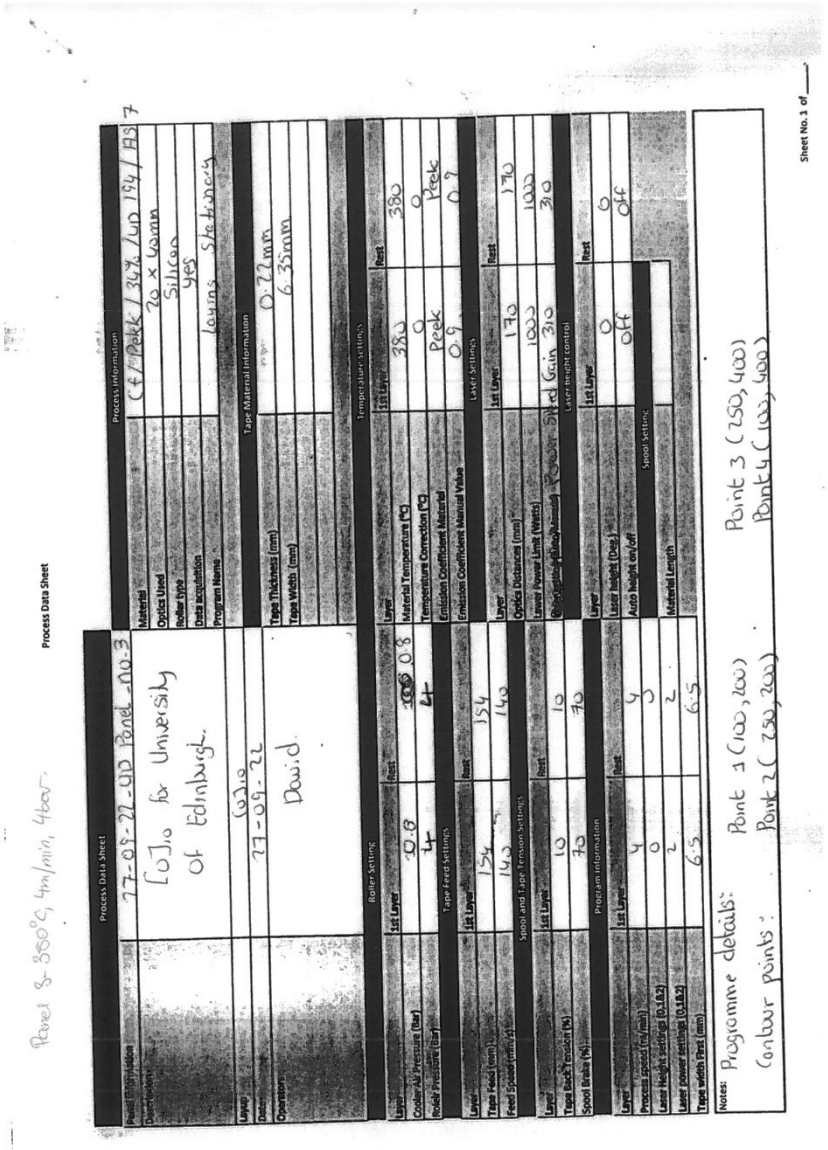

Process Data Sheet

Panel Information: 27-09-22-UD Panel .no.3

Operators: David

Layup: (a)to

Date: 27-09-22

Process Information

Material: CF/PEKK / 34% / UD 194 / 133

Optics Used: 70 x 10mm

Roller type: Silicon

Data acquisition: yes

Program Name: layup stationary

Tape Material Information

Tape Thickness (mm): 0.22mm

Tape Width: (mm): 6.35mm

Roller Setting

Layer	1st Layer	Rest
Cooler Air Pressure (bar)	0.8	0.8
Roller Pressure (bar)	4	4

Temperature Settings

Layer	1st Layer	Rest
Material Temperature (°C)	380	380
Temperature Correction (°C)	0	0
Emission Coefficient Material	Peek	Peek
Emission Coefficient Manual Value	0.9	0.9

Tape Feed Settings

Layer	1st Layer	Rest
Tape Feed (mm/s)	154	154
Feed Speed (mm/s)	140	140

Laser Settings

Layer	1st Layer	Rest
Optics Distances (mm)	190	190
Laser Power Limit (Watts)	1000	1000
Process (PEKK/Nylon)	PEKK	PEKK

Spool and Tape Tension Settings

Layer	1st Layer	Rest
Tape Back Tension (N)	10	10
Spool Brake (N)	70	70

Laser Height control

Layer	1st Layer	Rest
Laser height (Dec)	0	0
Auto Height On/Off	Off	Off

Program Information

Layer	1st Layer	Rest
Process passes (+/-1in)	4	4
Laser Height Settings (0.1in)	3	3
Laser power setting (0.1A)	2	2
Tape width Pass (mm)	6.5	6.5

Spool Setting

Material Length

Notes: Programme details: Point 1 (100, 200) Point 3 (250, 400)
Contour points: Point 2 (250, 200) Point 4 (100, 400)

Sheet No. 1 of ____

Panel 8- 350°C, 4m/min, 4bar.

Layup of panel

Ply	Orientation	Offset	Comments
1	0	0%	
2	0	50%	
3	0	0%	
4	0	50%	
5	0	0%	
6	0	50%	
7	0	0%	
8	0	50%	
9	0	0%	
10	0	50%	

Notes: 27-09-22-UD Panel .no.3

Programme data:

Flyheight = 120mm
Runup length = 150mm
Ramp = 30mm

Inclising length = 40mm
Laying length = 50mm
Finalising length = 50mm.
Laseroff = 25mm
Topespeed = 2m/min.

Process Data Sheet

Process Information

Date	27-09-22	Operators	David
Layup	CoJio		
Material	Cf / Pekk		
Program	laying Stationary		

Panel Information: 27-09-22-UD Panel - NO. 3

Date	Time	Layer No.	Orientation	Comments
				Material from 2022 batch
				Batch Number: 600M00792708, Serial-60M00794
		1	0.	RP = 4.00 CP: 0.8. 270042
				TCP x value = +8.5.
				Material used = 11.4m
		2	0	RP = 4.0 CP = 0.8
				TCP x value = +8.5
				Material used: 22.3m.
		3	0	RP = 4.0 CP = 0.8
				TCP x value = @ +8.5
				Material used = 33.4m
		4	0	RP = 4.0 CP = 0.8
				TCP x value = +8.5
				Material used = 44.4m
		5	0.	RP = 4.0 CP = 0.8
				TCP x value = +8.5.
				Material used = 55.6m
		6	0	RP = 4.0 CP = 0.8
				TCP x value = +8.5.
				Material used = 66.6m
		7	0	RP = 4.0. CP = 0.8
				TCP x value = +8.5.
				Material used = 77.6m

Sheet No. ___ of ___

Process Data Sheet

Process Information

Date	27-09-22	Operators	David
Layup	CoJio		
Material	Cf / Pekk		
Program	laying Stationary		

Panel Information: 27-09-22-UD Panel - NO. 3

Date	Time	Layer No.	Orientation	Comments
		8	0	RP = 4.00 CP = 0.8.
				TCP x value = +8.5.
				Material used = 88.8m
		9	0	RP = 4.0 CP = 0.8
				TCP x value = +8.5
				Material used = 99.9m
		10	0	RP = 4.0 CP = 0.8
				TCP x value = +8.5
				Material used = 110.9m
		10a	0	repass @ 600 watts on layer 10.
				Panel completed

Sheet No. ___ of ___

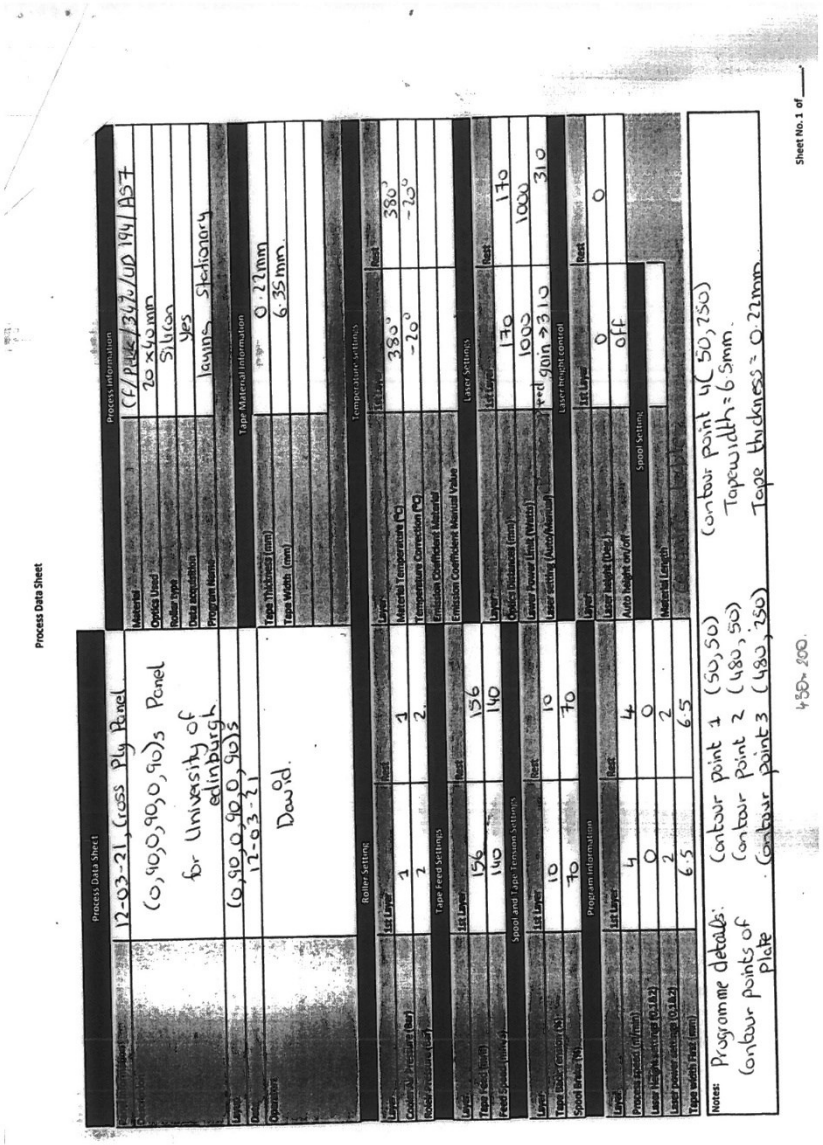

Process Data Sheet

Process Information	
Project Name	12-03-21, Cross Ply Panel
Description	(0,90,90,90,90)s Panel for University of Edinburgh
Layup	(0,90,0,90,0,90)s
Date	12-03-21
Operator	David.

Material Information	
Material	CF/PEEK/APC/UD 194/AS4
Optics Used	20 x 40 mm
Roller type	Silicon
Data acquisition	Yes
Program Name	Layup Stationary

Tape Material Information	
Tape Thickness (mm)	0.22mm
Tape Width (mm)	6.35mm

Roller Setting	Rest
Layer	
Coolerol Pressure (bar)	1
Roller Pressure (kg)	2

Temperature Settings	1st Layer	Rest
Material Temperature (°C)	380°	380°
Temperature Correction (°C)	-20°	-20°
Emission Coefficient Material		
Emission Coefficient Material Value		

Tape Feed Settings	1st Layer	Rest
Layer		
Tape Feed (mm)	156	156
Feed Speed (mm/s)	140	140

Laser Settings	1st Layer	Rest
Layer		
Optics Distance (mm)	170	170
Laser Power Limit (Watts)	1000	1000
Laser Power (Watts)	Feed 90in → 310	310

Spool and Tape Tension Settings	1st Layer	Rest
Layer		
Tape Brake Torque (%)	10	10
Spool Brake (%)	70	70

Laser Height Control	1st Layer	Rest
Layer		
Laser Height (Dz)	0	0
Auto Height On/Off	Off	

Program Information	1st Layer	Rest
Layer		
Process Speed (m/min)	4	
Laser Height Offset (0.1Hz)	0	
Laser Power Offset (0.1Hz)	2	
Tape Width Feed (mm)	65	

Spool Setting	
Material Length	

Notes: Programme details: Contour point 1 (50,50) Contour point 4 (50,250)
Contour points of Plate Contour Point 2 (480,50) Tapewidth = 6.5mm.
Contour point 3 (480,250) Tape thickness = 0.22mm.

Sheet No. 1 of ____

450 × 200

Layup of panel

Ply	Orientation	Offset	Comments
1	0	0%	
2	90	0%	
3	0	0%	
4	90	0%	
5	0	0%	
6	90	0%	
7	90	50%	
8	0	0%	
9	90	0%	
10	0	0%	
11	90	0%	
12	0	0%	

Notes: Panel 12-03-21 Cross Ply Panel.

Programme data.

flyheight = 120mm.
Runup length = 150mm.
ramp = 30mm.
Inicising length = 40mm.
laying length min = 80mm.
finalising length = 50mm.
laseroff = 25mm.
Tapespeed = 4 m/min.

Process Data Sheet

Process Information			
Date	12-03-21	Operators	David
Layup	(0,90,0,90,0,90)s		
Material	CF/PEKK		
Program	laying Stationary		

Panel Information:
12-03-21, Cross Ply panel.

Date	Time	Layer No.	Orientation	Comments
		1	0	CP= 1.00
				RP= 2.00
				TCP X Value= 12.5.
				Material used= 40.8m
		2	90	CP= 1.00
				RP= 2.00
				TCP X Value= 12.5
				Material used= 67.9m
				Spool changed @ end of layer. Some of the material on this spool seemed dry to the touch.
		3	0	CP= 1.00
				RP= 2.00
				TCP X Value= 12.5
				Material used= 95.0m
		4	90	CP= 1.00
				RP= 2.00
				TCP X Value= 12.5.
				Material used= 117.3m
		5	0	CP= 1.00
				RP= 2.00
				TCP X Value= 12.5.
				Material used= 148.9m
		6	90	CP= 1.00
				RP= 2.00, TCP X Value= 12.5.
				Material used= 171.2m

Finished for day.

Sheet No. ___ of ___

Process Data Sheet

Process Information			
Date	15-03-21	Operators	David.
Layup	(0,90,0,90,0,90)s		
Material	CF/PEKK		
Program	laying Stationary		

Panel Information:
12-03-21, Cross ply panel.

Date	Time	Layer No.	Orientation	Comments
15/3/21		7	90	CP=1.00
				RP= 2.00, TCP X Value= 12.5.
				Material used= 22.4m
		8	0	CP=1.00
				RP= 2.00 TCP X Value= 12.5.
				Material used= 54.1m
		9	90	CP=1.00
				RP= 2.00, TCP X Value= 12.5.
				Material used= 76.3m
		10	0	CP=1.00
				RP= 2.00 TCP X Value= 125
				Material used= 108m
		11	90	CP=1.00, RP=2.00
				TCP X Value= 12.5.
				Material used= 130.4m
		12	0	CP= 1.00, RP= 2.00
				TCP X Value= 12.5.
				Material used= 167.0m
				New spool fitted @ end of track 18.
		12a	0	Laser repass on layer 12.
				laser set @ 600 watts
				Panel completed

13a. laser repass on tool side of panel. This was needed due to some wrinkling of the tool side of panel when it was been removed from the adhesive tape. repass @ 600 watts

Sheet No. ___ of ___

Cross-ply ATP-360-4-2 (later post-processed in the hydraulic press at 220°C isothermal hold)

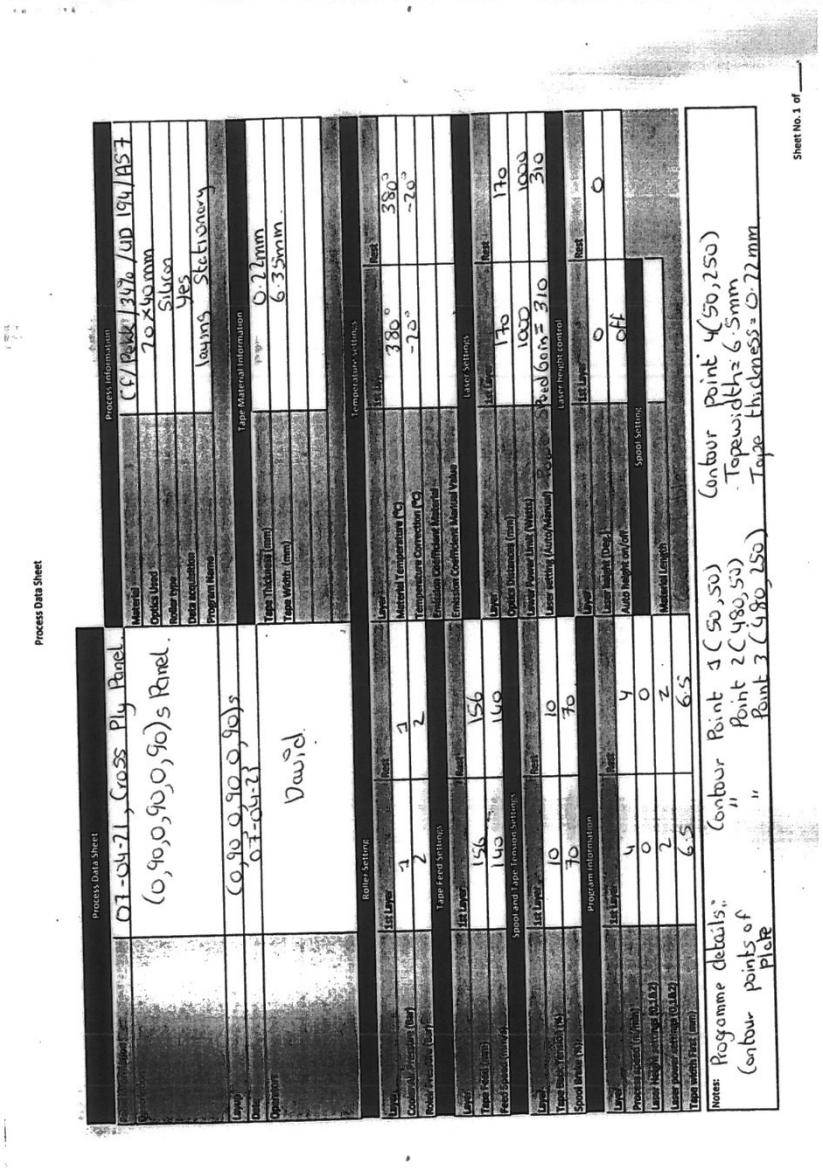

Process Data Sheet

07-04-21, Cross Ply Panel.
(0,90,90,90,90)s Panel.
(0,90,0,90,0,90)s
07-04-21
David

Process Information
Material: CF/PEKK/34% /UD 194/AS7
Optics Unit: 70x340mm
Roller type: Silicon
Data acquisition: Yes
Program Name: Lowes Stationary

Tape Material Information
Tape Thickness (mm): 0.22mm
Tape Width (mm): 6.35mm

Roller Setting
1st Layer: Pass 1
Consolidation Pressure (bar): 2
Pedal Pressure (bar): 2

Tape Feed Settings
1st Layer: Pass 156
Tape Feed (mm/s): 140
Pedal Speed Ratio (%):

Spool and Tape Tension Settings
1st Layer: Pass 10
Tape Brake Tension (N): 70
Spool Brake (%):

Program Information
1st Layer: Pass 4
Process Speed (m/min): 0
Laser Height Setting (0-1.2): 2
Laser power Setting (0-1.2): 0.5
Tape Width Fed (mm): 6.5

Temperature Settings
1st Layer: Pass 380°
Material Temperature (°C): -20°
Temperature Correction (°C):
Emission Coefficient (Material):
Emission Coefficient Material Value:

Laser Settings
1st Layer: Pass 170
Optics Distance (mm): 1000
Laser Power Line: 310
Laser setting (Auto/Manual): Pedal Gain = 310

Laser Height Control
1st Layer: Pass 0
Laser Height (Dec.): 0
Auto Height on/off: off

Spool Setting
Material (Length):

Notes: Progamme details: Contour Point 1 (50,50) Contour Point 4 (50,250)
Contour points of Plate: " Point 2 (480,50) Tapewidth = 6.5mm
" Point 3 (480,250) Tape thickness = 0.22mm

Sheet No. 1 of ____

Layup of panel

Ply	Orientation	Offset	Comments
1	0	0%	✓
2	90	0%	✓
3	0	0%	✓
4	90	0%	✓
5	0	0%	✓
6	90	0%	✓
7	90	50%	✓
8	0	0%	✓
9	90	0%	✓
10	0	0%	✓
11	90	0%	
12	0	0%	

Notes: Panel 07-04-21 Cross Ply Panel.

Programme data
flyheight = 120mm
runup length = 150mm
ramp = 30mm
incubsing length = 40mm
laying length min = 80mm
finclusing length = 50mm
lessroff = 25mm
Topespeed = 4m/min

Process Data Sheet

Process Information			
Date	07-04-21	Operators	David.
Layup	(0,90,0,90,0,90)s		
Material	CF/PEKK		
Program	laying Stationary		

Panel Information:
07-04-21, Cross Ply panel.

Date	Time	Layer No.	Orientation	Comments
		1	0	CP= 1.00 Started with Spool 5.
				RP= 2.00 from ID=85m588200721-04
				TCP X value = 12.5
				Material used= 31.7m
		2	90	CP= 1.00
				RP= 2.00
				TCP X value= 12.5
				Material used= 53.9m
		3	0	CP= 1.00
				RP= 2.00
				TCP X value = 12.5
				Material used = 85.6m
		4	90	CP= 1.00
				RP= 2.00
				TCP X value= 12.5
				Material used= 107.8m
		5	0	CP= 1.00
				RP= 2.00
				TCP X value= 12.5
				Material used= 139.5m
		6	90	CP= 1.00
				RP= 2.00
				TCP X value= 12.5
				Material used = 161.7m

Sheet No. ___ of ___

Process Data Sheet

Process Information			
Date	08-04-21	Operators	David.
Layup	(0,90,0,90,0,90)s		
Material	CF/PEKK		
Program	laying Stationary		

Panel Information:
07-04-21, Cross Ply Panel.

Date	Time	Layer No.	Orientation	Comments
		7	90	CP= 1.00
				RP= 2.00
				TCP X value= 12.5
				Material used= 183.9m
		8	0	CP= 1.00
				RP = 2.00
				TCP X value= 12.5
				Material used= 215.5m
		9	90	CP= 1.00
				RP= 2.00
				TCP X value= 12.5.
				Material used= 237.8m
				Spool changed @ end of layer 9
				Spool 07 from ID=85m588200721-02
				→Put on head
		10	0	CP= 1.00
				RP= 2.00
				TCP X value= 12.5
				Material used = 269.4m
		11	90	CP= 1.00
				RP= 2.00
				TCP X value = 12.5.
				Material used= 291.7m
		12	0	CP= 1.00
				RP= 2.00
				TCP X value= 12.5.
				Material used= 323.4m.

Sheet No. ___ of ___

Process Data Sheet

Process Information			
Date	08-04-21	Operators	David.
Layup	(0,90,0,90,0,90)s		
Material	CF/PAEK.		
Program	laying Stationary		

Panel Information:
07-04-21, Cross Ply panel.

Date	Time	Layer No.	Orientation	Comments
		12a	0	laser repass on layer 12.
				laser set @ 600 watts.

Sheet No. ___ of ___

Cross-ply ATP-360-4-2 (later post-processed in the hydraulic press at 300°C isothermal hold)

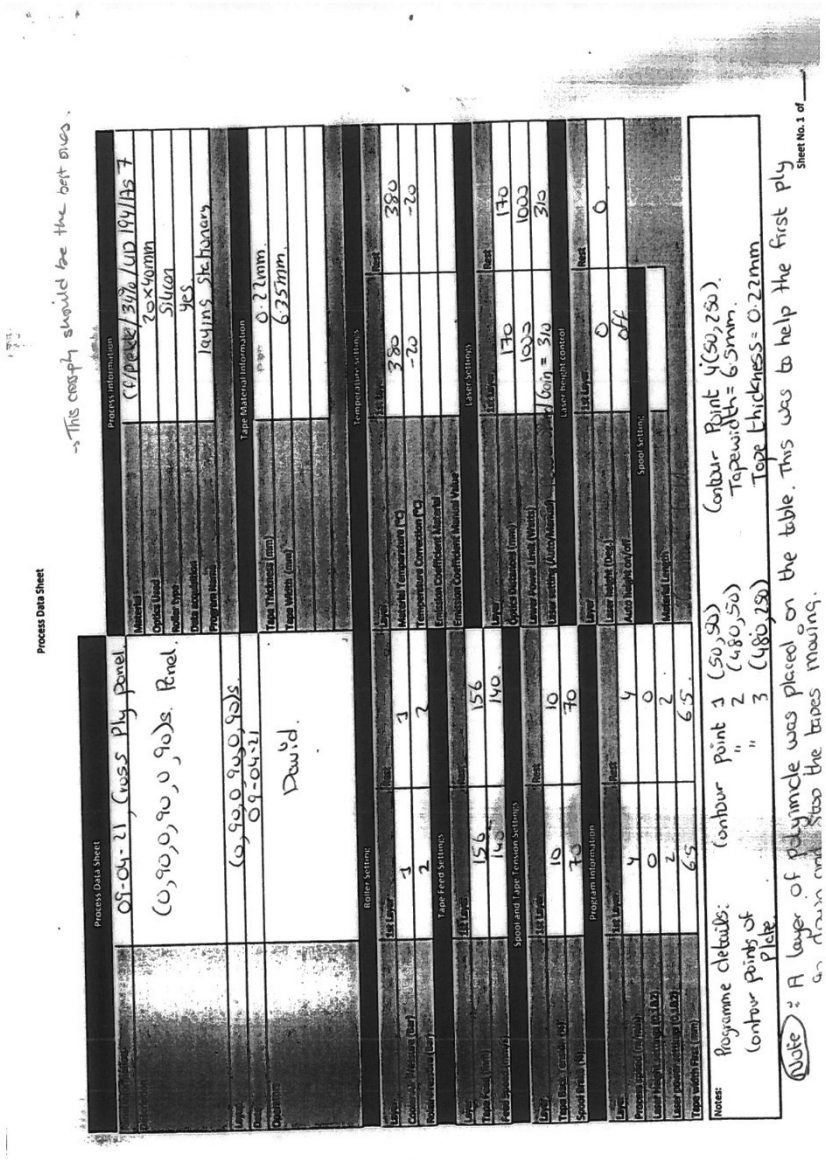

Process Data Sheet

→ This cosply should be the best ones.

Process Information	
Material	CF/peek/316/UD 194/AS 7
Optics Used	2×40mm
Roller Type	Silicon
Data Recorded	yes
Program Name	layins St.hoares

Tape Material Information	
Tape Thickness (mm)	0.22mm
Tape Width (mm)	6.25mm.

Roller Setting		Heat
1st Layer		
Consolidation Pressure (bar)	1	
Roller Temperature (°C)	2	

Temperature Settings		Heat
1st Layer		
Material Temperature (°C)		380
Temperature Correction (°C)		-20
Emission Coefficient Material		
Emission Coefficient Material Value		

Tape Feed Settings		Heat
1st Layer		
Fibre Area (mm²)	156	
Feed Rate (mm/s)	140	

Laser Settings		Heat
1st Layer		
Optics Distance (mm)		170
Laser Power Limit (Watts)		1003
Laser Setting (Auto/Manual)	Gain = 310	310

Spool and Tape Tension Settings		Heat
1st Layer		
Tape Tens. Control (%)	10	
Spool Rest. (%)	70	

Laser Height Control		Heat
1st Layer		
Laser Height (Dev.)		0
Auto Height On/Off		off

Program Information		Heat
1st Layer		
Recessed spaces (in Plate)	4	
Laser Height Setting (Plate)	0	
Laser Power Setting (Plate)	2	
Material Length	65	

Spool Setting		Heat
1st Layer		
Spool Diameter (mm)		
Spool Width (mm)		
Material Length		

Notes: Programme details: Contour Point 1 (50,50) Contour Point 4 (50,250).
" 2 (480,50) Tapewidth = 6.5mm.
" 3 (480,250) Tape Thickness = 0.22mm

Contour Points of Plate

Note: A layer of polymide was placed on the table. This was to help the first ply go down and stop the tapes moving.

Sheet No. 1 of ____

Layup of panel

Ply	Orientation	Offset	Comments
1	0	0	✓
2	90	0	
3	0	0	✓
4	90	0	
5	0	0	✓
6	90	0	
7	90	50%	
8	0	0	
9	90	0	
10	0	0	
11	90	0	
12	0	0	

Notes: Panel 09-04-21, Cross Ply Panel.

Programme data.

flyheight = 120mm.
Runup length = 150mm.
ramp = 30mm

Inclising length = 40mm
Layins length min = 80mm.
Finclising length = 50mm
Laseroff = 25mm.

Topespeed = 4 m/min.

Process Data Sheet

Process Information			
Date	09-04-21	Operators	David
Layup	(0,90,0,90,0,90)s		
Material	CF/PEKK		
Program	laying Stationary		

Panel Information:
09-04-21, Cross Ply Panel

Date	Time	Layer No.	Orientation	Comments
09/04/21		1	0	RP = 2.00
				CP = 1.00
				TCP x Value = 12.5.
				Material used = 37.0m.
		[illegible]		[illegible]
		2	90	RP = 2.00
				CP = 1.00
				TCP x Value = 12.5.
				[illegible]
				Dry tape @ end of track 16. Material
				fouled up in head. (material started chopping up)
				Dry tape @ end of track 17. Spool was
				Changed @ end of this track.
				Roll 8 from bobbin ID - 85MS88200771-02
				was put on head.
				Material used = 60.9m.
		3	0.	RP = 2.00
				CP = 1.00.
				TCP x Value = 12.5.
				Material used = 192.8m
		4	90.	RP = 2.00
				CP = 1.00
				TCP x Value = 12.5.
				Material used = 115.0m

Sheet No. ___ of ___

Process Data Sheet

Process Information			
Date	17-04-21	Operators	David
Layup	(0,90,0,90,0,90)s		
Material	CF/PEKK		
Program	laying Stationary		

Panel Information:
09-04-21, Cross Ply Panel.

Date	Time	Layer No.	Orientation	Comments
		5	0.	RP = 2.00
				CP = 1.00
				TCP x Value = 12.5.
				Material used = 146.9m.
		6	90.	RP = 2.00
				CP = 1.00
				TCP x Value = 12.5.
				Material used = 169.1m
		7	90	RP = 2.00
				CP = 1.00
				TCP x Value = 12.5.
				Material used = 191.3m
		8	0	RP = 2.00
				CP = 1.00
				TCP x Value = 12.5.
				Material used = 223.0m
		9	90	RP = 2.00
				CP = 1.00
				TCP x Value = 12.5.
				Material used = 245.2m
		10	0	RP = 2.00
				CP = 1.00
				TCP x Value = 12.5.
				Material used = 276.9m.

Sheet No. ___ of ___

Process Data Sheet

Process Information			
Date	12-04-21	Operators	David.
Layup	(0,90,0,90,0,90)3		
Material	CF/PEKK.		
Program	laying Stationary.		

Panel Information:
09-04-21 Cross Ply panel.

Date	Time	Layer No.	Orientation	Comments
		11	90	RP= 2.00
				CP= 1.00
				TCP x value = 12.5.
				Roll 9 from [redacted] bobbin ID-8SM588.2007.21-02
				was put on head @ 287.m
				Material used= 299.3m
		12	0	RP= 2.00
				CP= 1.00.
				TCP x value = 12.5.
				Material used= 330.9m
		12a	0	laser repass on layer 12.
				laser set @ 600 watts
				Panel Completed.
		13a		laser repass on tool side of panel. Repass @ 600 watts.

Sheet No. ___ of ___

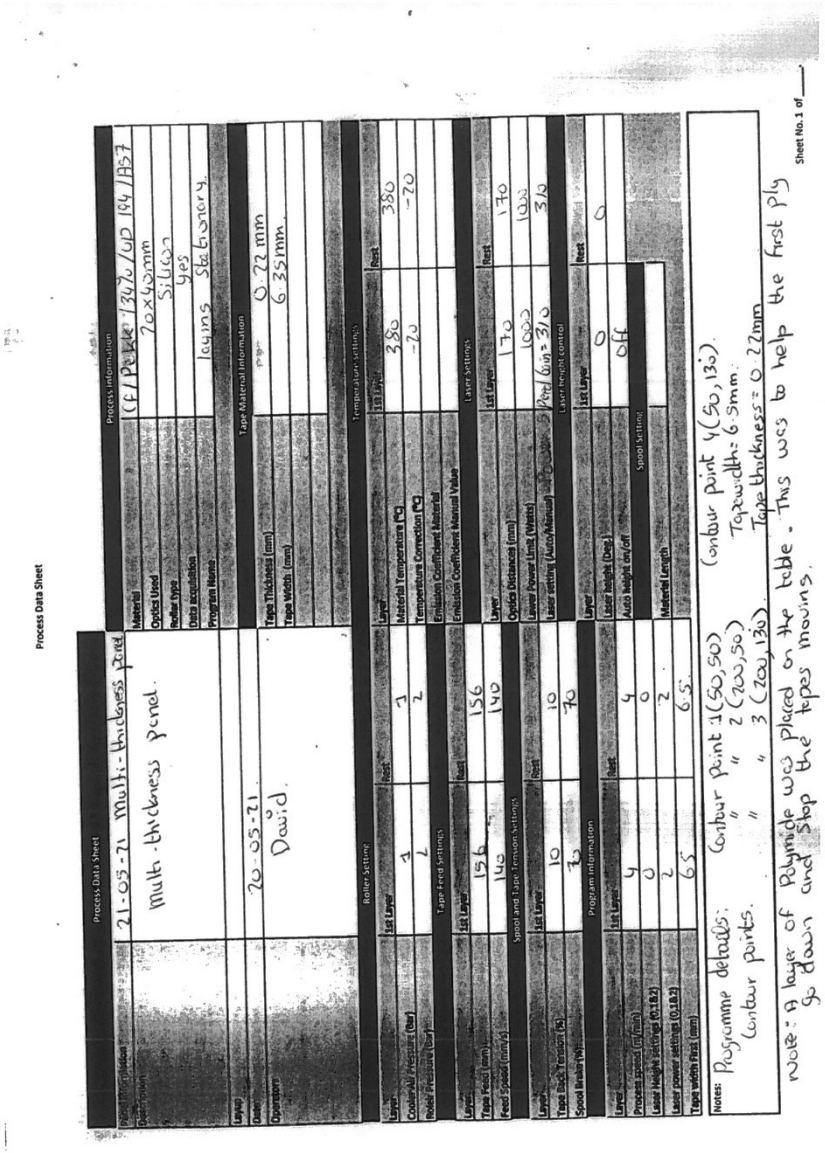

Process Data Sheet

Process Data Sheet

Process Information

Material: (E/Peek 1396/UD 194/AS7
Optics Used: 70x40mm
Roller type: Silicon
Data acquisition: yes
Program Name: layins Stationary

Tape Material Information

Tape Thickness (mm): 0.72 mm
Tape Width (mm): 6.35mm.

Roller Setting

Layup	1st Layer	Rest
Cooler Air Pressure (bar)	1	1
Roller Pressure (bar)	2	2

Temperature Settings

Layup	1st Layer	Rest
Material Temperature (°C)	380	380
Temperature Correction (°C)	-70	-70
Emission Coefficient Material		
Emission Coefficient Manual Value		

Tape Feed Settings

Layup	1st Layer	Rest
Tape Feed (mm/s)	156	
Feed Process (mm/s)	140	

Laser Settings

Layup	1st Layer	Rest
Layer	170	170
Optics Distances (mm)	1000	1000
Laser Power Limit (Watts)	310	310
Laser setting (Auto/Manual)	Man	Man

Spool and Tape Tension Settings

Layup	1st Layer	Rest
Tape Back Tension (N)	10	
Spool Brake (%)	70	

Laser Height Control

Layup	1st Layer	Rest
Laser Height (Dec)	0	0
Auto Height On/Off	Off	

Program Information

Layup	1st Layer	Rest
Process speed (m/min)	4	
Laser Height Settings (0-10)	3	
Laser power setting (0-10)	2	
Tape width Pass (mm)	6.5	

Spool Setting

Layup	1st Layer	Rest
Material Length		

Notes: Programme details: Contour Point 1(50,50) (Contour point 4(50,130).
" " 2(200,50) Tapewidth: 6.3mm.
Contour points. " " 3(200,130). Tape thickness = 0.22mm

Note: A layer of Polyimide was placed on the table. This was to help the first ply go down and stop the tapes moving.

Sheet No. 1 of ___

Layup of panel

Ply	Orientation	Offset	Comments
1	0	0	2mm thickness
2	0	50%	" "
3	0	0	"
4	0	50%	" "
5	0	0	" "
6	0	50%	" "
7	0	0	" "
8	0	50%	" "
9	0	0	" "
10	0	50%	4mm thickness
11	0	0	" "
12	0	50%	" "
13	0	0	" "
14	0	50%	" "
15	0	0	" "
16	0	50%	" "
17	0	0	" "
18	0	50%	" "
19	0	0	6mm thickness
20	0	50%	" "
21	0	0	" "
22	0	50%	" "
23	0	0	" "
24	0	50%	" "
25	0	0	" "
26	0	50%	" "
27	0	0	" "
28	0	50%	8mm thickness
29	0	0	" "
30	0	50%	" "
31	0	0	" "
32	0	50%	" "
33	0	0	" "
34	0	50%	" "
35	0	0	" "
36	0	50%	" "
37	0	0	10mm thickness
38	0	50%	" "
39	0	0	" "
40	0	50%	" "

Notes: 21-05-21 Multi-thickness panel.
Programme data.
Flyheight = 120mm
Runup length = 150mm
Ramp = 30mm
Inclusing length = 40mm
Laying length min = 80mm
finalising length = 50mm
laserOff = 75mm
Tapespeed = 4m/min

Layup of panel

Ply	Orientation	Offset	Comments
41	0	0	10mm thickness
42	0	50%	" "
43	0	0	" "
44	0	50%	" "
45	0	0	" "

Notes:

Contour points for multi-thickness panel:

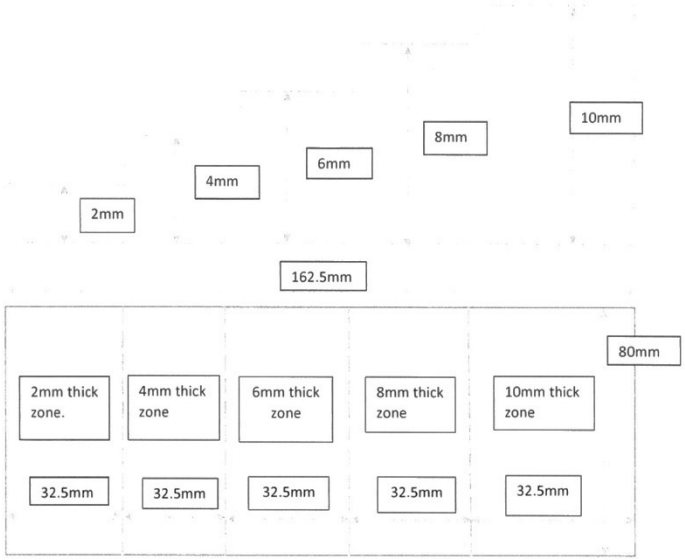

Contour points for robot programme:

- 2mm thickness- point 1(50,50), point 2(212.5,50), point 3(212.5,130,) and point 4(50,130).
- 4mm thickness- point 1(82.5,50), point 2(212.5,50), point 3(212.5,130,) and point 4(82.5,130).
- 6mm thickness- point 1(115,50), point 2(212.5,50), point 3(212.5,130,) and point 4(115,130).
- 8mm thickness- point 1(147.5,50), point 2(212.5,50), point 3(212.5,130,) and point 4(147.5,130).
- 10mm thickness- point 1(180,50), point 2(212.5,50), point 3(212.5,130,) and point 4(180,130).

Notes:

Tape width pre-set in programme is at 6.5mm.

Each of the five zones will be 5 tapes in width in the X-direction.

The panel will 80mm in length in the Y-direction.

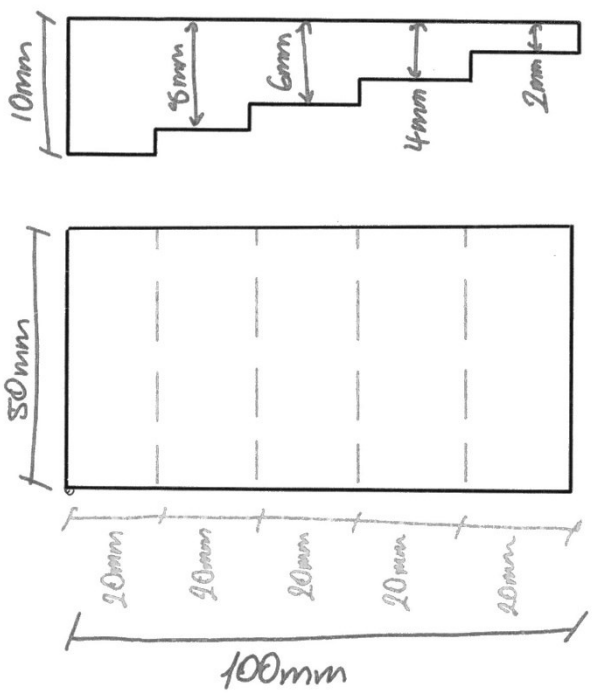

Process Data Sheet

Process Information			
Date	21-05-21 Multi-thickness	Operators	David
Layup			
Material	CF/PEKK 1367/UD 194		/AS7
Program	laying stationary		

Panel Information:

21-05-21 multi-thickness panel.

Date	Time	Layer No.	Orientation	Comments
		1	0	RP= 2.00 CP= 1.00 TCPX value= 12.5
				Material used = 9.6m
				Started @ start of layer with 5 plot 1
				bobbin ID - 60m588 200721003
		2	0	RP= 2.00 CP= 1.00 TCPX value= 12.5
				Material used = 18.5m
		3	0	RP= 2.00 CP= 1.00 TCPX value= 12.5
				Material used = 27.4m.
		4	0	RP= 2.00 CP= 1.00 TCP X value= 12.5
				Material used = 36.4m
		5	0	RP= 2.00 CP= 1.00 TCP X value= 12.5
				Material used = 45.3m
		6	0	RP= 2.00 CP= 1.00 TCP X value= 12.5.
				Material used = 54.2m
		7	0	RP= 2.00 CP= 1.00 TCP X value= 12.5
				Material used = 63.2m.
		8	0	RP= 2.00 CP= 1.00 TCPX value= 12.5.
				Material used = 72.1m
		9	0	RP= 2.00 CP= 1.00 TCP X value= 12.5.
				Material used = 81.1m
				2mm thickness section completed

Sheet No. ___ of ___

Process Data Sheet

Process Information			
Date	24-05-21	Operators	David
Layup			
Material	CF/Pekk/34%/UD194/AS7		
Program	laying Stationary		

Panel Information:
21-05-21 Multi-thickness panel.

Date	Time	Layer No.	Orientation	Comments
		10	0	RP=2.00 CP=1.00 TCP X value=12.5 Material used=88.4m
		11	0	RP=2.00 CP=1.00 TCP X value=12.5 Material used=95.5m
		12	0	RP=2.00 CP=1.00 TCP X value=12.5 Material used=101.7m
		13	0	RP=2.00 CP=1.00 TCP X value=12.5 Material used=109.8m
		14	0	RP=2.00 CP=1.00 TCP X value=12.5 Material used=117.0m
		15	0	RP=2.00 CP=1.00 TCP X value=12.5 Material used=124.1m
		16	0	RP=2.00 CP=1.00 TCP X value=12.5 Material used=131.7m
		17	0	RP=2.00 CP=1.00 TCP X value=12.5 Material used=138.4m
		18	0	RP=2.00 CP=1.00 TCP X value=12.5 Material used=145.5m
				4mm thickness section completed

Sheet No. ___ of ___

Process Data Sheet

Process Information			
Date	24-05-21	Operators	David
Layup			
Material	CF/Pekk/34%/UD194/AS7		
Program	laying Stationary		

Panel Information:
21-05-21 Multi-thickness panel.

Date	Time	Layer No.	Orientation	Comments
		19	0	RP=2.00 CP=1.00 TCP X value=12.5 Material used=151.1m.
		20	0	RP=2.00 CP=1.00 TCP X value=12.5 Material used=156.4m
		21	0	RP=2.00 CP=1.00 TCP X value=12.5 Material used=161.8m
		22	0	RP=2.00 CP=1.00 TCP X value=12.5 Material used=167.2m
		23	0	RP=2.00 CP=1.00 TCP X value=12.5 Material used=172.5m
		24	0	RP=2.00 CP=1.00 TCP X value=12.5 Material used=177.9m
		25	0	RP=2.00 CP=1.00 TCP X value=12.5 Material used=183.3m
		26	0	RP=2.00 CP=1.00 TCP X value=12.5 Material used=188.6m
		27	0	RP=2.00 CP=1.00 TCP X value=12.5 Material used=194.0m.
				6mm thick section piece completed

Sheet No. ___ of ___

Appendix E. Ultrasound scan

Figure E.1 shows an ultrasonic scan of a quasi-isotropic autoclave laminate, with prepreg tape laid down at 0°, 45°, 90° and -45°. The laminate is approximately 12 mm thick, approximately 6 times thicker than the laminates used in the main body of this work. This ultrasonic test is therefore not comparable with the ones presented in Chapter 6.

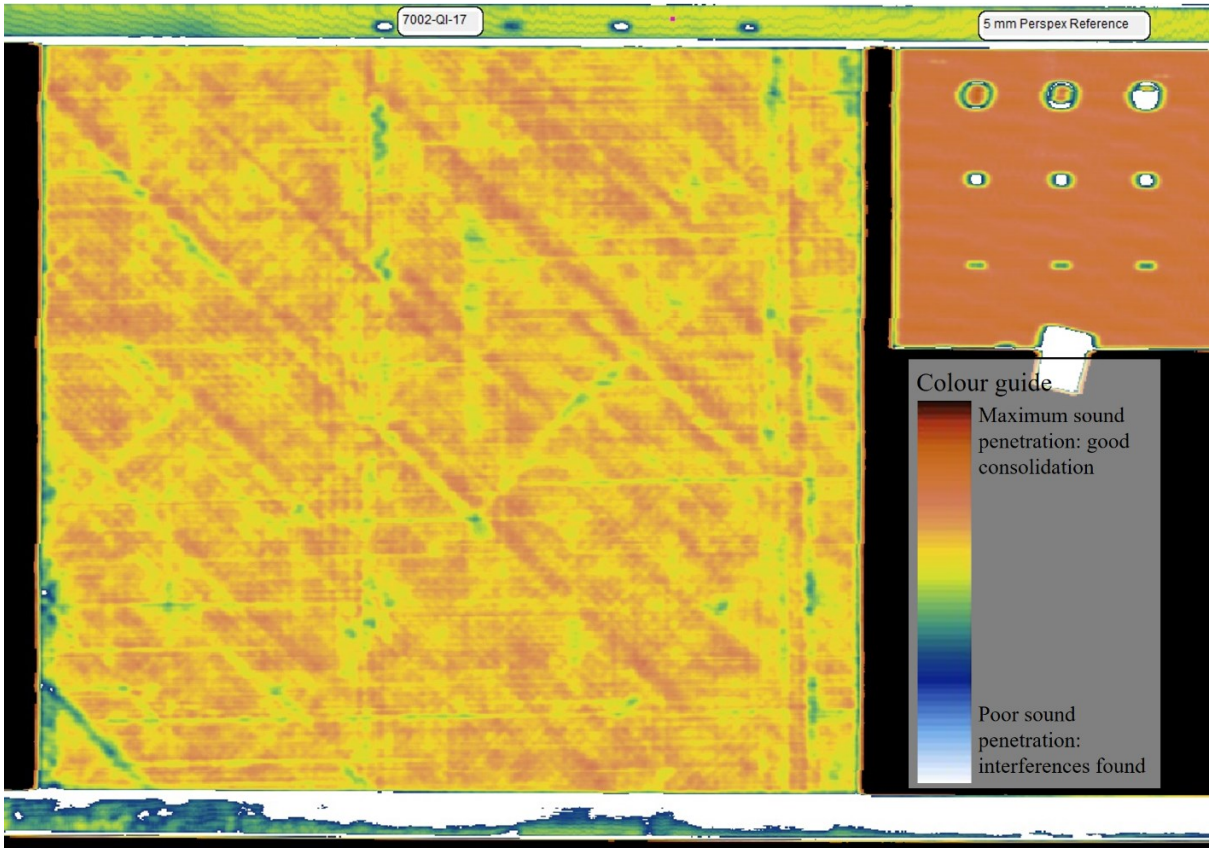

Figure E.1: Ultrasound c-scan of autoclaved CF/PEKK laminate with a 5 mm Perspex reference to the right.

Appendix F. Mechanical testing error analysis

Error analysis on the mechanical testing was performed for flexural, ILSS and in-plane shear testing. Table F.1 below outlines the equations used to estimate the absolute error in each property, as well as the equations used for each property calculation. These equations are taken from ASTM D7264 for flexural testing, ASTM D2344 for ILSS testing, and ASTM D3518 for in-plane shear testing. An explanation of each term, along with their reading error with the used equipment, is provided in Table F.2.

Table F.1: Property and error calculation equations for mechanical testing performed in this work.

Property equation	Error calculation
Flexural strength, $\sigma = \frac{3PL}{2bh^2}$	$\Delta\sigma = \sigma\left[\frac{\Delta P}{P} + \frac{\Delta L}{L} + \frac{\Delta b}{b} + 2\frac{\Delta h}{h}\right]$
Flexural modulus, $E_f^{chord} = \frac{\Delta\sigma}{\Delta\varepsilon}$, where $\varepsilon = \frac{6\delta h}{L^2}$	$\Delta E_f^{chord} = E_f^{chord}\left[\frac{\Delta P}{P} + 3\frac{\Delta L}{L} + \frac{\Delta\delta}{\delta} + \frac{\Delta b}{b} + 3\frac{\Delta h}{h}\right]$
ILSS, $F^{sbs} = \frac{0.75P}{bh}$	$\Delta F^{sbs} = F^{sbs}\left[\frac{\Delta P}{P} + \frac{\Delta b}{b} + \frac{\Delta h}{h}\right]$
IPS stress, $\tau_{12} = \frac{P}{2bh}$	$\Delta\,\tau_{12} = \tau_{12}\left[\frac{\Delta P}{P} + \frac{\Delta b}{b} + \frac{\Delta h}{h}\right]$
IPS strain, $\gamma_{12} = \varepsilon_x - \varepsilon_y$	$\Delta\gamma_{12} = \gamma_{12}\left[\frac{\Delta\varepsilon_x}{\varepsilon_x} + \frac{\Delta\varepsilon_y}{\varepsilon_y}\right]$

Table F.2: Reading error in the equipment used.

Absolute error	Definition	Value
ΔP	Load	20N (1/500th of load capacity)
ΔL	Specimen length	0.05mm
Δb	Specimen width	0.05mm
Δh	Specimen thickness	0.005mm
$\Delta\delta$	Displacement (as measured by Instron testing rig)	0.03mm
$\Delta\varepsilon_x$	Horizontal strain (as measured via DIC)	5 x 10^{-6}
$\Delta\varepsilon_y$	Vertical strain (as measured via DIC)	5 x 10^{-6}

Appendix G. ANOVA analysis of nanoindentation matrix bulk properties

A one-way ANOVA test was used to find out if the differences observed in the nanoindentation results of the matrix bulk are statistically significant. The following null and alternative hypotheses are used:

- H_0: all group means are equal (there is no statistically significant difference)
- H_1: at least one of the group means is statistically different.

The ANOVA test calculates an F_{crit} and F. If $F<F_{crit}$, H_0 is correct. if $F>F_{crit}$, H_1 is correct.

In the case that H1 is true, further testing is required to identify which of the groups is/are different.

G.1 Comparison across compression-moulded data

Hardness

CM-220	CM-260	CM-300
0.389	0.432	0.381
0.436	0.424	0.407
0.401	0.39	0.352
0.363	0.387	0.384
0.366	0.385	
0.32		
0.376		
0.375		

ANOVA						
Source of Variation	*SS*	*df*	*MS*	*F*	*P-value*	*F crit*
Between Groups	0.002127	2	0.001064	1.316012	0.29942	3.738892
Within Groups	0.011315	14	0.000808			
Total	0.013442	16				

F<Fcrit, therefore H0 is correct.

Elastic modulus

CM-220	CM-260	CM-300
6.91	7.3	5.98
7.37	6.98	7.59
7.94	6.8	5.71
6.66	5.99	6.23
6.68	6.05	
5.61		
5.77		
6.66		

ANOVA						
Source of Variation	*SS*	*df*	*MS*	*F*	*P-value*	*F crit*
Between Groups	0.280852	2	0.140426	0.261126	0.773853	3.738892
Within Groups	7.528795	14	0.537771			
Total	7.809647	16				

F<Fcrit, therefore H0 is correct.

G.2 Comparison across ATP-380 data

Hardness

380-4-2			380-2-2			380-4-4		
Top	Mid	Bot	Top	Mid	Bot	Top	Mid	Bot
0.254	0.276	0.262	0.247	0.261	0.253	0.23	0.291	0.231
0.26	0.282	0.294	0.252	0.273	0.27	0.27	0.281	0.289
0.248	0.279	0.24	0.283	0.287	0.271	0.264	0.255	0.275
0.259	0.261				0.246	0.263	0.251	0.237
	0.272				0.266		0.269	0.281
	0.277						0.232	
	0.273						0.267	
	0.284							
	0.285							
	0.284							

ANOVA						
Source of Variation	*SS*	*df*	*MS*	*F*	*P-value*	*F crit*
Between Groups	0.002546	8	0.000318	1.136616	0.364033	2.216675
Within Groups	0.009799	35	0.00028			
Total	0.012345	43				

F<Fcrit, therefore H0 is correct.

Elastic modulus

380-4-2			380-2-2			380-4-4		
Top	Mid	Bot	Top	Mid	Bot	Top	Mid	Bot
4.26	5.02	4.78	4.34	4.56	4.52	4.26	4.71	4.21
4.65	4.96	4.08	4.21	4.59	4.31	4.25	4.8	4.58
4.64	5.05	4.09	4.7		4.75		4.19	4.35
4.12	4.94				3.96		4.33	4.01
4.52	4.99				4.3		4.26	4.35
	4.51						4.61	

ANOVA						
Source of Variation	*SS*	*df*	*MS*	*F*	*P-value*	*F crit*
Between Groups	1.56299	8	0.195374	3.172369	0.010935	2.291264
Within Groups	1.72441	28	0.061586			
Total	3.2874	36				

F>Fcrit, therefore H1 is correct. This means that the mean of at least one data set is significantly different. Based on the results reported in the article, it is likely that ATP-380-4-2 MID is the data set causing the significant difference. The ANOVA test was rerun excluding this data set, see below.

380-4-2		380-2-2			380-4-4		
Top	Bot	Top	Mid	Bot	Top	Mid	Bot
4.26	4.78	4.34	4.56	4.52	4.26	4.71	4.21
4.65	4.08	4.21	4.59	4.31	4.25	4.8	4.58
4.64	4.09	4.7		4.75		4.19	4.35
4.12				3.96		4.33	4.01
4.52				4.3		4.26	4.35
						4.61	

ANOVA						
Source of Variation	*SS*	*df*	*MS*	*F*	*P-value*	*F crit*
Between Groups	0.228583	7	0.032655	0.493168	0.829726	2.442226
Within Groups	1.522927	23	0.066214			
Total	1.75151	30				

F<Fcrit, therefore H0 is correct. This means that none of the tested groups shows any significant different. Therefore, ATP 380-4-2 MID is the only data set causing a significant difference.

The next step would be to understand whether ATP-380-4-2 MID is significantly different to ALL groups or only to some. We want to know whether it is significantly different than the other locations of the ATP-380-4-2 laminate (next row in this table), as well as the MID locations from other laminates (final row on the next page).

380-4-2		
Top	Mid	Bot
4.26	5.02	4.78
4.65	4.96	4.08
4.64	5.05	4.09
4.12	4.94	
4.52	4.99	
	4.51	

ANOVA						
Source of Variation	*SS*	*df*	*MS*	*F*	*P-value*	*F crit*
Between Groups	0.95172	2	0.47586	6.990185	0.010987	3.982298
Within Groups	0.74883	11	0.068075			
Total	1.70055	13				

F>Fcrit, therefore H1 is correct. Even when compared with the TOP and BOT locations individually, ATP-380-4-2 MID is significantly different.

380-4-2	380-2-2	380-4-4
Mid	Mid	Mid
5.02	4.56	4.71
4.96	4.59	4.8
5.05		4.19
4.94		4.33
4.99		4.26
4.51		4.61

ANOVA						
Source of Variation	*SS*	*df*	*MS*	*F*	*P-value*	*F crit*
Between Groups	0.576133	2	0.288067	5.989289	0.017393	3.982298
Within Groups	0.529067	11	0.048097			
Total	1.1052	13				

F>Fcrit, therefore H1 is correct. Even when compared with the other MID locations individually, ATP-380-4-2 MID is significantly different.

G.3 Comparison across ATP-360 data

Hardness

ATP-360-4-2-2mm			ATP-360-4-2-4mm			ATP-360-4-2-6mm				
TOP	MID	BOT	MID	BOT-MID	BOT	TOP	TOP-MID	MID	BOT-MID	BOT
0.253	0.27	0.249	0.265	0.251	0.24	0.229	0.263	0.29	0.272	0.206
0.245	0.259	0.245	0.253	0.248	0.253	0.251	0.248	0.283	0.266	0.251
0.213	0.256	0.212	0.249		0.243	0.249		0.253	0.224	0.253
0.233	0.264	0.253	0.245		0.213			0.236	0.263	0.271
	0.258		0.246		0.259			0.234	0.254	0.255
					0.193			0.258		
					0.265			0.258		

ANOVA						
Source of Variation	*SS*	*df*	*MS*	*F*	*P-value*	*F crit*
Between Groups	0.003788	10	0.000379	1.076032	0.403831	2.090856
Within Groups	0.013379	38	0.000352			
Total	0.017167	48				

F<Fcrit, therefore H0 is correct.

Elastic modulus

ATP-360-4-2-2mm			ATP-360-4-2-4mm			ATP-360-4-2-6mm				
TOP	MID	BOT	MID	BOT-MID	BOT	TOP	TOP-MID	MID	BOT-MID	BOT
4.79	4.44	4.14	5.76	**4.45**	5.15	4.36	4.73	5.29	5.39	4.96
4.41	4.51	4.66	4.22		4.23	4.2	4.33	4.77	5.06	4.83
3.91	4.4		4.29		3.9			5.08	3.79	4.25
4.08	4.31				4.63			4.36	5.35	
	4.54				3.74			4.54	4.35	
					4.62					

ANOVA						
Source of Variation	*SS*	*df*	*MS*	*F*	*P-value*	*F crit*
Between Groups	1.488647	10	0.148865	0.627221	0.777594	2.204292
Within Groups	6.408185	27	0.23734			
Total	7.896832	37				

F<Fcrit, therefore H0 is correct.

G.4 Comparison across MID locations (compression-moulded vs. ATP-380)

Hardness

			380-4-2	380-2-2	380-4-4
CM-220	CM-260	CM-300	Mid	Mid	Mid
0.389	0.432	0.381	0.276	0.261	0.291
0.436	0.424	0.407	0.282	0.273	0.281
0.401	0.39	0.352	0.279	0.287	0.255
0.363	0.387	0.384	0.261		0.251
0.366	0.385		0.272		0.269
0.32			0.277		0.232
0.376			0.273		0.267
0.375			0.284		
			0.285		
			0.284		

ANOVA						
Source of Variation	*SS*	*df*	*MS*	*F*	*P-value*	*F crit*
Between Groups	0.12306	5	0.024612	52.73929	3.06E-14	2.522538
Within Groups	0.014467	31	0.000467			
Total	0.137527	36				

F>Fcrit, therefore H1 is correct. S.1 determined that there is no statistically significant difference between the hardness of CM laminates. S.2 also determined that there is no statistically significant difference between the hardness of the ATP-380 laminates. Rerunning the ANOVA test, or a t-test, comparing CM results with ATP-380 results still provides F>Fcrit. Therefore, there is a significant difference in the hardness of the compression-moulded laminates vs. the ATP-380 laminates.

Elastic modulus

			380-4-2	380-2-2	380-4-4
CM-220	CM-260	CM-300	Mid	Mid	Mid
6.91	7.3	5.98	5.02	4.56	4.71
7.37	6.98	7.59	4.96	4.59	4.8
7.94	6.8	5.71	5.05		4.19
6.66	5.99	6.23	4.94		4.33
6.68	6.05		4.99		4.26
5.61			4.51		4.61
5.77					
6.66					

ANOVA						
Source of Variation	*SS*	*df*	*MS*	*F*	*P-value*	*F crit*
Between Groups	29.21107	5	5.842215	18.12582	1.33E-07	2.602987
Within Groups	8.057862	25	0.322314			
Total	37.26894	30				

F>Fcrit, therefore H1 is correct. Same reasoning as in previous table. S.1 determined that there is no statistically significant difference between the elastic modulus of CM laminates. S.2 determined that ATP-380-4-2 MID ***is*** statistically different to the rest of the ATP-380 MID results. As seen in the article, the average values for all CM samples are considerably larger than the ATP-380 MID values. Rerunning the ANOVA test, or a t-test, comparing CM results with all ATP-380 MID results still provides F>Fcrit. Therefore, there is a significant difference in the hardness of the compression-moulded laminates vs. the ATP-380 laminates.

G.5 Comparison across MID locations (compression-moulded vs. ATP-360)

Hardness

			360-4-2-2mm	360-4-2-6mm
CM-220	CM-260	CM-300	MID	MID
0.389	0.432	0.381	0.27	0.29
0.436	0.424	0.407	0.259	0.283
0.401	0.39	0.352	0.256	0.253
0.363	0.387	0.384	0.264	0.236
0.366	0.385		0.258	0.234
0.32				0.258
0.376				0.258
0.375				

ANOVA						
Source of Variation	*SS*	*df*	*MS*	*F*	*P-value*	*F crit*
Between Groups	0.1146	4	0.02865	48.52255	3.68E-11	2.776289
Within Groups	0.014171	24	0.00059			
Total	0.128771	28				

F>Fcrit, therefore H1 is correct. We previously determined that there is no statistically significant difference between the CM laminates. We also determined that there is no statistically significant difference between the MID locations of the ATP-360 laminates. Therefore, any difference must come from comparing any CM laminate with any ATP-360 laminate. Performing further ANOVA or t-tests shows that all CM results are statistically different to all ATP-360 MID results.

Elastic modulus

			360-4-2-2mm	360-4-2-6mm
CM-220	CM-260	CM-300	MID	MID
6.91	7.3	5.98	4.44	5.29
7.37	6.98	7.59	4.51	4.77
7.94	6.8	5.71	4.4	5.08
6.66	5.99	6.23	4.31	4.36
6.68	6.05		4.54	4.54
5.61				
5.77				
6.66				

ANOVA						
Source of Variation	*SS*	*df*	*MS*	*F*	*P-value*	*F crit*
Between Groups	25.24771	4	6.311928	17.05408	1.69E-06	2.816708
Within Groups	8.142475	22	0.370113			
Total	33.39019	26				

F>Fcrit, therefore H1 is correct. Same reasoning as in previous table.

Appendix H. Fibre/matrix interphase of ATP laminates

Table H.1 and Table H.2 show B_H and B_M values for all ATP laminates, with the corresponding exponential decay curves shown in Figure H.1 and Figure H.2.

Table H.1: Summary of and B_H and B_M values for the exponential decay modelling of ATP CF/PEKK samples manufactured at T_{nip} = 380°C (on a metal tool). Values are given for each tested location on each sample. The cells shaded the darkest grey in the tables are a guide to the eye of the highest B values for each laminate (the steepest slope and the shortest fibre-matrix transition). The lower the B value, the lighter the cell shading is, with white cells indicating the lowest B value of each laminate (the softest gradient, and the longest fibre-matrix transition).

	ATP samples (metal tool)								
Laminate code	**380-4-2**			**380-2-2**			**380-4-4**		
Indentation distance from bottom surface (mm)	0.5 (bottom)	1 (middle)	1.5 (top)	0.5 (bottom)	1 (middle)	1.5 (top)	0.5 (bottom)	1 (middle)	1.5 (top)
B_H (Hardness)	3.280	3.816	2.509	2.237	2.263	2.334	2.040	4.139	2.178
B_M (Elastic modulus)	1.602	1.687	1.338	1.083	1.093	1.177	0.918	2.512	0.831

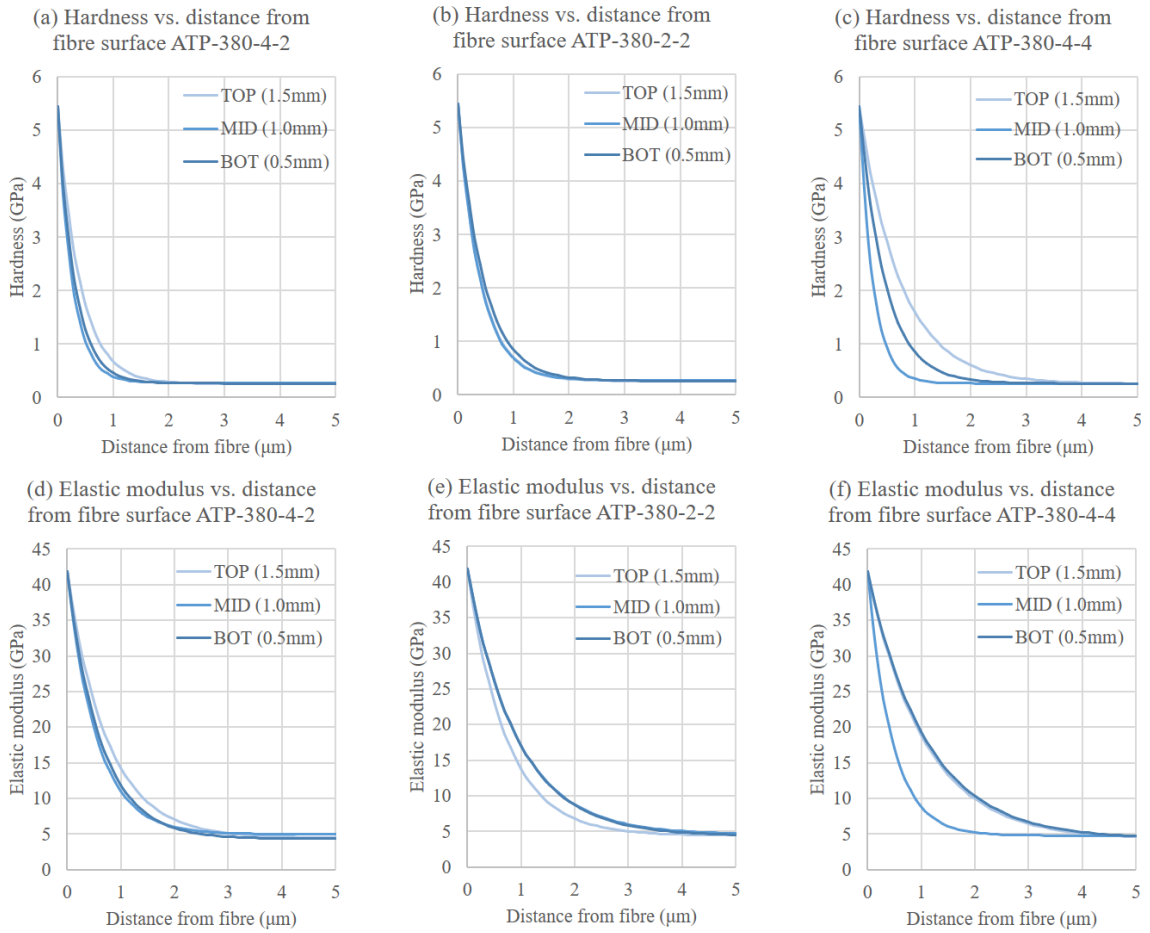

Figure H.1: (a, b, c) Hardness and (d, e, f) elastic modulus exponential decay curve fittings of ATP CF/PEKK T_{nip} = 380°C nanoindentation testing results. Each plot has the curve fittings of all locations of a single sample.

Table H.2: Summary of and B_H and B_M values for the exponential decay modelling of ATP CF/PEKK samples manufactured at T_{nip} = 360°C (on a ceramic tool). Values are given for each tested location on each sample. The cells shaded the darkest grey in the tables are a guide to the eye of the highest B values for each laminate (the steepest slope and the shortest fibre-matrix transition). The lower the B value, the lighter the cell shading is, with white cells indicating the lowest B value of each laminate (the softest gradient, and the longest fibre-matrix transition).

	ATP samples (ceramic tool)							
Laminate code	**360-4-2-2mm**			**360-4-2-6mm**				
Indentation distance from bottom surface (mm)	0.5 (bottom)	1 (middle)	1.5 (top)	0.5 (bottom)	1.75	3 (middle)	4.25	5.5 (top)
***B_H* (Hardness)**	2.766	3.096	2.340	2.414	2.352	2.508	3.456	2.484
***B_M* (Elastic modulus)**	1.291	0.985	0.910	1.198	1.588	1.615	1.379	1.347

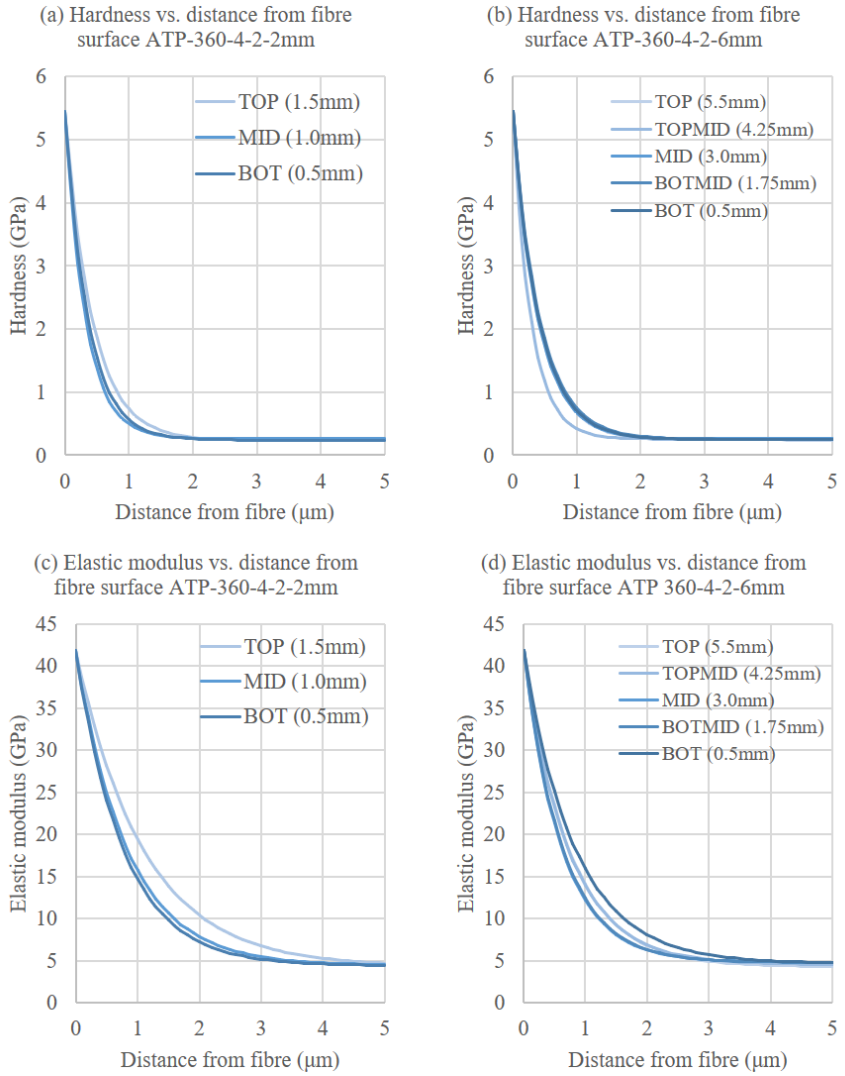

Figure H.2: (a, b) Hardness and (c. d) elastic modulus exponential decay curve fittings of ATP CF/PEKK T_{nip} = 360°C nanoindentation testing results. Each plot has the curve fittings of all locations of a single sample.

Generally, laminates showed slightly steeper slopes (higher *B* values) towards the middle of the laminate for both hardness and elastic modulus. This is not what was expected given the results discussed in Chapter 7, where a higher crystallinity in the middle of the laminates could be expected to

cause a longer transition distance between fibre and matrix properties, and therefore a softer slope. However, any crystallinity developed in the core of the ATP laminates is most likely a consequence of annealing due to heat repasses, during which molecular movement and rearrangement into crystal structure is considerably more restricted than during melt crystallisation. Therefore, any major rearrangement forming an interphase is unlikely.

The above argument still does not explain the reason for the steeper slopes (and therefore shorter transition region from fibre to matrix bulk properties) taking place mainly in the middle locations of laminates. The difference between most curves is quite small, and may not be significant. An exception to this is the considerably steeper MID curves for ATP-380-4-4, likely due to limited data points obtained at distances below 1 μm.

Overall, the changes introduced in lay down speed and roller pressure were not high enough as to introduce any distinctive changes at the fibre/matrix interface that can be captured via microproperty measurements. Hence, the observations are inconclusive. Further work would have to be performed in order to draw any conclusions from this work.

Appendix I. Peer-reviewed publications

Chapters 2, 4, 6 and 7 in this thesis present studies that are based on peer-reviewed publications. These are summarised in the List of publications found in page viii, as well as in a thesis chapter to publication mapping table in page 3. With the exception of the literature review paper, which is not open access, the complete publications can be found in the following pages.

Composites: Part A 159 (2022) 106992

Contents lists available at ScienceDirect

Composites Part A

journal homepage: www.elsevier.com/locate/compositesa

Crystallisation behaviour and morphological studies of PEKK and carbon fibre/PEKK composites

Helena Pérez-Martín [a], Paul Mackenzie [b], Alex Baidak [b], Conchúr M. Ó Brádaigh [a], Dipa Ray [a,*]

[a] School of Engineering, Institute for Materials and Processes, The University of Edinburgh, Edinburgh, United Kingdom
[b] Hexcel Composites Ltd, Duxford, Cambridge, United Kingdom

ARTICLE INFO

Keywords:
A. Polymer-matrix composites (PMCs)
A. Thermoplastic resin
B. Microstructures
B. Thermal properties
CF/PEKK composites
Crystallinity

ABSTRACT

The increased interest in carbon fibre/poly(etherketoneketone) (CF/PEKK) as an option for high-performance applications calls for a thorough understanding of the composite's crystallisation behaviour, due to the essential role that crystallinity plays in performance. In this study, differential scanning calorimetry was used with a variety of thermal cycles to evaluate the effect of thermal history on crystallinity development in unreinforced PEKK and CF/PEKK. Different isothermal holding temperatures during cooling affected the ratio between primary and secondary crystallisation, and non-isothermal cooling cycles influenced the extent of crystallisation. The inclusion of carbon fibres increased the proportion of secondary crystallisation in the matrix and slowed down crystallisation kinetics. A Velisaris-Seferis model was used to model crystallisation kinetics for the isothermal data, and adapted Nakamura models were used for the non-isothermal data. Based on this work, optimum isothermal hold temperatures during cooling for CF/PEKK are estimated to lie in the range of 220–260 °C.

1. Introduction

High-performance, semicrystalline thermoplastics are increasingly being studied as a matrix in structural composites destined for the aerospace industry. Poly(aryletherketones) (PAEKs) in particular, are a family of thermoplastics of interest due to their excellent properties, which also have the added benefit of shorter manufacturing processes that the more conventionally used thermosets lack [1–3]. Due to the higher melt temperatures of PAEK thermoplastics, however, composite manufacturing requires high processing temperatures (350–390 °C). The processing cycle plays a key role in the case of semicrystalline thermoplastic composites, as it controls the extent of crystallinity developed in the material and dictates the mechanical properties [4–6]. Therefore, it is of interest to further investigate the crystallisation behaviour of thermoplastics in order to maintain the performance required for aerospace applications.

Poly(etheretherketone) (PEEK) is the most widely studied polymer of the PAEK family, and has been one of the main candidates as a thermoplastic matrix for high-performance composite applications [1,3,7–10]. Poly(etherketoneketone) (PEKK) has been less studied to date, but is becoming an increasingly attractive option for advanced composites [2,4,11–14]. The reason for this is the difference in ether/ketone ratio between PEEK and PEKK: the ketone-ketone link in PEKK offers a tuneability that PEEK doesn't allow for, where this link can be either para- or meta-, as shown in Fig. 1. The amount of para- to meta-linkages that PEKK contains is commonly referred to as the *T/I ratio*, or *grade*. This is due to its preparation method, combining diphenyl ether (DPE) with terephthalic acid (T), which leads to para- linkages, or with isophthalic acid (I), which creates meta- linkages [2].

The grade has a large effect on the properties of PEKK: a high T/I ratio results in a higher content of *para*-linkages, leading to stiffer molecular chains which in turn allows better chain-packing and a higher melting temperature. This increases viscosity and hinders manufacturing, but results in higher crystallinity and faster crystallisation kinetics due to an increased chain linearity. Conversely, a low T/I ratio will result in more flexible chains and a lower melting temperature, benefitting manufacturability but limiting crystallisation kinetics due to the chain irregularity disrupting crystal packing [15].

The crystallisation mechanism of different PEKK grades has been investigated by several authors [9,11–14,16–19]. Similarly to PEEK, PEKK has been found to crystallise following two distinct crystallisation mechanisms:

* Corresponding author at: 1.140 Sanderson Building, King's Buildings, Edinburgh EH9 3FB, Scotland, UK.
E-mail address: Dipa.Roy@ed.ac.uk (D. Ray).

https://doi.org/10.1016/j.compositesa.2022.106992
Received 17 December 2021; Received in revised form 22 April 2022; Accepted 6 May 2022
Available online 11 May 2022
1359-835X/© 2022 The Author(s). Published by Elsevier Ltd. This is an open access article under the CC BY license (http://creativecommons.org/licenses/by/4.0/).

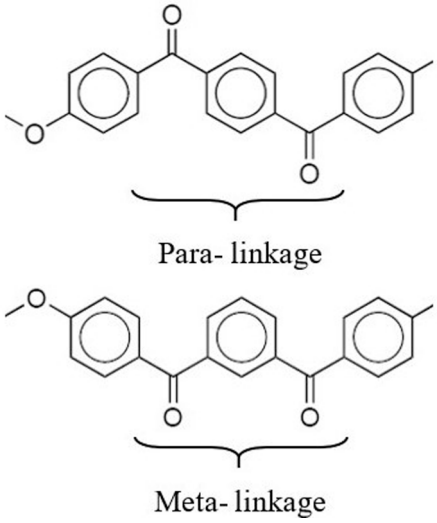

Fig. 1. Molecular structure of PEKK with para- (top) and meta- (bottom) links.

- Primary crystallisation, where amorphous material nucleates and spherulitic growth takes place.
- Secondary crystallisation, where amorphous material between the lamellae of the already established spherulites crystallises.

Fig. 2 depicts these two mechanisms. Spherulitic growth is shown first, indicated by the arrows; and the interlamellar material which undergoes secondary crystallisation is shown magnified.

Literature has highlighted the presence of these two crystallisation modes forming during isothermal holds [2,11–14,16,19,20,22–28]. This is observable in DSC melting curves, where the presence of two (endothermic) melting peaks has been attributed to the dual crystallisation mechanism:

- A higher temperature endotherm (HTE), corresponding to the melting of the primary crystallisation phase (conventional melting). The temperature at which this endotherm takes place is not affected by the isothermal hold temperature.
- A lower temperature endotherm (LTE), associated with the melting of the secondary crystallisation structures. This peak takes place earlier in the heating process, approximately 10–15 °C above the isothermal hold temperature.

Quiroga Cortés et al. [12] observed that the LTE increased in size with higher temperatures and longer holding times of unreinforced PEKK, suggesting an increase in the contribution of secondary crystallisation to the overall crystallisation mechanism. Both peaks contribute towards the total crystallinity of the material. An example of these two peaks is shown in Fig. 3.

However, associating the primary and secondary crystalline phases to the presence of two distinct endothermic peaks poses a limitation in the case of non-isothermal crystallisation studies. In non-isothermal studies of several grades of PEKK by Quiroga Cortés et al. [12] the DSC melting curves showed a single melting endotherm, corresponding to conventional melting (the HTE), as well as a cold crystallisation exotherm, indicating the presence of amorphous material in the samples as a consequence of the faster cooling rates. The absence of an LTE is not addressed in this case. Bessard et al. [24] performed a similar study on PEEK, where they observed a shoulder at the beginning of the single melting endotherm for the slower cooling rates, indicating some contribution from the secondary crystallisation. Similar observations were made by Regis et al. [29] and by Lustiger et al. [30] in their work

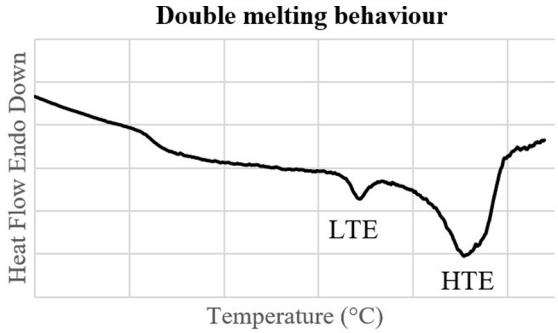

Fig. 3. Representative thermogram of double melting behaviour.

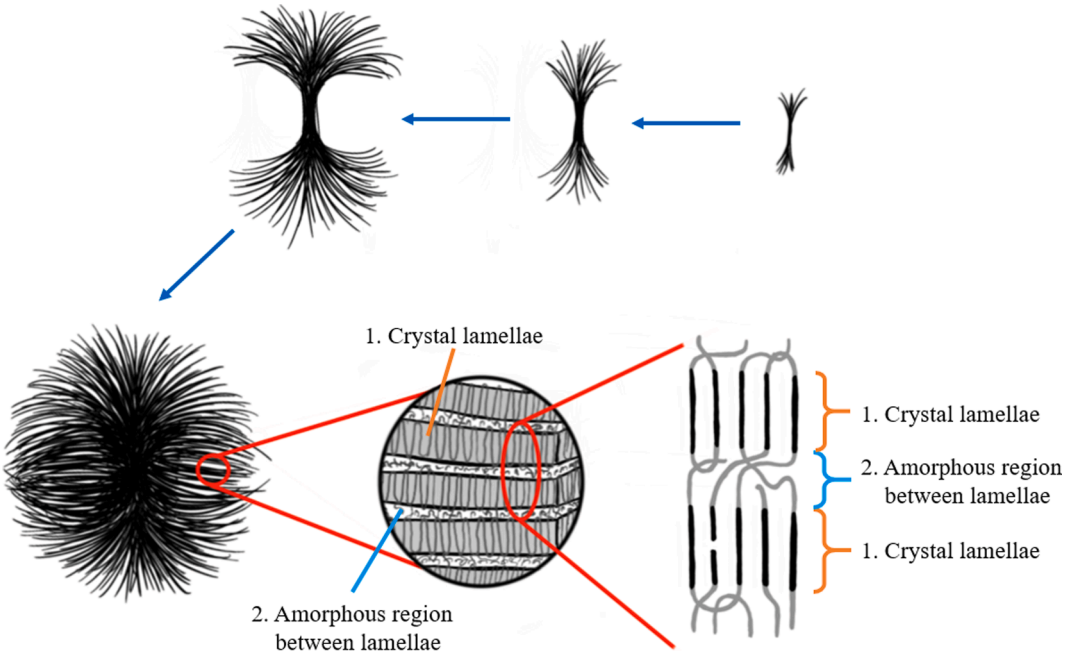

Fig. 2. Schematic depicting spherulitic formation, showing lamellae (crystal) and amorphous regions of a spherulite. Drawn after [2,20,21].

on PEEK and carbon fibre (CF)/PEEK. The presence of secondary crystallisation in slow-cooled PEEK can be explained by the faster kinetics that the PEEK possesses compared to PEKK, due to PEEK's higher chain linearity and lower ketone content. Since the development of secondary crystallisation is determined by time, it is therefore logical that there will be a lower contribution of secondary crystallinity (if at all) at faster cooling rates. The lack on an LTE in non-isothermal PEKK studies may suggest that there is no secondary crystallisation phase present in PEKK after undergoing cooling from the melt, however this has not been explored or discussed in depth to date.

Several studies have integrated both primary and secondary crystallisation mechanisms into crystallisation kinetic models, many of which are based on the Avrami equation [17,22,31,32]:

$$\alpha(t) = 1 - \exp(-kt^n) \tag{1.1}$$

where $\alpha(t)$ is the relative volume fraction crystallinity attained at time t, k is the crystallisation rate constant (which is temperature dependent), and n is the Avrami exponent. Both the crystallisation rate constant and the Avrami exponent are dependent on the nature of the crystallisation, namely the crystalline growth geometry and whether crystallisation is instantaneous or sporadic [2,11,17,33]. k is generally expressed as a function of potential nuclei N and crystal growth rate G. The exact relation is dependent on the nature of crystallisation, and will be defined later in this article. G can be expressed following the Hoffmann-Lauritzen theory [11,34]:

$$G(T) = G_0 \exp\left(-\frac{U^*}{R(T-T_0)}\right)\exp\left(-\frac{K_g}{T\Delta \times T \times f}\right) \tag{1.2}$$

G_0 is a pre-exponential factor independent of temperature. The first exponent contains the contribution of the macromolecular chain diffusion in the melt, whereas the second exponential term corresponds to the contribution of the nucleation process. U^* is the activation energy of the molecular transfer from the melt to the crystal surface, T_∞ is the temperature below which diffusion stops ($T_\infty = T_g - 30$), R is the universal gas constant, K_g is the activation energy of nucleation for a crystal with a critical size, ΔT is the degree of supercooling ($\Delta T = T_m^0 - T$) with T_m^0 as the equilibrium melting temperature, and f is a correction coefficient to account for the temperature dependence of the melting enthalpy ($f = 2T/(T_m^0 + T)$). This model has been successfully implemented to describe crystal growth on PEKK by several authors [11,17,35], and is used later in this article.

It is worth noting, however, that the Avrami equation on its own doesn't allow for the existence of the secondary crystallisation mechanism that takes place in PEKK. This is observable from an Avrami plot, where a plot of $\ln[-\ln(1-\alpha)]$ against $\ln(t)$ will result in a straight line of gradient n and intercept $\ln k$ if the fit is successful. This is not the case for PEKK due to the presence of this secondary mechanism, which is observed later in this article, as well as in literature [11,13]. The most relevant models for dual crystallisation adapt the Avrami equation to take this into account. One of these is the Velisaris-Seferis model [32], in which two separate Avrami crystallisation processes are considered in parallel, representing primary and secondary crystallisation (Eq. (1.3)):

$$\alpha(t) = w_1[1 - \exp(-k_1 t^{n_1})] + w_2[1 - \exp(-k_2 t^{n_2})] \tag{1.3}$$

Subscripts 1 and 2 refer to primary and secondary crystallisation respectively. w_1 and w_2 are weight factors corresponding to each crystallisation mechanism, where $w_1 + w_2 = 1$. This model has been successfully applied to PEEK [32,36], CF/PEEK [32] and PEKK [13].

A different two-stage crystallisation model, originally developed by Hillier and later modified by Hsiao et al. [13] and Choupin et al. [11] has been implemented on PEEK, CF/PEEK and PEKK as well. In this case, the secondary crystallisation is expressed in an integral form. Choupin et al. [17] developed a derivative Hillier model in later work, which has been successfully implemented on unreinforced PEKK. A more thorough explanation of the above can be found in the cited articles, as well as in [2].

The Velisaris-Seferis model is adequate for isothermal crystallisation modelling, however in non-isothermal instances, the variation of the crystallisation rate constant k with respect to temperature must be accounted for. This was carried out by Nakamura in their adaptation of the Avrami equation as follows [37]:

$$\alpha(t) = 1 - exp\left[-\left(\int_0^t K\, dt\right)^n\right] \tag{1.4}$$

where K is temperature dependent and connected with the isothermal crystallisation rate constant k through the relation:

$$K = k^{1/n} \tag{1.5}$$

An equation for K can therefore be determined by first finding a temperature-dependent equation for k based on isothermal crystallisation experiments and the Hoffmann-Lauritzen model, and then substituting into Eq. (1.5).

As per the Avrami equation, the Nakamura model only takes into account a single crystallisation mechanism. In a similar manner to the Velisaris-Seferis model, the secondary mechanism can be accounted for by having two separate Nakamura models acting in parallel:

$$\alpha(t) = w_1\left(1 - exp\left[-\left(\int_0^t k_1^{1/n_1} dt\right)^{n_1}\right]\right) + w_2\left(1 - exp\left[-\left(\int_0^t k_2^{1/n_2} dt\right)^{n_2}\right]\right) \tag{1.6}$$

with substitutions for K_1 and K_2 as shown in Eq. (1.5). Bessard et al. [24] used a differential form of Eq. (1.6) to model non-isothermal crystallisation kinetics of unreinforced PEEK. Their investigation resulted in a successful fit where a gradual decrease in the secondary crystallisation contribution to the total crystallinity was observed with a faster cooling rate.

Despite this understanding of the crystallisation mechanisms, kinetics and modelling of different grades of PEKK developed by several authors, an investigation and comparison of crystallisation between unreinforced PEKK and CF/PEKK has not been performed in depth. Some published literature discussing the impact of carbon fibres on crystallinity development is available for PEEK, where fibre inclusions were found to decrease overall crystallinity [5]. Research on kinetics is somewhat inconclusive, where some work proposes that the inclusion of fibres has no major effect on PEKK crystallisation kinetics [13], but other research suggests that this varies with isothermal temperature hold, leading to faster kinetics in composite samples at higher temperatures (reported in theses work on PEEK [38] and PEKK [39]). These are discussed in more detail in [2].

Further to this, the discussion of dual crystallisation kinetics during non-isothermal crystallisation is sparse, now that a secondary crystallisation peak is not obvious in heat scans performed in literature. Consequently, non-isothermal crystallisation models are sparsely implemented on PEKK compared to isothermal ones.

This article offers a detailed study of PEKK with a T/I ratio of 70/30 in both unreinforced and composite forms, undergoing a variety of isothermal and non-isothermal cycles in order to study the effect of carbon fibre inclusions on the crystallisation mechanism and kinetics. The Velisaris-Seferis and dual Nakamura models discussed above are then implemented to interpret the results. This work first covers the crystallinity, morphology, kinetics and modelling of the isothermal cycles that unreinforced and composite PEKK are exposed to, followed by the non-isothermal studies and models. A brief discussion focussing on the relevance of this work in high-performance thermoplastic composite applications is also included.

2. Material and methods

2.1. Materials

In this study, KEPSTAN PEKK 7002PT by Arkema is used in powder form, provided by Hexcel Composites Ltd. This grade of PEKK has a T/I ratio of 70/30, with glass transition temperature and melting temperature measured at 161 °C and 338 °C respectively. This grade in particular is intended for the manufacturing of unidirectional prepreg tape with carbon fibres [40].

The composite material used is unsized AS7 CF/PEKK unidirectional prepreg tape, provided by Hexcel Composites Ltd. The PEKK matrix in the tape is the same grade as the powder. The fibre volume fraction of the prepreg material was measured to be 60.8% by acid digestion (68.3% fibre weight content).

2.2. Differential scanning calorimetry (DSC)

Isothermal and non-isothermal crystallisation analyses were carried out using a PerkinElmer DSC 8000, with aluminium pans non-hermetically sealed with aluminium lids. Indium was used to calibrate the temperature and heat of fusion prior to any experiments. Sample weights of 5–7 mg of neat PEKK powder were used, whereas sample weights of 10–12 mg of CF/PEKK prepreg tape were used. All experiments were run twice in order to ensure repeatability, and under a nitrogen environment to avoid any sample degradation.

In order to erase any thermal history, samples were initially heated to 370 °C, and held in the melt for 5 min. For isothermal analysis, samples were cooled at a rate of 150 °C/min down to the temperature of interest (220, 240, 260, 280, or 300 °C), held for 60 min, and then further cooled at a rate of 150 °C/min to room temperature. For non-isothermal crystallisation analysis, samples were cooled at the rate of interest (5, 10, 20, 40, 60, 100 or 150 °C/min) from the melt to room temperature. All samples then underwent a second heat ramp at 20 °C/min to measure the effect of the crystallisation cycle on the glass transition, melting temperature and crystallinity. The temperature–time plots of these thermal cycles are shown in Fig. 4.

Performing the second heat ramp at the end of the cycle removes all thermal history. In order to later observe the impact of the thermal history at microscopic scale under scanning electron microscopy (SEM), CF/PEKK samples underwent the same cycle once again with the exception of the final heating ramp.The crystallinity of a sample can be estimated with:

$$\chi = \frac{\Delta H_m - \Delta H_{cc}}{\alpha \times \Delta H_{100\%}} \tag{2.1}$$

where ΔH_m is the melting enthalpy, ΔH_{cc} is the cold crystallisation enthalpy, α is the weight fraction of matrix content (100% in the case of the unreinforced PEKK powder, 31.7% in the case of CF/PEKK prepreg tape) and $\Delta H_{100\%}$ is the theoretical melting enthalpy of 100% crystalline PEKK. This has been calculated to be 130 J/g by Chang and Hsiao [16].

2.3. Scanning electron microscopy

SEM was performed on cryofractured CF/PEKK prepreg tape samples after undergoing the DSC cycles described above, in order to qualitatively examine the effect that crystallinity had on fibre–matrix interfacial adhesion and matrix morphology. Cryofracture involved submerging the samples in liquid nitrogen, followed by fracturing to expose their cross-section. Samples were prepared with a 15 nm sputter coating of gold to enhance surface conductivity, and then imaged with a JEOL JSM-IT100 instrument at 20 kV.

3. Results and discussion

3.1. Isothermal crystallisation

3.1.1. Crystallisation at different isothermal temperatures

Fig. 5 shows the heat flow variation of one set of runs of unreinforced PEKK powder and CF/PEKK prepreg tape, during a heat ramp of 20 °C/min from room temperature to 370 °C, after undergoing different isothermal temperatures from the melt held for 60 min. Table 1 shows average data from this portion of the cycle for both performed runs.

Two melting endotherms are observed in the heat scans in Fig. 5, corresponding to the LTE and HTE as discussed in Section 1. The LTE is approximately 15 °C above the isothermal temperature throughout for both unreinforced and composite PEKK. In the case of the 280 °C and 300 °C isothermal holds where the two endotherms overlap, the area corresponding to each endotherm was calculated by drawing a line perpendicular to the baseline, crossing the curve at its inflection point between the two peaks. This is illustrated on the 300 °C isothermal curve in Fig. 5a.

As the isothermal hold temperature increases, the LTE:HTE ratio can be seen to increase, the variation of which can be observed in Table 1 and Fig. 6. The reasoning for this may be as follows. In order for secondary crystallisation to take place, primary crystallisation (formation of spherulites) must be established first. As primary crystallisation takes

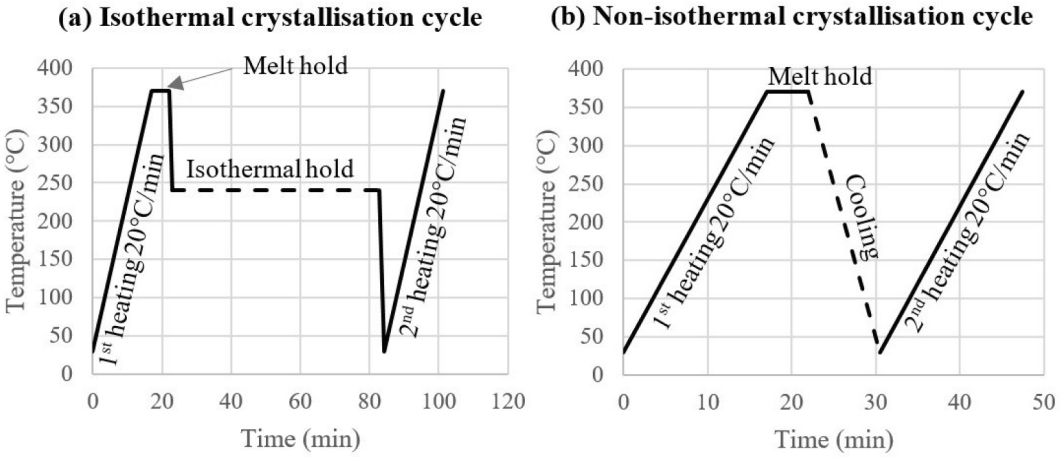

Fig. 4. DSC heat cycle of all samples undergoing (a) isothermal crystallisation analysis and (b) non-isothermal or dynamic crystallisation analysis. The dotted sections of the plot indicate (a) the isothermal hold of the cycle, which can be at 220, 240, 260, 280 or 300 °C; and (b) the cooling section of the cycle, which can be 5, 10, 20, 40, 60, 100 or 150 °C/min cooling rate.

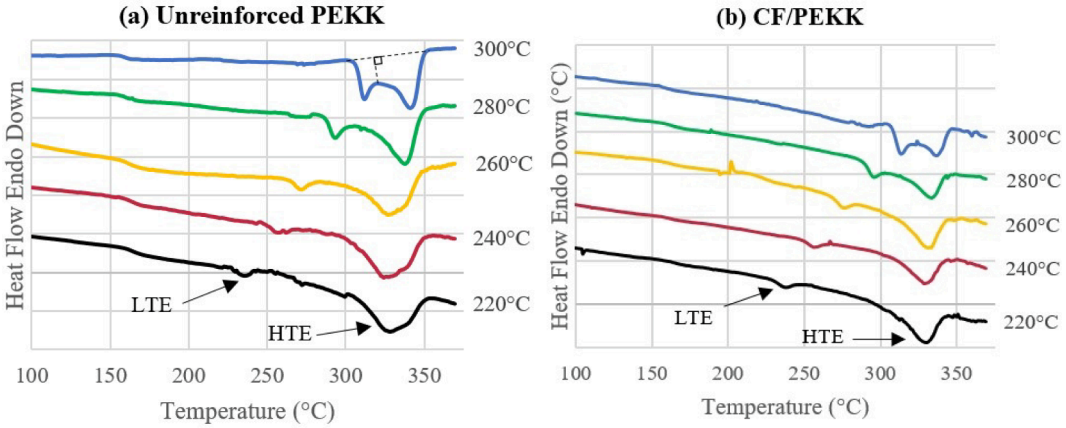

Fig. 5. DSC thermograms (second heating cycles in Fig. 4a) of (a) unreinforced PEKK powder and (b) CF/PEKK prepreg tape after undergoing isothermal crystallisation at different temperatures with a hold time of 60 min. Dotted lines in the 300 °C curve in (a) demonstrate how the area corresponding to each endotherm (LTE and HTE) was calculated in instances where the two peaks overlap.

Table 1
Average values for transition temperatures, melting enthalpies and total crystallinity of unreinforced PEKK powder and CF/PEKK prepreg tape after undergoing different isothermal holds.

Isothermal temp. (°C)	Unreinforced PEKK						
	T_g (°C)	T_{LTE} (°C)	ΔH_{LTE} (J/g)	T_{HTE} (°C)	ΔH_{HTE} (J/g)	LTE:HTE	χ (%)
220	165.5 ± 1.1	239.6 ± 4.4	1.8 ± 0.2	328.6 ± 0.5	29.7 ± 0.1	5:95 ± 1	24.2 ± 0.2
240	163.5 ± 0.3	258.4 ± 2.0	2.3 ± 0.3	324.0 ± 0.2	29.1 ± 0.4	7:93 ± 1	24.1 ± 0.2
260	162.0 ± 0.8	274.9 ± 3.3	2.5 ± 0.2	331.9 ± 5.0	26.9 ± 0.2	8:92 ± 1	22.6 ± 0.1
280	159.7 ± 0.8	298.1 ± 4.9	7.3 ± 0.3	337.5 ± 0.1	28.4 ± 0.4	20:80 ± 1	27.5 ± 0.5
300	158.5 ± 0.1	315.5 ± 3.8	10.4 ± 0.5	341.7 ± 0.5	20.4 ± 1.8	34:66 ± 3	23.7 ± 1.1
				CF/PEKK			
220	164.3 ± 0.9	239.8 ± 2.1	1.0 ± 0.1	329.4 ± 0.3	9.1 ± 0.1	10:90 ± 0	24.3 ± 0.6
240	158.5 ± 1.8	258.9 ± 2.5	1.1 ± 0.2	329.2 ± 0.3	8.5 ± 0.1	10:90 ± 1	23.0 ± 0.5
260	160.4 ± 1.4	277.0 ± 1.2	1.1 ± 0.2	334.1 ± 2.7	8.2 ± 0.5	12:88 ± 1	22.5 ± 1.5
280	159.6 ± 2.8	300.4 ± 5.0	3.1 ± 0.4	335.5 ± 2.2	7.9 ± 0.1	28:72 ± 2	26.6 ± 1.2
300	161.4 ± 2.0	316.3 ± 2.8	4.7 ± 0.5	338.8 ± 2.1	5.2 ± 0.1	47:53 ± 3	23.7 ± 1.0

T_g: Glass transition temperature.
T_{LTE}: Low temperature endotherm.
ΔH_{LTE}: Low temperature endotherm enthalpy.
T_{HTE}: High temperature endotherm.
ΔH_{HTE}: High temperature endotherm enthalpy.
LTE:HTE: Low temperature endotherm to high temperature endotherm ratio.
χ: Total crystallinity.

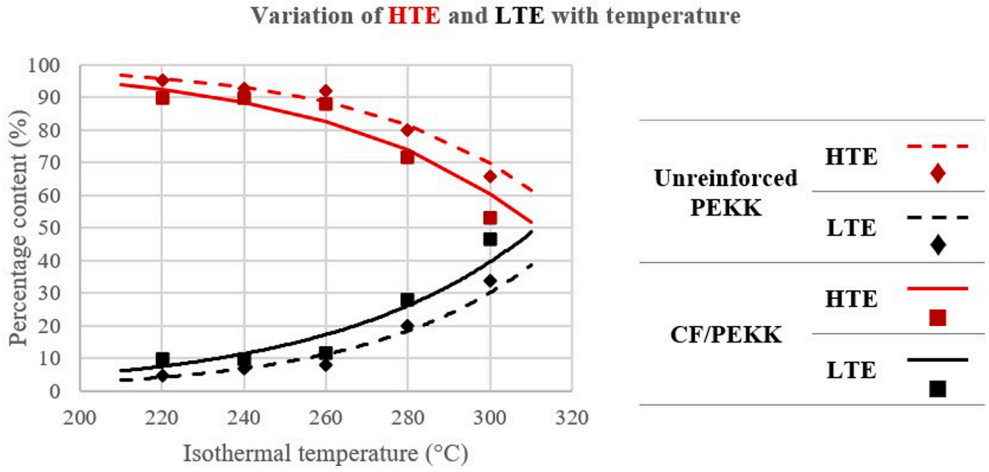

Fig. 6. Variation of LTE and HTE with isothermal temperature for unreinforced PEKK powder and CF/PEKK prepreg tape. Solid and dotted lines are exponential lines of best fit.

place and spherulites develop, the spherulites' lamellae expand and branch out, becoming larger and therefore creating more interlamellar space for secondary crystallisation to happen. The extent to which spherulites grow is determined by general polymeric nucleation theory, where at lower temperatures the formation of new spherulite nuclei takes precedence over spherulitic growth. This results in a high number of small spherulites. On the other hand, at higher temperatures, spherulitic growth predominates over the formation of new nuclei, resulting in a smaller number of spherulites but larger in size. It is therefore possible that, at higher isothermal temperatures, there is more interlamellar space created by the larger spherulites, allowing for a larger volume of interlamellar growth (secondary crystallisation) to take place than at low isothermal temperatures. This therefore results in a larger presence of secondary crystallites, and a larger LTE:HTE endotherm ratio. A schematic portraying this is shown in Fig. 7.

From the above results in Table 1 and Fig. 6, it can also be observed that CF/PEKK has a slightly larger LTE:HTE ratio than the unreinforced PEKK (a higher presence of secondary crystallisation) throughout all isothermal hold temperatures. A possible reason for this could be the presence of densely-packed fibres supressing spherulitic development, causing a slower growth of the primary crystallisation phase in CF/PEKK compared to the neat samples at a given time *t*, as shown in Fig. 8.

Spherulitic growth is governed by primary crystallisation, which in turn affects the extent to which secondary crystallisation can take place. However, secondary crystallisation takes place at a smaller scale and does not require major molecular rearrangement in the manner that primary crystallisation does (since it occurs in already established interlamellar regions), and it is therefore possible that it *locally* progresses at the same speed as in the unreinforced case. This would result in a larger percentage of the crystallinity contribution in CF/PEKK being from the secondary phase, resulting in a larger LTE:HTE ratio as seen in Fig. 6.

Another potential explanation for the larger proportion of the LTE could be a different nucleation density and crystal growth at the fibre surface. Fibres may be a source of heterogeneous nucleation and transcrystallinity, which may possess a higher fraction of secondary crystallisation than spherulites developed in the bulk of the matrix via homogeneous nucleation.

Fig. 9a, b and c show SEM images of cryofractured CF/PEKK samples after undergoing the previously described DSC isothermal cycles at 220, 260 and 300 °C respectively. Spherulite structures can be observed in Fig. 9c, these becoming smaller and slightly less defined in Fig. 9b and even less so in Fig. 9a. As described previously, higher isothermal hold temperatures induce a lower nucleation density and larger spherulitic growth, which is the case in the 300 °C isotherm. Consequently, the largest and most defined spherulites can be observed in Fig. 9c. On the other hand, at lower isothermal temperatures, nucleation density is higher and therefore smaller spherulites are formed due to an early impingement between growth fronts. This may be the reason why spherulitic structures in Fig. 9a are the least defined. However, this could also be due to the proximity of the fibres limiting the crystallisation to purely perpendicular to the fibre surface.

Another potential explanation for the matrix morphology seen in these figures is the presence of transcrystallinity. It is possible that with lower isothermal hold temperatures, the growth of a transcrystalline interface is incentivised as a consequence of primary nucleation dominating at lower temperatures and the fibre surfaces inducing such nucleation. In Fig. 9b (260 °C isotherm), some epitaxial growth can be observed perpendicular to the fibre surfaces, which then seem to change orientation and form more spherulite-like structures in the bulk. In Fig. 9a, this perpendicular growth seems to be the most obvious.

3.1.2. *Crystallisation kinetics at different isothermal holds*

Fig. 10 shows heat flow – time thermograms of unreinforced PEKK and CF/PEKK samples during the DSC isothermal holds. Crystallisation occurs in the first minutes of the isothermal hold, and therefore only the first 20 min of the 60-minute hold are shown (minutes 20–60 do not show any variation in heat flow).

In the case of unreinforced PEKK, crystallisation kinetics curves for 220 °C and 240 °C are not present and the peak for 260 °C is only partially present. This is because unreinforced PEKK is partially crystallised when reaching these isothermal temperatures. When cooling from the melt at 150 °C/min, crystallisation takes place in the temperature range 260–210 °C (shown later in Fig. 17a in Section 3.2.2, where crystallisation kinetics under non-isothermal conditions is discussed). By the time that the isothermal temperature (240 or 220 °C) is reached when cooling from the melt, crystallisation has already occurred. Therefore, when the isotherm hold begins, there is no crystallisation

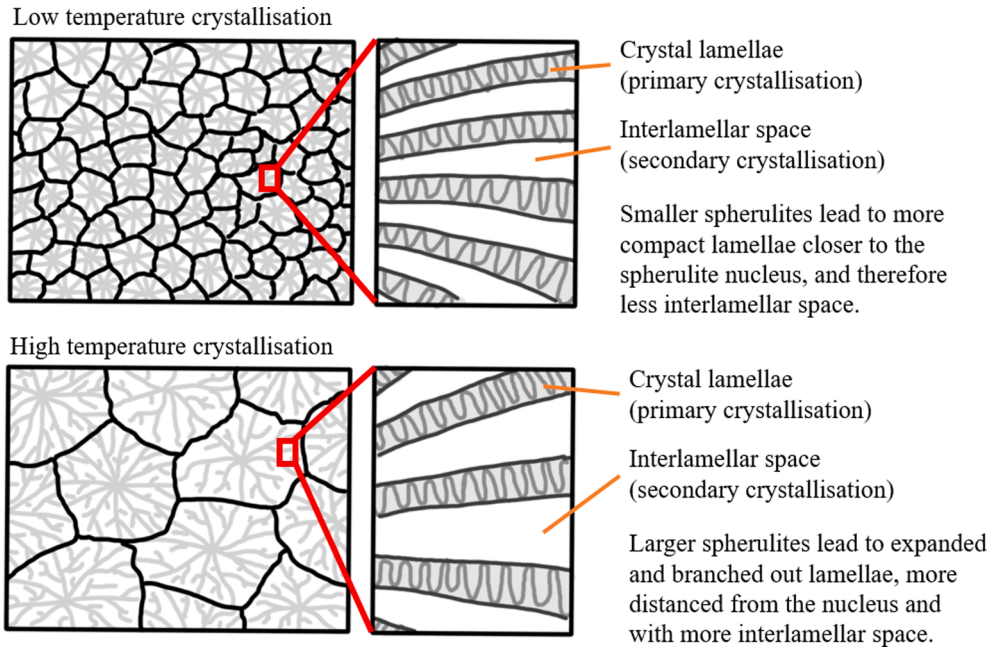

Fig. 7. Schematic showing spherulite size at low and high temperature isotherms, and the consequent interlamellar spacing in which secondary crystallisation takes place.

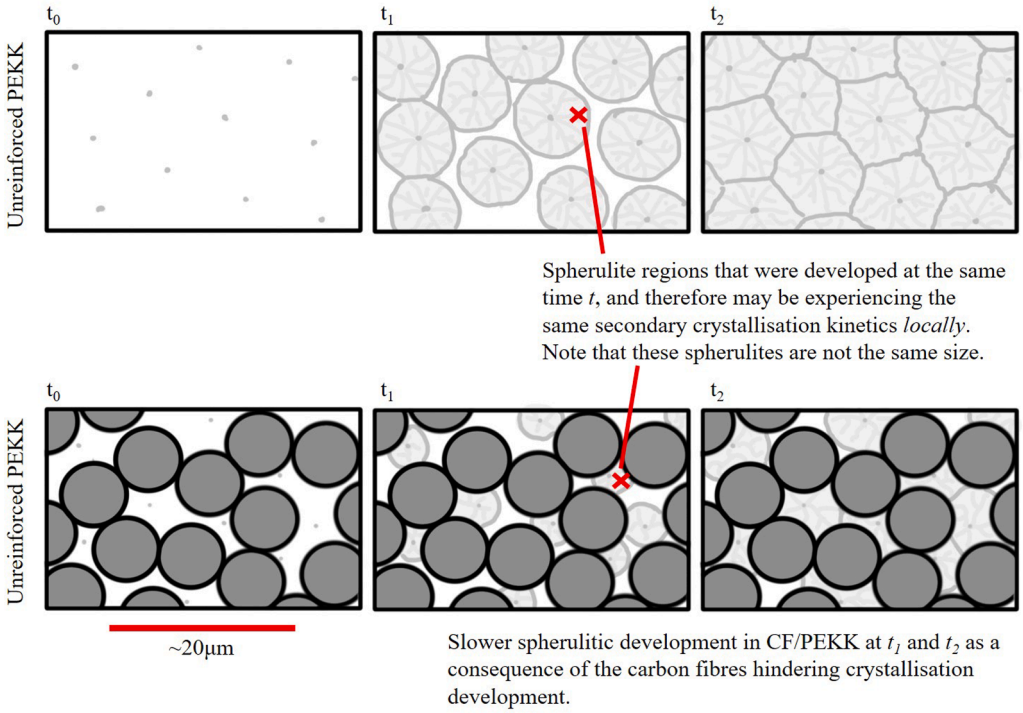

Fig. 8. Schematic representation of spherulitic development in unreinforced PEKK and CF/PEKK, depicting the difference in growth kinetics at different times as a consequence of CFs inhibiting spherulitic growth. Schematics of CF/PEKK are based on an SEM micrograph of the cross-section of a CF/PEKK prepreg sample. The regions marked with an X indicate areas in the two different samples that crystallised at the same time t.

taking place. In order to assess the crystallisation kinetics at the lower isotherms, a faster cooling rate would have to be applied. Kinetics and modelling of unreinforced PEKK will therefore only be discussed for the isothermal holds at 260, 280 and 300 °C henceforth.

Other authors have assessed the crystallisation kinetics of unreinforced PEKK in literature. Choupin et al. [17] used KEPSTAN PEKK 7002 in their studies, a similar grade of PEKK with the same T/I ratio as the one used in this article (KEPSTAN PEKK 7002PT). While they found peak kinetics to take place at approximately 245 °C (which would be in line with this article's results), kinetics were considerably slower. They observed a clear crystallisation peak at ~ 0.8 min during an isothermal hold of 250 °C after cooling at 40 °C/min, a cooling rate which they determined was fast enough to not result in any crystallisation before reaching the isothermal temperature. This is not the case in this study, where both unreinforced and composite PEKK do crystallise at rates above 40 °C/min, as will be shown in Section 3.2.

In a different article, Chelaghma et al. [35] used KEPSTAN PEKK 7003, which also possesses a T/I ratio of 70/30 but has a lower viscosity than the KEPSTAN PEKK 7002 series [15]. This material still displayed slower crystallisation kinetics (~1.8 min peak time at 270 °C) than the grade being studied in this article (~0.5 min peak time at 280 °C). This may be a consequence of different syntheses or modifications of the different grades, as they are intended for different applications [40].

A comparison of the rest of the unreinforced PEKK isothermal holds with their composite counterparts clearly revealed that CF/PEKK has slower crystallisation kinetics, peaking between 240 and 260 °C. This is likely due to the high carbon fibre content hindering the growth and development of spherulites as previously discussed, resulting in slower kinetics. Hsiao et al. [13] found peak kinetics to take place at 255 °C and reported minimal impact of fibres on the crystallisation rate of PEKK under isothermal conditions, however there could be differences in the matrix composition, which in Hsiao et al.'s case was provided by DuPont. It is also possible that the different carbon fibres used (AS4 carbon fibres in Hsiao et al.'s work) cause the difference in results.

3.1.3. Modelling of isothermal crystallisation kinetics

In order to implement the Velisaris-Seferis model discussed in Section 1, a plot of the relative crystallinity of each sample against time is needed. This can be obtained by dividing the area under the curves in Fig. 10 at time t by the area under the entire curve. This is defined by Eq. (3.1):

$$\alpha(t) = \frac{\int_0^t Q(t)dt}{\int_0^{t_\infty} Q(t)dt} \tag{3.1}$$

where $Q(t)$ is the heat flow measured at time t, and t_∞ is the time when the polymer is fully crystallised. The resulting relative crystallinity-time curves are shown in Fig. 11. In the cases where some data points at the beginning of the isothermal crystallisation exotherm are missing in Fig. 10 as a consequence of partial crystallisation during the cooling step, the curves shown in Fig. 11 do not start at a relative volume crystallinity of 0.

Avrami plots can be obtained by plotting $\ln[-\ln(1-\alpha)]$ against $\ln(t)$, shown in Fig. 12. As discussed in Section 1, these do not provide a straight line of best fit, implying that there is more than a single crystallisation mechanism taking place. An estimated Avrami exponent for the primary crystallisation stage can be obtained by calculating the slope of the first part of the curves [11,13,32].

In the case of unreinforced PEKK, the linear sections of the plots average to 2.9, making 3 the closest integer. This is in line with the instantaneous nature of crystallisation, as observed by other authors in hot stage microscopy [11,35], as well as its three-dimensional, spherulitic form. For CF/PEKK however, these slopes average to 2.5. A potential cause for this could be restricted growth as a consequence of fibre proximity, which may limit the three-dimensional spherulitic growth in the matrix bulk, inducing early impingement and reducing the value of n_1. High nucleation density on the fibre surface may be another reason for the lower n_1 value: this may cause a transcrystalline region, which resembles a unidirectional growth from the nucleation site as opposed to the three-dimensional growth of spherulites in the bulk.

Values for n_2 were not determined from the Avrami plots in Fig. 12,

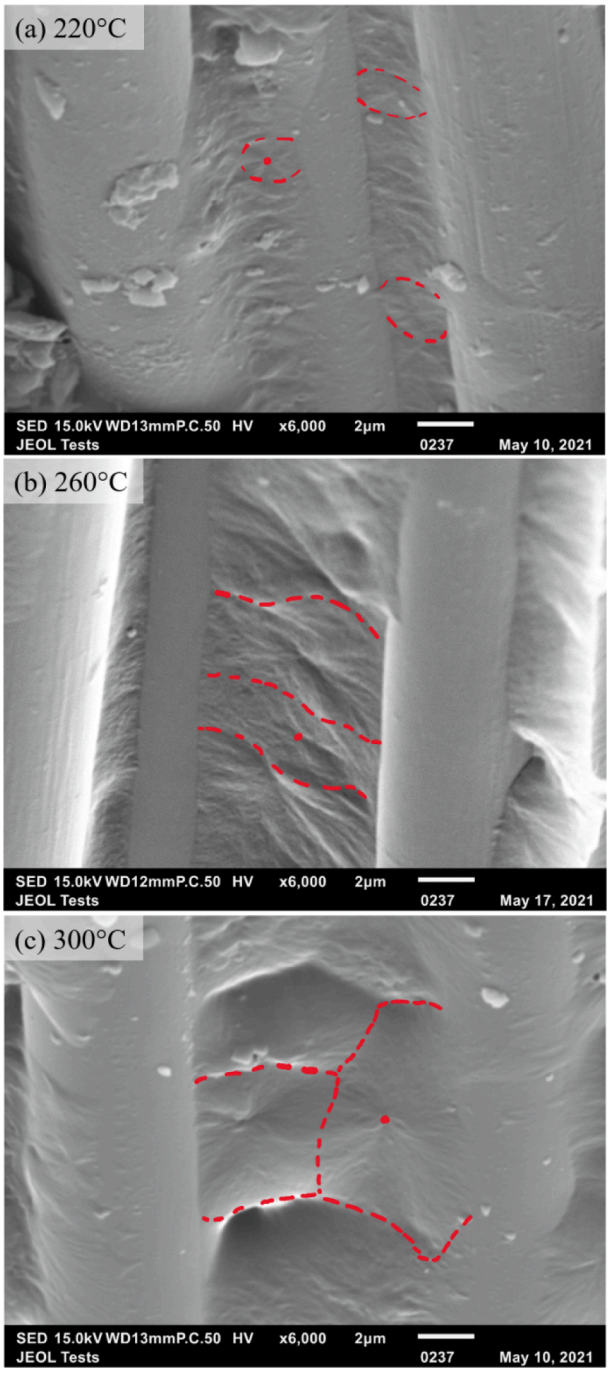

Fig. 9. SEM of cryofractured CF/PEKK samples after undergoing an isothermal hold of (a) 220 °C, (b) 260 °C and (c) 300 °C from the melt. Red annotations highlight spherulitic structures, with a red dot providing an example of a nucleus location. (For interpretation of the references to colour in this figure legend, the reader is referred to the web version of this article.)

now that the gradients obtained at the upper tail of the curves varied between 0.6 and 0.8, and these proved to provide very poor fits. Further to this, other authors have used both integer and non-integer values ranging between 1 and 3 to model secondary crystallisation kinetics of PEEK and PEKK with Avrami-based models [17,22,32,35]. This value would be picked based on which one provided the best fit with the experimental data, and some authors allowed the value for n_2 to vary with the isothermal hold temperature [28]. This further highlights the more complicated nature of secondary crystallisation, which suggests that the growth of secondary crystallisation structures may consist of different dimensions, the proportions of which may vary with isothermal holding temperature.

For modelling purposes, the Avrami exponents (n_1 and n_2) were kept constant across different temperatures in this work. The Velisaris-Seferis model was scripted in MATLAB, setting n_1 to 3 and 2.5 for unreinforced and composite PEKK respectively. A value for n_2 was determined by the script that provided the best fit for all curves, which for both unreinforced and composite PEKK was $n_2 = 2$. w_1 and w_2 were set according to the LTE:HTE ratios calculated in Table 1 for each individual isotherm. k_1 and k_2 were optimised by the script using a non-linear least squares method. All parameters are summarised in Table 2.

The obtained models are shown in Fig. 13. The Velisaris Seferis model (solid lines) achieves a good fit with the provided Avrami exponents (n_1 and n_2) and weight factors (w_1 and w_2), and with the optimised crystallisation rate constants (k_1 and k_2). The contributions of the primary and secondary crystallisations to the overall model are depicted by the different dotted lines in the plots.

Plots showing the variation of $\ln(k_1)$ and $\ln(k_2)$ against the isothermal temperatures are shown in Fig. 14. Hoffmann-Lauritzen models were fitted to these values, which will be used when modelling crystallisation kinetics at different cooling rates in Section 3.2.3. The equations for these curves are summarised below.

For spherulitic growth during primary crystallisation, k_1 is expressed as per Eq. (3.2), which results in the Hoffmann-Lauritzen model in Eq. (3.3) used in Fig. 14a.

$$k_1 = \frac{4}{3}\pi N_{01} G_1^3 \tag{3.2}$$

$$k_1 = k_{01}\left[\exp\left(-\frac{3U^*}{R(T-T_\infty)}\right) \times \exp\left(-\frac{3K_{g1}}{T\Delta Tf}\right)\right] \tag{3.3}$$

where $k_{01} = \frac{4}{3}\pi N_{01} G_{01}^3$. G_1 is the crystal growth rate described in Eq. (1.2), N_{01} is the initial number of potential nuclei and G_{01} is a pre-exponential factor independent of temperature.

For crystal growth during secondary crystallisation, k_2 is expressed as per Eq. (3.4) and Eq. (3.5), used in Fig. 14b.

$$k_2 = \pi N_{02} G_2^2 \tag{3.4}$$

$$k_2 = k_{02}\left[\exp\left(-\frac{2U^*}{R(T-T_\infty)}\right) \times \exp\left(-\frac{2K_{g2}}{T\Delta Tf}\right)\right] \tag{3.5}$$

where $k_{02} = \pi N_{02} G_{02}^2$. Parameter definitions are as per Eqs. (3.2) and (3.3). Table 3 provides the parameters used for the models, as well as results for k_{01}, k_{02}, K_{g1} and K_{g2}. Note that, while all temperature values are given in °C, modelling was performed with temperature in units of Kelvin.

Fig. 14a and Fig. 14b show slower crystallisation kinetics for the secondary crystallisation mechanism k_2, due to this step requiring an established primary crystallisation and a longer time to develop. This is in line with what was previously discussed in Section 1.

Hoffmann-Lauritzen model fitting show that the fastest crystallisation kinetics for both unreinforced PEKK and PEKK composites occur at circa 255 °C and 260 °C for k_1 and k_2 respectively. This is in line with what has been reported in literature to date, where the fastest kinetics were identified to take place at approximately 255 °C [13].

3.2. Non-isothermal crystallisation

3.2.1. Crystallisation at different cooling rates

Fig. 15 shows the heat flow variation of one set of runs of PEKK powder and CF/PEKK respectively, when heated from room temperature to 370 °C at a rate of 20 °C/min, after undergoing different cooling rates. Table 4 shows average data from this portion of the cycle for both performed runs.

The crystallinity of unreinforced PEKK powder decreases with an

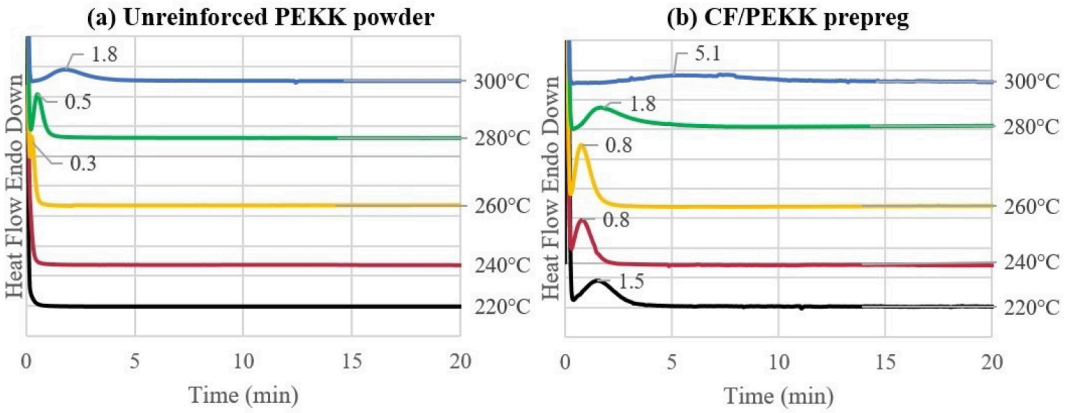

Fig. 10. DSC thermograms of (a) unreinforced PEKK powder and (b) CF/PEKK prepreg tape while undergoing isothermal holds at different temperatures showing peak crystallisation kinetics times in minutes.

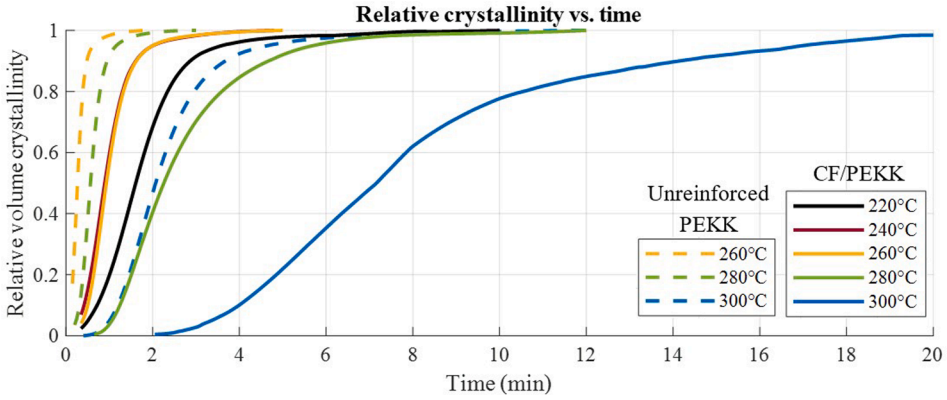

Fig. 11. Relative crystallinity against time of unreinforced PEKK (dotted lines) and CF/PEKK (solid lines) at different isothermal holds.

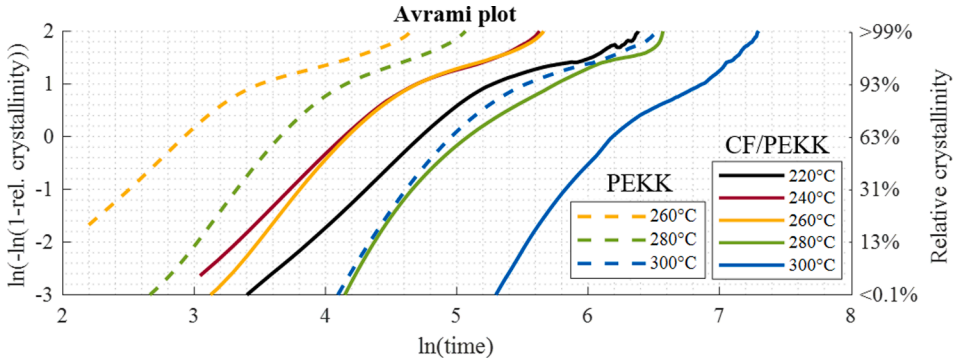

Fig. 12. Avrami plots of the relative crystallinity of unreinforced PEKK and CF/PEKK.

increase in cooling rate, due to faster temperature drops inhibiting chain movement and therefore limiting diffusion onto the growing crystal front [5]. There is therefore a small cold crystallisation peak developed at the faster cooling rates (100 °C/min, 150 °C/min). This agrees with results from Quiroga Cortés et al. [12], where this peak takes place at the fastest cooling rates across different PEKK grades.

The crystallinity of CF/PEKK, on the other hand, is affected more significantly by the cooling rate, as is observable from Table 4. An increasingly larger cold crystallisation peak develops with higher cooling rates in Fig. 15b, and therefore a drop in crystallinity from 25.7% at 5 °C/min to 1.5% at 150 °C/min takes place. This drastic difference is likely due to carbon fibres suppressing spherulitic development as discussed in Section 2, which becomes increasingly significant at faster cooling rates. It is possible that, while carbon fibre surfaces can act as nucleation sites, densely packed fibres are likely to supress chain mobility and spherulitic growth, and will have a larger impact in the overall crystallisation. Similar observations were made by Gao and Kim [5] when evaluating the impact of CF inclusions on the crystallisation capability of PEEK. They observed lower crystallinities in CF/PEEK with a fibre volume fraction of 61% in comparison to PEEK powder when undergoing different cooling rates.

As discussed in Section 1, the characteristic double melting endotherm observed in Fig. 5 is not present during non-isothermal crystallisation. This absence could be a consequence of secondary crystallisation being a slower mechanism that requires an established primary crystallisation and time to develop, both of which are reduced

Table 2
Summary of Velisaris-Seferis model parameters for the isothermal crystallisation modelling of unreinforced PEKK and CF/PEKK. w_1 and w_2 are extracted from the LTE:HTE ratios in Table 1.

Isothermal temperature (°C)	Unreinforced PEKK ($n_1 = 3$, $n_2 = 2$)				CF/PEKK ($n_1 = 2.5$, $n_2 = 2$)			
	w_1	w_2	k_1	k_2	w_1	w_2	k_1	k_2
220	–	–	–	–	0.90	0.10	0.2363	0.0556
240	–	–	–	–	0.90	0.10	1.0109	0.1914
260	0.92	0.08	38.8591	1.3068	0.88	0.12	0.9123	0.2539
280	0.80	0.20	4.3684	1.0171	0.74	0.26	0.1107	0.0472
300	0.69	0.31	0.0961	0.0838	0.55	0.45	0.0069	0.0084

w_1: primary crystallisation weight factor.
w_2: secondary crystallisation weight factor.
k_1: primary crystallisation rate constant.
k_2: secondary crystallisation rate constant.

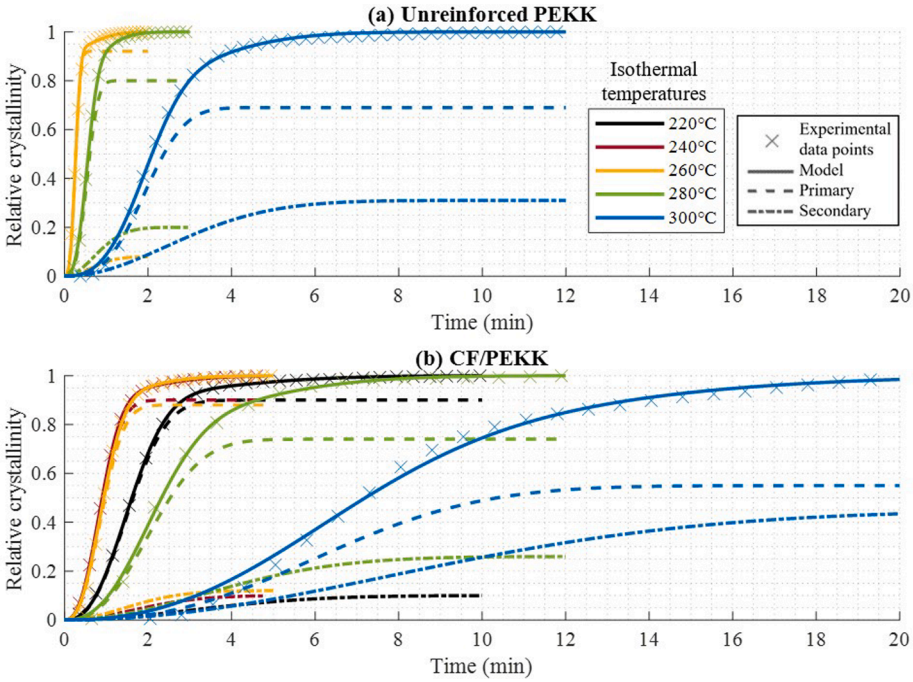

Fig. 13. Relative crystallinity against time of (a) unreinforced PEKK and (b) CF/PEKK at different isothermal holds, showing a comparison of the Velisaris-Seferis model with the experimental data, as well as the contribution of primary and secondary crystallisation mechanisms to the model.

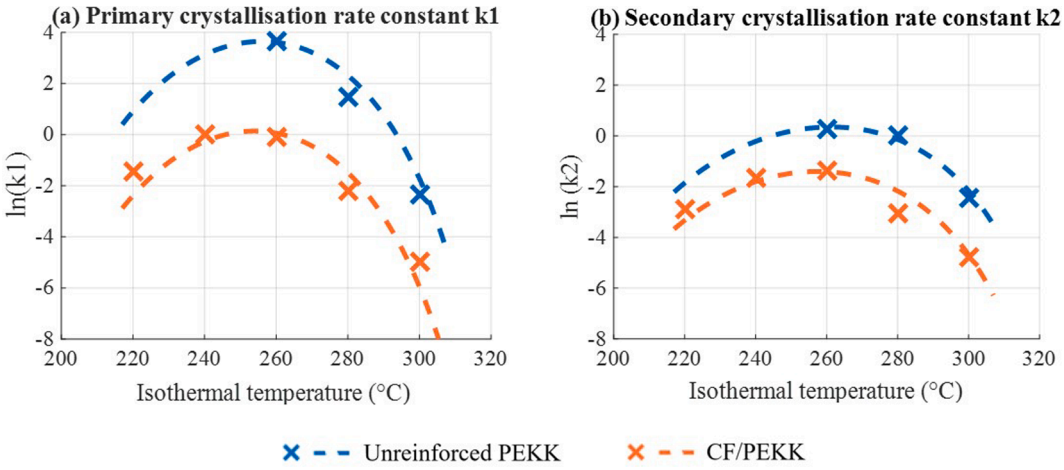

Fig. 14. Logarithmic plot of (a) k_1 and (b) k_2 against isothermal temperature for unreinforced PEKK and CF/PEKK. Dotted lines show the Hoffmann-Lauritzen models fitted to the experimental data.

Table 3
Parameters used for Hoffmann-Lauritzen modelling.

Parameters	Unreinforced PEKK	CF/PEKK
U^* (J mol^{-1})	4700 (Ref [17])	4700 (Ref [17])
R (m^3 Pa K^{-1} mol^{-1})	8.314	8.314
T_m^0 (used for T_∞, ΔT and f) (°C)	356 (Ref [16])	356 (Ref [16])
T_∞ (°C)	131	131
k_{01} (min^{-3})	1.500×10^{14}	1.5460×10^{13}
k_{02} (min^{-2})	5.041×10^{7}	3.593×10^{7}
K_{g1} (K^2)	2.486×10^{5}	2.687×10^{5}
K_{g2} (K^2)	2.025×10^{5}	2.359×10^{5}

with increasingly faster cooling rates. An LTE or a small shoulder at slow cooling rates has been observed in literature for PEEK [24,29,30], however PEEK possesses a more linear structure than any grade of PEKK, resulting in faster chain-packing and therefore a faster secondary crystallisation mechanism.

Fig. 16 shows SEM images of cryofractured CF/PEKK samples after undergoing 5 °C/min and 100 °C/min cooling rates respectively, with high and low crystallinities. Fig. 16a shows highly coated fibres, whereas clean, exposed fibres are observed in the lower crystallinity case in Fig. 16b. Similar behaviour has been observed in CF/PEEK in published literature [5,41]. This suggests that higher crystallinity in the matrix will improve fibre–matrix adhesion when compared to a more amorphous matrix.

3.2.2. Crystallisation kinetics at different cooling rates

Fig. 17 shows heat flow – temperature thermograms of PEKK and CF/PEKK samples while undergoing different cooling rates, showing melt crystallisation exotherms as the material cools and solidifies.

In both unreinforced PEKK and CF/PEKK composite, crystallisation takes place at progressively lower temperatures with faster cooling rates. At slower rates, chains have more time to move, and therefore begin to crystallise at higher temperatures. As the cooling rate is progressively increased, the polymer begins diffusion at lower temperatures.

Comparing PEKK and CF/PEKK, the composite samples in Fig. 17b consistently begin crystallisation at lower temperatures than their neat counterparts in Fig. 17a. The introduction of carbon fibres clearly obstructs the crystallisation mechanism of the matrix, resulting in a delayed crystallisation compared to unreinforced PEKK. This progressively lowers the total crystallinity developed with faster cooling rates, as discussed in the previous section. The crystallisation peak completely disappears at the fastest cooling rates for CF/PEKK in Fig. 17b, whereas unreinforced PEKK in Fig. 17a still shows a crystallisation peak at 150 °C/min cooling rate.

3.2.3. Modelling of non-isothermal crystallisation kinetics

Similar to isothermal crystallisation kinetics, relative crystallinity plots of each sample are required to implement any model. Using Eq. (3.1), such a plot is obtained, shown in Fig. 18. The kinetics for CF/PEKK at 150 °C/min are not evaluated, as the achieved crystallinity was very low (0.7%). Note that, while all samples reach a relative volume crystallinity of 1 in Fig. 18, this does not mean that all samples achieved the same level of absolute crystallinity (listed in Table 4). As observed in Section 3.2.2, unreinforced PEKK undergoes a faster crystallisation than its composite counterpart for each given cooling rate.

As discussed in Section 1, Avrami-based modelling includes the temperature-dependent crystallisation rate constant k. Therefore, creating an Avrami plot as shown in Fig. 12 (by plotting $\ln[-\ln(1-\alpha)]$ against $\ln(t)$) in order to find information on the possible primary crystallisation mechanism (a value for n_1) is not suitable in this instance, now that k varies with temperature under non-isothermal conditions.

Further to this, changing the thermal cycle that the sample undergoes is not likely to change the spherulitic (or otherwise) nature of crystallisation, but rather the extent to which it occurs (the total crystallinity achieved). Therefore, n_1 and n_2 have been kept the same as in Section 3.1.3: $n_1 = 3$ and $n_2 = 2$ for unreinforced PEKK; and $n_1 = 2.5$ and $n_2 = 2$ for CF/PEKK composite.

In order to model dynamic behaviour, the dual Nakamura model, Eq. (1.6), presented in Section 1 was scripted in MATLAB. Substituting k_1 and k_2 with Hoffmann-Lauritzen model Eqs. (3.3) and (3.5) yields the following model:

$$\alpha(t) = w_1\left(1 - exp\left[-\left(\int_0^t \left(k_{01}\left[\exp\left(-\frac{3U^*}{R(T-T_\infty)}\right)\times\exp\left(-\frac{3K_{g1}}{T\Delta Tf}\right)\right]\right)^{1/n_1} dt\right)^{n_1}\right]\right) + w_2\left(1 - exp\left[-\left(\int_0^t \left(k_{02}\left[\exp\left(-\frac{2U^*}{R(T-T_\infty)}\right)\times\exp\left(-\frac{2K_{g2}}{T\Delta Tf}\right)\right]\right)^{1/n_2} dt\right)^{n_2}\right]\right) \tag{3.6}$$

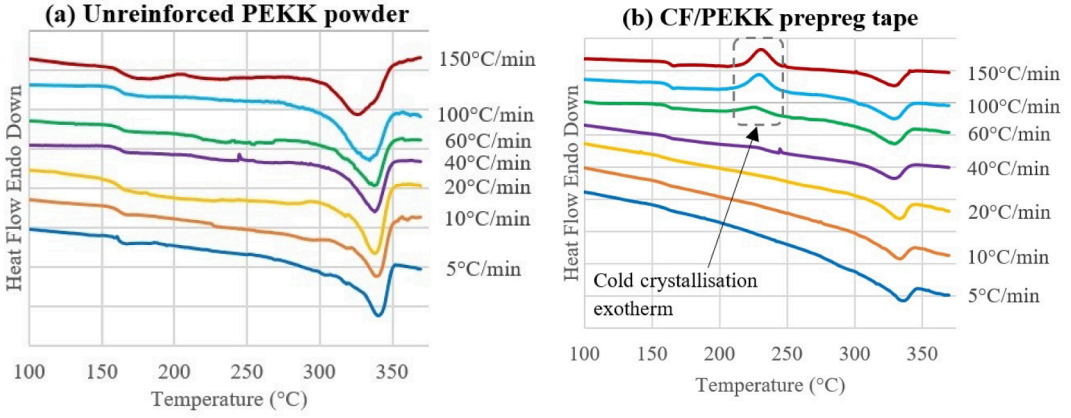

Fig. 15. DSC thermograms of (a) unreinforced PEKK and (b) CF/PEKK prepreg at 20 °C/min heat ramp after different cooling rates.

Table 4
Average values for transition temperatures, enthalpies and total crystallinity of PEKK powder and CF/PEKK prepreg tape after undergoing different cooling rates.

Cooling rate (°C/min)	Unreinforced PEKK					
	T_g (°C)	T_{cc} (°C)	ΔH_{cc} (J/g)	T_m (°C)	ΔH_m (J/g)	χ (%)
5	160.9 ± 0.8	–	–	341.5 ± 1.5	33.1 ± 0.3	25.5 ± 0.2
10	161.1 ± 0.7	–	–	340.0 ± 1.2	29.2 ± 3.1	22.5 ± 2.5
20	162.8 ± 1.8	–	–	338.0 ± 0.3	27.2 ± 0.1	20.9 ± 0.1
40	164.0 ± 1.9	–	–	337.4 ± 0.4	28.3 ± 1.0	21.8 ± 0.8
60	161.4 ± 0.1	–	–	337.0 ± 0.4	27.4 ± 1.2	21.1 ± 0.9
100	161.9 ± 0.7	212.3 ± 4.7	0.6 ± 0.2	331.9 ± 2.4	26.2 ± 0.6	19.7 ± 0.3
150	159.5 ± 3.9	210.9 ± 8.7	1.9 ± 0.1	326.0 ± 0.8	26.7 ± 0.4	19.0 ± 0.2
CF/PEKK						
5	159.2 ± 1.8	–	–	334.4 ± 0.7	10.6 ± 0.0	25.7 ± 0.0
10	160.6 ± 3.6	–	–	335.0 ± 2.2	7.8 ± 0.7	18.9 ± 1.6
20	158.8 ± 3.0	–	–	334.9 ± 2.5	7.0 ± 0.0	16.9 ± 0.2
40	161.9 ± 1.5	–	–	333.1 ± 4.6	6.6 ± 0.7	16.1 ± 0.6
60	161.2 ± 0.1	222.0 ± 4.2	2.1 ± 1.6	333.2 ± 3.3	7.8 ± 1.6	14.0 ± 0.1
100	162.8 ± 0.8	226.8 ± 2.2	5.8 ± 1.3	331.9 ± 3.5	8.7 ± 1.4	6.8 ± 0.1
150	162.0 ± 1.4	226.1 ± 4.7	7.7 ± 0.4	330.9 ± 1.8	8.3 ± 0.7	1.5 ± 0.8

T_g: Glass transition temperature.
T_{cc}: Cold crystallisation temperature.
ΔH_{cc}: Cold crystallisation enthalpy.
Tm: High temperature endotherm enthalpy.
ΔH_m: Melting enthalpy.
χ: Total crystallinity.

T is the temperature at time t, dependent on the cooling rate r:

$$T = T_m - rt \tag{3.7}$$

where T_m is the melt temperature from which the cooling begins (in this case, 370 °C).

3.2.3.1. Unreinforced PEKK. The heat scan curves of unreinforced PEKK in Fig. 15 show a single melting endotherm, and therefore values for w_1 and w_2 cannot be set according to LTE:HTE ratios as in the isothermal modelling. Therefore, the ratio of w_1 and w_2 was optimised by the script. The resulting fits are shown in Fig. 19. These show a decreasing contribution of secondary crystallisation as the cooling rate increases, in line with the observations by Bessard et al. [24] and Regis et al. [29] on the presence of secondary crystallisation under non-isothermal crystallisation. The resulting variation of w_1 and w_2 with cooling rate is shown in Fig. 20.

The model can be adapted to account for this variation in w_1 by introducing Eq. (3.8) (obtained from the fit in Fig. 20) in Eq. (3.6) and remembering that $w_1 + w_2 = 1$.

$$w_1 = -1.399r^{-0.8707} + 1 \tag{3.8}$$

where r is the applied cooling rate.

The contribution of w_2 necessary to achieve a better fit in the models above suggests that there may be some secondary crystallisation taking place in the material, despite no presence of an LTE endotherm in Fig. 15a. While the LTE:HTE ratio may be a good estimate of primary and secondary crystallisation content in the case of isothermal studies, this is not the case in non-isothermal studies. Therefore, a LTE may not be the sole indicator of presence of secondary crystallisation in PEKK.

3.2.3.2. CF/PEKK composite. In the case of CF/PEKK composite, performing the fitting while allowing the script to optimise the values of w_1 and w_2 resulted in $w_1 = 1$ for all curves. It is likely that only primary crystallisation occurs in the case of CF/PEKK, now that kinetics are slower than in unreinforced PEKK and there may not be enough time for the slower secondary crystallisation mechanism to take place.

Even when only accounting for primary crystallisation, however, the model underpredicts the kinetics of the composite, and at increasingly faster rates the crystallinity achieved in the experiments is not reached by the model. This is shown in Fig. 21. This may be due to the crystallisation rate equation for k_1 (Eq. (3.4)) underestimating the crystallisation capability of the polymer under non-isothermal conditions, particularly at higher cooling rates. Including a secondary crystallisation step would only delay kinetics further, as this is a slower mechanism than primary crystallisation.

In order to successfully model dynamic crystallisation of composite PEKK, a z coefficient was introduced to Eq. (3.6), which was optimised by the MATLAB script. This coefficient is bespoke for the specific grade of composite PEKK, as it would be beneficial to use for instance in the modelling of crystallinity development across a laminate experiencing different temperature gradients and distributions.

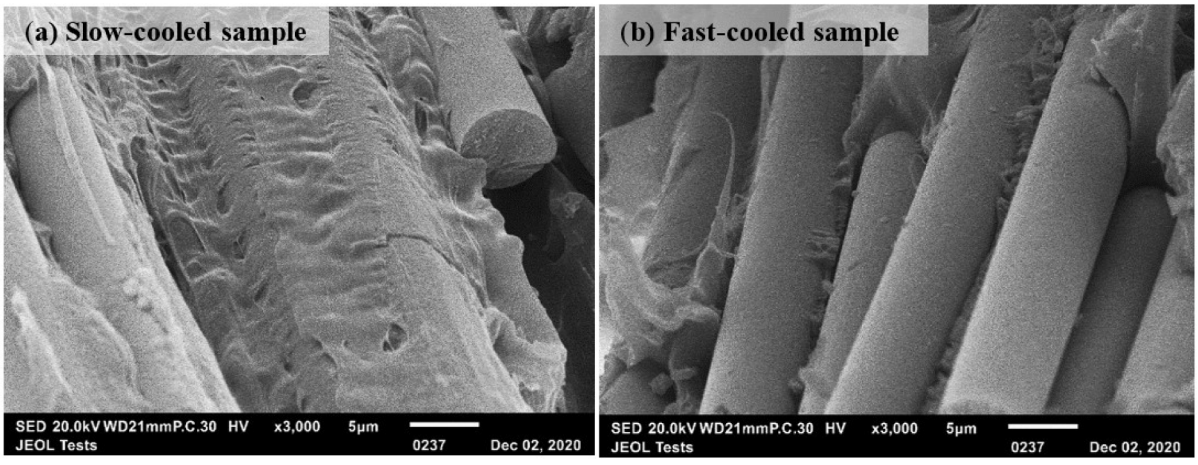

Fig. 16. SEM of cryofractured CF/PEKK sample after undergoing a cooling rate of (a) 5 °C/min from the melt to room temperature (25.6% crystallintiy) and (b) 100 °C/min from the melt to room temperature (6.9% crystallinity).

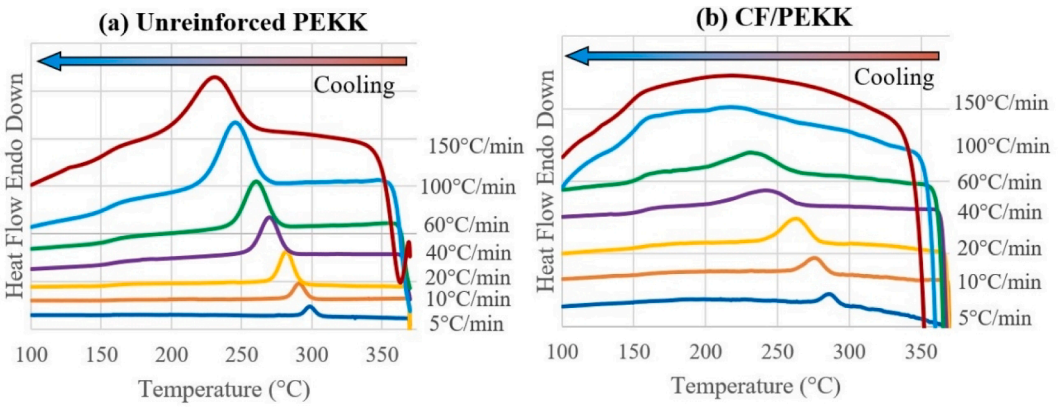

Fig. 17. DSC thermograms of (a) Unreinforced PEKK powder and (b) CF/PEKK prepreg tape while undergoing different cooling rates.

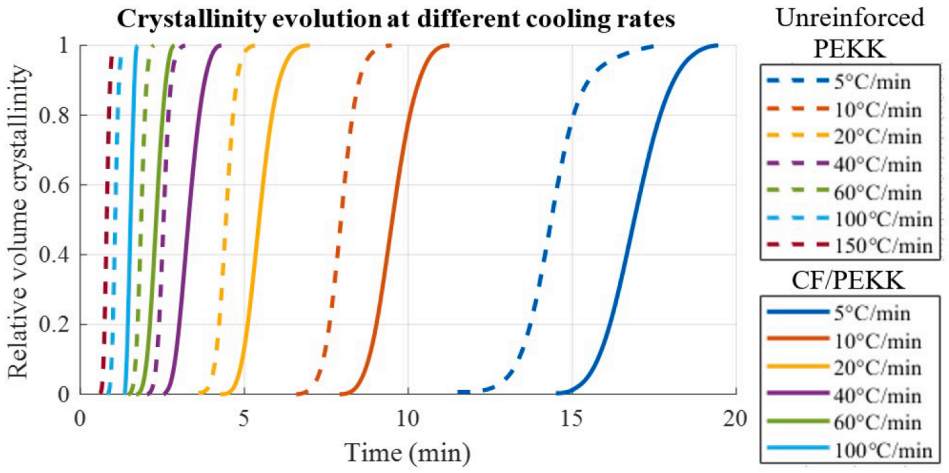

Fig. 18. Relative crystallinity against time of unreinforced PEKK (dotted lines) and CF/PEKK (solid lines) at different cooling rates.

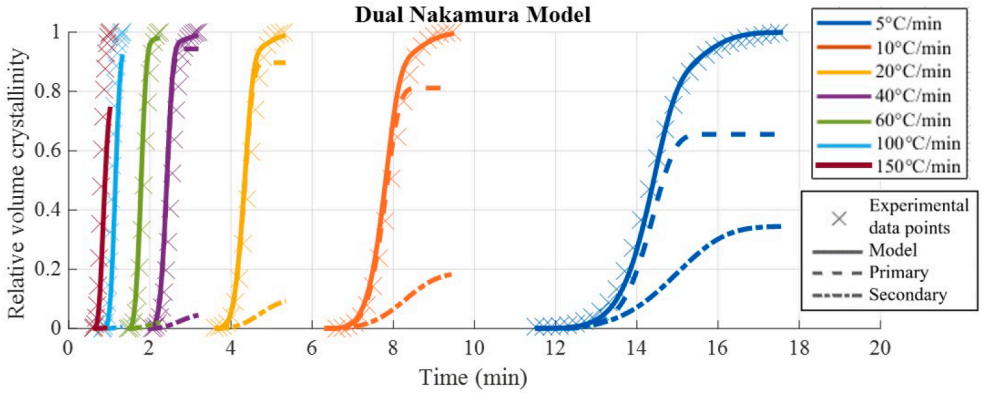

Fig. 19. Dual Nakamura model fits to non-isothermal crystallisation experimental data of unreinforced PEKK powder undergoing a range of cooling rates.

Since, as discussed above, $w_1 = 1$ and $w_2 = 0$, the second half of Eq. (3.6) can be ignored, and becomes:

$$\alpha(t) = z\left(1 - \exp\left[-\left(\int_0^t \left(k_{01}\left[\exp\left(-\frac{3U^*}{R(T-T_\infty)}\right)\times\exp\left(-\frac{3K_{g1}}{T\Delta Tf}\right)\right]\right)^{1/n_1} dt\right)^{n_1}\right]\right) \tag{3.9}$$

The expression obtained for z is shown in Eq. (3.10), where r is the cooling rate, and the resulting fittings are shown in Fig. 22.

$$z = 0.00229\exp(0.109r) + 1 \tag{3.10}$$

3.3. End-use applicability

It is of interest to reflect on which of the studied processing conditions would result in the best performance of CF/PEKK composites within the context of high-performance applications. To determine this, a structure–property correlation has to be established via manufacturing and mechanical testing. As this is outside the scope of the current work,

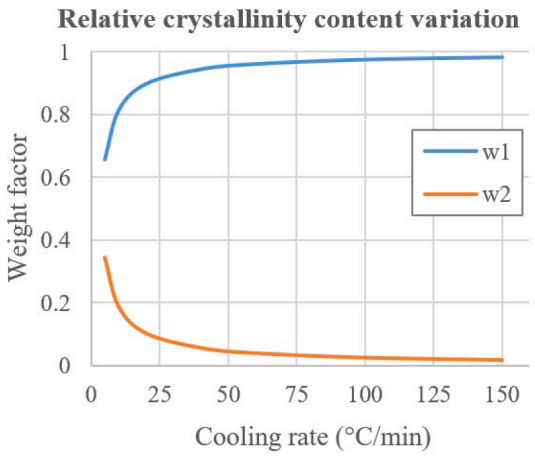

Fig. 20. Variation of crystallisation relative content (w_1 and w_2) with cooling rate for crystallisation kinetics modelling of unreinforced PEKK powder.

the remainder of this discussion will be based on the understanding of crystallinity that has been developed in this article, as well as the existing understanding of crystalline morphology from literature.

A high crystallinity content may be desirable [1,4] in order to achieve specific performance requirements, such as high strength, stiffness, or chemical resistance, which usually entails using slow cooling rates or isothermal holds. Deciding what isothermal temperature hold or cooling rate will result in a better response is therefore worth investigating and discussing. In this work, different applied thermal cycles have been observed to influence the formation of crystals. Some literature has reported that larger spherulite sizes reduce the mechanical performance of PEEK [30,42] and other polymers [43,44]. Larger crystal sizes in PEKK and CF/PEKK are shown here to develop at high isothermal hold temperatures, and are also likely developed at slow cooling rates (crystallisation takes place at higher temperatures with slower rates, as seen in Fig. 17). This suggests lower isothermal holds, in the range of 220–260 °C, may result in improved mechanical properties, and may therefore be more attractive to designers and manufacturers. The higher end of this range (240–260 °C), while resulting in larger spherulites, will undergo faster crystallisation kinetics, which may lead to shorter processing times. Time-temperature-transformation diagrams based on the isothermal Velisaris-Seferis modelling have been included in Fig. 23, which allow for the relative crystallinity of the material to be determined at any holding temperature and time. A relative crystallinity of 1 means the material has reached its full crystallisation potential, absolute percentage values of which are presented in Table 1.

Time-temperature transformation diagrams have also been included for non-isothermal instances in Fig. 24, based on the performed Nakamura modelling. In this instance, a relative crystallinity of 1 refers to the crystallinity achieved by cooling at 5 °C/min (absolute crystallinity of 25.5% and 25.7% for unreinforced and composite PEKK respectively). As faster cooling rates are performed (indicated by the labelled slopes), lower crystallinities are achieved, as outlined in Table 4.

It is worth considering, however, that holding temperature or cooling rate are not the only factors influencing physical and mechanical properties. The melt temperature will have a large effect on resin flow and part consolidation, as will the application of sufficient processing pressure, without which defects like voids or non-homogeneous consolidation may arise, possibly impacting mechanical performance. Further to this, the experiments performed in this work have all focussed on small amounts of material under the highly controlled, inert environment that DSC provides. This may not be directly applicable to an industrial manufacturing setting, where larger parts are unlikely to undergo highly controlled cooling and may experience a temperature

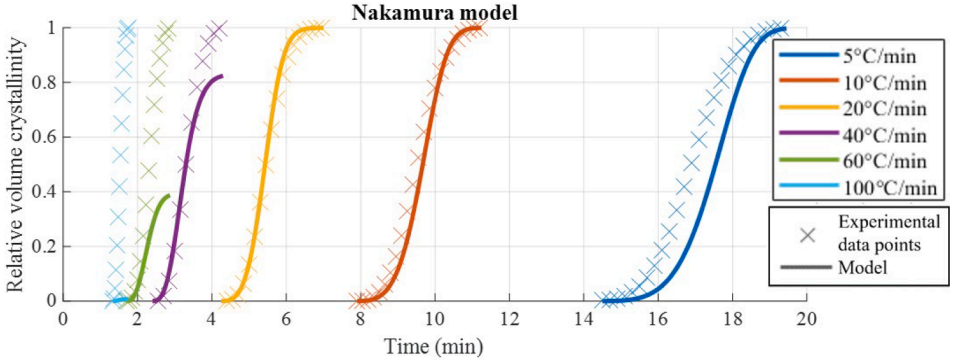

Fig. 21. Single Nakamura model fits to non-isothermal crystallisation experimental data of CF/PEKK composite undergoing a range of cooling rates.

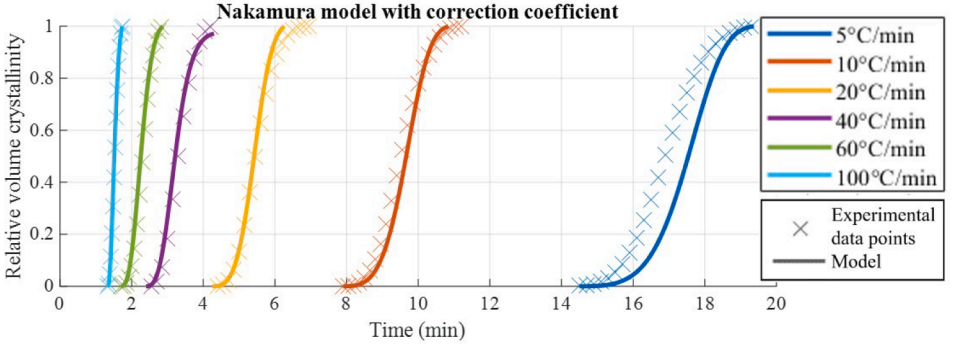

Fig. 22. Single Nakamura with correction coefficient fits to non-isothermal crystallisation experimental data of CF/PEKK composite undergoing a range of cooling rates.

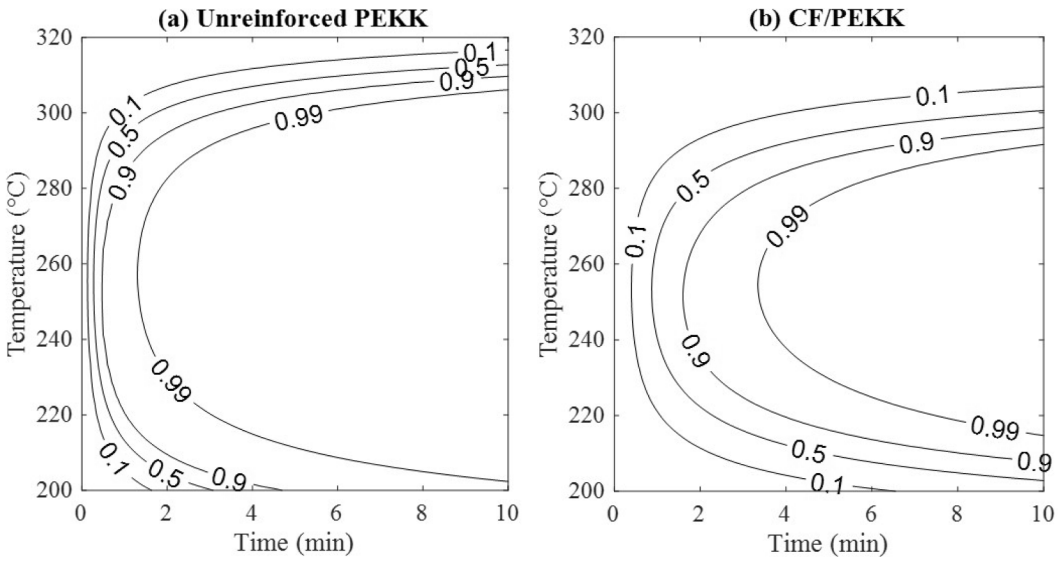

Fig. 23. Time-temperature-transformation diagrams of relative crystallinity development for (a) unreinforced PEKK and (b) CF/PEKK at different isothermal holds. A relative crystallinity of 1 means the material has achieved its full crystallisation potential, based on the crystallinity values shown in Table 1.

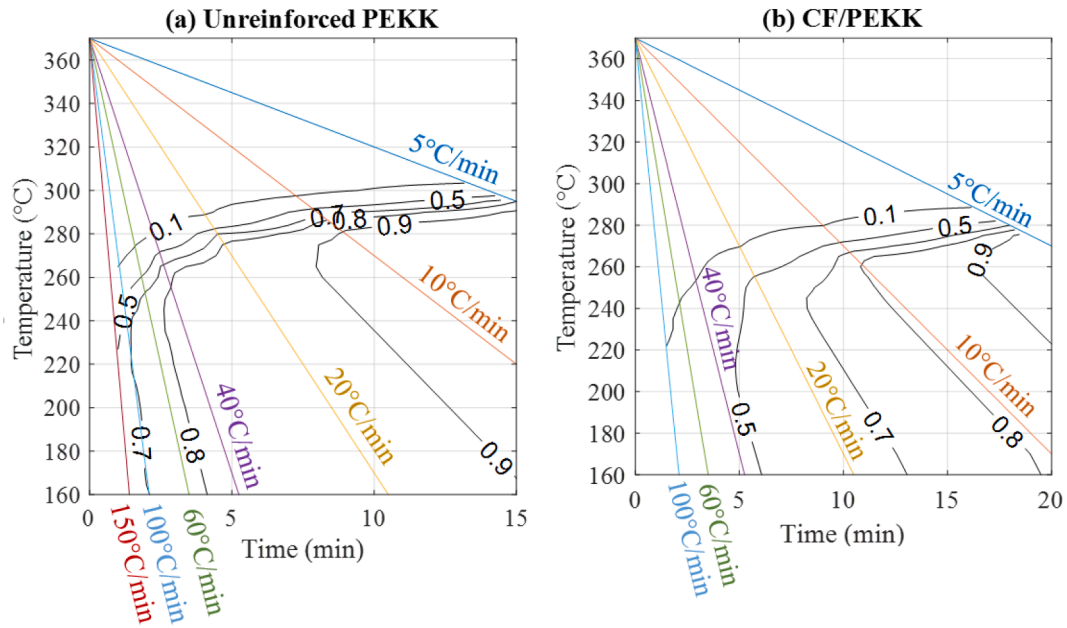

Fig. 24. Time-temperature-transformation diagrams of relative crystallinity development for (a) unreinforced PEKK and (b) CF/PEKK when undergoing different cooling rates. The coloured straight lines denote the performed cooling rates in this study. A relative crystallinity of 1 refers to the total crystallinity achieved after cooling at 5 °C/min.

gradient across their thickness. The results in this work will, however, form a solid guideline for industrial-scale processing of CF/PEKK composite parts.

4. Conclusions

When undergoing non-isothermal crystallisation, PEKK in unreinforced form crystallises even at the fastest cooling rate tested in this study (150 °C/min, achieving partial crystallisation), whereas CF/PEKK, possessing slower crystallisation kinetics, remains amorphous at the fastest cooling rate. Fibre-matrix adhesion is enhanced in more crystalline samples than in amorphous ones, as observed in cryofractured CF/PEKK samples. During dynamic crystallisation, the secondary crystallisation behaviour is not obvious, due to the slower nature of this mechanism. Slow-cooled CF/PEKK samples with higher levels of crystallinity were observed to have a stronger fibre–matrix interphase than amorphous (fast-cooled) samples, as examined by SEM.

Crystallisation kinetics for both isothermal and non-isothermal conditions have been studied using Avrami-based models, where two parallel Avrami-based expressions are used to account for primary and secondary crystallisation respectively. For the isothermal instances, the Velisaris-Seferis model was implemented, and a correlation between the isothermal holding temperature and the crystallisation rate constants was established. This was then used in the non-isothermal crystallisation cases in the implementation of adapted versions of the Nakamura model: a dual Nakamura model with a decreasing contribution of secondary crystallisation with faster cooling rates for unreinforced PEKK, and a single Nakamura model with a material-specific correction factor for

CF/PEKK. Successful fits were achieved in all instances, which will allow for the prediction of crystallisation evolution at other different rates and isothermal holds.

Overall, the findings of this work lead to a better understanding of the effect that different processing cycles might have on crystal structure development in CF/PEKK composite parts. Given the results in this work, a preliminary isothermal holding temperature range that provides optimum spherulitic development for its intended application in high-performance environments is found at 220–260 °C. The limitations of this work within the context of industrial applications must, however, be taken into account, namely the differences in scale, processing parameters and environment control when comparing small scale DSC studies and industrial-scale manufacturing.

CRediT authorship contribution statement

Helena Pérez-Martín: Conceptualization, Investigation, Formal analysis, Project administration, Writing – original draft. **Paul Mackenzie:** Supervision, Resources, Writing – review & editing. **Alex Baidak:** Supervision, Resources, Writing – review & editing. **Conchúr M. Ó Brádaigh:** Supervision, Resources, Writing – review & editing. **Dipa Ray:** Conceptualization, Supervision, Resources, Project administration, Writing – review & editing.

Declaration of Competing Interest

The authors declare that they have no known competing financial interests or personal relationships that could have appeared to influence the work reported in this paper.

Acknowledgements

The authors acknowledge the financial support received from the National Manufacturing Institute for Scotland (NMIS-IDP/009) and Hexcel Composites Limited.

References

[1] Comer AJ, Ray D, Obande WO, Jones D, Lyons J, Rosca I, et al. Mechanical characterisation of carbon fibre–PEEK manufactured by laser-assisted automated-tape-placement and autoclave. Compos Part Appl Sci Manuf 2015;69:10–20.
[2] Pérez-Martín H, Mackenzie P, Baidak A, Ó Brádaigh CM, Ray D. Crystallinity studies of PEKK and carbon fibre/PEKK composites: a review. Compos Part B Eng 2021;223:109127. https://doi.org/10.1016/j.compositesb:2021.109127.
[3] Flanagan M, Goggins J, Doyle A, Weafer B, Ward M, Bizeul M, et al. Out-of-autoclave manufacturing of a stiffened thermoplastic carbon fibre PEEK panel. In: AIP Conf Proc 2017;1896. 10.1063/1.5008001.
[4] Choupin T, Debertrand L, Fayolle B, Régnier G, Paris C, Cinquin J, et al. Influence of thermal history on the mechanical properties of poly(ether ketone ketone) copolymers. Polym Cryst 2019;2(6). https://doi.org/10.1002/pcr2.v2.610.1002/pcr2.10086.
[5] Gao S-L, Kim J-K. Cooling rate influences in carbon fibre/PEEK composites. Part I. Crystallinity and interface adhesion. Compos Part Appl Sci Manuf 2000;31:517–30. https://doi.org/10.1016/S1359-835X(00)00009-9.
[6] Gao S-L, Kim J-K. Cooling rate influences in carbon fibre/PEEK composites. Part II: interlaminar fracture toughness. Compos A Appl Sci Manuf 2001;32(6):763–74.
[7] Deignan A, Stanley WF, McCarthy MA. Insights into wide variations in carbon fibre/polyetheretherketone rheology data under automated tape placement processing conditions. J Compos Mater 2018;52(16):2213–28. https://doi.org/10.1177/0021998317740733.
[8] Lee Y, Porter RS. Crystallization of poly(etheretherketone) (PEEK) in carbon fiber composites. Polym Eng Sci 1986;26(9):633–9. https://doi.org/10.1002/pen.760260909.
[9] Gardner KH, Hsiao BS, Faron KL. Polymorphism in poly (aryl ether ketone). Polymer 1994;35:2290–5. https://doi.org/10.1016/0032-3861(94)90763-3.
[10] Tencé-Girault S, Quibel J, Cherri A, Roland S, Fayolle B, Bizet S, et al. Quantitative Structural Study of Cold-Crystallized PEKK. ACS Appl Polym Mater 2021;3(4):1795–808. https://doi.org/10.1021/acsapm.0c0138010.1021/acsapm.0c01380.s001.
[11] Choupin T, Fayolle B, Régnier G, Paris C, Cinquin J, Brulé B. Isothermal crystallization kinetic modeling of poly(etherketoneketone) (PEKK) copolymer. Polymer 2017;111:73–82. https://doi.org/10.1016/j.polymer.2017.01.033.
[12] Quiroga Cortés L, Caussé N, Dantras E, Lonjon A, Lacabanne C. Morphology and dynamical mechanical properties of poly ether ketone ketone (PEKK) with meta phenyl links. J Appl Polym Sci 2016;133(19):n/a–. https://doi.org/10.1002/app.43396.
[13] Hsiao BS, Chang IY, Sauer BB. Isothermal crystallization kinetics of poly(ether ketone ketone) and its carbon-fibre-reinforced composites. Polymer 1991;32(15):2799–805. https://doi.org/10.1016/0032-3861(91)90111-U.
[14] Gardner KH, Hsiao BS, Matheson RR, Wood BA. Structure, crystallization and morphology of poly (aryl ether ketone ketone). Polymer 1992;33(12):2483–95. https://doi.org/10.1016/0032-3861(92)91128-O.
[15] Arkema. Introduction to ultra high-performance Kepstan® PEKK 2020.
[16] Chang IY, Hsiao BS. Thermal properties of high performance thermoplastic composites based on poly(ether ketone ketone). In: (PEKK). 36th Int SAMPE Symp; 1991. p. 1587–601.
[17] Choupin T, Fayolle B, Régnier G, Paris C, Cinquin J, Brulé B. A more reliable DSC-based methodology to study crystallization kinetics: Application to poly(ether ketone ketone) (PEKK) copolymers. Polymer 2018;155:109–15. https://doi.org/10.1016/j.polymer.2018.08.060.
[18] Ho R-M, Cheng SZD, Hsiao BS, Gardner KH. Crystal morphology and phase identifications in poly(aryl ether ketone)s and their copolymers. 1. Polymorphism in PEKK. Macromolecules 1994;27(8):2136–40. https://doi.org/10.1021/ma00086a023.
[19] Ho RM, Cheng SZD, Hsiao BS, Gardner KH. Crystal morphology and phase identifications in poly(aryl ether ketone)s and their copolymers. 3. Polymorphism in a polymer containing alternated terephthalic acid and isophthalic acid isomers. Macromolecules 1995;28:1938–45. https://doi.org/10.1021/ma00110a030.
[20] Jin L, Ball J, Bremner T, Sue H-J. Crystallization behavior and morphological characterization of poly(ether ether ketone). Polymer 2014;55(20):5255–65. https://doi.org/10.1016/j.polymer.2014.08.045.
[21] Painter PC, Coleman MM. Polymer Morphology. Fundam. Polym. Sci. Introd. Text. 2nd ed. Routledge; 1997, p. 250–3.
[22] Hsiao BS, Gardner KH, Cheng SZD. Crystallization of poly(aryl ether ketone ketone) copolymers containing terephthalate/isophthalate moieties. J Polym Sci Part B Polym Phys 1994;32:2585–94. https://doi.org/10.1002/polb.1994.090321604.
[23] Bassett D, Olley R, Alraheil I. On crystallization phenomena in PEEK. Polymer 1988;29(10):1745–54. https://doi.org/10.1016/0032-3861(88)90386-2.
[24] Bessard E, De Almeida O, Bernhart G. Unified isothermal and non-isothermal modelling of neat PEEK crystallization. J Therm Anal Calorim 2014;115(2):1669–78. https://doi.org/10.1007/s10973-013-3308-8.
[25] Blundell DJ, Osborn BN. The morphology of poly(aryl-ether-ether-ketone). Polymer 1983;24(8):953–8. https://doi.org/10.1016/0032-3861(83)90144-1.
[26] Cebe P, Hong S-D. Crystallization behaviour of poly(ether-ether-ketone). Polymer 1986;27(8):1183–92. https://doi.org/10.1016/0032-3861(86)90006-6.
[27] Lattimer MP, Hobbs JK, Hill MJ, Barham PJ. On the origin of the multiple endotherms in PEEK. Polymer 1992;33(18):3971–3. https://doi.org/10.1016/0032-3861(92)90391-9.
[28] Tardif X, Pignon B, Boyard N, Schmelzer JWP, Sobotka V, Delaunay D, et al. Experimental study of crystallization of PolyEtherEtherKetone (PEEK) over a large temperature range using a nano-calorimeter. Polym Test 2014;36:10–9. https://doi.org/10.1016/j.polymertesting.2014.03.013.
[29] Regis M, Zanetti M, Pressacco M, Bracco P. Opposite role of different carbon fiber reinforcements on the non-isothermal crystallization behavior of poly (etheretherketone). Mater Chem Phys 2016;179:223–31. https://doi.org/10.1016/j.matchemphys.2016.05.034.
[30] Lustiger A, Uralil FS, Newaz GM. Processing and structural optimization of PEEK composites. Polym Compos 1990;11(1):65–75. https://doi.org/10.1002/pc.750110109.
[31] Avrami M. Kinetics of phase change. I: General theory. J Chem Phys 1939;7(12):1103–12. https://doi.org/10.1063/1.1750380.
[32] Velisaris CN, Seferis JC. Crystallization kinetics of polyetheretherketone (peek) matrices. Polym Eng Sci 1986;26(22):1574–81. https://doi.org/10.1002/pen.760262208.
[33] Cowie JMG. The crystalline state: Kinetics of crystallization. In: Polym. Chem. Phys. Mod. Mater. 2nd ed. Blackie Academic & Professional; 1998.
[34] Hoffman JD, Lauritzen JI. Crystallization of bulk polymers with chain folding: theory of growth of lamellar spherulites. J Res Natl Bur Stand Sect Phys Chem 1961;65A(4):297. https://doi.org/10.6028/jres.065A.035.
[35] Chelaghma SA, De Almeida O, Margueres P, Passieux J-C, Perie J-N, Vinet A, et al. Identification of isothermal crystallization kinetics of poly(ether-ketone-ketone)

based on spherulite growth measurements and enthalpic data. Polymer Crystallization 2020;3(4). https://doi.org/10.1002/pcr2.v3.410.1002/pcr2.10141.
[36] Cebe P. Application of the parallel Avrami model to crystallization of poly (etheretherketone). Polym Eng Sci 1988;28(18):1192–7. https://doi.org/10.1002/pen.760281809.
[37] Nakamura K, Katayama K, Amano T. Some aspects of nonisothermal crystallization of polymers. II. Consideration of the isokinetic condition. J Appl Polym Sci 1973;17:1031–41. https://doi.org/10.1002/app.1973.070170404.
[38] Harris L. A study of the crystallisation kinetics on PEEK and PEEK composites. University of Birmingham, 2011.
[39] Choupin T. Mechanical performances of PEKK thermoplastic composites linked to their processing parameters. École nationale supérieure d'arts et métiers, 2017.
[40] Arkema. Kepstan® PEKK Brochure 2018.
[41] Saiello S, Kenny J, Nicolais L. Interface morphology of carbon fibre/PEEK composites. J Mater Sci 1990;25(8):3493–6. https://doi.org/10.1007/BF00575375.
[42] Chu J-N, Schultz JM. The influence of microstructure on the failure behaviour of PEEK. J Mater Sci 1990;25(8):3746–52. https://doi.org/10.1007/BF00575414.
[43] Ehrenstein GW, Theriault RP. Polymeric Materials: Structure, Properties, Applications. Hanser Publishers; 2001.
[44] Starkweather Jr HW, Brooks RE. Effect of spherulites on the mechanical properties of nylon 66. J Appl Polym Sci 1959;1:236–9. https://doi.org/10.1002/app.1959.070010214.

Materials Today Communications 36 (2023) 106442

Contents lists available at ScienceDirect

Materials Today Communications

journal homepage: www.elsevier.com/locate/mtcomm

Effect of crystallinity and morphology on the mechanical properties of CF/PEKK composites manufactured under compression moulding and automated tape placement

Helena Pérez-Martín [a], Stefan Buchalik-Bopp [b], Barbara E. Guettler [b], Paul Mackenzie [c], Alex Baidak [c], Conchúr M. Ó Brádaigh [a], Dipa Ray [a,*]

[a] School of Engineering, Institute for Materials and Processes, The University of Edinburgh, Edinburgh, United Kingdom
[b] Leibniz-Institut für Verbundwekstoffe GmbH, Kaiserslautern, Germany
[c] Hexcel Composites Ltd., Duxford, Cambridge, United Kingdom

ARTICLE INFO

Keywords:
Polymer-matrix composites (PMCs)
Thermoplastic resin
Mechanical properties
Compression moulding
Automated tape placement
Carbon fibre
PEKK

ABSTRACT

The present work aims to establish to what extent crystallisation morphology and kinetics affect the matrix-dominated properties of CF/PEKK composites, two factors which have been minimally investigated together in existing literature. Different compression-moulding cycles and automated tape placement (ATP) were used as the processing routes. Their effects on void content, crystallinity development, morphology and mechanical performance were investigated. Results showed that ~~all~~ compression-moulded laminates undergoing different isothermal crystallisation conditions achieved similar levels of consolidation and crystallinity, although the spherulitic development varied considerably. The effect of different crystalline structures was not evident on the properties investigated, as all compression-moulded laminates performed similarly. However, ATP laminates displayed a higher void content and low crystallinity, resulting in a lower performance across the investigated mechanical properties. While the modification of some ATP parameters resulted in slight improvements in performance in some testing, the results indicated that a thorough understanding of the correlation between processing conditions and development of crystalline structures in PEKK is needed in order to produce good-quality CF/PEKK parts under very rapid processing conditions and ensure the repeatability of this.

1. Introduction

The use of high-performance thermoplastic matrices in structural composites is of high interest in the aerospace industry. Poly(ether-ketoneketone) (PEKK) in particular is a semicrystalline thermoplastic, attractive due to its excellent mechanical properties, chemical inertness and resistance to high temperatures [1–4]. The range of PEKK grades that can be achieved, allowing manufacturers to choose which grade better suits their application, makes it a versatile and interesting material in industry. Using PEKK, or any other thermoplastic polymer, as a matrix in composites is also advantageous for manufacturers as they have the potential to undergo single-step processing, and have a better starting point to mechanically recycle the components at their end of life.

An example of such a process is automated tape placement (ATP), which is designed for fast production, energy consumption and cost reduction, automation and repeatability of part manufacturing. However, such fast manufacturing techniques (consolidation times of seconds or a fraction of a second [5]) can result in lower quality and performance when compared to slower processing techniques such as compression moulding or autoclaving (consolidation times of 20–60 + minutes [6–8]). The temperature, pressure and environmental control that autoclave manufacturing provides is often considered the golden standard in composite manufacturing. When compared to this, the fast-paced nature of the ATP manufacturing process results in very short exposure times to high temperatures and pressures. This limits the time window for resin flow, adhesion between the laid plies and void reduction, which are factors that play key roles in consolidation quality, part integrity and properties [5,6,9–11].

The use of thermoplastics for in-situ manufacturing comes with several challenges regarding their processing. Thermoplastics possess high viscosities in molten conditions when compared to thermosetting

* Correspondence to: 1.140 Sanderson Building King's Buildings, Edinburgh EH9 3FB, Scotland, UK.
E-mail address: Dipa.Roy@ed.ac.uk (D. Ray).

https://doi.org/10.1016/j.mtcomm.2023.106442
Received 28 April 2023; Received in revised form 6 June 2023; Accepted 13 June 2023
Available online 14 June 2023
2352-4928/© 2023 The Author(s). Published by Elsevier Ltd. This is an open access article under the CC BY license (http://creativecommons.org/licenses/by/4.0/).

resins, hindering fibre impregnation, interply contact and polymer chain reptation. The processing conditions add a further layer of complexity in the case of semicrystalline thermoplastics such as PEKK, as their crystallinity content and morphology are dependent on the thermal history that the part undergoes. This in turn affects the mechanical and chemical performance of the manufactured part, which are critical in high-performance applications such as aerospace [5,12,13].

Consequently, optimising the processing parameters is of paramount importance for thermoplastics, particularly offering temperature and pressure control and exposure times catered to the material being used. It is common to perform some form of secondary processing, involving reheating and reconsolidation of ATP-manufactured thermoplastic composite parts to improve mechanical performance [10,14]. In the case of CF/PEKK, a previous study has shown an improvement in crystallinity and reduction in void content with increasing number of layers as a consequence of repeated heat exposure and slower cooling profiles when further away from the lay-down surface [15]. In order to fully optimise the processing of such materials, however, it is important to establish an understanding of the effect of thermal history on the morphology and properties of the composite matrix.

Differential scanning calorimetry (DSC) studies have shown a dual melting behaviour in both unreinforced and CF-reinforced PEKK after undergoing isothermal crystallisation [1–3,16–20], also observed in the widely-studied poly(etheretherketone) (PEEK) [21–26]. This consists of a lower temperature endotherm (LTE) that varies in temperature and area based on the isothermal hold temperature, and a higher temperature endotherm (HTE) corresponding to conventional melting that takes place at the same temperature (~336 °C) irrespective of thermal history. This suggests there are two different crystal structures present with different thermal stability, one of them being more reliant on the material's thermal history. In literature, these have been assigned to primary and secondary crystallisation, where the primary spherulitic structure forms first, followed by a secondary slower interlamellar crystallisation once the primary structure is established. The latter has slower kinetics and its thermal stability is dependent on the processing conditions, hence melting in the LTE during heating; whereas the main spherulitic structure melts during the HTE [1,2,16–18,20,27–29].

This dual melting behaviour is not observed in samples that undergo non-isothermal crystallisation. Crystallisation kinetics modelling shows that, during slow non-isothermal crystallisation where this dual melting behaviour is not observed, a dual crystallisation model is still necessary to obtain a good fit [20,30]. Some literature has highlighted the presence of a slight shoulder below the melting peak of PEEK after undergoing slow cooling, attributing it to the secondary crystallisation phase [23]. This shoulder is significantly less prominent than the distinct LTE observed after isothermal crystallisation and is absent during faster cooling rates. Such a shoulder is observable in some literature for higher PEKK grades [2] (higher crystallisation capability and faster kinetics), however, its nature is not discussed.

The impact of thermal history on the morphology has been studied on CF/PEEK, and more recently on CF/PEKK. Brittle fracture and matrix residue of CF/PEEK composites are present in slow-cooled [31] and isothermally crystallised [32] samples, indicative of high crystallinity content and a good fibre/matrix interface; whereas amorphous samples presented clean fibre surfaces and plastic yielding of the matrix [31,32]. Similar results were seen in a recent study on fractured CF/PEKK samples [20] after undergoing fast and slow cooling rates, as well as different spherulitic sizes as a consequence of isothermal hold in DSC cycles. Observations followed general nucleation theory, where at lower isothermal temperatures many, small spherulites were formed, and at higher temperatures, a lower number of spherulites but of larger dimensions could be seen.

While the above crystallisation studies are comprehensive, these have been performed with 5–20 mg of material in highly controlled, inert environments such as differential scanning calorimetry (DSC). Such conditions are unlikely to take place during manufacturing within an industrial context. It is therefore important to understand to what extent crystallinity influences mechanical performance under different manufacturing conditions. Studies correlating crystallinity with matrix-dominated properties of CF/PEEK overall show improved mechanical properties with a higher crystallinity [7,33,34], but as discussed in Pérez-Martín et al.'s review [3], diligent studies on the impact of thermal cycles on crystallinity and matrix performance are minimal. A study on the crystallinity and mechanical properties of CF/PEKK as a consequence of different processing methods has been recently published [35], however this does not evaluate the impact of varying individual process parameters on the crystallinity and performance. Outside of this, there are no studies correlating crystallinity with mechanical properties of CF/PEKK that the authors of this work are aware of. It is therefore of interest to understand how different processing conditions and resulting crystalline structures influence the performance of PEKK composites with high volume fraction of carbon fibres. This work compares the flexural 0 °, flexural 90 ° and interlaminar shear strength of unidirectional CF/PEKK laminates compression-moulded under different processing conditions and laminates manufactured by ATP. Laminates were also analysed via DSC and microscopy to obtain crystallinity levels and void contents, in order to establish the impact of different processing conditions on their mechanical performance and microstructure. Chemical etching was performed on the cross-section of some laminates to observe the impact of processing conditions on the developed crystal structures.

2. Materials and methods

2.1. Materials

In this study, laminates were produced using PEKK prepreg tapes unidirectionally reinforced with AS7 carbon fibres, provided by Hexcel Composites Ltd. The PEKK matrix is KEPSTAN PEKK 7002PT manufactured by Arkema. The polymer's glass transition temperature and melting temperature were measured at 160 °C and 337 °C respectively via DSC. The thickness of the prepreg tape was 0.2 mm. Two different rolls were used; one for compression moulding (150 mm wide prepreg roll), with a crystallinity of 18.2% and an average fibre volume fraction of 60.6% (measured via acid digestion); and one for ATP manufacturing (6.4 mm width prepreg tape), with a crystallinity of 19.2% and an average fibre volume fraction of 58.4%. For compression moulding, the prepreg roll was cut into 300 mm long prepreg sheets with a guillotine and stacked into layers.

2.2. Compression moulding

Unidirectional laminates were manufactured in a Pinette Emidecau Industries (PEI) LAB 450 P hydraulic press. Cooling of the press is provided by an integrated Frigosystem chiller. All laminates were made by stacking 10 plies of prepreg sheets with a layup $[0\ °]_{10}$ to achieve a thickness of 2 mm. A 3-part mould was used, consisting of a 2 mm-thick frame and a top and bottom plate, as shown in Fig. 1.

This resulted in laminates with dimensions 300 mm x 150 mm x 2 mm. Four laminates were manufactured undergoing the following

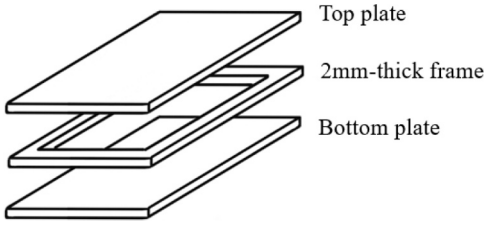

Fig. 1. Schematic of frame and plates used for compression-moulding manufacturing.

processing cycles. The selected isothermal and holding temperatures in the melt were chosen based on a previous study on the crystallisation behaviour and morphology of PEKK and CF/PEKK composites [20].

1. Heat from room temperature to holding temperature in the melt (370 °C or 380 °C) at 10 °C/min.
2. Hold in the melt for 25 min.
3. Cool down to isothermal temperature (220 °C, 260 °C or 300 °C) at 10 °C/min.
4. Hold at the isothermal temperature for 60 min.
5. Cool from the isothermal temperature to room temperature at 10 °C/min.

An additional laminate was manufactured undergoing a different processing cycle with no isothermal hold:

1. Heat from room temperature to holding temperature in the melt (370 °C) at 10 °C/min.
2. Hold in the melt for 25 min.
3. Cool from the melt temperature to room temperature at 5 °C/min.

A temperature-time plot of the described cycles is shown in Fig. 2. All laminates underwent a pressure of 1 bar during the heating step, and 28 bar for the remainder of the processing cycle. The laminates were named as shown in Fig. 2. The laminate code consists of three parts, denoting the nature of cooling ("I" for isothermal or "C" for dynamic cooling) followed by isothermal hold temperature (220 °C, 260 °C or 300 °C) or a cooling rate (5 °C/min), and finally the holding temperature in the melt (370 °C or 380 °C).

2.3. Automated Tape Placement (ATP)

Unidirectional ATP laminates were manufactured at the University of Limerick (Ireland) using a laser-assisted tape placement head (AFPT, GmbH) attached to a robot arm (Kuka, KR240 L210–2). A total of 10 layers of prepreg tape were placed per laminate, as per the compression-moulded laminates, resulting in 2 mm-thick laminates. A diagram of the process highlighting the ATP settings is shown in Fig. 3, and the names of the laminates with the parameters that were varied in this study are given in Table 1. The laminate code consists of the nip temperature (370, 380 or 390 °C), lay-down speed (2 or 4 m/min) and roller pressure (2 or 4 bar). Comparisons in laminate properties and performance have been drawn across these three parameters in Section 3.

In this work, the tool on which the laminates were manufactured was unheated and made out of mild steel, and a repass on the final layer of each laminate was done. Repasses are often performed to improve interply consolidation, crystallinity and hence mechanical performance of the part [12].

While in this work it is not possible to assess the cooling rates that the tape undergoes during lay-down, previous literature [15] has reported steep temperature drops in CF/PEKK tapes when manufactured on an unheated tool using ATP. Using a laser source, cooling rates between 150 and 220 °C/min were achieved in the first second of cooling, the rates being higher on the first layers of prepreg tape that were laid on the unheated surface of the tool.

2.4. Microscopy

Void content was calculated using optical microscopy images taken with a Leica DM6000 M microscope after casting, grinding and polishing the laminate samples. These images were then analysed with ImageJ software, using the threshold tool to calculate void content area. This calculates the area that pixels above or below a certain threshold value take up of the image being analysed. An example of how this was done is shown in Fig. 4. Void content was taken from images that encompassed the entire thickness of a laminate cross-section ignoring defects close to the laminate surfaces (6 images per laminate). The total evaluated area per laminate was approximately 1250 μm x 1400 μm.

2.5. Differential scanning calorimetry (DSC)

Crystallinity measurements were obtained by cutting three samples from randomly selected locations of each laminate. Scans at dynamic heating rates of 20 °C/min from room temperature to 370 °C were carried out using a Mettler Toledo DSC 3 + , with aluminium pans non-hermetically sealed with aluminium lids. Sample masses of 10–20 mg were used. All experiments were performed under a nitrogen environment to avoid any sample degradation.

The crystallinity of a sample was estimated with:

$$\chi = \frac{\Delta H_m - \Delta H_{cc}}{\alpha \times \Delta H_{100\%}} \quad (1)$$

where ΔH_m is the melting enthalpy, ΔH_{cc} is the cold crystallisation enthalpy, α is the weight fraction of matrix content (31.7% for the compression moulding tape and 34.5% for the ATP tape) and $\Delta H_{100\%}$ is the theoretical melting enthalpy of 100% crystalline PEKK. This has been calculated to be 130 J/g by Chang and Hsiao [15].

2.6. Chemical etching

Chemical etching was performed on laminates I-220–370, I-260–370 and I-300–370 to observe the impact of isothermal temperature on the matrix morphology. Cross-section samples of the laminates were cast in

Compression-moulded laminates

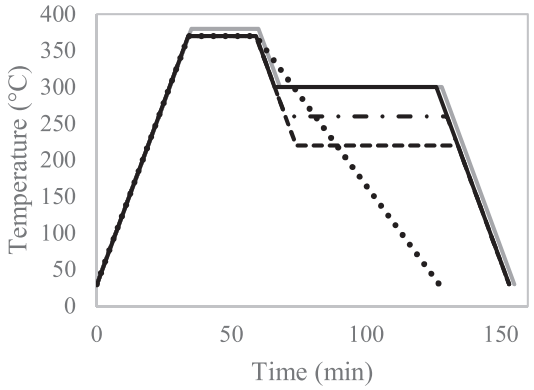

Legend	Laminate code	Hold melt temp. (°C)	Isothermal hold temp. (°C)
– – –	I-220-370	370	220
– · ·	I-260-370	370	260
———	I-300-370	370	300
———	I-300-380	380	300

Legend	Laminate number	Hold melt temp. (°C)	Cooling rate (°C/min)
▪▪▪▪	C-5-370	370	5

Fig. 2. Summary of processing parameters for the compression-moulded laminates.

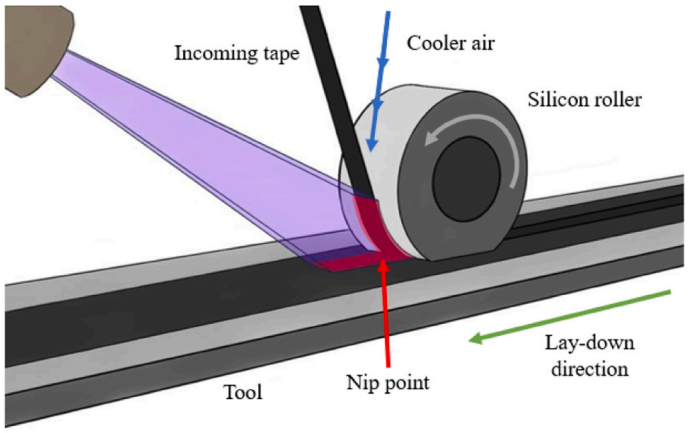

Cooler air pressure	1 bar
Incoming tape dimensions	6.4mm wide x 0.2mm thick
Laser-nip point optical distance	170mm
Laser power limit	1000W
Tape/laminate laser split	Approx. 50/50
Tool temperature	Unheated

Fig. 3. Schematic of ATP lay-up process and processing parameters. ATP schematic drawn after [5].

Table 1
Summary of processing parameters for the ATP-manufactured laminates.

Laminate code	Nip temperature (°C)	Lay-down speed (m/min)	Roller pressure (bar)
370–4–2	370	4	2
380–4–2	380	4	2
390–4–2	390	4	2
380–2–2	380	2	2
380–4–4	380	4	4

epoxy resin, and polished with silicon carbide discs of grits up to P2500, followed by diamond suspensions of down to 1 μm particle size. These were then etched following the steps below, based on the etching methods reported in literature for CF/PEEK, where spherulitic structures have been successfully observed [22,36]:

1. Immerse in a stirred solution of 1% potassium permanganate in a 5:2:2 solution of sulphuric acid, orthophosphoric acid and distilled water. Constant stirring was provided by a magnetic stirrer at approximately 100 rpm.
2. Carefully wash in a 7:2 solution of sulphuric acid and distilled water.
3. Wash in 30% hydrogen peroxide solution.
4. Wash in distilled water.

This procedure was performed twice. The first time, steps 1 and 2 were carried out for 7 and 3 min respectively; the second time they were carried out for 10 and 5 min respectively.

2.7. Mechanical testing

2.7.1. Flexural testing

0 ° and 90 ° flexural testing were performed in accordance with ASTM D7264, using a span-to-thickness ratio of 32:1 and a specimen length about 20% longer than the support span. This resulted in coupon dimensions of 80 mm x 13 mm, and a span of 64 mm. Eight coupons were tested per laminate in each orientation. A crosshead speed of 3 mm/min was used until failure on an Instron 3369 testing system.

2.7.2. Short beam shear testing (interlaminar shear strength)

Interlaminar shear performance was assessed in accordance with ASTM D2344, using a span-to-thickness ratio of 4:1, a length-to-thickness ratio of 6:1 and a width-to-thickness ratio of 2:1. Eight coupons were tested per laminate. Coupon dimensions were therefore 12 mm x 4 mm, with a span of 8 mm. Testing was performed at 1 mm/min on an Instron 3369 testing system.

2.8. Scanning electron microscopy (SEM)

SEM was performed on post-mortem flexural and ILSS coupons in order to qualitatively assess failure behaviour. Flexural coupons were cut down to a size that allowed for SEM observation of the fracture area, taking care to not affect the region of interest. ILSS coupons were cast exposing the edges of the samples and polished. SEM was also performed on the aforementioned etched samples, in order to observe differences in the crystalline structures. Samples were prepared with a 15 nm sputter coating of gold to enhance surface conductivity and imaged with a JEOL

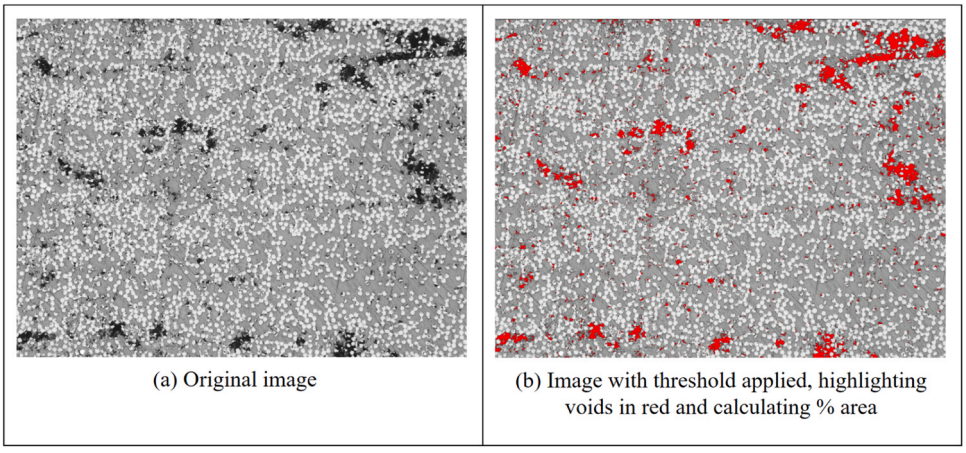

Fig. 4. Sample image from ATP laminate 380–4–2 (a) original image (b) after applying the threshold tool on ImageJ.

JSM-IT100 instrument at 20 kV.

3. Results and discussion

The manufactured laminates were examined for their consolidation quality and crystalline morphology, and were tested for flexural (longitudinal and transverse) and interlaminar shear strength properties. The following sections discuss the results of these tests.

3.1. Laminate consolidation

Fig. 5 shows sample microscopy images of mounted and polished compression-moulded and ATP samples, where fibre, matrix and any voids present can be observed. Table 2 shows the average thickness and per cent void content for each laminate taken from Fig. 5.

Overall, no significant variability was observed in the thickness or void content across the compression-moulded laminates. Although the thermal history of each laminate is different, these were held in the melt and at the isothermal temperatures for long times (60 min) under high pressure (28 bar), and therefore a low void content was expected. This processing, along with the frame used, limited the laminate thickness of the compression-moulded laminates to the thickness of the frame, explaining the low variability in thickness across the different laminates. The different prepreg layers are still distinguishable in the micrographs of all the laminates.

On the other hand, the ATP laminates showed a significantly higher void content. This is a consequence of the much shorter exposure time to high temperatures and pressures which limit flow of the matrix into voids and the extent of interply contact, evident in the interply voids highlighted with blue squares in Fig. 5. Intraply voids (highlighted with red arrows) are also present, which could be attributed to the inadequate penetration of the matrix into the fibres in the prepreg tape. The pressure during compression moulding is high enough to minimise these, but not during the ATP lay-down process. Other authors have made similar

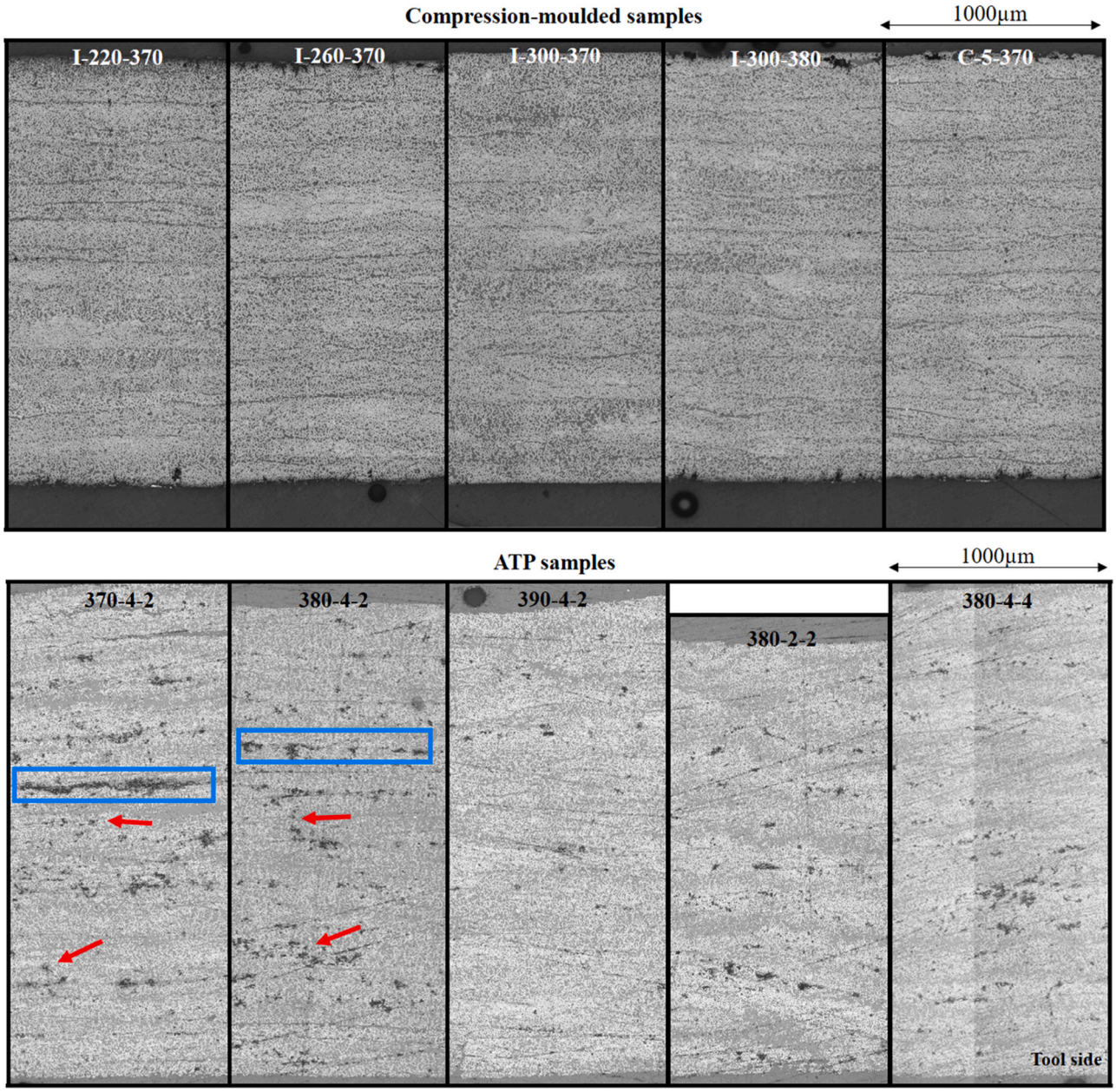

Fig. 5. Microscopy images of the cross sections of all compression-moulded laminates and the ATP-manufactured laminates with annotations highlighting examples of interply voids (blue squares) and intraply voids (red arrows).

Table 2
Laminate thickness and void content of compression-moulded and ATP laminates, taken from microscopy images in Fig. 5.

	Laminate	Laminate thickness (mm)	Void content (%)
Compression-moulded	I-220–370	1.92 ± 0.00	0.4 ± 0.2
	I-260–370	1.89 ± 0.01	0.1 ± 0.1
	I-300–370	1.93 ± 0.00	0.1 ± 0.1
	I-300–380	1.92 ± 0.01	0.2 ± 0.0
	C-5–370	1.91 ± 0.01	0.4 ± 0.1
ATP	370–4–2	2.20 ± 0.03	7.9 ± 2.7
	380–4–2	2.13 ± 0.01	8.0 ± 1.1
	390–4–2	2.11 ± 0.03	3.7 ± 0.5
	380–2–2	1.95 ± 0.02	6.0 ± 0.5
	380–4–4	2.24 ± 0.02	5.7 ± 1.8

observations when comparing CF/PEEK ATP-manufactured laminates with autoclaved laminates. For example, in Comer et al.'s work [6], void content was measured at 2.83% and 0.08% in ATP and autoclaved laminates respectively. They also cited other works on ATP-manufactured CF/PEEK laminates [37–39] where void content varied from 1.65% to 7%, in line with the observations in this study. Qureshi et al. [10] also drew qualitative comparisons between microscopy images of autoclaved and ATP CF/PEEK laminates where the higher void content in the ATP-manufactured laminates was evident.

The effect of the lower pressure applied for shorter times also became obvious when comparing the ATP laminate thicknesses with that of the compression moulded laminates: with the same number of plies, thicknesses were 1.89–1.93 mm for the compression-moulded laminates and 1.95–2.24 mm for the ATP laminates.

Some differences, albeit less significant, can also be observed across the different ATP laminates. A slower lay-down speed resulted in a thinner laminate, less defined interply boundaries and a lower void content, visible when comparing laminates 380–4–2 and 380–2–2. Roller pressure may have also impacted the presence of voids: interply voids appear more localised in 380–4–4, whereas in 380–4–2 they seem more elongated and distributed along interply boundaries.

Higher nip temperatures clearly caused a decrease in void content, particularly noticeable in Fig. 5 when comparing 370–4–2 and 390–4–2. A higher temperature likely resulted in the polymer being held at a lower viscous state for longer, resulting in better interply adhesion. Consequently, the thickness also decreased with a higher nip temperature, but the drop is less significant.

3.2. Crystallinity and spherulitic morphology

Table 3 shows the average glass transition temperatures, enthalpies and total crystallinities achieved in the manufactured laminates, with Fig. 6 showing heat flow variation against temperature in DSC for one sample of each laminate. All the compression-moulded laminates crystallised to the maximum extent (~29%), whereas the ATP-manufactured laminates only achieved 6–8.3% crystallinity and contained a significant amorphous fraction. This amorphous content is denoted by the cold crystallisation peak and the much more prominent glass transition in the ATP sample curves in Fig. 6.

The melting behaviour of the isothermally compression-moulded laminates in DSC denote a dual crystallisation mechanism previously observed for both PEEK and PEKK systems[1–3,17,20,22,24,27,40,41]. The LTEs (marked * in Fig. 6) are observed to shift, depending on the isothermal temperature (T_{iso}) the material underwent, always remaining approximately 10 °C above T_{iso}. The proportion of LTE:HTE also increased with T_{iso}, as observed in a previous study performed on the same prepreg tape undergoing different cycles in DSC [20]. The proportion of HTE is higher in the current study, which may be a consequence of the slower cooling rate the material undergoes to reach T_{iso} (10 °C/min instead of 150 °C/min used in DSC), as well as the sample size: the laminates consist of 10 layers of prepreg tape across which heat flow may be slower than the small prepreg sample used in the previous DSC studies. During non-isothermal processing (as per laminate C-5–370), PEKK does not display this dual melting behaviour, but rather a single melting peak (corresponding to the HTE in the isothermal laminates).

In the case of laminates I-300–370 and I-300–380, where the holding temperatures in the melt were 370 °C and 380 °C respectively and isothermal hold temperature was 300 °C, both endotherms in Fig. 6 (LTE and HTE) began to overlap, as observed in previous studies [2,17,20]. In this case, the area corresponding to each endotherm was calculated as done in [20]. There is no significant difference observed as a consequence of the different holding temperatures in the melt.

The ATP-manufactured laminates, on the other hand, achieved a

Table 3
Average values for glass transition temperatures, enthalpies and total crystallinity of CF/PEKK laminates manufactured under different processing conditions.

	Laminate	T_g (°C)	T_{LTE} (°C)	ΔH_{LTE} (J/g)	T_{HTE} (°C)	ΔH_{HTE} (J/g)	LTE:HTE	X (%)
Compression-moulded	I-220–370	155.5 ± 1.4	231.6 ± 0.5	0.27 ± 0.01	341.3 ± 0.6	11.8 ± 0.6	2:98 ± 0	29.3 ± 1.4
	I-260–370	157.0 ± 3.2	271.0 ± 0.7	0.38 ± 0.03	340.8 ± 0.6	10.7 ± 0.4	3:97 ± 0	27.0 ± 1.0
	I-300–370	156.6 ± 205	309.9 ± 0.2	2.9 ± 0.2	341.4 ± 0.8	9.1 ± 0.5	24:76 ± 1	29.1 ± 1.3
	I-300–380	160.2 ± 0.4	306.6 ± 0.1	2.9 ± 0.2	340.9 ± 0.7	10.0 ± 0.4	22:78 ± 1	31.2 ± 0.4
	C-5–370	151.9 ± 0.8	-	-	341.7 ± 1.1	11.7 ± 0.2	-	28.5 ± 0.4
ATP		**T_g (°C)**	**T_{cc} (°C)**	**ΔH_{cc} (J/g)**	**T_m (°C)**	**ΔH_m (J/g)**	**-**	**X (%)**
	370–4–2	162.6 ± 1.0	220.5 ± 0.3	9.0 ± 0.5	337.8 ± 1.3	11.7 ± 0.7	-	6.0 ± 0.5
	380–4–2	165.3 ± 4.1	220.2 ± 3.8	9.1 ± 0.3	339.2 ± 2.7	12.5 ± 0.5	-	6.8 ± 1.3
	390–4–2	164.7 ± 0.4	223.5 ± 2.6	9.0 ± 1.0	339.2 ± 0.4	11.8 ± 1.0	-	6.1 ± 0.5
	380–2–2	162.6 ± 0.3	217.8 ± 0.4	8.6 ± 0.2	338.2 ± 0.6	12.5 ± 0.9	-	8.3 ± 1.0
	380–4–4	163.8 ± 2.1	220.5 ± 1.3	9.0 ± 0.1	338.4 ± 1.7	11.7 ± 0.7	-	6.0 ± 1.6

T_g = glass transition temperature
T_{LTE} = low endotherm temperature
ΔH_{LTE} = low endotherm enthalpy
T_{HTE} = high endotherm temperature
ΔH_{HTE} = high endotherm enthalpy
LTE:HTE = low endotherm to high endotherm ratio
X = total crystallinity
T_{cc} = cold crystallisation temperature
ΔH_{cc} = cold crystallisation enthalpy
T_m = melting temperature
ΔH_m = melting enthalpy

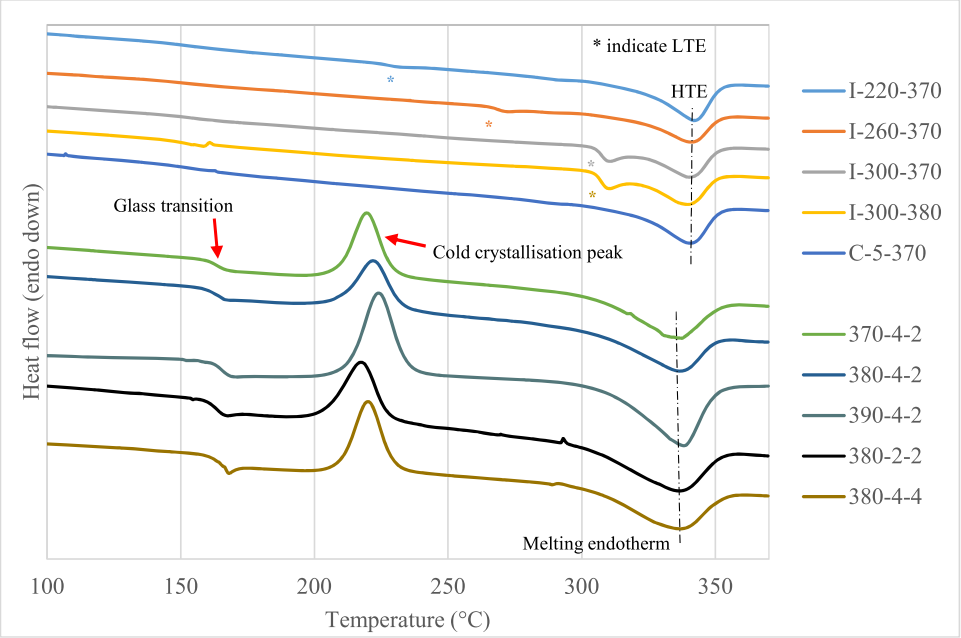

Fig. 6. Sample DSC heat scans of CF/PEKK laminates manufactured under different processing conditions.

lower crystallinity than what the prepreg tape originally contained, and did not show any form of dual melting behaviour in the DSC heat scan. This may be attributed to the slower crystallisation kinetics of PEKK compared to PEEK [3] and the short time that the matrix is exposed to temperatures at which it can undergo crystallisation, developing a limited amount of primary crystallisation and no secondary crystallisation phase due to its slower forming nature. This is further evidenced by the cold crystallisation peak that takes place during heating (Fig. 6), showing that the matrix did not fully crystallise during processing. Laminate 380–2–2, with a slower lay-down speed of 2 m/min, achieved a slightly higher crystallisation, likely due to this lower speed resulting in longer exposure times of the material to temperatures within crystallisation range (between glass transition temperature and melting temperature). Nip temperature and roller pressure did not seem to have an effect on the crystallisation extent.

Fig. 7a, b and c show etched samples from laminates I-220–370, I-

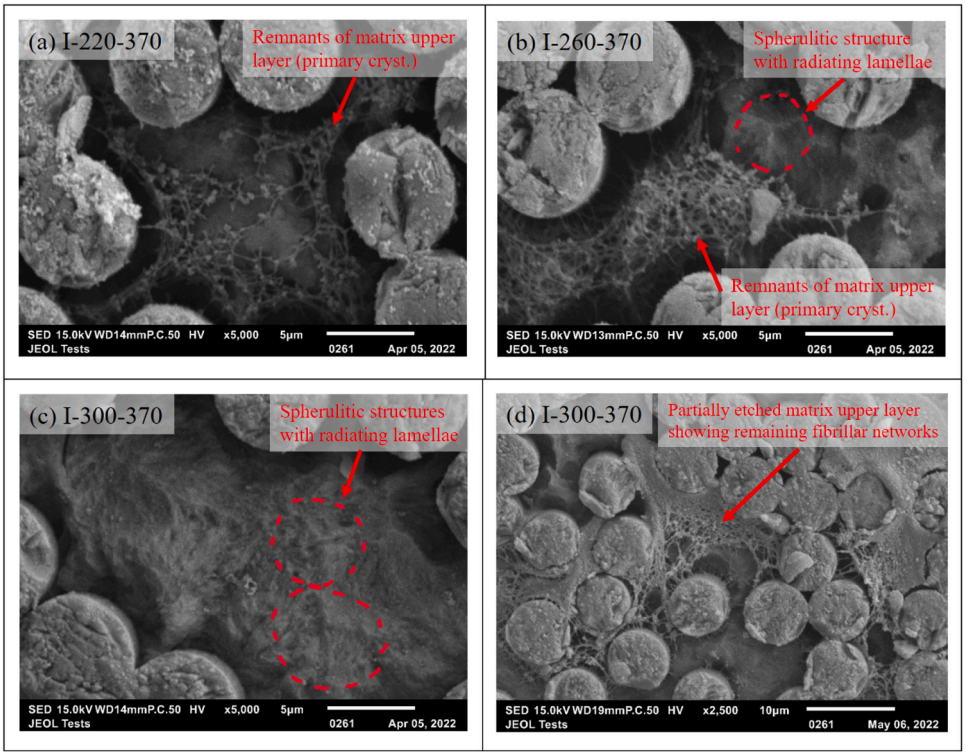

Fig. 7. SEM micrographs of etched CF/PEKK samples from different compression-moulded laminates: (a) Laminate I-220–270 (b) Laminate I-260–370 and (c) Laminate I-300–370 (d) example of partially etched sample showing remaining fibrillar networks in the matrix as a consequence of partial etching.

260–370 and I-300–370 respectively. These samples were selected to observe the effect of different isothermal holding temperatures on the developed matrix morphology. Fig. 7d shows a partially etched sample, where the top layer of the matrix has not been fully etched. Here the fibrillar networks in the matrix can be observed to be the last to remain from the top matrix layer as the etchant exposes the lower layer of the matrix. These networks are likely to be remnants of the primary crystal structure of the matrix, with amorphous material being etched first, followed by secondary crystals, and finally the primary crystalline structures.

Across all images in Fig. 7 it is obvious that the fibre-matrix interface region was more severely impacted by the etching than the bulk matrix. This suggests a fibre-matrix interface with a lower chemical resistance than the matrix bulk. This could be due to the presence of a trans-crystalline region with lower chemical resistance.

In the bulk matrix of the samples in Fig. 7b and c, the preferential etching of the amorphous regions revealed radiating patterns typical of spherulitic crystallisation. The spherulite size is larger in Fig. 7c where the sample was held at the higher isotherm (300 °C), a consequence of the lower nucleation density at higher isothermal temperatures. The spherulite sizes are therefore expected to be the smallest in Fig. 7a with the highest nucleation density out of the three samples. These are not particularly obvious potentially due to spherulites being very small, as well as the network-like structure present over the etched surface in Fig. 7a. While these network structures were present in all samples, these were observed the most in the etched sample of laminate I-220–370 and I-260–370, and the least in the laminate I-300–370. From the DSC results shown in Fig. 6 and Table 3, there is a larger proportion of material that melts under the HTE in samples undergoing lower T_{iso}, and therefore a larger proportion of the more stable primary crystalline structure. It is therefore logical that there is more of this residual primary structure present in Fig. 7a, and the least in Fig. 7c.

Similar conclusions on the variation of spherulite size have been observed in literature. As discussed in Section 1, a preceding study [20] observed cryofractured CF/PEKK samples undergoing isothermal holds in DSC cycles to develop small spherulites at lower isothermal temperatures, and larger spherulites at higher isothermal holds. Other work on CF/PEEK also observed such behaviour [36].

3.3. Mechanical performance

The results of the mechanical testing are discussed in this section. Overall, there was no significant difference in the performance of the different compression-moulded laminates, except for a marginally improved performance of Laminate I-300–380 in Flexural 90°. On the other hand, lower properties were observed in the ATP-manufactured laminates across all tests. A summary of all mechanical testing results is presented in Table 4, and will be discussed in detail in the following sub-sections. Mechanical testing data reported in literature for ATP-manufactured CF/PEKK (AS7 fibres as used in this study) laminates is scarce, and therefore available results on CF/PEEK with different fibre types (AS4, IM7) are also included for comparative purposes.

3.3.1. Flexural 0 ° (longitudinal) testing

Representative flexural 0 ° stress-strain curves for each laminate are shown in Fig. 8. Coupon failure in this testing mode commenced by compression on the top surface of the specimens (where the load was being applied), followed by tension failure on the bottom surface. While flexural 0 ° testing response is dominated by the fibres, the matrix also plays a role in providing compression strength in particular, and therefore may influence flexural properties to some extent.

No significant difference in flexural strength or modulus was observed across the different compression-moulded laminates, implying that differences in the crystal morphology, as a consequence of the differing isothermal holds or holding temperatures in the melt, have not resulted in significant differences in the behaviour of the matrix when loaded under 0 ° flexure. This was expected, as longitudinal flexural testing is dominated by fibre strength rather than the matrix. The failure of the composites was also abrupt and explosive, with the majority of the samples splitting in two when reaching the maximum load. It is obvious, however, that processing conditions did have an effect on flexural 0 ° performance to a certain extent, as shown by the lower flexural strength and modulus of the ATP specimens by 62% and 25% respectively on average. The higher void content is likely to lead to lower mechanical properties; as well as the amorphous nature of the matrix in the ATP specimens resulting in a more ductile behaviour. This therefore resulted in sample deformation and failure under lower loads than the compression-moulded specimens. This more plastic behaviour is also reflected in the fact that, unlike the compression-moulded specimens, the ATP flexural specimens did not experience an explosive fracture nor completely split into two. Instead, a jagged fracture curve was observed in Fig. 8, indicating that the ATP samples failed in various steps. This is due to the poorer consolidation of the laminates observed in Section 3.1, which resulted in different groups of plies failing at different stages. This is visible in the SEM images of the fracture surfaces shown in Fig. 9 – in the compression-moulded sample, single compression and tension regions are visible, whereas in the ATP sample these can be seen to alternate, indicating several steps to failure.

Comparing the results in Table 4 for the different ATP laminates, it is obvious that higher nip temperatures (380 and 390 °C) increase 0 ° flexural performance, particularly flexural strength, possibly a consequence of achieving a better interlayer adhesion during material lay-down. A slower lay-down speed likely had the same impact, marginally increasing the performance of laminate 380–2–2 compared to laminate 380–4–2. This may have also been influenced by the slightly higher crystallinity content resulting from a slower lay-down speed. Laminate 380–4–4, with a higher roller pressure, did not show any significant difference, potentially indicating that at this nip temperature and lay-down speed, increasing roller pressure does not have an impact on laminate consolidation.

Higher magnification SEM images of the fracture surfaces of a compression-moulded specimen and an ATP specimen are shown in

Table 4
Mechanical testing results of compression-moulded and ATP CF/PEKK laminates.

	Laminate	Flexural 0°		Flexural 90°		ILSS
		Strength (MPa)	Modulus (GPa)	Strength (MPa)	Modulus (GPa)	SBS Strength (MPa)
Compression-moulded	I-220–370	1824 ± 119	120.1 ± 1.7	75.5 ± 2.0	8.6 ± 0.2	97.9 ± 0.5
	I-260–370	1825 ± 135	120.6 ± 2.6	75.8 ± 3.0	8.6 ± 0.2	97.9 ± 1.8
	I-300–370	1770 ± 107	120.1 ± 1.7	77.6 ± 7.3	8.6 ± 0.2	99.4 ± 3.0
	I-300–380	1772 ± 95	119.2 ± 2.5	93.9 ± 7.0	8.6 ± 0.2	100.1 ± 3.1
	C-5–370	1855 ± 64	121.2 ± 2.0	81.0 ± 3.5	8.7 ± 0.1	93.0 ± 4.6
ATP	370–4–2	457.8 ± 35.8	88.8 ± 7.4	20.8 ± 4.9	2.2 ± 0.6	22.0 ± 1.6
	380–4–2	718.8 ± 73.1	95.8 ± 2.8	31.3 ± 2.3	3.4 ± 0.3	24.4 ± 2.0
	390–4–2	755.7 ± 58.9	91.9 ± 6.1	27.1 ± 4.4	2.6 ± 0.5	29.3 ± 1.7
	380–2–2	761.0 ± 50.1	87.1 ± 4.8	24.1 ± 2.1	2.9 ± 0.6	27.0 ± 2.4
	380–4–4	741.7 ± 98.9	86.9 ± 8.7	24.1 ± 1.6	3.1 ± 0.2	26.6 ± 2.0

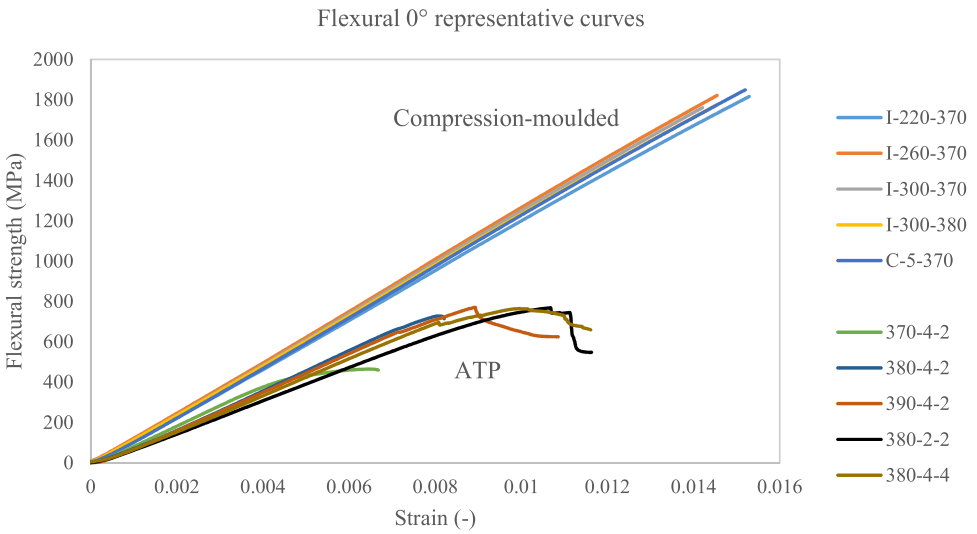

Fig. 8. Representative stress-strain curves for flexural 0° coupons of compression-moulded and ATP laminates.

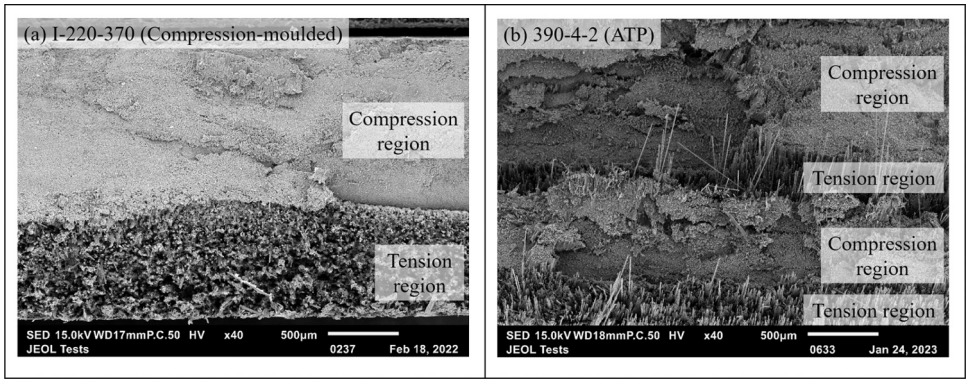

Fig. 9. SEM images of 0 ° flexural fracture surfaces of specimens extracted from (a) I-220–370 (compression moulded) and (b) 390–4–2 (ATP-manufactured) laminates at × 40 magnification, with labelled tension and compression failure regions.

Fig. 10. Across all compression-moulded specimens, fibre surfaces were observed to be coated with matrix, with no major differences across the different samples, whereas the ATP specimens showed bare fibres. This suggests that the processing conditions influenced the fibre-matrix interface, with a higher crystallinity resulting in better adhesion of the matrix to the fibre surface. As mentioned in Section 1, this is in line with what has previously been observed in literature, with high crystallinity content in CF/PEEK [31,32] and CF/PEKK [20] fracture samples displaying a significant amount of matrix residue on fibres, whereas amorphous samples resulted in clean fibre surfaces.

A comparison of the above results of CF/PEKK with results from the literature on CF/PEEK is given in Table 5. The compression-moulded CF/PEKK samples performed comparably to autoclaved CF/PEEK samples, whereas the ATP laminates tested in this work underperformed in comparison to reported CF/PEEK values. This may be a consequence of the ATP process parameters selected in the current study limiting interply consolidation and resulting in higher void content, as discussed in Section 3.1.

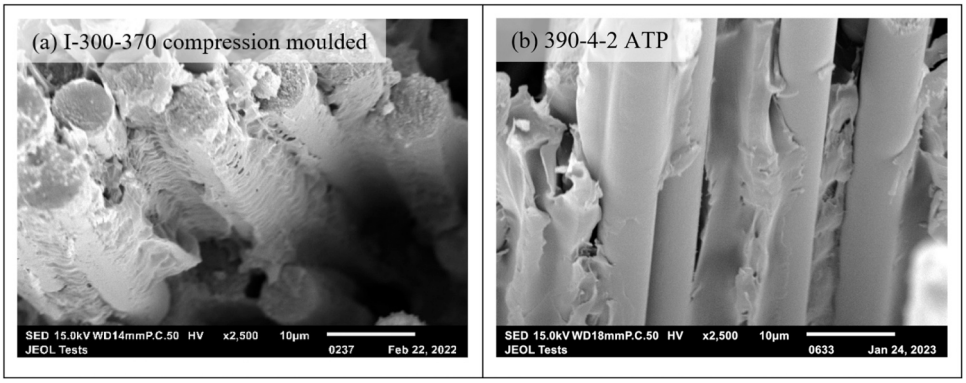

Fig. 10. SEM images of 0 ° flexural fracture surfaces of specimens extracted from (a) I-300–370 (compression moulded) and (b) 390–4–2 (ATP).

Table 5
Flexural 0 ° results in this work and in literature.

Material [Ref]	Autoclave	Laser ATP					
	Flexural 0 ° (MPa)	Nip temp. (°C)	Tool temp. (°C)	Tool material	Lay-down speed (m/min)	Roller pressure (bar)	Flexural 0 ° Strength (MPa)
AS4/PEEK[42]	1650	420	Unheated	Stainless steel	9	3.8	1143
AS4/PPS/PEEK[42]	1650	400	Unheated	Stainless steel	9	3.8	1035
This work, AS7/PEKK	1770–1855 (comp. moulding)	370	Unheated	Mild steel	4	2	457.8
		380	Unheated	Mild steel	4	2	718.8
		390	Unheated	Mild steel	4	2	755.7
		380	Unheated	Mild steel	2	2	761.0
		380	Unheated	Mild steel	4	4	741.7

3.3.2. *Flexural 90 ° (transverse) testing*

Representative flexural 90 ° stress-strain curves for each laminate are shown in Fig. 11. In this testing mode, failure was caused purely by tension, which began on the bottom surface of the samples (side under tension). Fibre contribution to strength and stiffness is minimal in this case, and therefore this test can provide a better indication of any variation in matrix properties as a consequence of processing.

There was a significant increase of approximately 23% in the 90 ° flexural strength of laminate I-300–380 compared to the remaining compression-moulded laminates, which showed no significant difference in performance. This suggests that a different crystalline morphology as a consequence of different isothermal holds (large vs. small spherulites) does not majorly dictate flexural performance when loaded under 90° flexure as long as the material is crystallised to its maximum extent (~29%). The crystallinity of laminate I-300–380 (shown in Table 3) was also the highest, which may contribute to the better performance. All compression-moulded samples exhibited immediate load drop after reaching the peak load.

The ATP specimens showed significantly lower flexural strength and modulus (~68% and 67% respectively) compared to the compression-moulded laminates. The more amorphous nature of the matrix resulted in lower material strength and stiffness, as mentioned before. The higher ductility in the material is once again apparent in the representative curves in Fig. 11, where the load did not immediately drop after failure. The ATP laminates manufactured with higher nip temperatures (380 and 390 °C) performed best, indicating that higher processing temperatures contributed towards a better performance. This may be a consequence of the lower void content and an overall better consolidation as observed in the laminate thickness in Section 3.1. A slower lay-down speed and a higher roller pressure did not seem to have a significant impact on changing matrix flexural strength in this case.

SEM images of the 90 ° flexural fracture surfaces of compression-moulded and ATP specimens in Fig. 12 show coated fibres in the compression-moulded specimen, and clean fibres in the ATP sample. Similarly to 0 ° flexural fracture images, this suggests a weak fibre-matrix interface with an amorphous matrix in the ATP specimen, causing failure at said interface rather than in the matrix bulk.

Comparing the flexural 90 ° results to literature, the compression-moulded CF/PEKK laminates in this study (75–94 MPa) performed comparably with CF/PEEK laminates manufactured via autoclave (~90 MPa [8]) and compression moulding (55–130 MPa [7,43]). Literature covering flexural 90 ° testing of ATP-manufactured CF/PEEK or CF/PEKK laminates has not been found.

3.3.3. *Interlaminar shear strength (ILSS)*

Representative stress-displacement curves from the ILSS tests are shown in Fig. 13. No significant variation in performance was observed across the isothermally compression-moulded laminates, with a marginally lower performance in the ILSS of dynamically cooled laminate C-5–370 (−6%). As this laminate underwent non-isothermal cooling at a rate of 5 °C/min, there was a steady decrease in the matrix molecular movement with the drop in temperature as the material cooled down. The laminate was also exposed to temperatures in which interply consolidation could happen above glass transition temperature for a shorter time than the rest of the compression-moulded laminates. This is visible in Fig. 1, where the temperature in laminate C-5–370 dropped below 160 °C (T_g) after 100 min, whereas the rest of the compression-moulded laminates dropped below 160 °C after approximately 140 min. Therefore, it is possible that a slower cooling rate, particularly at the temperature range where a better interply consolidation can be achieved (above T_g), might improve this result. However, if the difference in performance is marginal between laminates

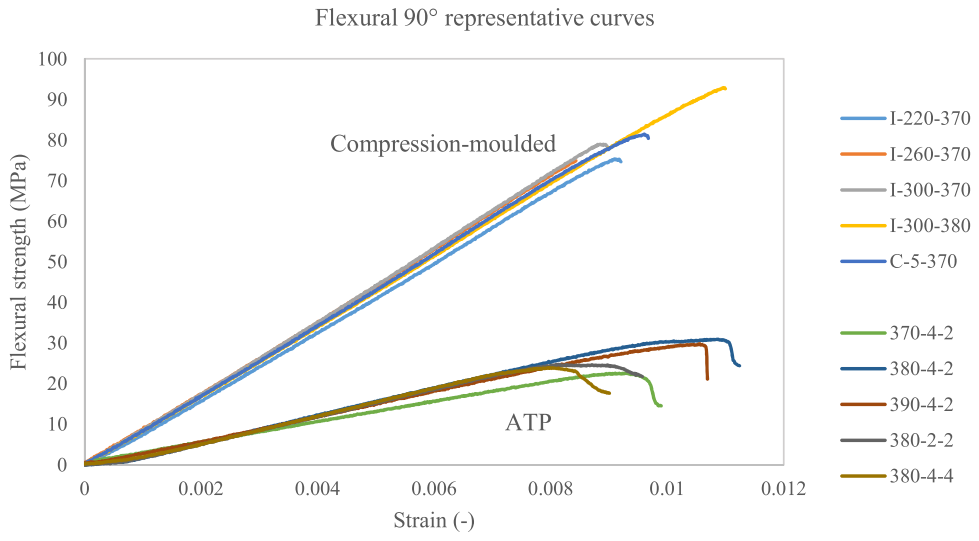

Fig. 11. Representative stress-strain curves for flexural 90 ° coupons of compression-moulded and ATP laminates.

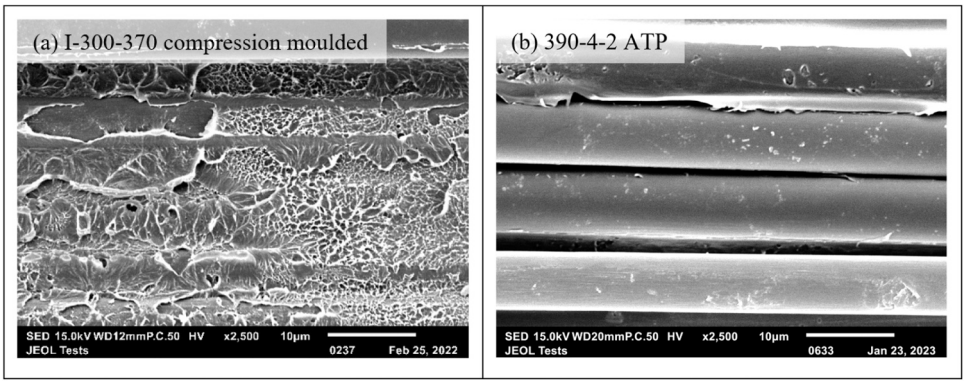

Fig. 12. SEM images of 90 ° flexural fracture surfaces of specimens extracted from (a) I-300–370 (compression moulded) and (b) 390–4–2 (ATP).

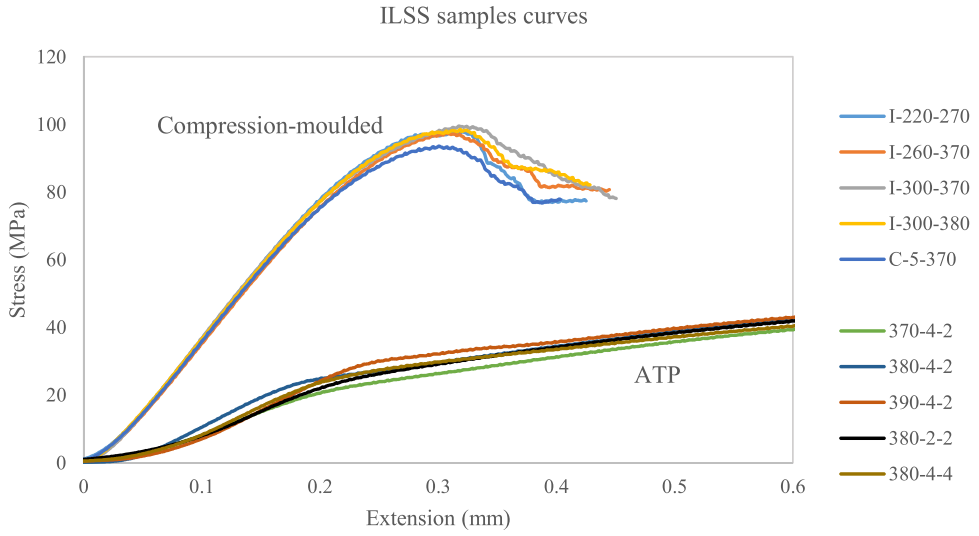

Fig. 13. Representative ILSS stress-displacement curves of compression-moulded and ATP laminates.

undergoing a slower cooling rate or undergoing an isothermal hold at a higher temperature for a definite period of time, then the more energy-efficient cycle should be considered in large-scale manufacturing.

The ATP laminate specimens, on the other hand, exhibited 73% lower ILSS compared to the compression-moulded laminates. This is very likely due to the much shorter exposure times to heat and pressure experienced during manufacturing, which resulted in a higher void content and lower interply consolidation than that achieved by compression moulding. It can also be observed in Fig. 13 that the response of the ATP specimens was unlike the other specimens and not what is commonly seen in an ILSS load-displacement curve (no ILSS peak). Instead, they displayed much more plastic deformation after the initial linear portion of the graph. Similar behaviour was observed in Chanteli et al.'s work on CF/PEEK [12], where the influence of repass on laser-ATP-manufactured laminates was studied, and no distinct peak was observed in their load-displacement curves. In this case, the authors argued that the non-linear response was a consequence of the visco-elastic behaviour of the matrix. Comer et al. [6] observed a slightly more defined curvature in the fail response of laser-ATP manufactured CF/PEEK, potentially due to the faster crystallising nature of PEEK compared to PEKK; however performance compared to autoclaved samples was still significantly lower.

As with the previous testing, the ILSS performance of the laminates can be observed to marginally increase with a higher nip temperature, again potentially indicating a better interlayer adhesion. As per the 0 ° flexural testing, there was also a marginal increase in ILSS with a slower lay-down speed (380−2−2) and a higher roller pressure (380−4−4) when compared to 380–4–2. This is likely due to the better consolidation reflected in the lower void content observed in Section 3.1.

The difference in performance between compression-moulded and ATP ILSS coupons becomes obvious in the SEM images shown in Fig. 14. The compression-moulded laminates showed a kink in the fibres under the location of the loading nose (flexural failure by compression) and/or ply separation (interlaminar shear) (Fig. 14a). On the other hand, the ATP specimens did not show either of these features, and instead displayed inelastic deformation (Fig. 14b). The voids visible in Fig. 14b(iv) have also been observed in untested specimens to a lesser extent (see Fig. 15). It is possible that the voids already present in the untested samples were exacerbated during ILSS testing, specifically those present between plies (particularly obvious in Fig. 14b(iv)). This is the case in Chanteli et al.'s work [12], where side-images of ILSS coupons from CF/PEEK ATP laminates show some elongated voids from interlayer separation/delamination and no brittle deformation as per the compression-moulded laminates in this work.

A comparison of ILSS results of CF/PEKK with that of CF/PEEK in literature, as well as a recent study on CF/PEKK, is given in Table 6. The compression-moulded laminates in our work performed similarly to the autoclaved CF/PEEK [12] and CF/PEKK [35] laminates reported in literature. This was also the case for the ATP laminates when compared to published work with similar nip temperatures and an unheated tool, showing a significant drop of 57% for CF/PEEK [12] and 77% for CF/PEKK [35] when compared to their respective autoclaved results.

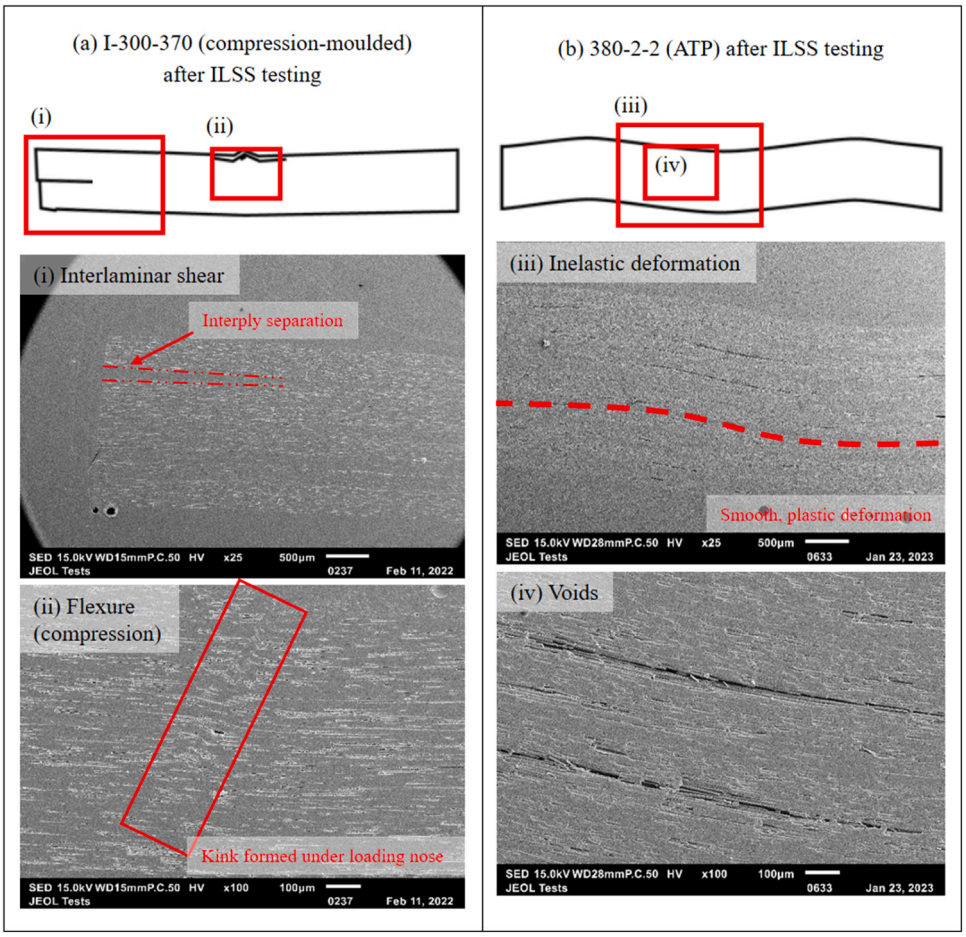

Fig. 14. Schematics and SEM images of cast ILSS specimens extracted from (a) I-300–370 (compression moulded) and (b) 380–2–2 (ATP) with sketches highlighting failure modes. Images are of the side of the specimens.

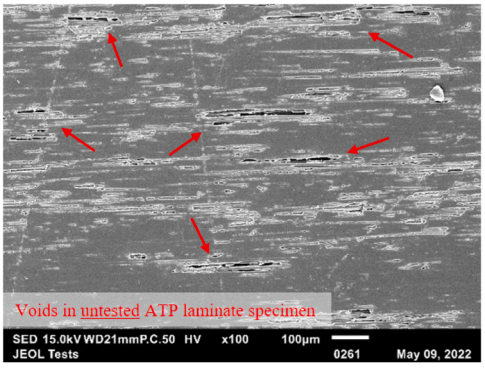

Fig. 15. SEM image of an untested ATP laminate sample showing intra-ply voids.

3.4. ATP manufacturing insights

As evidenced in Section 3, the ATP laminates studied displayed inferior performance when compared to the compression-moulded laminates in this work and other ATP-manufactured CF/PEEK laminates in literature, particularly in the case of flexural 0 ° testing. While PEEK has faster crystallisation kinetics than PEKK [3,15], which is generally beneficial for achieving higher crystallinities in ATP manufacturing, the results of the CF/PEKK laminates in this work show considerable scope for improvement. The underperformance is likely a consequence of suboptimal processing parameters, perhaps the most significant ones being the material temperature at nip and tool temperature (unheated). This was also apparent for CF/PEKK in Hoang et al.'s work [35] with an unheated tool, where with slightly higher nip temperatures (417–430 °C) than in the current study (370–390 °C), ILSS testing resulted in very similar values to the work presented in this article. Exposure to higher temperatures will lower polymer viscosity during tape placement, which could result in improved interply bonding and polymer chain reptation [44,45]. This was particularly evident in Stokes-Griffin et al.'s work on CF/PEEK [5], where nip temperatures significantly higher than melting temperature (400–600 °C, significantly higher than those used in this work) resulted in an ATP laminate performance comparable to autoclaved counterparts. It is worth noting, however, that PEEK is faster crystallising than PEKK, and therefore the fast cooling that the material undergoes in ATP manufacturing may be more adequate for PEEK than PEKK. Introducing a heated tool is likely to help with the material's exposure to higher temperatures, aiding with interply consolidation and crystallisation extent while working at lower nip temperatures. This was demonstrated in Esguerra-Arce et al.'s work [15], where using a heated tool at 200 °C reduced void content and improved the crystallinity of CF/PEKK. Saenz-Castillo et al.'s work on CF/PEEK [46] also observed similar results, where using similar nip temperatures to this study but with a heated tool at 200 °C resulted in an ILSS performance close to autoclaved samples.

Literature has highlighted, however, the problem of void rebound if the material is held at higher temperatures once roller pressure is removed (the re-emergence of pre-existing voids after these have been compressed during tape lay-down) [6,44,47]. This therefore poses conflicting mechanisms for PEKK, where high temperatures and slow

Table 6
ILSS results in this work and in literature.

Material	Autoclave	Laser ATP					
	ILSS (MPa)	Nip temp (°C)	Tool temperature (°C)	Tool material	Lay-down speed (m/min)	Roller pressure/load	ILSS (MPa)
IMS65/PEEK[12]	105	380	Unheated	Aluminium	3	2.5 bar	42.5
AS4D/PEKK[35]	~90	417	Unheated	Not specified	2.4	1000 N	~20
		430	Unheated	Not specified	2.4	1000 N	~20
		430	Unheated	Not specified	6	1000 N	~20
This work, AS7/PEKK	93–101 (compression moulding)	370	Unheated	Mild steel	4	2 bar	22.0
		380	Unheated	Mild steel	4	2 bar	24.4
		390	Unheated	Mild steel	4	2 bar	29.3
		380	Unheated	Mild steel	2	2 bar	27.0
		380	Unheated	Mild steel	4	4 bar	26.6

cooling are desirable for adequate crystallinity levels and interply chain reptation, but prolonged exposure to temperatures above T_g with no consolidation pressure may result in void rebound. Further to this, high lay-down speeds have been shown to not offer sufficient compaction time to achieve a good interply bond [47]. This requires an optimisation exercise of material temperature, tool temperature, lay-down speed and roller pressure, to establish optimal parameters regarding exposure to heat and compressive loads, and achieve acceptable levels of crystallinity, interply consolidation and void reduction for the composite material in question. These parameters will be highly dependent on the material type and its inherent crystallisation ability, average molecular weight and molecular weight distribution, and polydispersity index. Lamontia and Gruber [9] have suggested a modular lay-down head providing further heating, compaction and cooling steps, however these result in bulkier equipment pieces which may limit the equipment's ability to manufacture geometrically complex shapes, which is an attractive quality of ATP manufacturing.

4. Conclusions

In this work, CF/PEKK laminates were processed using different cycles under compression moulding (holding temperatures in the melt of 370 and 380 °C, followed by isothermal holds of 220, 260 and 300 °C or a cooling rate of 5 °C/min) and ATP (nip temperatures of 370, 380 and 390 °C, lay-down speeds of 2 and 4 m/min, and roller pressures of 2 and 4 bar). Their consolidation quality, crystallinity development in the matrix and flexural and interlaminar performance were evaluated. Overall, it was observed that compression-moulded laminates achieved a very good consolidation and all compression-moulded laminates performed similarly regardless of their processing history, with a marginally higher transverse flexural performance of the laminate manufactured at a higher holding temperature in the melt. The highest extent of crystallinity development was achieved across all the compression-moulded laminates. Differences were observed in their morphology as expected by general polymeric theory, where higher isothermal temperatures result in a lower nucleation density and therefore larger spherulitic entities. Chemical etching to expose these structures also highlighted the potential presence of a transcrystalline region at the fibre-matrix interface that the chemical etching attacked more aggressively.

Comparing the ATP laminates' performance with the compression-moulded laminates showed overall lower properties and quality. This is expected, due to the differences between the two processing techniques. The more rapid heating and cooling in the ATP manufacturing process resulted in poor consolidation quality, a higher void content, lower crystallinity and a significant reduction in mechanical performance. This is more prominent in slower crystallising PEKK than that in faster crystallising PEEK-based composites. In this study, increasing the nip temperature in ATP manufacturing had the most noticeable effect on mechanical performance, followed by a slower lay-down speed resulting in a lower void content and a marginal increase in both mechanical performance and crystallinity. However, these differences were not significant when compared to the performance of the compression-moulded laminates. Optimising the parameters of ATP manufacturing to better suit the PEKK matrix would likely improve all of the above properties. Specifically, the use of a higher temperature at nip and the use of a heated tool is likely to improve the consolidation quality and crystallinity of ATP laminates; and a higher roller pressure may contribute to void content reduction.

CRediT authorship contribution statement

Helena Pérez-Martín: Conceptualisation, Investigation, Formal analysis, Project administration, Writing – original draft. **Stefan Buchalik-Bopp:** Investigation, Resources, Writing – review & editing. **Barbara E. Guettler:** Supervision, Resources, Writing – review & editing. **Paul Mackenzie:** Supervision, Resources, Writing – review & editing. **Alex Baidak:** Supervision, Resources, Writing – review & editing. **Conchúr M. Ó Brádaigh:** Supervision, Resources, Writing – review & editing. **Dipa Ray:** Conceptualisation, Supervision, Resources, Project administration, Writing – review & editing.

Declaration of Competing Interest

The authors declare that they have no known competing financial interests or personal relationships that could have appeared to influence the work reported in this paper.

Data availability

Data will be made available on request.

Acknowledgements

The authors acknowledge the financial support received from the National Manufacturing Institute for Scotland (NMIS-IDP/009) and Hexcel Composites Limited. The authors would also like to thank Ms. Pia Eichert at the Leibniz-Institut für Verbundwerkstoffe GmbH for their support and thermal analysis facilities; as well as Mr. David Jones for their help in manufacturing the ATP laminate at the University of Limerick.

References

[1] T. Choupin, B. Fayolle, G. Régnier, C. Paris, J. Cinquin, B. Brulé, Isothermal crystallization kinetic modeling of poly(etherketoneketone) (PEKK) copolymer, Polymer 111 (2017) 73–82, https://doi.org/10.1016/j.polymer.2017.01.033.
[2] L. Quiroga Cortés, N. Caussé, E. Dantras, A. Lonjon, C. Lacabanne, Morphology and dynamical mechanical properties of poly ether ketone ketone (PEKK) with meta phenyl links, J. Appl. Polym. Sci. 133 (2016) 1–10, https://doi.org/10.1002/app.43396.
[3] H. Pérez-Martín, P. Mackenzie, A. Baidak, C.M. Ó Brádaigh, D. Ray, Crystallinity studies of PEKK and carbon fibre/PEKK composites: A review, Compos Part B Eng. 223 (2021), 109127, https://doi.org/10.1016/j.compositesb.2021.109127.

[4] S.Z.D. Cheng, R.M. Ho, B.S. Hsiao, K.H. Gardner, Polymorphism and crystal structure identification in poly(aryl ether ketone ketone)s, Macromolecules 197 (1996) 185–213, https://doi.org/10.1002/macp.1996.021970115.
[5] C.M. Stokes-Griffin, P. Compston, The effect of processing temperature and placement rate on the short beam strength of carbon fibre-PEEK manufactured using a laser tape placement process, Compos Part Appl. Sci. Manuf. 78 (2015) 274–283, https://doi.org/10.1016/j.compositesa.2015.08.008.
[6] A.J. Comer, D. Ray, W.O. Obande, D. Jones, J. Lyons, I. Rosca, et al., Mechanical characterisation of carbon fibre–PEEK manufactured by laser-assisted automated-tape-placement and autoclave, Compos Part Appl. Sci. Manuf. 69 (2015) 10–20, https://doi.org/10.1016/j.compositesa.2014.10.003.
[7] A. Beehag, L. Ye, Role of cooling pressure on interlaminar fracture properties of commingled CF/PEEK composites, Compos Part Appl. Sci. Manuf. 27 (1996) 175–182, https://doi.org/10.1016/1359-835X(95)00027-Y.
[8] J.P. Kilroy, C.M. Ó Brádaigh, C.O.A. Semprimoschnig, Mechanical and physical evaluation of a new carbon fibre/PEEK composite system for space applications, SAMPE J. (2008) 1–12.
[9] M. Lamontia, M. Gruber, Remaining developments required for commercializing in situ thermoplastic ATP, SAMPE Eur. Conf. (2007) 1–15.
[10] Z. Qureshi, T. Swait, R. Scaife, H.M. El-Dessouky, In situ consolidation of thermoplastic prepreg tape using automated tape placement technology: potential and possibilities, Compos Part B Eng. 66 (2014) 255–267, https://doi.org/10.1016/j.compositesb.2014.05.025.
[11] F. Shadmehri, S.V. Hoa, J. Fortin-Simpson, H. Ghayoor, Effect of in situ treatment on the quality of flat thermoplastic composite plates made by automated fiber placement (AFP, Adv. Manuf. Polym. Compos Sci. 4 (2018) 41–47, https://doi.org/10.1080/20550340.2018.1444535.
[12] A. Chanteli, A.K. Bandaru, D. Peeters, R.M. O'Higgins, P.M. Weaver, Influence of repass treatment on carbon fibre-reinforced PEEK composites manufactured using laser-assisted automatic tape placement, Compos Struct. 248 (2020), 112539, https://doi.org/10.1016/j.compstruct.2020.112539.
[13] J. Denault, M. Dumouchel, Consolidation Process of PEEK/Carbon Composite for Aerospace Applications, Adv. Perform. Mater. 5 (1998) 83–96, https://doi.org/10.1023/A:1008638105370.
[14] K. Kozaczuk, Automated fiber placement systems overview, Trans. Inst. Aviat. 245 (2016) 52–59, https://doi.org/10.5604/05096669.1226355.
[15] Esguerra-Arce I., Martín M.I., Pérez-Pastor A., García-Martínez V. Evolution of crystallinity with multiple lamination steps in high performance thermoplastic composites by in-situ consolidation process. Twenty-Second Int Conf Compos Mater, 2019.
[16] T. Choupin, B. Fayolle, G. Régnier, C. Paris, J. Cinquin, B. Brulé, A more reliable DSC-based methodology to study crystallization kinetics: Application to poly(ether ketone ketone) (PEKK) copolymers, Polymer 155 (2018) 109–115, https://doi.org/10.1016/j.polymer.2018.08.060.
[17] K.C.H. Gardner, B.S. Hsiao, R.R. Matheson, B.A. Wood, Structure, crystallization and morphology of poly (aryl ether ketone ketone, Polymer 33 (1992) 2483–2495, https://doi.org/10.1016/0032-3861(92)91128-O.
[18] R.M. Ho, S.Z.D. Cheng, B.S. Hsiao, K.H. Gardner, Crystal morphology and phase identifications in poly(aryl ether ketone)s and their copolymers. 1. Polymorphism in PEKK, Macromolecules 27 (1994) 2136–2140, https://doi.org/10.1021/ma00086a023.
[19] I.Y. Chang, B.S. Hsiao, Thermal properties of high performance thermoplastic composites based on poly(ether ketone ketone) (PEKK), 36th Int SAMPE Symp. (1991) 1587–1601.
[20] H. Pérez-Martín, P. Mackenzie, A. Baidak, C.M. Ó Brádaigh, D. Ray, Crystallisation behaviour and morphological studies of PEKK and carbon fibre/PEKK composites, Compos Part Appl. Sci. Manuf. 159 (2022), 106992, https://doi.org/10.1016/j.compositesa.2022.106992.
[21] L. Jin, J. Ball, T. Bremner, H.-J. Sue, Crystallization behavior and morphological characterization of poly(ether ether ketone, Polymer 55 (2014) 5255–5265, https://doi.org/10.1016/j.polymer.2014.08.045.
[22] D.C. Bassett, R.H. Olley, I.A.M. Al Raheil, On crystallization phenomena in PEEK, Polymer 29 (1988) 1745–1754, https://doi.org/10.1016/0032-3861(88)90386-2.
[23] E. Bessard, O. De Almeida, G. Bernhart, Unified isothermal and non-isothermal modelling of neat PEEK crystallization, J. Therm. Anal. Calor. 115 (2014) 1669–1678, https://doi.org/10.1007/s10973-013-3308-8.
[24] D.J. Blundell, B.N. Osborn, The morphology of poly(aryl-ether-ether-ketone, Polymer 24 (1983) 953–958, https://doi.org/10.1016/0032-3861(83)90144-1.
[25] M.P. Lattimer, J.K. Hobbs, M.J. Hill, P.J. Barham, On the origin of the multiple endotherms in PEEK, Polymer 33 (1992) 3971–3973, https://doi.org/10.1016/0032-3861(92)90391-9.
[26] Y. Lee, R.S. Porter, J.S. Lin, On the double-melting behavior of poly(ether ether ketone, Macromolecules 22 (1989) 1756–1760, https://doi.org/10.1021/ma00194a043.
[27] B.S. Hsiao, I.Y. Chang, B.B. Sauer, Isothermal crystallization kinetics of poly(ether ketone ketone) and its carbon-fibre-reinforced composites, Polymer 32 (1991) 2799–2805, https://doi.org/10.1016/0032-3861(91)90111-U.
[28] S. Tencé-Girault, J. Quibel, A. Cherri, S. Roland, B. Fayolle, S. Bizet, et al., Quantitative Structural Study of Cold-Crystallized PEKK, ACS Appl. Polym. Mater. 3 (2021) 1795–1808, https://doi.org/10.1021/acsapm.0c01380.
[29] B.S. Hsiao, K.H. Gardner, S.Z.D. Cheng, Crystallization of poly(aryl ether ketone ketone) copolymers containing terephthalate/isophthalate moieties, J. Polym. Sci. Part B Polym. Phys. 32 (1994) 2585–2594, https://doi.org/10.1002/polb.1994.090321604.
[30] J. Seo, X. Zhang, R.P. Schaake, A.M. Rhoades, R.H. Colby, Dual Nakamura model for primary and secondary crystallization applied to nonisothermal crystallization of poly(ether ether ketone, Polym. Eng. Sci. 61 (2021) 2416–2426, https://doi.org/10.1002/pen.25767.
[31] S.-L. Gao, J.-K. Kim, Cooling rate influences in carbon fibre/PEEK composites. Part I. Crystallinity and interface adhesion, Compos Part Appl. Sci. Manuf. 31 (2000) 517–530, https://doi.org/10.1016/S1359-835X(00)00009-9.
[32] S. Saiello, J. Kenny, L. Nicolais, Interface morphology of carbon fibre/PEEK composites, J. Mater. Sci. 25 (1990) 3493–3496, https://doi.org/10.1007/BF00575375.
[33] Weiss R. Influence of production parameters on the mechanical behaviour of CF/PEEK. Dev. Sci. Technol. Compos. Mater., Stuttgart: 1990, p. 1007–12.
[34] Y. Lee, R.S. Porter, Crystallization of poly(etheretherketone) (PEEK) in carbon fiber composites, Polym. Eng. Sci. 26 (1986) 633–639, https://doi.org/10.1002/pen.760260909.
[35] V.-T. Hoang, B.-S. Kwon, J.-W. Sung, H.-S. Choe, S.-W. Oh, S.-M. Lee, et al., Postprocessing method-induced mechanical properties of carbon fiber-reinforced thermoplastic composites, J. Thermoplast. Compos Mater. 36 (2023) 432–447, https://doi.org/10.1177/0892705720945376.
[36] D.J. Blundell, R.A. Crick, B. Fife, J. Peacock, A. Keller, A. Waddon, Spherulitic morphology of the matrix of thermoplastic PEEK/carbon fibre aromatic polymer composites, J. Mater. Sci. 24 (1989) 2057–2064, https://doi.org/10.1007/BF02385421.
[37] M.A. Lamontia, M.B. Gruber, A. Systems, S. Drive, J. Tierney, J.W. Gillespie, Modeling the Accudyne Thermoplastic In Situ ATP Process, Proc. SAMPE Conf. (2009) 8.
[38] Schledjewski R., Miaris A. Thermoplastic tape placement by means of diode laser heating. vol. 54, 2009.
[39] Chen J., Yousefpour A., Hojjati M., Cai X., Hoa S. Automated fiber placement of thermoplastic composites—lessons learned, 2013.
[40] R.M. Ho, S.Z.D. Cheng, B.S. Hsiao, K.H. Gardner, Crystal morphology and phase identifications in poly(aryl ether ketone)s and their copolymers. 3. Polymorphism in a polymer containing alternated terephthalic acid and isophthalic acid isomers, Macromolecules 28 (1995) 1938–1945, https://doi.org/10.1021/ma00110a030.
[41] X. Tardif, B. Pignon, N. Boyard, J.W.P. Schmelzer, V. Sobotka, D. Delaunay, et al., Experimental study of crystallization of PolyEtherEtherKetone (PEEK) over a large temperature range using a nano-calorimeter, Polym. Test. 36 (2014) 10–19, https://doi.org/10.1016/j.polymertesting.2014.03.013.
[42] S. Risteska, A.T. Petkoska, S. Samak, M. Drienovsky, Annealing Effects on the Crystallinity of Carbon Fiber-Reinforced Polyetheretherketone and Polyohenylene Laminate Composites Manufactured by Laser Automatic Tape Placement, Mater. Sci. 26 (2020) 308–316, https://doi.org/10.5755/j01.ms.26.3.21489.
[43] A. Beehag, L. Ye, Influence of cooling rate on interlaminar fracture properties of unidirectional commingled CF/PEEK composites, Appl. Compos Mater. 2 (1995) 135–151, https://doi.org/10.1007/BF00567748.
[44] Gruber M.B., Lockwood I.Z., Dolan T.L., Funck S.B., Tierney J.J., Simacek P., et al. Thermoplastic in situ placement requires better impregnated tapes and tows. Int SAMPE Tech Conf, 2012.
[45] A. Deignan, W.F. Stanley, M. McCarthy, Insights into wide variations in carbon fibre/polyetheretherketone rheology data under automated tape placement processing conditions, J. Compos Mater. 52 (2018) 2213–2228, https://doi.org/10.1177/0021998317740733.
[46] D. Saenz-Castillo, M.I. Martín, S. Calvo, F. Rodríguez-Lence, A. Güemes, Effect of processing parameters and void content on mechanical properties and NDI of thermoplastic composites, Compos Part Appl. Sci. Manuf. (2019), https://doi.org/10.1016/j.compositesa.2019.03.035.
[47] G. Clancy, D. Peeters, V. Oliveri, D. Jones, R.M. O'Higgins, P.M. Weaver, A study of the influence of processing parameters on steering of carbon fibre/PEEK tapes using laser-assisted tape placement, Compos Part B Eng. 163 (2019) 243–251, https://doi.org/10.1016/j.compositesb.2018.11.033.

Materials & Design 234 (2023) 112359

Contents lists available at ScienceDirect

Materials & Design

journal homepage: www.elsevier.com/locate/matdes

Microstructural and micromechanical property characterisation of CF/PEKK composites using nanoindentation

Helena Pérez-Martín [a], Paul Mackenzie [b], Alex Baidak [b], Conchúr M. Ó Brádaigh [a], Dipa Ray [a,*]

[a] School of Engineering, Institute for Materials and Processes, The University of Edinburgh, Edinburgh, United Kingdom
[b] Hexcel Composites Ltd., Duxford, Cambridge, United Kingdom

ARTICLE INFO

Keywords:
CF/PEKK
Composite
Automated tape placement
Nanoindentation
Thermoplastic matrix
Interphase

ABSTRACT

The present work seeks to characterise the micromechanical properties of carbon fibre/poly(etherketoneketone) (CF/PEKK) composites with different crystallinity levels and morphologies. CF/PEKK laminates were manufactured under various compression-moulding and automated tape placement (ATP) conditions. Nanoindentation experiments were performed at different locations across the thickness of the laminates to evaluate hardness and elastic modulus at the micron scale. The polymer matrix of compression-moulded laminates, which was found to be fully crystallised, performed significantly better than the matrix of the ATP laminates. The central region of the ATP laminates performed slightly better than regions close to the top and bottom surfaces, likely due to a higher crystallisation development in the central area. A transition in response from the fibre to the matrix bulk was observed across all samples via nanoindentation testing. Overall, the study of micromechanical properties can provide insight into the impact of manufacturing conditions on the composite's performance at the macro scale, ultimately contributing towards higher-quality end products. To the authors' best knowledge, the in-depth work presented in this article is the first to use nanoindentation to characterise the effect of manufacturing processes on the micromechanical properties of CF/PEKK laminates.

1. Introduction

Poly(aryletherketones) (PAEKs) are a family of semicrystalline thermoplastics of high interest as a polymer matrix in composites, due to their suitability for high-performance applications. Poly(ether-etherketone) (PEEK), the most established of this polymer family, has been widely studied and is currently a popular option for advanced composites [1,2]. In recent years, poly(etherketoneketone) (PEKK) is also becoming an increasingly attractive choice due to the tuneability of the molecule's backbone chain, allowing control of material density, crystallisation rate and resulting properties [3–5]. Studies have characterised crystallisation kinetics of various grades of unreinforced PEKK and CF/PEKK [4–7], as well as the composite's mechanical performance when manufactured using various techniques [8].

In-situ manufacturing techniques are of interest as these are more energy and time efficient than other conventional processing methods, such as compression moulding and autoclaving. Automated tape placement (ATP) is one of such manufacturing methods, attractive due to its automation, part repeatability, potential as a single-step process and lower waste production. In-situ manufacturing processes such as ATP, however, can compromise part quality due to very short exposure times to heat and pressure, resulting in limited consolidation and non-uniform crystallinity development. Published studies on in-situ manufacturing of CF/PEEK demonstrate that ATP can achieve properties close to autoclave values [9–12], however, in the case of CF/PEKK, whose crystallisation kinetics are slower, this needs further research [13].

The fast nature of ATP manufacturing also leads to uncertainties in the crystallinity evolution when the part is manufactured, as the already laid material sees heat repasses as more material is laid on top. At the same time, the tool upon which the material is laid can act as a heat sink if kept unheated; whereas, if heated, can cause void rebound within the part being manufactured when held above glass transition temperature after roller pressure is lost [14–16]. It is therefore essential to understand how processing conditions affect the final part's performance.

Work has been done on tracking the evolution of heat transfer [10,17] and its modelling [18–21], as well as some investigations on how this impacts crystallinity development [17,21]. The generation of uniform crystallinity throughout the bulk of a manufactured part is a key requirement for reliable performance during the service life. This is

* Corresponding author at: 1.140 Sanderson Building, King's Buildings, Edinburgh EH9 3FB, Scotland, United Kingdom.
E-mail address: Dipa.Roy@ed.ac.uk (D. Ray).

https://doi.org/10.1016/j.matdes.2023.112359
Received 17 July 2023; Received in revised form 13 September 2023; Accepted 24 September 2023
Available online 25 September 2023
0264-1275/© 2023 The Authors. Published by Elsevier Ltd. This is an open access article under the CC BY license (http://creativecommons.org/licenses/by/4.0/).

quite challenging to achieve when a thermoplastic part is manufactured using ATP. The measurement of crystallinity across the thickness of laminates can provide insight into the effectiveness of the manufacturing method and potential areas of improvement during the manufacturing process. Differential scanning calorimetry (DSC) has been used by many researchers to evaluate crystallinity and morphology of ATP samples [8,9,11,12,14,17], however, DSC provides an average value of the entire sample being assessed. Lamontia and Gruber [22] assessed crystallinity variation of a CF/PEKK ATP laminate by milling different layers of a sample and then performing DSC, however, this is a quite laborious and time-intensive process. A different way of indirectly evaluating through-thickness crystallinity requiring less sample preparation is via micromechanical property characterisation with nanoindentation.

Nanoindentation is a technique that can be used to measure elastic modulus and hardness at micron and nano scales, which can thereby infer crystallinity. A method most commonly used in the field of metals and ceramics, it is increasingly used on a variety of polymers to test local properties [23–26]. Recent studies on unreinforced semicrystalline thermoplastics have shown that nanoindentation can be used to indirectly measure crystallinity of a sample by measuring their micromechanical properties. Christöfl et al. [25] successfully measured the variation in elastic modulus across an injection-moulded polyoxymethylene sample cross-section as a consequence of crystallinity and morphology variation. Indentations close to the sample surface displayed a lower elastic modulus than indentations in the bulk, due to top and bottom surfaces being in contact with injection-moulding tooling and cooling at a faster rate during manufacturing, therefore having a lower crystallinity. Similar behaviour has been observed in unreinforced PEEK [24,26,27], where a higher crystallinity resulted in increased hardness and elastic modulus values. A bimodal behaviour in fully crystallised PEEK was reported by Iqbal et al. [24], which was initially associated with the semicrystalline nature of the material. However, the indentation depths (6 μm) and reported spherulitic sizes of PEEK spherulites (10–20 μm) most likely provided the homogenised properties of the polymer rather than the two different phases, due to the resulting indentation being too large (a triangle with sides of about 30 μm [26]) to distinguish between the phases within a spherulitic structure. Voyiadjis et al. [26] suggested that this bimodal behaviour could therefore be due to surface inhomogeneities and studied the importance of surface finish in tough polymers (specifically PEEK) for nanoindentation to obtain consistent results. To the knowledge of the authors, no nanoindentation testing on unreinforced PEKK has been published.

The use of nanoindentation to characterise composite materials has risen since the 2000 s, with research characterising the reinforcement and matrix constituents of composites. The performance of the polymer matrix during nanoindentation experiments is influenced by the presence of fibres, particularly at large penetration depths [28], and polymer hardness and elastic modulus values are generally greater as a matrix in a composite than in neat form [29,30]. Nanoindentation has also been used to assess reinforcement-matrix interface and interphase properties. Interface generally refers to interfacial shear strength between fibre and matrix, where nanoindentation is used for fibre push-in testing; whereas interphase refers to a “third” transition phase between the fibre and matrix, tested via grid nanoindentation. Gibson [29] provides a review of work done on interfaces and interphases for a variety of polymer composites.

Nanoindentation has been used in the more recent years to characterise CF/PEEK ATP-manufactured laminates, some examples being as follows. Ray et al. [28] performed nanoindentation on CF/PEEK autoclaved and ATP laminates, corroborating previous findings that the presence of crystallinity results in a performance increase. Molazemhosseini et al. [31] studied PEEK-based composites with short CFs and nano-silica, successfully characterising fibre, matrix and interphase performance, as well as demonstrating an improvement in the performance of PEEK composites compared to its unreinforced form. Gain et al. [32] performed a study where the impact of consolidation force and hot gas torch temperature on the matrix and interphase properties were assessed, finding that increasing both parameters resulted in hardness and elastic modulus increases during nanoindentation testing. Additionally, nanoindentation has been used to evaluate the effect of ion irradiation on the micromechanical properties of unreinforced PEKK, [33] as well as its thermal degradation behaviour as a consequence of laser heating [34].

Nano-indentation research on CF/PEKK, on the other hand, is more limited, with no literature available on ATP-manufactured CF/PEKK composites. Gaillard and Amiot [35] performed nanoindentation testing on CF/PEKK prepreg tape in an attempt to observe and model the presence of an interphase with very low maximum loads of 60μN (and therefore very small indentations), achieving a very high spatial resolution. The matrix regions close to the fibre were found to be affected by the presence of the fibre, presenting a fibre-to-matrix modulus gradient ring around the fibre of approximately 800 nm thickness. It is important to keep in mind, however, that very small indentations (<50 nm depth) may produce unreliable results that are influenced by tip blunting or surface roughness [36]. Ramaswamy et al. [37] employed a nanoindenter to characterise fibre/matrix interfacial shear strength via fibre-pushout tests on autoclave-manufactured CF/PEKK laminates. Any further nanoindentation studies on crystallinity, the effects of varying parameters in a manufacturing process, or interphase characterisation of CF/PEKK have not been found by the authors of this work.

This work evaluates micromechanical properties of CF/PEKK laminates manufactured via compression moulding and ATP using nanoindentation, in order to indirectly measure crystallinity development and variation. DSC is initially used to assess the average crystallinity developed in each laminate as a consequence of the processing conditions. The impact of varying manufacturing parameters on the micromechanical properties is then studied via nanoindentation, as well as any variation in properties across the thickness of the ATP laminates. Additionally, the presence of any fibre/matrix property transition is evaluated.

2. Materials and methods

2.1. Materials

In this study, samples were manufactured with AS7 CF/PEKK unidirectional prepreg tape, provided by Hexcel Composites Ltd. The PEKK matrix was KEPSTAN PEKK 7002PT by Arkema. The tape for the compression-moulded laminates was 150 mm wide and had an average fibre volume fraction of 60.6 % (measured via acid digestion). The tape for the ATP laminates was 6.4 mm wide and had an average fibre volume fraction of 58.4 %. Both tapes had an average thickness of 0.2 mm.

2.2. Compression moulding manufacturing

Unidirectional compression-moulded laminates were manufactured using a 3-part mould (a 2 mm-thick frame with top and bottom plates). 10 sheets of prepreg tape were stacked and placed in the mould. A Pinette Emidecau Industries (PEI) LAB 450P hydraulic press was used, with a Frigosystem chiller providing the cooling.

A total of three laminates were manufactured with dimensions 300 mm × 150 mm × 2 mm, undergoing the following cycle:

1. Heat up from 20 °C to 370 °C at 10 °C/min.
2. Hold at 370 °C for 25 min.
3. Cool down from 370 °C to isothermal temperature (220 °C, 260 °C or 300 °C) at 10 °C/min.
4. Hold at isothermal temperature for 60 min.
5. Cool down from isothermal temperature to 20 °C at 10 °C/min.

The isothermal temperatures were selected based on a previous study on the crystallisation behaviour and morphology of PEKK and CF/PEKK composites [7]. The holding temperature in the melt of 370 °C is above the polymer's melting temperature (338 °C), and therefore ensures the removal of the matrix's thermal history. All laminates underwent a platen pressure of 1 bar during step 1, and 28 bar for the remaining steps.

A temperature–time plot of the above cycles is shown in Fig. 1. The laminate code denotes the processing condition ("CM" for compression moulding) and the isothermal hold temperature (220 °C, 260 °C or 300 °C).

2.3. Automated tape placement manufacturing

Unidirectional ATP laminates were manufactured using a laser-assisted tape placement head (AFPT, GmbH) attached to a robot arm (Kuka, KR240 L210-2). A total of 10 layers of prepreg tape were placed per laminate, with a laser repass performed on the final layer of each laminate. A diagram of the process and a summary of the ATP settings is shown in Fig. 2.

Three laminates with dimensions 300 mm × 150 mm × 2 mm were manufactured on a metallic tool, with a nip temperature (T_{nip}) of 380 °C, laydown speed of 2 or 4 m/min, roller pressure of 2 or 4 bar, and a laminate thickness of 2 mm.

Additionally, a multi-thickness laminate was manufactured on a ceramic tool, with a T_{nip} = 360 °C, lay-down speed of 4 mm/min, roller pressure of 2 bar. A section of this laminate was 2 mm thick (10 layers), and another 6 mm-thick (30 layers). A schematic of this laminate is shown in Fig. 3.

The laminate codes are given in Table 1. These denote the processing condition (ATP), T_{nip} (360 or 380 °C), lay-down speed (2 or 4 m/min) and roller pressure (2 or 4 bar). In the case of the 360 °C laminates, the code also includes the laminate thickness (2 or 6 mm). Comparisons of laminate properties and performance have been drawn across these three parameters in Section 3.

While recording the thermal history that the tape undergoes during lay-down was not possible during manufacturing, literature [17] has reported steep temperature drops during ATP manufacturing of CF/PEKK laminates on a cold tool, reaching cooling rates of 150–220 °C/min during the first seconds of cooling. These were observed to be higher on the first layers of prepreg tape laid on an unheated tool, likely due to the tool acting as a heat sink and the progressively larger amount of material between the tool and the incoming tape holding on to the heat produced by the ATP laser.

2.4. Differential scanning calorimetry (DSC)

Crystallinity measurements of the ATP samples with T_{nip} = 360 °C were carried out with a PerkinElmer DSC 8000. For the rest of the samples, this was done with a Mettler Toledo DSC 3+. In both instances, DSC scans from room temperature to 370 °C at 20 °C/min were run with non-hermetically sealed aluminium pans and lids under a nitrogen environment. Indium was used to calibrate the temperature and heat of fusion prior to any experiments. All samples weighed 8–20 mg. These were performed to evaluate the average crystallinity across the entire thickness of the manufactured laminates.

The crystallinity of a sample was calculated using:

$$\chi = \frac{\Delta H_m - \Delta H_{cc}}{\alpha \times \Delta H_{100\%}} \quad (1)$$

where ΔH_m is the melting enthalpy, ΔH_{cc} is the cold crystallisation enthalpy, α is the matrix weight fraction (31.7 % for the compression moulding tape and 34.5 % for the ATP tape, both measured via acid digestion) and $\Delta H_{100\%}$ is the theoretical melting enthalpy of 100 % crystalline PEKK. This has been calculated to be 130 J/g by Chang and Hsiao [38].

2.5. Nanoindentation

Samples measuring approximately 1 cm × 1 cm (2 mm thick) were cut out of the laminates with a hand saw and were mounted in epoxy resin, exposing the cross-section of the laminate. These were polished with silicon carbide discs of up to P2500, followed by diamond suspension polishing down to 1 μm particle size.

The nanoindentation tests were performed using a KLA iMicro Nanoindenter, with a diamond Berkovich-type indenter tip (ID: DC2/BERKOVICH/015). An initial calibration was performed with silica and glassy carbon to measure the frame stiffness and the area function of the tip.

Load-unload indentation cycles were performed using continuous stiffness measurement testing, at an indentation strain rate of 0.2 s^{-1}, a frequency of 110 Hz and frequency amplitude of 2 nm. Elastic modulus and hardness can be determined from the load–displacement curves obtained during testing, an example of which is shown in Fig. 4.

The contact stiffness S, which is the initial slope at the beginning of the unloading curve, can be expressed as defined by Pharr and Oliver

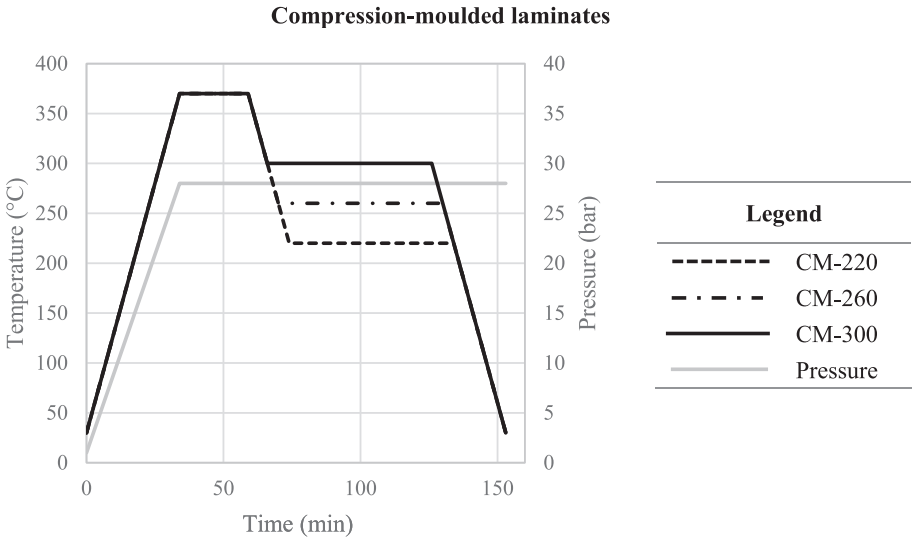

Fig. 1. Summary of processing parameters for the compression-moulded laminates.

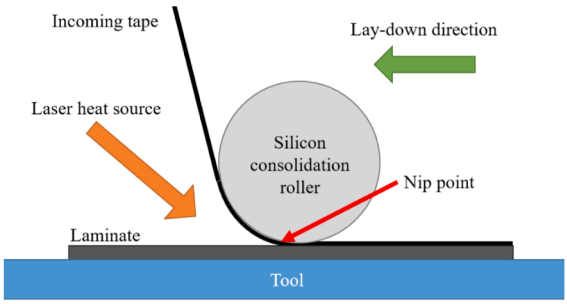

Cooler air pressure	1 bar
Incoming tape dimensions	6.4mm wide x 0.2mm thick
Laser-nip point optical distance	170mm
Laser power limit	1000W
Tape/laminate laser split	Approx. 50/50
Tool temperature	Unheated

Fig. 2. Schematic of ATP lay-up process and processing parameters.

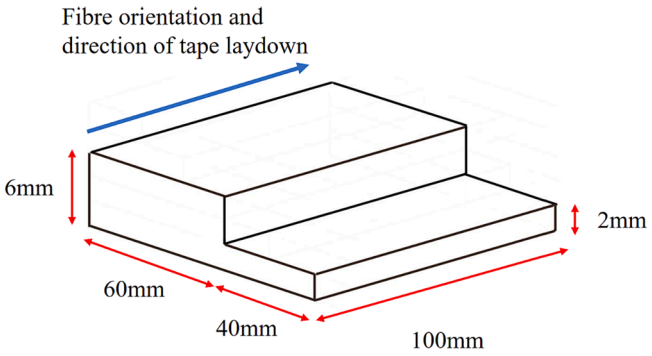

Fig. 3. Schematic of multi-thickness laminate, showing 2 mm and 6 mm thicknesses (not to scale).

Table 1
Summary of processing parameters for the ATP-manufactured laminates.

Laminate code	Tool material	Nip temperature (°C)	Lay-down speed (m/min)	Roller pressure (bar)	Laminate thickness (mm)
ATP-380-4-2	Mild steel	380	4	2	2
ATP-380-2-2	Mild steel	380	2	2	2
ATP-380-4-4	Mild steel	380	4	4	2
ATP-360-4-2-2 mm	Ceramic	360	4	4	2
ATP-360-4-2-6 mm	Ceramic	360	4	4	6

[39]:

$$S = \frac{2\beta}{\sqrt{\pi}} \times E_r \sqrt{A_c} \tag{2}$$

where E_r is the reduced elastic modulus and A_c is the indenter contact area (a function of the indenter depth in contact with the sample during testing). β is an indenter geometry constant introduced by Hay et al. [40] to account for different indenter tip geometries. E_r represents the elastic deformation that takes place in both the indenter and the sample, and is given by:

$$E_r = \left(\frac{1-\nu_i^2}{E_i} + \frac{1-\nu_s^2}{E_s} \right)^{-1} \tag{3}$$

where ν is Poisson's ratio, and the subscripts i and s denote the indenter and sample materials respectively. Assuming that $E_i \gg E_s$, the first term of Eq. (2) becomes negligible. Substituting Eq. (3) into Eq. (2) and rearranging,

$$E_s = \left(1-\nu_s^2\right) \times \frac{\sqrt{\pi}}{2\beta} \times \frac{S}{\sqrt{A_c}} \tag{4}$$

If the indenter is considered to be much stiffer than the sample, the sample hardness H can be defined by [41]:

$$H = \frac{P_{max}}{A_c} \tag{5}$$

where P_{max} is the maximum loading force achieved.

A 2 μm trial indentation in a matrix pocket, as shown in Fig. 5a, was performed to determine an adequate indentation depth. Fig. 5b shows that, above 1100 μm, there is a sharp increase in elastic modulus, indicating that fibres in the vicinity significantly influenced the matrix response at these depths. A lower depth is therefore preferable, in order to successfully evaluate the response of the composite's different constituents [29]. Based on this and previous work performed on CF/PEEK [26,28], a target indentation depth of 400 nm was chosen to take all elastic modulus and hardness values. In Fig. 5a, a 2 μm-deep indentation can be observed to be too large to do this in matrix areas closer to the fibre surface.

All samples were indented at locations marked with a square □ as shown in Fig. 6. At each location, a series of indentations were performed as given below:

- An array of nanoindentations to obtain hardness and elastic modulus values of the fibres and the matrix at different distances from the fibre surface, as shown with triangles Δ in Fig. 6;
- Two individual indents on matrix pockets to obtain matrix bulk properties, shown with stars ☆ in Fig. 6 (to ensure matrix bulk properties are characterised);
- Two individual indents on fibres to obtain fibre properties, as shown with crosses x in Fig. 6 (to ensure fibre properties are characterised).

A micrograph of an array and a matrix indent is shown in Fig. 8. The distance of the indentations to the closest fibre surface was measured using ImageJ software from the centre of the indentations to the surface of the nearest fibre edge.

The location and amount of nanoindentation arrays performed were chosen based on the expected crystallinity distribution across the thickness of the laminates. In the case of the compression-moulded laminates, crystallinity and morphology were assumed to be constant throughout the thickness due to the long holding times at crystallisation temperatures. Previous work done on these laminates [7] supported this assumption, showing homogeneous consolidation, high average crystallinity content and good mechanical performance. Therefore, a 5 × 5 array, two matrix indentations and two fibre indentations were performed at a single location (as shown in Fig. 6b) on compression-moulded samples, totalling 29 indentations per location □.

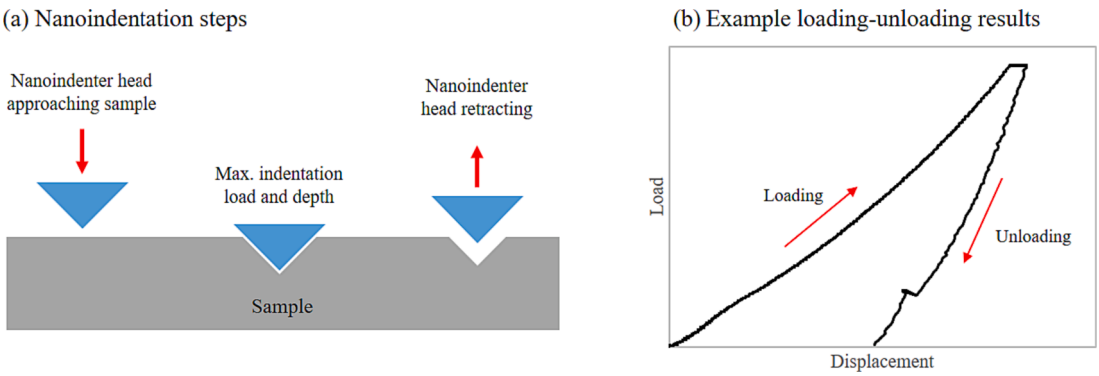

Fig. 4. (a) Nanoindentation loading and unloading schematic; and (b) sample load–displacement curve generated from a nanoindentation test.

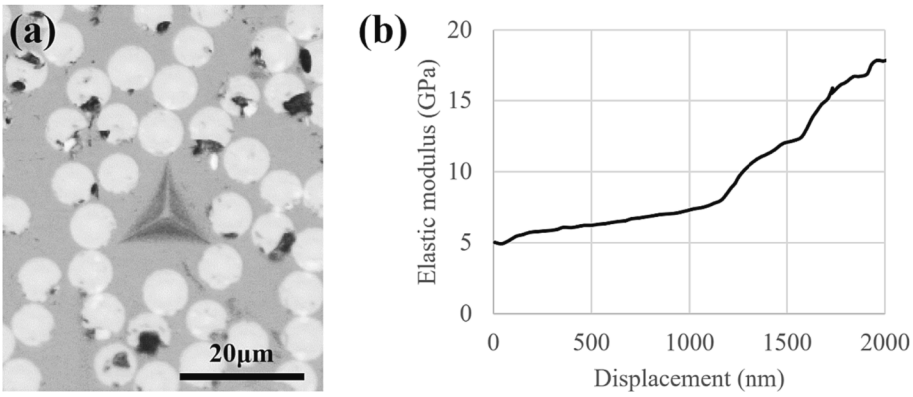

Fig. 5. (a) Micrograph of 2 µm depth indentation at a matrix pocket; and (b) elastic modulus-displacement plot of said indentation.

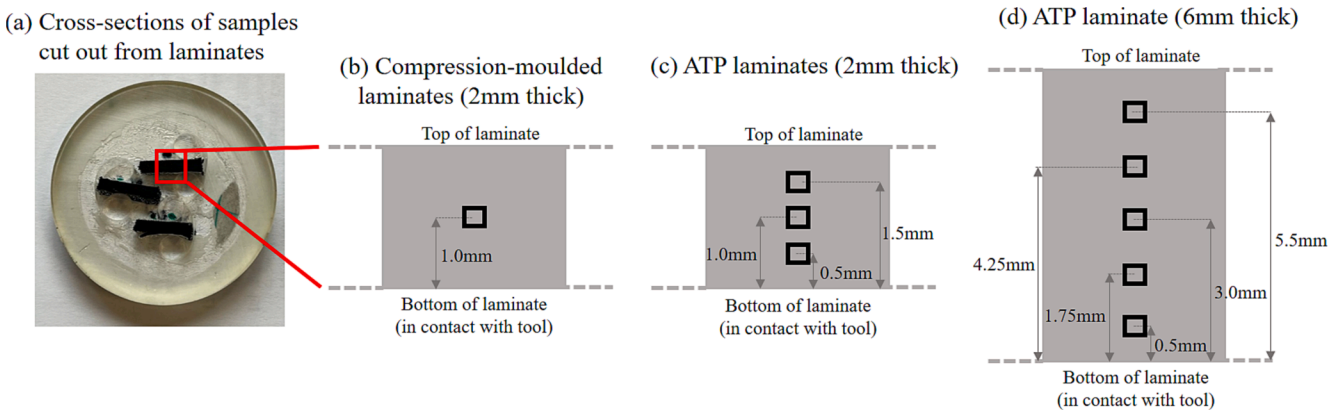

Fig. 6. Schematics of laminate cross-sections, showing the location of performed indentations with a square □.

On the other hand, the fast nature of ATP manufacturing is likely to result in a difference in crystallinity and morphology across the laminate thickness. This is supported by observations of poor laminate consolidation and low average crystallinity in our previous work [7], as well as a varying crystallinity content across the thickness of CF/PEEK and CF/PEKK ATP laminates as reported in literature [17,22]. Therefore, 3 × 5 arrays (plus two matrix and two fibre indentations) were performed at several locations across thicknesses of the ATP samples to assess this variation, resulting in 19 indentations per location □. For 2 mm-thick ATP laminates, 3 locations were tested (as shown in Fig. 6c); for the 6 mm-thick laminate, 5 locations were tested (as shown in Fig. 6d).

3. Results and discussion

3.1. Crystallinity content

Table 2 shows the total crystallinity achieved in the manufactured laminates. All compression-moulded laminates crystallised to the highest extent (~29 %), as expected due to the long holding times within crystallisation temperatures; whereas the ATP-manufactured laminates only achieved crystallinities up to 3–8 % overall. The marginally higher crystallinity of ATP-380-2-2 is likely due to the slower lay-down speed during manufacturing, keeping the material at temperatures which allow for crystallisation to take place for longer. Further discussion of the crystallinity content, morphology and DSC curves for the compression-moulded laminates and the ATP laminates with T_{nip} =

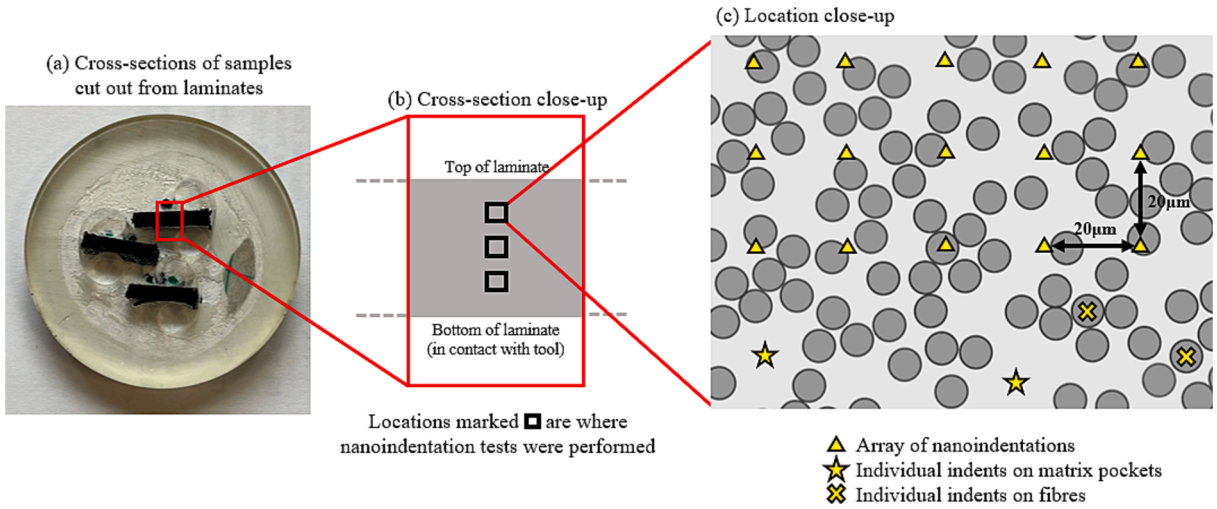

Fig. 7. Schematic example of an indentation array and fibre and matrix indents on an ATP sample. In this case, 19 indentations are being performed per location marked with a square □, with each of them giving hardness and elastic modulus data.

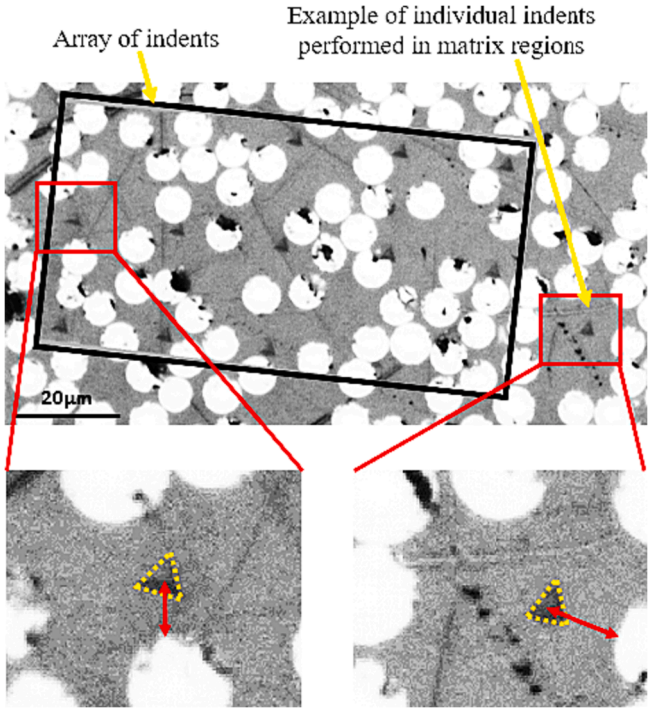

Fig. 8. A micrograph showing array and a matrix indent. A close-up of two indentations shows nanoindentation distances to the closest fibre surface marked with red arrows, measured using ImageJ. (For interpretation of the references to colour in this figure legend, the reader is referred to the web version of this article.)

380 °C can be found in our previous work [8], and a comprehensive study of crystallisation kinetics and modelling of the prepregs used in this work can be found in [7].

3.2. Nanoindentation

The following sections discuss the differences observed in load–displacement curves for compression-moulded and ATP laminates. This is followed by a brief explanation of the data processing procedure. Then matrix bulk properties are analysed and compared across different laminates and locations, as well as any variation in properties across the fibre/matrix interphase.

Table 2
Total crystallinity of CF/PEKK laminates manufactured under different processing conditions.

Laminate	Crystallinity (%)
CM-220	29.3 ± 1.4
CM-260	27.0 ± 1.0
CM-300	29.1 ± 1.3
ATP-380-4-2	6.8 ± 1.3
ATP-380-2-2	8.3 ± 1.0
ATP-380-4-4	6.0 ± 1.6
ATP-360-4-2-2 mm	3.4 ± 0.9
ATP-360-4-2-6 mm	4.6 ± 3.1

3.2.1. Load-displacement curves

Fig. 9a and b show load–displacement curves for all indentations done on sample CM-220 and the top location of ATP-380–4-2 respectively. These are provided as representative examples of the response of compression-moulded and ATP laminates, as this section draws a general comparison of the two manufacturing techniques, and not of the individual laminates. In these, as well as the rest of the nanoindentation results, three distinct responses can be observed, denoted as "fibre", "matrix" and "interphase" in Fig. 9. Note that results obtained by indentations marked with a star ☆ in Fig. 7 fall in the matrix response, and results obtained by indentations marked with a cross x fall in the fibre response. Indentations marked with a triangle Δ may fall within any of these three categories, depending on where the indentation is made (on the fibre, in the matrix bulk, or in the matrix closer to a fibre surface).

The fibre response is the stiffest among all regions, experiencing the largest elastic recovery compared to matrix and interphase responses. This is observed in existing nanoindentation work on CF/PEEK [31]. While the fibres in all samples are identical, a lower peak load response in the ATP sample of 17-20mN can be observed, against 20-25mN of the compression-moulded sample. This may be due to the fibre behaving as part of a composite during nanoindentation rather than in isolation. Due to the elastic response of the fibre, no permanent dents were left after nanoindentation testing – this is visible in the nanoindentation array in Fig. 8, where permanent dents on matrix regions are visible but those that fell on fibres are not. Because of this, the indentation distance from the centre of the fibre could not be measured.

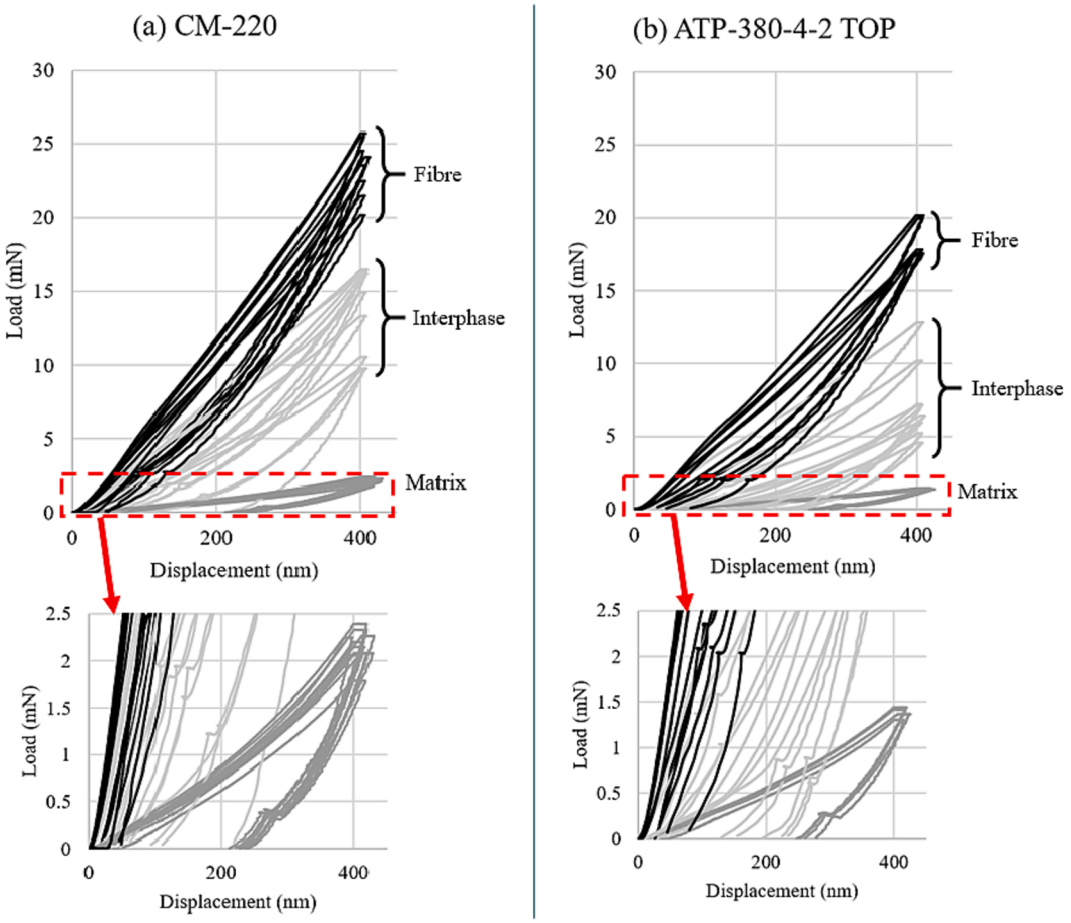

Fig. 9. Load-displacement results of nanoindentation experiments on (a) CM-220 and (b) the top location of ATP-380-4-2.

Matrix behaviour refers to the bulk response far away from any fibres, where performance remained similar across all load–displacement curves irrespective of the distance from fibre surfaces. An example location of this can be seen in Fig. 7 marked with stars ☆. A prominent hysteresis loop can be observed, related to the viscoelastic behaviour of PEKK. The compression-moulded sample withstood a higher load and experienced a smaller hysteresis loop. This is visible in the zoomed-in plots in Fig. 9a and b, where the indentation depth retained after the nanoindenter head is withdrawn ranges from 210 to 235 nm for the compression-moulded sample and 245–280 nm for the ATP sample (values read from the x-axes in Fig. 9). This can be attributed to the high crystallinity content in the compression-moulded samples resulting in a stiffer, more elastic response compared to that observed in the amorphous matrix of the ATP sample.

The interphase region refers to the response that does not match the fibre or matrix bulk response, but instead varies with the distance from the fibre surface at which the indentation was made. In the following section, it will be observed that nanoindentation tests closer to the fibre surface resulted in a stiffer response. The stiffer responses shown in Fig. 9 (higher loads at the same displacement) also possess smaller hysteresis loops, in line with the more elastic response as indentations are performed closer to fibre surfaces.

Similar observations have been made for a variety of polymers and polymer composites in literature. Molazemhosseini et al. [31] performed nanoindentation testing on short CF/PEEK samples (some reinforced with nano silica particles) and reported similar fibre/matrix/interphase responses as observed in this work. In their case, fibres exhibited perfect elastic response, likely due to the lower depth of indentations in all the testing (10–70 nm). Shen et al. [42] observed an increase in indentation resistance with a higher crystallinity content in unreinforced PA6, in a similar way to the stiffer performance of the more crystallised compression-moulded samples in this work. Klapperich et al. [23] tested a range of unreinforced PE grades with different molecular weights, and found those with lower crystallinity to exhibit a more pronounced hysteresis loop, and experience a significantly higher amount of deformation under the same load due to a more compliant response of the amorphous fraction in the sample.

3.2.2. *Hardness and elastic modulus against indentation distance from fibre surface: curve fitting*

The nanoindentation results for each location marked with a square □ in Fig. 6 provided hardness and elastic modulus data, which were plotted against the distance from the fibre surface at which each data point was taken. An example of this is given in Fig. 10, where hardness and elastic modulus results for the single location in laminate CM-260 are plotted. These results show a plateau far away from the fibre surface. For results analysis and comparative purposes, an exponential decay function was fitted to the results of each location. Examples of these are shown with the dotted curves in Fig. 10.

The exponential decay equation in question has the following form:

$$y = Aexp(-Bx) + C \tag{6}$$

where x is the distance from the fibre surface (μm), y is fibre hardness (or elastic modulus) (GPa), and A, B and C are constants. The number of constants to be found can be reduced by introducing the following boundary conditions:

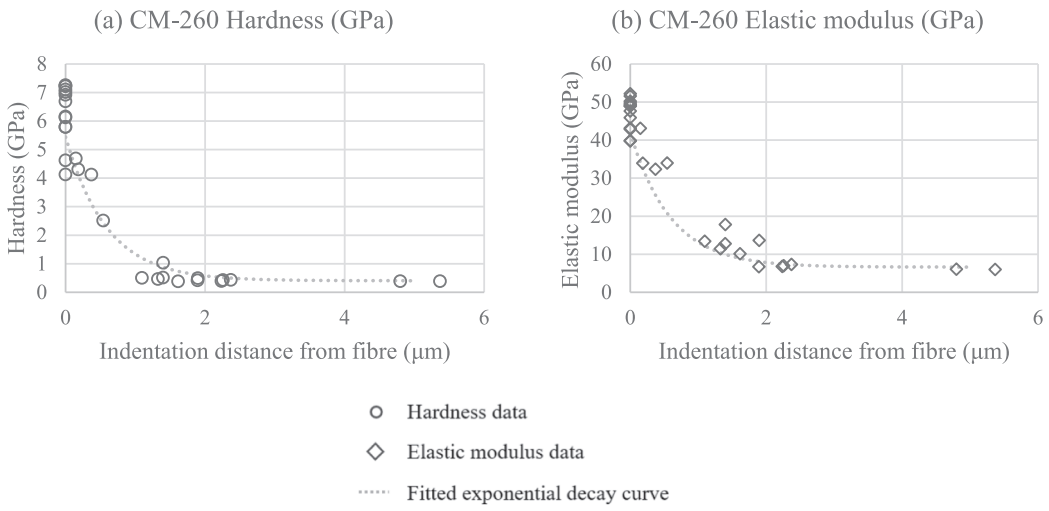

Fig. 10. (a) Hardness and (b) elastic modulus results against indentation distance from fibre surface for CM-260. The experimental data includes the nanoindentation array and individual indents performed on matrix pockets and fibres. The curves are fitted to the experimental data, and correspond to Eq. (9) and (10) for (a) and (b) respectively.

- When $x = 0$, $y = H_F$ (or M_F), the fibre hardness (or fibre elastic modulus). This value remains the same across all locations, as they all use the same fibre type. Substituting and rearranging:

$$y = Aexp(-Bx) + H_F - A \tag{7}$$

$$y = Aexp(-Bx) + M_F - A \tag{8}$$

- When $x = \infty$, $y = H_M$ (or M_M), the matrix hardness (or matrix elastic modulus). This value changes with each location, now that the processing conditions will affect the matrix morphology and crystallinity, and therefore its properties. This includes different locations within the same sample, as is the case with ATP samples. Substituting and rearranging:

$$y = (H_F - H_M)\exp(-B_H x) + H_M \tag{9}$$

$$y = (M_F - M_M)\exp(-B_M x) + M_M \tag{10}$$

Values for H_F and M_F were found by averaging the fibre indentation results across all locations, and were found to be $H_F = 5.44$ GPa and $M_F = 41.9$ GPa. Values for H_M and M_M are discussed in Section 3.2.3, and were found by averaging the matrix indentation results of each individual location after they stabilised into a plateau. For example, in Fig. 10a and b, this would be after $\times \approx 1.75$ μm and $\times \approx 2$ μm respectively.

A one-way ANOVA test was used to evaluate whether there was a significant difference in H_M and M_M results across the different tested locations (across the thickness of samples and across the same location of different samples), with a probability threshold value $\alpha = 0.05$. Whenever a significant difference is found, a one-way ANOVA test does not highlight which groups differ specifically. Therefore, when this happened, different result sets were tested together, and a T-test was performed whenever necessary to evaluate exactly which groups had a significant difference. This analysis can be found in the supplementary document.

Once these values were established, a MATLAB script was used to fit Eq. (9) and (10) to the raw data and find B_H (for hardness) and B_M (for elastic modulus) at each location □. These constants represent the gradient of the exponential decay function – the larger the value, the faster the transition from fibre to matrix hardness (or elastic modulus).

3.2.3. Matrix bulk properties (H_M and M_M)

In this section, a general comparison between compression-moulding and ATP results is drawn, followed by discussions within individual manufacturing processes (compression-moulded, ATP with T_{nip} 380 °C and ATP with T_{nip} 360 °C) addressed separately.

Note that ATP laminates with different nip temperatures are manufactured on different types of tools ($T_{nip} = 360$ °C on a ceramic tool and $T_{nip} = 380$ °C on a mild steel tool). This likely resulted in different cooling profiles in the laminates due to the different thermal conductivity of the tools. Therefore, results are not directly comparable.

Compression-moulded vs. ATP-380 laminates

The graphs in Fig. 11a and b show matrix bulk hardness and elastic modulus results for the compression-moulded laminates (single location tested as shown in Fig. 6b) and across the thickness of the ATP laminates with $T_{nip} = 380$ °C (3 locations tested as shown in Fig. 6c). These show that the compression-moulded laminates have significantly higher hardness (34–53 %) and elastic modulus (22–48 %) values than the ATP laminates (see supplementary document Section S.4). This is expected due to the extended holding times at crystallisation temperatures during manufacturing resulting in a crystalline matrix, whereas ATP laminates experienced fast-cooling, resulting in a softer, amorphous structure and lower hardness and elastic modulus responses.

Differences in compression-moulded laminates

Among the compression-moulded laminates, CM-260 performed marginally better (~9% higher hardness and 8–11 % higher elastic modulus), even though this difference was found not statistically significant (see supplementary document Section S.1). CM-220 and CM-300 performed similarly, as observed in Fig. 11. Previous work [7] performed on the same CF/PEKK prepreg tape showed that laminate CM-260 exhibited the fastest crystallisation rates. CM-220 and CM-300 possessed the smallest (~2 μm diameter) and largest (~6 μm) spherulites respectively (with CM-260 having intermediate-sized spherulites, ~4 μm). The faster crystallisation rates that CM-260 experienced might be an indication that these processing conditions are optimal for the polymer's most effective crystallisation, which has been reflected in its performance during nanoindentation testing.

On the other hand, mechanical properties of these samples reported in previous work (ILSS, 0° and 90° flexural [8]) did not show any significant effect of the spherulitic size. Tensile testing on other polymers with similar spherulite sizes (unreinforced PP-PE, 3–7 μm diameter) [43] reported similar findings. Polymers with larger variations in spherulitic diameter (1–30 μm), however, have shown a variation in mechanical performance (tensile and flexural), with unreinforced PA66 achieving a higher flexural modulus and yield point and a lower ultimate elongation with smaller spherulites [44]. Therefore, it might be

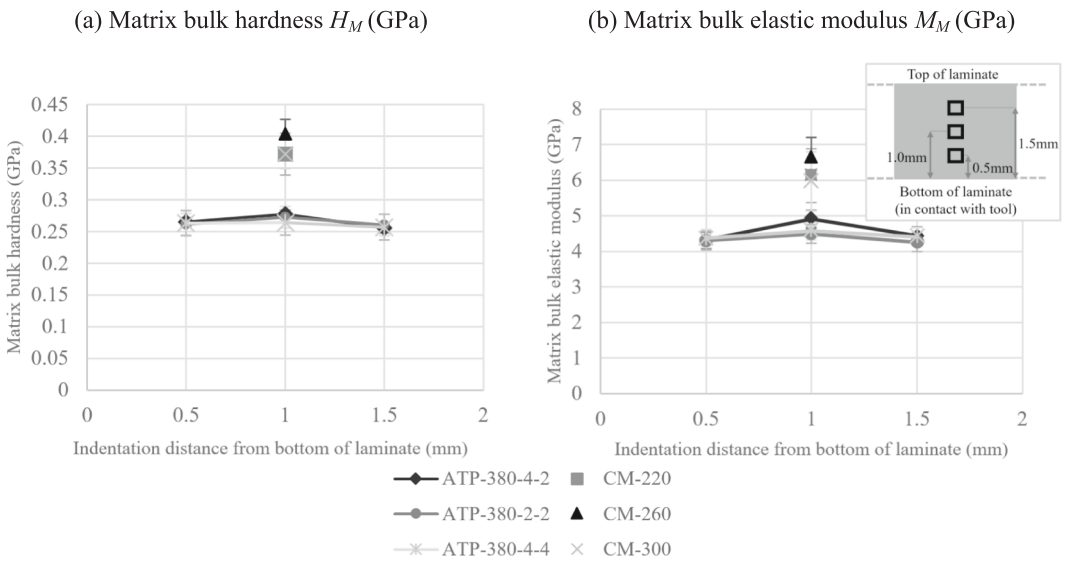

Fig. 11. (a) Matrix bulk hardness and (b) matrix bulk elastic modulus of all compression-moulded laminates and ATP laminates manufactured at $T_{nip} = 380$ °C. Top-right schematic shows the locations where the indentations were performed, measured from the bottom of the laminate (taken from Fig. 6).

possible that small variations in spherulite size may not have a significant impact on all mechanical properties at the macro scale, but their effects are more detectable at micron or nano-scale. The knowledge and understanding of such microstructures can improve the performance and failure at macroscopic level during the service life.

Differences in ATP-380 laminates (metal tool)

The results of all the ATP laminates (2 mm thick) shown in Fig. 11 follow a similar trend: a peak in properties in the middle of the laminate compared to the tested locations close to the bottom (tool side) and top surfaces. Percentage differences between the performance of the middle location and the top/bottom locations in the ATP laminates are as follows:

- ATP-380–4-2: 5–9 % hardness increase, 11–14 % elastic modulus increase.
- ATP-380–2-2: ~5% hardness increase, 4–5 % elastic modulus increase.
- ATP-380–4-4: 0–3 % hardness increase, 4–5 % elastic modulus increase.

This is likely due to the presence of two competing mechanisms during ATP manufacturing that influence crystallinity and mechanical properties:

- Proximity to the metal tool: the tool surface acts as a heat sink, contributing towards the fast cooling of the prepreg tape laid on it. As more layers of the laminate are laid, there is more material between the new prepreg layers and the tool. This can result in better heat retention and a reduction in the cooling speed, which contributes to crystallinity development. This has been observed for CF/PEEK [17], where prepreg layer crystallinity was found to be higher the further away the layer was from the bottom of the laminate (which was in contact with the tool surface), eventually plateauing to the maximum achievable crystallinity given the heat retention capability of the material and the ATP parameters. Ref. [17] also showed similar results on CF/PEKK, however, due to slower crystallisation kinetics, maximum achievable crystallinity was reached at a higher number of layers. The contribution of the proximity to the tool to crystallinity development is represented in Fig. 12 with a grey line, which resembles the results reported in [17] for the crystallinity evolution for every added layer.
- Heat repasses: as the prepreg layers are laid, the incoming heat diffuses into the layers that are already in place. This causes annealing of the polymer, which contributes towards enhanced crystallisation. The lower layers of the laminate undergo more of these repasses than the top layers. The through-thickness temperature profile of ATP-manufactured CF/PEEK laminates has been validated via

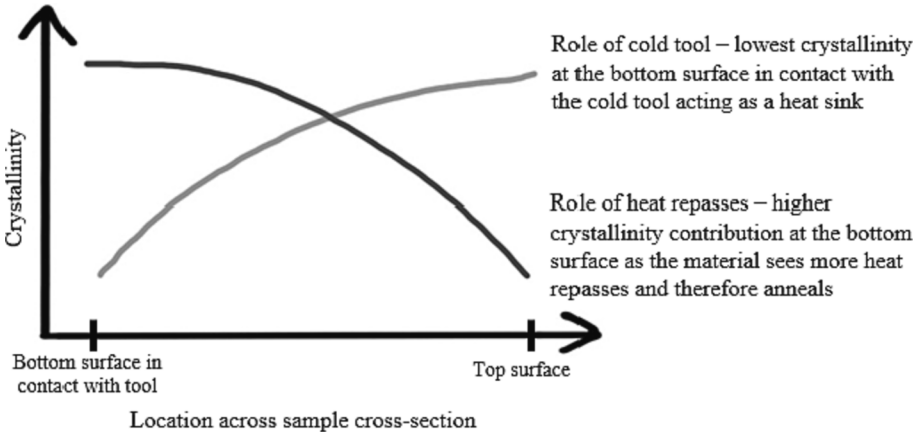

Fig. 12. Schematic of contribution to crystallinity development of the ATP unheated tool acting as a heat sink and the heat repasses seen by a layer of material as more layers are placed on top.

thermocouples during manufacturing [15,18,19] and modelled [15,18,20] in literature. The published literature shows that already laid material is repeatedly heated as more layers are placed. The contribution of heat repasses to crystallinity development is represented in Fig. 12 with a black line.

The optimal combination of these two competing mechanisms for the highest achievable crystallinity development may be reached around the middle layers of the laminate. The contribution of each mechanism is likely to change along with manufacturing parameters and the type of tool.

The difference in hardness and elastic modulus between ATP-380-4-2, ATP-380-2-2 and ATP-380-4-4 at the top and bottom locations is negligible and showed no statistically significant differences (see supplementary document Section S.2). This is likely due to the proximity to the tool on the bottom surface and the low number of (if any) repasses experienced by the top surface, where any variation in manufacturing parameters likely had a negligible effect on performance. It is therefore hypothesised that the fast-cooling and/or minimal annealing resulted in lower crystallinity compared to the middle location.

The middle location of the ATP-380-4-2 sample displayed a slightly higher hardness and elastic modulus than in the other two laminates, (2–5 % increase in hardness and 7–10 % in elastic modulus). The difference in elastic modulus particularly was statistically significant (supplementary document Section S.2).

Differences in ATP-360 laminates (ceramic tool)

The plots in Fig. 13 show matrix hardness and elastic modulus results for the compression-moulded laminates (single location tested as shown in Fig. 6b) and across the thickness of the 2 mm and 6 mm laminates with $T_{nip} = 360$ °C (3 locations tested as shown in Fig. 6c). The difference in performance between the compression-moulded laminates and the ATP-360 laminates (42–56 % hardness and 38–49 % elastic modulus) is similar to the ATP-380 laminates, for the same reasons as previously discussed, and is also statistically significant (see supplementary document Section S.5). Both ATP-360 laminates also displayed the same behaviour as the ATP-380 laminates, where the middle location of the laminates performed better than the top/bottom locations, with percentage differences as follows:

- 2 mm-thick laminate: 9–11 % hardness increase, 1–3 % elastic modulus increase.
- 6 mm thick laminate: 5–7 % hardness increase, 3–12 % elastic modulus increase.

This might be due to the central location having a higher crystallinity than the other tested locations, as described for the ATP-380 laminates. These differences were not statistically different (see supplementary document Section S.3).

3.2.4. Fibre/matrix interphase

As observed in Section 3.2.1, there is a fibre/matrix property transition in samples, whose response varies with the distance from the fibre surface. Section 3.2.2 introduced Eq. (9) and (10) to model this transition where B_H and B_M control the gradient of the fitted curves for hardness and elastic modulus data respectively. This section comments on any observed variations on these gradients across all compression-moulded laminates, as well as middle locations of ATP-380-4-2 and ATP-360-4-2-2 mm as representative ATP laminates to compare with the compression-moulding results.

Compression-moulded laminates

Table 3 provides B_H and B_M values and their 95 % confidence intervals for the compression-moulded laminates as calculated in

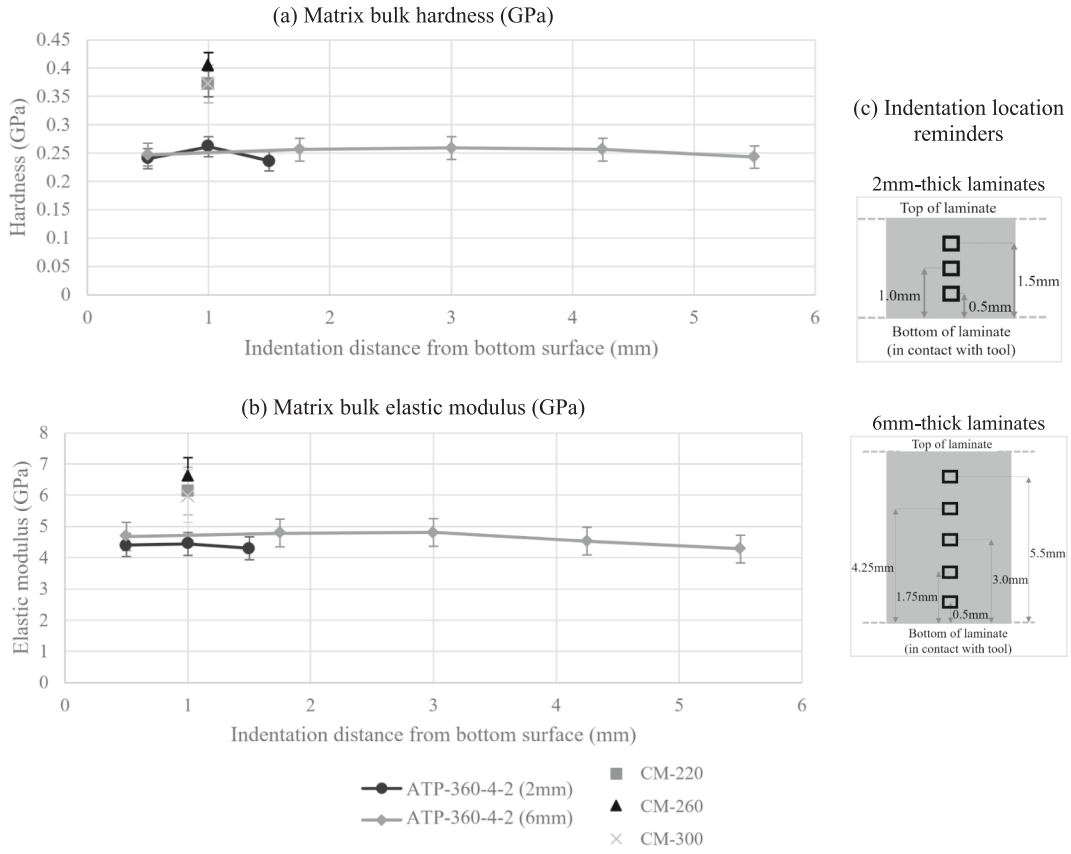

Fig. 13. (a) Matrix bulk hardness and (b) matrix bulk elastic modulus of all compression-moulded laminates and ATP laminates manufactured at $T_{nip} = 360$ °C. Schematics in (c) show the locations where the indentations were performed, measured from the bottom of the laminate (taken from Fig. 6).

Table 3
Summary of B_H and B_M values and 95% confidence intervals for the exponential decay modelling of compression-moulded CF/PEKK samples.

Laminate code	CM-220		CM-260		CM-300	
	Value	95 % confidence interval	Value	95 % confidence interval	Value	95 % confidence interval
B_H (Hardness)	1.918	±0.394	1.687	±0.344	1.924	±0.723
B_M (Elastic modulus)	1.421	±0.286	1.200	±0.197	1.411	±0.374

MATLAB. Fig. 14 shows the fitted exponential decay curves with the confidence intervals applied to the curves with shaded regions.

While gradient differences are subtle and all confidence intervals overlap with the plotted curves, these show that CM-260 is the laminate with the lowest B_H and B_M (the softest gradients), implying that this sample might have a slightly larger interphase than the other compression-moulded samples. This phenomenon could be explained with general polymeric nucleation theory, along with previous observations made on spherulite sizes of CF/PEKK at the temperatures used for compression moulding in this work. Fig. 15 has been included to aid with the explanation that follows.

- At lower crystallisation temperatures (the holding isothermal temperature at which the material is allowed to crystallise), primary nucleation dominates and there is minimal secondary nucleation. This means there will be a higher number of small spherulites, as shown in Fig. 15a. This is likely to also contribute towards the establishment of crystal nuclei (primary nucleation) on the fibre surface, but crystal growth as a consequence of secondary nucleation will be minimal. This might also result in a transcrystalline region at the fibre/matrix interface where any lamellar growth from the fibre is potentially very short and perpendicular to the fibre surface. This is likely the case for CM-220, as reported in our previous work [7] where SEM imaging of cryofractured CF/PEKK prepreg samples isothermally crystallised at 220 °C showed the formation of small spherulites, with some growth perpendicular to the fibre surface.
- At higher crystallisation temperatures, on the other hand, secondary nucleation dominates, resulting in a lower number of spherulites, but larger in size, as shown in Fig. 15c. This results in minimal primary nucleation taking place at the fibre surface, and so any crystals growing from the fibre surface will likely resemble spherulites from the bulk. It is therefore unlikely for there to be a significant interphase present. This is likely to be the case for CM-300, also shown in our previous work [7], where large spherulitic structures were observed on CF/PEKK samples isothermally crystallised at 300 °C.
- At the mid-range of crystallisation temperatures, however, there is a balance of both nucleation mechanisms, resulting in medium-sized spherulites. This might also allow for some primary nucleation to take place at the fibre surfaces but also for these nucleation sites to undergo secondary nucleation and develop a crystal structure/transcrystalline interphase between the fibre and the matrix. This is shown in Fig. 15b, and is likely representative of CM-260. CF/PEKK prepreg tape isothermally crystallised at 260 °C was observed to develop spherulites of intermediate size and perpendicular crystal growth from fibre surfaces, as reported in our previous work [7].

Compression-moulded vs. ATP laminates

Table 4 provides B_H and B_M values and their 95 % confidence intervals for CM-260, ATP-380-4-2 and ATP-360-4-2-2 mm as example laminates that underwent compression moulding, ATP with T_{nip} = 380 °C (with a metallic tool) and T_{nip} = 360 °C (with a ceramic tool). Fig. 16 shows the fitted exponential decay curves for each of these laminates, with their corresponding 95 % confidence intervals indicated by the shaded regions. CM-260 properties can be observed to plateau at a slightly higher value than the ATP laminates. This is due to the higher matrix bulk properties that compression-moulded samples possess, as discussed in Section 3.2.3.

In the case of the ATP laminates, the fast nature of the manufacturing is not ideal for developing a crystalline structure, as determined by the DSC results in Table 2. This is also the case for any fibre–matrix interphase formation. Even in the event of polymer melting during heating, the cooling rates that the material undergoes are too fast for any significant crystallinity to form in this grade of CF/PEKK [7]. Any further

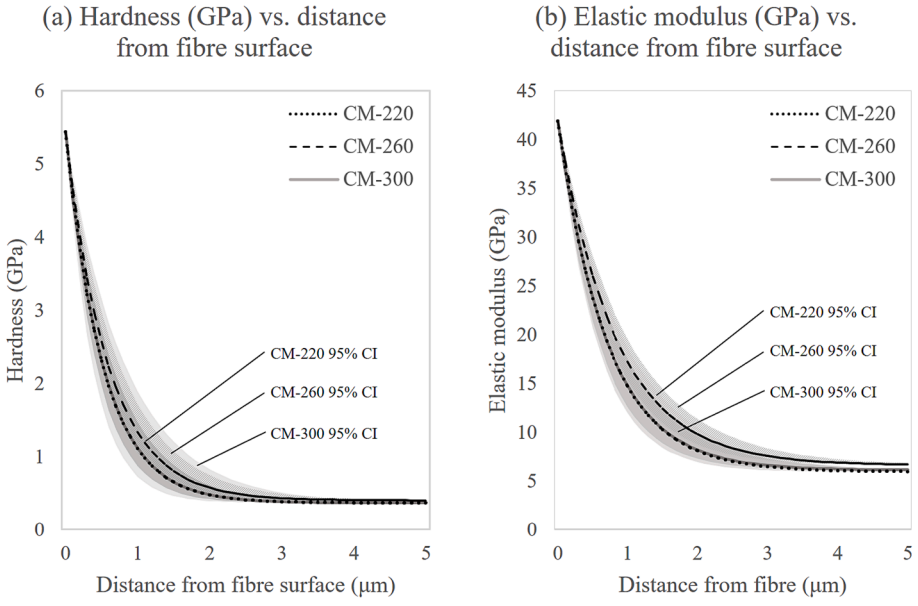

Fig. 14. (a) Hardness and (b) elastic modulus exponential decay curve fittings to nanoindentation test results of compression moulded samples, with 95% confidence intervals shown by the shaded regions. Note that the curves for CM-220 and CM-300 overlap in both plots.

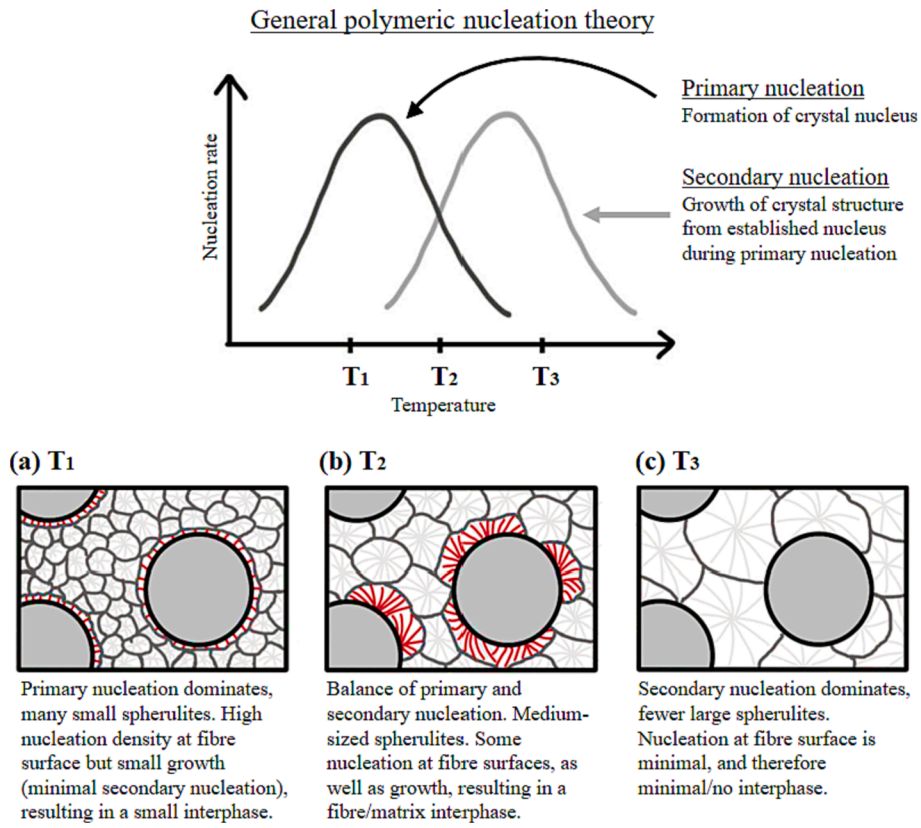

Fig. 15. Schematic demonstrating the effect of temperature on crystal growth in CF/PEKK, based on general polymeric nucleation theory, where $T_1 < T_2 < T_3$.

Table 4
Summary of B_H and B_M values and 95 % confidence intervals for the exponential decay modelling of CM-260, ATP-380-4-2 and ATP-360-4-2–2 mm.

Laminate code	CM-260		ATP-380–4-2 (MID)		ATP-360-4-2-2 mm (MID)	
	Value	95 % confidence interval	Value	95 % confidence interval	Value	95 % confidence interval
B_H (Hardness)	1.687	±0.344	3.816	±0.592	3.096	±0.885
B_M (Elastic modulus)	1.200	±0.197	1.687	±0.191	0.985	±0.211

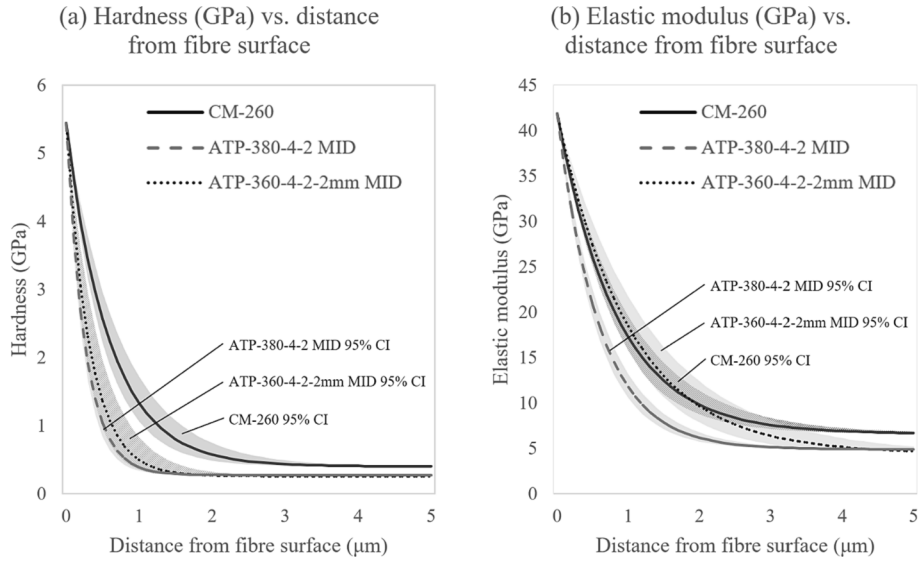

Fig. 16. (a) Hardness and (b) elastic modulus exponential decay curve fittings to nanoindentation test results of CM-260, ATP-380-4-2 and ATP-360-4-2-2 mm, with confidence intervals shown by the shaded regions.

crystallinity content developed during heat repasses is likely to take place at a smaller scale in the matrix bulk rather than at the interphase, due to molecular movement being considerably more restricted during annealing than during melt crystallisation. Therefore, any major rearrangement forming an interphase is unlikely.

The effect of overall crystallinity achieved is clearly reflected in the hardness results shown in Fig. 16a. Hardness is dictated by the load applied as per Eq. (4), and is more influenced by surface properties. Both ATP laminates possess a similar hardness response in the fibre/matrix transition region, whereas the compression-moulded laminate (with much higher crystallinity) shows a distinctly longer transition from fibre to matrix properties. This behaviour is not as obvious in Fig. 16b, where CM-260 and ATP-360-4-2-2 mm follow a similar transition path for the first micron from the fibre surface, after which CM-260 plateaus first to a higher value. The elastic modulus is influenced by the stiffness of the sample, as shown in Eq. (3), which is more interlinked with matrix bulk properties rather than surface properties as is the case of hardness. The marginally enhanced fibre–matrix transition behaviour in ATP-360 laminate might be attributed to the enhanced heat retention with the ceramic tool.

4. Conclusions

In this work, a series of CF/PEKK laminates were manufactured under a variety of compression-moulding and ATP conditions. DSC was carried out with each laminate in order to determine the crystallinity level achieved in each case. Nanoindentation experiments were performed that measured the hardness and elastic modulus of the samples reflecting their microstructural differences. A significant difference was observed in the performance of the matrix bulk across the different manufacturing techniques and conditions. A distinct variation in properties of the matrix bulk across the thickness of the ATP laminates was evident, for both 2 mm and 6 mm thickness, showing the presence of a crystallinity gradient. The presence of a fibre–matrix interphase and its variation under different processing conditions was also observed.

The matrix bulk of the compression-moulded laminates performed better than that of the ATP laminates by 34–53 % in hardness and 22–48 % in elastic modulus. This is expected, due to the higher crystallinity content of the compression-moulded laminates as a consequence of the longer holding times at crystallisation temperatures. CM-260, which had been observed to possess the fastest crystallisation rates in our previous work [7], performed the best among all the compression-moulded laminates by 9 % in hardness and 8–11 % in elastic modulus.

Variation in hardness and elastic modulus across the thickness of the ATP laminates was observed, with these properties being the highest in the middle of the laminate in all instances. This was likely due to the central region of the laminate cross-section achieving higher crystallinity, due to a combined effect of heat repasses from the added layers of material on top, and heat retention of the already laid material, allowing this middle section to hold heat for longer undergoing annealing.

Declaration of Competing Interest

The authors declare that they have no known competing financial interests or personal relationships that could have appeared to influence the work reported in this paper.

Data availability

Data will be made available on request.

Acknowledgements

The authors acknowledge the financial support received from the National Manufacturing Institute for Scotland (NMIS-IDP/009) and Hexcel Composites Limited.

The authors also wish to acknowledge the support of the Henry Royce Institute for Ms Helena Pérez-Martín through the Royce PhD Equipment Access Scheme, enabling access to nanoindentation facilities at the Materials Research Facility (UK Atomic Energy Authority).

Appendix A. Supplementary data

Supplementary data to this article can be found online at https://doi.org/10.1016/j.matdes.2023.112359.

References

[1] F. Rodríguez-Lence, M. Zuazo, S. Calvo, In-situ consolidation of PEEK composites by automated placement technologies, 20th Int. Conf. Compos. Mater. (2015) 19–24.
[2] J.P. Kilroy, C.M. Ó Brádaigh, C.O.A. Semprimoschnig, Mechanical and physical evaluation of a new carbon fibre/PEEK composite system for space applications, SAMPE J. (2008) 1–12.
[3] H. Pérez-Martín, P. Mackenzie, A. Baidak, C.M. Ó Brádaigh, D. Ray, Crystallinity studies of PEKK and carbon fibre/PEKK composites: A review, Compos. B Eng. 223 (2021) 109127.
[4] L. Quiroga Cortés, N. Caussé, E. Dantras, A. Lonjon, C. Lacabanne, Morphology and dynamical mechanical properties of poly ether ketone ketone (PEKK) with meta phenyl links, J. Appl. Polym. Sci. 133 (2016) 1–10, https://doi.org/10.1002/app.43396.
[5] T. Choupin, B. Fayolle, G. Régnier, C. Paris, J. Cinquin, B. Brulé, Isothermal crystallization kinetic modeling of poly(etherketoneketone) (PEKK) copolymer, Polymer 111 (2017) 73–82, https://doi.org/10.1016/j.polymer.2017.01.033.
[6] T. Choupin, B. Fayolle, G. Régnier, C. Paris, J. Cinquin, B. Brulé, A more reliable DSC-based methodology to study crystallization kinetics: application to poly(ether ketone ketone) (PEKK) copolymers, Polymer 155 (2018) 109–115, https://doi.org/10.1016/j.polymer.2018.08.060.
[7] H. Pérez-Martín, P. Mackenzie, A. Baidak, C.M. Ó Brádaigh, D. Ray, Crystallisation behaviour and morphological studies of PEKK and carbon fibre/PEKK composites, Compos. Part Appl. Sci. Manuf. 159 (2022) 106992.
[8] H. Pérez-Martín, S. Buchalik-Bopp, B.E. Guettler, P. Mackenzie, A. Baidak, C.M. Ó Brádaigh, et al., Effect of crystallinity and morphology on the mechanical properties of CF/PEKK composites manufactured under compression moulding and Automated Tape Placement, Mater. Today Commun. 36 (2023), https://doi.org/10.1016/j.mtcomm.2023.106442.
[9] S. Risteska, A.T. Petkoska, S. Samak, M. Drienovsky, Annealing effects on the crystallinity of carbon fiber-reinforced polyetheretherketone and polyohenylene laminate composites manufactured by laser automatic tape placement, Mater. Sci. 26 (2020) 308–316, https://doi.org/10.5755/j01.ms.26.3.21489.
[10] C.M. Stokes-Griffin, P. Compston, The effect of processing temperature and placement rate on the short beam strength of carbon fibre-PEEK manufactured using a laser tape placement process, Compos. Part Appl. Sci. Manuf. 78 (2015) 274–283, https://doi.org/10.1016/j.compositesa.2015.08.008.
[11] D. Saenz-Castillo, M.I. Martín, S. Calvo, F. Rodriguez-Lence, A. Güemes, Effect of processing parameters and void content on mechanical properties and NDI of thermoplastic composites, Compos. Part Appl. Sci. Manuf. 121 (2019) 308–320.
[12] A. Chanteli, A.K. Bandaru, D. Peeters, R.M. O'Higgins, P.M. Weaver, Influence of repass treatment on carbon fibre-reinforced PEEK composites manufactured using laser-assisted automatic tape placement, Compos. Struct. 248 (2020), 112539, https://doi.org/10.1016/j.compstruct.2020.112539.
[13] V.-T. Hoang, B.-S. Kwon, J.-W. Sung, H.-S. Choe, S.-W. Oh, S.-M. Lee, J.-H. Kweon, Y.-W. Nam, Postprocessing method-induced mechanical properties of carbon fiber-reinforced thermoplastic composites, J. Thermoplast. Compos. Mater. 36 (1) (2023) 432–447.
[14] A.J. Comer, D. Ray, W.O. Obande, D. Jones, J. Lyons, I. Rosca, R.M. O' Higgins, M. A. McCarthy, Mechanical characterisation of carbon fibre–PEEK manufactured by laser-assisted automated-tape-placement and autoclave, Compos. Part Appl. Sci. Manuf. 69 (2015) 10–20.
[15] M.B. Gruber, I.Z. Lockwood, T.L. Dolan, S.B. Funck, J.J. Tierney, P. Simacek, et al., Thermoplastic in situ placement requires better impregnated tapes and tows, Int. SAMPE Tech. Conf. (2012).
[16] G. Clancy, D. Peeters, V. Oliveri, D. Jones, R.M. O'Higgins, P.M. Weaver, A study of the influence of processing parameters on steering of carbon fibre/PEEK tapes using laser-assisted tape placement, Compos. B Eng. 163 (2019) 243–251, https://doi.org/10.1016/j.compositesb.2018.11.033.
[17] I. Esguerra-Arce, M.I. Martín, A. Pérez-Pastor, V. García-Martínez, Evolution of crystallinity with multiple lamination steps in high performance thermoplastic composites by in-situ consolidation process, Twenty-Second Int. Conf. Compos. Mater. (2019).
[18] A. Kollmannsberger, R. Lichtinger, F. Hohenester, C. Ebel, K. Drechsler, Numerical analysis of the temperature profile during the laser-assisted automated fiber placement of CFRP tapes with thermoplastic matrix, J. Thermoplast. Compos. Mater. 31 (2018) 1563–1586, https://doi.org/10.1177/0892705717738304.
[19] Lamontia MA, Gruber MB, Systems A, Drive S, Tierney J, Gillespie JW. Modeling the Accudyne Thermoplastic In Situ ATP Process. Proc SAMPE Conf 2009:8.

[20] J. Tierney, J.W. Gillespie, Modeling of heat transfer and void dynamics for the thermoplastic composite tow-placement process, J. Compos. Mater. 37 (19) (2003) 1745–1768.
[21] J.J. Tierney, J.W. Gillespie, Crystallization kinetics behavior of PEEK based composites exposed to high heating and cooling rates, Compos. Part Appl. Sci. Manuf. 35 (2004) 547–558, https://doi.org/10.1016/j.compositesa.2003.12.004.
[22] M.A. Lamontia, M.B. Gruber, Limitations on mechanical properties in thermoplastic laminates fabricated by two processes: automated thermoplastic tape placement and filament winding, SAMPE Eur. Conf. Exhib. (2005).
[23] C. Klapperich, K. Komvopoulos, L. Pruitt, Nanomechanical properties of polymers determined from nanoindentation experiments, J. Tribol. 123 (2000) 624–631, https://doi.org/10.1115/1.1330736.
[24] T. Iqbal, B.J. Briscoe, S. Yasin, P.F. Luckham, Nanoindentation response of poly (ether ether ketone) surfaces-A semicrystalline bimodal behavior, J. Appl. Polym. Sci. (2013), https://doi.org/10.1002/app.39723.
[25] P. Christöfl, C. Czibula, T. Seidlhofer, M. Berer, A. Macher, E. Helfer, T. Schrank, G. Oreski, C. Teichert, G. Pinter, Morphological characterization of semi-crystalline POM using nanoindentation, Int. J. Polym. Anal. Charact. 26 (8) (2021) 692–706.
[26] G.Z. Voyiadjis, A. Samadi-Dooki, L. Malekmotiei, Nanoindentation of high performance semicrystalline polymers: A case study on PEEK, Polym. Test. 61 (2017) 57–64, https://doi.org/10.1016/j.polymertesting.2017.05.005.
[27] B.R. Murray, A. Doyle, P.J. Feerick, C.O.A. Semprimoschnig, S.B. Leen, C.M. Ó Brádaigh, Rotational moulding of PEEK polymer liners with carbon fibre/PEEK over tape-placement for space cryogenic fuel tanks, Mater. Des. 132 (2017) 567–581, https://doi.org/10.1016/j.matdes.2017.07.026.
[28] D. Ray, A.J. Comer, J. Lyons, W. Obande, D. Jones, R.M.O. Higgins, M. A. McCarthy, Fracture toughness of carbon fiber/polyether ether ketone composites manufactured by autoclave and laser-assisted automated tape placement, J. Appl. Polym. Sci. (2014), https://doi.org/10.1002/app.41643.
[29] R.F. Gibson, A review of recent research on nanoindentation of polymer composites and their constituents, Compos. Sci. Technol. 105 (2014) 51–65, https://doi.org/10.1016/j.compscitech.2014.09.016.
[30] J.R. Gregory, S.M. Spearing, Nanoindentation of neat and in situ polymers in polymer–matrix composites, Compos. Sci. Technol. 65 (2005) 595–607, https://doi.org/10.1016/j.compscitech.2004.09.001.
[31] A. Molazemhosseini, H. Tourani, M.R. Naimi-Jamal, A. Khavandi, Nanoindentation and nanoscratching responses of PEEK based hybrid composites reinforced with short carbon fibers and nano-silica, Polym. Test. 32 (2013) 525–534, https://doi.org/10.1016/j.polymertesting.2013.02.001.
[32] A.K. Gain, E. Oromiehie, B.G. Prusty, Nanomechanical characterisation of CF-PEEK composites manufactured using automated fibre placement (AFP), Compos. Commun. 31 (2022), 101109, https://doi.org/10.1016/j.coco.2022.101109.
[33] E. Oromiehie, V. Nair, K. Short, T. Wei, D. Bhattacharyya, P.B. Gangadhara, Effect of He 2+ ion irradiation on the mechanical properties of automated fibre placement (Afp) Cf-peek thermoplastics, Composites (2023). https://doi.org/10.21203/rs.3.rs-3027646/v1.
[34] D. Gaitanelis, A. Chanteli, C. Worrall, P.M. Weaver, M. Kazilas, A multi-technique and multi-scale analysis of the thermal degradation of PEEK in laser heating, Polym. Degrad. Stab. 211 (2023), 110282, https://doi.org/10.1016/j.polymdegradstab.2023.110282.
[35] Y. Gaillard, F. Amiot, Grid nano-indentation as full-field measurements, Compos. Part Appl. Sci. Manuf. 132 (2020), 105807, https://doi.org/10.1016/j.compositesa.2020.105807.
[36] M. Hardiman, T.J. Vaughan, C.T. McCarthy, A review of key developments and pertinent issues in nanoindentation testing of fibre reinforced plastic microstructures, Compos. Struct. 180 (2017) 782–798, https://doi.org/10.1016/j.compstruct.2017.08.004.
[37] K. Ramaswamy, V. Modi, P.S. Rao, P.P. Martin, C.T. McCarthy, R.M. O'Higgins, An investigation of the influence of matrix properties and fibre–matrix interface behaviour on the mechanical performance of carbon fibre-reinforced PEKK and PEEK composites, Compos. A Appl. Sci. Manuf. 165 (2023) 107359.
[38] I.Y. Chang, B.S. Hsiao, Thermal properties of high performance thermoplastic composites based on poly(ether ketone ketone) (PEKK), in: 36th Int. SAMPE Symp., 1991, pp. 1587–1601.
[39] G.M. Pharr, W.C. Oliver, F.R. Brotzen, On the generality of the relationship among contact stiffness, contact area, and elastic modulus during indentation, J. Mater. Res. 7 (1992) 613–617, https://doi.org/10.1557/JMR.1992.0613.
[40] J.C. Hay, A. Bolshakov, G.M. Pharr, A critical examination of the fundamental relations used in the analysis of nanoindentation data, J. Mater. Res. 14 (1999) 2296–2305, https://doi.org/10.1557/JMR.1999.0306.
[41] W.C. Oliver, G.M. Pharr, An improved technique for determining hardness and elastic modulus using load and displacement sensing indentation experiments, J. Mater. Res. 7 (1992) 1564–1583, https://doi.org/10.1557/JMR.1992.1564.
[42] L. Shen, I.Y. Phang, T. Liu, Nanoindentation studies on polymorphism of nylon 6, Polym. Test. 25 (2006) 249–253, https://doi.org/10.1016/j.polymertesting.2005.09.019.
[43] J.C. Viana, A.M. Cunha, N. Billon, The effect of the skin thickness and spherulite size on the mechanical properties of injection mouldings, J. Mater. Sci. 36 (2001) 4411–4418.
[44] H.W. Starkweather, R.E. Brooks, Effect of spherulites on the mechanical properties of nylon 66, J. Appl. Polym. Sci. 1 (1959) 236–239, https://doi.org/10.1002/app.1959.070010214.